coatings

Special Issue Reprint

Development of Low-Carbon Coatings/Materials and Intelligent Construction Protection Technology

Edited by
Tian Su, Fubo Cao and Jianwen Shao

mdpi.com/journal/coatings

MDPI

Development of Low-Carbon Coatings/Materials and Intelligent Construction Protection Technology

Development of Low-Carbon Coatings/Materials and Intelligent Construction Protection Technology

Guest Editors

Tian Su
Fubo Cao
Jianwen Shao

MDPI

Basel • Beijing • Wuhan • Barcelona • Belgrade • Novi Sad • Cluj • Manchester

Guest Editors

Tian Su
School of Civil Engineering and Geomatics
Shandong University of Technology
Zibo
China

Fubo Cao
School of Civil Engineering
Inner Mongolia University of Science & Technology
Baotou
China

Jianwen Shao
School of Civil Engineering
Ludong University
Yantai
China

Editorial Office
MDPI AG
Grosspeteranlage 5
4052 Basel, Switzerland

This is a reprint of the Special Issue, published open access by the journal *Coatings* (ISSN 2079-6412), freely accessible at: https://www.mdpi.com/journal/coatings/special_issues/9W2G3EJ27M.

For citation purposes, cite each article independently as indicated on the article page online and as indicated below:

Lastname, A.A.; Lastname, B.B. Article Title. *Journal Name* **Year**, *Volume Number*, Page Range.

ISBN 978-3-7258-9263-1 (Hbk)
ISBN 978-3-7258-9264-8 (PDF)
https://doi.org/10.3390/books978-3-7258-9264-8

© 2026 by the authors. Articles in this reprint are Open Access and distributed under the Creative Commons Attribution (CC BY) license. The reprint as a whole is distributed by MDPI under the terms and conditions of the Creative Commons Attribution-NonCommercial-NoDerivs (CC BY-NC-ND) license (https://creativecommons.org/licenses/by-nc-nd/4.0/).

Contents

About the Editors . . . . . **vii**

Preface . . . . . **ix**

Tian Su and Jianwen Shao
Development of Low-Carbon Coatings/Materials and Intelligent Construction Protection Technology
Reprinted from: *Coatings* **2026**, *16*, 1068, https://doi.org/10.3390/coatings16091068 . . . . . **1**

Miao Yu, Zehui Zhang, Changgui Xu, Tian Su and Zhenyu Tan
Research Progress on Microbially Induced Calcium Carbonate Precipitation (MICP) for Reinforcing Fractured Rock Masses
Reprinted from: *Coatings* **2026**, *16*, 413, https://doi.org/10.3390/coatings16040413 . . . . . **8**

Sa Lv, Shiyi Wang, Runsheng Wang, Huan Wang, Xuefeng Chu, Fan Yang, et al.
Hierarchical Engineering of $CuCo_2O_4$/Nickel–Cobalt–Sulfide Electrode for Improved Energy Storage
Reprinted from: *Coatings* **2026**, *16*, 270, https://doi.org/10.3390/coatings16030270 . . . . . **54**

Zhanfeng Wang, Chao Yin and Jingjing Li
Landslide Susceptibility Mapping Considering Time-Varying Factors Based on Different Models
Reprinted from: *Coatings* **2026**, *16*, 207, https://doi.org/10.3390/coatings16020207 . . . . . **68**

Haoran Zhai, Aizhu Liu, Huiqing Yang, Dong Gao, Chunguang Liu, Wenda Yan and Whengyu Du
Research on the Mechanism of Steel Slag Fine Aggregate Damaging the Volume Stability of Cement-Based Materials
Reprinted from: *Coatings* **2026**, *16*, 132, https://doi.org/ **105**

Zeyi Liu, Huan Wang, Xuefeng Chu, Wanyue Diao, Chao Wang, Shiyi Wang, et al.
Hierarchical Design of EA ZnCo-LDH/NCS Electrode for Enhanced Electrochemical Performance
Reprinted from: *Coatings* **2026**, *16*, 113, https://doi.org/10.3390/coatings16010113 . . . . . **129**

Lei Zhang, Xinxin Cao, Xuefeng Mei, Xinhui Fu and Huanhuan Zhang
Analysis of Failure Characteristics and Mechanisms of Asphalt Pavements for Municipal Landscape Roads
Reprinted from: *Coatings* **2026**, *16*, 28, https://doi.org/10.3390/coatings16010028 . . . . . **143**

Sanan Song, Yan Yan, Yu Liu, Chao Wang, Liyan Wang, Liping Zhang and Huan Wang
Synthesis and Performance of Triisopropanolamine-Modified Polycarboxylate Cement Grinding Aid
Reprinted from: *Coatings* **2025**, *15*, 1478, https://doi.org/10.3390/coatings15121478 . . . . . **165**

Yanjiao Gao, Jiale Chen, Qing Li, Tian Su, Meng Li, Bangxiang Li and Xuefeng Mei
Research Progress on the Preparation and Performance of Recycled Mortars Using Solid Waste-Based Cementitious Materials
Reprinted from: *Coatings* **2025**, *15*, 1483, https://doi.org/10.3390/coatings15121483 . . . . . **180**

Yu Yan, Qifei Du, Wanyue Diao, Chao Wang, Liyan Wang, Sa Lv, et al.
Sustainable Biomass Functional Monomer-Modified Polycarboxylate Superplasticizers Enable the Creation of High-Performance Cement Pastes
Reprinted from: *Coatings* **2025**, *15*, 1459, https://doi.org/10.3390/coatings15121459 . . . . . **224**

Yun Lin, Qin Hu, Shuzeng Shen, Mo Zhou, Jintuan Zhang, Siqing Zhang, et al.
Influence of Cellulose Ether on Properties of Premixed Mortar Based on Orthogonal Test Method
Reprinted from: *Coatings* **2025**, *15*, 1395, https://doi.org/10.3390/coatings15121395 . . . . . **241**

Jiagu Chen, Chao Yin, Tianqi Sun and Jiaxu Li
Seismic Damage Risk Assessment of Reinforced Concrete Bridges Considering Structural Parameter Uncertainties
Reprinted from: *Coatings* **2025**, *15*, 1242, https://doi.org/10.3390/coatings15111242 . . . . . **259**

Meng Li, Huaiqin Liu, Bangxiang Li, Shangwei Gong, Changgui Xu, Tian Su, et al.
Frost Resistance and Damage Mechanism of Recycled Aggregate Concrete
Reprinted from: *Coatings* **2025**, *15*, 1169, https://doi.org/10.3390/coatings15101169 . . . . . **285**

Zhaorui Ji, Bin Peng, Wendong Guo and Mingyang Sun
Simulation of Macroscopic Chloride Ion Diffusion in Concrete Members
Reprinted from: *Coatings* **2025**, *15*, 1131, https://doi.org/10.3390/coatings15101131 . . . . . **304**

Mo Zhou, Guimeng Ban, Yuanming Luo, Qin Hu, Jintuan Zhang, Ke Yu, et al.
Influence of Wood Fiber on Mechanical and Thermal Insulation Properties of Lightweight Mortar
Reprinted from: *Coatings* **2025**, *15*, 1094, https://doi.org/10.3390/coatings15091094 . . . . . **319**

Jianping Gao, Le Liu, Xuefeng Mei, Dengfeng Li, Jianli Wu and Peng Cui
Dynamic Response and Energy Dissipation Mechanisms of Soil–Lightweight Foam Composite Protective Layers Under Impact Loading
Reprinted from: *Coatings* **2025**, *15*, 1074, https://doi.org/10.3390/coatings15091074 . . . . . **335**

Xuechao Yang, Zehui Zhang, Hsing-Wei Tai, Bangxiang Li, Jiahui Li, Weishen Zhang, et al.
Frost Resistance and Life Prediction of Waste Polypropylene Fibre-Reinforced Recycled Aggregate Concrete
Reprinted from: *Coatings* **2025**, *15*, 1070, https://doi.org/10.3390/coatings15091070 . . . . . **357**

Linxin Qi, Hongmin Kan, Tingting Yue and Jiang Wu
Effect of Y_2O_3 Particle Size on the Microstructure and Properties of Ni-Co-Y_2O_3 Composite Coatings
Reprinted from: *Coatings* **2025**, *15*, 1009, https://doi.org/10.3390/coatings15091009 . . . . . **387**

About the Editors

Tian Su

Tian Su is a Master's supervisor at Shandong University of Technology and a doctoral supervisor at the University of Malaya. He received his Ph.D. degree from Nanjing University of Aeronautics and Astronautics and previously conducted postdoctoral research at Wuhan University. His research interests encompass low-carbon materials and public space design, microbial construction technologies, and intelligent structural health monitoring and maintenance. He has led more than 10 research projects, including those supported by the China Postdoctoral Science Foundation and the Natural Science Foundation of Shandong Province. He has published more than 80 SCI- and EI-indexed papers, including over 60 as the first or corresponding author. His publications include papers recognized as ESI Hot Papers and Highly Cited Papers. He holds five invention patents and five utility model patents and has contributed to the development of three standards, one monograph, and one textbook. He was selected as an Outstanding Postdoctoral Researcher in Innovation and Entrepreneurship by the Ministry of Human Resources and Social Security of China. He has also received several national- and provincial-level awards for research and teaching. In addition, he serves as an editor, editorial board member, guest editor, and reviewer for several international academic journals.

Fubo Cao

Fubo Cao is a professor and master's supervisor at the School of Civil Engineering, Inner Mongolia University of Science and Technology. He holds a Doctor of Engineering degree from Nanjing University of Aeronautics and Astronautics and has undertaken academic visits at the University of Alabama, USA, and the University of Nottingham, UK. His principal research interests include recycled concrete and its durability, steel–concrete composite structures, and structural reliability analysis, with particular emphasis on the bond behavior between steel reinforcement or structural steel and recycled concrete, freeze–thaw-induced damage, and numerical simulation of composite structural systems. He has served as the principal investigator of several projects funded by the National Natural Science Foundation of China and the Natural Science Foundation of Inner Mongolia. He has published more than 50 academic papers, over 20 of which have been indexed by SCI or EI, and has been granted several invention patents and utility model patents related to structural strengthening and bond-slip testing. He serves as a reviewer for several leading domestic and international journals, including *Journal of Building Structures, Engineering Mechanics*, and *Construction and Building Materials*, and as a Deputy Editor-in-Chief of *Bridge and Structural* and *Chinese Journal of Science and Technology*. He also serves on professional committees in the fields of recycled concrete, steel–concrete composite structures, and solid waste resource utilization.

Jianwen Shao

Jianwen Shao received his Ph.D. degree from Tianjin University and currently serves as a master's supervisor at Ludong University. His research focuses on cement-based/solid waste-based/polymer-based composites, low-carbon cementitious materials, novel high-performance concrete materials and structures, and the resource utilization of solid waste in building materials. He has presided over one Youth Fund project of the Shandong Provincial Natural Science Foundation, participated in three national-level projects and more than five provincial/ministerial and enterprise-commissioned projects. He received the third award in China, "Building Materials Innovation Award", in 2020 and guided students to success in the National College Students' Innovation and Entrepreneurship Training Program. Moreover, he serves as an editorial board member of several Chinese journals and one English journal, a guest editor of two English journals and a reviewer of over 10 SCI journals. He has published over 20 SCI-indexed papers, with over 10 as the first or corresponding author.

Preface

The construction industry is undergoing a profound transition toward low-carbon development, resource efficiency, enhanced durability, and intelligent management. Against this background, this Reprint was prepared to present recent research progress in sustainable coatings and construction materials, durability enhancement, environmental protection, and intelligent technologies for infrastructure assessment and maintenance. The contributions reflect the growing need to integrate material innovation with advanced sensing, artificial intelligence, structural health monitoring, and data-driven decision-making. Through this interdisciplinary collection, we aim to provide a broader understanding of how low-carbon materials and intelligent protection technologies can jointly improve the sustainability, safety, resilience, and service life of civil infrastructure. This Reprint is intended for researchers, engineers, practitioners, and graduate students working in coatings, construction materials, civil engineering, structural durability, and intelligent infrastructure. We sincerely thank all authors, reviewers, and editorial staff whose efforts made this Reprint possible.

Tian Su, Fubo Cao, and Jianwen Shao
Guest Editors

coatings

MDPI

Editorial

Development of Low-Carbon Coatings/Materials and Intelligent Construction Protection Technology

Tian Su [1,2,3] and Jianwen Shao [4,5,*]

[1] Department of Civil Engineering, School of Civil Engineering and Geomatics, Shandong University of Technology, Zibo 255000, China
[2] Department of Civil Engineering, Faculty of Engineering, Universiti Malaya, Kuala Lumpur 50603, Malaysia
[3] Department of Engineering and Management, International College, Krirk University, No. 3 Soi Ramintra 1, Ramintra Road, Anusaowaree, Bangkhen, Bangkok 10220, Thailand
[4] Shandong Key Laboratory of Estuary, Coast and Nuclear Environment, Yantai 264025, China
[5] School of Hydraulic and Civil Engineering, Ludong University, Yantai 264025, China
* Correspondence: jwshao@ldu.edu.cn

1. Introduction and Scope

Global urbanization continues to accelerate, driving rapid growth in demand for new buildings and infrastructure, as well as further exacerbating natural resource consumption, ecological degradation, and greenhouse gas emissions [1–3]. In this context, the research and application of low-carbon materials and coatings, resource recycling technology, and intelligent construction and protection technology have received widespread attention. At present, urban construction is gradually moving from the traditional resource-based development model to a new stage of coordinated promotion of low-carbon materials, resource recycling, and engineering digitization.

The low-carbon transformation of the built environment is difficult to achieve through a single material or technology, and requires coordinated efforts from multiple aspects such as reducing the amount of cement clinker, developing alternative cementitious materials, utilizing recycled components, optimizing material mix ratios, improving durability, and extending the service life of structures [4–6]. Meanwhile, circular construction is transforming construction and demolition waste, metallurgical by-products, waste plastics, and biomass residues from conventional wastes into recyclable resources with engineerable performance and controllable processing, thereby providing an important pathway for reducing virgin-resource consumption and environmental burdens and promoting the sustainable development of the construction industry [7,8].

Moreover, the development of low-carbon materials should account for both material durability and the long-term performance of structures in service [9]. Chloride ingress, freeze–thaw cycling, friction and wear, and environmental and loading actions such as impact and earthquakes can all degrade material and structural performance [10–13]. It is therefore necessary to integrate the transport of aggressive agents, microscale damage evolution, macroscopic performance deterioration, and service-life prediction, thereby providing a theoretical basis and technical support for improving the in-service reliability of infrastructure [14–16].

At the same time, infrastructure protection is shifting from localized inspection and reactive repair toward intelligent sensing, risk prediction, and proactive maintenance. Technologies such as structural health monitoring, intelligent sensing, computer vision, machine learning, and artificial intelligence can effectively improve the efficiency of defect identification [17,18]. On this basis, by further integrating physical models, probabilistic

risk analysis, and long-term monitoring data, intelligent evaluation technology is expected to develop into a comprehensive tool that integrates material state perception, structural performance evaluation, and maintenance decision optimization.

Surface and interface engineering further expands the functional boundaries of low-carbon materials and engineering protection. Advanced coatings such as diamond-like carbon films can improve the wear resistance, friction reduction, and protective properties of the substrate with minimal increase in material usage [19,20]. Multiphase composite coatings, graded electrodes, and heterogeneous interface materials can achieve synergistic improvements in mechanical, anti-corrosion, friction, and electrochemical properties through structural design and interface regulation. From this, it can be seen that innovation in low-carbon and resilient materials is gradually shifting from single-component substitution to multiscale collaboration in resource recycling, durability design, functional interfaces, and intelligent management.

In this context, this Special Issue "Development of Low-Carbon Coatings/Materials and Intelligent Construction Protection Technology" includes a total of 17 papers covering solid waste and biomass resource utilization, green cement-based materials, durability degradation and life prediction, advanced functional coatings and energy storage electrodes, as well as infrastructure resilience and intelligent risk assessment. The research objects and technological paths are different, and their common goal is to improve material performance, structural service reliability, and the scientific nature of engineering protection decisions while reducing resource consumption and environmental loads. The following text will summarize and discuss the papers in this Special Issue under four interrelated themes.

2. Contributions

2.1. Sustainable Utilization and Performance Improvement of Building Materials

One of the important themes of this Special Issue is the high-value utilization of waste resources in building materials and the improvement of the performance of recycled materials. Gao et al. [21] reviewed the application of solid waste-based cementitious materials in recycled mortar. Solid waste such as construction waste powder, slag, and fly ash has the potential to replace some cement, but their activity needs to be improved through thermal activation, carbonation activation, or alkali activation. Moderate addition of solid waste can improve pore structure and durability, while excessive addition can lead to a decrease in strength. Synergistic utilization of multi-source solid wastes, composite activation, and low-energy activation are important development directions for achieving high-performance and low-carbon recycled mortar.

Zhai et al. [22] reviewed the influence of steel slag fine aggregate on the volume stability of cement-based materials. Steel slag has the potential to replace natural fine aggregates, but the continuous hydration expansion of free CaO and free MgO can easily lead to particle damage, crack propagation, and mechanical property degradation. Among them, free CaO mainly affects early stability, while free MgO has a more significant impact on long-term service safety. The engineering application of steel slag fine aggregate should be combined with reasonable dosage control and pre-stabilization treatment to ensure the long-term stability of the material.

Lin et al. [23] analyzed the effects of cellulose ether, stone powder, manufactured sand, polyvinyl alcohol, and bentonite on the properties of premixed mortar. Cellulose ether is a key component in regulating fluidity and water retention, while stone powder and manufactured sand mainly affect strength development. Polyvinyl alcohol can improve crack resistance, while bentonite improves thickening and water retention effects. The article reveals the synergistic mechanism of organic–inorganic composite components and

https://doi.org/10.3390/coatings16091068

establishes prediction and optimization methods for mortar flowability, water retention, and compressive strength.

Yan et al. [24] developed a biomass functional monomer-modified polycarboxylate superplasticizer using renewable raffinose as a functional monomer. Research has shown that this polycarboxylate superplasticizer can enhance the dispersibility of cement particles, improve the fluidity and flow retention of cement paste, delay early hydration, and optimize the microstructure of the hardened cement paste, thereby improving the compressive and flexural properties of mortar.

Song et al. [25] prepared a triisopropanolamine-modified polycarboxylate cement grinding aid. Research has shown that this grinding aid can reduce particle agglomeration, optimize particle-size distribution, improve grinding efficiency, improve cement paste fluidity, and promote hydration reactions, thereby enhancing the early and later strength of mortar and providing a reference for the development of high-performance and environmentally friendly cement grinding aids.

Zhou et al. [26] studied the effect of waste wood fibers on the properties of lightweight mortar. The results indicate that an appropriate amount of wood fiber can improve interfacial bonding, suppress crack propagation, and enhance the mechanical and thermal insulation properties of mortar. However, excessive dosage can easily lead to fiber aggregation and interface defects, reducing the overall performance of the material. Therefore, the dosage of wood fibers should be reasonably controlled.

Li et al. [27] studied the effects of recycled coarse aggregate replacement rate and freeze–thaw cycles on the frost resistance of recycled aggregate concrete. The results indicate that recycled aggregates increase the initial defects of concrete and exacerbate freeze–thaw damage, with the degree of damage increasing as the replacement rate and number of freeze–thaw cycles increase. The old interfacial transition zone is a weak point for crack initiation and propagation. The study also established a freeze–thaw damage prediction model based on the relative dynamic modulus of elasticity, which can better describe the degradation law of material properties.

Yang et al. [28] studied the improvement effect of waste polypropylene fibers on the frost resistance of recycled aggregate concrete. The results indicate that waste polypropylene fibers can slow down mass loss and the degradation of stiffness and strength by bridging cracks, optimizing pore structure, and improving interfacial properties, thereby enhancing the frost resistance and durability of recycled aggregate concrete. It is also pointed out that using a comprehensive evaluation of relative dynamic modulus of elasticity and strength loss can more accurately reflect the freeze–thaw resistance.

Yu et al. [29] reviewed the application of Microbially Induced Calcium Carbonate Precipitation (MICP) technology in the reinforcement and seepage control of fractured rock masses. Research has shown that MICP can fill cracks, improve strength, and reduce permeability by generating calcium carbonate. Its repair effect is influenced by factors such as bacterial strains, environmental conditions, and construction processes. The article believes that optimizing mineralization pathways, selecting bacterial strains, and improving construction processes are key to promoting the engineering application of MICP.

2.2. Durability Degradation, Transport Processes, and Intelligent Maintenance Decision-Making

For the long-term safe service of infrastructure, durability research is gradually expanding from material degradation mechanisms and aggressive-medium transport simulations to intelligent defect detection, performance degradation prediction, and life-cycle maintenance decision-making. Ji et al. [30] established a numerical model for macroscopic chloride ion diffusion in concrete based on the peridynamic differential operator (PDDO). Research has shown that this model can simulate the chloride ion transport process under

https://doi.org/10.3390/coatings16091068

complex boundary and material defect conditions, revealing that internal defects accelerate the migration of chloride ions to the surface of reinforcing steel, increasing the risk of steel bar corrosion. It can provide a reference for concrete durability evaluation and service-life prediction.

Zhang et al. [31] studied the pavement distress identification and aging damage mechanism of asphalt pavement in municipal landscape roads. The results indicate that the shadow removal method based on SpA-Former can improve the accuracy of crack detection. Asphalt aging, temperature changes, and freeze–thaw cycles are the main causes of transverse crack formation. The study combines intelligent image recognition with material performance analysis, providing a reference for pavement distress detection and life-cycle maintenance.

2.3. Advanced Functional Coatings, Hierarchical Electrodes, and Interface Control

Regarding the optimization of material surface structure and improvement of interface function, this Special Issue explores the implementation path of enhancing the performance of composite coatings and energy storage electrodes from the aspects of particle-size regulation, hierarchical structure construction, and electrochemical activation. Qi et al. [32] prepared Ni–Co–Y_2O_3 composite coatings and studied the effect of Y_2O_3 particle size on coating properties. The results indicate that particle size and particle-size combinations can regulate the microstructure, hardness, tribological performance, and corrosion resistance of coatings. Reasonable optimization of particle size can help achieve a synergistic improvement in the comprehensive performance of coatings.

Lv et al. [33] constructed a $CuCo_2O_4$/nickel–cobalt–sulfide hierarchical electrode and studied the effect of electrodeposition time on its energy storage performance. The results indicate that the hierarchical structure can increase active sites and promote ion transport. By optimizing the electrodeposition time, the specific capacitance, rate performance, and cycling stability of the electrode can be improved.

Liu et al. [34] prepared an electrochemically activated ZnCo-LDH/NCS hierarchical electrode (EA ZnCo-LDH/NCS), and systematically analyzed the effects of activation conditions and synergistic effects of different components on energy storage performance. Research has shown that hierarchical architecture and electrochemical activation can synergistically improve electrode reaction kinetics, enhance specific capacitance, rate performance, and cycling stability, providing a reference for the design of high-performance energy storage electrodes.

2.4. Infrastructure Resilience and Intelligent Risk Assessment

In the face of sudden disasters such as impacts, earthquakes, and landslides, infrastructure security needs to coordinate the design of protective materials and energy-dissipating structures, structural vulnerability analysis, and intelligent prediction of regional disasters, in order to achieve a transition from passive disaster resistance to risk identification, active protection, and resilience enhancement. Gao et al. [35] studied the impact response characteristics of EPS and EPE foams and soil–lightweight foam composite protective layers. The results indicate that EPE has better stress wave attenuation and energy absorption capabilities, making it suitable as an impact-resistant protective material. The performance of composite protective layer is affected by the thickness of foam and the proportion of soil, so the structural design should be optimized according to the engineering needs.

Chen et al. [36] established a comprehensive seismic assessment system for bridges that considers seismic hazard, structural vulnerability, and damage risk. Research has shown that side piers and bearings are weak areas for seismic resistance in bridges. Therefore, it is necessary to focus on strengthening bearings, unseating-prevention devices, and seismic

isolation and energy dissipation designs, providing a reference for seismic reinforcement and resilience enhancement of bridges.

Wang et al. [37] studied the applicability of conditioning factors and prediction models in landslide susceptibility mapping. The results indicate that introducing dynamic factors can improve the accuracy of landslide susceptibility prediction, and different factor combinations and models have a significant impact on the evaluation results. The study screened for better dynamic factor expression methods and prediction models, providing a reference for landslide risk identification and regional disaster prevention and reduction.

Overall, the 17 papers in this Special Issue cover multiple directions, including solid waste resource utilization, material performance regulation, durability improvement, functional interface design, and infrastructure risk assessment. Related studies have shown that the development of green engineering materials not only relies on the high-value utilization of waste resources, but also requires strengthened regulation of pore structure, interfacial characteristics, transport processes, and damage evolution, combined with intelligent detection, service-life prediction, and risk analysis, to achieve synergistic improvement of material performance, structural safety, and environmental benefits.

3. Conclusions and Outlook

This Special Issue showcases the latest research progress in solid waste resource utilization, green cementitious materials, functional additives, durability improvement, advanced coatings and energy storage electrodes, and infrastructure risk assessment. The included papers comprehensively adopt methods such as material testing, microscopic characterization, numerical simulation, statistical analysis, machine learning, and probabilistic risk analysis, extending from material composition, microstructure, transmission and damage processes to structural safety and regional disaster assessment, reflecting the deepening cross-integration between material science, civil engineering, surface engineering, and intelligent analysis technology.

In the future, research on green building materials should balance resource utilization efficiency and long-term service performance [5,7,38]. For solid waste such as steel slag, recycled aggregates, and waste fibers, the focus should be on addressing issues such as raw material fluctuations, interface defects, volume stability, and durability, and improving performance stability through pretreatment, composite activation, and synergistic proportioning. Biomass additives and green grinding aids need to be strengthened in terms of large-scale preparation, system adaptability, and long-term performance verification, in order to promote the transformation of achievements into engineering applications.

Durability research should strengthen the connection between micromechanisms, accelerated testing, numerical simulation, and actual service environments, focusing on freeze–thaw, salt erosion, chloride ion transport, material aging, and crack propagation, and improve evaluation indicators and life prediction methods [39,40]. Coatings, electrodes, and other functional materials should further optimize their interface structure, component coordination, and preparation parameters to achieve coordinated improvement of multiple properties.

In the field of infrastructure security, intelligent detection and risk assessment should develop from a single identification model to a comprehensive decision-making system, integrating computer vision, physical models, probability analysis, real-time monitoring and maintenance data to improve the ability to identify, predict and warn of disasters and long-term deterioration risks [17,41,42].

The Guest Editors expect this Special Issue to further promote cross-disciplinary collaboration in fields such as materials science, coating engineering, civil and geotechnical engineering, and data science. Through collaborative promotion of low-carbon material

https://doi.org/10.3390/coatings16091068

development, durability design, intelligent risk assessment, and full life-cycle management, related research is expected to gradually shift from single material or performance optimization to systematic solutions that balance resource recycling, long-term safety, and engineering resilience, thereby reducing primary resource consumption and repetitive maintenance, as well as improving the reliability and sustainability of infrastructure throughout the service life.

Author Contributions: Conceptualization, T.S. and J.S.; methodology, T.S. and J.S.; writing—original draft preparation, T.S. and J.S.; writing—review and editing, T.S. and J.S.; supervision, J.S. All authors have read and agreed to the published version of the manuscript.

Acknowledgments: The Guest Editors thank all authors, reviewers, and the editorial staff of Coatings for their contributions to this Special Issue.

Conflicts of Interest: The authors declare no conflicts of interest.

References

1. Chen, L.; Liu, Z.; Liu, Y.; Chen, Z.; Huang, L.; Dong, L.; Li, X.; Xie, Z.; Hua, J.; Shi, J. Green construction strategies to combat climate change and public-health issues. *Cell Rep. Phys. Sci.* **2026**, *7*, 103044. [CrossRef]
2. Zhou, Y.; Jin, H.; Li, C.; Ding, L. Spatio-temporal patterns and impact mechanisms of CO_2 emissions from China's construction industry under urbanization. *Sustain. Cities Soc.* **2024**, *106*, 105353. [CrossRef]
3. Huang, X.; Su, T.; Wang, J.; Cao, F.; Wang, C. Bond performance of corroded steel reinforcement and recycled coarse aggregate concrete after freeze–thaw cycles. *Sustainability* **2023**, *15*, 6122. [CrossRef]
4. Liu, H.; Yi, H.; Gao, Y.; Tan, Z.; Liu, C.; Wang, T.; Su, T.; Yap, S.P. Valorization of industrial solid wastes for sustainable acid-resistant cement: Microstructural mechanisms of GGBFS mitigating anhydrite-induced sulfuric acid degradation. *J. Environ. Chem. Eng.* **2026**, *14*, 124367. [CrossRef]
5. Azarhomayun, F.; Wei, J.; Khayat, K.H. Low-carbon concrete for sustainable construction: A comprehensive review of performance characteristics, implementation challenges, and decarbonization pathways. *J. Build. Eng.* **2026**, *128*, 116731. [CrossRef]
6. Fan, H.; Yu, H.; Ma, H.; Chen, X.; Li, L.; Du, Q.; Zhang, M.; Ma, H.; Wu, C. Refinement and application of life cycle assessment (LCA) for concrete: Development of a carbon emission metric normalized by salt-freezing durability and its use in designing high-durability, low-carbon, high-performance concrete. *Sustain. Mater. Technol.* **2025**, *45*, e01622. [CrossRef]
7. Alsharari, F. Utilization of industrial, agricultural, and construction waste in cementitious composites: A comprehensive review of their impact on concrete properties and sustainable construction practices. *Mater. Today Sustain.* **2025**, *29*, 101080. [CrossRef]
8. Dassanayake, C.; Mashaan, N.S.; Galagedara, R. Waste material utilization in civil engineering applications: Advances, challenges, and future directions—A scoping review. *Materials* **2026**, *19*, 3154. [CrossRef] [PubMed]
9. Khan, S.; Al-Deen, S.; Lee, C.K. Mechanical and durability behaviours of low carbon concrete: A systematic review. *J. Build. Eng.* **2025**, *100*, 111633. [CrossRef]
10. Das, C.S.; Zheng, H.; Dai, J.-G. A review of chloride-induced steel corrosion in coastal reinforced concrete structures: Influence of micro-climate. *Ocean Eng.* **2025**, *325*, 120794. [CrossRef]
11. Guler, S.; Akbulut, Z.F. A comprehensive review of concrete durability in freeze-thaw conditions: Mechanisms, prevention, and mitigation strategies. *Structures* **2025**, *75*, 108804. [CrossRef]
12. Zhang, P.; Zhang, L.; Wang, K.; Zhang, T.; Hu, S. A state-of-the-art review on abrasion resistance of concrete. *J. Build. Eng.* **2025**, *111*, 113277. [CrossRef]
13. Barbosa dos Santos, A.; Conde Bandini, P.A.; Segura, R.L.; Paultre, P. Dynamic tensile strength of concrete: A review of mechanisms, test results, and applications for dam safety. *Materials* **2025**, *18*, 5669. [CrossRef] [PubMed]
14. Feng, T.; Miao, Y.; Tan, Y.; Yang, Z.; Cao, T.; Wang, F.; Jiang, J. Prediction methodology for the service life of concrete structures in marine environment: From materials to performance. *Engineering* **2026**, *61*, 109–119. [CrossRef]
15. Li, P.; Li, K.; Li, J.; Chen, H. Degradation and service life prediction of reinforced concrete beams under coupled fatigue loading and chloride ingress: A review. *Case Stud. Constr. Mater.* **2026**, *24*, e06031. [CrossRef]
16. Flah, M.; Marani, A.; Suleiman, A.R.; Nehdi, M.L. Durability-informed life cycle assessment of concrete through machine learning for service life prediction. *Renew. Sustain. Energy Rev.* **2026**, *231*, 116730. [CrossRef]
17. Spencer, B.F., Jr.; Sim, S.-H.; Kim, R.E.; Yoon, H. Advances in artificial intelligence for structural health monitoring: A comprehensive review. *KSCE J. Civ. Eng.* **2025**, *29*, 100203. [CrossRef]
18. Bodke, K.; Bhirud, S.; Sangle, K.K. Structural health monitoring using image processing and advanced technologies for the identification of deterioration of building structure: A review. *Struct. Durab. Health Monit.* **2025**, *19*, 1547–1562. [CrossRef]

19. Liu, Y.; Li, X.; Xu, P.; Zhang, H.; Liu, L. Recent advances and challenges in tribology of diamond-like carbon films: A critical review. *Diam. Relat. Mater.* **2025**, *154*, 112206. [CrossRef]
20. Liu, H.; Li, C.; Ye, Q.; Chen, L.; Qiao, L.; Yan, Y. Inhibition mechanism of a diamond-like carbon (DLC) coating on the fretting crevice corrosion of stainless steel in artificial crevices. *Corros. Sci.* **2025**, *253*, 112995. [CrossRef]
21. Gao, Y.; Chen, J.; Li, Q.; Su, T.; Li, M.; Li, B.; Mei, X. Research Progress on the Preparation and Performance of Recycled Mortars Using Solid Waste-Based Cementitious Materials. *Coatings* **2025**, *15*, 1483. [CrossRef]
22. Zhai, H.; Liu, A.; Yang, H.; Gao, D.; Liu, C.; Yan, W.; Du, W. Research on the Mechanism of Steel Slag Fine Aggregate Damaging the Volume Stability of Cement-Based Materials. *Coatings* **2026**, *16*, 132. [CrossRef]
23. Lin, Y.; Hu, Q.; Shen, S.; Zhou, M.; Zhang, J.; Zhang, S.; Ban, G.; Lee, Z.-J. Influence of Cellulose Ether on Properties of Premixed Mortar Based on Orthogonal Test Method. *Coatings* **2025**, *15*, 1395. [CrossRef]
24. Yan, Y.; Du, Q.; Diao, W.; Wang, C.; Wang, L.; Lv, S.; Kong, L.; Zhang, L.; Xi, Y.; Wang, H. Sustainable Biomass Functional Monomer-Modified Polycarboxylate Superplasticizers Enable the Creation of High-Performance Cement Pastes. *Coatings* **2025**, *15*, 1459. [CrossRef]
25. Song, S.; Yan, Y.; Liu, Y.; Wang, C.; Wang, L.; Zhang, L.; Wang, H. Synthesis and Performance of Triisopropanolamine-Modified Polycarboxylate Cement Grinding Aid. *Coatings* **2025**, *15*, 1478. [CrossRef]
26. Zhou, M.; Ban, G.; Luo, Y.; Hu, Q.; Zhang, J.; Yu, K.; Hong, X.; Zhong, H. Influence of Wood Fiber on Mechanical and Thermal Insulation Properties of Lightweight Mortar. *Coatings* **2025**, *15*, 1094. [CrossRef]
27. Li, M.; Liu, H.; Li, B.; Gong, S.; Xu, C.; Su, T.; Mei, X.; Xu, S. Frost Resistance and Damage Mechanism of Recycled Aggregate Concrete. *Coatings* **2025**, *15*, 1169. [CrossRef]
28. Yang, X.; Zhang, Z.; Tai, H.-W.; Li, B.; Li, J.; Zhang, W.; Su, T.; Liu, J. Frost Resistance and Life Prediction of Waste Polypropylene Fibre-Reinforced Recycled Aggregate Concrete. *Coatings* **2025**, *15*, 1070. [CrossRef]
29. Yu, M.; Zhang, Z.; Xu, C.; Su, T.; Tan, Z. Research Progress on Microbially Induced Calcium Carbonate Precipitation (MICP) for Reinforcing Fractured Rock Masses. *Coatings* **2026**, *16*, 413. [CrossRef]
30. Ji, Z.; Peng, B.; Guo, W.; Sun, M. Simulation of Macroscopic Chloride Ion Diffusion in Concrete Members. *Coatings* **2025**, *15*, 1131. [CrossRef]
31. Zhang, L.; Cao, X.; Mei, X.; Fu, X.; Zhang, H. Analysis of Failure Characteristics and Mechanisms of Asphalt Pavements for Municipal Landscape Roads. *Coatings* **2026**, *16*, 28. [CrossRef]
32. Qi, L.; Kan, H.; Yue, T.; Wu, J. Effect of Y_2O_3 Particle Size on the Microstructure and Properties of Ni-Co-Y_2O_3 Composite Coatings. *Coatings* **2025**, *15*, 1009. [CrossRef]
33. Lv, S.; Wang, S.; Wang, R.; Wang, H.; Chu, X.; Yang, F.; Zhang, Z.; Yang, X.; Wang, C. Hierarchical Engineering of $CuCo_2O_4$/Nickel–Cobalt–Sulfide Electrode for Improved Energy Storage. *Coatings* **2026**, *16*, 270. [CrossRef]
34. Liu, Z.; Wang, H.; Chu, X.; Diao, W.; Wang, C.; Wang, S.; Zhang, Z.; Lv, S. Hierarchical Design of EA ZnCo-LDH/NCS Electrode for Enhanced Electrochemical Performance. *Coatings* **2026**, *16*, 113. [CrossRef]
35. Gao, J.; Liu, L.; Mei, X.; Li, D.; Wu, J.; Cui, P. Dynamic Response and Energy Dissipation Mechanisms of Soil–Lightweight Foam Composite Protective Layers Under Impact Loading. *Coatings* **2025**, *15*, 1074. [CrossRef]
36. Chen, J.; Yin, C.; Sun, T.; Li, J. Seismic Damage Risk Assessment of Reinforced Concrete Bridges Considering Structural Parameter Uncertainties. *Coatings* **2025**, *15*, 1242. [CrossRef]
37. Wang, Z.; Yin, C.; Li, J. Landslide Susceptibility Mapping Considering Time-Varying Factors Based on Different Models. *Coatings* **2026**, *16*, 207. [CrossRef]
38. Gong, S.; Wang, T.; Hasan, M.M.; Mei, X.; Tan, Z.; Su, T.; Cao, F. Effect of polypropylene fiber and nano-silica on the compressive strength and frost resistance of recycled brick aggregate concrete. *Nanotechnol. Rev.* **2023**, *12*, 20230174. [CrossRef]
39. Muhit, I.B.; Al-Fakih, A.; Suntharalingam, T.; Michel, A. Progress in computational modelling for concrete durability and its integration with artificial intelligence and life-cycle assessment. *Arch. Comput. Methods Eng.* **2026**, *33*, 2751–2783. [CrossRef]
40. Mei, X.; Zhang, Y.; Ni, D.; Yang, D.; Su, T. Analysis of the ion diffusion mechanism affecting the durability of concrete in saline-alkali soils in Western China. *Constr. Build. Mater.* **2025**, *475*, 141213. [CrossRef]
41. Plevris, V.; Papazafeiropoulos, G. AI in structural health monitoring for infrastructure resilience: A review. *Infrastructures* **2024**, *9*, 225. [CrossRef]
42. Kamariotis, A.; Chatzi, E.; Straub, D.; Dervilis, N.; Goebel, K.; Hughes, A.J.; Lombaert, G.; Papadimitriou, C.; Papakonstantinou, K.G.; Pozzi, M.; et al. Monitoring-supported value generation for managing structures and infrastructure systems. *Data-Centric Eng.* **2024**, *5*, e27. [CrossRef]

Disclaimer/Publisher's Note: The statements, opinions and data contained in all publications are solely those of the individual author(s) and contributor(s) and not of MDPI and/or the editor(s). MDPI and/or the editor(s) disclaim responsibility for any injury to people or property resulting from any ideas, methods, instructions or products referred to in the content.

coatings

MDPI

Review

Research Progress on Microbially Induced Calcium Carbonate Precipitation (MICP) for Reinforcing Fractured Rock Masses

Miao Yu [1], Zehui Zhang [2], Changgui Xu [3,*], Tian Su [1,4,5,*] and Zhenyu Tan [4]

[1] Department of Civil Engineering, School of Civil Engineering and Geomatics, Shandong University of Technology, Zibo 255000, China
[2] China Design Group Co., Ltd., 9 Ziyun Avenue, Nanjing 210000, China
[3] Department of Landscape Architecture, School of Civil Engineering and Architecture, Hebei University of Engineering Science, Shijiazhuang 050011, China
[4] Department of Civil Engineering, Faculty of Engineering, Universiti Malaya, Kuala Lumpur 50603, Malaysia
[5] Department of Engineering and Management, International College, Krirk University, No. 3 Soi Ramintra 1, Ramintra Road, Anusaowaree, Bangkhen, Bangkok 10220, Thailand
* Correspondence: changguixu123@163.com (C.X.); sutian@sdut.edu.cn (T.S.)

Abstract

The deterioration of mechanical properties and seepage issues in fractured rock masses represent critical technical bottlenecks in the field of geotechnical engineering. Traditional remediation techniques suffer from drawbacks such as environmental pollution, poor filling effects in microfissures, and susceptibility to secondary cracking, making it difficult to meet the requirements for long-term effectiveness and environmental compatibility in fractured rock mass reinforcement. Microbially induced calcium carbonate precipitation (MICP) technology, which drives the formation of calcium carbonate crystals through microbial metabolic activities, achieves fracture filling and rock mass reinforcement. This technology offers several advantages, including environmental friendliness, high permeability, and excellent compatibility; thus, it represents a cutting-edge direction for green remediation in geotechnical engineering. In this paper, the core mineralization mechanisms of MICP technology, key influencing factors, and engineering applications in fractured rock masses are systematically analysed. Research has indicated that MICP can significantly increase the compressive strength, impermeability, and liquefaction resistance of fractured rock masses, enabling both self-healing of rock fractures and precise filling of existing fissures. Compared with traditional techniques, it demonstrates superior environmental compatibility and remediation efficacy. This review aims to serve as a reference for theoretical research and engineering applications of MICP in fractured rock mass reinforcement.

Keywords: microbially induced calcium carbonate precipitation (MICP); fractured rock mass reinforcement; mineralization mechanism; engineering application

1. Introduction

Fractured rock masses are widely distributed in geotechnical engineering scenarios such as slope engineering, underground caverns, hydraulic dams, and oil and gas well walls. The randomly developed internal fracture network directly leads to a reduction in compressive strength and deterioration of impermeability, serving as a primary inducement for engineering disasters, including slope instability, cavern seepage, and dam piping [1]. Traditional remediation techniques for fractured rock masses predominantly employ physical or chemical methods to achieve fracture reinforcement through material grouting [2,3].

Cement-based repair represents the most prevalent physical remediation approach, with cementitious materials being most widely applied in engineering practice because of their low cost, easy accessibility, and mature construction techniques [4–6]. However, cement production generates substantial greenhouse gas emissions [7,8], accounting for 5%–7% of global greenhouse gas emissions [9]. Cement-based repair materials exhibit substantial particle sizes, elevated slurry viscosity, and inadequate fluidity, which collectively result in limited efficacy for filling fine cracks. Furthermore, the hydration heat of cement [10] induces post-hardening shrinkage, predisposing the material to secondary cracking and consequently compromising the attainment of ideal remediation outcomes. Conversely, although chemical grouts possess advantageous characteristics such as low viscosity and superior fluidity [11] that enable effective microcrack infiltration, they present critical limitations, including prohibitive costs and poor environmental compatibility. These drawbacks pose potential risks to human health and ecological systems, thereby limiting their applicability in green engineering contexts.

A wide variety and large number of microbial communities inhabit rock masses. During long-term geological evolution, these microorganisms have evolved unique biomineralization capabilities, which can regulate the nucleation, growth and deposition processes of calcium carbonate in the environment through their own metabolic activities, a phenomenon known as microbially induced calcium carbonate precipitation (MICP) [12]. Among the numerous microbial groups, bacteria have become the core application carrier of MICP technology because of their high abundance of 10^9–10^{10} cells per gram in the soil environment, wide ecological distribution and diverse metabolic pathways [13]. The cell diameter of bacteria is usually only 0.5–3 μm, and the spore diameter of some Bacillus species can even be as small as 0.2 μm [14]. This tiny size endows them with a unique permeability advantage, enabling them to easily penetrate micron-scale and even nanometer-scale small pores and fractures in geotechnical masses and reach areas that are difficult for traditional repair materials to access, providing an ideal reaction site for the subsequent mineralization reaction. The calcium carbonate crystals generated during microbial metabolism do not exist in isolation but cement the geotechnical particles and fill the pore spaces between the particles at the same time, bonding the loose particles into an integral body with a certain strength and integrity [12]. Following MICP treatment, the unconfined compressive strength and impermeability of sand columns or geotechnical specimens are significantly enhanced [15].

In recent years, against the backdrop of increasingly prominent environmental issues caused by global warming and the widespread consensus among nations on the concept of "green and low-carbon" development [16], MICP technology has emerged as a highly promising green remediation technique [17]. This technology harnesses the metabolic processes of naturally occurring microorganisms to achieve mineralization under mild reaction conditions, generating few harmful by-products and significantly reducing environmental disturbance and pollution. Furthermore, MICP exhibits unique self-healing potential: when new micro-cracks form in a geotechnical mass due to external forces, the mineralization process can be re-initiated as long as active microorganisms and sufficient reaction substrates are present in the environment. This enables autonomous crack repair, thereby substantially enhancing the long-term service performance of engineering structures [18].

To ensure the systematic rigor and reproducibility of this review, we adhered to the retrieval principles of systematic literature reviews to conduct a comprehensive search of studies on the reinforcement of fractured rock masses using microbially induced calcium carbonate precipitation (MICP). This review systematically analyzes the mineralization mechanisms of various functional microorganisms, elucidating the core pathways through

https://doi.org/10.3390/coatings16040413

which different types of microorganisms regulate the physicochemical properties of the microenvironment and induce calcium carbonate precipitation. Additionally, it synthesizes the key influencing factors and their coupling effects, thereby contributing to a deeper understanding of the behavioral principles and application performance of MICP technology in the reinforcement of fractured rock masses. These findings provide a scientific reference for strain selection, parameter optimization, and process design across various engineering scenarios, including slope engineering, hydraulic dams, and underground caverns.

Literature Search Strategy

For the sake of systematicity and replicability, a comprehensive literature search was conducted on studies related to MICP for reinforcing fractured rock masses. The search was performed in the following databases: CNKI, Wanfang Data, Web of Science, Scopus, and Google Scholar. The search time frame spanned from 1990 to 2026. The keyword combinations used were: MICP, ("microbially induced carbonate precipitation" OR "MICP") AND ("fractured rock" OR "rock fracture" OR "crack repair" OR "Reinforcing Fractured Rock Masses"). Figure 1 illustrates the annual publication volume based on keyword searches, and Figure 2 presents the global distribution of publications by country.

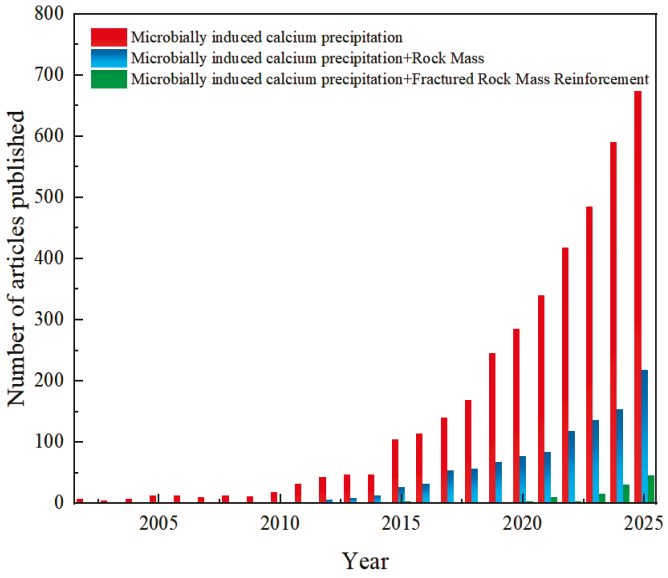

Figure 1. Annual number of peer-reviewed publications on microbial-induced carbonate precipitation with different keyword combinations, 2002–2025. (Note: Data were retrieved from the ScienceDirect database on March 20, 2026, using the keywords "Microbial-induced carbonate precipitation" (MICP), "MICP + Rock Mass", and "MICP + Fractured Rock Mass Reinforcement").

The inclusion criteria for the literature were: (I) research content directly related to the principles of MICP technology, mineralization mechanisms, or engineering applications; (II) research objects involving fractured rock masses, rock fractures, or concrete cracks; (III) sources from peer-reviewed journals, authoritative conference proceedings, or high-quality dissertations; and (IV) inclusion of clear data or conclusions to support the findings.

It should be noted that the application of MICP technology in geotechnical engineering can be divided into two typical scenarios. One is porous media, where the primary objective is to cement loose particles and fill intergranular pores. The other is fractured media, where the core focus lies in filling and bridging pre-existing fractures to restore the continuity and overall strength of the rock mass. Although the mineralization mechanisms underlying these two scenarios share certain commonalities, they exhibit fundamental differences in terms of bacterial transport, spatial constraints on precipitation, and mechanical response

mechanisms [19]. This paper focuses on fractured rock masses and systematically reviews the latest research progress in this field.

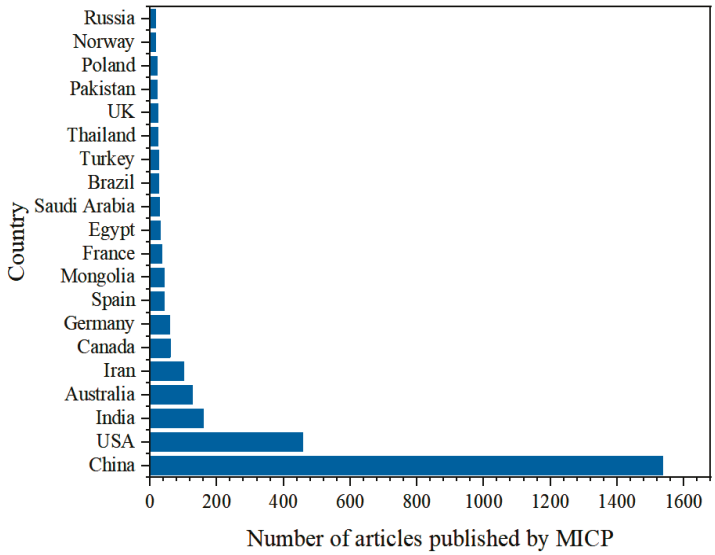

Figure 2. Top 20 countries in terms of MICP research publications.

2. Microbial Mineralization Reaction Mechanism

Biologically induced mineralization refers to the process in which microorganisms indirectly induce mineral precipitation by altering the physicochemical properties of their surrounding environment through metabolic activities [20]. The underlying mechanism involves the generation of carbonate ions by microbes while simultaneously regulating the ambient pH to alkaline conditions, thereby facilitating the combination of metal ions, such as calcium, with carbonate ions to ultimately form stable carbonate precipitates [21]. MICP technology involves various types of mineralization reactions, with the functional microorganisms that are typically involved primarily being ureolytic bacteria, sulfate-reducing bacteria, and denitrifying bacteria.

2.1. Urease-Producing Bacteria Reaction Mechanism

Within the mineralization mechanism of MICP for geotechnical fracture remediation, the urea hydrolysis pathway has emerged as the most extensively applied and rigorously investigated approach owing to its high reaction efficiency, ease of control, and excellent stability of its mineralized products [14]. The process of calcium carbonate precipitation induced by ureolytic bacteria is shown in Figure 3. These microorganisms, capable of synthesizing and secreting urease, drive the hydrolysis of urea within the environment to initiate carbonate precipitation, thereby serving as the key functional flora for achieving geotechnical fracture reinforcement and repair via MICP technology. The urease-producing bacteria currently widely investigated and applied include multiple genera, with representative strains [22] such as *Sporosarcina pasteurii* (formerly *Bacillus pasteurii*), *Bacillus sphaericus*, *Bacillus subtilis*, *Escherichia coli*, and *Staphylococcus* spp.

Studies have confirmed the dual core role of urease-producing bacteria in the mineralization repair of geotechnical fractures [23]. Urea hydrolysis catalyzed by secreted urease yields NH_3 and CO^2. Elevated NH_3 concentrations increase the ambient pH and drive the formation of carbonate ions in solution. Sustained urease secretion promotes efficient urea hydrolysis, providing a sufficient material basis for carbonate precipitation at fracture sites [24]. Surface functional groups, charge characteristics and negatively charged organic layers enable continuous Ca^{2+} chelation and offer stable heterogeneous nucleation sites for calcium carbonate crystals. Regulated crystal growth and morphology favour the

https://doi.org/10.3390/coatings16040413

integration of precipitated calcium carbonate with the geotechnical matrix, enhancing fracture repair performance [25]. Microorganisms contribute to microbially induced calcium carbonate precipitation not only through urease production but also by providing essential nucleation sites for effective fracture remediation.

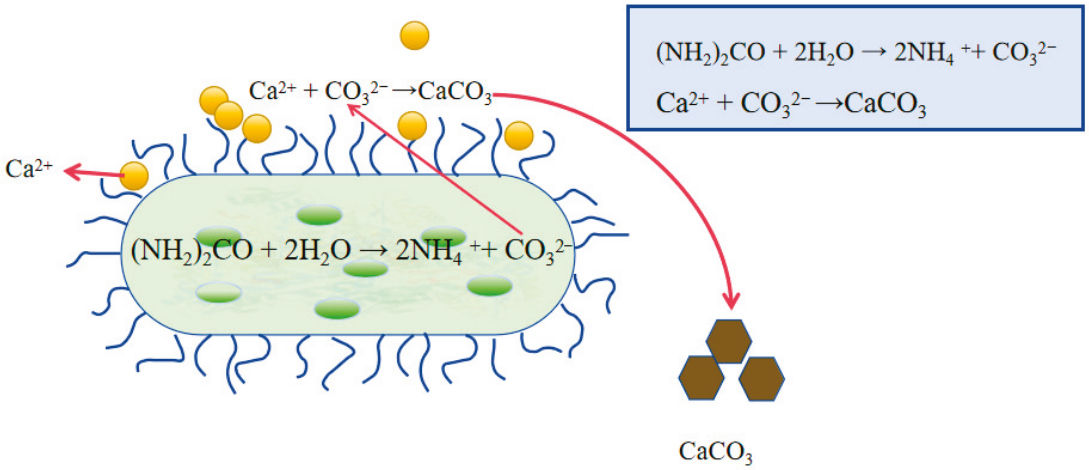

Figure 3. Schematic diagram of calcium carbonate precipitation induced by urease-producing bacteria.

2.2. Sulfate-Reducing Bacteria Reaction Mechanism

Sulfate-reducing bacteria (SRB) are a class of anaerobic microorganisms characterized by unique metabolic capabilities. In anoxic microenvironments within geotechnical fractures that are rich in organic matter, SRB utilize sulfate as an electron acceptor, reducing sulfate ions to hydrogen sulfide gas, which is subsequently released [26]. This metabolic process simultaneously generates bicarbonate ions. These bicarbonate ions then combine with metal ions present in the geotechnical environment to precipitate carbonate, as shown in Figure 4. Furthermore, the sulfate reduction activity of the SRB increases the pH of the surrounding microenvironment within the fractures, thereby further promoting precipitation formation [27]. Common SRB predominantly belong to the genus Desulfovibrio, as do 11 other genera, including *Desulfomonas* and *Desulfosarcina* [28]. Mineralization technology based on SRB metabolism has unique advantages in the engineering application of microbially induced carbonate precipitation (MICP) for repairing geotechnical fractures. It is particularly suitable for fractured zones in organic-rich cohesive or silty soils, roadbeds with sulfate-rich backgrounds, and geotechnical fracture zones in tailings dams [29].

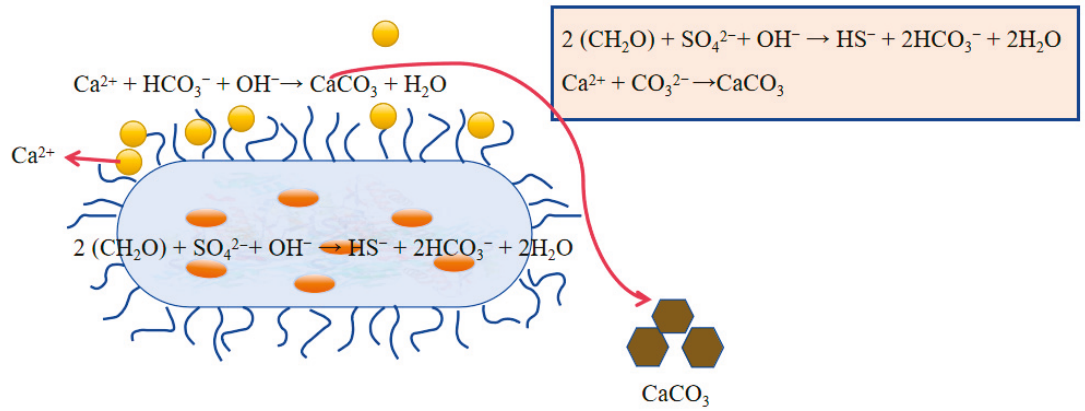

Figure 4. Schematic Diagram of Calcium Carbonate Precipitation Induced by Sulfate-Reducing Bacteria.

2.3. Iron Salt-Reducing Bacteria Reaction Mechanism

Iron-reducing bacteria (IRBs) are widely distributed in natural environments, particularly in iron-rich soils, groundwater sediments, and anoxic geotechnical fracture media. These microorganisms possess a unique dissimilatory iron reduction metabolic capability, which drives the valence transformation of iron ions and induces the precipitation of stable iron-based minerals. This provides a novel technical pathway for the MICP-based remediation of geotechnical fractures [30]. During metabolism, IRB reduces insoluble Fe^{3+} to soluble Fe^{2+}, which subsequently reacts with oxidizing agents in the environment to form insoluble iron-based precipitates [31,32], as shown in Figure 5. In addition, their metabolic activity modulates the local redox potential and pH, establishing thermodynamically favourable conditions for iron mineral formation [33]. These biogenic precipitates fill fracture pores and cement loose particles, ultimately achieving effective plugging and mechanical reinforcement of geotechnical fractures.

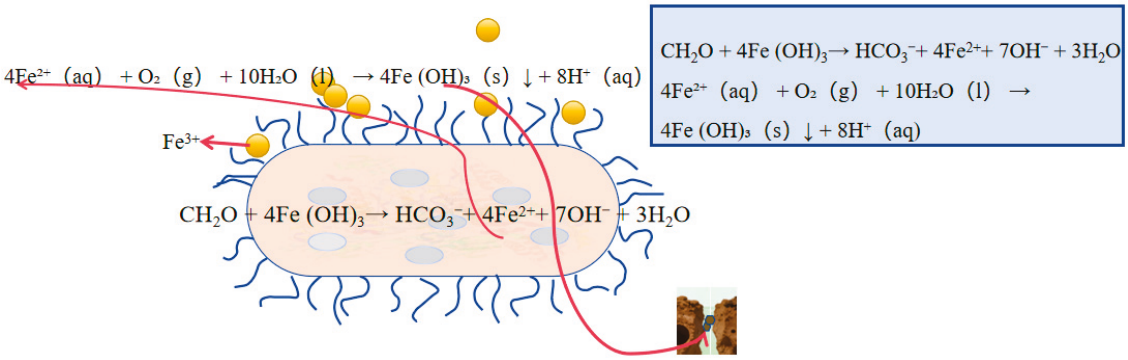

Figure 5. Schematic Diagram of the Calcium Carbonate Precipitation Induced by Iron Salt-Reducing Bacteria.

2.4. Denitrifying the Bacteria Reaction Mechanism

Denitrifying bacteria are typical facultative anaerobes whose metabolic characteristics render them particularly well suited to the anoxic or microaerophilic conditions often encountered in geotechnical fractures. These microorganisms utilize organic carbon as an electron donor and energy source, progressively reducing nitrate to nitrogen gas via enzyme-catalyzed reactions [34]. Throughout this dissimilatory process, hydrogen ions are continuously consumed, leading to a marked increase in the pH of the local microenvironment. This alkalinization establishes favourable conditions for carbonate precipitation [35]. The bicarbonate ions generated through denitrification subsequently combine with free calcium ions present in the geotechnical medium. Under the nucleation effect provided by functional groups on the bacterial cell surface, insoluble calcium carbonate precipitates are rapidly formed, as shown in Figure 6. These precipitates predominantly consist of stable polymorphs such as calcite or aragonite, which exhibit strong integration with the surrounding geotechnical matrix [36]. The accumulated calcium carbonate progressively fills the void spaces within fractures and effectively cements adjacent loose particles—including soil grains, rock fragments, or concrete matrix constituents—thereby forming a continuous and structurally stable solidified layer [37]. A notable advantage of this pathway over other MICP mechanisms, such as urea hydrolysis, is that it eliminates the need for exogenous strain introduction [38]. The resulting biomineralized layer serves a dual function: it achieves efficient fracture sealing, thereby reducing groundwater seepage and mitigating medium erosion while also significantly enhancing the compressive strength and shear performance of the fractured zone. This contributes to the long-term recovery of structural stability in the treated geotechnical mass [39].

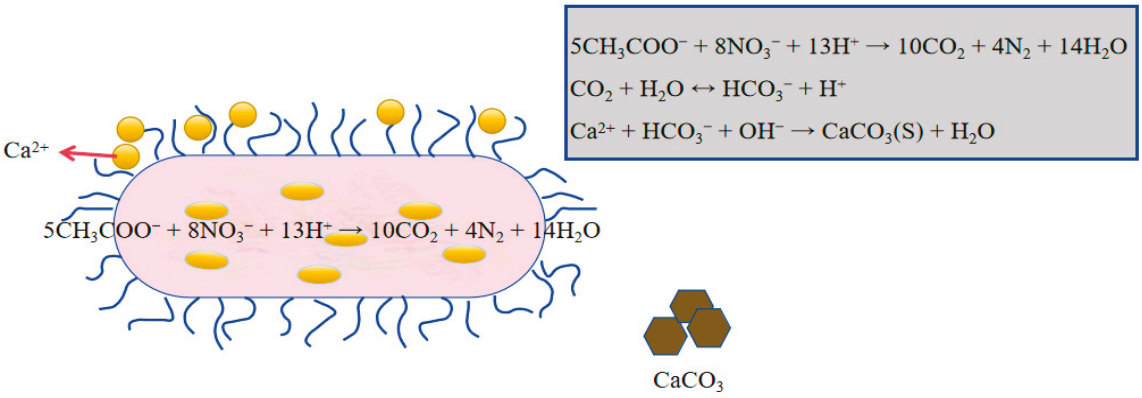

Figure 6. Schematic diagram of calcium carbonate precipitation induced by denitrifying bacteria.

Nevertheless, incomplete denitrification reactions may lead to the accumulation of toxic intermediates such as nitrite and nitrous oxide. These byproducts pose potential environmental risks because of their toxicity and pollutant characteristics, which could adversely affect surrounding water bodies and soil ecosystems if not adequately controlled [35].

2.5. Methanotroph Mineralization

In low-oxygen or anaerobic environments such as deep fractures in geotechnical engineering and underground excavation engineering, methanotrophs, as core anaerobic functional microorganisms, can mediate the microbially induced calcium carbonate precipitation (MICP) process through metabolic activities driven by formic acid oxidation, providing a new path for green and nonsecondary pollution for geotechnical fracture repair in such special scenarios [40]. With methane as the sole carbon source and formic acid as the electron donor, methane is converted into carbon dioxide through an anaerobic oxidation reaction [41]. The generated carbon dioxide combines with pore water in geotechnical fractures to form carbonic acid, providing a material basis for the subsequent generation of carbonate ions. Moreover, the synchronous consumption of methane can also achieve the additional benefit of atmospheric methane removal. Proton in the environment is consumed through metabolic processes, and the pH of the local microenvironment gradually increases [42]. Methanotrophs can adapt to the anaerobic conditions in fractures through their own metabolism and construct an alkaline environment in a complex geotechnical microenvironment, providing an efficient material guarantee for fracture filling and cementation [43]. Compared with traditional urea hydrolysis-type MICP, this pathway can also avoid the secondary pollution problems caused by ammonia release and nitric acid formation [44].

The core chemical reaction Equations (1)–(3) for calcium carbonate precipitation induced by methanotrophs are as follows:

Without sulfate participation (typical reaction):

$$CH_4 + 2H_2O \rightarrow CaCO_3 + 4H_2 \quad (1)$$

$$CO_2 + H_2O + Ca^{2+} \rightarrow CaCO_3 \downarrow + 2H^+ \quad (2)$$

In the presence of sulfate (sulfur-containing environment):

$$CH_4 + Ca^{2+} + SO_4^{2+} \rightarrow CaCO_3 \downarrow + H_2O + H_2S \quad (3)$$

2.6. Mineralization Mechanisms of Other Microorganisms

Photosynthetic microorganisms, such as cyanobacteria and microalgae, are autotrophic organisms that utilize CO_2 in the environment as their primary carbon source through photosynthetic metabolism and physiological characteristics. The photosynthetic process directly alters the speciation of inorganic carbon within the system, facilitating the conversion of CO_2 into available forms such as bicarbonate ions. Concurrently, the metabolic process generates OH^-, leading to a significant increase in the pH of the surrounding environment [45]. Ultimately, this elevated pH reduces the solubility of carbonates, promoting the combination of metal ions (primarily Ca^{2+}) in the environment with the converted bicarbonate ions to induce carbonate precipitation. These precipitates achieve remediation by filling pores in the rock or soil mass and cementing loose particles, as shown in Figure 7. Furthermore, this entire process proceeds without the involvement of urease, thereby avoiding environmental pollution caused by ammonia and offering the advantage of being ecologically friendly [46].

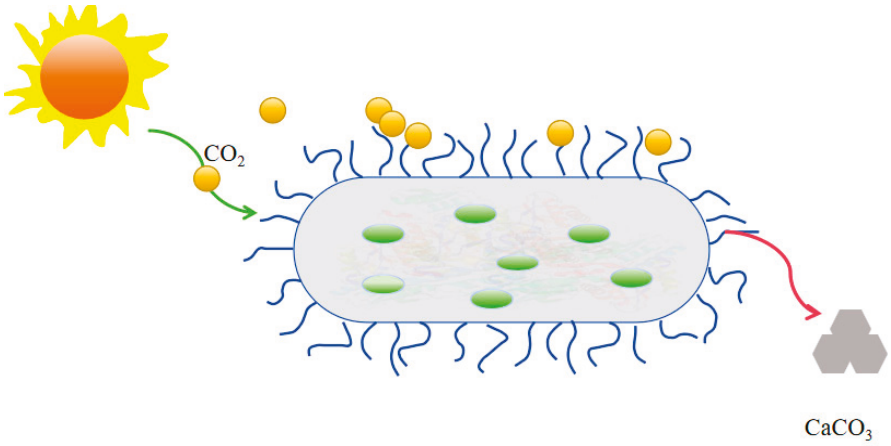

Figure 7. Schematic diagram of calcium carbonate precipitation induced by photosynthetic microorganisms.

As indicated by the metabolic mechanisms and application characteristics of different functional microorganisms shown in Table 1, significant differences exist in both the application performance and the required reaction conditions of microbially induced calcium carbonate precipitation (MICP) technology for geotechnical fracture remediation. For each mole of $CaCO_3$ produced via ureolytic MICP, 2 moles of NH_4^+ are generated [47]. If left untreated, this byproduct can cause environmental pollution. Although current post-treatment technologies can achieve 80%–90% ammonium removal, they increase process complexity [48]. Denitrification-based MICP requires strict control of the nitrate loading rate ($\leq$0.7 mol/m^2·day) to avoid nitrite accumulation. SRB-based MICP is constrained by the toxicity of H_2S and is only suitable for specific scenarios with a sulfate-rich background. From an economic perspective, the use of low-cost calcium sources (e.g., agricultural fertilizers, industrial byproducts) can increase $CaCO_3$ yield by 2.3–2.5 times; however, challenges such as compositional variability and potential impurity toxicity remain unresolved. Therefore, the large-scale application of MICP necessitates a balance between environmental benefits and process costs. Future research should focus on the development of low-toxicity or non-toxic metabolic pathways (e.g., carbonic anhydrase-engineered bacteria) and the resource utilization of byproducts.

Table 1. Metabolic Mechanisms and Application Characteristics of Microorganisms with Different Functions.

Microbial Type	Core Metabolic Reaction	Product Type	pH Adaptation Range	Advantages	By-Product	Engineering Applicability	Mineralization Efficiency	Ref.
Urease-producing bacteria	Urea hydrolysis to produce ammonia and carbonate	Calcium carbonate	7.0–10.0	Fast metabolic rate, high precipitation yield	Ammonia	Good injectability; suitable for shallow or well-ventilated fractures; low cost; controllable.	Extremely high	[14,21–25]
Sulfate-reducing bacteria	Sulfate reduction to produce sulfide	Calcium sulfide, ferrous sulfide	6.0–8.5	Suitable for sulfate environment	toxic hydrogen sulfide	Suitable for anaerobic conditions; applicable to underground or deep oxygen-deficient fractures.	Moderate	[26–29]
Iron salt-reducing bacteria	Ferrous ion oxidation to produce iron hydroxide	Iron hydroxide	2.0–6.0	Suitable for iron-bearing rock	solid secondary iron minerals	Suitable for anaerobic or iron-rich environments; applicable to iron-bearing rock masses and mining fractures; suitable for specialized pollution remediation scenarios.	Moderate	[30–33]
Denitrifying bacteria	Nitrate reduction to produce nitrogen and carbonate	Calcium carbonate	6.5–9.0	No urea needed, low cost	N_2, N_2O	Applicable to both underground and shallow settings; moderate efficiency; suitable for nitrate-rich or oxygen-deficient environments.	Moderate	[34–39]
Methanotrophs	Anaerobic oxidation reaction	Calcium carbonate	7.5–9.0	Low cost, carbon sequestration	produces no toxic byproducts	Suitable for deep anaerobic environments; applicable to deep fractures, underground caverns, and oil/gas wellbores.	Moderate	[40–44]
Photosynthetic	Autophototrophy	Calcium carbonate	6.5–9.0	No urea needed, low cost	produces no toxic byproducts	Suitable for surface or shallow engineering applications; surface solidification; dust control; desertification management.	Moderately low	[45,46]

3. Influencing Factors of Microbial Mineralization for Reinforcing Fractured Rock

In practical applications, microbially induced calcium carbonate precipitation (MICP) technology is constrained by multiple factors that directly influence its mineralization

efficiency [47]. The primary factors influencing the solidification performance of MICP are shown in Figure 8, including the bacterial concentration, bacterial and urease activity, pH, temperature, fracture characteristics, and calcium source type and concentration. These factors collectively impact the engineering properties of reinforced or remediated rock masses through their effects on the amount of precipitation, crystal morphology, distribution uniformity, and cementation characteristics of calcium carbonate.

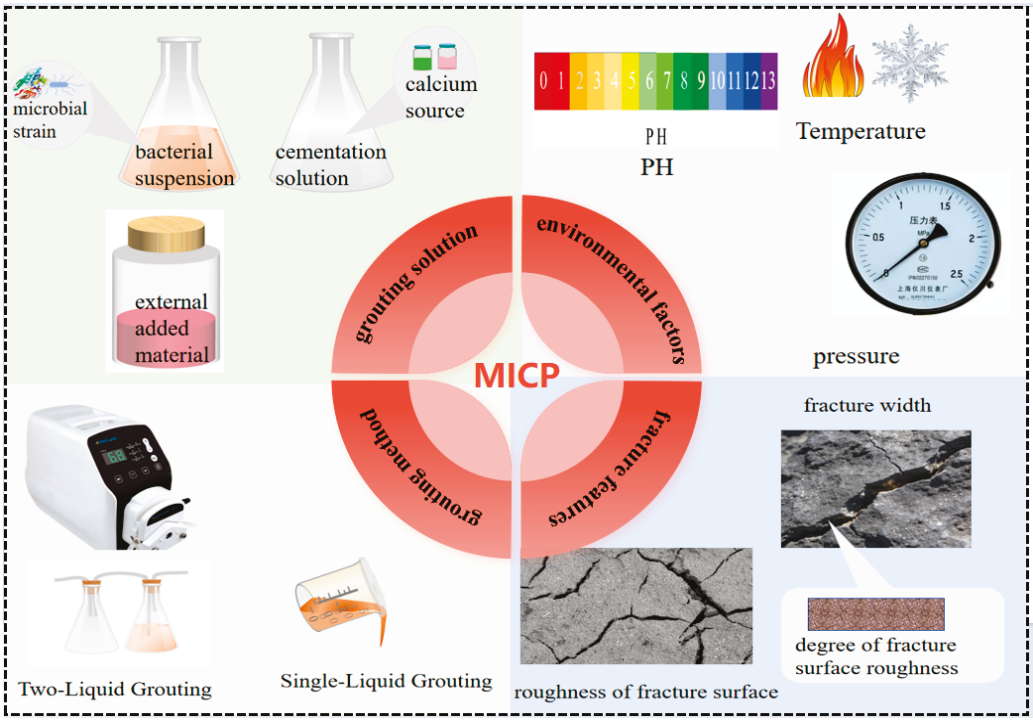

Figure 8. Schematic Diagram of the Influencing Factors for Microbially Induced Calcium Carbonate Precipitation.

3.1. Species and Concentrations of Bacterial Strains

The efficacy of microbial mineralization is directly influenced by the microbial species employed, as significant variations in mineralization capacity exist among different microbial taxa [48], which directly affects the efficiency and effectiveness of geotechnical fracture remediation. Urease-producing microorganisms represent the most commonly utilized functional strains in fracture repair, primarily *Bacillus sphaericus*, *Sporosarcina pasteurii*, *Bacillus megaterium*, and *Bacillus subtilis* [49,50]. Under identical environmental conditions, inherent differences in urea hydrolysis rates among bacterial species lead to corresponding variations in calcium carbonate precipitation kinetics [51]. A comparative analysis of mineralization rates across different bacterial strains, as shown in Table 2, revealed that the mineralization rate of *Sporosarcina pasteurii* ranged from 80% to 90%, with calcium carbonate production reaching 21.83 g/L, whereas that of *Bacillus megaterium* ranged from only 40%–70%. Within the context of MICP-based geotechnical fracture remediation, *Sporosarcina pasteurii* is recognized as the most promising ureolytic bacterium, possessing advantages such as high enzyme production capacity, superior mineralization efficiency, excellent precipitate characteristics, and robust environmental adaptability, enabling rapid acclimatization to fracture environments [51].

In addition to microbial species, bacterial concentration constitutes a core factor that regulates the MICP mineralization process, directly influencing the precipitation efficiency and cementation quality of calcium carbonate within fractures [52]. The bacterial concentration, which is typically characterized by the OD600 value (optical density at 600 nm),

https://doi.org/10.3390/coatings16040413

serves as a critical parameter affecting mineralization efficiency. Under conditions where the urea concentration sufficiently supports bacterial metabolic activity, the urea hydrolysis rate accelerates with increasing bacterial concentration, thereby promoting the generation and deposition of calcium carbonate precipitates [39]. The growth curve of *Sporosarcina pasteurii* is shown in Figure 9, which clearly demonstrates that under appropriate culture conditions, the bacterial concentration progressively increases with extended cultivation time. When the cultivation period exceeds 25 h, nutrient depletion and the accumulation of toxic metabolites gradually reduce the rate of bacterial growth and reproduction. The temporal variation in urease activity, shown in Figure 10, reveals that urease activity increases synchronously with cultivation time; specifically, when the bacterial concentration (OD600) increases from 0.4 to 0.7, urease activity increases 2.5-fold [52]. Similarly, the calcium carbonate precipitation rate increases concomitantly, establishing a positive correlation between the bacterial concentration and calcium carbonate yield [53]. Furthermore, elevated bacterial concentrations accelerate calcite formation. The cementation efficacy of calcium carbonate is also intimately associated with the spatial distribution of bacteria within fractures; when substantial bacterial populations adhere to fracture walls and surrounding geotechnical media surfaces, the formation of sufficient quantities of well-cemented calcium carbonate crystals is facilitated [54]. In summary, an optimal bacterial concentration ensures adequate bacterial colonization within fractures and on fracture surfaces, efficiently induces calcium carbonate mineralization, and forms continuous, dense calcium carbonate cementitious structures within fracture spaces, thereby enhancing the overall cementation strength and impermeability of remediated fractures.

Table 2. Comparison of Urease Activity, Calcium Carbonate Mineralization Characteristics, and the Application Potential of Different Spore-Forming Bacteria.

Bacterial Name	Effect of Bacterial Concentration on Urease Activity	Effect of Bacterial Concentration on Calcium Carbonate Yield	Application Potential/Advantages	Suitable pH Value	Calcium Carbonate Yield Under the Same External Conditions	Ref.
Bacillus sphaericus	Positive correlation	Positive correlation	Flexible environmental adaptability, alkali resistance, calcium tolerance, low temperature adaptability	Suitable working pH 7–11	High yield >80%	[47,55,56]
Sporosarcina pasteurii	Positive correlation	Positive correlation	High urease activity and mineralization efficiency, strong environmental adaptability, cell characteristics suitable for mineralization	Suitable working pH 6–9	Yield up to more than 80%–90%	[57,58]
Bacillus megaterium	Positive correlation	Positive correlation	Outstanding environmental repair capacity, suitable for working in low-temperature environment	Suitable working pH range 6–8	Yield approximately 40%–70%	[59–62]
Bacillus subtilis	Positive correlation	Positive correlation	Wide adaptation range	Suitable working pH range 6–10	Yield approximately 50%–80%	[63,64]

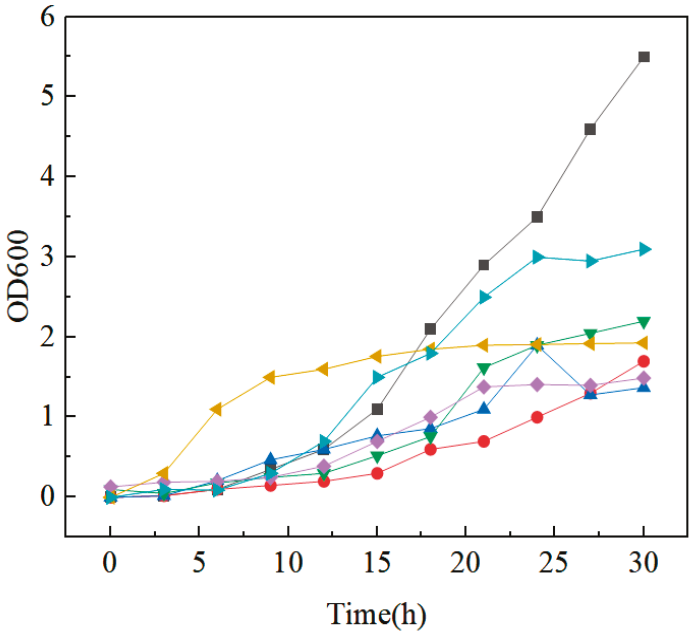

Figure 9. Growth curve of *Sporosarcina pasteurii*: Change in bacterial concentration with time: Black squares [52], red circles [65], blue upward triangles [66], green downward triangles [67], purple diamonds [68], orange left-pointing triangles [69], and cyan right-pointing triangles [70].

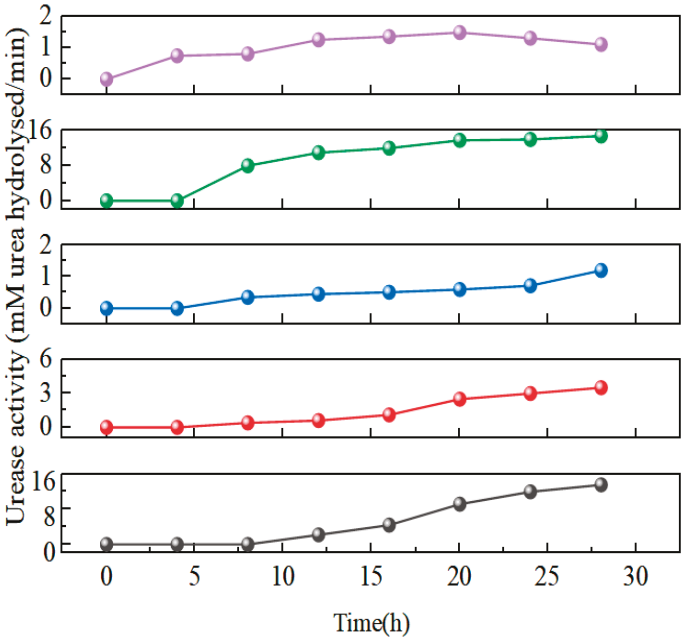

Figure 10. Growth curve of *Sporosarcina pasteurii*: Change in urease activity with time: Purple diamonds [52], green downward triangles [65], blue upward triangles [66], red circles [68], and black squares [69].

The urea concentration in the cementation solution directly influences the amount of calcium carbonate produced; higher urea concentrations lead to an increased hydrolysis rate, thereby generating more calcium carbonate precipitates. However, excessively high urea concentrations can inhibit the production of microbially induced calcium carbonate. When the concentration exceeds 1.0 mol/L, an inhibitory effect gradually emerges, becoming significantly pronounced at concentrations of 1.5–2.0 mol/L [23,71]. Similarly, an excessively high bacterial concentration can result in an uneven distribution of calcium carbonate [72,73], often causing clogging near the injection port and consequently limiting

the effective penetration range of the grout. To address the limitations associated with high-concentration bacterial suspensions in the remediation of geotechnical fractures, studies on MICP grouting [74] have demonstrated that compared with a single injection of a high-concentration bacterial suspension, multiple injections of low-concentration suspensions significantly increase the unconfined compressive strength of sand columns. This improvement is attributed to the slower attenuation of bacterial activity and reduced flocculation at lower concentrations, which extends the effective grouting window. Furthermore, this approach facilitates the formation of large calcium carbonate crystals that effectively fill the pores between soil particles and geotechnical fractures, thereby establishing a more stable granular cementation network.

The morphological characteristics of calcium carbonate crystals under different bacterial concentrations are shown in Figure 11. The regulatory effect of bacterial concentration on the mineralization process is also reflected in the morphology of calcium carbonate crystals, and this effect increases with increasing bacterial concentration [71,75]. SEM results [69] revealed that in the bacterial liquid system with different concentrations containing both bacterial cells and secretions, calcium carbonate crystals were mainly spherical and hexagonal. In environments containing only bacterial secretions, the crystals are mostly spindle-shaped and spherical, with stable calcite and metastable vaterite coexisting. In the environment containing only bacterial cells, it is regular hexagonal calcite. These findings indicate that bacterial secretions are the key to controlling crystal morphology and that bacterial cells provide nucleation sites for calcium carbonate deposition, thereby guiding the deposition and growth of calcium carbonate crystals and improving the compactness and stability of the cemented structure [68]. Regulating different concentrations of bacterial liquid to form stable calcite crystals with mainly spherical and hexagonal shapes can adapt to the multiscale pore-filling requirements of geotechnical fractures, form a mineralized cemented layer with high compactness and excellent cementation effects, and significantly improve the fracture plugging stability, impermeability and shear strength [76].

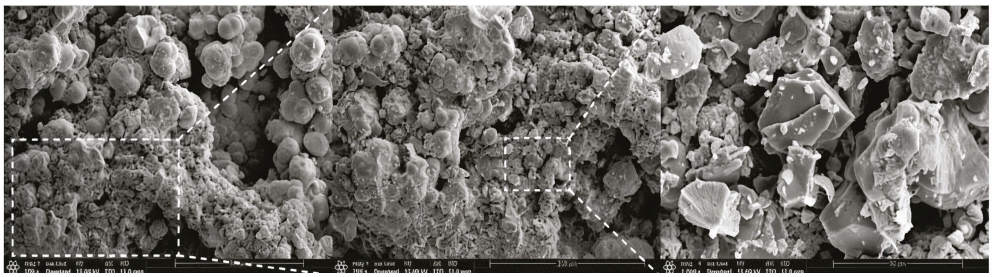

(a) OD_{600}=0.5

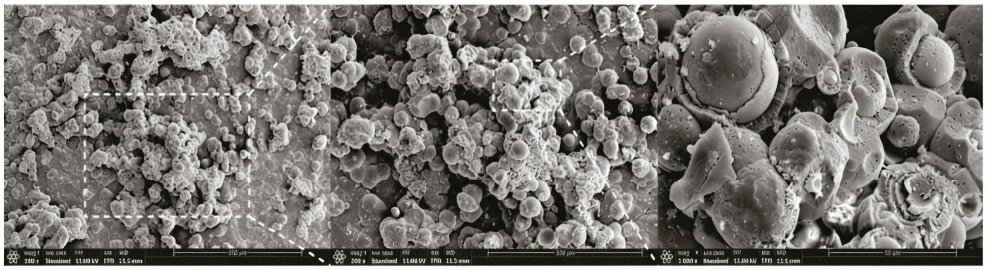

(b) OD_{600}=2.0

Figure 11. Morphological characteristics of calcium carbonate crystals with different bacterial solution concentrations. (Reprinted from Cui et al., Journal of Rock Mechanics and Geotechnical Engineering, 2026, 18, 1213–1232, Figure 18 [75]).

https://doi.org/10.3390/coatings16040413

In summary, the concentration and activity of urease are directly related to the bacterial concentration. Within a certain range, the higher the bacterial concentration is, the stronger the catalytic activity of urease, and the higher the urea hydrolysis rate, thereby generating more calcium carbonate crystals and ultimately accelerating the mineralization process of MICP.

3.2. Temperature

Temperature plays a pivotal role in determining the efficiency of microbially induced calcium carbonate precipitation (MICP) for fracture remediation. Suitable temperatures significantly increase the metabolic activity of microorganisms and the catalytic efficiency of urease, thereby promoting the generation and stabilization of calcium carbonate precipitates. This provides a favourable basis for the effective remediation of geotechnical fractures.

Research on the influence of temperature on fracture remediation and soil reinforcement efficacy indicates that within the environmental range of 10–30 °C, elevated temperatures are positively correlated with the strength of geotechnical masses following fracture repair [77]. Concurrently, the permeability of fractured zones decreases significantly with increasing temperature, providing empirical support for MICP-based fracture remediation projects in temperate climate regions [78]. Within a broader temperature spectrum [79], as illustrated in Figure 12, which depicts the morphological characteristics of calcium carbonate crystals at different temperatures, both the yield and size of calcium carbonate crystals employed for fracture filling initially increase but subsequently decrease with increasing temperature [80]. During the temperature increase phase, microbial activity and crystal growth conditions continuously improve, facilitating the dense filling of multiscale fracture pores. However, when the temperature reaches 50 °C, both the crystal yield and size markedly decrease, highlighting the inhibitory effects of high-temperature environments on the MICP reaction system, which adversely affects the formation of mineralized fracture layers. Therefore, when geotechnical fracture remediation is being conducted in high-temperature regions, targeted temperature control measures must be implemented to mitigate the inhibitory effects of elevated temperatures on mineralization reactions, thereby ensuring the compactness and cementation quality of mineralized fracture fill [81].

Taking urea hydrolysis-based MICP technology for geotechnical fracture remediation as an example, the temperature response characteristics of urease activity—the core driving factor of the MICP reaction—are particularly critical. As shown in Figure 13, which presents the influence of environmental temperature on the concentration of different bacterial strains, the urease activity of *Sporosarcina pasteurii* peaks at 30 °C and thereafter gradually declines with increasing temperature [65]. In contrast, *Bacillus subtilis* exhibits peak urease activity at 36 °C [77]. Corresponding mechanical property studies [79] have demonstrated that fracture-repaired samples treated at 35 °C achieve the highest peak strength and residual strength, followed by those treated at 20 °C. This trend aligns with the response patterns of *Sporosarcina pasteurii* bacterial concentration and urease activity under varying temperatures shown in Figure 14, further confirming the regulatory role of enzymatic activity in controlling the solidification effectiveness of fracture remediation. Conducting rock fracture remediation within an appropriate temperature range maximizes the mineralization efficiency at fracture sites, thereby significantly enhancing both the structural stability and shear-bearing capacity of the remediated geotechnical mass [77].

Although urease catalytic activity decreases exponentially in low-temperature environments below 15 °C—with urea hydrolysis efficiency falling below 30% of that observed under optimal thermal conditions [79,82], thereby presenting significant challenges for fracture remediation in cold climates—it is noteworthy that MICP technology has considerable

https://doi.org/10.3390/coatings16040413

application potential for low-temperature fracture repair. Specifically, elevated bacterial concentrations can effectively offset the temperature-induced reduction in urease activity, thereby ensuring the continuity of mineralized fracture filling. Furthermore, freeze-thaw cycling studies [83] have demonstrated that under adverse environmental conditions, such as cyclic freeze-thaw exposure, the *Sporosarcina pasteurii* employed in MICP-based fracture remediation is capable of forming endospores to preserve metabolic viability. Upon the return of favourable environmental conditions, these dormant spores can germinate and reestablish functionally active bacterial populations. These reactivated microorganisms subsequently utilize the nutrients available within the soil matrix and surrounding fracture zones to sustain microbial mineralization reactions, continuously generating calcium carbonate precipitates that progressively infill fracture networks. This adaptive resilience provides a robust theoretical foundation for the application of MICP-based fracture remediation technologies in cold regions, positioning this approach as a promising strategy for soil stabilization and frost-resistant crack repair in low-temperature environments [84].

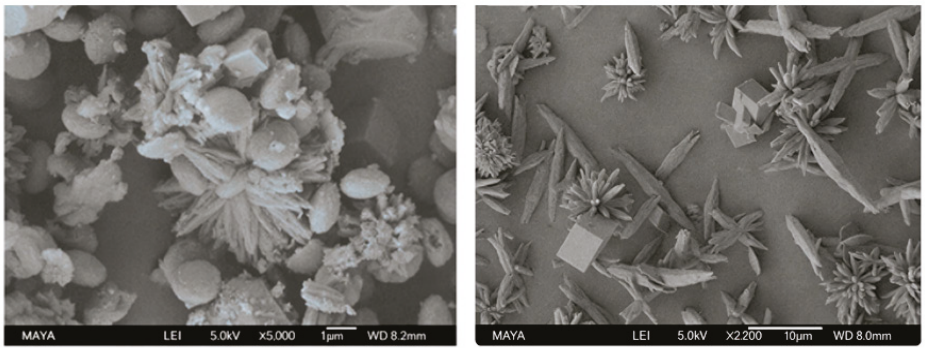

(a) 25°C (b) 55°C

Figure 12. Morphology of Calcium Carbonate Crystals at Different Temperatures. (Reprinted from Wang et al., ACS Applied Materials & Interfaces, 2013, 5, 4884–4892, Figures 6 and 8 [79]).

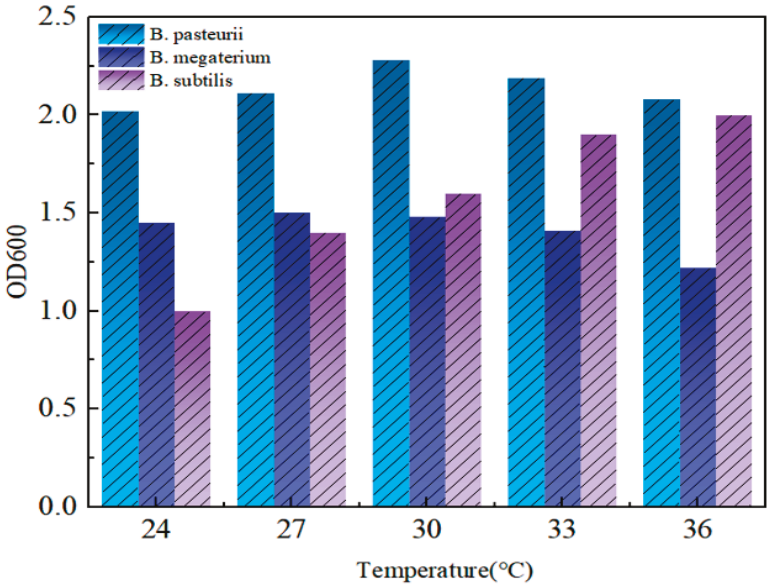

Figure 13. Effects of Ambient Temperature on Bacterial Concentrations: teal [65], blue [85], purple [86].

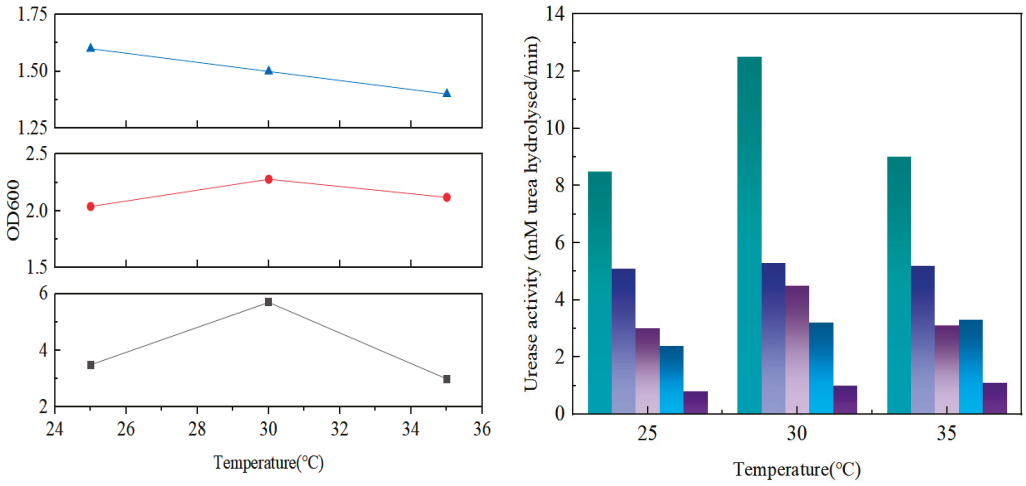

Figure 14. Influence of Temperature on the Cell Concentration and Urease Activity of *Sporosarcina pasteurii*: Blue upward triangles [52], red circles [65], black squares [85]; Muted teal [52], dusty blue [65], dusty purple [67], blue [85], purple [87].

3.3. pH Value

To a certain extent, the pH directly affects the total calcium carbonate yield and crystalline quality within the mineralization reaction system in rock fractures, thereby influencing the final compactness and mechanical performance of geotechnical fracture remediation. Urease, the core biological enzyme driving the MICP repair reaction, is essentially a protein. All the enzyme preparations possess a corresponding optimal pH range, within which only urease can maintain high activity [88]. If the pH of the filling system within the geotechnical fracture deviates from this suitable range, an excessively high or low acidic–alkaline environment will directly compromise the molecular structure of urease, resulting in a significant attenuation of enzyme activity or even complete deactivation [23]. Therefore, during the MICP repair process of geotechnical fractures, regulating the internal pH of the fissure environment to the optimal range can significantly increase the catalytic efficiency of urease. This ensures the continuous and efficient progression of the urea hydrolysis reaction, thereby providing stable reaction conditions for the in situ generation of calcium carbonate precipitates and the filling of fracture pores [89].

The regulatory effect of pH on urease activity is shown in Figure 15. A weakly acidic, low-pH environment markedly compromises the catalytic function of urease [89], thereby decelerating the urea hydrolysis rate and consequently decreasing the quantity of calcium carbonate crystals formed within the fracture [90]. If the pH becomes excessively low, the hydrolytic mineralization reaction within the fissure may even cease entirely, rendering the effective cementation and filling of the fracture unattainable [91]. Within a complete bacterial reaction system for geotechnical fracture remediation, the buffering effect of bacterial metabolism and extracellular secretions establishes an optimal pH range of 6.0–8.5 for efficient urease activity [23]. This range aligns closely with the complex media environment of actual fissures, offering more pertinent guidance for in situ remediation construction.

The direct effect of pH on calcium carbonate yield during fracture remediation is equally significant. As shown in Figure 16, which shows the morphological characteristics of calcium carbonate precipitated by *Sporosarcina pasteurii* under different pH conditions, pH has a negligible influence on calcium carbonate yield and longitudinal distribution when it is controlled within the range of 4–7. Within the pH range of 7–10, calcium carbonate production first increases but then decreases with increasing pH. The precipitation yield remains at a peak level within pH 8–9, which favours the dense filling of multiscale pores in geotechnical fractures and improves the cementation performance of the remediation

https://doi.org/10.3390/coatings16040413

interface [92]. Further studies have indicated that over a broad pH range of 6–13, urease activity also first increases but then decreases with changes in environmental acidity and alkalinity [93], reaching maximum activity at pH 7–8 [94]. Overall, maintaining the reaction system pH within the optimal range of 7–9 during both in situ geotechnical fracture remediation and laboratory experiments maximizes the efficiency of calcium carbonate production and the quality of crystal development. When combined with suitable temperature control, this strategy further improves the fracture filling density, interfacial cementation strength, and overall durability of the repaired geotechnical mass, thus providing a fundamental basis for optimizing environmental parameters in MICP-based fracture remediation technology [95].

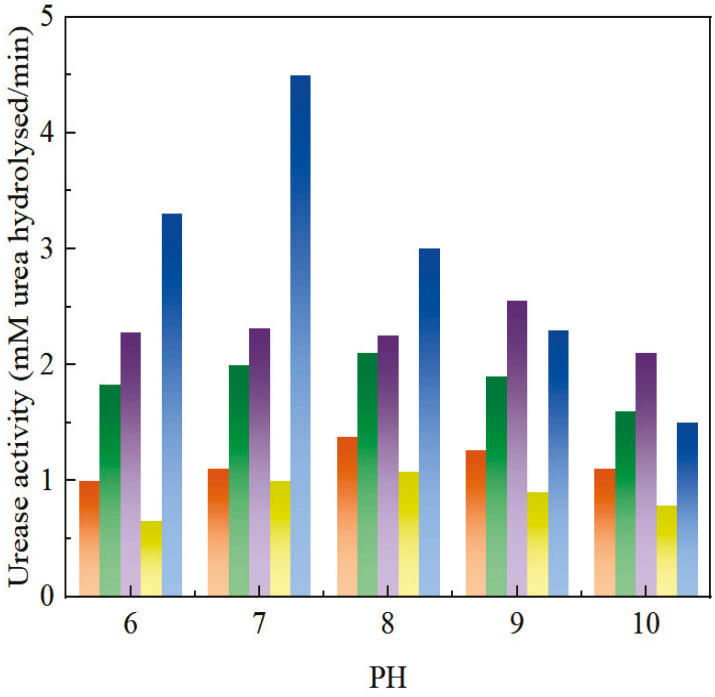

Figure 15. Effect of Different pH Values on Urease Activity of Sporosarcina pasteurii: orange [65], green [94], purple [85], yellow [87], blue [67].

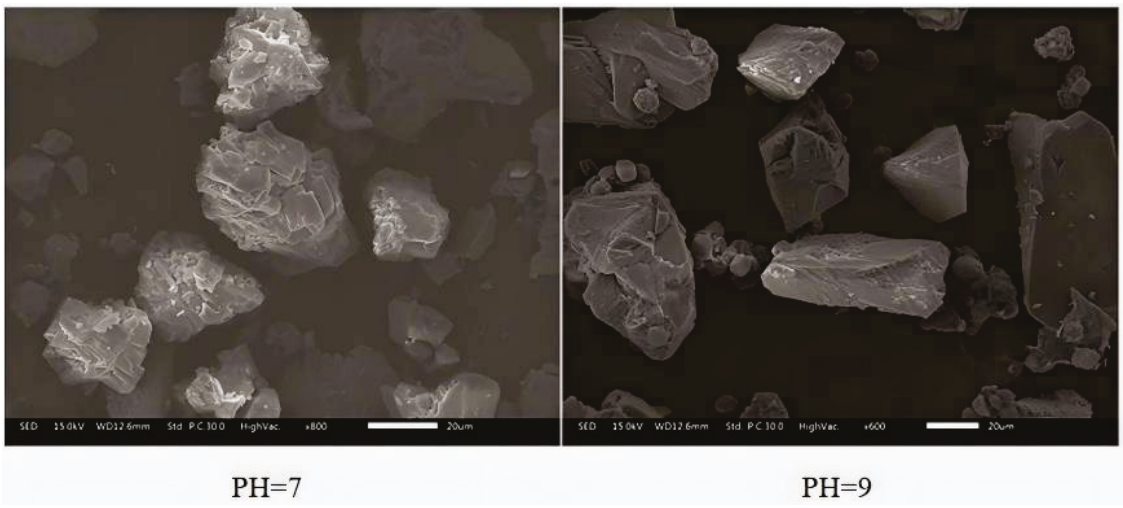

Figure 16. Morphological Characteristics of Calcium Carbonate Crystals Under Different pH Values. (Reprinted from Wang et al., ACS Applied Materials & Interfaces, 2013, 5, 5204–5213, Figure 4 [82]).

https://doi.org/10.3390/coatings16040413

3.4. Type and Concentration of the Calcium Source

Calcium sources, as the fundamental substrate in microbially induced calcium carbonate precipitation (MICP) technology for geotechnical fracture remediation, provide the Ca^{2+} ions essential for the formation of calcium carbonate minerals, which are required for fracture cementation. In the absence of Ca^{2+}, the mineral precipitation necessary for fracture filling and cementation cannot proceed [96]. The type and concentration of calcium sources directly dictate the yield, crystal size, and distribution uniformity of calcium carbonate precipitated within fractures, thereby influencing the remediation efficacy and cementation stability of MICP-treated geotechnical fractures. Accordingly, calcium source parameters represent critical factors governing the quality of mineralized fracture filling.

Comparative MICP-based fracture remediation experiments were systematically conducted using calcium sources of varying types and concentrations, as shown in Figures 17 and 18, followed by electron microscopic characterization of the resulting calcium carbonate crystal morphologies [97–105]. The experimental findings reveal that calcium sulfate, characterized by its inherently low solubility, fails to provide a sustained and sufficient flux of Ca^{2+} ions to the fracture zone. When calcium carbonate is applied as the sole calcium source, the resulting calcium carbonate precipitation is quantitatively inadequate to achieve effective fracture cementation, thereby yielding only marginal improvements in the mechanical strength of the remediated geotechnical matrix. In contrast, the calcium chloride treatment group generated hexagonal calcite crystals with atomically smooth surfaces and well-defined crystallographic facets, characterized by high structural regularity and density, rendering them particularly suitable for filling and cementing macroscopic fracture voids. The calcium nitrate treatment group produced hexagonal calcite crystals with notably roughened surface topography; this enhanced surface roughness substantially improved interfacial adhesion between the precipitated crystals and fracture wall surfaces, thereby significantly increasing cementation stability and long-term durability [96]. The calcium acetate treatment group predominantly generated acicular aragonite crystals, whose elongated morphology enables effective penetration into microscale interstitial spaces within the fracture network, thereby compensating for the inherent filling limitations of larger, equant crystal morphologies and ensuring comprehensive void occupation across multiple length scales. These findings establish a robust scientific basis for the tailored selection of calcium sources in MICP-based remediation strategies targeting fractures of varying geometrical characteristics and scale distributions [106–109].

In microbially induced calcium carbonate precipitation (MICP) for geotechnical fracture remediation, the calcium ion concentration, together with the calcium source type, constitutes a critical determinant of remediation efficacy, directly influencing the sealing density of fractures and the postremediation stability of the treated geotechnical mass [110]. The results demonstrate that elevated calcium ion concentrations promote increased calcium carbonate precipitation, thereby enhancing fracture remediation and reinforcement performance [111]. MICP-based fracture remediation experiments employing analytical-grade calcium chloride as the calcium source revealed that all treated geotechnical samples achieved compressive strengths exceeding 600 kPa, with maximum values approaching 4 MPa. The calcium carbonate mass fraction within the solidified matrix remained stable within the range of 12.2%–16.6% [99], facilitating the formation of a dense cemented layer that effectively impedes water infiltration and mitigates the loss of geotechnical particles. Within the MICP remediation framework, the strength improvement of the treated geotechnical material is positively correlated with the calcium ion concentration in the cementation solution [112]: Within the low-concentration range, increasing the calcium ion concentration promotes calcium carbonate precipitation, thereby improving fracture filling and cementation efficiency. In sand solidification experiments using calcium chloride as

the calcium source [96], it was found that when the calcium ion concentration exceeded 1.25 mol/L, the increase in calcium carbonate precipitation gradually plateaued, adversely affecting both remediation efficiency and cost control. Under the specific experimental conditions of that study (sand matrix, Sporosarcina pasteurii, and laboratory scale), a calcium ion concentration in the range of 0.5–1.0 mol/L promoted relatively uniform calcium carbonate precipitation, enhanced the strength of fracture remediation, and improved the compactness of the cemented layer. It should be noted that the above concentration threshold was obtained under specific experimental conditions, and its applicability may vary depending on factors such as rock lithology, bacterial strain characteristics, and grouting processes. In engineering applications, it is advisable to use these literature-derived values as references and to optimize parameters according to site-specific conditions.

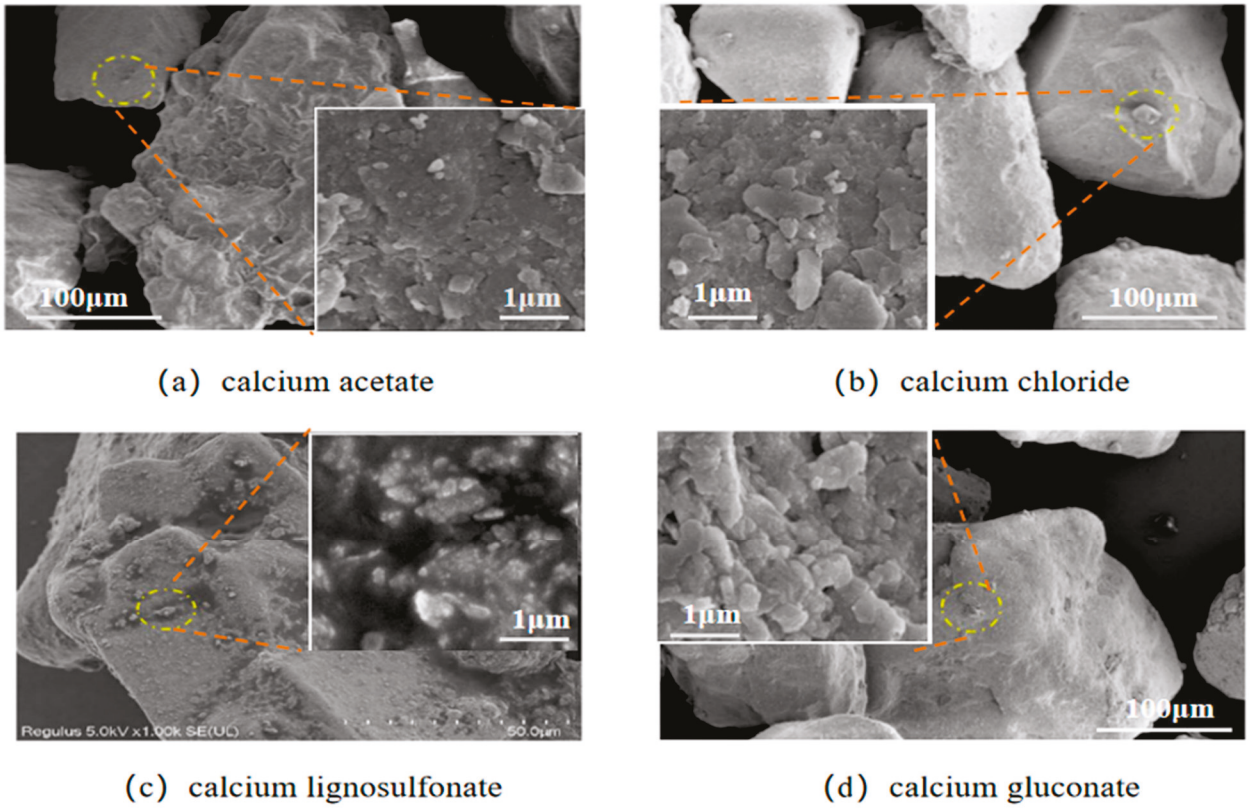

Figure 17. Morphological Characteristics of Calcium Carbonate Crystals with Different Calcium Sources. (Reprinted from Tao et al., Scientific Reports, 2025, 15, 9149, Figure 14 [108]).

3.5. Fracture Characteristics

In microbially mediated geotechnical fracture remediation, fracture characteristics constitute a governing factor that regulates the efficacy of microbially induced calcium carbonate precipitation (MICP) reinforcement. These characteristics directly influence the closure rate of geotechnical fractures and the efficiency of calcium carbonate accumulation by governing bacterial transport within fracture channels, the diffusion uniformity of cementation solutions, and the spatial distribution of calcium carbonate precipitates [113]. A schematic illustration of microbially mediated geotechnical fracture remediation is shown in Figure 19, which reveals that under favourable conditions, microbial mineralization effectively fills and rehabilitates rock fractures. Research has indicated [114] that when the fracture aperture is within the range of 0.5–2.0 mm, calcium carbonate precipitation tends to significantly increase with increasing aperture, and the fracture sealing efficacy progressively improves with increasing width. Specifically, fractures with apertures of 1.5–2.0 mm demonstrate sealing rates approximately 5%–15% higher than those of 1.0 mm

https://doi.org/10.3390/coatings16040413

fractures [115,116], accompanied by superior bond strength at the cementation interface. Under conditions where commonly used *Sporosarcina pasteurii*, conventional grouting processes, and calcium chloride as the calcium source are employed, existing studies indicate that an aperture range of 0.5–2.0 mm represents a preferable width interval for MICP-based fractured rock mass remediation.

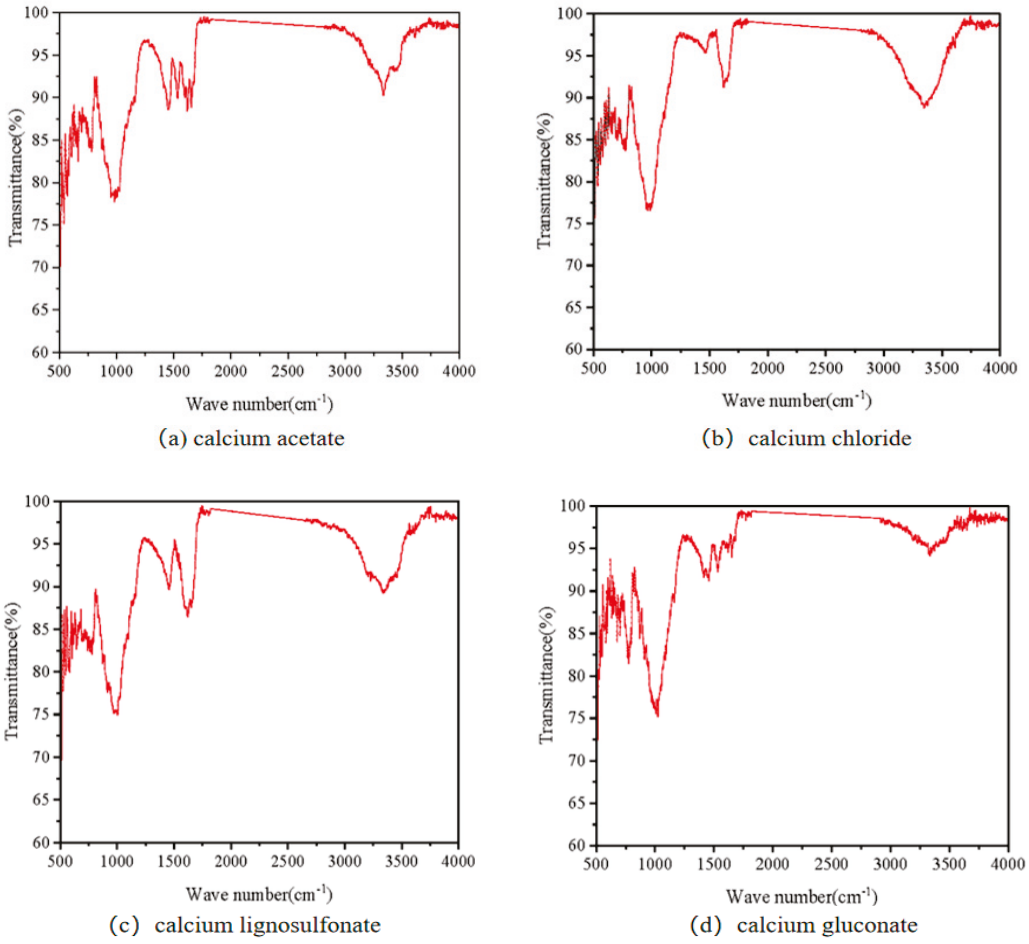

Figure 18. FTIR Spectra of Mineralized Products Under Different Calcium Sources. (Reprinted from Tao et al., Scientific Reports, 2025, 15, 9149, Figure 17 [108]).

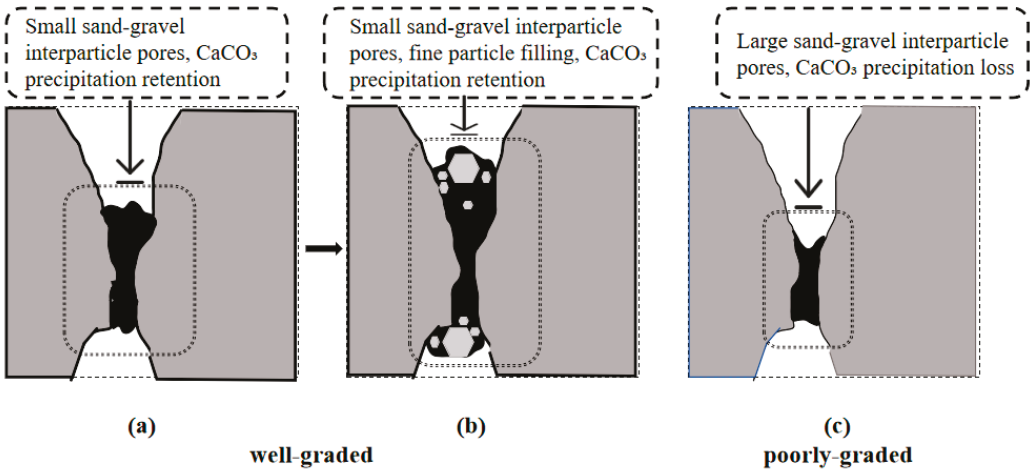

Figure 19. Schematic Diagram of Microbial-Induced Calcium Carbonate Precipitation (MICP) for Geotechnical Crack Remediation.

Larger fracture apertures provide more ample physical space for microbial metabolic activity and calcium carbonate precipitation, facilitating both efficient urease-catalyzed urea hydrolysis [117] and favourable conditions for crystal growth and deposition. This prevents premature pore throat clogging caused by crystal aggregation, accommodates greater volumes of bacterial suspension and cementation solution, prolongs contact time between microorganisms and reactive substrates, and sustains material supply for substantial calcium carbonate generation [118]. Conversely, when the fracture aperture falls below 0.5 mm, the confined space readily induces rapid accumulation of reaction-generated calcium carbonate, forming localized blockages that impede subsequent infiltration and diffusion of the bacterial suspension and cementation solution, thereby significantly compromising the overall sealing efficacy [119]. When the fracture width exceeds 2 mm, despite ample spatial availability, the bacterial suspension and cementation solution tend to rapidly decrease along the fracture network. Furthermore, calcium carbonate precipitates, lacking effective attachment sites, fail to adhere stably to geotechnical particle surfaces and predominantly exist as loosely aggregated crystals, resulting in substantially diminished sealing density and durability [120].

The influence of fracture surface roughness on MICP remediation efficacy has a dualistic nature [120,121]: moderate roughness provides abundant attachment sites for calcium carbonate crystals, promoting crystal deposition and bridging interactions. When the fracture roughness is 0.414 mm, the remediation rate reaches 27.06%. As the roughness increases to 0.873 mm, the remediation rate further improves to 33.55% [117]. However, excessive roughness tends to induce localized overdeposition of calcium carbonate, thereby compromising the overall uniformity of the remediation process and decreasing the effectiveness of the reinforcement. However, it is worth noting that the remediation capability of MICP technology with respect to fracture aperture is not fixed, but is governed by multifactor coupling, including bacterial type, injection method, and calcium source. For instance, the choice of bacterial strain directly influences the achievable repair width. Using agar-immobilized Bacillus megaterium, the maximum repairable aperture was increased to 0.66 mm, significantly outperforming the 0.29 mm achieved by the injection method [122]. This improvement can be attributed to the enhanced retention and localized activity of the immobilized bacterial carriers within wider fractures. Injection strategy also plays a critical role. By optimizing the injection flow rate, higher calcium carbonate retention can be achieved in larger-aperture fractures than in smaller-aperture ones [123], suggesting that flow dynamics can be tailored to overcome the challenges posed by increased fracture width. Furthermore, a three-stage grouting strategy achieved a high bridging rate of 89.5% in meter-long fractures [124], demonstrating that multi-step injection protocols can substantially extend the effective repair scale.

These findings collectively indicate that the capability of MICP technology to remediate wide fractures still holds considerable potential for improvement through process innovation. Future efforts may focus on synergistic optimization of bacterial carriers, grouting procedures, and calcium source chemistry to further expand the applicable fracture aperture range and enhance remediation reliability in field-scale applications.

3.6. Grouting Method

An appropriate injection strategy is critically important for the efficacy of microbially mediated rock fracture reinforcement, as it directly governs the penetration depth of the bacterial suspension and cementation solution within fractures, the uniformity of their distribution, and the degree of contact with geotechnical particles, thereby determining both the efficiency of calcium carbonate precipitation and the ultimate remediation strength [125]. The bacterial suspension and cementation solution are mixed and then injected into the

fractured rock mass in a single step. This method is simple to operate and allows for rapid construction, and was widely adopted in early MICP studies. However, injecting a mixture of high-concentration bacterial suspension and cementation solution in a single step leads to rapid calcium carbonate precipitation near the injection port, forming a "filter cake effect" that hinders the further penetration of subsequent slurry into deeper zones. This issue directly results in a highly uneven distribution of calcium carbonate within the solidified body, with precipitation accumulating near the injection port while almost no reinforcement effect is observed at the distal end [21]. Therefore, this method is only suitable for shallow reinforcement or scenarios with large fracture apertures (>2 mm), and its effectiveness in repairing deep micro-fractures is limited. Currently, the most mature grouting process in both laboratory research and field applications is the staged injection method [126]. The "two-phase cementation process" effectively delays the rapid reaction that occurs upon contact between the bacterial suspension and cementation solution, significantly alleviates clogging at the injection port, and improves the penetration of the slurry into sand columns. However, this method still suffers from a relatively long treatment cycle. For wide fractures (>2 mm), the bacterial suspension is prone to loss, necessitating the use of filling materials [127]. Comparative studies have shown that, compared with single-step high-concentration injection, the use of low-concentration multiple injections achieves a more uniform distribution of calcium carbonate within sand columns, resulting in larger crystal sizes and a denser cementation structure [71]. After six repeated treatments with low-concentration cementation solution, the unconfined compressive strength of the treated specimen increased by approximately 2.3 times, while the coefficient of variation of calcium carbonate distribution decreased by over 60% [64]. Although this approach requires multiple grouting rounds in practical engineering, leading to higher time costs, it is suitable for projects requiring high uniformity of reinforcement and for environmentally sensitive areas.

Different injection strategies significantly influence the reinforcement efficacy of MICP in fractured rock masses. The injection approach strongly affects mineralization uniformity, sealing effectiveness, and mechanical performance during remediation, as shown in Table 3. Various injection strategies are suited to different application scenarios: the mixing method improves the distribution uniformity of calcium carbonate, the spraying method facilitates the formation of fine crystals, and the injection method achieves better reinforcement efficacy through flow rate control. Techniques such as direct grouting, grouting after filling, immersion, brushing, mixing, and the two-phase cementation process are applicable to different fracture characteristics and geotechnical conditions. In consideration of the specific properties of rock fractures, appropriate grouting techniques should be selected accordingly: fractures with widths less than 0.5 mm can be effectively sealed using direct grouting, whereas fractures with larger apertures require preliminary filling with fine sand or similar media before grouting treatment [125]. Under equivalent microbial treatment cycles, specimens reinforced by the mixing method and the grouting method show minimal differences in calcium carbonate content; however, specimens treated by the mixing method exhibit better uniformity in the distribution of precipitated calcium carbonate [128].

Research on the number of immersion cycles indicates that compared with those receiving fewer treatment cycles, specimens subjected to multiple immersion treatments exhibit significantly higher compressive strength [129]. Comparative experimental analysis using immersion, spraying, and brushing methods revealed distinct differences in the formation characteristics of calcium carbonate crystals under different application techniques [130]. In the samples treated by the spraying method, the nucleation function of the microorganisms was effective, resulting in uniformly distributed calcium carbonate precipitate particles on the surface of the solidified samples. In terms of crystal morphology

and dimensions, the immersion method generated irregular spheroidal calcium carbonate crystals with relatively large sizes; the spraying method produced relatively small crystals (with a mean diameter of approximately 10 μm), whereas the brushing method yielded the smallest crystals, which were predominantly concentrated in the surface layer of the samples. In studies on calcareous sand solidification, the spraying method has been shown to effectively promote calcium carbonate crystal formation between desert soil particles [131]. Furthermore, experiments using the mixing method for calcareous sand solidification and fracture remediation systematically analysed its one-dimensional consolidation characteristics, revealing that microbially mineralized calcareous sand exhibited significantly reduced permeability and effectively enhanced structural stability [132].

Table 3. Effects of Perfusion-related Factors on the Microbial Reinforcement Performance of Rock Fractures.

Influence Dimension	Specific Grouting Method	Conditions	Impact on Reinforcement Effect	Ref.
Classification of grouting methods	Stirring method	Universal	Excellent distribution uniformity of calcium carbonate	[128]
	Spraying method	Universal	Bacteria play a nucleation role, small crystal size, can promote the formation of calcareous sand crystals	[130,131]
	Injection method	Universal	The smaller the slurry flow rate, the longer the solidification time, but the better the reinforcement effect	[133]
	Perfusion method—direct grouting method	Plugging of rock fractures with width less than 0.5 mm	Can realize fracture plugging, the specific calcium carbonate content, distribution, etc., are not clearly mentioned	[127]
	Perfusion method—grouting after filling method	Reinforcement of rock fractures with larger width	Need to fill with fine sand and other media first, then grout, can realize fracture plugging	[127]
	Immersion method	Universal, focusing on plugging effect and crystal morphology	Large crystal size (irregular spherical), excellent plugging effect, higher compressive strength with multiple immersions	[129,130,134]
	Brushing method	Universal	The generated calcium carbonate crystals are small in size and basically concentrated on the surface of the specimen	[130]
	Mixing method	Calcareous sand solidification scenario	The permeability of solidified calcareous sand is significantly reduced	[132]
	Two-phase cementation process (grout bacterial liquid first, then cementing liquid)	Solve the blockage problem in the solidification of sand by *Sporosarcina pasteurii*	Alleviate grouting port blockage and improve penetration effect	[23]

The flow rate of the grouting solution during injection critically influences the reinforcement efficacy of MICP technology, an effect particularly pronounced in the strength anisotropy resulting from heterogeneous calcium carbonate distribution. Experiments on sand solidification using the injection method revealed that lower flow rates extend the duration required for solidification but yield superior reinforcement outcomes [133]. Comparative investigations on rock fracture reinforcement demonstrated that all the samples treated with different injection methods exhibited macroscopically visible calcium carbonate precipitates, indicating that fracture filling occurred. Notably, specimens treated by peristaltic pump injection, characterized by slower flow rates, displayed smoother surfaces

with relatively limited calcium carbonate attachment and fracture filling, accompanied by finer precipitate particles. In contrast, specimens subjected to immersion grouting exhibited rougher surfaces because of substantial precipitate attachment, with abundant interfracture precipitates aggregating into cohesive clusters, thereby achieving superior sealing effectiveness [134].

Laboratory investigations into the factors influencing microbial mineralization have further elucidated [96] that when the grout flow rate falls below 0.042 (mol/L)/h, the MICP efficiency in a closed system can reach 100%. Conversely, if the flow rate is excessively high, the urea hydrolysis rate fails to match the grout flow velocity, resulting in diminished solidification efficiency. Furthermore, within the optimal flow rate range, the medium concentration does not significantly influence the total calcium carbonate precipitation but significantly alters its distribution characteristics, with lower concentration conditions favouring a more uniform distribution of calcium carbonate precipitates.

3.7. Admixtures

The introduction of various admixtures into the microbially induced calcium carbonate precipitation (MICP) reaction system constitutes a pivotal strategy for enhancing the efficiency of microbial reinforcement technologies. Different exogenous materials optimize the reinforcement effect by modulating the reaction environment, microbial activity, or product characteristics. However, the dosage and underlying mechanisms of these admixtures require precise control.

(1) Sodium Silicate

When geotechnical fractures are remediated, the incorporation of sodium silicate into the cementation solution significantly enhances the effectiveness of MICP treatment. Sodium silicate rapidly adjusts the pH of the cementation solution to form a weakly alkaline environment, thereby improving the activity of functional bacteria such as *Sporosarcina pasteurii*, promoting efficient urea hydrolysis, and consequently increasing calcium carbonate yield while accelerating the precipitation rate [135]. The morphological characteristics of geotechnical fractures after the addition of sodium silicate reveal the formation of amorphous porous layered materials that fill the microvoids within the fractures and establish bridging connections between the rock particles and calcium carbonate crystals [136]. This promotes the formation of a continuous spatial network cementation structure, improving the fracture sealing density and rock mass integrity and thereby enhancing the mechanical strength of the remediated rock mass. Stringent control of the sodium silicate dosage is needed, with its addition not exceeding 0.3%; excessive dosage leads to excessively rapid calcium carbonate formation, inducing hardening and clogging at the injection port, as well as heterogeneous distribution of precipitates, thereby reducing the overall load-bearing capacity of the rock mass [136].

(2) Ferric Chloride

The incorporation of ferric chloride solution into the cementation solution indirectly enhances the reinforcement efficacy by reducing the number of grouting cycles [137]. The addition of ferric chloride lowers the pH of the cementation solution, which, although delaying the rate of calcium carbonate precipitation, enables more uniform diffusion and penetration of the cementation solution through soil fractures and pores, effectively mitigating localized clogging at the injection port. As shown in Figure 20, which presents the morphological characteristics of calcium carbonate crystals before and after the addition of ferric chloride, calcium carbonate and ferric hydroxide coprecipitate simultaneously at the sand particle interface, forming a continuous cementitious bonding layer that substantially enhances the overall mechanical strength of the sand column samples. Furthermore,

https://doi.org/10.3390/coatings16040413

iron ions exert significant regulatory effects on the crystal morphology of calcium carbonate [138]: with increasing iron ion concentration, the formation of flat calcium carbonate is readily induced. This morphological variant densely fills the interstitial spaces within the soil matrix, significantly improving the impermeability of the treated soil. However, excessive iron ions reduce the pH of the cementation solution below the optimal range for bacterial activity, suppressing the metabolic function of *Sporosarcina pasteurii* and ultimately diminishing calcium carbonate yield, thereby compromising the effectiveness of the reinforcement.

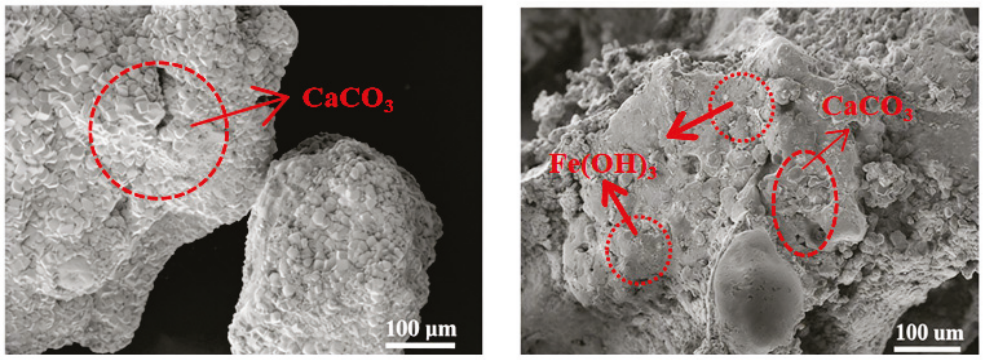

Figure 20. Morphological characteristics of calcium carbonate crystals before and after ferric chloride addition. (Reprinted from Zhu et al., PLoS One, 2025, 20(7), e0327568, Figure 9 [137]).

(3) Carbonic Anhydrase

Carbonic anhydrase (CA), a functional biological enzyme secreted by CA-producing bacteria, enhances the MICP reaction in geotechnical fracture remediation. As shown in Figure 21, which presents a schematic diagram of calcium carbonate generation via the synergistic induction of urease and carbonic anhydrase, carbonic anhydrase accelerates CO_2 hydration and increases carbonate ion production, thereby promoting calcium ion deposition to form calcium carbonate while simultaneously achieving carbon dioxide fixation and environmentally beneficial carbon sequestration [139]. To address the issue where Ca^{2+} concentrations in the cementation solution exceeding 1.25 mol/L inhibit urease activity and reduce calcium carbonate yield, the addition of carbonic anhydrase alleviates this inhibition and accelerates ionic binding, thereby improving mineralization efficiency [140]. When it is combined with urease, carbonic anhydrase rapidly increases the strength of remediated samples, and its dosage is positively correlated with both the rate and amount of calcium carbonate generation within a certain range [141]. The application of carbonic anhydrase in microbially mediated geotechnical fracture remediation optimizes the efficiency and uniformity of calcium carbonate deposition within fractures, mitigates the limitations of conventional MICP reactions under high calcium concentrations, and achieves efficient and environmentally sustainable fracture remediation.

(4) Fly Ash

When MICP technology is employed for geotechnical fracture remediation, the addition of fly ash to the cementation solution enhances the unconfined compressive strength of the treated geotechnical mass while reducing its permeability coefficient [142]. The incorporation of fly ash not only provides nucleation sites for bacteria to participate in the mineralization reaction but also increases the immobilization rate of bacterial cells. This enables a greater number of bacteria to participate in the MICP process, thereby increasing the yield of calcium carbonate [143]. Furthermore, fly ash adsorbs the ammonia generated during the MICP reaction, achieving an ammonia nitrogen removal efficiency of up to

62.6% [144]. Silicon and aluminum components within fly ash are solubilized under alkaline conditions and react with calcium ions in the solution to form cementitious materials such as calcium silicate hydrate (C-S-H) and calcium aluminosilicate hydrate. These gel-like substances, together with the precipitated calcium carbonate crystals, collectively fill the interstitial voids between the sand and gravel particles [145]. At an optimal dosage of 7%, the compressive strength of MICP-solidified sand is increased by a factor of 2.6 [144]. Conversely, excessive fly ash content can clog rock fractures, thereby reducing the overall efficiency of the MICP remediation process.

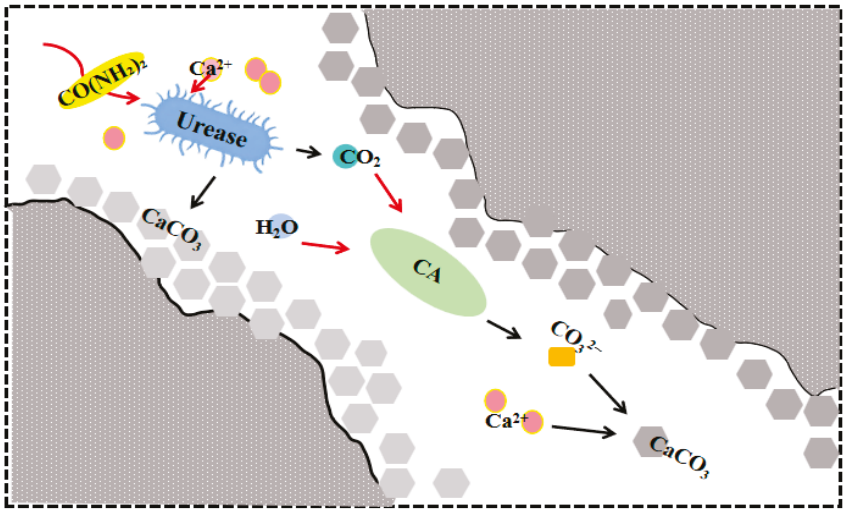

Figure 21. Schematic Diagram of Calcium Carbonate Production Induced by the Synergistic Effects of Urease and Carbonic Anhydrase.

(5) Jute Fibre

The incorporation of jute fibres into the cementation solution during preparation significantly enhances both the compressive strength and the tensile strength of the remediated geotechnical mass. The inherently rough surface of jute fibres provides an increased surface area for microbial adhesion and colonization, thereby sustaining bacterial growth and consequently enhancing urease activity [146]. As shown in Figure 22, which presents a schematic diagram of geotechnical particle cementation following the addition of jute fibres, the inclusion of jute fibres improves microbial viability, enabling enhanced mineralization and the formation of dense calcium carbonate crystals, thereby increasing the overall strength of the geotechnical mass [147]. With increasing fibre content, the unconfined compressive strength of the remediated rock mass correspondingly increases, indicating a positive correlation between the jute fibre content and the compressive strength of the treated geotechnical mass within a certain range. Research has indicated [146,148] that the optimal jute fibre content is 3%, with an optimal fibre length of 15–20 mm. When the quantity and length of incorporated jute fibres exceed these optimal levels, fibres tend to entangle during the fracture remediation process, thereby impeding bacterial access to interstitial spaces between sand particles, reducing the available habitat for microorganisms, and consequently diminishing calcium carbonate production [149].

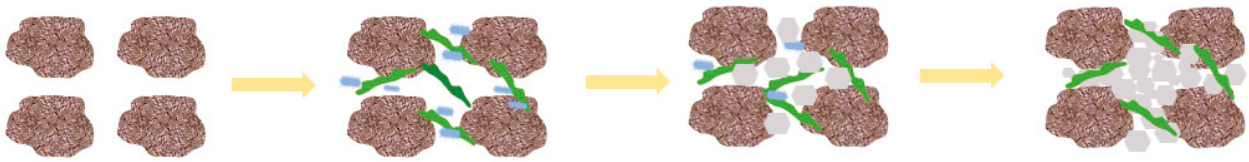

Figure 22. Schematic diagram of cementing geotechnical particles after the addition of jute fibres.

Furthermore, synergistic solidification technology combining nanosilica with MICP has been demonstrated as a green, low-carbon, and highly efficient approach suitable for enhancing silt [150–154]. Compared with the MICP treatment alone, the porous structure of the biochar adsorbs urea and calcium ions, enabling the slow release of these compounds from the substrate and resulting in enhanced heavy metal immobilization rates [155]. Polyacrylamide (PAM) increases calcium carbonate yield and calcium ion utilization efficiency, thickens the hardened surface layer, and improves both penetration resistance and water stability [156]. In summary, the selection of exogenous materials for incorporation into the MICP reaction system necessitates comprehensive consideration of the target soil type, engineering requirements, and environmental conditions. Through precise control of the dosage and optimization of compounding strategies, a balance among reaction efficiency, reinforcement effectiveness, and engineering efficiency can be achieved. Future research directions will likely emphasize the development of multimaterial synergistic formulations and functionalized admixtures as important pathways for enhancing the application potential of MICP technology.

3.8. Coupling Effects of Multiple Factors

In engineering practice, factors such as temperature, pH, calcium source concentration, and injection strategy do not operate independently; rather, they exhibit multiple types of coupling effects that directly influence the regulatory precision of MICP mineralization outcomes.

(1) Biochemical Coupling Effect

This is primarily manifested as the antagonistic effect between the "cementation solution concentration and pH" and the synergistic effect between the "calcium source type and microbial activity" [157]. For instance, when the concentration of calcium chloride exceeds 1.0 mol/L, the ambient pH rapidly increases to above 9.5, thereby inhibiting urease activity. Under such conditions, even increasing the urea concentration does not improve mineralization efficiency [158]. In contrast, when calcium acetate is employed as the calcium source, the acetate ions generated from its hydrolysis exert a buffering effect on the pH, enabling microorganisms to maintain relatively high activity even at calcium source concentrations up to 1.5 mol/L. This finding demonstrates the synergistic protective mechanism between calcium source type and microbial activity [159]. To address these coupling effects in engineering practice, a combined strategy of "gradient regulation of calcium source concentration coupled with pH buffering" can be adopted: for strongly alkaline calcium sources such as calcium chloride, the concentration should be controlled within 1.0 mol/L, supplemented with 0.05 mol/L phosphate buffer solution to stabilize the reaction environment [23]; for weakly alkaline calcium sources such as calcium acetate, the concentration can be appropriately increased to 1.2–1.5 mol/L without the need for additional buffering agents [159].

(2) Physical–biological Coupling Effect

This is manifested primarily as synergistic effects between "temperature and injection efficiency" and between "fracture roughness and the microbial retention rate". For example, under low-temperature conditions (<10 °C), the viscosity of the bacterial suspension increases, leading to reduced grout penetration depth, whereas microbial metabolic rates concurrently slow, resulting in significantly diminished mineralization efficiency [160]. However, when the rock fracture roughness exceeds 50 μm, the microbial retention rate increases by more than 40%, which can partially offset the inhibitory effect of low temperature on metabolic activity. This finding demonstrates the compensatory role of "fracture roughness–microbial retention" coupling in low-temperature environments [161]. To ad-

https://doi.org/10.3390/coatings16040413

dress these coupling effects in engineering practice, a strategy of "environmental adaptation coupled with process optimization" can be employed: under low-temperature conditions, water-reducing agents are added to the bacterial suspension to reduce viscosity, while the injection pressure is increased to 0.3–0.5 MPa [126,162]. For fractured rock masses with smooth surfaces, sandblasting can be applied to increase surface roughness, or surfactants can be incorporated into the bacterial suspension to increase microbial retention rates [163].

(3) Physical–chemical–biological Coupling Effect

This represents the most complex type of coupling in engineering practice, characterized by three-dimensional interactions among "temperature, pH value, and calcium source concentration". For instance, under high-temperature conditions (>40 °C), urease is susceptible to thermal denaturation. If calcium chloride is employed as the calcium source under such conditions, the resulting increase in pH further exacerbates urease inactivation [23]. Conversely, when calcium nitrate is used as the calcium source in conjunction with denitrifying bacteria, mineralization can be achieved under neutral pH conditions (7.0–7.5), thereby avoiding the dual inhibitory effects of high-temperature and alkaline environments [164]. To address this coupling effect, the establishment of a "multifactor response model" is necessary, enabling the selection of appropriate bacterial strains, calcium sources, and injection processes on the basis of site-specific temperature conditions and fracture characteristics [165]. For example, in open-pit high-temperature slope engineering, denitrification-mediated mineralization is preferentially selected, employing calcium nitrate as the calcium source and vacuum injection processes [166]. For underground low-temperature cavern engineering, *Sporosarcina pasteurii* is preferentially selected, employing calcium chloride supplemented with phosphate-buffered solution and pressure injection processes [23].

Microbially induced calcium carbonate precipitation (MICP) technology represents an environmentally friendly and sustainable approach for the reinforcement and remediation of geotechnical fractures. The remediation efficacy of this technology is contingent upon the interplay of multiple factors, including bacterial strain characteristics, environmental conditions, and substrate parameters, rather than being dominated by any single variable. These factors collectively govern the yield, crystal morphology, distribution, and cementation quality of calcium carbonate precipitates, thereby ultimately determining the mechanical properties and durability of the fractured rock mass after remediation.

4. Engineering Applications of MICP in Rock Fracture Repair

The low viscosity and excellent fluidity of the bacterial suspension and cementation solution enable effective infiltration and filling of micropores and fractures within geotechnical masses under gravitational seepage or low-pressure grouting conditions, achieving nondestructive reinforcement of in situ soil. This constitutes a critical advantage of MICP technology for in situ soil improvement [167]. Consequently, this approach enhances the mechanical properties and overall stability of the treated soil, thereby improving the strength, stability, and impermeability of foundations, slopes, dams, and other geotechnical structures.

4.1. Microbial Reinforcement of Fractured Rock

Under the action of microbial mineralization, the fracture-filled regions exhibit pronounced integrity, and the compressive strength of the treated samples is significantly enhanced [65]. A remediation approach that uses loose materials such as sand as microbial carriers for filling geotechnical fractures rationally utilizes the cementation effect of biobinders. The pores and particles within the sand matrix provide sufficient space and nucleation sites for the precipitation of mineralization products. Untreated loose sand

https://doi.org/10.3390/coatings16040413

(particle size 0.1–0.5 mm) typically exhibits a compressive strength below 0.5 MPa [168,169]. Following MICP treatment, calcium carbonate precipitates fill the interparticle pores within the sand, transforming loose particles into an integrated structure, with the compressive strength increasing to 2–10 MPa depending on the treatment process employed [170,171]. It has been widely reported in the literature [172,173] that the cementitious structure formed by calcium carbonate precipitates between particles constitutes the key mechanism for soil strength enhancement. The correlation between the unconfined compressive strength and the corresponding calcium carbonate content in solidified sand, as reported by different research teams [174–178], is shown in Figure 23. The data presented in the figure reveal a significant positive correlation between the unconfined compressive strength of solidified sand and calcium carbonate content [179]. Notably, the increase in calcium carbonate content strongly strengthened the unconfined compressive strength of the soil, indicating that the calcium carbonate content directly governs the mechanical properties of the remediated geotechnical mass.

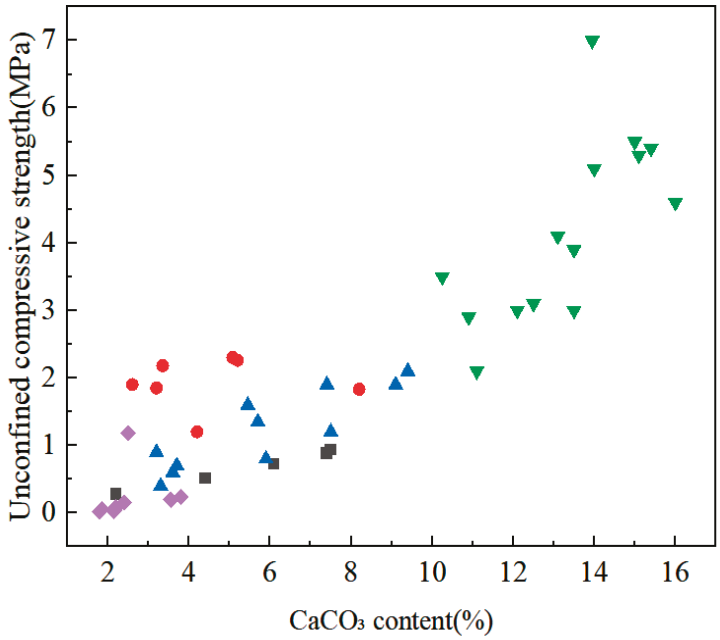

Figure 23. Relationship between the unconfined compressive strength and calcium carbonate content of the MICP-treated sand: black [174], red [175], blue [176], green [177], purple [178].

In addition to enhancing compressive strength, microbial mineralization technology significantly improves the tensile strength of geotechnical masses [180]. With a cementation solution concentration of 1.0 mol/L [181], the tensile strength of the treated soil markedly increased. Following MICP treatment, the geotechnical mass exhibits residual strength even after experiencing compressive or shear failure. Compared with untreated loose sand, MICP-cemented sand demonstrates a substantially enhanced capacity to retain strength after failure, indicating a significant improvement in residual strength [182]. To address the apparent brittle failure observed in MICP-treated geotechnical materials, research has confirmed that the combination of fibre reinforcement technology with microbial mineralization soil consolidation significantly enhances the tensile strength of treated soil. Fibres bridge particles, span fractures, and provide attachment sites for calcium carbonate crystals, thereby forming a reinforced structure [183]. This combination effectively mitigates the brittle behavior of solidified soil and significantly enhances its toughness [184].

https://doi.org/10.3390/coatings16040413

4.2. Impermeability of Microbially Repaired Fractured Rock Masses

In engineering application research on seepage control and crack remediation, the technical application scenarios have progressively expanded from traditional crack repair to the regulation and improvement of sand permeability. Numerous studies have confirmed that the continuous generation and accumulation of microbial metabolic byproducts within soil can effectively fill soil pores and play an auxiliary role in significantly reducing soil permeability. The integration of microbially induced mineralization technology with fractured rock and soil remediation not only achieves self-healing and long-term sealing of cracks but also improves the compactness and impermeability of the geotechnical mass at the microstructural level, providing a green and sustainable approach for seepage control and reinforcement in hydraulic engineering, subgrade construction, and slope engineering [185,186]. Research has demonstrated the dual efficacy of MICP technology in soil seepage control and dam protection: On the one hand, it can form a low-permeability layer in sandy soils; on the other hand, it can be employed for surface reinforcement of dams. Through dam model experiments [187], surface MICP solidification and crack remediation were achieved by spraying a bacterial suspension and nutrient solution. Flume tests revealed the formation of a 20–30 mm calcium carbonate protective layer on the model surface (with the surface 5 mm exhibiting a dense structure). Furthermore, specialized investigations into the effectiveness of seepage control of biological slurries in rock fractures [188] have demonstrated that MICP treatment resulted in reduced permeability of the samples, indicating significant antiseepage efficacy. Erosion tests conducted on fine sand after MICP solidification revealed that MICP technology significantly enhanced the scour resistance of fine sand. Further analysis indicated that the erosion resistance performance is closely correlated with the quantity of calcium carbonate generated within the system and the microstructural characteristics of the solidified matrix [189].

The performance data presented in Table 4 are primarily derived from studies using ureolytic bacteria (particularly Sporosarcina pasteurii), which currently represent the most mature and well-documented MICP pathway for engineering applications. For fractured rock masses, nuclear magnetic resonance testing has shown that after 42 days of treatment, the compressive strength of fractured yellow sandstone increased by 30.52%, impermeability improved by 94.62%, and porosity decreased by 36.41% [41]. Studies have demonstrated that the Darcy permeability coefficient of fractured rock can be reduced by three to four orders of magnitude following MICP grouting [115]. Using an enzyme-induced carbonate precipitation (EICP) combined with calcium acetate process, the peak load of fractured rock increased by 12.03 times after seven reinforcement cycles [75,190]. In granite fractures, excellent results were achieved, including a four-order-of-magnitude reduction in transmissivity, shear strength reaching 512–688 kPa, and a fracture filling rate of 85% [191].

Table 4. Summary of application effects and influencing factors of MICP technology for fractured rock mass reinforcement.

Application Scenario	Reinforcement Effect	Typical Data	Key Influencing Factors	Ref.
Fractured rock mass reinforcement	Compressive strength improvement	+30.52% (after 42 days of treatment)	Treatment duration, bacterial activity	[41,192]
	Impermeability improvement	+94.62%	Degree of pore filling	[41]
	Porosity reduction	–36.41%	Uniformity of calcium carbonate distribution	[193]
	Permeability coefficient reduction	3–4 orders of magnitude	Fracture aperture, confining pressure	[21,115]

Notable differences exist in the reinforcement effects of different microbial mineralization pathways, with their typical characteristics summarized as follows: Ureolytic bacteria: Most significant strength improvement [65], permeability reduction of three to four orders of magnitude [117]; suitable for most geotechnical fracture repair scenarios, but ammonia release remains a concern. Denitrifying bacteria: Slightly lower strength improvement than ureolytic bacteria, permeability reduction of approximately two orders of magnitude [38]; suitable for water-sensitive areas where ammonia nitrogen introduction is undesirable, but reaction rate is relatively slow. Sulfate-reducing bacteria: Moderate strength improvement; primarily applicable to sulfate-rich environments [29]. Methanotrophs and photosynthetic microorganisms: Relatively lower strength improvement but produce no toxic byproducts; suitable for shallow surface engineering or deep anaerobic environments [42,46].

4.3. Practical Engineering Applications of MICP

A CO_2 geological storage project in Montana, USA, targeted the sealing of fractures in a diorite formation at a depth of 340.8 m to prevent CO_2 leakage [194]. A "two-step" grouting strategy was adopted, in which bacterial suspension and cementation solution were injected alternately to promote calcium carbonate precipitation within the fractures. Complete fracture sealing was achieved within four days, effectively reducing the permeability of the formation and demonstrating the feasibility of MICP technology under deep geological conditions [195]. For micro-fractures smaller than 0.2 mm, which are difficult to treat with cement grout, a field grouting trial was conducted using a low-viscosity microbial slurry prepared with indigenous bacterial strains. A "multi-stage quantitative injection" process was employed to achieve effective slurry diffusion within the fractures. The slurry diffusion distance reached over 0.4 m, and the permeability of the rock mass after grouting was reduced to approximately 0.1 Lu, demonstrating a significant anti-seepage effect [196]. Against the engineering backdrop of seepage control in a large underground water-sealed oil storage cavern, a study on MICP sealing of micro-fractures in the rock mass was conducted (Figure 24). Using a self-designed visual fracture model test apparatus, the study revealed a "stepwise" decrease in fracture permeability and established the concept of a "critical fracture sealing threshold." Although this study was conducted as a detailed laboratory experiment, its engineering background was clearly defined, and its findings directly support seepage control requirements for underground energy storage facilities. In summary, based on the above field application examples, MICP technology for fractured rock mass reinforcement is currently in a critical transition stage from laboratory research to field application. Although several successful field trials have demonstrated the feasibility of the technology, large-scale application still faces challenges related to precipitation uniformity, long-term stability, and cost-effectiveness. Future research should further promote the integration of laboratory and field experiments, optimize grouting processes and bacterial strain performance, reduce engineering costs, and provide technical support for practical applications under complex geological conditions.

4.4. Current Status of MICP Technical Specifications and Standardization

As an emerging geotechnical remediation technology, MICP has not yet established dedicated national or international technical specifications specifically for the reinforcement of fractured rock masses. Nevertheless, with the advancement of research and the expansion of engineering applications, relevant standardization efforts have gradually been initiated.

https://doi.org/10.3390/coatings16040413

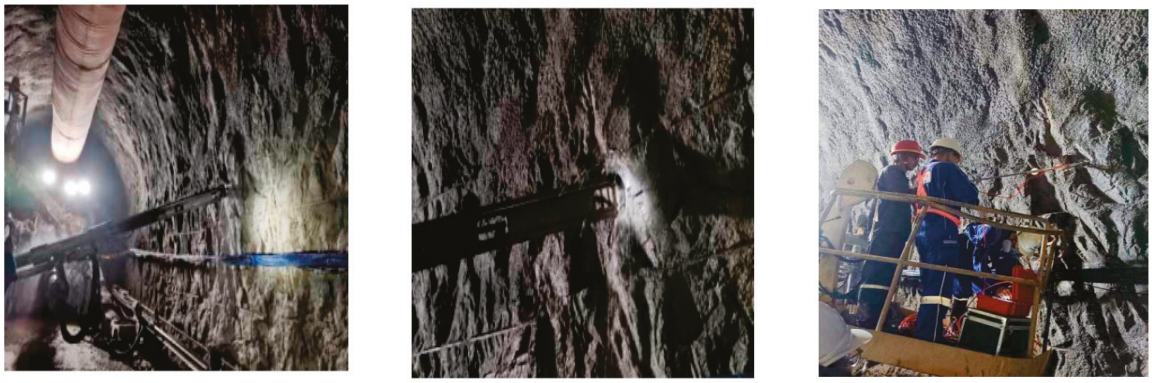

(**a**) Field borehole grouting operation



(**b**) White calcium carbonate precipitates are clearly visible in the pores

Figure 24. Field observation of grouting sealing effect. (Reprinted from Liu QL, China University of Geosciences (Beijing), 2024, Figures 6–9, 6–10 and 6–21 [197]).

(1) International Specifications and Guidelines

At the international level, ASTM International issued ASTM D8260-20 [198], Standard Test Method for Microbial Calcite Precipitation in Soil Specimens, in 2020. This standard represents the most directly relevant testing standard for MICP currently available, specifying experimental procedures for microbially induced calcite precipitation in soil specimens, encompassing aspects such as bacterial solution preparation, grouting processes, and strength testing. It provides a unified testing framework for laboratory-scale investigations of MICP technology.

The International Organization for Standardization (ISO) published ISO/TR 23262:2021, Geotechnics—Use of microorganisms in soil improvement—Technical report, in 2021 [199]. This technical report systematically summarizes the current state of application, underlying mechanisms, and engineering considerations pertaining to the use of microorganisms in soil improvement, serving as a foundational document for the standardization of MICP technology and providing technical support for the subsequent development of formal standards. Additionally, the Federal Highway Administration (FHWA) of the United States released Bio-mediated Soil Improvement: A Review of Recent Advances and Applications in 2016 [200], which offers technical guidance for the application of MICP technology in highway engineering, covering aspects such as material selection, construction processes, and quality control.

(2) Analysis and Outlook of Standardization Status

Standardization efforts for MICP technology remain in their nascent stages and face the following principal challenges:

I. Diversity of bacterial strains and processes: The substantial influence exerted by different bacterial strains (e.g., *Sporosarcina pasteurii*, *Bacillus sphaericus*), grouting processes (e.g., one-phase method, two-phase method, staged injection), and material formulations on reinforcement performance renders the unification of technical parameters challenging.
II. Lack of long-term performance evaluation systems: Unified evaluation methodologies and acceptance criteria for long-term durability, freeze–thaw resistance, aging resistance, and chemical erosion resistance of MICP-reinforced materials remain absent.
III. Environmental impact assessment standards: Byproducts such as ammonia released from ureolytic MICP and nitrite potentially generated from denitrification-based MICP necessitate the establishment of clear environmental control standards and emission limits.
IV. Field quality control methods: Rapid and effective detection methods for real-time monitoring of bacterial activity, calcium carbonate production, and reinforcement effectiveness during field construction are currently lacking.

4.5. Current Commercialization Status of MICP Technology

According to the Global Bio Cement Market Report published by HTF Market Intelligence, MICP-related technologies are experiencing rapid market growth in the fields of geotechnical engineering and infrastructure repair. The market size for related applications was approximately USD 198 million in 2024 and is projected to reach USD 1.34 billion by 2033, growing at a compound annual growth rate (CAGR) of 23.7% [201]. BioCement Technologies (Netherlands): Provides MICP-based soil stabilization solutions primarily for foundation reinforcement, slope stabilization, and erosion control. The underlying technical principles are also applicable to the filling and cementation of rock fractures. StoneBio (UK): Develops MICP-based bio-remediation materials focused on the restoration and conservation of historical buildings and stone cultural heritage, filling stone cracks and surface damage through induced calcium carbonate precipitation. Halliburton (USA): A globally leading oilfield service company that applies MICP technology for fracture sealing in oil and gas wellbores and for lost circulation control, representing a typical industrial application of MICP technology in deep rock fracture repair. BASF SE (Germany): A global chemical giant currently expanding into bio-based construction materials, with MICP-related products being one of its research and development directions, with potential applications including concrete crack repair and geotechnical reinforcement.

MICP technology has transitioned from laboratory research to engineering applications, with the global related market experiencing rapid growth. The aforementioned companies have launched mature products in their respective niche areas and have successfully applied them in practical engineering projects. Particularly in fields such as crack repair in hydraulic tunnels and dams, rock fracture reinforcement on slopes, restoration of historical stone structures, and fracture sealing in oil and gas wellbores, MICP technology has demonstrated strong engineering applicability and environmental benefits. With ongoing cost optimization and the advancement of standardization efforts, MICP technology is expected to achieve large-scale application across a broader range of engineering scenarios, including rock fracture repair.

4.6. Cost Analysis of MICP Technology

The cost of MICP technology represents one of the main bottlenecks limiting its large-scale commercial application [202]. The cost of MICP technology mainly comprises three components: bacterial strain and culture medium expenses, grouting equipment

https://doi.org/10.3390/coatings16040413

and labor costs, and testing and acceptance fees [98]. From a material perspective, the cost of preparing a 1 mol/L cementation solution (equimolar concentrations of urea and calcium chloride) in the laboratory is approximately RMB 7.0–8.0 per liter, of which bacterial culture medium accounts for 50%–80% [203,204]. Notably, the cultured bacterial strains can be reused, which helps to further reduce the process cost [205]. In practical engineering, material dosage and ratios must be adjusted according to variations in geological conditions and remediation objectives, leading to significant cost fluctuations [206].

Studies have shown that, excluding the time costs associated with microbial cultivation and grouting construction, the cost of microbial grouting engineering is only 55% of that of cement grouting [207]. However, when related costs such as bacterial solution preparation and specimen curing are taken into account, the overall cost of MICP technology is typically higher than that of conventional chemical grouting processes. To address this, researchers have conducted numerous optimization studies aimed at cost reduction and efficiency improvement. One important direction involves the use of industrial solid waste as a substitute for conventional reagents to serve as low-cost nutrient substrates and calcium sources [208,209]. In addition to optimizing material costs, enhancing mineralization efficiency is key to reducing overall costs. By introducing specific additives (e.g., organic polymers, inorganic ions, or bioactive substances) into the MICP reaction system, urease activity can be effectively enhanced, additional nucleation sites can be provided, and calcium carbonate crystal growth can be regulated, thereby significantly improving mineralization rates and product stability [210,211]. Concurrently, researchers have employed genetic engineering and synthetic biology approaches to directionally modify functional strains. For example, heterologous expression of a highly efficient urease gene cluster in Bacillus subtilis has successfully yielded engineered strains with substantially improved mineralization efficiency [212]. Furthermore, the application of non-destructive monitoring techniques such as ultrasound, X-ray computed tomography, and electrical resistivity tomography enables real-time dynamic monitoring of the grouting and sealing process, allowing timely adjustments to grouting strategies, ensuring uniformity of calcium carbonate deposition, and effectively reducing waste of materials and construction resources.

5. Current Challenges and Future Research Directions

5.1. Current Challenges

Although MICP technology exhibits broad application prospects in the field of fractured rock mass reinforcement, existing processes still face challenges related to byproduct generation, reinforcement uniformity, and long-term durability. Considering the characteristics of different microbial mineralization pathways, future research should focus on the following directions:

(1) Spatial distribution heterogeneity and long-term stability of mineralized products

When MICP technology is applied to fractured rock mass reinforcement, the complex and irregular geometry of fractures significantly restricts the seepage and diffusion of reaction solutions, leading to uneven distribution of calcium carbonate precipitation within the fracture space. This heterogeneous deposition can easily cause localized sealing failure, ultimately compromising the overall structural strength and stability of the rock mass [213]. Moreover, fractured rock masses reinforced by MICP are subjected to complex environmental conditions during service, including wetting–drying cycles, freeze–thaw cycles, acid rain erosion, and long-term loading [214]. Currently, research on the long-term durability of MICP-reinforced rock masses remains severely insufficient, representing a critical bottleneck limiting the application of this technology. Existing studies have demonstrated that optimized grouting processes—such as staged injection and low-concentration repeated treatment—can effectively improve the distribution of reaction solutions within

https://doi.org/10.3390/coatings16040413

fractures and enhance the uniformity of calcium carbonate precipitation [64,109]. However, research on the long-term performance of calcium carbonate precipitates remains limited, particularly regarding resistance to dissolution and erosion under conditions of water scouring, freeze–thaw cycles, and acidic environments.

(2) Adaptability of functional strains to extreme geological environments

Fractured rock masses are often situated in extreme geological environments, including deep subsurface, anaerobic conditions, high or low temperatures, and acidic or alkaline settings. However, the functional strains currently used in mainstream applications have stringent environmental requirements and suffer from issues such as poor environmental adaptability, rapid decline in metabolic activity, and significantly reduced mineralization efficiency, making them unsuitable for complex engineering scenarios [215]. Progress in screening indigenous stress-tolerant strains and engineering strain modification for extreme environments in fractured rock masses remains slow. A strain system that combines both high enzyme activity and strong environmental adaptability has yet to be established. Furthermore, in-depth research on the colonization, proliferation, and metabolic behavior of strains within the fracture microenvironment is lacking, limiting the application of MICP technology in complex fracture scenarios such as acidic, low-temperature, and deep subsurface environments.

(3) Control of harmful byproducts

The issue of byproducts represents a core controversy regarding the environmental friendliness of MICP technology and constitutes a critical bottleneck restricting its application in environmentally sensitive areas. Significant differences exist in the types and emission intensities of byproducts among different mineralization pathways: ammonia emissions from ureolytic MICP, N_2O and nitrite accumulation from denitrification-based MICP, and H_2S release from sulfate-reducing MICP all require targeted management. Future research should focus on [216,217]: low-cost, high-efficiency in situ byproduct immobilization technologies (e.g., the MISP method); the optimization and application of novel bacterial strains with no ammonia or greenhouse gas emissions; and the establishment of monitoring and evaluation systems for the long-term environmental behavior of byproducts.

5.2. Future Research Directions

Although MICP technology demonstrates broad application prospects in the field of fractured rock mass reinforcement, existing processes still face challenges such as byproduct generation, reinforcement uniformity, and long-term durability. Considering the characteristics of different microbial mineralization pathways, future research should focus on the following directions:

(1) Ureolytic MICP: This pathway offers high mineralization efficiency and is the most mature in terms of application; however, the issue of ammonia release urgently needs to be addressed. Future research could explore low-cost ammonia recovery technologies, develop modified strains with low ammonia emissions, or adopt plant-derived urease (EICP) as an alternative. In addition, optimization of grouting processes (e.g., low-concentration multiple injections) and the development of novel admixtures (e.g., sodium silicate, ferric chloride) can help improve the uniformity of calcium carbonate distribution.

(2) Denitrification-based MICP: This pathway does not require exogenous urea and is suitable for sensitive water areas where ammonia nitrogen introduction is undesirable. However, it suffers from a relatively slow reaction rate and may produce intermediates such as nitrite. Future research should focus on precise regulation of reaction condi-

tions to avoid intermediate accumulation, while exploring synergistic applications with ureolytic bacteria to achieve complementary advantages.

(3) Sulfate-reducing MICP: This pathway is suitable for sulfate-rich environments (e.g., marine environments, tailings dams). However, the generation of hydrogen sulfide poses a threat to construction safety. Future research should develop safe and reliable hydrogen sulfide capture and treatment systems, and explore its application potential in extreme environments such as deep sea and deep subsurface.

(4) Methanotrophs and photosynthetic microorganisms: Both pathways produce no toxic byproducts and offer the best environmental friendliness, but their reaction rates are relatively slow. Methanotrophs are suitable for deep anaerobic environments (e.g., underground caverns, oil/gas wellbores) and can provide the added benefit of methane emission reduction. Photosynthetic microorganisms are suitable for shallow surface engineering (e.g., desert solidification, dust control). Future research should aim to improve their mineralization efficiency through strain acclimatization and optimization of light conditions.

(5) Synthetic biology-engineered bacteria: Our research team has constructed a carbonic anhydrase heterologously expressed engineered bacterium (CA-HEEB) based on synthetic biology approaches [218]. Figure 25 illustrates the preparation of CA-HEEB and its application process in bio-cementation of fractured rock masses. By heterologously expressing carbonic anhydrase, this strain achieves mineralization efficiency comparable to that of ureolytic bacteria without generating ammonia, while also possessing carbon dioxide fixation capability. Preliminary assessments in recycled aggregate concrete indicate a potential carbon emission reduction of 3.74%. This technology offers a new direction for the green development of MICP, although its engineering application data and long-term stability require further validation.

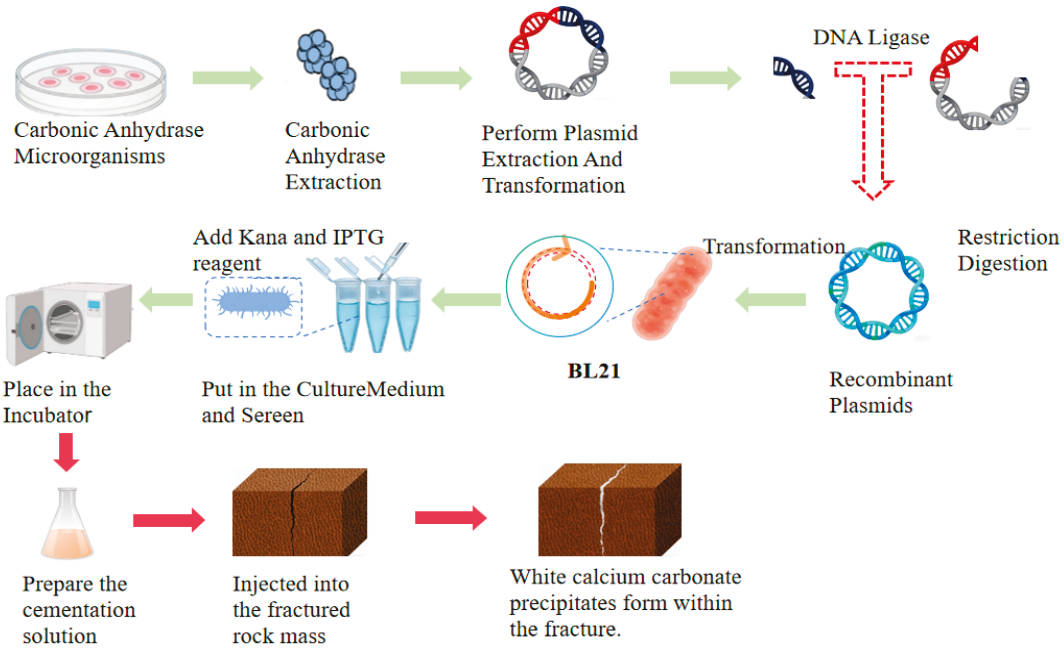

Figure 25. Schematic diagram of the preparation of CA-HEEB and its application in bio-cementation of fractured rock masses. (Adapted from Li JH, Cao FB, Yang QF, et al. 2025, Construction and Building Materials, 490: 142425; Figure 4 [218]).

In summary, future development of MICP technology should adopt a pathway-specific approach, selecting the most suitable microbial pathway according to the specific engineering scenario, and advancing technological maturity through interdisciplinary integration

(microbiology, materials science, geotechnical engineering). Meanwhile, closer integration of laboratory and field studies should be promoted to accelerate the transition of the technology from laboratory research to engineering applications.

6. Conclusions

This paper provides a systematic analysis of the microbial mineralization mechanism, the influence of various factors on mineralization reactions, and the engineering applications of MICP technology. The following conclusions are drawn:

(1) Compared with traditional rock fracture remediation methods, MICP technology offers the advantage of self-healing, eliminating the need for repeated manual intervention. By leveraging microbial metabolism, it continuously facilitates fracture remediation, achieving long-term repair. Furthermore, when new cracks develop in the same area, the microorganisms can be reactivated by external environmental stimuli and perform secondary crack repair through their inherent mineralization activity.

(2) Among the various microbial mineralization pathways, the ureolytic pathway exhibits high environmental adaptability and mineralization efficiency, making it the most widely applied approach; however, it requires exogenous nutrients and generates ammonia as a byproduct. Pathways such as denitrification and sulfate reduction offer application value under specific environmental conditions but are limited by slow reaction rates or the production of toxic byproducts, respectively. In recent years, a carbonic anhydrase-engineered bacterium (CA-HEEB) constructed based on synthetic biology has achieved mineralization under ammonia-free conditions while also possessing carbon fixation capability, offering a new direction for MICP technology; however, its engineering application data still require further validation. Overall, each pathway has its own characteristics, and the selection in practical applications should be based on a comprehensive consideration of engineering scenarios and environmental requirements.

(3) The mineralization efficacy of MICP is governed by a synergistic regulatory mechanism involving "single-factor and multifactor coupling". Individual factors—including bacterial strain characteristics, temperature, pH, calcium source type and concentration, fracture characteristics, and injection methods—directly influence the quantity and crystalline quality of calcium carbonate precipitates. However, multifactor coupling effects, such as "biochemical" and "physical–biological" interactions, are more decisive for engineering applications and require precise control through parameter optimization.

(4) The engineering application of MICP technology necessitates the selection of suitable functional bacterial strains on a project scale and under site-specific environmental conditions. Simultaneously, the reliability and stability of the remediation effect must be ensured through the optimization of admixture combinations and injection processes, thereby providing a foundation for large-scale implementation in scenarios such as slope reinforcement and dam seepage control.

Author Contributions: M.Y.: Writing—original draft, Investigation, Data curation. Z.Z.: Conceptualization, Methodology, Writing—original draft, Resources, Writing—review and editing, Supervision. C.X.: Writing—review and editing, Writing—original draft, Supervision, Investigation, Funding acquisition. T.S.: Conceptualization, Methodology, Writing—original draft, Resources, Writing—review and editing, Supervision. Z.T.: Investigation, Data curation. All authors have read and agreed to the published version of the manuscript.

Funding: This work was supported by the Shandong University of Technology Young and Middle-aged Key Teachers Overseas Visit Program Funds (Tian Su); the Natural Science Foundation of Shandong Province (ZR2025MS802) (Tian Su).

Data Availability Statement: The data presented in this study are available on request from the corresponding authors.

Conflicts of Interest: Author Zehui Zhang employed by the company China Design Group (China). The remaining authors declare that the research was conducted in the absence of any commercial or financial relationships that could be construed as a potential conflict of interest.

References

1. Chen, W.Z.; Wang, L.Y.; Tan, X.J.; Yang, D.S.; Yuan, J.Q.; Yang, J.P. Development trends in stability research of fractured rock mass underground engineering. *Chin. J. Rock Mech. Eng.* **2021**, *40*, 1945–1961. (In Chinese)
2. Luo, C.J. Application of curtain grouting technology in soluble rock dam foundations of existing earth dams. *Chin. J. Rock Mech. Eng.* **2004**, *22*, 3910–3916. (In Chinese)
3. Liu, Z.J.; Qi, X.B.; Ke, J.; Shui, Z.H. Enhancing the toughness of ultra-high performance concrete through improved fiber-matrix interface bonding. *Constr. Build. Mater.* **2025**, *491*, 142616. [CrossRef]
4. Achal, V.; Mukherjee, A.; Reddy, M.S. Microbial concrete: Way to enhance the durability of building structures. *J. Mater. Civ. Eng.* **2011**, *23*, 730–734. [CrossRef]
5. Choi, S.G.; Wu, S.; Chu, J. Biocementation for sand using an eggshell as calcium source. *J. Geotech. Geoenvironmental Eng.* **2016**, *142*, 06016010. [CrossRef]
6. Luo, B.; Su, Y.H.; Hu, X.; Chen, Z.F.; Chen, Y.H.; Ding, X.H. Strength behavior and microscopic mechanisms of geopolymer-stabilized waste clays considering clay mineralogy. *J. Clean. Prod.* **2025**, *530*, 146877. [CrossRef]
7. Bremner, T.W.; Eng, P. Environmental aspects of concrete: Problems and solutions. In Proceedings of the 1st All-Russian Conference on Concrete and Reinforced Concrete, Moscow, Russia, 14 September 2001.
8. Worrell, E.; Price, L.; Martin, N.; Hendriks, C.; Meida, L.O. Carbon dioxide emissions from the global cement industry. *Annu. Rev. Energy Env.* **2001**, *26*, 303–329. [CrossRef]
9. Benhelal, E.; Zahedi, G.; Shamsaei, E.; Bahadori, A. Global strategies and potentials to curb CO_2 emissions in cement industry. *Clean. Prod.* **2013**, *51*, 142–161. [CrossRef]
10. Liu, H.Q.; Yi, H.H.; Cao, F.B.; Liu, C.J.; Li, B.X.; Gao, Y.J.; Su, T. Multi-component synergistic regulation of hydration behavior and microstructure in solid waste-based high belite calcium sulphoaluminate cement: Hydration-microstructure-performance correlation. *Constr. Build. Mater.* **2025**, *505*, 144750. [CrossRef]
11. Naeimi, M.; Haddad, A. Environmental impacts of chemical and microbial grouting. *Environ. Sci. Pollut. Res.* **2020**, *27*, 2264–2272. [CrossRef]
12. Wang, S.J.; Li, Z.Q.; Tian, Y.F.; Li, Y.M.; Zhou, Y.X.; Li, D.D. The past, present and future of microbial geotechnical engineering technology. *J. Eng. Geol.* **2024**, *32*, 236–264. (In Chinese)
13. Tecon, R.; Or, D. Biophysical processes supporting the diversity of microbial life in soil. *FEMS Microbiol. Rev.* **2017**, *41*, 599–623. [CrossRef]
14. Geng, Y.Y.; Wang, S.M.; Tang, L.Y.; Shen, Z.T. Influence of typical soil minerals on ureolytic bacteria-induced carbonate precipitation. *Soil Use Manag.* **2024**, *40*, e13149. [CrossRef]
15. Vekariya, M.S.; Pitroda, J. Bacterial concrete: New era for construction industry. *Int. J. Eng. Trends Technol.* **2013**, *4*, 4128–4137.
16. Wang, P.F.; Tan, W.H.; Ma, X.W.; Li, Z.J.; Liu, J.J.; Wu, Y.F. Experimental study of seepage characteristics of consecutive and filling fracture with different roughness levels and gap-widths. *Rock Soil Mech.* **2019**, *40*, 3062–3070. (In Chinese)
17. Qian, C.X.; Wang, J.Y.; Wang, R.X.; Guo, H.D.; Li, L. Yield of microbial sedimentary calcite. *J. Inorg. Chem.* **2006**, *4*, 618–621. (In Chinese)
18. Wong, P.Y.; Mal, J.; Sandak, A.; Luo, L.; Jian, J.; Pradhan, N. Advances in microbial self-healing concrete: A critical review of mechanisms, developments, and future directions. *Sci. Total Environ.* **2024**, *947*, 174553. [CrossRef] [PubMed]
19. Fouladi, A.S.; Arulrajah, A.; Chu, J.; Horpibulsuk, S. Application of Microbially Induced Calcite Precipitation (MICP) technology in construction materials: A comprehensive review of waste stream contributions. *Constr. Build. Mater.* **2023**, *388*, 131546. [CrossRef]
20. Han, X.; Schultz, L.; Zhang, W.; Zhu, J.; Meng, F.; Geesey, G.G. Mineral formation during bacterial sulfate reduction in the presence of different electron donors and carbon sources. *Chem. Geol.* **2016**, *435*, 49–59. [CrossRef]
21. Gollapudi, U.K.; Knutson, C.; Bang, S.S.; Islam, M.R. A new method for controlling leaching through permeable channels. *Chemosphere* **1995**, *30*, 695–705. [CrossRef]

22. Jiang, N.; Soga, K.; Kuo, M. Microbially Induced Carbonate Precipitation for Seepage-Induced Internal Erosion Control in Sand-Clay Mixtures. *J. Geotech. Geoenviron.* **2017**, *143*, 4016100. [CrossRef]
23. Whiffin, V.S.; van Paassen, L.A.; Harkes, M.P. Microbial carbonate precipitation as a soil improvement technique. *Geomicrobiol. J.* **2007**, *24*, 417–423. [CrossRef]
24. Wang, M.L.; Wu, S.J.; Yang, Y.Q.; Chen, F.R. Advances in microbial-induced carbonate precipitation and its application in heavy metal fixation. *Chin. J. Environ. Sci.* **2018**, *31*, 206–214. (In Chinese) [CrossRef]
25. Dhami, N.K.; Reddy, M.S.; Mukherjee, A. Biomineralization of calcium carbonates and their engineered applications: A review. *Front. Microbiol.* **2013**, *4*, 314. [CrossRef]
26. Li, J.Y.; Huang, W.B.; Wang, X.L.; Zou, Z.R. Isolation and physiological characteristics of sulfate-reducing bacteria. *J. Anhui Agric. Sci.* **2010**, *38*, 16092–16123. [CrossRef]
27. Baumgartner, L.K.; Reid, R.P.; Dupraz, C.; Decho, A.W.; Buckley, D.H.; Spear, J.R.; Przekop, K.M.; Visscher, P.T. Sulfate reducing bacteria in microbial mats: Changing paradigms, new discoveries. *Sediment. Geol.* **2006**, *185*, 131–145. [CrossRef]
28. Dai, Y.D. *Biomineralogy*; Petroleum Industry Press: Beijing, China, 1994. (In Chinese)
29. Chen, Q.Y.; Min, Q.; Wu, H.; Zhang, L.; Si, Y.B. Biomineralization of Cd^{2+} and Pb^{2+} by sulfate-reducing bacteria Desulfovibrio desulfuricans and Desulfobulbus propionicus. *Front. Environ. Sci.* **2025**, *13*, 1591564. [CrossRef]
30. Ivanov, V.; Stabnikov, V.; Zhuang, W.Q.; Tay, J.H.; Tay, S.T.L. Phosphate removal from the returned liquor of municipal wastewater treatment plant using iron-reducing bacteria. *J. Appl. Microbiol.* **2005**, *98*, 1152–1161. [CrossRef]
31. Maitte, B.; Jorand, F.P.A.; Grgic, D.; Abdelmoula, M.; Carteret, C. Remineralization of ferrous carbonate from bioreduction of natural goethite in the Lorraine iron ore (Minette) by Shewanella putrefaciens. *Chem. Geol.* **2015**, *412*, 48–58. [CrossRef]
32. Ju, J.F.; Li, Q.S.; Xu, J.L.; Li, J.J.; Cao, Z.G. Experimental study on seepage reduction characteristics of chemical precipitation remediation for fractured/porous rock mass disturbed by mining. *Coal Sci. Technol.* **2020**, *48*, 89–96. (In Chinese)
33. Roden, E.E.; Leonardo, M.R.; Ferris, F.G. Immobilization of strontium during iron biomineralization coupled to dissimilatory hydrous ferric oxide reduction. *Geochim. Cosmochim. Acta* **2002**, *66*, 2823–2839. [CrossRef]
34. Zhu, T.; Dittrich, M. Carbonate precipitation through microbial activities in natural environment, and their potential in biotechnology: A review. *Front. Bioeng. Biotechnol.* **2016**, *4*, 4. [CrossRef]
35. Seifan, M.; Khajeh Samani, A.; Berenjian, A. Bioconcrete: Next generation of self-healing concrete. *Appl. Microbiol. Biotechnol.* **2016**, *100*, 2591–2602. [CrossRef] [PubMed]
36. Martin, D.; Dodds, K.; Butler, I.; Ngwenya, B.T. Carbonate precipitation under pressure for bioengineering in the anaerobic subsurface via denitrification. *Environ. Sci. Technol.* **2013**, *47*, 8238–8245. [CrossRef]
37. Karatas, I. Microbiological Improvement of the Physical Properties of Soils. Ph.D. Thesis, Arizona State University, Tempe, AZ, USA, 2008.
38. Erşan, Y.Ç.; de Belie, N.; Boon, N. Microbially induced $CaCO_3$ precipitation through denitrification: An optimization study in minimal nutrient environment. *Biochem. Eng. J.* **2015**, *101*, 108–118. [CrossRef]
39. Liu, H.L.; Xiao, P.; Xiao, Y.; Chu, J. State-of-the-art review of biogeotechnology and its engineering applications. *J. Civ. Environ. Eng.* **2019**, *41*, 101030. (In Chinese)
40. Ganendra, G.; De Muynck, W.; Ho, A.; Arvaniti, E.C.; Hosseinkhani, B.; Ramos, J.A.; Rahier, H.; Boon, N. Formate oxidation-driven calcium carbonate precipitation by Methylocystis parvus OBBP. *Appl. Environ. Microbiol.* **2014**, *80*, 4659–4667. [CrossRef]
41. Riding, R. Cyanobacterial calcification, carbon dioxide concentrating mechanisms, and Proterozoic-Cambrian changes in atmospheric composition. *Geobiology* **2006**, *4*, 299–316. [CrossRef]
42. Gao, X.B.; Pan, Z.D.; Gong, P.L.; Jiang, Y.; Li, C.C.; Li, H.Y. Process and mechanism of microbial induced carbonate precipitation. *Carsologica Sin.* **2022**, *41*, 441–452. (In Chinese)
43. Deng, H.J.; Luo, Y.L.; Wu, L.J.; Zhang, Y.N.; Peng, S.H. Experimental study of improving impermeability and strength of fractured rock by microbial induced carbonate precipitation. *Rock Soil Mech.* **2019**, *40*, 3542–3548. (In Chinese)
44. Latif, D.O.; Diana, W.; Daga, W.; Apriyono, A. A PRISMA-guided systematic review of MICP and EICP in clayey soils: Mineralogy-aware mechanisms, injection control, and multi-scale performance synthesis. *Results Eng.* **2026**, *29*, 109337. [CrossRef]
45. Reeburgh, W.S. Oceanic methane biogeochemistry. *Chem. Rev.* **2007**, *107*, 486–513. [CrossRef]
46. Zúñiga-Barra, H.; Ostojic, C.; Torres-Aravena, Á.; Rivas, M.; Vílchez, C.; Jeison, D. Use of photosynthetic MICP to induce calcium carbonate precipitation: Prospecting the role of the microorganism in the formation of $CaCO_3$ crystals. *Algal Res.* **2024**, *80*, 103499. [CrossRef]
47. Dong, Y.; Gao, Z.; Wang, D.; Di, J.; Guo, X.; Yang, Z.; Li, Y.; Wang, Y.; Wang, Y. Optimization of growth conditions and biological cementation effect of Sporosarcina pasteurii. *Constr. Build. Mater.* **2023**, *395*, 132288. [CrossRef]
48. Chuo, S.C.; Mohamed, S.F.; Mohd Setapar, S.H.; Ahmad, A.; Jawaid, M.; Wani, W.A.; Yaqoob, A.A.; Mohamad Ibrahim, M.N. Insights into the current trends in the utilization of bacteria for microbially induced calcium carbonate precipitation. *Materials* **2020**, *13*, 4993. [CrossRef]

49. Le Métayer, É.; Castanier, S.; Le Borgne, T.; Perito, B.; Ménez, B.; Delaunay, A.; Orial, G.; Servant-Vildary, S.; Tiano, P. Influence of temperature on the effectiveness of a biogenic carbonate surface treatment for limestone conservation. *Appl. Microbiol. Biotechnol.* **2013**, *97*, 1335–1347.
50. Dhami, N.K.; Reddy, M.S.; Mukherjee, A. Biomineralization of calcium carbonate polymorphs by the bacterial strains isolated from calcareous sites. *J. Microbiol. Biotechnol.* **2013**, *23*, 707–714. [CrossRef]
51. Okwadha, G.D.O.; Li, J. Optimum conditions for microbial carbonate precipitation. *Chemosphere* **2010**, *81*, 1143–1148. [CrossRef]
52. Zhao, Q. Experimental Study on Soil Improvement Using Microbial Induced Calcite Precipitation (MICP). Ph.D. Thesis, China University of Geosciences (Beijing), Beijing, China, 2014. (In Chinese)
53. Liu, S.Y.; Yu, J.; Zeng, W.L.; Peng, X.Q.; Cai, Y.Y.; Tu, B.X. Repair effect of tabia cracks with microbially induced carbonate precipitation. *Chin. J. Rock Mech. Eng.* **2020**, *39*, 191–204.
54. Prajapati, N.K.; Agnihotri, A.K.; Basak, N. Microbial induced calcite precipitation (MICP) a sustainable technique for stabilization of soil: A review. *Mater. Today Proc.* **2023**, *93*, 357–361. [CrossRef]
55. Liu, Y.; Ali, A.; Su, J.F.; Li, K.; Hu, R.Z.; Wang, Z. Microbial-induced calcium carbonate precipitation: Influencing factors, nucleation pathways, and application in waste water remediation. *Sci. Total Environ.* **2023**, *860*, 160439. [CrossRef]
56. Li, H.D.; Jiao, X.Y.; Li, J.; Su, M.X.; Wu, S.Y.; Liu, Y. Using microbe-induced calcite precipitation and enzyme-induced carbonate precipitation to cement slopes of earth ditches. *Guan'gai Paishui Xuebao* **2021**, *40*, 59–65.
57. Carter, M.S.; Tuttle, M.J.; Mancini, J.A.; Martineau, R.; Hung, C.S.; Gupta, M.K. Microbially induced calcium carbonate precipitation by Sporosarcina pasteurii: A case study in optimizing biological $CaCO_3$ precipitation. *Appl. Environ. Microbiol.* **2023**, *89*, e01794-22. [CrossRef] [PubMed]
58. Seifan, M.; Khajeh Samani, A.; Berenjian, A. Beneficial factors for biomineralization by ureolytic bacterium Sporosarcina pasteurii. *Microb. Cell Factories* **2020**, *19*, 12. [CrossRef] [PubMed]
59. Shi, W.; Wang, M.; Wu, L.; Xie, X.H.; Wang, M.; Lu, T.J. Study of concrete crack repair using Bacillus megaterium. *Adv. Mater. Sci. Eng.* **2022**, *2022*, 6188680. [CrossRef]
60. Shen, T.Y.; Li, X.; Wang, S.J.; Xu, C.; Xue, L. Triaxial shear strength and immersion compressive strength of sandy clayey purple soil treated by microbial induced calcite precipitation. *Trans. Chin. Soc. Agric. Eng. (Trans. CSAE)* **2019**, *35*, 135–143. (In Chinese)
61. Qin, Y.F.; Lu, W.; Yuan, M.X.; Shen, T.Y.; Li, X.; Wang, S.J. An experimental study of Handan strong expansive soil enhanced by Bacillus megaterium. *J. Southwest China Norm. Univ. (Nat. Sci. Ed.)* **2020**, *45*, 87–95. (In Chinese)
62. Zhao, S.M. Enhancement Effect of Bacillus Megaterium LY02 on Phytoremediation of Heavy Metal-Contaminated Soil by Ryegrass. Master's thesis, Zhejiang A&F University, Lin'an, China, 2018. (In Chinese)
63. Peng, J.; He, X.; Liu, Z.M.; Feng, Q.P.; He, J. Experimental study on microbial induced calcium carbonate precipitation for soil stabilization under low temperature conditions. *Chin. J. Geotech. Eng.* **2016**, *38*, 1801–1807. (In Chinese)
64. Tran, T.K.; Nguyen, T.P.; Le, Q.L.; Tran, T.M.N.; Vu, T.T.N.; Duong, T.H.D.; Tran, Q.V.; Nguyen, H.D. Effect of culture conditions on bacteria-induced calcite precipitation of Bacillus subtilis QN7 strain. *Huit. J. Sci.* **2024**, *24*, 3–11.
65. Deng, J.R. Mechanical Behavior and Microscopic Characterization of Rock Materials After Microbial Remediation. Ph.D. Thesis, Central South University, Changsha, China, 2023. (In Chinese)
66. Sun, X.H. Study on Mechanism of Microbial Mineralization and Application of it to Repair Concrete Cracks. Ph.D. Thesis, Southeast University, Nanjing, China, 2019. (In Chinese)
67. Li, D. Investigation of Solidifying Desert Aeolian Sand Using Microbially Induced Calcite Precipitation. Master's thesis, Northwest A&F University, Yangling, China, 2018. (In Chinese)
68. Liu, D.; Shao, A.L.; Zhao, X.; Jin, C.Y. Experimental study on rock mass structural plane repair based on microbially induced calcium carbonate precipitation. *J. Northeast. Univ. (Nat. Sci.)* **2018**, *39*, 961–965. (In Chinese)
69. Zhang, H.N. Experimental Study on Microbial Induced Calcium Carbonate Precipitation Technology for Sand Solidification. Ph.D. Thesis, China University of Geosciences (Beijing), Beijing, China, 2019. (In Chinese)
70. Pei, D. Studies on *Sporosarcina pasteurii* Induced Mineralization and Its Mechanism. Ph.D. Thesis, National University of Defense Technology, Changsha, China, 2021. (In Chinese)
71. van Paassen, L.A. Biogrout: Ground Improvement by Microbial Induced Carbonate Precipitation. Ph.D. Thesis, Delft University of Technology, Delft, The Netherlands, 2009.
72. Wang, J.Y.; Jonkers, H.M.; Boon, N.; De Belie, N. Bacillus sphaericus LMG 22257 is physiologically suitable for self-healing concrete. *Appl. Microbiol. Biotechnol.* **2017**, *101*, 5101–5114. [CrossRef]
73. Cheng, L.; Cord-Ruwisch, R. In situ soil cementation with ureolytic bacteria by surface percolation. *Ecol. Eng.* **2012**, *42*, 64–72. [CrossRef]
74. Yi, H.H.; Zheng, T.W.; Jia, Z.R.; Su, T.; Wang, C.G. Study on the influencing factors and mechanism of calcium carbonate precipitation induced by urease bacteria. *J. Cryst. Growth* **2021**, *564*, 126113. [CrossRef]
75. Cui, Z.H.; He, X.; Dai, F.; Liu, Y.; Yang, S.H. Influence of bacterial concentration and fissure aperture on improving dynamic mechanical properties of MICP repaired fissured sandstone. *J. Rock Mech. Geotech. Eng.* **2026**, *18*, 1213–1232. [CrossRef]

76. Wu, D.D.; Zhang, J.G.; Wang, P.Z.; Gao, P.; Liu, Y.Z.; Zhou, A.J. Optimizing the self-healing of concrete cracks under actual service oxygen conditions via mineralization of facultatively aerobic microbial consortia. *Cem. Concr. Compos.* **2026**, *165*, 106319. [CrossRef]
77. Li, K.L.; Yan, C.; Chen, X.; Chen, A.J.; Du, X.M.; Li, W.H. Comparative analysis of the repair effect of three methods of microbial induced calcium carbonate precipitation on recycled aggregate concrete cracks. *Mater. Rep.* **2025**, *39*, 59–66. (In Chinese)
78. Peng, J.; Feng, Q.P.; Sun, Y.C. Influences of temperatures on MICP-treated soils. *Chin. J. Geotech. Eng.* **2018**, *40*, 1048–1054. (In Chinese)
79. Wang, H.; Alfredsson, V.; Tropsch, J.; Ettl, R.; Nylander, T. Formation of $CaCO_3$ Deposits on Hard Surfaces—Effect of Bulk Solution Conditions and Surface Properties. *ACS Appl. Mater. Interfaces* **2013**, *5*, 5204–5213. [CrossRef]
80. Wang, Y.Z.; Wang, Y.; Soga, K.; DeJong, J.T.; Kabla, A.J. Microscale investigations of temperature-dependent microbially induced carbonate precipitation (MICP) in the temperature range 4–50 °C. *Acta Geotech.* **2023**, *18*, 2239–2261. [CrossRef]
81. Cheng, M.; Jiang, L.; Hu, S.; Zhao, X.; Wang, W.; Zhang, Y.; Paine, K.; Liu, Y. Mechanism and application of a coating-free microbial self-healing agent in cement-based composites. *Cem. Concr. Compos.* **2025**, *163*, 106213. [CrossRef]
82. Chen, J.; Liu, B.L.; Zhong, M.; Jing, C.; Guo, B.Y. Research status and development of microbial induced calcium carbonate mineralization technology. *PLoS ONE* **2022**, *17*, e0271761. [CrossRef]
83. Kang, B.; Zha, F.S.; Li, J. Study of self-healing capability of MICP technology under freeze-thaw cycle conditions. *J. Eng. Geol.* **2025**, *33*, 1271–1279. (In Chinese)
84. Liu, H.Q.; Chen, J.L.; Zhang, P.; Li, W.; Su, W.; Su, T.; Gong, S.W.; Li, B.X. Freeze-Thaw Behavior and Damage Prediction of Mixed Recycled Coarse Aggregate Concrete. *Buildings* **2026**, *16*, 368. [CrossRef]
85. Wang, S. Study on the Effect and Mechanism of Microbial Reinforcement of Fractured Rock Mass. Master's thesis, Xi'an University of Technology, Xi'an, China, 2023. (In Chinese)
86. Li, D.; Niu, C.H.; Jiang, Y.Y.; Wang, J.H. Optimization of high density fermentation conditions of Bacillus subtilis NKY1145. *China Brew.* **2015**, *34*, 75–78. (In Chinese)
87. Gao, G.Y. Experimental study on microbial dust suppressant for solidified dust based on MICP. *Coal Mine Saf.* **2024**, *55*, 91–98. (In Chinese)
88. Kappaun, K.; Piovesan, A.R.; Carlini, C.R.; Ligabue-Braun, R. Ureases: Historical aspects, catalytic, and non-catalytic properties-A review. *J. Adv. Res.* **2018**, *13*, 3–17. [CrossRef] [PubMed]
89. Zhang, Q.C.; Zheng, Y.F.; Huang, M.Z.; Shen, X.K.; Wu, L.L.; Zhang, Z.J. Experimental and Computational Investigation of pH-Dependent Urease Conformational Dynamics and Its Impact on MICP Efficiency. *Chin. J. Biochem. Mol. Biol.* **2025**, *41*, 879–894. (In Chinese)
90. Lai, H.J.; Cui, M.J.; Chu, J. Effect of pH on soil improvement using one-phase-low-pH MICP or EICP biocementation method. *Acta Geotech.* **2023**, *18*, 3259–3272. [CrossRef]
91. Risdanareni, P.; Fatkhurrahman, M.; Hastuti, A.A.M.; Zai, K.; Karolina, R.; Mustafa, I.; Kristiawan, S.A.; Kusbiantoro, A. pH responsive natural-based hydrogel: Application in bacteria-based self-healing mortar. *Results Eng.* **2025**, *28*, 107932. [CrossRef]
92. Stocks-Fischer, S.; Galinat, J.K.; Bang, S.S. Microbiological precipitation of $CaCO_3$. *Soil Biol. Biochem.* **1999**, *31*, 1563–1571. [CrossRef]
93. Cui, R. Experimental Study on Mechanical Properties of Remolded Mudstone Cemented and Reinforced by MICP Method. Master's thesis, Hubei University of Technology, Wuhan, China, 2020. (In Chinese)
94. Zhang, Y. Experimental Study on Microorganisms Applied to Sand Cementation and Concrete Crack Repair. Master's thesis, Tsinghua University, Beijing, China, 2014. (In Chinese)
95. Zheng, Y.F.; Wu, L.L.; Zhang, Q.C.; Hu, L.; Tian, Y.K.; Wang, M.; Zheng, H.M.; Zhang, Z.J. A constant pH molecular dynamics and experimental study on the effect of different pH on the structure of urease from Sporosarcina pasteurii. *J. Mol. Model.* **2025**, *31*, 164. [CrossRef]
96. Lv, C.; Tang, C.S.; Zhang, J.Z.; Pan, X.H.; Liu, H. Effects of calcium sources and magnesium ions on the mechanical behavior of MICP-treated calcareous sand: Experimental evidence and precipitated crystal insights. *Acta Geotech.* **2023**, *18*, 2703–2717. [CrossRef]
97. Zhao, T.; Du, H.; Shang, R. The Effect of Bacteria-to-Calcium Ratio on Microbial-Induced Carbonate Precipitation (MICP) under Different Sequences of Calcium-Source Introduction. *Materials* **2024**, *17*, 1881. [CrossRef]
98. Lajmiri, A.; Sharafi, H.; Khayat, N. Evaluation of low-cost calcium sources for microbially induced calcite precipitation (MICP): Implications for sustainable bio-cementation. *Results Eng.* **2025**, *28*, 107638. [CrossRef]
99. Zhao, Z.F.; Duan, R. Effect of different calcium sources on MICP biocementation of silt. *J. Wuhan Univ. (Eng. Sci.)* **2025**, *58*, 1–9. (In Chinese)
100. Zheng, T.W.; Qian, C.X.; Su, Y.L. Influences of different calcium sources on the early age cracks of self-healing cementitious mortar. *Biochem. Eng. J.* **2021**, *166*, 107849. [CrossRef]

101. Zhang, Y.H.; Guo, H.X.; Cheng, X.H. Influences of calcium sources on microbially induced carbonate precipitation in porous media. *Mater. Res. Innov.* **2014**, *18*, S2-79–S2-84. [CrossRef]
102. Wang, W.L.; Qin, S.Y.; Xiao, Y.; Xiao, Z.Y.; Zheng, C.L. Effect of different calcium sources on MICP solidification of cyanide tailings. *Nonferrous Met. (Smelt. Part)* **2022**, 85–111. (In Chinese)
103. Ming, D.G.; Qiu, M.X.; Yin, L.J.; Zhang, J.M.; Zhu, J.K.; Zhou, Y. Experimental study on the effect of calcium sources on microbial solidification of aeolian sand. *Yellow River* **2020**, *42*, 85–88. (In Chinese)
104. Achal, V.; Pan, X.L. Influence of calcium sources on microbially induced calcium carbonate precipitation by Bacillus sp. CR2. *Appl. Biochem. Biotechnol.* **2014**, *173*, 307–317. [CrossRef]
105. Su, Y.L.; Qu, F.L.; Meng, Y.; Xu, W.J.; Zhu, X.H.; Zhang, C.; Tsang, D.C.W. Microbial-induced carbonate precipitation (MICP) modified biochar for low-carbon cementitious materials. *Constr. Build. Mater.* **2024**, *451*, 138644. [CrossRef]
106. Gorospe, C.M.; Han, S.H.; Kim, S.G. Effects of different calcium salts on calcium carbonate crystal formation by Sporosarcina pasteurii KCTC3558. *Biotechnol. Bioprocess Eng.* **2013**, *18*, 903–908. [CrossRef]
107. Liang, S.H.; Niu, J.G.; Fang, C.T.; Dai, J.; Yin, Y.M.; Liu, Y.J. Experimental study on the effect of nutrient solution calcium source on microbial solidification of sand. *J. Disaster Prev. Mitig. Eng.* **2018**, *38*, 781–786. (In Chinese)
108. Tao, H.; Jiang, P.P.; Qu, J.L.; Huang, Y.D. The impact of various calcium ion sources on the curing efficacy of MICP. *Sci. Rep.* **2025**, *15*, 9149. [CrossRef] [PubMed]
109. Gu, T.Q.; Xu, X.; Wang, Z.; Zheng, C.L. Study on the effect of different calcium sources on the solidification of cyanide tailings by microbial induced carbonate precipitation. *Nonferrous Met. (Smelt. Part)* **2025**, 2327–2336. (In Chinese) [CrossRef]
110. Zhu, W.K.; Luo, X.G. Optimization of Calcium Carbonate Precipitation Conditions Induced by Carbonate Mineralization Bacteria. *Non-Met. Mines* **2012**, *35*, 1–4. (In Chinese)
111. Al Qabany, A.; Soga, K. Effect of chemical treatment used in MICP on engineering properties of cemented soils. *Geotechnique* **2014**, *63*, 331–339. [CrossRef]
112. Huang, C.C.; Du, Q.; Qu, L.Q.; Liu, X.M.; Xue, J.L. Effect of calcium sources and solidification methods on the uniformity and strength of MICP-treated sandy loess. *J. Civ. Environ. Eng.* **2024**, *46*, 1–3. (In Chinese)
113. Peng, S.Q.; Kang, J.Y.; Zhang, K.J.; Fan, L.; Chen, S.F.; Wang, F. Seepage law of fractured rock mass sealed with microbiologically induced $CaCO_3$ precipitation. *Min. Metall. Eng.* **2020**, *40*, 15–19. (In Chinese)
114. Wu, Y.R.; Zhang, Y.; Xiao, Y.; Liu, H.L. Study on the influence of crack opening on the shear performance of rock fractures repaired by microbial mineralization. *J. Xi'an Univ. Archit. Technol. (Nat. Sci. Ed.)* **2025**, *57*, 636–638. (In Chinese)
115. Jia, Q.; Zhao, Q.C.; Sun, Z.C. Study on impermeability of concrete cracks repaired by microbial calcium carbonate precipitation. *Chin. J. Appl. Basic Sci. Eng.* **2017**, *25*, 141–148. (In Chinese)
116. Shen, J.W.; Du, Z.H.; Li, H.; Li, L.; Wang, F.B.; Ni, J.J.; Teng, G.G. Fracture gas invasion mechanism and plugging method of shale gas layer. *J. Chengdu Univ. Technol.* **2022**, *49*, 579–585. (In Chinese)
117. Peng, S.Q.; Di, H.; Fan, L.; Fan, W.; Qin, L. Factors Affecting Permeability Reduction of MICP for Fractured Rock. *Front. Earth Sci.* **2020**, *8*, 217. [CrossRef]
118. Wang, J.; Li, Y.; Zhang, S.; Zhang, H.; Li, Z. Mechanical behavior and microscale mechanisms of grout-consolidated fractured coal rock: Integrated 3D In-Situ CT reconstruction modeling and multiscale experimental analysis. *Results Eng.* **2026**, *29*, 108901.
119. Zhang, S.X.; Shen, D.Y.; Zhang, R.Z.; Wu, C.Z. The high-strength method of reinforcing sand particles using MICP combined with coconut fiber under unsaturated conditions in marine and coastal regions. *Case Stud. Constr. Mater.* **2025**, *22*, e04550. [CrossRef]
120. Zhong, L.; Islam, M. A New Microbial Plugging Process and Its Impact on Fracture Remediation. In Proceedings of the SPE Annual Technical Conference and Exhibition, Dallas, TX, USA, 22–25 October 1995.
121. Cardoso, R.; Arbabbzadeh, E.; Lima, J.T.; Flores-Colen, I.; Pereira, M.F.C.; Silva, M.C.; Duarte, S.O.D.; Monteiro, G.A. The influence of stone joints width and roughness on the efficiency of biocementation sealing. *Constr. Build. Mater.* **2021**, *283*, 122743. [CrossRef]
122. Song, C.P.; Elsworth, D.; Zhi, S.; Zhang, X. Impact of flow-direction and gravitational settling on microbially-induced calcium carbonate precipitation (MICP) in rock fractures. *Bull. Eng. Geol. Environ.* **2024**, *83*, 261. (In Chinese) [CrossRef]
123. Dai, Q.C.; Pan, X.H.; Zhang, Y.C.; Tang, C.S. A high-bridging-rate MICP repair method for non-penetrating steeply inclined rock fractures based on three-step grouting strategy. *Geol. J. China Univ.* **2025**, *31*, 562–571. (In Chinese) [CrossRef]
124. Tobler, D.J.; Minto, J.M.; Mountassir, G.E.; Lunn, R.J.; Phoenix, V.R. Microscale Analysis of Fractured Rock Sealed With Microbially Induced $CaCO_3$ Precipitation: Influence on Hydraulic and Mechanical Performance. *Water Resour. Res.* **2018**, *54*, 8295–8308. [CrossRef]
125. Jia, Q.; Jiang, H.; Zhang, X. Experimental study on microbial deposition of calcium carbonate for sealing concrete cracks. *J. Build. Mater.* **2018**, *21*, 663–666. (In Chinese)
126. Gao, R.X.; Wang, J.Y. Influence of Repairing Technical Parameters on the Healing Efficiency of Biological Calcium Carbonate–Based Mortar Crack Healing Efficiency. *J. Mater. Civ. Eng.* **2026**, *38*, 04025548. [CrossRef]
127. Cheng, L.; Shahin, M.; Cord-Ruwisch, R. Bio-cementation of sandy soil using microbially induced carbonate precipitation for marine environments. *Geotechnique* **2014**, *64*, 1010. [CrossRef]

128. Pang, Y.S. Study on Grouting Method of Microbial Induced Calcium Carbonate Precipitation. Master's thesis, Yangzhou University, Yangzhou, China, 2017. (In Chinese)
129. Li, Y.; Wen, K.J.; Li, L.; Huang, W.; Bu, C.M.; Amini, F. Experimental investigation on compression resistance of bio-bricks. *Constr. Build. Mater.* **2020**, *265*, 120751. [CrossRef]
130. Qian, C.X.; Wang, R.X.; Cheng, L.; Wang, J.Y. Theory of microbial carbonate precipitation and its application in restoration of cement-based materials defects. *Chin. J. Chem.* **2010**, *28*, 847–857. [CrossRef]
131. Zheng, Y.L.; Li, R.L.; Wang, J.Q.; Pan, H.Z.; Zhang, G.Y.; Cheng, L. Innovative and environmentally friendly MICP surface curing: Enhancing mechanical and durability properties of concrete. *J. Clean. Prod.* **2024**, *478*, 143962. [CrossRef]
132. Guo, X.X.; Li, D.R.; Ma, R.N.; Cheng, X.H. One-dimensional consolidation test of MICP mixed and solidified calcareous sand. *J. Tsinghua Univ. (Sci. Technol.)* **2019**, *59*, 593–600. (In Chinese)
133. Peng, J.; Huang, M.F.; Xie, G.Q.; Tian, Y.M. Grouting method for microbial induced calcium carbonate precipitation to solidify soil. *J. Hohai Univ. (Nat. Sci.)* **2019**, *47*, 259–264. (In Chinese)
134. Shan, Z.G.; Zhou, N.; Hou, W.X.; Chen, Q.; Kou, H.J. Influence of different treatment processes on the reinforcement effect of microorganisms on rock cracks. *J. Water Resour. Water Eng.* **2022**, *33*, 70–75.
135. Xu, J.; Wang, X.; Yao, W.; Kulinskaya, A.; Shah, S.P. Microbial-inspired self-healing of concrete cracks by sodium silicate-coated recycled concrete aggregates served as bacterial carrier. *Front. Struct. Civ. Eng.* **2024**, *18*, 14–29. [CrossRef]
136. Shang, Z.Y.; Peng, J.; Wei, R.J.; Li, L.L.; Jiang, R.; Dai, D. Experimental study on sodium silicate enhanced microbial grouting reinforcement effect. *J. Civ. Environ. Eng.* **2025**, *47*, 3–8. (In Chinese)
137. Zhu, J.; Wei, R.J.; Dai, D.; Li, L.L.; Shang, Z.Y.; Jiang, Z.; Peng, J. Enhancing microbial-induced calcium carbonate precipitation efficiency in calcareous sands through ferric ion additives: A comprehensive experimental investigation. *PLoS ONE* **2025**, *20*, e0327568. [CrossRef]
138. Wei, R.J.; Tang, P.Y.; Peng, J.; Li, L.L.; Shang, Z.Y.; Jiang, R. Experimental study on the strengthening effect of ferric chloride on microbial mineralization of sand. *Chin. J. Geotech. Eng.* **2025**, *47*, 949–955. (In Chinese)
139. Al Jaber, M.; Muhammad, N.; Ahmad, H.F. Sustainable Stabilization Using Gypsum and Concrete Waste Enhanced Microbially Induced Calcium Precipitation (MICP) Activities in Peat Soil. *Biogeotechnics* **2026**, 100233. [CrossRef]
140. Liu, P.; Cao, Y.X.; Cheng, Y.; Bai, Y.B. Experimental study on the effect of carbonic anhydrase enhanced microbial mineralization for soil stabilization. *Rock Soil Mech.* **2024**, *45*, 2555–2561. (In Chinese) [CrossRef]
141. Chen, Y. Experimental Study on Sand Solidification by Carbonic Anhydrase Bacteria and Urease Bacteria Combined with Active Magnesium Oxide. Master's thesis, Nanjing Forestry University, Nanjing, China, 2025. (In Chinese)
142. Li, M.; Liu, S.; Hu, G.H.; Zhang, J.X.; Guo, S.J.; Huo, B.B.; Zhao, Y. Study on properties and cementation mechanism of microbial modified coal-based solid waste backfill materials. *J. Min. Saf. Eng.* **2025**, *42*, 937–948. (In Chinese)
143. Wang, Z.W.; Wei, R.; Wu, S.F.; Tian, J.X.; Liang, S.J. Strength effect and mechanism analysis of MICP-solidified coal ash. *Chin. J. Geotech. Eng.* **2023**, *45*, 88–91. (In Chinese)
144. Zhang, P.; Li, Z.H.; Yu, J.L.; Gong, Y.H.; Tang, Y.Z. Experimental study on the performance of alkali modified fly ash enhanced MICP solidified sand. *Chin. J. Geotech. Eng.* **2025**, *47*, 1295–1303. (In Chinese)
145. Li, M.M.; Fang, C.L.; Kawasaki, S.; Achal, V. Fly ash incorporated with biocement to improve strength of expansive soil. *Sci. Rep.* **2018**, *8*, 2565. [CrossRef]
146. He, G.C.; Tang, M.Y.; Li, Y.M.; Li, C.G.; Zhang, Z.J.; Wu, L.L. Experiment on the impermeability of uranium tailings treated by microbial induced calcium carbonate precipitation combined with modified jute fiber. *Rock Soil Mech.* **2023**, *44*, 3459–3470. (In Chinese)
147. Spencer, C.A.; van Paassen, L.; Sass, H. Effect of jute fibres on the process of MICP and properties of biocemented sand. *Materials* **2020**, *13*, 5429. [CrossRef] [PubMed]
148. Al Imran, M.D.; Gowthaman, S.; Nakashima, K.; Kawasaki, S. The influence of the addition of plant-based natural fibers (jute) on biocemented sand using MICP method. *Materials* **2020**, *13*, 4198. [CrossRef]
149. Al Imran, M.D.; Nakashima, K.; Evelpidou, N.; Kawasaki, S. Durability improvement of biocemented sand by fiber-reinforced MICP for coastal erosion protection. *Materials* **2022**, *15*, 2389. [CrossRef]
150. Su, T.; Yu, X.H.; Jin, H.S.; Chen, L.K.; Tan, Z.Y.; Ngo, T. Macro-mechanical properties and freeze thaw evaluation of innovative nano-silica modified concrete reinforced by recycled carpet fibers. *Constr. Build. Mater.* **2025**, *492*, 142894.
151. Chen, H. Evaluation of efficiency and driving mechanism of nano-SiO_2-MICP synergistic solidification of sludge. *J. Yangtze River Sci. Res. Inst.* **2024**, *41*, 117–125. (In Chinese)
152. Hu, Z.; Yang, Y.; Zhang, H. Durability and damage evolution of steel fiber and Nano-SiO_2 reinforced concrete under freeze-thaw and salt erosion environments based on acoustic emission and Computed Tomography analysis. *J. Build. Eng.* **2025**, *115*, 114595. [CrossRef]
153. Hu, Z.; Zhou, X.; Yu, L. An intelligent prediction method for rock core integrity based on deep semantic segmentation. *Rock Mech. Rock Eng.* **2026**. [CrossRef]

154. Li, W.; Chen, Y.; Zhan, X.; Lv, G.; Huang, X. An experimental study on the densification mechanism of coarse-grained landslide deposits from Southeastern Tibet under dynamic compaction. *Soil Dyn. Earthq. Eng.* **2026**, *202*, 110023.
155. Cui, X.L.; Li, J.X.; Xie, J.M. Experimental study on improvement of soft soil mechanical properties by biochar combined with microbial mineralization technology. *Water Resour. Hydropower Eng.* **2024**, *55*, 134–146. (In Chinese)
156. Wang, J. Experimental Study on Sand Fixation and Dust Suppression by Polyacrylamide Combined with MICP. Master's thesis, Nanjing Forestry University, Nanjing, China, 2023; pp. 80–82. (In Chinese)
157. Huang, Y.; Liu, F.; Zhang, X. A One-Phase Injection Method with Dual Inhibition for Improving the Strength and Uniformity of MICP. *Materials* **2025**, *18*, 2514. [CrossRef]
158. Jia, Q.; Wang, Y.C. Study on Calcium Carbonate Deposition of Microorganism Bottom Grouting to Repair Concrete Cracks. *Sustainability* **2023**, *15*, 3723. [CrossRef]
159. Xiang, J.; Qiu, J.; Wang, Y.; Gu, X. Calcium acetate as calcium source used to biocement for improving performance and reducing ammonia emission. *J. Clean. Prod.* **2022**, *348*, 131286. [CrossRef]
160. Kim, G.; Kim, J.; Youn, H. Effect of Temperature, pH, and Reaction Duration on Microbially Induced Calcite Precipitation. *Appl. Sci.* **2018**, *8*, 1277. [CrossRef]
161. Xiao, Y.; Wang, Y.; Wang, S.; Evans, T.M.; Stuedlein, A.W.; Chu, J.; Zhao, C.; Wu, H.; Liu, H. Homogeneity and mechanical behaviors of sands improved by a temperature-controlled one-phase MICP method. *Acta Geotech.* **2021**, *16*, 1417–1427. [CrossRef]
162. Wu, C.; Song, Z.; Jang, B.A.; Song, H.G.; Ni, P. Strength improvement of rock fractures and aggregates cemented with bio-slurry. *Mater. Lett.* **2021**, *305*, 130866. [CrossRef]
163. Li, S.; Li, X.; Zhong, J.M.; Zhu, Z.Y.; Xiao, W.M. Experimental study on the effect of contact area on the impermeability of rough rock joints treated by MICP. *J. Eng. Geol.* **2025**, *33*, 2126–2137. (In Chinese)
164. Pham, V.P.; Nakano, A.; van der Star, W.R.L.; Heimovaara, T.J.; van Paassen, L.A. Applying MICP by denitrification in soils: A process analysis. *Environ. Geotech.* **2017**, *5*, 79–93. [CrossRef]
165. Erdmann, N.; de Payrebrune, K.M.; Ullher, R.; Strieth, D. Optimizing compressive strength of sand treated with MICP using response surface methodology. *SN Appl. Sci.* **2022**, *4*, 282. [CrossRef]
166. Kakelar, M.M.; Ebrahimi, S. Up-scaling application of microbial carbonate precipitation: Optimization of urease production using response surface methodology and injection modification. *Int. J. Environ. Sci. Technol.* **2016**, *13*, 2619–2628. [CrossRef]
167. Liu, H.L. Biological construction system and prospects. *J. Civ. Environ. Eng.* **2024**, *46*, 1–22. (In Chinese)
168. Feng, Q.; Liu, J.; Lu, Y.; Wang, Y.; Zhang, D.; Qi, X.H.; Liu, R.T. Experimental study on strength of sand reinforced with composite reinforcement agent. *J. Eng. Geol.* **2017**, *25*, 903–911. (In Chinese)
169. Xu, G.; Pei, X.J.; Yuan, J.K.; Chen, J.; Ren, H. A study of the engineering characteristics of reinforced loose sand by modified nano-Si materials. *Hydrogeol. Eng. Geol.* **2019**, *46*, 142–149. (In Chinese)
170. Wu, L.Y.; Miao, L.C.; Sun, X.H.; Chen, R.F.; Wang, C.C. Experimental study on sand solidification using plant-derived urease-induced calcium carbonate precipitation. *Chin. J. Geotech. Eng.* **2020**, *42*, 714–720. (In Chinese)
171. Zhao, X.B.; Ma, J.J.; Du, J.; Jiang, L. Microbially induced calcite precipitation for soil solidification and erosion mitigation: A review. *Bull. Eng. Geol. Environ.* **2026**, *85*, 90. [CrossRef]
172. Li, Z.; Zhang, Y.; Yao, W.J. Review of research on monitoring and prediction technologies for gully erosion. *Sci. Soil Water Conserv.* **2012**, *10*, 110. (In Chinese)
173. Arias, D.; Gallardo, K.; Saldana, M.; Galleguillos-Madrid, F. Urease-Driven Microbially Induced Carbonate Precipitation (MICP) for the Circular Valorization of Reverse Osmosis Brine Waste: A Perspective Review. *Minerals* **2025**, *15*, 543. [CrossRef]
174. Dong, Y.R.; Gao, Z.Q.; Di, J.Z.; Wang, D.; Yang, Z.H.; Wang, Y.F.; Guo, X.Y.; Li, K.F. Experimental study on solidification and remediation of lead–zinc tailings based on microbially induced calcium carbonate precipitation (MICP). *Constr. Build. Mater.* **2023**, *369*, 130611. [CrossRef]
175. Zhang, J.K.; Su, P.D.; Li, L. Microbial induced carbonate precipitation modified steel slag: Mechanical improvement and erosion resistance to sulfate attack. *J. Clean. Prod.* **2023**, *405*, 136982. [CrossRef]
176. Yang, Y.; Chu, J.; Cao, B.; Liu, H.; Cheng, L. Biocementation of soil using non-sterile enriched urease-producing bacteria from activated sludge. *J. Clean. Prod.* **2020**, *262*, 121315. [CrossRef]
177. Lin, W.B.; Gao, Y.P.; Lin, W.; Zhuo, Z.L.; Wu, W.T.; Cheng, X.H. Seawater-based bio-cementation of natural sea sand via microbially induced carbonate precipitation. *Environ. Technol. Innov.* **2023**, *29*, 103010. [CrossRef]
178. Dagliya, M.; Satyam, N.; Sharma, M.; Garg, A. Experimental study on mitigating wind erosion of calcareous desert sand using spray method for microbially induced calcium carbonate precipitation. *J. Rock Mech. Geotech. Eng.* **2022**, *14*, 1556–1567. [CrossRef]
179. Meng, H.; Gao, Y.F.; He, J.; Qi, Y.S.; Hang, L. Microbially induced carbonate precipitation for wind erosion control of desert soil: Field-scale tests. *Geoderma* **2021**, *383*, 114723. [CrossRef]
180. Ahenkorah, I.; Rahman, M.M.; Karim, M.R.; Beecham, S. Unconfined compressive strength of MICP and EICP treated sands subjected to cycles of wetting-drying, freezing-thawing and elevated temperature: Experimental and EPR modelling. *J. Rock Mech. Geotech. Eng.* **2023**, *15*, 1226–1247. [CrossRef]

181. Liu, L.; Liu, H.; Stuedlein, A.W.; Evans, T.M.; Xiao, Y. Strength, stiffness, and microstructure characteristics of biocemented calcareous sand. *Can. Geotech. J.* **2019**, *56*, 1502–1513. [CrossRef]
182. DeJong, J.T.; Mortensen, B.M.; Martinez, B.C.; Nelson, D.C. Bio-mediated soil improvement. *Ecol. Eng.* **2010**, *36*, 197–210. [CrossRef]
183. Wang, D.L.; Tang, C.S.; Pan, X.H.; Liu, B.; Li, H.; Lv, C.; Cheng, Y.J. Tensile strength of fiber-reinforced MICP-treated calcareous sand. *Geol. J. China Univ.* **2021**, *27*, 670–678. (In Chinese)
184. Han, Q.; Jiang, L.; Zhang, Y.; Wang, W.; Li, P.; Lu, W.; Xia, H.; Li, Z. Study on crack-healing effect of cement mortar with fiber under dynamic water environment. *J. Build. Eng.* **2023**, *72*, 106567. [CrossRef]
185. Chen, X.; Zhang, D.; Larson, S.L.; Ballard, J.H.; Knotek-Smith, H.M.; Nie, J.; Hu, N.; Ding, D.; Han, F.X. Microbially induced carbonate precipitation techniques for the remediation of heavy metal and trace element–polluted soils and water. *Water Air Soil Pollut.* **2021**, *232*, 268. [CrossRef]
186. Song, H.W.; Sha, J.Q.; Wei, S.H.; An, J. Low nitrogen MICP remediation of Pb contaminated water by multifunctional microbiome UN-1. *Environ. Technol. Innov.* **2025**, *38*, 104097. [CrossRef]
187. Duan, Y.T.; Yuan, Q.; Yu, C.Q.; Zheng, C.L. A large-scale study on solidification of gold tailings based on microbially induced carbonate precipitation (MICP). *Biogeotechnics* **2025**, *3*, 100164. [CrossRef]
188. Abharian, S.; Sadrekarimi, A. Development of a low-cost MICP protocol for strengthening mine tailings. *Constr. Build. Mater.* **2026**, *518*, 145828. [CrossRef]
189. Wang, J.; Li, Y.; Zhang, S.; Zhang, H.; Li, Z. Decoupling of permeability and strength recovery in microbial-induced calcium carbonate precipitation (MICP) for concrete crack repair. *Results Eng.* **2026**, *29*, 109910. [CrossRef]
190. Zhang, A.; Xu, S.H.; Zhou, C.J.; Shi, G.M.; Yang, D.J.; Guan, W.M.; Zhang, J.H.; Jin, C.; Wang, D.Y.; Pan, X.H. Enhancing mechanical strength of Yili loess soil using microbial-induced calcite precipitation (MICP). *Mater. Today Commun.* **2026**, *52*, 114931. [CrossRef]
191. Dong, Z.H.; Pan, X.H.; Tang, C.S.; Lv, C.; Shi, B. An adjustable bio-sealing method for rock fracture leakage mitigation. *J. Rock Mech. Geotech. Eng.* **2025**, *17*, 220–232. [CrossRef]
192. Fan, L.; Wang, C.B.; Hu, D. Experimental Study on Acoustic Emission Characteristics of Uniaxial Compression of MICP-Filled Sandstone. *Materials* **2023**, *16*, 3428. [CrossRef]
193. Sang, G.J.; Lunn, R.J.; Minto, J.M.; El Mountassir, G. Microbially induced calcite precipitation for sealing anhydrite fractures with gouges. In *Proceedings of the 56th US Rock Mechanics/Geomechanics Symposium, 26–29 June 2022, New Mexico/Online*; ARMA USA: Carson City, NV, USA, 2022.
194. Li, Z.Y.; Wu, C.Z.; He, J.; Cheng, L.; Zhang, F.S. Advance in microbial mineralization for fractured rock mass reinforcement and its application. *J. Zhejiang Univ. (Eng. Sci.)* **2025**, *59*, 2336–2351. [CrossRef]
195. Dai, Q.C.; Pan, X.H.; Tang, C.S.; Shi, B. A bio-healing method for underground long rock fractures with high bridging rate. *J. Rock Mech. Geotech. Eng.* **2026**, *18*, 1359–1367. [CrossRef]
196. Qi, Y.M.; Wang, W.Z.; Fu, P. Field experimental study on MICP technology applied to rock fracture grouting. *J. Water Resour. Archit. Eng.* **2024**, *22*, 127–133. [CrossRef]
197. Liu, Q.L. Seepage Reduction Mechanism of Microbial Mediated Rock Fine Fracture Mineralization Sealing and Its Application in Underground Water-Sealed Oil Storage. Ph.D. Thesis, China University of Geosciences (Beijing), Beijing, China, 2024. (In Chinese)
198. *ASTM D8260-20*; Standard Test Method for Microbial Calcite Precipitation in Soil Specimens. ASTM International: West Conshohocken, PA, USA, 2020.
199. *ISO/TR 23262:2021*; Geotechnics-Use of Microorganisms in Soil Improvement-Technical Report. International Organization for Standardization: Geneva, Switzerland, 2021.
200. FHWA. *Bio-Mediated Soil Improvement: A Review of Recent Advances and Applications*; Federal Highway Administration: Washington, DC, USA, 2016.
201. HTF Market Intelligence. *Global Bio Cement Market Professional Survey Report 2025–2033*; HTF Market Intelligence: Pune, India, 2025.
202. Zhu, J.; Wei, R.J.; Peng, J.; Dai, D. Improvement Schemes for Bacteria in MICP: A Review. *Materials* **2024**, *17*, 5420. [CrossRef] [PubMed]
203. Yan, Z.; Nakashima, K.; Takano, C.; Kawasaki, S. Strategies for cost-optimized biocement production: A comprehensive review. *World J. Microbiol. Biotechnol.* **2025**, *41*, 67. [CrossRef]
204. Song, Z.C.; Shen, D.Y.; Liu, Z.Y.; Wu, C.Z. A rapid and costeffective biogrouting method for forming bio-piles considering in-situ situation. *Acta Geotech.* **2024**, *19*, 5597–5609. [CrossRef]
205. Li, J.H.; Wang, T.; Du, C.Y.; Wang, C.X.; Cao, F.B.; Su, T. Multi-faceted assessment of microbial-reinforced recycled brick aggregate concrete. *Chem. Eng. J.* **2024**, *497*, 154481. [CrossRef]

206. Zúñiga-Barra, H.; Toledo-Alarcón, J.; Torres-Aravena, Á.; Jorquera, L.; Rivas, M.; Gutiérrez, L.; Jeison, D. Improving the sustainable management of mining tailings through microbially induced calcite precipitation: A review. *Miner. Eng.* **2022**, *189*, 107855. [CrossRef]
207. Suer, P.; Hallberg, N.; Carlsson, C.; Bendz, D.; Holm, G. Biogrouting compared to jet grouting: Environmental (LCA) and economical assessment. *J. Environ. Sci. Health Part A Toxic/Hazard. Subst. Environ. Eng.* **2009**, *44*, 346–353. [CrossRef]
208. Wang, J.Q.; Hu, X.M.; Zhao, Y.Y.; Li, X.; Zhao, P.D.; Guo, Y.X. Effects of molasses-based microbial dust suppressant on soil dust and microbial community. *Powder Technol.* **2024**, *441*, 119831. [CrossRef]
209. Liang, S.H.; Chen, J.T.; Niu, J.G.; Gong, X.; Feng, D.L. Using recycled calcium sources to solidify sandy soil through microbial induced carbonate precipitation. *Mar. Georesources Geotechnol.* **2020**, *38*, 393–399. [CrossRef]
210. Wang, Z.X.; Qin, H.C.; Dong, X.; Zhang, W.C. Classification of additives and their influence mechanisms in improving the performance of biologically induced carbonate precipitation. *Environ. Res.* **2025**, *275*, 121376. [CrossRef] [PubMed]
211. Zhang, X.S.; Wang, H.Y.; Wang, Y.; Wang, J.H.; Cao, J.; Zhang, G. Improved methods, properties, applications and prospects of microbial induced carbonate precipitation (MICP) treated soil: A review. *Biogeotechnics* **2025**, *3*, 100123. [CrossRef]
212. Hoffmann, T.D.; Paine, K.; Gebhard, S. Genetic optimisation of bacteria-induced calcite precipitation in Bacillus subtilis. *Microb. Cell Factories* **2021**, *20*, 214. [CrossRef]
213. Wu, C.Z.; Chu, J.; Wu, S.F.; Hong, Y. 3D characterization of microbially induced carbonate precipitation in rock fracture and the resulted permeability reduction. *Eng. Geol.* **2019**, *249*, 23–30. [CrossRef]
214. Xiao, Y.; Zhao, H.H.; Wu, H.R.; Zaman, M.; Liu, H.L. Degradation characteristics of sandstone with inclined biotreated fractures under dry–wet cycles. *Acta Geotech.* **2026**, *21*, 31–39. [CrossRef]
215. Chen, Y.Q.; Liu, Z.Y.; Xia, Z.; Li, L.; Huang, D.W.; Kang, X. Leveraging the Fine-Control MICP framework for cross-scale geoenvironmental applications: A roadmap of innovations and challenges. *Geoenviron. Disasters* **2026**, *13*, 21. [CrossRef]
216. Naveed, M.; Duan, J.G.; Uddin, S.; Suleman, M.; Hui, Y.; Li, H.Y. Application of microbially induced calcium carbonate precipitation with urea hydrolysis to improve the mechanical properties of soil. *Ecol. Eng.* **2020**, *153*, 105885. [CrossRef]
217. Yu, X.N.; Chu, J.; Yang, Y.; Qian, C.X. Reduction of ammonia production in the biocementation process for sand using a new biocement. *J. Clean. Prod.* **2021**, *286*, 124928. [CrossRef]
218. Li, J.H.; Cao, F.B.; Yang, Q.F.; Yi, H.H.; Yang, X.C.; Wang, C.X.; Su, T. Carbon-capture heterologous expression engineering bacteria based on synthetic biology and comprehensive evaluation of its modifying effect on recycled aggregate concrete. *Constr. Build. Mater.* **2025**, *490*, 142425. [CrossRef]

Disclaimer/Publisher's Note: The statements, opinions and data contained in all publications are solely those of the individual author(s) and contributor(s) and not of MDPI and/or the editor(s). MDPI and/or the editor(s) disclaim responsibility for any injury to people or property resulting from any ideas, methods, instructions or products referred to in the content.

coatings

MDPI

Article

Hierarchical Engineering of $CuCo_2O_4$/Nickel–Cobalt–Sulfide Electrode for Improved Energy Storage

Sa Lv [1], Shiyi Wang [1], Runsheng Wang [2], Huan Wang [1], Xuefeng Chu [1], Fan Yang [3], Zehao Zhang [1], Xiaotian Yang [1] and Chao Wang [3,*]

[1] Key Laboratory for Architectural Cold Climate Energy Management, Ministry of Education, Jilin Jianzhu University, Changchun 130118, China; lvsa@jlju.edu.cn (S.L.)
[2] Beijing Xiaomi Mobile Software Co., Ltd., Beijing 100085, China
[3] Provincial Key Laboratory of Architectural Electricity & Comprehensive Energy Saving, Jilin Jianzhu University, Changchun 130118, China
* Correspondence: wangchao@jlju.edu.cn; Tel.: +86-0431-8456-6181

Abstract

The $CuCo_2O_4$/nickel–cobalt–sulfide (NCS) composite electrode was fabricated on nickel foam (NF) substrate using a combination of hydrothermal method and constant-potential electrodeposition. Supported by the underlying $CuCo_2O_4$, the NCS layer was then systematically deposited by varying the deposition time to achieve the optimal deposition amount. This hierarchical architecture maximizes the exposure and utilization of electrochemically active sites from both components. The optimized $CuCo_2O_4$/NCS electrode delivers an areal specific capacitance (*C*s) of 5.18 F cm^{-2} at a discharge current density of 2 mA cm^{-2}, with a coulombic efficiency of 99.61%. Upon increasing the current density 30-fold to 60 mA cm^{-2}, the electrode retains 67.95% of its original capacitance. The equivalent series resistance (R_{ESR}) is 0.96 Ω cm^{-2}. Cycling stability tests show that 90% of the initial *C*s is maintained after 2200 cycles, dropping to 80% at 2900 cycles and remaining stable thereafter.

Keywords: hierarchical structures; chronoamperometry; hydrothermal method; energy storage

1. Introduction

The explosive growth of portable electronics and electric vehicles has created an urgent demand for developing high-performance electrochemical energy-storage devices [1]. Although these systems bridge the power–energy gap between dielectric capacitors and conventional batteries, their large-scale deployment is hindered by low energy density and short cycle life. As the key determinant of device performance, electrode materials must overcome intrinsic limitations such as long ion-diffusion paths, scarce electrochemically active sites, and structural pulverization induced by cyclic volume changes [2–4]. Precise construction of atom-to-nanoscale frameworks with high specific surface areas and hierarchical porosity can simultaneously shorten diffusion distances, increase active sites, and buffer volume variations, thereby overcoming these bottlenecks. Such architectures facilitate rapid transport pathways for ions and electrons, leading to substantial gains in capacitance and energy density [5–7].

Among various structural design strategies, a widely adopted approach involves sequentially growing different active components on conductive substrates such as carbon

cloth, nickel foam (NF), and stainless steel mesh to construct hierarchical core–shell or multilayer composite architectures [8,9]. In this regard, hydrothermal synthesis and electrodeposition have become the preferred methods for the in situ fabrication of such structures, owing to their short preparation periods, excellent reproducibility, and facile control of deposition amounts [10,11]. For the selection of active components, metal oxide/hydroxide-based electrode materials are particularly attractive owing to their superior theoretical specific capacities and abundant pseudocapacitive active sites [12]. Meanwhile, controllable synthesis strategies enable uniform and stable nanostructures, avoiding issues commonly encountered in carbon materials, such as stacking-induced aggregation and surface chemical inertness, thereby demonstrating greater development potential for practical applications [13].

Typical binary metal oxides include $NiCo_2O_4$, $CuCo_2O_4$, and $NiMo_2O_4$ [14–16]. For instance, Liu et al. reported the fabrication of a $CuCo_2O_4$ nanoflower electrode with enriched oxygen vacancies, achieving a *C*s of 1.2 F cm^{-2} at 1.2 mA cm^{-2} [17]. In another study, You et al. designed a $NiCo_2O_4/NiMoO_4$ composite electrode on conductive carbon cloth via a two-step hydrothermal method, with the optimized hierarchical electrode delivering a high *C*s of 3.85 F cm^{-2} at 4 mA cm^{-2} [18]. Similarly, Zhao et al. synthesized a $NiMoO_4@Ni_3S_2$ electrode through a two-step hydrothermal reaction, which also exhibited a high *C*s of 2.3 F cm^{-2} at 1 mA cm^{-2} [19]. In these examples, binary metal oxides functioned as active electrode components and structural supports simultaneously, thereby combining high specific surface area, abundant active sites, and rapid ion/electron transport.

Based on the above analysis, this study employed a combined strategy of hydrothermal synthesis and electrodeposition to in situ construct the $CuCo_2O_4$/NCS electrode. Initially, a Cu-Co hydroxide precursor was grown on the NF substrate via the hydrothermal method and subsequently converted into $CuCo_2O_4$ nanorod arrays through high-temperature calcination. Thereafter, an NCS layer was controllably deposited onto the $CuCo_2O_4$ surface using chronoamperometry. By regulating the electrodeposition time, precise optimization of the NCS loading was achieved, ultimately yielding a $CuCo_2O_4$/NCS composite electrode with superior energy storage properties. This stepwise construction strategy enables controlled integration of metal oxide and metal sulfide components, promoting interfacial coupling between the $CuCo_2O_4$ scaffold and NCS. The hierarchical architecture enhances electrochemical active site utilization and charge transfer efficiency, leading to improved *C*s compared to the individual components. This approach offers a promising direction for optimizing composite electrode design for energy storage systems.

2. Materials and Methods

2.1. Materials

NF was cut into pieces of 1.0 cm × 1.5 cm and rinsed sequentially with dilute HCl, ethanol, and deionized water to remove surface oxides and contaminants. All chemicals used were of analytical grade.

2.2. Hierarchical Construction of $CuCo_2O_4$/NCS Electrode

Step 1. A mixed solution containing 0.025 M $Cu(NO_3)_2 \cdot 3H_2O$, 0.05 M $Co(NO_3)_2 \cdot 6H_2O$ and 0.3 M urea was subjected to hydrothermal treatment at 120 °C for 6 h. The resulting Cu-Co precursor was collected, repeatedly washed with absolute ethanol and deionized water, and then calcined at 350 °C for 6 h to obtain $CuCo_2O_4$.

Step 2. A mixed electrolyte containing 0.05 M $Co(NO_3)_2 \cdot 6H_2O$, 0.05 M $NiCl_2 \cdot 6H_2O$ and 0.5 M thiourea was prepared. Potentiostatic electrodeposition was carried out at

https://doi.org/10.3390/coatings16030270

−1.1 V (vs. SCE) in a three-electrode configuration, using the $CuCo_2O_4$ obtained in Step 1 as the working electrode, a saturated calomel electrode (SCE) as the reference, and a Pt foil as the counter electrode. Deposition times of 60 s, 150 s, 300 s and 450 s were applied, and the resulting samples were denoted as S-60, S-150, S-300 and S-450, respectively. After deposition, the electrodes were rinsed with absolute ethanol followed by deionized water.

2.3. Characterization

The samples were characterized by X-ray diffraction (XRD, Cu Kα radiation with λ = 1.5406 Å, Shimadzu Co., Ltd., Kyoto, Japan), field-emission scanning electron microscopy (FE-SEM, JSM-7610F 15.0 kV, Tokyo, Japan) and X-ray photoelectron spectroscopy (XPS, ESCALAB 250Xi, ThermoFisher Scientiffffc Co., Ltd., Waltham, MA, USA, Al Kα as X-ray source). The electrochemical properties were investigated via cyclic voltammetry (CV), galvanostatic charge–discharge (GCD), electrochemical impedance spectroscopy (EIS) and cycling stability measurements using a CHI 760E electrochemical workstation configured in a three-electrode mode: $CuCo_2O_4$/NCS working electrode, Pt foil counter electrode, Ag/AgCl reference electrode, and 2 M NaOH aqueous electrolyte.

3. Results

Figure 1 provides a schematic of the synthesis of $CuCo_2O_4$/NCS electrode. After hydrothermal reaction, a blue-green Cu-Co hydroxide precursor layer formed on the NF substrate and turned into black $CuCo_2O_4$ upon high-temperature calcination. An NCS layer was then electrodeposited onto the $CuCo_2O_4$ surface by chronoamperometry, yielding the $CuCo_2O_4$/NCS composite electrode.

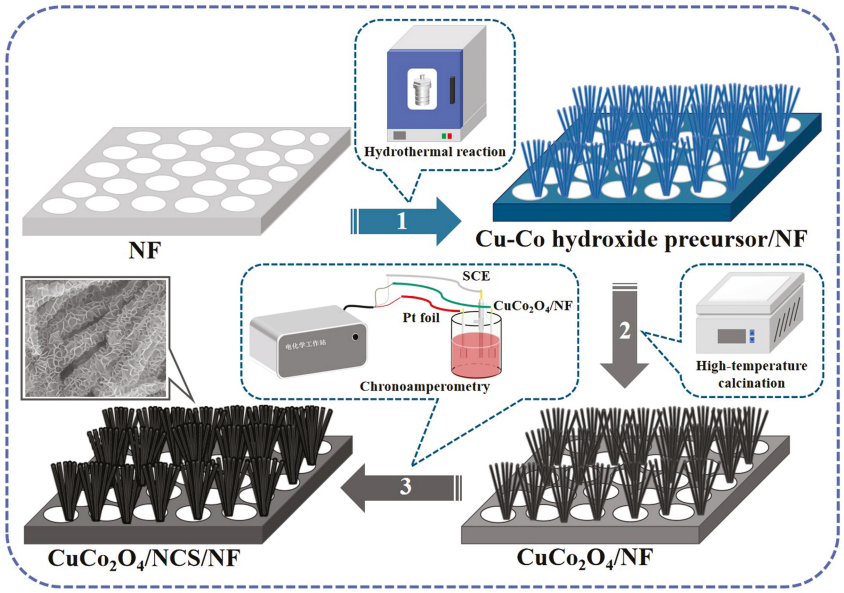

Figure 1. Fabrication schematic of $CuCo_2O_4$/NCS electrode.

The XRD pattern of the $CuCo_2O_4$/NCS electrode (Figure S1) displays two intense peaks-marked with stars-that can be indexed to the NF substrate (JCPDS 01-1258). Additionally, the diffraction peaks designated by squares and diamonds match the $CuCo_2O_4$ (JCPDS No. 37-0878) and NCS (JCPDS No. 43-1477) components, respectively. These relatively weak signals arise because the nanoscale active film electrodeposited on the macroporous NF has an ultra-low mass loading and high dispersion, yielding insufficient long-range order to produce sharp peaks distinguishable from the intense substrate signals [20]. The XPS spectra of the $CuCo_2O_4$/NCS electrode are presented in Figure 2. The survey scan (Figure 2a) exhibits distinct photoelectron peaks for Cu, Co, Ni, O and S, con-

firming the formation and elemental composition of the composite. In the high-resolution Cu 2p spectrum (Figure 2b), spin–orbit–split Cu $2p_{1/2}$ and Cu $2p_{3/2}$ peaks are observed at 954.22 and 934.53 eV, respectively, together with their shake-up satellites (labeled sat.) at 962.97 and 942.18 eV [21]. The Co 2p region (Figure 2c) shows Co $2p_{1/2}$ and Co $2p_{3/2}$ main peaks centered at 796.68 and 781.03 eV, with attendant satellites at 802.55 and 786.37 eV. Deconvolution further resolves each spin–orbit component into Co^{2+} (797.55 and 781.77 eV) and Co^{3+} (796.42 and 780.65 eV) contributions [22]. The Ni 2p spectrum (Figure 2d) displays principal Ni $2p_{1/2}$ and Ni $2p_{3/2}$ peaks at 873.84 and 856.02 eV, accompanied by shake-up satellites at 880.12 and 861.75 eV. Fitted components at 873.93 and 856.26 eV are assigned to Ni^{3+}, whereas those at 872.53 and 855.09 eV are attributed to Ni^{2+} [23]. In the O 1s region (Figure 2e), bands at 531.48 and 530.82 eV are assigned to OH^- and metal–oxygen (M–O) bonds, respectively [24]. Finally, the S 2p spectrum (Figure 2f) exhibits S $2p_{1/2}$ and S $2p_{3/2}$ peaks at 162.70 and 160.27 eV, while features at 168.58 and 167.44 eV correspond to S–O $2p_{1/2}$ and S–O $2p_{3/2}$ [25].

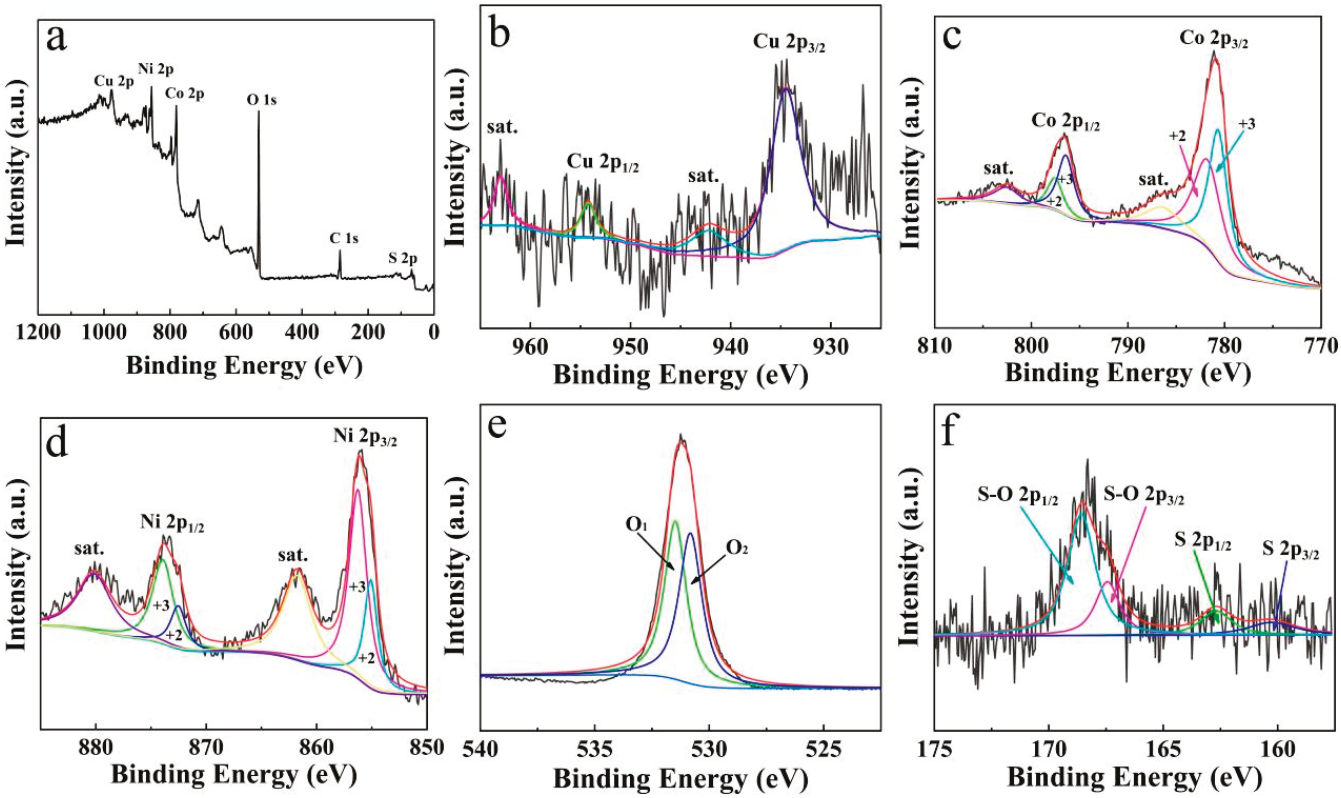

Figure 2. XPS analysis of $CuCo_2O_4$/NCS electrode: (**a**) survey scan, (**b**) Cu 2p, (**c**) Co 2p, (**d**) Ni 2p, (**e**) O 1s and (**f**) S 2p.

Figure 3a presents FE-SEM images of the Cu-Co hydroxide precursor prepared by a hydrothermal method. A dense, uniform precursor layer fully covers the NF surface. Higher-magnification inspection (Figure 3b) reveals that the layer consists of slender, needle-like nanostructures arranged in a radial array, approximately 140 nm in diameter, with smooth side surfaces. After high-temperature calcination, the resulting $CuCo_2O_4$ is shown in Figure 3c. Dehydration renders the nanorods thinner and slightly curved, and their diameter shrinks to 80–110 nm, with occasional micro-cracks visible along the nanorods (Figure 3d).

https://doi.org/10.3390/coatings16030270

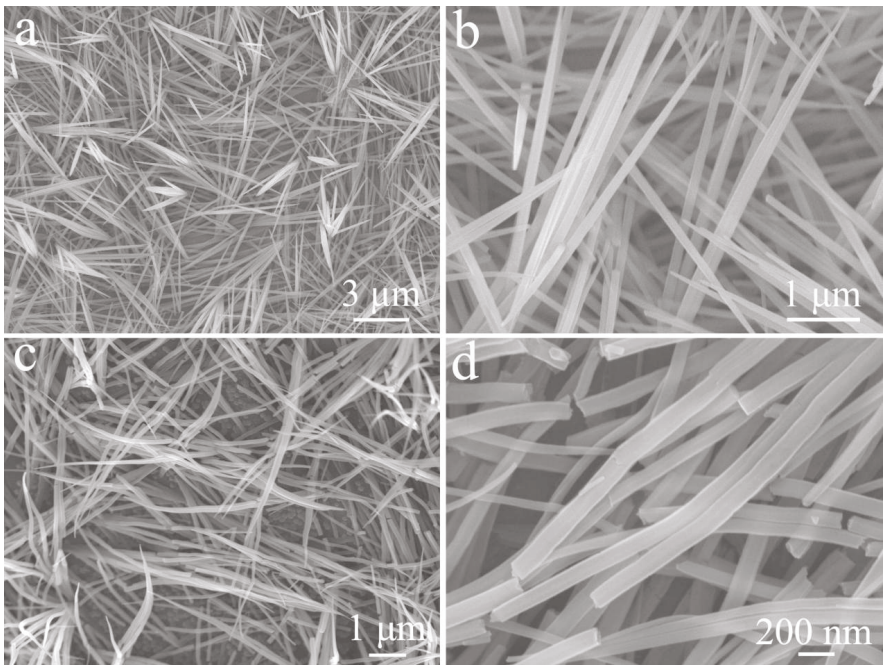

Figure 3. FE-SEM images of (**a**,**b**) Cu-Co hydroxide precursor and (**c**,**d**) $CuCo_2O_4$ at different magnifications.

Figure 4 shows FE-SEM images of the $CuCo_2O_4$/NCS electrode prepared by electrodepositing an NCS layer (300 s) on the $CuCo_2O_4$ surface. At low magnification (Figure 4a,b), the rod-like architecture of $CuCo_2O_4$ was preserved and each rod was uniformly and conformally sheathed by a dense NCS layer of homogeneous thickness, with no bulk aggregation. Higher-magnification images (Figure 4c,d) reveal that the NCS layer is constructed from interconnected, curved nanosheets approximately 10 nm in thickness, whose interconnection creates numerous small chambers.

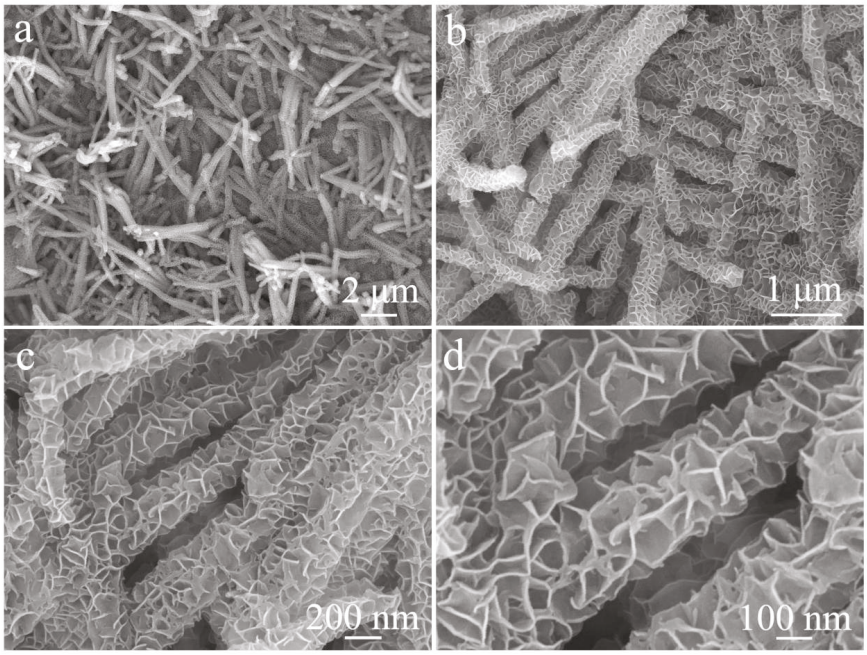

Figure 4. FE-SEM images of the $CuCo_2O_4$/NCS electrode at different magnifications: (**a**,**b**) low magnification; (**c**,**d**) high magnification.

https://doi.org/10.3390/coatings16030270

In fact, the morphology of the single-component NCS layer was also recorded, as shown in Figure S2. Without the support of the underlying $CuCo_2O_4$, the curved NCS nanosheets—approximately 15 nm thick—interconnected, forming a uniform, dense coverage on the NF surface.

Figure 5a presents a comparison of the CV profiles of $CuCo_2O_4$/NCS, $CuCo_2O_4$ and NCS electrodes recorded at 10 mV s^{-1}. All display well-defined, symmetric redox peaks, indicating pronounced pseudocapacitive behavior and highly reversible faradaic reactions. The $CuCo_2O_4$/NCS composite electrode delivers a substantially larger CV-integrated area, evidencing superior charge–storage capacity. The GCD curves of the three electrodes measured at 2 mA cm^{-2} are shown in Figure 5b. The $CuCo_2O_4$/NCS electrode exhibits a markedly longer discharge duration than the single-component $CuCo_2O_4$ and NCS electrodes, confirming enhanced energy storage performance consistent with the CV results. This enhancement stems from Faradaic redox processes involving multiple redox couples [23,26,27]:

$$CuCo_2O_4 + H_2O + e^- \leftrightarrow 2CoOOH + CuOH \quad (1)$$

$$CoOOH + OH^- \leftrightarrow CoO_2 + H_2O + e^- \quad (2)$$

$$CuOH + OH^- \leftrightarrow Cu(OH)_2 + e^- \quad (3)$$

$$NiS + OH^- \leftrightarrow NiSOH + e^- \quad (4)$$

$$CoS + OH^- \leftrightarrow CoSOH + e^- \quad (5)$$

$$CoSOH + OH^- \leftrightarrow CoSO + H_2O + e^- \quad (6)$$

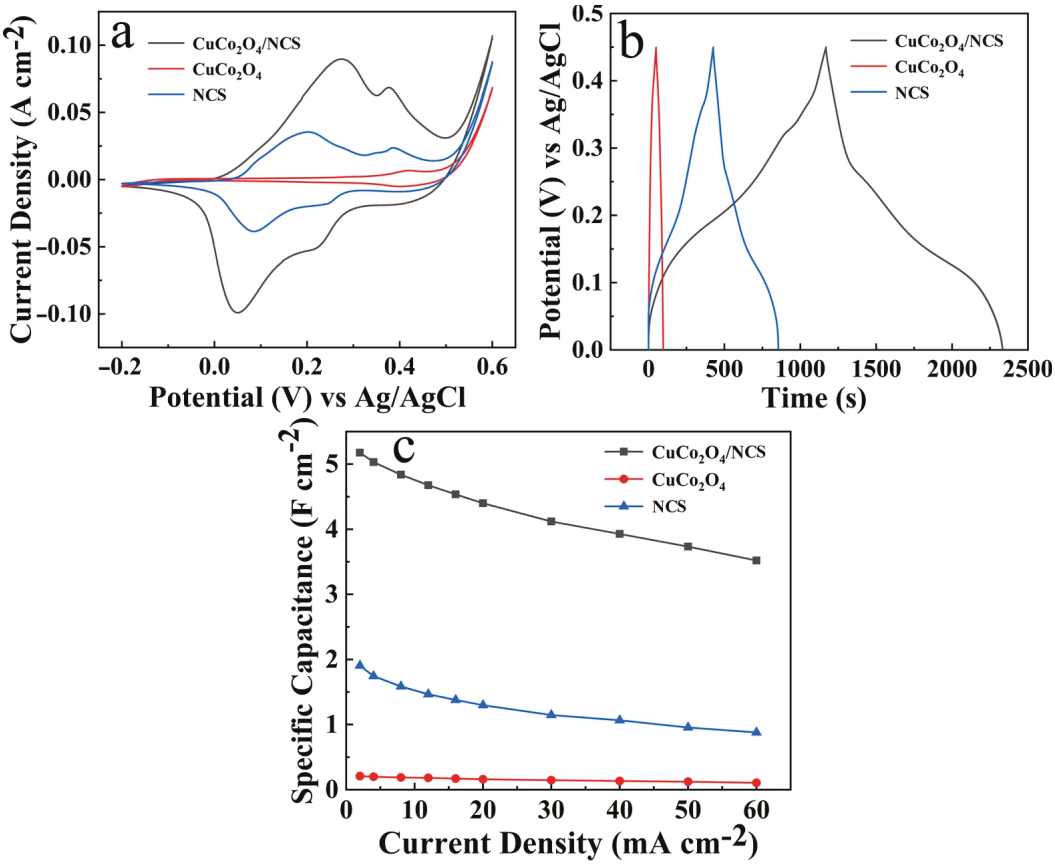

Figure 5. Electrochemical performance of $CuCo_2O_4$/NCS, $CuCo_2O_4$ and NCS electrodes: (**a**) CV curves; (**b**) GCD curves; (**c**) Cs at various current densities.

https://doi.org/10.3390/coatings16030270

*C*s calculations based on the discharge times (formula given in the SI) yield values of 5.18, 0.21 and 1.91 F cm^{-2} at 2 mA cm^{-2} for the $CuCo_2O_4$/NCS, $CuCo_2O_4$ and NCS electrodes, respectively (Figure 5c), further validating the rationality and effectiveness of the hybridization strategy. In addition, the EIS spectra were employed to evaluate the $CuCo_2O_4$/NCS, $CuCo_2O_4$, and NCS electrodes (Figure S3). The significantly reduced *R*ct value observed for the $CuCo_2O_4$/NCS composite relative to pristine $CuCo_2O_4$ and NCS suggests accelerated ion transport across the interface, thereby facilitating enhanced electrochemical reaction kinetics [16].

Driven by the above comparative analysis, a set of parallel experiments was conducted in which the NCS electrodeposition time on the $CuCo_2O_4$ underlayer was systematically varied to tune the $CuCo_2O_4$/NCS electrode morphology and thus identify the optimal fabrication condition. Figure 6 reveals the microstructure of the $CuCo_2O_4$/NCS electrode prepared with different NCS deposition times. At the earliest stage (60 s), as shown in Figure 6a, the $CuCo_2O_4$ nanorods appear slightly rough. Higher magnification (Figure 6b) reveals that they are uniformly wrapped by a layer of curved NCS nanoflakes. When the deposition time is increased to 150 s, the nanorods become thicker, and the overlying NCS nanoflakes are more distinct, denser, and larger (Figure 6c,d). This trend persists at 300 s, rendering the $CuCo_2O_4$ nanorods even more robust (Figure 6e,f). However, prolonging the electrodeposition to 450 s (Figure 6g,h) leads to excessive NCS growth, and most $CuCo_2O_4$ nanorods are buried, with only a few protruding nanorods remaining visible beneath the thick NCS coating.

Subsequently, the electrochemical properties of the four parallel electrodes were systematically assessed. The CV curves of the four electrodes under a scan rate of 10 mV s^{-1} are depicted in Figure 7a. It is evident that the integrated area of the CV curves increases systematically with prolonging NCS deposition time, indicating enhanced charge–storage capacity [24,28]. Figure 7b further compares the GCD profiles of them set at 2 mA cm^{-2}. The same trend is observed, as the discharge time increases systematically with NCS deposition time, leading to higher *C*s values. Figure 7c presents the *C*s of them at different current densities. At 2 mA cm^{-2}, the *C*s values for S-60, S-150, S-300 and S-450 are 6.55, 5.18, 4.53 and 1.88 F cm^{-2}, respectively. Although S-450 delivers the highest *C*s, it decays much more rapidly than S-300 as the current density increases. Consequently, S-300 exhibits the best rate capability, retaining 67.95% of its initial capacitance upon increasing the current density 30-fold from 2 to 60 mA cm^{-2} (Figure 7d). Additionally, Figure 7e records the voltage drop across each electrode at various current densities. The equivalent series resistance (R_{ESR}) of S-300, calculated using the formula provided in the SI, is 0.96 Ω cm^{-2}, significantly lower than that of the other samples. Accordingly, S-300, identified as the optimal sample, was selected for further investigation.

Figure 8a presents the CV curves of the $CuCo_2O_4$/NCS (S-300) electrode recorded at various scan rates. A pair of well-defined, nearly symmetric redox peaks is observed, confirming that charge storage is dominated by Faradaic reactions—that is, a typical pseudocapacitive mechanism. As the scan rate increases, the peak currents grow systematically, indicating fast electrode kinetics [29]. Figure 8b shows the GCD data. Significantly, the GCD profiles preserve near-ideal symmetry across elevated current densities, evidencing highly reversible redox kinetics [15]. Lower current densities result in longer discharge times, corresponding to higher *C*s. This trend is quantified in Figure 8c, where *C*s drops from 5.18 to 3.52 F cm^{-2} across the current density range of 2–60 mA cm^{-2}, retaining 67.96% of its initial value even after a 30-fold current increase. Figure 8d displays the voltage-drop curve, and the R_{ESR} of the $CuCo_2O_4$/NCS electrode, calculated from the slope, is 0.96 Ω cm^{-2}, a value also labeled in Figure 7e.

https://doi.org/10.3390/coatings16030270

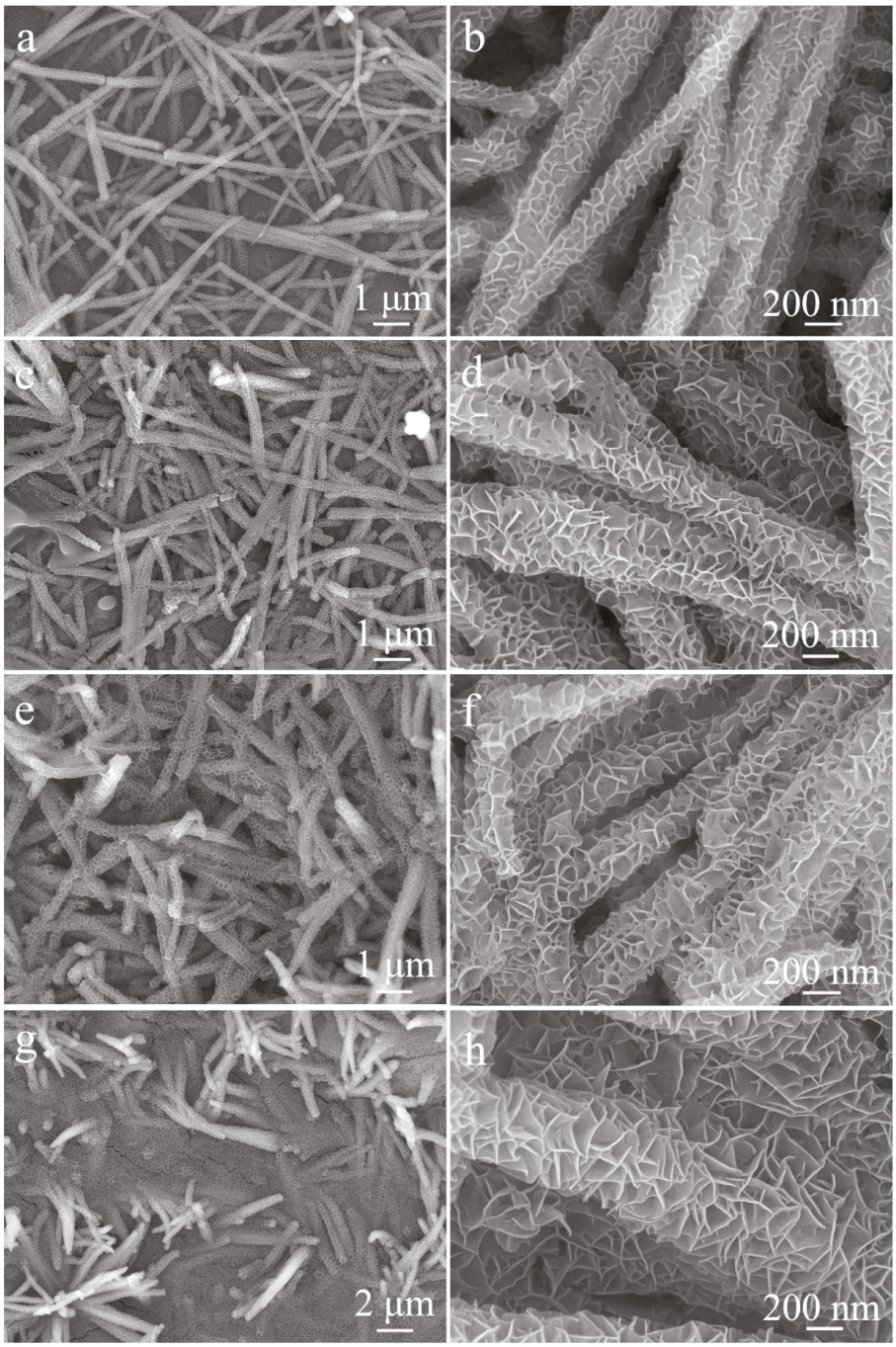

Figure 6. FE-SEM images of the $CuCo_2O_4$/NCS electrode at different NCS deposition times: (**a**,**b**) 60 s (S-60); (**c**,**d**) 150 s (S-150); (**e**,**f**) 300 s (S-300); (**g**,**h**) 450 s (S-450).

Figure S4 presents the electrochemical response of the single-component $CuCo_2O_4$ and NCS electrodes. CV plots (Figure S4a,b) reveal that both materials exhibit Faradaic pseudocapacitance through broad redox humps. The integrated area under the CV curve for the NCS electrode is markedly larger than that for $CuCo_2O_4$, indicating superior charge-storage capability. GCD profiles (Figure S4c,d) show the same trend, with the NCS electrode delivering significantly longer discharge times than the $CuCo_2O_4$ electrode at any given current density. CS data (Figure S4e,f) quantify this difference. $CuCo_2O_4$ provides 0.96 F cm^{-2} at 2 mA cm^{-2} and retains 0.63 F cm^{-2} at 60 mA cm^{-2}, whereas NCS decreases from 1.92 to 0.81 F cm^{-2} over the same range. These results demonstrate that using $CuCo_2O_4$ as a scaffold allows a larger amount of the higher-performance NCS to

https://doi.org/10.3390/coatings16030270

be deposited. Through this synergistic effect, the $CuCo_2O_4$/NCS composite electrode exhibits significantly enhanced performance, validating the original design strategy.

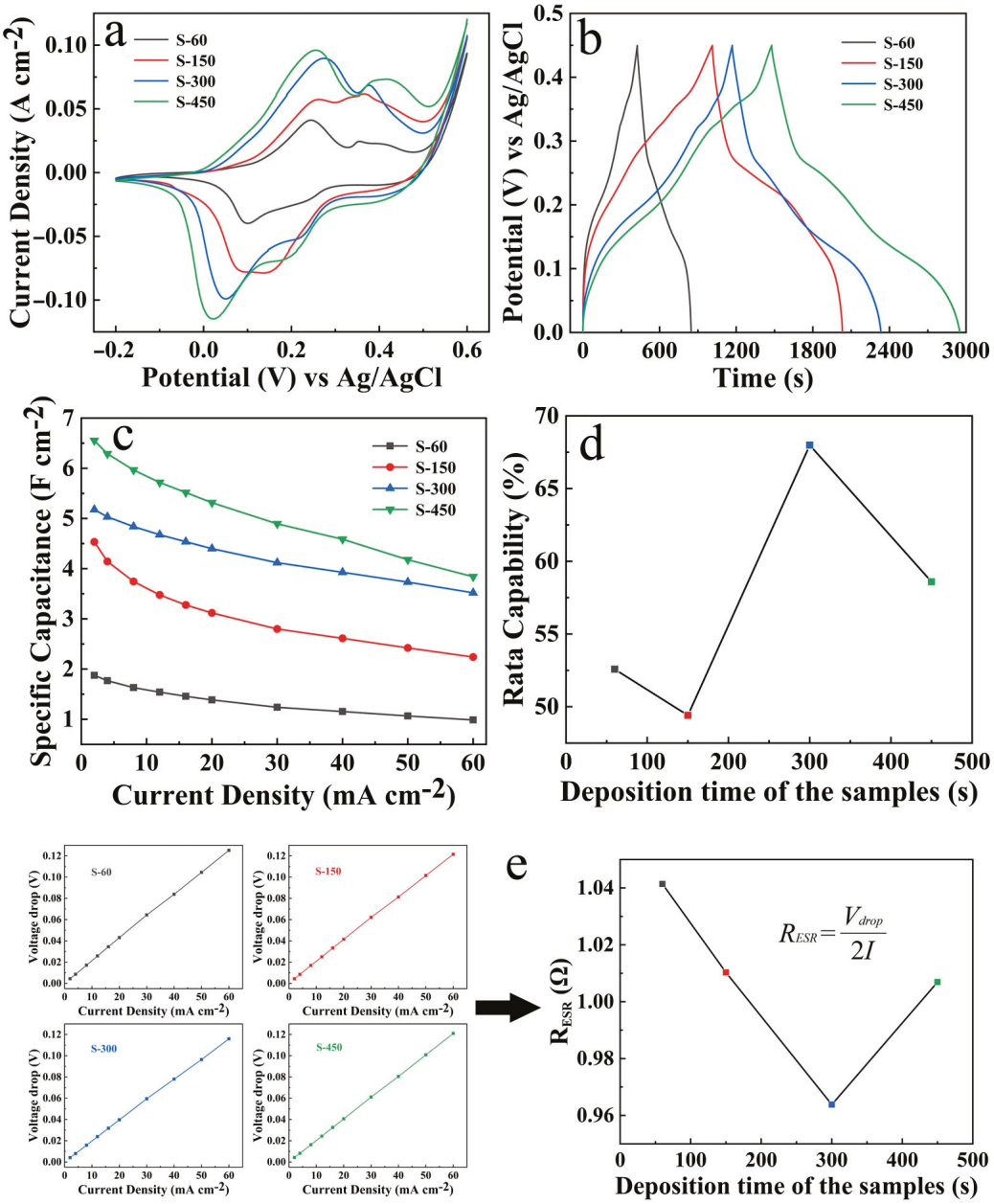

Figure 7. Electrochemical performance comparison of S-60, S-150, S-300 and S-450: (**a**) CV (10 mV s^{-1}); (**b**) GCD (2 mA cm^{-2}); (**c**) C_S at different current densities; (**d**) rate capability; (**e**) voltage-drop curves at various current densities and the corresponding R_{ESR}.

The cycling stability of the $CuCo_2O_4$/NCS electrode was further evaluated (Figure 9). After 2200 charge–discharge cycles, about 90% of the initial *C*s was retained. Approximately 20% decay had occurred by the 2900th cycle, and 80% of the initial capacitance was maintained steadily until the test was completed at 5000 cycles. As shown in Figure S5a, the CV curves maintained a similar shape after 5000 cycles. Likewise, the GCD profiles (Figure S5b) exhibited discharge times of roughly 80% relative to those before the stability test; consequently, the *C*s is also retained at approximately 80% of the original value. Additionally, the EIS spectra (Figure S5c) show an extremely slight increase in charge transfer resistance after cycling, which is virtually negligible, rendering the curves before and after cycling nearly identical and demonstrating satisfactory structural and electrochemical sta-

bility of the $CuCo_2O_4$/NCS electrode. FE-SEM analysis was subsequently performed to investigate the cause of this moderate capacitance decay. As shown in Figure 10, the hierarchical architecture of the $CuCo_2O_4$/NiCoS electrode remained essentially unchanged after electrochemical testing, with no large-scale collapse or agglomeration observed. However, repeated redox reactions slightly reduced the packing density of the NiCoS nanosheets, accounting for the observed ~20% *C*s decay.

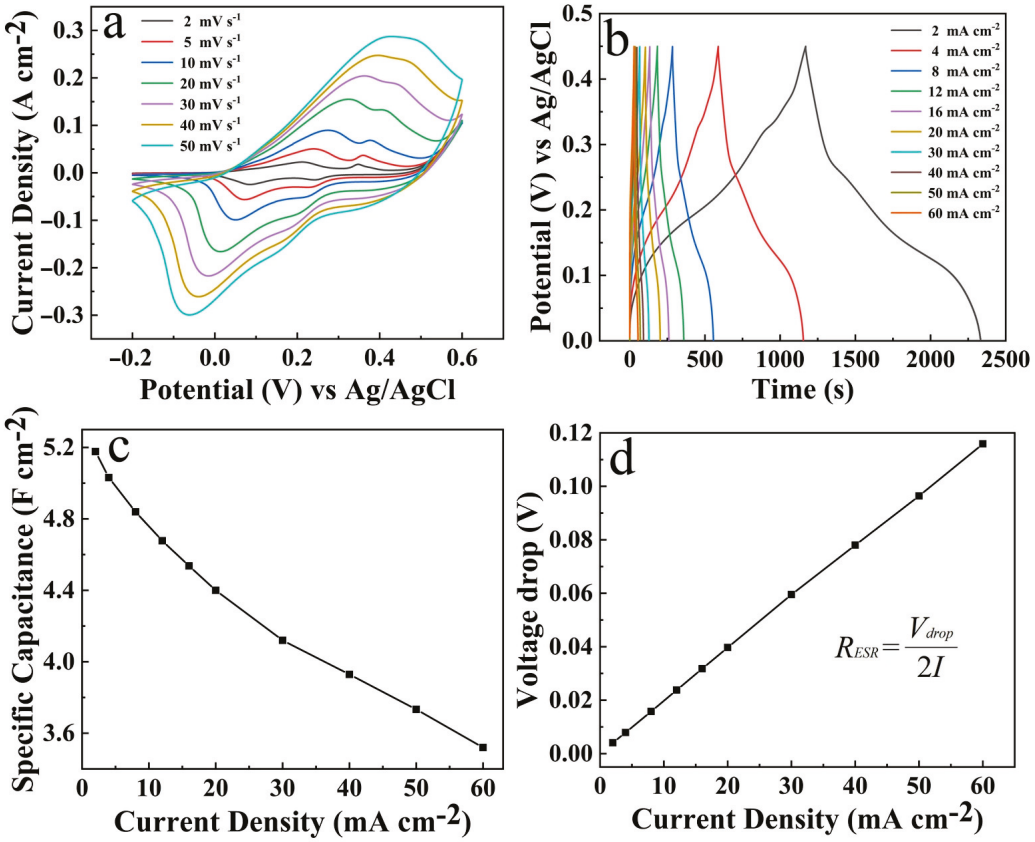

Figure 8. Electrochemical performance of $CuCo_2O_4$/NCS electrode: (**a**) CV curves; (**b**) GCD curves; (**c**) *C*s and (**d**) voltage drops at various current densities.

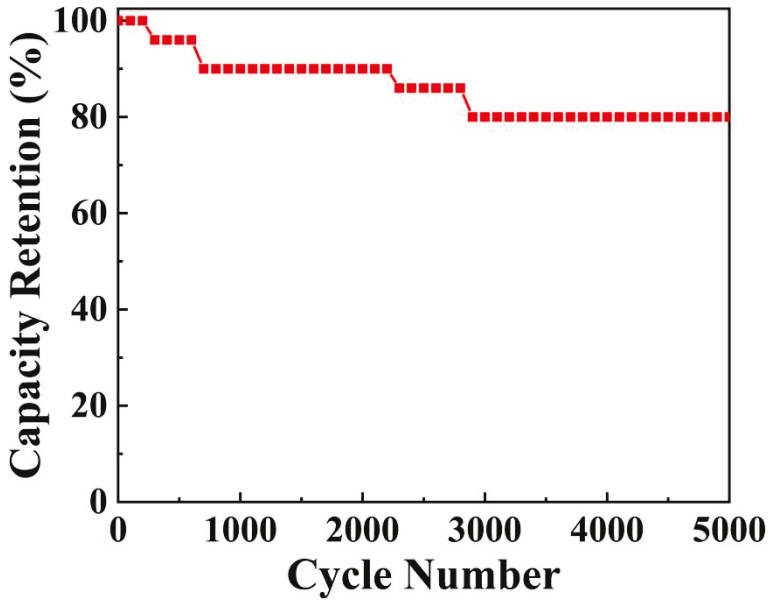

Figure 9. Cycling stability of $CuCo_2O_4$/NCS electrode.

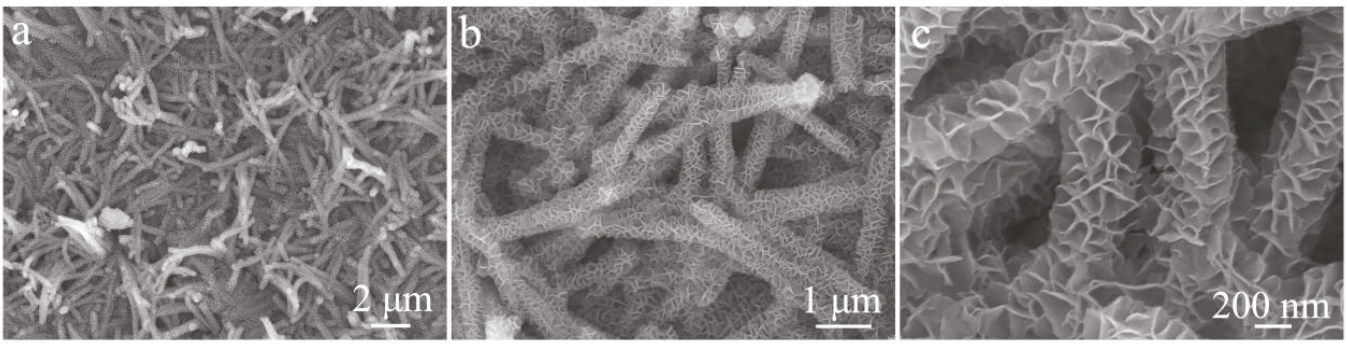

Figure 10. FE-SEM image of the $CuCo_2O_4$/NCS electrode subsequent to electrochemical measurements: (**a**,**b**) low magnification; (**c**) high magnification.

Table 1 presents a comparison of test conditions and Cs values between reported representative electrodes and the as-prepared hierarchical $CuCo_2O_4$/NCS electrode. The superior capacitive performance is mainly attributed to the following factors: (1) Scalable and controllable composite synthesis strategy. Uniform $CuCo_2O_4$ nanorod arrays are first grown hydrothermally and then calcined at high temperature; subsequently, an NCS layer is deposited potentiostatically without any post-treatment. Simply adjusting the electrodeposition time from 60 s to 450 s allows continuous optimization of the active layer deposition amount and surface morphology. The optimum is reached at 300 s, yielding a *C*s of 5.18 F cm^{-2} at 2 mA cm^{-2} and 67.95% retention upon increasing the current 30-fold. This overlap between the processing window and the performance maximum confirms the protocols controllability, reproducibility and high efficiency [29]. (2) Multi-component synergistic effect. $CuCo_2O_4$ provides a robust scaffold and extra pseudocapacitance, whereas the conformal NCS nanosheets form a hierarchical architecture. Together they multiply active sites and facilitate charge transport, surpassing the limitations of either single component [22]. (3) Optimized microstructure design. The interlaced voids formed between $CuCo_2O_4$ nanorods and NCS nanosheets enlarge the electrodes specific surface area, ensure full contact between electrolyte and active material, and shorten ion-diffusion paths, thereby markedly reducing charge–transfer resistance and endowing the electrode with superior rate capability and long-term cycling stability [9,28].

Table 1. Comparison of *C*s values for representative electrodes.

Electrode	Substrate	Electrolyte	Current Density (mA cm^{-2})	*C*s (F cm^{-2})	Ref.
$NiCo_2O_4$/NiCo-LDO	Ni foam	3 M KOH	6	3.85	[14]
$CuCo_2O_4$	Ni foam	3 M KOH	1.2	1.20	[17]
$NiCo_2O_4$/$NiMoO_4$	carbon cloth	2 M KOH	4	3.85	[18]
$NiMoO_4$@Ni_3S_2	Ni foam	3 M KOH	1	2.30	[19]
NiCoS	Ni foam	1 M KOH	1ă	3.31ă	[30]
Se–NiCoS	Ni foam	3 M KOH	1	2.00	[31]
Ni_3S_4/CoS	carbon fiber	1 M KOH	2	5.10	[32]
NiCoSe@CoS	Ni foam	3 M KOH	3	3.28	[33]
$Cu(OH)_2$/Ni_3S_2	Cu foam	2 M NaOH	2	4.85	[34]
$CuCo_2O_4$/NCS	Ni foam	2 M NaOH	2	5.18	this work

https://doi.org/10.3390/coatings16030270

4. Conclusions

A hierarchical $CuCo_2O_4$/NCS electrode was constructed by growing $CuCo_2O_4$ nanorod arrays on NF via a hydrothermal–calcination route and subsequently depositing NCS nanosheets potentiostatically. This two-step protocol is robust, scalable and parameter-tunable. Merely adjusting the electrodeposition time from 60 s to 450 s allows precise control of active-layer loading and morphology without any post-treatment. At the optimum time (300 s) the electrode delivers 5.18 F cm^{-2} at 2 mA cm^{-2} and retains 67.95% of its capacity when the current is stepped up 30-fold, demonstrating exceptional rate capability. Additionally, 80% of the initial *C*s is preserved after 5000 cycles. Characterized by operational simplicity, flexible tunability and high reproducibility, the hierarchical construction strategy provides a practical and readily adaptable route for the controllable fabrication of multilayer composite electrodes.

Supplementary Materials: The following supporting information can be downloaded at https://www.mdpi.com/article/10.3390/coatings16030270/s1, Figure S1: XRD pattern of $CuCo_2O_4$/NCS electrode; Figure S2: FE-SEM images of single-component NCS at different magnifications; Figure S3: EIS spectra of $CuCo_2O_4$/NCS, $CuCo_2O_4$ and NCS electrodes; Figure S4: Electrochemical performance of single-component $CuCo_2O_4$ and NCS electrodes: (**a**,**b**) CV; (**c**,**d**) GCD; (**e**,**f**) *C*s at various current densities; Figure S5: Electrochemical performance of the $CuCo_2O_4$/NiCoS electrode: (**a**) CV and (**b**) GCD curves after the stability test; (**c**) EIS spectra before and after the stability test; Formula for calculating the *C*s and R_{ESR}.

Author Contributions: Conceptualization, H.W.; methodology, F.Y. and C.W.; software, R.W.; formal analysis, X.C. and X.Y.; investigation, Z.Z. and S.W.; writing—original draft preparation, S.W. and R.W.; writing—review and editing, S.L.; supervision, C.W.; funding acquisition, X.Y. and S.L. All authors have read and agreed to the published version of the manuscript.

Funding: This research was funded by National Natural Science Foundation of China (Grant No. 62374073) and the Scientific Research Project of the Education Department of Jilin Province, China (Grant No. JJKH20240363KJ).

Institutional Review Board Statement: Not applicable.

Informed Consent Statement: Not applicable.

Data Availability Statement: The original contributions presented in this study are included in the article/Supplementary Materials. Further inquiries can be directed to the corresponding author.

Conflicts of Interest: Author Runsheng Wang was employed by the company Beijing Xiaomi Mobile Software Co., Ltd. The remaining authors declare that the research was conducted in the absence of any commercial or financial relationships that could be construed as a potential conflict of interest.

References

1. Sun, Z.X.; Wang, R. Emerging nanomaterials for energy storage: A critical review of metrics, hotspots, and future directions. *Renew. Sustain. Energy Rev.* **2025**, *224*, 116093. [CrossRef]
2. Dorji, G.; Minakshi, M.; Ariga, K.; Shrestha, L.K. Binary transition metal oxides vs. binary metal oxides for electrochemical supercapacitors: Performance, challenges, and future prospects. *J. Energy Storage* **2026**, *147*, 120116. [CrossRef]
3. Irfan, M.; Shahi, A.; Bari, M.A.; Laiba; Atiq, S.; Shakoor, A.; Sadiq, I.; Tariq, A.; Adnan, M.; Shahzad, A.; et al. Emerging composite electrode architectures based on transition metal oxides for high-performance Li-ion capacitors. *RSC Adv.* **2026**, *16*, 4801–4840. [CrossRef]
4. Reddy, B.P.; Pabba, D.P.; Sreedevi, G.; Alzahrani, F.M.A.; Al-Buriah, M.S.; Alsaiari, N.S.; Park, S.H.; Mangiri, R. Self-assembled porous $Ni(HCO_3)_2$ microspheres with ultrahigh-capacity for battery-type supercapacitors. *J. Phys. Chem. Solids* **2026**, *208*, 113141.
5. Xu, Z.H.; Li, X.L.; Li, Q.W.; Lv, K.; Liu, J.S.; Hang, X.K.; Bayaguud, A. Mechanism research progress on transition metal compound electrode materials for supercapacitors. *Rare Metals* **2024**, *43*, 4076–4098. [CrossRef]

6. Chen, J.M.; Zhang, H.L.; Peng, X.; Shao, X.; Chai, Y.F.; Ma, M.; Li, Z.L.; Liu, S.D.; Ding, B. Heterostructure engineering of transition metal dichalcogenides for high-performance supercapacitors. *Rare Metals.* **2025**, *44*, 8198–8236. [CrossRef]
7. Zainul, R.; Hsu, C.-Y.; Basem, A.; Jasim, D.J.; Conde, Á.A.S.; Ajaj, Y.; Muzammil, K.; Islam, S.; Elawady, A. In-situ growth of MCo_2O_4 nanospheres (M: Mn, Ni) over g-C_3N_4@PPy as high-performance and novel composites for sustainable supercapacitors. *J. Energy Storage* **2024**, *90*, 111727. [CrossRef]
8. Zhang, X.; Yang, S.; Cao, Y.; Liang, C.; Geng, S.; Guo, H.; Liu, Y.; Luo, Y.; Zhang, W.; Li, L. $CuCo_2O_4$@$NiFe_2O_4$ core-shell structure array based on carbon paper is used as high-performance counter electrode of liquid thin film solar cells. *Surf. Interfaces* **2022**, *34*, 102374. [CrossRef]
9. Narale, D.K.; Kumbhar, P.D.; Bhosale, R.R.; Patil, K.D.; Jambhale, C.L.; Kim, J.H.; Kolekar, S.S. Engineering of both binder-free $CuCo_2O_4$ nanorod@CuO flower-like nanosheet core-shell heterostructure and $NiFe_2O_4$ nanoflake electrodes for asymmetric supercapacitor. *J. Energy Storage* **2024**, *84*, 110942. [CrossRef]
10. Zhang, P.; He, H. Rational rope-like $CuCo_2O_4$ nanosheets directly on Ni foam as multifunctional electrodes for supercapacitor and oxygen evolution reaction. *J. Alloys Compd.* **2020**, *826*, 153993. [CrossRef]
11. Shivani; Duddi, R.; Singh, A.K.; Kamboj, N.; Singh, G.; Kumar, S. Progress and outlook of electrochemically deposited metal-oxides based materials for energy storage applications. *Coord. Chem. Rev.* **2026**, *547*, 217082. [CrossRef]
12. Arishi, M. Morphologically engineered mixed metal oxides on carbon fibers as a binder-free electrode for diffusion capacitance-dominated hybrid supercapacitors. *Rare Met.* **2025**, *44*, 8548–8564. [CrossRef]
13. Song, L.; Zhong, X.H.; Wang, F.L.; Huang, Z.H.; Hong, Z.; Gao, Y.F.; Wang, H.D.; Ren, J.W.; Peng, S.J.; Li, L. Convenient room-temperature synthesis of sulfur and nitrogen co-doped NiCo-LDH coupled with CNTs on NiCo foam as battery-type electrode for high performance hybrid supercapacitor. *Rare Met.* **2024**, *43*, 4286–4301. [CrossRef]
14. Gao, Y.; Cao, P.; Cai, B.; Xu, R.; Gu, H.; Zhou, J.; Sun, Y.; Jiang, J.; Yu, F. $Nico_2O_4$/NiCo layered double oxide heterojunction nanocomposite as a cathode material for supercapacitors. *ACS Appl. Nano Mater.* **2025**, *8*, 9448–9459. [CrossRef]
15. Zhang, P.; Yang, Z. Leaf-like $CuCo_2O_4$@$CuCo_2O_4$ core-shell nanowires as binder-free electrode for high-performance flexible supercapacitors. *ChemistrySelect* **2022**, *7*, e202104112. [CrossRef]
16. Wang, T.; Ma, W.; Zhang, Y.; Guo, J.; Li, T.; Wang, S.; Yang, D. Construction of $CoMoO_4$@Ni_3S_2 core-shell heterostructures nanorod arrays for high-performance supercapacitors. *J. Energy Storage* **2021**, *35*, 102319. [CrossRef]
17. Wang, X.; Jiang, J. Oxygen vacancies enhance supercapacitive performance of $CuCo_2O_4$ in high-energy-density asymmetric supercapacitors. *J. Power Sources* **2020**, *458*, 228005.
18. Wang, L.; Li, J.; You, J.; Wang, Z.; Qi, X.; Xu, J. Hierarchical structure $NiCo_2O_4$/$NiMoO_4$ supported by carbon cloth for high-performance supercapacitors. *Ionics* **2023**, *29*, 2925–2933. [CrossRef]
19. Xing, B.; Zhao, J.; Jiang, S.; Pang, M.; Pan, Q.; Geng, Y.; Ma, G.; Li, Z.; Han, P. $NiMoO_4$@Ni_3S_2 core-shell composites grown in situ on nickel foam for applications in supercapacitors. *Synth. Met.* **2021**, *271*, 116638. [CrossRef]
20. Ma, F.; Dai, X.Q.; Jin, J.; Tie, N.; Dai, Y.T. Hierarchical core-shell hollow $CoMoS_4$@Ni-Co-S nanotubes hybrid arrays as advanced electrode material for supercapacitors. *Electrochim. Acta* **2020**, *331*, 135459. [CrossRef]
21. Zhang, L.; Li, R.; Li, W.; Li, R.; Li, C.; Zhou, Y. $CuCo_2O_4$ nanoneedle array with high stability for high performance asymmetric supercapacitors. *RSC Adv.* **2020**, *10*, 22775. [CrossRef]
22. Zhang, C.; Sui, Q.; Lu, L.; Zou, Y.; Xu, F.; Sun, L.; Cai, D.; Xiang, C. Hollow core-shell $CuCo_2O_4$@MoNi-layered double hydroxides as an electrode material for supercapacitors. *J. Energy Storage* **2023**, *61*, 106691. [CrossRef]
23. Li, P.; Liu, S.; Mao, Y.; Yin, H.; Chen, S.-M.; Liu, X. Surface self-reconstruction and sulfidation strategy to fabricate flower-like $NiCo_2S_4$ hollow nanospheres: Formation, storage mechanism, and application in hybrid supercapacitors. *ACS Appl. Energy Mater.* **2021**, *4*, 9178–9189. [CrossRef]
24. Kamble, G.P.; Rasal, A.S.; Gaikwad, S.B.; Gurav, V.S.; Chang, J.-Y.; Kolekar, S.S.; Ling, Y.-C.; Ghule, A.V. $CuCo_2O_4$ nanorods coated with CuO nanoneedles for supercapacitor applications. *ACS Appl. Nano Mater.* **2021**, *4*, 12702–12711. [CrossRef]
25. Zhao, X.; Ma, Q.; Tao, K.; Han, L. ZIF-derived porous $CoNi_2S_4$ on intercrosslinked polypyrrole tubes for high-performance asymmetric supercapacitors. *ACS Appl. Energy Mater.* **2021**, *4*, 4199–4207. [CrossRef]
26. George, A.; Kundu, M. Construction of self-supported hierarchical $CuCo_2O_4$ dendrites as faradaic electrode material for redox-based supercapacitor applications. *Electrochim. Acta* **2022**, *433*, 141204. [CrossRef]
27. Yewale, M.A.; Kadam, R.A.; Nakate, U.T.; Teli, A.M.; Kumar, V.; Beknalkar, S.A.; Jadhavar, A.A.; Kadam, S.L.; Shelke, N.T.; Shin, D.K. Sphere-shaped $CuCo_2O_4$ nanostructures battery type electrode for supercapacitor via hydrothermal synthesis approach. *Colloids Surf. A* **2023**, *679*, 132541. [CrossRef]
28. Chen, S.; Cui, S.; Chandrasekaran, S.; Ke, C.; Li, Z.; Chen, P.; Zhang, C.; Jiang, Y. Growth of $CuCo_2O_4$@$MnMoO_4$ core/shell nanosheet arrays for high energy density asymmetric supercapacitors. *Electrochim. Acta* **2020**, *341*, 135893. [CrossRef]
29. Sun, W.; Gao, B.; Li, Y.; Wang, X.; Song, X.-Z.; Tan, Z. Hierarchical heterostructured $CuCo_2O_4$@Ni_3Co_1-layered double hydroxide electrode with cobalt-ion internal stress for high performance hybrid supercapacitors. *J. Power Sources* **2025**, *630*, 236085. [CrossRef]

30. Prabakaran, P.; Prabhu, S.; Selvaraj, M.; Navaneethan, M.; Ramu, P.; Ramesh, R. Design and preparation of NiCoS nanostructures on Ni foam for high-performance asymmetric supercapacitor application. *J. Mater. Sci. Mater. Electron.* **2022**, *33*, 9256–9268. [CrossRef]
31. Zhou, A.; Chi, R.T.; Liu, R.; Shi, Y.J.; Zhang, Z.X.; Che, H.W.; Wang, G.S.; Mu, J.B.; Wang, Y.M.; Zhang, X.R. Se-doped nickel-cobalt sulfide nanotube arrays with 3D networks for high-performance hybrid supercapacitor. *Ceram. Int.* **2022**, *48*, 30536–30545. [CrossRef]
32. Zhang, Q.; Pan, S.J.; Wang, Z.P.; Yang, Y.Q.; Li, S.Z. MOF-derived porous Ni_3S_4/CoS nanosheet arrays for flexible supercapacitor electrode. *Ionics* **2024**, *30*, 343–351. [CrossRef]
33. Zhang, Z.X.; Shi, Y.J.; Zhao, X.; Zhou, A.; Liu, R.; Che, H.W.; Wang, G.S.; Mu, J.B.; Zhang, X.L.; Zhang, X.R. Construction of hierarchical NiCoSe@CoS core–shell nanotube arrays for high-performance hybrid supercapacitor. *J. Alloys Compd.* **2022**, *919*, 165824. [CrossRef]
34. Lv, S.; Shang, W.S.; Wang, H.; Chu, X.F.; Chi, Y.D.; Wang, C.; Yang, J.; Geng, P.Y.; Yang, X.T. Design and Construction of $Cu(OH)_2$/Ni_3S_2 Composite Electrode on Cu Foam by Two-Step Electrodeposition. *Micromachines* **2022**, *13*, 237. [CrossRef] [PubMed]

Disclaimer/Publisher's Note: The statements, opinions and data contained in all publications are solely those of the individual author(s) and contributor(s) and not of MDPI and/or the editor(s). MDPI and/or the editor(s) disclaim responsibility for any injury to people or property resulting from any ideas, methods, instructions or products referred to in the content.

coatings

MDPI

Article

Landslide Susceptibility Mapping Considering Time-Varying Factors Based on Different Models

Zhanfeng Wang [1], Chao Yin [2,*] and Jingjing Li [1]

[1] School of Highway Engineering, Shaanxi College of Communication Technology, Xi'an 710018, China; wang0133@163.com (Z.W.); lijingjingqi@chd.edu.cn (J.L.)
[2] School of Architecture Engineering and Geomatics, Shandong University of Technology, Zibo 255049, China
* Correspondence: yinchao1987611@163.com

Abstract

The selection of hazard factors is an important factor affecting the accuracy of landslide susceptibility mapping (LSM). The systematic development of an integrated input framework, incorporating both static and time-varying factors, as well as comparative studies of different input frameworks, remains at a preliminary stage. The degree of fit between each data-driven method and landslide-prone environment cannot be known in advance, so the best modeling method can only be determined through comparative studies. Therefore, the Pearson correlation coefficient method and collinearity diagnostics were used to screen the hazard factors, and three hazard factor combinations, considering both static and time-varying factors, were established. A total of 4498 landslide grids and 4498 non-landslide grids were determined, among which 70% (3149 landslide grids and 3149 non-landslide grids) were training samples, and the remaining 30% (1349 landslide grids and 1349 non-landslide grids) were verification samples. The three combinations were input to five models (Support Vector Machine, Random Forest, Convolutional Neural Network-Random Forest, Convolutional Neural Network-Support Vector Machine and Deep Belief Network-Multilayer Perceptron). The results show that the LSM results of different combinations and models are quite varied, and the combination No.3 and the Deep Belief Network-Multilayer Perceptron are the best. The study area is divided into extremely low susceptible areas, low susceptible areas, medium susceptible areas, high susceptible areas and extremely high susceptible areas, and the extremely high susceptible areas mainly distribute in the northwest, south and east. The other models overestimate the distance from the fault and underestimate the distance from the road. The extreme tendency of LSM results of the combinations No.1 and No.2 are strong, and they are easy to produce error estimation areas, which overestimate the elevation and underestimate the distance from the river. The LSM results of the Convolutional Neural Network-Support Vector Machine are closer to those of the benchmark, which underestimates the distance from the road and overestimates the distance from the fault. This study selected the best combination and model through comparative studies and revealed the degree of influence of each hazard factor on landslide susceptibility, greatly improving LSM accuracy, which can provide a scientific basis for land use planning.

Keywords: landslide susceptibility mapping; time-varying factor; hazard factor combination; Deep Belief Network-Multilayer Perceptron

1. Introduction

Landslides are defined as the downward movement of rock and soil masses, either intact or disrupted, along a weak surface or zone under gravitational influence [1]. According to the China Institute for Geo-Environmental Monitoring, 5659 geological disasters were recorded in 2022, causing more than 140 casualties and economic losses exceeding 1.5 billion yuan. Among these, landslides numbered 3919, accounting for 69.25% of the total occurrences [2]. Landslide susceptibility mapping (LSM) quantifies the spatial probability of landslide occurrence and classifies the study area into different susceptible levels, thereby providing a scientific basis for land-use planning and landslide risk mitigation policies [3,4].

The factors governing landslide susceptibility encompass both static and time-varying (dynamic) elements, with the latter inducing dynamic spatial-temporal shifts in susceptibility distributions [5]. Some studies in LSM consider only static factors or treat time-varying factors as constants, while other studies have analyzed the relationship between time-varying factors and landslide susceptibility [6]. However, due to the highly complex mechanisms through which time-varying factors influence landslide susceptibility, the systematic development of an input framework for landslide susceptibility assessment that incorporates both static and time-varying factors, as well as comparative studies of different input frameworks, remains in its early stages [7]. Soma and Kubota [8] applied frequency ratio and Logistic regression methods to demonstrate that land-use changes reduce slope stability and elevate landslide likelihood. Alberto et al. [9] integrated land-use change and Normalized Difference Vegetative Index (NDVI) variation to assess landslide susceptibility, reporting peak landslide probability 5–7 years after human disturbances such as deforestation. Jin et al. [10] combined static and dynamic factors to produce time-sensitive susceptibility maps, noting improved predictive performance and enhanced spatial alignment with observed landslide patterns when dynamic variables were incorporated. Francis and Bryson [11] introduced a novel workflow for dynamic susceptibility and forecastable hazard analysis in eastern Kentucky, integrating static geomorphic parameters with temporally varying vegetation data. Lamichhane et al. [12] generated multi-temporal susceptibility maps (1995–2020) that accounted for urbanization trends and climatic variations, highlighting the combined influence of static and dynamic factors on landslide prediction. Jia et al. [13] developed input datasets using twelve continuous and three discrete factors, combined through two distinct connection methods. Their findings emphasized the importance of accounting for the varying data characteristics and selecting suitable environmental factor integration strategies to enhance the accuracy of LSM. Similarly, He et al. [14] constructed an interpretable machine learning model to examine changes in landslide susceptibility and their underlying driving mechanisms amid urbanization between 2000 and 2020. The results demonstrated that urbanization elevated landslide susceptibility and underscored the value of employing interpretable machine-learning approaches to elucidate this relationship.

LSM approaches can be broadly categorized into two groups: deterministic and data-driven methods, the latter of which includes statistical, shallow learning and deep learning models [15,16]. A defining strength of deep learning models lies in their capacity for automated feature extraction. These automatically learned features generally offer greater representational power and robustness compared to manually engineered ones, underscoring that feature learning is central to deep learning methodologies [17,18]. Deep neural networks, constructed through stacked layers of nonlinear transformations, provide the foundational architecture for deep learning and have shown significant promise for LSM [19]. Youssef et al. [20] applied Support Vector Machine (SVM), 1D-

https://doi.org/10.3390/coatings16020207

Convolutional Neural Network (1D-CNN) and 2D-CNN to LSM in Saudi Arabia's Asir Region. Their results indicated that the CNN-based models outperformed SVM, with 1D-CNN and 2D-CNN achieving accuracy improvements of 4.9% and 7.9%, respectively, while 2D-CNN surpassed 1D-CNN by 3.5%. Ge et al. [21] compared five deep learning architectures (AlexNet, Inception-v3, Xception, ResNet-101 and DenseNet-201) with two conventional models (SVM and Artificial Neural Network (ANN)) in a study along a transmission line corridor. Deep learning models attained high area-under-the-curve (AUC) values and demonstrated superior predictive accuracy and capability for deep feature extraction. Wang et al. [22] introduced a CNN model for LSM and assessed it against the Classification and Regression Trees (CART) and Multilayer Perceptron (MLP) using the Receiver Operating Characteristic (ROC) analysis. The CNN consistently outperformed both traditional models, with MLP ranking second and CART least effective. Bhattacharya et al. [23] also reported the advantage of deep learning in the Chamoli District of India, where the Deep Learning Neural Network (DLNN) achieved higher predictive performance compared to Random Forest (RF) and ANN. Similarly, Zhang et al. [24] introduced a novel multi-classification machine learning framework for LSM, designed to address the limitations inherent in conventional binary classification models. Experiments conducted in Lvliang City, Shanxi Province, employing eight machine learning algorithms, showed that the multi-classification approach achieved superior performance compared to binary modeling, with an average improvement of 6.71% in predictive accuracy.

Different regions are characterized by distinct geological, topographic and hydrological conditions, leading to variations in landslide types, triggering mechanisms and evolutionary processes [25,26]. LSM methods also differ substantially in their logical frameworks and mathematical underpinnings. The compatibility between a landslide-prone environment and a specific modeling approach cannot be predetermined and must be evaluated through comparative analysis [27,28]. Owing to the complex mechanisms by which time-varying factors influence landslide susceptibility, the systematic development of an integrated input framework, incorporating both static and time-varying factors, as well as comparative studies of different input frameworks, remains at a preliminary stage [29]. In this study, landslide hazard factors were selected by correlation analysis and collinearity diagnostics. A total of 4498 landslide grids and 4498 non-landslide grids were used to construct training and verification datasets. Three hazard factor combinations were formulated based on the information value method: (1) static factors + values of time-varying factors in 2021, (2) static factors + annual values of time-varying factors, (3) static factors + interannual variation values of time-varying factors. These combinations were fed into five predictive models: SVM, RF, CNN-RF, CNN-SVM and Deep Belief Network (DBN)-MLP. The combination and model yielding the highest accuracy were identified, and the study area was classified into five susceptible levels. The resulting LSM outputs from different combinations and models were compared, and the influence of selected hazard factors on landslide susceptibility was examined. The methodological workflow is shown in Figure 1.

https://doi.org/10.3390/coatings16020207

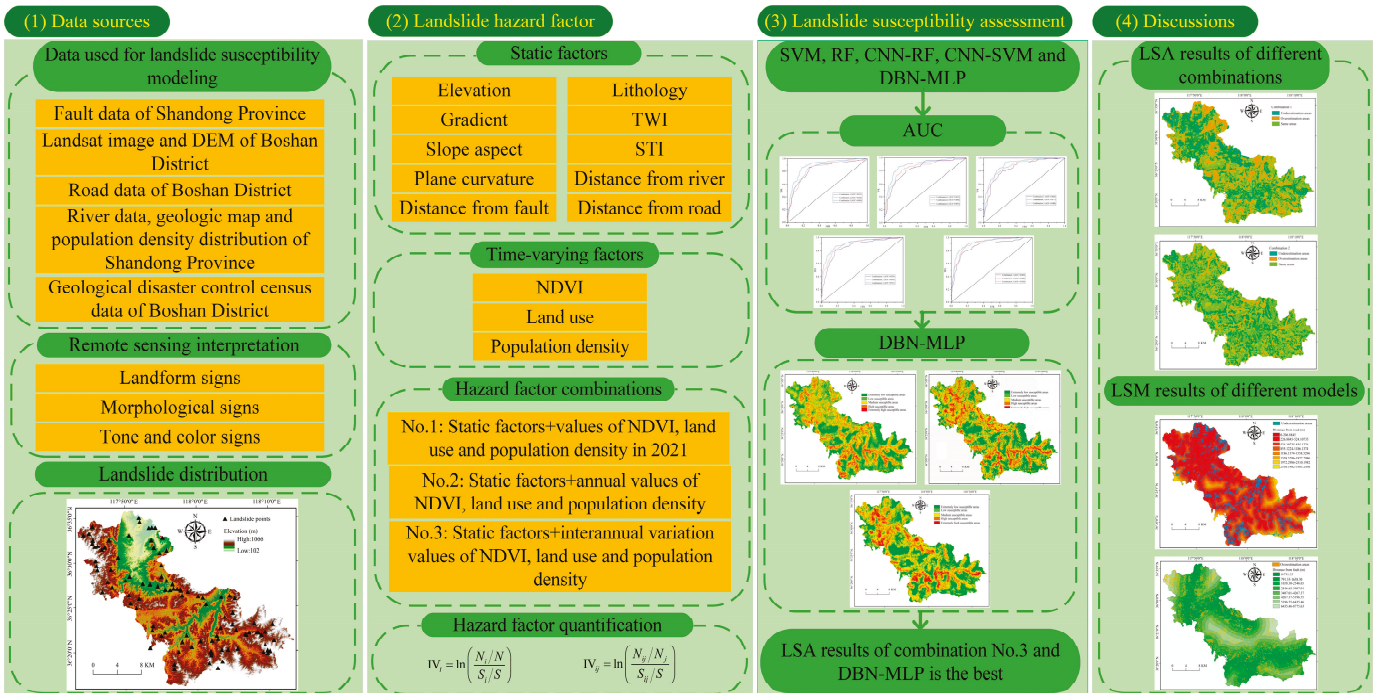

Figure 1. Methodological workflow.

2. Study Area and Data

2.1. Overview of the Study Area

The study area is Boshan District, Zibo City, Shandong Province, China, ranging from 117°43′ E to 118°42′ E and 36°16′ N to 36°31′ N. It extends approximately 20.0 km from east to west and 49.4 km from north to south, covering a total area of 698.2 km^2, as shown in Figure 2. Boshan District experiences a typical warm temperate semi-humid continental monsoon climate. From 1951 to 2023, precipitation ranged from 304.6 mm to 1853.1 mm, with a mean of 726.5 mm. Precipitation is unevenly distributed throughout the year, with 60%–70% concentrated between June and August. Intense summer rainfall serves as a major triggering factor for landslides, debris flows, and flash floods [30].

Boshan District lies on the southeastern margin of the North China Plate (Craton), specifically on the northern flank of the Luxi Uplift (Central Shandong Uplift), adjacent to the western side of the prominent Yishu Fault Zone (the Shandong segment of the Tanlu Fault Zone) [31], characterized by typical tectonic-erosion low mountain and hilly terrain. The topography slopes from higher elevations in the south to lower elevations in the north. Major geomorphological units include [32]:

(1) Southern low-middle mountain area: the northern extension of the Lu Mountain range, featuring steep slopes and deeply incised valleys dominated by tectonic erosion landforms and Karst topography.
(2) Central hilly valley area: Centered on the belt-shaped valley formed by the Xiaofu River and its tributaries, consisting of river terraces, alluvial fans, and denudational hills.
(3) Northern gentle hill-plain area: Composed mainly of denudation-accumulation hills and piedmont alluvial-proluvial plains, with elevations generally below 200 m.

https://doi.org/10.3390/coatings16020207

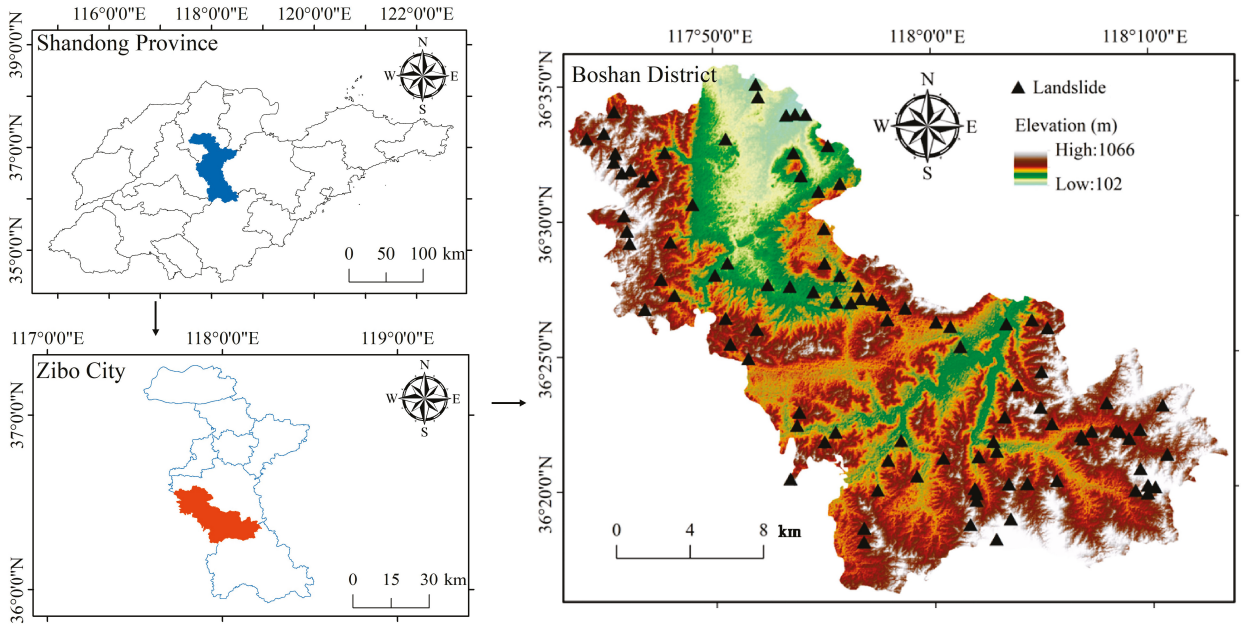

Figure 2. Location and landslide distribution of Boshan District. Source: Geospatial Data Cloud, available online: http://www.gscloud.cn/ (accessed on 10 October 2025).

The stratigraphic sequence in Boshan District is relatively complete, ranging from ancient basement rocks to Cenozoic unconsolidated sediments [33], as shown in Table 1.

Table 1. Geological and lithological characteristics of the study area.

Eon	Era	Period	Lithology
Archean			Taishan group: composed of high-grade metamorphic rocks such as gneiss and amphibolite.
Phanerozoic	Paleozoic	Cambrian	Lower part: purple-red shale and sandstone (Mantou formation); Middle to upper part: thick-bedded oolitic limestone, edgewise limestone and shale (Zhangxia formation, Chaomidian formation).
		Ordovician	Majiagou formation: thick-bedded pure limestone and dolomitic limestone, interbedded with thin layers of shale.
		Carboniferous-Permian	Benxi formation/Taiyuan formation: a paralic coal-bearing sequence consisting of sandstone, shale, limestone and multiple coal seams; Shanxi formation/Shihezi formation: continental sandstone and shale containing coal seams.
	Mesozoic		Jurassic sandstone and shale (Fangzi formation).
	Cenozoic	Paleogene	Conglomerate and sandstone (Guanzhuang group).
		Quaternary	Loess, fluvial gravels and alluvial-proluvial clay.

Key structural features in Boshan District include folds and faults. The fold axes are generally oriented NNE, with the core structure being the Boshan Syncline, whose axis roughly follows the Xiaofu River valley. The western branch of the Yishu Fault Zone is a regional-scale fracture whose intense activity profoundly influences crustal stability, seismic activity and modern geomorphic patterns. The Boshan Fault and other secondary faults form a system of NNE- and NW-trending fractures that control the orientation of mountain ranges and valleys [34].

2.2. Data Sources

The sources and download links of the data used for landslide susceptibility modeling are shown in Table 2.

Table 2. Data used for landslide susceptibility modeling.

Data	Source and Download Link
Fault data of Shandong Province	Geological Professional Knowledge Service System (http://103.85.177.213:9080/mlr)
Landsat image and GDEMV3 of Boshan District	Geospatial Data Cloud (http://www.gscloud.cn/)
Road data of Boshan District	Open Street Map (OSM) (https://www.openstreetmap.org)
River data, geologic map and population density distribution of Shandong Province	Institute of Geographic Science and Natural Resource, Chinese Academy of Sciences (http://www.resdc.cn/)
Geological disaster control census data of Boshan District	Zibo Natural Resource and Plan Bureau (https://gtj.zibo.gov.cn/)

According to the geological disaster control census data of Boshan District released by Zibo Natural Resource and Plan Bureau, combined with the remote sensing interpretation and on-site investigation, 99 landslides were determined in the study area. On satellite imagery, notable distinctions between landslide and non-landslide areas include [35,36]:

(1) Landform signs: incoordination between the local landform and the overall landform, sudden destruction of the continuous landform.
(2) Morphological signs: shape and boundary of the landslide can be clearly seen, and usually manifested as a special plane shape such as ring chair type, oval type and arc type.
(3) Tone and color signs: the color of the surface coverage changes continually. The plant coverage is bad; the color is light, and the sliding mass is well preserved.

The results show that the total volume of the landslides is 2,732,400 m^3 and the total area is 0.442 km^2. The largest landslide is in Boshan Town, with a volume of 74,160 m^3 and an area of 0.021 km^2. Chishang Town has the largest number of landslides (19). The landslides are shown in Figure 2 and Table 3.

https://doi.org/10.3390/coatings16020207

Table 3. Landslide overview in Boshan District.

No.	Location	Volume	Area	No.	Location	Volume	Area	No.	Location	Volume	Area	No.	Location	Volume	Area
1	Chishang Town	15,321 m^3	2927 m^2	26	Boshan Town	74,160 m^3	21,343 m^2	51	Shima Town	16,934 m^3	2244 m^2	76	Baita Town	34,783 m^3	6375 m^2
2	Chishang Town	58,763 m^3	8123 m^2	27	Boshan Town	27,689 m^3	4522 m^2	52	Shima Town	33,284 m^3	5435 m^2	77	Baita Town	12,093 m^3	1671 m^2
3	Chishang Town	37,145 m^3	5390 m^2	28	Boshan Town	31,543 m^3	4820 m^2	53	Shima Town	53,521 m^3	9245 m^2	78	Baita Town	26,387 m^3	3886 m^2
4	Chishang Town	29,542 m^3	5414 m^2	29	Boshan Town	15,231 m^3	2803 m^2	54	Shima Town	10,162 m^3	1404 m^2	79	Baita Town	25,896 m^3	5054 m^2
5	Chishang Town	16,378 m^3	2075 m^2	30	Boshan Town	28,347 m^3	5796 m^2	55	Shima Town	16,745 m^3	2593 m^2	80	Yucheng Town	35,027 m^3	4697 m^2
6	Chishang Town	18,451 m^3	2857 m^2	31	Boshan Town	47,965 m^3	7103 m^2	56	Shima Town	40,527 m^3	7137 m^2	81	Yucheng Town	26,765 m^3	7501 m^2
7	Chishang Town	26,987 m^3	4661 m^2	32	Boshan Town	31,876 m^3	6222 m^2	57	Shima Town	13,376 m^3	1695 m^2	82	Yucheng Town	6271 m^3	1024 m^2
8	Chishang Town	39,874 m^3	5347 m^2	33	Boshan Town	14,765 m^3	1980 m^2	58	Shima Town	17,031 m^3	2781 m^2	83	Yucheng Town	35,294 m^3	6083 m^2
9	Chishang Town	45,789 m^3	6744 m^2	34	Boshan Town	28,129 m^3	4512 m^2	59	Shima Town	6578 m^3	1055 m^2	84	Yucheng Town	11,548 m^3	2011 m^2
10	Chishang Town	9123 m^3	1672 m^2	35	Yuanquan Town	47,754 m^3	8249 m^2	60	Shima Town	43,796 m^3	7565 m^2	85	Yucheng Town	26,158 m^3	3852 m^2
11	Chishang Town	36,654 m^3	5066 m^2	36	Yuanquan Town	32,189 m^3	4519 m^2	61	Shima Town	22,891 m^3	3213 m^2	86	Yucheng Town	15,693 m^3	3063 m^2
12	Chishang Town	30,215 m^3	4450 m^2	37	Yuanquan Town	14,432 m^3	2235 m^2	62	Badou Town	26,897 m^3	3961 m^2	87	Shantou Town	5518 m^3	740 m^2
13	Chishang Town	15,983 m^3	3119 m^2	38	Yuanquan Town	7891 m^3	1389 m^2	63	Badou Town	26,432 m^3	6525 m^2	88	Shantou Town	51,327 m^3	8233 m^2
14	Chishang Town	48,876 m^3	6555 m^2	39	Yuanquan Town	17,543 m^3	2223 m^2	64	Badou Town	34,018 m^3	4311 m^2	89	Shantou Town	46,047 m^3	7954 m^2
15	Chishang Town	17,231 m^3	2764 m^2	40	Yuanquan Town	42,457 m^3	6934 m^2	65	Badou Town	22,654 m^3	3508 m^2	90	Shantou Town	25,532 m^3	3022 m^2
16	Chishang Town	30,678 m^3	5299 m^2	41	Yuanquan Town	34,198 m^3	5485 m^2	66	Badou Town	26,765 m^3	4623 m^2	91	Shantou Town	45,763 m^3	6424 m^2
17	Chishang Town	10,999 m^3	1544 m^2	42	Yuanquan Town	47,632 m^3	8228 m^2	67	Badou Town	16,287 m^3	2286 m^2	92	Shantou Town	25,936 m^3	4017 m^2
18	Chishang Town	39,321 m^3	5435 m^2	43	Yuanquan Town	17,328 m^3	2432 m^2	68	Badou Town	34,275 m^3	5498 m^2	93	Chengxi Town	35,984 m^3	6337 m^2
19	Chishang Town	26,897 m^3	3961 m^2	44	Yuanquan Town	42,768 m^3	6624 m^2	69	Badou Town	22,437 m^3	4112 m^2	94	Chengxi Town	20,432 m^3	2589 m^2
20	Boshan Town	30,984 m^3	3926 m^2	45	Yuanquan Town	23,987 m^3	4224 m^2	70	Badou Town	26,634 m^3	3468 m^2	95	Chengxi Town	25,815 m^3	4216 m^2
21	Boshan Town	5543 m^3	1081 m^2	46	Yuanquan Town	17,465 m^3	2213 m^2	71	Badou Town	11,145 m^3	1726 m^2	96	Chengxi Town	25,178 m^3	5714 m^2
22	Boshan Town	18,569 m^3	4065 m^2	47	Yuanquan Town	17,129 m^3	2797 m^2	72	Baita Town	14,512 m^3	2555 m^2	97	Chengdong Town	36,195 m^3	5003 m^2
23	Boshan Town	27,432 m^3	3679 m^2	48	Yuanquan Town	33,015 m^3	6051 m^2	73	Baita Town	10,218 m^3	1799 m^2	98	Chengdong Town	20,217 m^3	2977 m^2
24	Boshan Town	31,127 m^3	4584 m^2	49	Yuanquan Town	13,754 m^3	1901 m^2	74	Baita Town	38,508 m^3	4880 m^2	99	Chengdong Town	15,697 m^3	3064 m^2
25	Boshan Town	15,876 m^3	2796 m^2	50	Shima Town	27,298 m^3	5215 m^2	75	Baita Town	56,014 m^3	9148 m^2				

https://doi.org/10.3390/coatings16020207

The 30 m resolution GDEMV3 data (Source: Geospatial Data Cloud; Download link: http://www.gscloud.cn/) was first reprojected into a projected coordinate system using ArcGIS 10.2. Subsequently, a 10 m resolution dataset was generated by applying the "Resample" tool with the bilinear interpolation method. Based on this enhanced DEM, a total of 6,983,061 grids and 4498 landslide grids, each measuring 10 m × 10 m, were delineated, corresponding to a total area of 698.2 km^2 and landslide area of 0.442 km^2 across 99 identified landslides in the study area. It should be noted that this "upsampling" operation of the original DEM, while increasing the spatial resolution from 30 m to 10 m, does not introduce any additional genuine topographic detail. All newly generated details are mathematical estimates and do not represent actual measurement accuracy. Landslide susceptibility modeling requires both positive and negative samples; an additional 4498 grids were randomly selected from non-landslide areas to serve as negative samples. The method for selecting non-landslide grids was as follows:

(1) 4498 landslide grids and those located within a 50 m buffer distance from landslide grids were removed, resulting in 514,673 remaining grids.
(2) Using the reclassification tool in ArcGIS 10.2, the 514,673 grids were categorized into 4499 groups. The first 4498 groups each contained 114 spatially adjacent grids, while the last group contained the remaining 1901 grids.
(3) From each of the first 4498 groups, one grid was randomly selected to form the negative samples.

2.3. Typical Landslide

Liujiadayu landslide (No.26) is a typical accumulation layer-bedrock contact surface landslide. After a sliding event in July 1998, cracks appeared at the rear part, and the leading edge blocked the road. No significant changes have been observed in recent years.

The exposed stratum is the Cambrian Mantou formation, consisting mainly of limestone, mudstone and shale. The primary groundwater type is carbonate rock fissure-karst water. Its water abundance is related to lithology, with precipitation as the main recharge source. It generally exhibits short runoff paths and discharges over short distances; no stable groundwater table was observed. The landslide body has a semi-circular planform with a slope angle of 25°. It is 156 m long longitudinally and 140 m wide transversely, with a main sliding direction of N26° E. The landslide boundary is clear: the rear is bounded by a detachment surface formed by tensile cracks, and the sides are defined by gullies. The elevation of the rear scarp ranges from 400 to 410 m, while the leading edge features a free face, 2–10 m high, created by road construction, with a toe elevation between 359 and 366 m. The thickness of the landslide mass varies: 1.0–6.7 m in the front part, 2.2–5.3 m in the middle part and 3.3–7.5 m in the rear part, with an average thickness of 3.47 m. It covers a plan area of approximately 21,343 m^2 and has an estimated volume of about 74,160 m^3, classifying it as a small-scale retrogressive landslide.

According to borehole data, the landslide body consists of silty clay containing rock fragments, which is a common colluvium in Shandong Province. The soil is in a plastic to hard plastic state, yellowish-brown in color, with a non-uniform texture containing a small amount of fine-grained rock fragments measuring 0.5–5 cm in diameter, comprising 10%–20% of the total volume. Beneath the colluvium is moderately weathered limestone, with a bedding dip angle of 13°. The limestone is relatively dense and has high strength; it was encountered in all boreholes, but its base was not reached. Investigation revealed that several days of continuous rainfall in July 1998 increased the water content within the accumulation layer, triggering a slide with a movement distance of about 20 m, which blocked the road at the landslide's toe. Currently, sliding cracks approximately 2–4 m deep and 1–3 m wide are still visible in the middle and rear parts of the landslide body. Multiple

https://doi.org/10.3390/coatings16020207

tensile cracks have developed in the front part, generally linear in distribution, with a trend of about 10°, widths of about 0.5 m, depths of about 1.0 m, and extensions of 8–20 m in length, as shown in Figure 3.

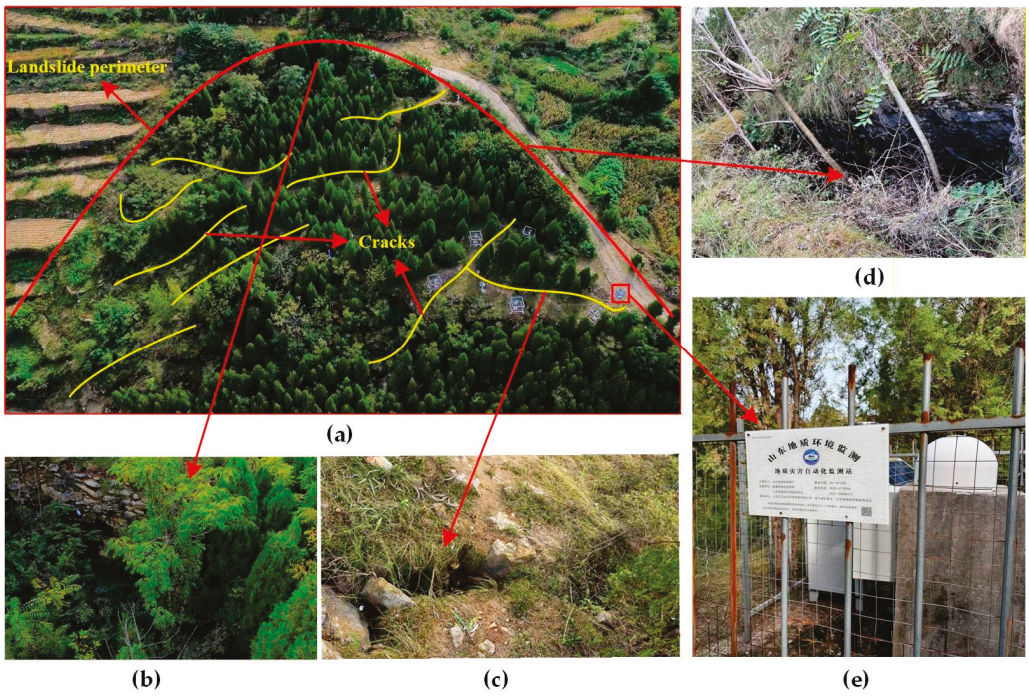

Figure 3. Liujiadayu landslide: (**a**) Landslide morphology; (**b**) Landslide scarp; (**c**) Transverse crack; (**d**) Longitudinal crack; (**e**) Monitoring equipment.

3. Landslide Hazard Factor Selection and Classification

3.1. Landslide-Prone Environment

Landslide-prone environment involves topographic and geological factors (elevation, gradient, slope aspect, plane curvature, profile curvature, lithology, distance from fault), hydrological and vegetation factors (distance from river, topographic wetness index (TWI), sediment transport index (STI), stream power index (SPI), NDVI) and human activity factors (distance from road, land use, population density) [37]. Among them, TWI quantifies the control of terrain on the basic hydrological process, which is used to describe the degree of surface saturated runoff [38]. STI is a comprehensive topographic variable, which indicates the extent of surface sand and other materials carried with water flow [39]. SPI is a parameter to quantify the erosion capacity of surface water flow, which is used to identify the areas susceptible to gully erosion and the strong water flow path [40]. NDVI measures the extent of vegetation coverage, which ranges from −1.0–1.0 [41]. TWI, STI, SPI and NDVI are shown in Equations (1)–(4).

$$\mathrm{TWI} = \ln\left(\frac{A_s}{\tan\beta}\right) \tag{1}$$

$$\mathrm{STI} = \left(\frac{A_s}{22.13}\right)^{0.6} \cdot \left(\frac{\sin\beta}{0.0896}\right)^{1.3} \tag{2}$$

$$\mathrm{SPI} = A_s \cdot \tan\beta \tag{3}$$

$$\mathrm{NDVI} = \frac{NIR - R}{NIR + R} \tag{4}$$

where: A_s is the upstream area of surface water flowing on the contour length, which is calculated by the cumulative confluence area and length of the upstream water flow; β is the terrain gradient; *NIR* is the reflecting value of the near-infrared band; *R* is the reflecting value of the red band.

3.2. Hazard Factor Screening

Too many hazard factors may exacerbate the collinearity problem, resulting in redundant information and unreliable results. Too few hazard factors may ignore important factors. Therefore, it is necessary to carry out correlation analysis and collinearity test on the hazard factors [42].

3.2.1. Correlation Analysis

The correlation between two variables can be measured using the Pearson correlation coefficient method [43], with values ranging from −1.0–1.0, as shown in Equation (5).

$$\rho_{x,y} = \frac{\mathrm{cov}(x,y)}{\sigma_x \cdot \sigma_y} = \frac{E\left[(x-\mu_x)\cdot(y-\mu_y)\right]}{\sigma_x \cdot \sigma_y} \tag{5}$$

where: $\rho_{x,y}$ is the Pearson correlation coefficient of x and y; μ_x, μ_y are the mean values of x and y; σ_x, σ_y are the variances of x and y; E is the expectation. $\rho_{x,y} = 1.0$ means x and y fall on a straight line, and y increases with the increase of x. $\rho_{x,y} = -1.0$ also means x and y fall on a straight line, but y decreases with the increase of x. $\rho_{x,y} = 0$ means no linear relationship between x and y, while $|\rho_{x,y}| > 0.4$ means strong correlation.

The Pearson correlation coefficients of the fifteen hazard factors (elevation, gradient, slope aspect, plane curvature, profile curvature, lithology, distance from fault, distance from river, TWI, STI, SPI, NDVI, distance from road, land use, population density) were calculated by SPSS23.0, as shown in Figure 4.

Among them, the coefficient between plane curvature and profile curvature is −0.599, and between SPI and STI is 0.816. The coefficients of other hazard factors are between −0.4–0.4, and the independence is strong. Therefore, profile curvature and SPI were excluded.

3.2.2. Collinearity Diagnostic

Variance inflation factor (*VIF*) is a measure of the severity of complex collinearity in multiple linear regression models [44]. It represents the ratio of the variance of the regression coefficient estimator to the variance when the independent variables are assumed not to be linearly correlated. When the correlation between independent variables is very low, *VIF* is close to 1. The larger the *VIF*, the larger the collinearity [45]. *VIF* > 10 means there is a serious collinearity problem in the variables, and *VIF* is shown in Equation (6).

$$\mathrm{VIF}_i = \frac{1}{1-R_i^2} \tag{6}$$

where: ${R_i}^2$ is the correlation coefficient of x_i for regression analysis of the other variables.

SPSS23.0 was used to test the collinearities of the thirteen hazard factors, and the results are shown in Table 4.

https://doi.org/10.3390/coatings16020207

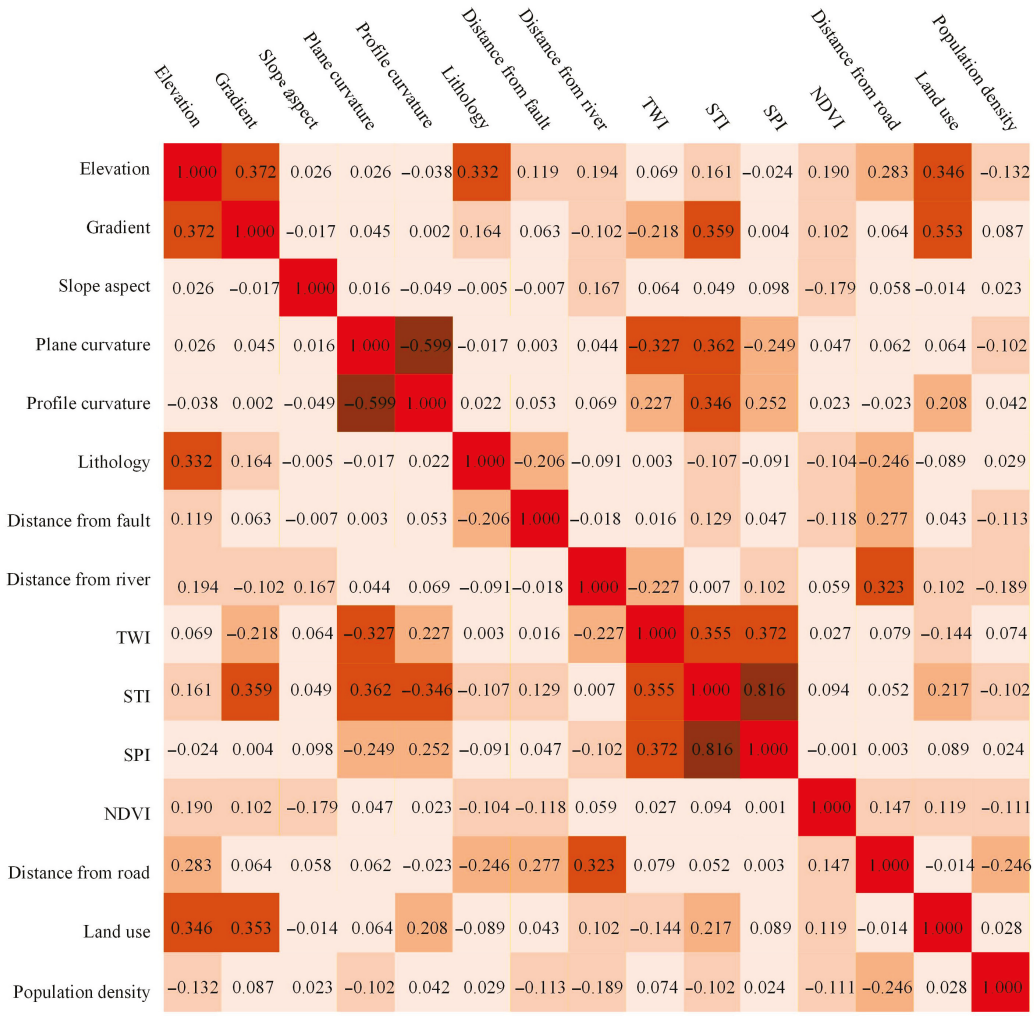

Figure 4. Pearson correlation coefficient calculation results.

Table 4. Collinearity diagnostic results.

Hazard Factor	Elevation	Gradient	Slope Aspect	Plane Curvature	Lithology	Distance from Fault	Distance from River
VIF	3.337	1.940	1.050	1.124	1.815	1.224	1.633
Hazard Factor	**TWI**	**STI**	**NDVI**	**Distance from Road**	**Land Use**	**Population Density**	
VIF	1.855	1.406	2.452	1.904	1.024	1.174	

The *VIF* of each hazard factor is <10, and the collinearity is low, indicating the hazard factors can be used for the establishment of hazard factor combinations.

3.3. Landslide Hazard Factor Classification

Elevation, gradient, plane curvature, distance from fault, distance from river, TWI, STI, NDVI, distance from road and population density were classified by the natural breakpoint method. Taking elevation as an example, the principle of the natural breakpoint method is explained as follows [46,47]:

(1) The elevation of the 6,983,061 grids was determined, with a minimum elevation of 102 m and a maximum elevation of 1066 m.

(2) The classification number (c_n) and breakpoints were set, and all grids were classified in ascending order of elevation.
(3) The mean and variance of elevations within each class were calculated, followed by the computation of the sum of variances (Var_a) across all c_n classes.
(4) Global searches for c_n and the breakpoints were conducted using MATLAB R2024b software to identify the combination that resulted in the smallest Var_a.

This study set the initial c_n = 5, with initial breakpoints at 295 m, 490 m, 695 m, and 825 m. The results showed that Var_a was minimized when c_n = 8 and the breakpoints were 240 m, 329 m, 402 m, 475 m, 555 m, 645 m and 769 m, representing the optimal classification number and breakpoints. Besides, slope aspect, lithology and land use were divided into 9, 16 and 6 categories respectively, as shown in Table 5 and Figure 5.

Table 5. Landslide hazard factor classifications.

Hazard Factor	Classification
Elevation (m)	0–240; 240–329; 329–402; 402–475; 475–555; 555–645; 645–769; 769–1066.
Gradient (°)	0–5.9328; 5.9328–10.4418; 10.4418–15.1881; 15.1881–19.9344; 19.9344–24.6806; 24.6806–29.9016; 29.9016–36.5463; 36.5463–60.5150.
Plane curvature	−7.9765–−2.0350; −2.0350–−1.1948; −1.1948–−0.5946; −0.5946–−0.1145; −0.1145–0.3056; 0.3056–0.8457; 0.8457–1.6259; 1.6259–7.3274.
Distance from fault (m)	0–791.53; 791.53–1686.30; 1686.30–2546.65; 2546.65–3407.01; 3407.01–4267.37; 4267.37–5196.55; 5196.55–6435.46; 6435.46–8775.63.
Distance from river (m)	0–214.9345; 214.9345–470.1691; 470.1691–711.9704; 711.9704–953.7717; 953.7717–1209.0063; 1209.0063–1504.5412; 1504.5412–1920.9767; 1920.9767–3425.5180.
TWI	3.0010–5.1384; 5.1384–6.1674; 6.1674–7.4341; 7.4341–9.0965; 9.0965–11.0755; 11.0755–13.4504; 13.4504–16.6960; 16.6960–23.1873.
STI	0–1.0421; 1.0421–2.1134; 2.1134–12.9532; 12.9532–24.2145; 24.2145–42.7421; 42.7421–61.5125; 61.5125–101.0528; 101.0528–182.0463.
NDVI	−1–−0.0270; −0.0270–0.0844; 0.0844–0.1444; 0.1444–0.1823; 0.1823–0.2561; 0.2561–0.3720; 0.3720–0.4501; 0.4501–0.7202.
Distance from road (m)	0–206.8845; 206.8845–524.1073; 524.1073–855.1225; 855.1225–1186.1376; 1186.1376–1558.5296; 1558.5296–1972.2986; 1972.2986–2510.1982; 2510.1982–3503.2436.
Population density (p/km^2)	23.1670–544.5703; 544.5703–646.6793; 646.6793–737.5949; 737.5949–764.0146; 764.0146–1100.3417; 1100.3417–1145.4753; 1145.4753–1201.6171; 1201.6171–1280.8762.
Slope aspect	Plane; North; Northeast; East; Southeast; South; Southwest; West; Northwest.
Lithology	Silty sand, sandy clay; Thick limestone, medium-thickness dolomite; Mudstone, shale with sandstone; Arkose; Yellowish·green sandstone; Edgewise limestone; Silty mudstone; Gabbro; Dolomitic limestone; Mudstone, shale with limestone; Gneissie monzogranite; Weak gneissic orthogranite; Tonalitic gneiss; Homblendite; Fine-grined granite; Micrite, micritic limestone.
Land use	Water area; Garden plot; Cultivated land; Reclaimed land; Bare land; Forest land.

https://doi.org/10.3390/coatings16020207

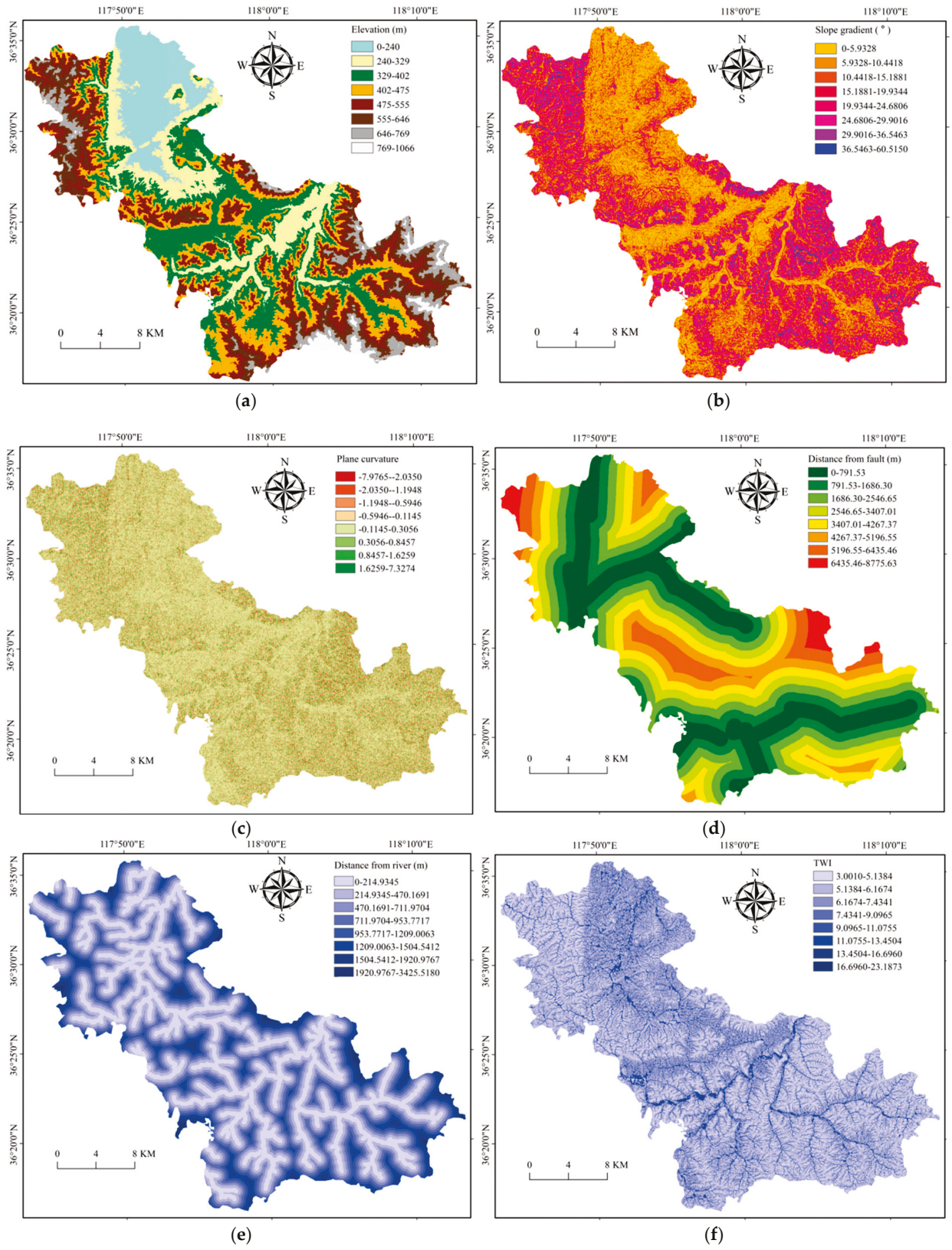

Figure 5. *Cont.*

https://doi.org/10.3390/coatings16020207

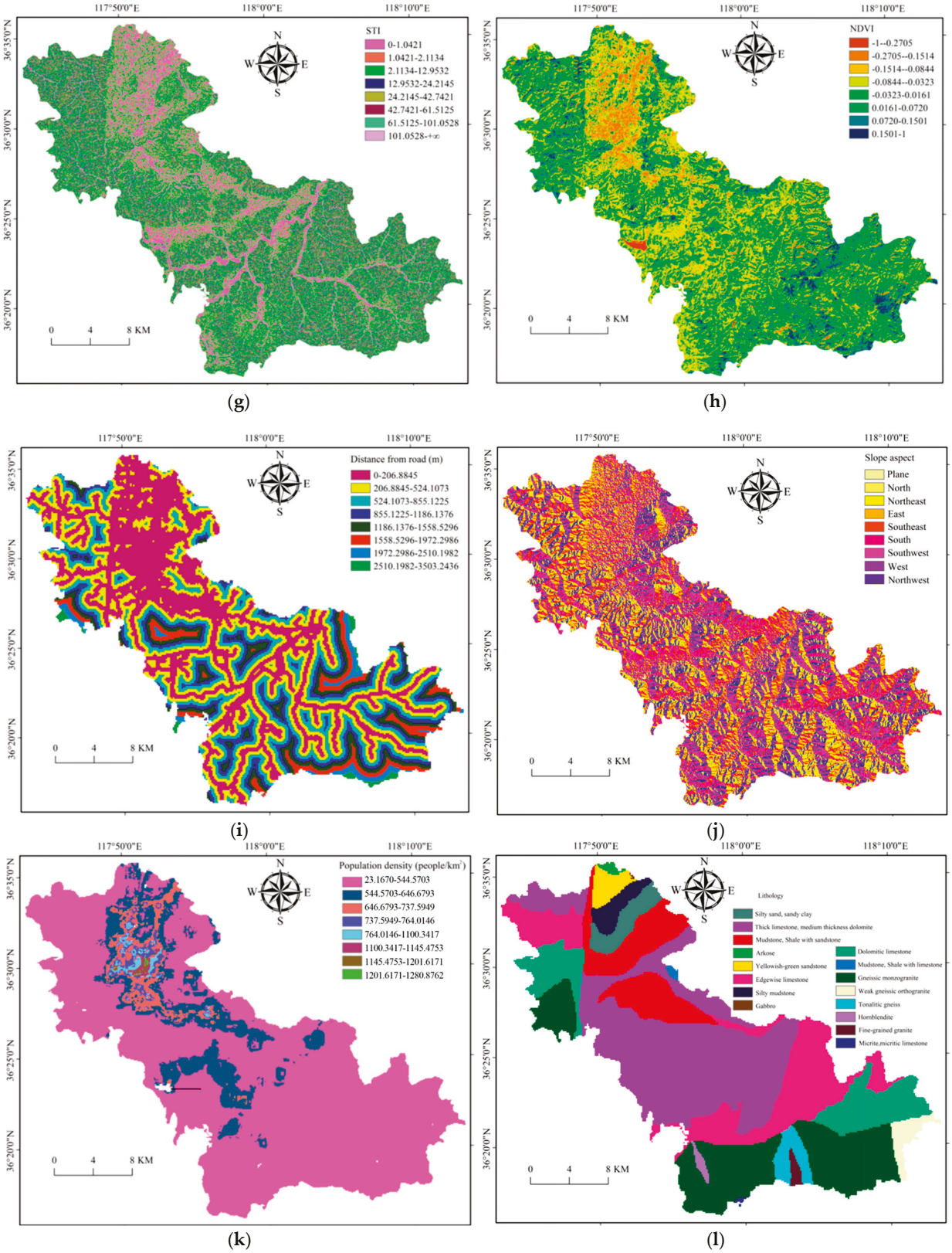

Figure 5. *Cont.*

https://doi.org/10.3390/coatings16020207

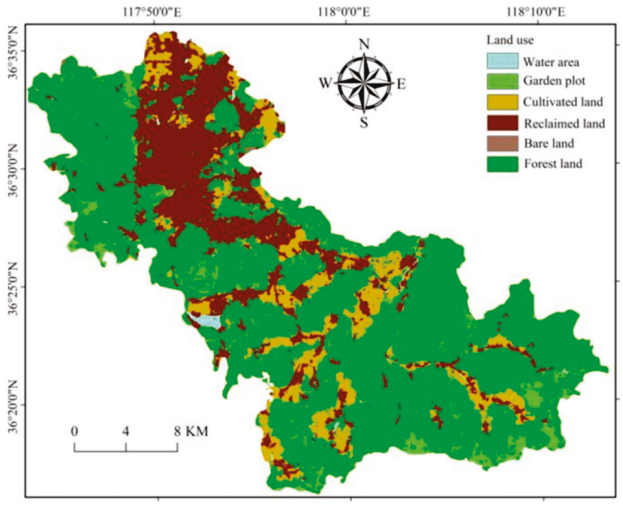

(**m**)

Figure 5. Landslide hazard factor classification maps: (**a**) Elevation; (**b**) Gradient; (**c**) Plane curvature; (**d**) Distance from fault; (**e**) Distance from river; (**f**) TWI; (**g**) STI; (**h**) NDVI; (**i**) Distance from road; (**j**) Slope aspect; (**k**) Population density; (**l**) Lithology; (**m**) Land use. Source: Geospatial Data Cloud, available online: http://www.gscloud.cn/ (accessed on 10 October 2025).

4. Landslide Hazard Factor Combination and Quantification

4.1. Hazard Factor Combination

The thirteen hazard factors were divided into ten static factors (elevation, gradient, slope aspect, plane curvature, distance from fault, lithology, TWI, STI, distance from river, distance from road) and three time-varying factors (NDVI, land use, population density). The selection of NDVI, land use and population density as time-varying factors was based on long-term monitoring and tracking of the landslide-prone environment in the study area. We have observed that, with intensified engineering activities and accelerated urbanization, NDVI, land use and population density in the study area have undergone significant changes over the past two decades, which constitutes a major reason for the frequent occurrence of landslides in this region. The combinations were established, as shown in Table 6.

Table 6. Hazard factor combinations.

No.	Static Factor	Time-Varying Factor
1	Elevation, gradient, slope aspect, plane curvature, distance from fault, lithology, TWI, STI, distance from river, distance from road	Values of NDVI, land use and population density in 2021.
2		Annual values of NDVI, land use and population density.
3		Interannual variation values of NDVI, land use and population density.

Combination No.1 represents the conventional approach commonly used in LSM, treating time-varying factors as constants. The values for the year 2021 were selected because that year recorded the highest number of landslides (12 events) in Boshan District. Combination No.2 assigns to each of the 4498 landslide grids the values of time-varying factors corresponding to the year in which the landslide occurred. This enables a precise match between the landslide-prone environment and the susceptibility conditions at the time of failure. Combination No.3 further refines combination No.2 by using the interannual variation values (i.e., changes relative to the previous year) of the time-varying factors for each landslide grid cell in the year of occurrence. These variation values better capture the intensity of human engineering activities and the degree of change in the landslide-prone environment, thereby offering higher interpretability for landslide susceptibility. By incorporating such temporal dynamics, combination No.3 provides a more comprehensive

https://doi.org/10.3390/coatings16020207

representation of the combined effects of internal and external driving forces that contribute to landslide initiation.

4.2. Hazard Factor Quantification

The information value (IV) method was used to quantify the hazard factors [48], and the IV calculation method for combination No.1 is shown in Equation (7).

$$\mathrm{IV}_i = \ln\left(\frac{N_i/N}{S_i/S}\right) \tag{7}$$

where: N_i is the number of landslide grids in the i-th interval, N is the total number of landslide grids and N = 4498, S_i is the number of grids in the i-th interval, S is the total number of grids and S = 6,983,061.

IV_i reflects the favorable degree of landslide occurrence of the i-th interval. The larger the IV_i, the larger the landslide susceptible probability. $\mathrm{IV}_i > 0$ indicates that the i-th interval is conducive to landslide, while $\mathrm{IV}_i < 0$ indicates not conducive to landslide, and $\mathrm{IV}_i = 0$ indicates the impact of the i-th interval on landslide is not obvious.

When adding j to Equation (7), the IV calculation method is shown in Equation (8).

$$\mathrm{IV}_{ij} = \ln\left(\frac{N_{ij}/N_j}{S_{ij}/S}\right) \tag{8}$$

where: N_{ij} is the number of landslide grids in the i-th interval and j-th year, N_j is the number of landslide grids in the j-th year, S_{ij} is the number of grids in the i-th interval and j-th year.

(1) Static factor quantification

The IVs of the static factors were calculated according to Equation (7), as shown in Table 7.

Table 7. IVs of the static factors.

Static Factor	Classification	Number of Grids	Proportion of Grids	Number of Landslide Grids	Proportion of Landslide Grids	IV
Elevation (m)	0–240	85,557	0.110	74	0.051	−0.7687
	240–329	108,070	0.140	236	0.162	0.1460
	329–402	165,856	0.214	339	0.232	0.0808
	402–475	141,223	0.182	295	0.202	0.1043
	475–555	114,264	0.148	221	0.151	0.0201
	555–645	92,237	0.119	162	0.111	−0.0696
	645–769	54,820	0.071	89	0.061	−0.1518
	769–1066	12,543	0.016	44	0.030	0.6286
Gradient (°)	0–5.9328	148,948	0.192	142	0.097	−0.6828
	5.9328–10.4418	168,743	0.218	210	0.144	−0.4147
	10.4418–15.1881	141,830	0.183	221	0.151	−0.1922
	15.1881–19.9344	112,992	0.147	256	0.175	0.1744
	19.9344–24.6806	84,716	0.109	203	0.140	0.2503
	24.6806–29.9016	62,658	0.081	196	0.134	0.5034
	29.9016–36.5463	39,853	0.051	161	0.110	0.7687
	36.5463–60.5150	14,830	0.019	71	0.049	0.9474

https://doi.org/10.3390/coatings16020207

Table 7. *Cont.*

Static Factor	Classification	Number of Grids	Proportion of Grids	Number of Landslide Grids	Proportion of Landslide Grids	IV
Slope aspect	Plane	4893	0.006	0	0	0
	North	120,794	0.156	237	0.162	0.0377
	Northeast	101,005	0.130	234	0.160	0.2076
	East	78,792	0.102	161	0.110	0.0755
	Southeast	91,177	0.118	219	0.150	0.2400
	South	106,066	0.137	199	0.136	−0.0073
	Southwest	92,830	0.120	161	0.110	−0.0870
	West	76,958	0.099	94	0.064	−0.4362
	Northwest	102,054	0.132	155	0.106	−0.2194
Plane curvature	−7.9765–−2.0350	7311	0.009	15	0.010	0.1054
	−2.0350–−1.1948	37,545	0.048	85	0.058	0.1892
	−1.1948–−0.5946	99,773	0.129	161	0.110	−0.1593
	−0.5946–−0.1145	183,022	0.236	339	0.232	−0.0171
	−0.1145–0.3056	199,852	0.258	432	0.296	0.1374
	0.3056–0.8457	150,018	0.195	263	0.180	−0.0800
	0.8457–1.6259	75,910	0.098	108	0.074	−0.2809
	1.6259–7.3274	21,140	0.027	58	0.040	0.3930
Lithology	Silty sand, sandy clay	11,696	0.015	89	0.061	1.4028
	Thick limestone, medium thickness dolomite	146,576	0.188	192	0.132	−0.3536
	Mudstone, shale with sandstone	46,060	0.059	324	0.222	1.3083
	Arkose	1228	0.002	9	0.006	1.0986
	Yellowish·green sandstone	6895	0.009	46	0.032	1.2685
	Edgewise limestone	74,976	0.097	225	0.154	0.4622
	Silty mudstone	8221	0.011	35	0.024	0.7802
	Gabbro	88	0.001	0	0	0
	Dolomitic limestone	372,558	0.481	348	0.238	−0.7036
	Mudstone, shale with limestone	833	0.001	23	0.016	2.7726
	Gneissie monzogranite	85,193	0.110	127	0.087	−0.2346
	Weak gneissic orthogranite	7180	0.009	11	0.007	−0.2513
	Tonalitic gneiss	8660	0.011	29	0.02	0.5978
	Homblendite	1885	0.001	0	0	0
	Fine-grined granite	2137	0.003	2	0.001	−1.0986
	Micrite, micritic limestone	384	0.001	0	0	0
Distance from fault (m)	0–791.53	138,669	0.178	361	0.247	0.3276
	791.53–1686.30	141,261	0.182	342	0.234	0.2513
	1686.30–2546.65	128,384	0.166	208	0.142	−0.1562
	2546.65–3407.01	115,321	0.149	199	0.136	−0.0913

https://doi.org/10.3390/coatings16020207

Table 7. *Cont.*

Static Factor	Classification	Number of Grids	Proportion of Grids	Number of Landslide Grids	Proportion of Landslide Grids	IV
Distance from fault (m)	3407.01–4267.37	107,743	0.139	169	0.116	−0.1809
	4267.37–5196.55	77,871	0.101	106	0.073	−0.3247
	5196.55–6435.46	48,623	0.063	61	0.042	−0.4055
	6435.46–8775.63	16,697	0.022	14	0.010	−0.7885
TWI	3.0010–5.1384	205,825	0.266	350	0.240	−0.1029
	5.1384–6.1674	257,617	0.333	467	0.320	−0.0398
	6.1674–7.4341	154,815	0.200	257	0.176	−0.1278
	7.4341–9.0965	70,567	0.091	164	0.112	0.2076
	9.0965–11.0755	41,059	0.053	91	0.062	0.1568
	11.0755–13.4504	28,852	0.037	82	0.056	0.4144
	13.4504–16.6960	11,951	0.015	38	0.026	0.5500
	16.6960–23.1873	3884	0.005	12	0.008	0.4700
STI	0–1.0421	70,660	0.091	117	0.080	−0.1288
	1.0421–2.1134	75,635	0.098	107	0.073	−0.2945
	2.1134–12.9532	320,212	0.413	622	0.426	0.0310
	12.9532–24.2145	159,093	0.205	304	0.208	0.0145
	24.2145–42.7421	98,176	0.127	204	0.140	0.0975
	42.7421–61.5125	23,917	0.031	44	0.030	−0.0328
	61.5125–101.0528	14,535	0.019	35	0.024	0.2336
	101.0528–+∞	12,341	0.016	28	0.019	0.1719
Distance from river (m)	0–214.9345	179,016	0.231	480	0.329	0.3536
	214.9345–470.1691	176,585	0.228	388	0.266	0.1542
	470.1691–711.9704	138,670	0.179	286	0.196	0.0907
	711.9704–953.7717	116,996	0.151	169	0.116	−0.2637
	953.7717–1209.0064	82,748	0.107	98	0.067	−0.4681
	1209.0064–1504.5413	50,404	0.065	24	0.016	−1.4018
	1504.5413–1920.9768	24,358	0.031	12	0.008	−1.3545
	1920.9768–3425.5181	5793	0.008	3	0.002	−1.3863
Distance from road (m)	0–206.8845	275,173	0.355	690	0.472	0.2849
	206.8845–524.1073	186,514	0.241	420	0.288	0.1782
	524.1073–855.1225	126,167	0.163	226	0.155	−0.0503
	855.1225–1186.1376	83,471	0.108	58	0.040	−0.9933
	1186.1376–1558.5296	51,968	0.067	38	0.026	−0.9466
	1558.5296–1972.2986	31,294	0.040	18	0.012	−1.2040
	1972.2986–2510.1982	14,583	0.019	7	0.005	−1.3350
	2510.1982–3503.2436	5401	0.007	3	0.002	−1.2528

(2) Time-varying factor quantification for combination No.1

The IVs of the time-varying factors for combination No.1 were calculated according to Equation (7), as shown in Table 8.

Table 8. IVs of the time-varying factors for combination No.1.

Time-Varying Factor	Classification	Number of Grids	Proportion of Grids	Number of Landslide Grids	Proportion of Landslide Grids	IV
NDVI	−1–−0.0270	1897	0.002	3	0.002	0
	−0.0270–0.0844	34,037	0.044	69	0.047	0.0660
	0.0844–0.1444	53,816	0.069	153	0.105	0.4199
	0.1444–0.1823	84,993	0.110	203	0.139	0.2340
	0.1823–0.2561	161,857	0.209	289	0.198	−0.0541
	0.2561–0.3720	190,692	0.246	336	0.230	−0.0673
	0.3720–0.4501	167,148	0.216	287	0.197	−0.0921
	0.4501–0.7202	80,129	0.103	120	0.082	−0.2280
land use	Cultivated land	77,374	0.0999	63	0.043	−0.8430
	Forest land	498,863	0.6441	839	0.574	−0.1152
	Garden plot	39,280	0.0507	255	0.175	1.2390
	Water area	4763	0.0061	8	0.006	−0.0165
	Reclaimed land	153,664	0.1984	295	0.202	0.0180
	Bare land	626	0.0008	0	0	0
Population density (p/km^2)	23.1670–544.5703	619,476	0.7998	1185	0.8116	0.0146
	544.5703–646.6793	106,265	0.1372	202	0.1384	0.0087
	646.6793–737.5949	27,770	0.0358	36	0.0247	−0.3711
	737.5949–764.0146	12,023	0.0155	22	0.0151	−0.0261
	764.0146–1100.3417	5351	0.0069	9	0.0061	−0.1232
	1100.3417–1145.4753	2475	0.0032	4	0.0027	−0.1699
	1145.4753–1201.6171	1053	0.0014	2	0.0014	0
	1201.6171–1280.8762	157	0.0002	0	0	0

(3) Time-varying factor quantification for combination No.2

The IVs of the time-varying factors for combination No.2 were calculated according to Equation (8), and the calculation results of NDVI during 2014–2021 are shown in Table 9.

Table 9. IVs of NDVI during 2014–2021 for combination No.2.

Year	Classification	Number of Grids	Proportion of Grids	Number of Landslide Grids	Proportion of Landslide Grids	IV
2014	−0.3996–−0.0687	40,701	0.052	0	0	0
	−0.0687–0.0016	91,310	0.118	26	0.137	0.1493
	0.0016–0.0719	126,257	0.163	40	0.211	0.2581
	0.0719–0.1422	135,607	0.175	38	0.200	0.1335
	0.1422–0.2208	137,015	0.177	32	0.168	−0.0522
	0.2208–0.3118	116,312	0.150	28	0.147	−0.0202
	0.3118–0.4193	81,211	0.105	18	0.095	−0.1001
	0.4193–0.6551	46,157	0.060	8	0.042	−0.3567

https://doi.org/10.3390/coatings16020207

Table 9. *Cont.*

Year	Classification	Number of Grids	Proportion of Grids	Number of Landslide Grids	Proportion of Landslide Grids	IV
2015	−0.5383–−0.2274	1044	0.001	0	0	0
	−0.2274–−0.0134	56,703	0.073	8	0.076	0.0403
	−0.0134–0.1088	93,448	0.121	20	0.191	0.4565
	0.1088–0.2210	112,590	0.145	18	0.171	0.1649
	0.2210–0.3331	134,557	0.174	19	0.181	0.0394
	0.3331–0.4452	137,682	0.178	16	0.152	−0.1579
	0.4452–0.5624	124,556	0.161	15	0.143	−0.1186
	0.5624–0.7612	113,990	0.147	9	0.086	−0.5361
2016	−0.2953–−0.0401	47,593	0.062	0	0	0
	−0.0401–0.0436	87,315	0.113	21	0.131	0.1478
	0.0436–0.1236	91,747	0.118	25	0.156	0.2792
	0.1236–0.2036	125,703	0.162	33	0.206	0.2403
	0.2036–0.2797	129,420	0.167	28	0.175	0.0468
	0.2797–0.3597	121,893	0.157	24	0.150	−0.0456
	0.3597–0.4435	103,774	0.134	19	0.119	−0.1187
	0.4435–0.6721	67,125	0.087	10	0.063	−0.3228
2017	−0.4567–−0.1691	2479	0.003	0	0	0
	−0.1691–−0.0041	64,557	0.083	19	0.092	0.1029
	−0.0041–0.1090	92,183	0.119	35	0.169	0.3508
	0.1090–0.2221	103,690	0.134	36	0.174	0.2612
	0.2221–0.3259	133,741	0.173	35	0.169	−0.0234
	0.3259–0.4296	143,714	0.186	35	0.169	−0.0958
	0.4296–0.5333	128,762	0.166	29	0.140	−0.1703
	0.5333–0.7455	105,444	0.136	18	0.087	−0.4467
2018	−0.3397–−0.0236	43,113	0.056	0	0	0
	−0.0236–0.0614	72,003	0.093	19	0.117	0.2296
	0.0614–0.1505	84,846	0.110	28	0.173	0.4528
	0.1505–0.2356	94,081	0.121	23	0.142	0.16
	0.2356–0.3207	128,899	0.166	27	0.167	0.006
	0.3207–0.4058	136,939	0.177	28	0.173	−0.0229
	0.4058–0.4990	118,750	0.153	21	0.130	−0.1629
	0.4990–0.6935	95,939	0.124	16	0.098	−0.2353
2019	−0.5500–−0.2012	2169	0.003	0	0	0
	−0.2012–−0.0242	62,839	0.081	8	0.029	−1.0272
	−0.0242–0.0818	94,569	0.122	36	0.131	0.0712
	0.0818–0.1880	113,783	0.147	59	0.215	0.3802
	0.1880–0.2941	133,347	0.172	47	0.171	−0.0058
	0.2941–0.4053	136,153	0.176	52	0.189	0.0713
	0.4053–0.5166	121,229	0.156	40	0.145	−0.0731
	0.5166–0.7390	110,481	0.143	33	0.120	−0.1754

https://doi.org/10.3390/coatings16020207

Table 9. *Cont.*

Year	Classification	Number of Grids	Proportion of Grids	Number of Landslide Grids	Proportion of Landslide Grids	IV
2020	−0.2628–−0.0207	43,526	0.056	0	0	0
	−0.0207–0.0588	72,067	0.093	19	0.100	0.0726
	0.0588–0.1350	74,359	0.096	22	0.116	0.1892
	0.1350–0.2080	101,841	0.132	30	0.158	0.1798
	0.2080–0.2743	136,331	0.176	39	0.205	0.1525
	0.2743–0.3406	142,707	0.184	37	0.195	0.0581
	0.3406–0.4070	123,713	0.160	28	0.147	−0.0847
	0.4070–0.5827	80,026	0.103	15	0.079	−0.2653
2021	−0.3211–−0.0270	1897	0.002	0	0	0
	−0.0270–0.0844	34,037	0.044	8	0.047	0.0660
	0.0844–0.1444	53,816	0.070	15	0.088	0.2288
	0.1444–0.1823	84,993	0.110	24	0.14	0.2412
	0.1823–0.2561	161,857	0.209	34	0.199	−0.0490
	0.2561–0.3720	190,692	0.246	40	0.234	−0.0500
	0.3720–0.4501	167,148	0.216	34	0.199	−0.0820
	0.4501–0.7202	80,130	0.103	16	0.093	−0.1021

(4) Time-varying factor quantification for combination No.3

The interannual variation values of NDVI, land use and population density during 2014–2021 were extracted. The variation values of NDVI and population density were divided into eight categories by the natural breakpoint method. The land use variation was divided into 36 categories. The distributions of interannual variation values of NDVI, land use and population density in 2016 are shown in Figure 6.

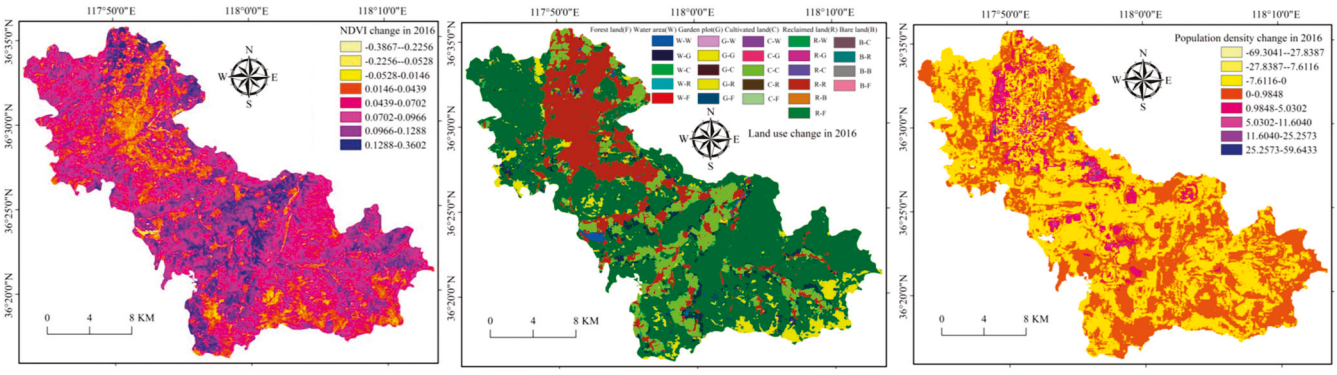

(**a**) (**b**) (**c**)

Figure 6. Distributions of the time-varying factors for combination No.3: (**a**) NDVI variation in 2016; (**b**) Land use variation in 2016; (**c**) Population density variation in 2016. Source: Geospatial Data Cloud, available online: http://www.gscloud.cn/ (accessed on 10 October 2025).

The IVs of the time-varying factors for combination No.3 were calculated according to Equation (8), and the calculation results of the land use variation in 2016 are shown in Table 10.

Table 10. IVs of the land use variation in 2016.

Land Use Variation	Number of Grids	Proportion of Grids	Number of Landslide Grids	Proportion of Landslide Grids	IV
Cultivated land → Water area	345	0.00045	0	0	0
Cultivated land → Garden plot	775	0.001	0	0	0
Cultivated land → Cultivated land	103,524	0.13365	6	0.0375	1.2709
Cultivated land → Reclaimed land	6881	0.00888	2	0.0125	0.3419
Cultivated land → Bare land	0	0	0	0	0
Cultivated land → Forest land	16,155	0.02086	6	0.0375	0.5865
Forest land → Water area	379	0.00049	0	0	0
Forest land → Garden plot	5023	0.00649	1	0.00625	0.0377
Forest land → Garden plot	15,646	0.0202	2	0.0125	0.4799
Forest land → Reclaimed land	7507	0.00969	2	0.0125	0.2546
Forest land → Bare land	330	0.00042	0	0	0
Forest land → Forest land	418,614	0.54044	66	0.4125	0.2701
Garden plot → Water area	9	0.00001	0	0	0
Garden plot → Garden plot	54,135	0.06989	27	0.16875	0.8815
Garden plot → Garden plot	371	0.00048	0	0	0
Garden plot → Reclaimed land	294	0.00038	3	0.01875	3.8988
Garden plot → Bare land	0	0	0	0	0
Garden plot → Forest land	4692	0.00606	11	0.06875	2.4288
Water area → Water area	4056	0.00524	0	0	0
Water area → Garden plot	24	0.00003	0	0	0
Water area → Garden plot	72	0.00009	0	0	0
Water area → Reclaimed land	223	0.00029	0	0	0
Water area → Bare land	0	0	0	0	0
Water area → Forest land	583	0.00075	2	0.0125	2.8134
Reclaimed land → Water area	211	0.00027	0	0	0
Reclaimed land → Garden plot	118	0.00015	5	0.03125	5.3391
Reclaimed land → Garden plot	1772	0.00229	0	0	0
Reclaimed land → Reclaimed land	121,419	0.15676	23	0.14375	0.0866
Reclaimed land → Bare land	52	0.00007	0	0	0
Reclaimed land → Forest land	10,306	0.01331	3	0.01875	0.3427
Bare land → Water area	0	0	0	0	0
Bare land → Garden plot	0	0	0	0	0
Bare land → Garden plot	35	0.00005	0	0	0
Bare land → Reclaimed land	100	0.00013	0	0	0
Bare land → Bare land	662	0.00085	0	0	0
Bare land → Forest land	257	0.00033	1	0.00625	2.9412

5. Landslide Susceptibility Mapping

5.1. LSM Model Construction

SVM is a generalized linear classifier that performs binary classification on data through supervised learning, with its decision boundary being the maximum-margin hyperplane derived from the training samples [49]. RF is an ensemble machine learning

https://doi.org/10.3390/coatings16020207

algorithm employed for both classification and regression tasks. It operates by constructing a multitude of decision trees and aggregating their predictions to yield more accurate and stable results than those achievable by a single model. CNN leverages the structural advantages of parameter sharing and local connectivity, enabling efficient processing of grid-like data without relying on additional features [50]. CNN-RF integrates the spatial feature-extraction strengths of CNN with the high stability and strong robustness of RF, thereby enhancing the analysis of landslide features and the exploration of disaster-causing patterns. DBN-MLP provides a new technical pathway for LSM by combining the efficient feature pre-training capability of DBN and the powerful nonlinear classification ability of MLP [51]. This paper employed SVM, RF, CNN, CNN-RF, and DBN-MLP models to conduct LSM, respectively. The hardware environment for modeling was a CPU i7-6700 processor, 8G memory, GTX1050 Ti-8G graphics card. A total of 70% grids (3149 landslide grids and 3149 non-landslide grids) were selected as training samples, and the remaining 30% grids (1349 landslide grids and 1349 non-landslide grids) were selected as verification samples.

5.1.1. SVM

SVM separates data by finding the optimal maximum-margin hyperplane, demonstrating strong robustness against noise and outliers. The loss function employed by SVM not only considers classification accuracy but also maximizes the margin width, which prevents overfitting on training data while effectively mitigating computational burdens caused by the curse of dimensionality. This gives SVM distinct advantages in solving nonlinear problems. However, SVM has limitations in parameter selection, as critical parameters like the penalty coefficient and kernel functions significantly impact prediction results, and improper choices may reduce model accuracy [52].

When applied to LSM, SVM treats hazard factors as independent variables (x), and a binary dependent variable (Y), where -1 indicates a non-landslide, and 1 indicates a landslide. It distinguishes between a landslide and a non-landslide in n-dimensional space by constructing an n-1-dimensional hyperplane, as shown in Equation (9).

$$y_i \cdot \left(\omega^T \cdot x_i + b\right) \geq 1 \tag{9}$$

where: b is the bias term. For linearly inseparable cases, SVM introduces slack variables (ξ) to allow approximate classification with tolerable misclassification, as shown in Equation (10).

$$y_i \cdot \left(\omega^T \cdot x_i + b\right) \geq 1 - \xi_i \tag{10}$$

By incorporating Lagrange multipliers (λ_i), the Lagrangian function is derived, as shown in Equation (11).

$$L = \frac{1}{2} \cdot \|\omega\|^2 + \sum_{i=1}^{n} \lambda_i \left(1 - y_i \cdot \left(\omega^T \cdot x_i + b\right)\right) \tag{11}$$

where: $\|\omega\|$ denotes the norm of the hyperplane's normal vector. Taking partial derivatives with respect to ω and b yields an expression containing λ_i, as shown in Equation (12).

$$\sum_{i=1}^{n} \lambda_i \cdot y_i = 0, \;\; \lambda_i \geq 0 \tag{12}$$

The SVM was constructed with key parameters listed in Table 11.

https://doi.org/10.3390/coatings16020207

Table 11. Key parameters of the SVM in this paper.

Parameter	Kernel Function	γ	C	Gamma	Shrinking	Tol
Value	RBF	0.1	5	Scale	False	1×10^{-4}

5.1.2. RF

RF is an ensemble learning model based on decision trees, used for regression and classification analysis. It employs the bootstrap method to randomly select n sample sets with replacement from the original training dataset, selects the optimal splitting attributes to construct CART decision trees, and integrates n decision trees through the Bagging algorithm to form a random forest. In essence, it is an improvement over the decision tree algorithm, combining multiple decision trees, with each tree's construction relying on an independently sampled dataset. The CART decision tree algorithm performs binary splits (rather than multi-way splits) on the values of a specific feature each time, resulting in the construction of binary trees instead of multi-way trees. The CART decision tree uses the *Gini* index to select the optimal splitting attribute. The *Gini* index represents the impurity of the model: the lower the *Gini* index, the lower the impurity and the better the features [53]. The calculation methods of the *Gini* index are shown in Equations (13) and (14).

$$gini(A) = 1 - \sum_{i=1}^{n} p_i^2 \tag{13}$$

$$gini(A, B) = \sum_{j=1}^{m} \frac{|A_j|}{|A|} gini(A_j) \tag{14}$$

where: $gini(A)$ is the *Gini* index of sample A, n is the number of categories of sample A, p_i is the proportion of the i-th category of sample A, $gini(A, B)$ is the *Gini* index after splitting sample A using sample B, m is the number of samples, $|A_j|$ is the size of the j-th subset.

The RF was constructed with key parameters listed in Table 12.

Table 12. Key parameters of the RF in this paper.

Parameter	N_Estimators	Criterion	Bootstrap	Random_State
Value	77	Gine	Sampling with replacement	None
Parameter	**Max_Features**	**Max_Depth**	**Min_Samples_Leaf**	**Min_Samples_Split**
Value	3	4	4	3

5.1.3. CNN

CNN is a feed-forward neural network with deep structure, which can learn features from data and effectively identify characteristics like edges, textures and shapes through convolutional kernels, synthesizing this information to enhance data processing efficiency. CNN includes an input layer, a convolutional layer, a pooling layer, a fully connected layer and output layer. Convolutional layer parameters include the size, step size and filling method of the convolutional kernel. Pooling operation is divided into maximum pooling and average pooling. Maximum pooling selects the maximum value of the element as the value after pooling, while average pooling selects the average value. Fully connected layer nonlinearly combines the features extracted by convolution and pooling, and the feature matrix is expanded into a one-dimensional vector. The output layer uses the Logical function to output the classification label, and assesses the similarity between the predicted value and the actual value of the model by the loss function [54]. The convolutional operation is shown in Figure 7.

https://doi.org/10.3390/coatings16020207

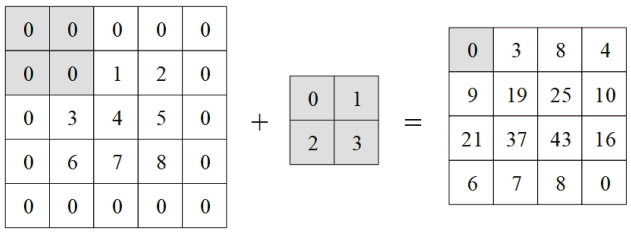

Figure 7. Convolutional operation.

In the training process of CNN, the landslide grids are converted into a two-dimensional square matrix with equal rows and columns. The specific steps are as follows:

(1) Comparing the number of factors in the three combinations and the number of grades of each factor, the larger one is selected as the size of the matrix.

(2) Each column of the matrix represents the corresponding factor. If the attribute value of the *m*-th factor of a grid is in the *n*-th grade, the element of the *m*-th column and the *n*-th row is calibrated to 1, and the other elements of the *n*-th column are calibrated to 0. For example, the categories of lithology in combination No.1 and No.2 are the largest (16), so the matrix size is 16 × 16. The categories of the land use variation in combination No.3 are 36, and the size is 36 × 36.

Taking a landslide grid in 2015 as an example, the hazard factors in combination No.2 are as follows: elevation is 832 m, gradient is 32.0752°, slope aspect is northeast, plane curvature is 1.3528, distance from river is 232.4534 m, STI is 23.0425, TWI is 21.6551, distance from road is 455.4205 m, land use is forest land, distance from fault is 2813.95 m, lithology is dolomitic limestone, NDVI is 0.1856, and population density is 128.7560 p/km^2. The corresponding two-dimensional square matrix is shown in Figure 8.

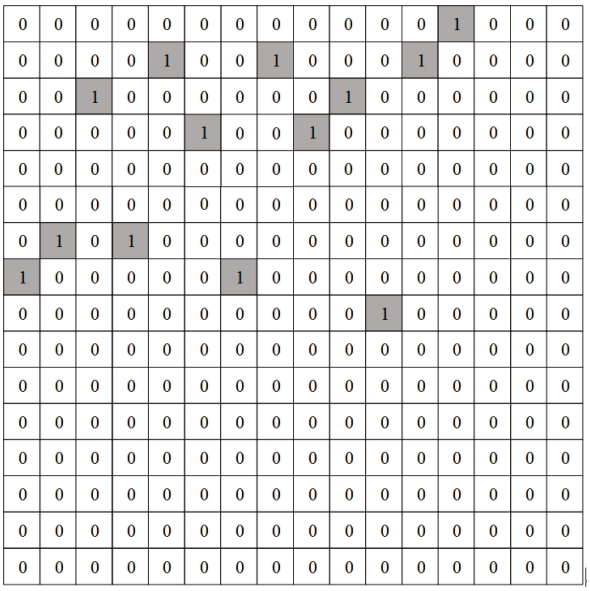

Figure 8. The corresponding two-dimensional square matrix.

The model structures of inputs are shown in Table 13, including one input layer, two convolutional layers, two pooling layers, one fully connected layer and one output layer.

https://doi.org/10.3390/coatings16020207

Table 13. CNN model structures.

No.	Layer	Model Size	Filter Size	Step	Zero Fill Way
1	Input	$16 \times 16/36 \times 36$	0	0	NONE
2	Conv-1	$16 \times 16/36 \times 36$	$3 \times 3 \times 4/5 \times 5 \times 4$	1	SAME/VALID
3	Pool-1	$16 \times 16 \times 4/32 \times 32 \times 4$	2×2	2	VALID
4	Conv-2	$8 \times 8 \times 4/16 \times 16 \times 4$	$3 \times 3 \times 8/9 \times 9 \times 8$	1	SAME/VALID
5	Pool-2	$8 \times 8 \times 8/8 \times 8 \times 8$	2×2	2	VALID
6	F-layer	128	NONE	NONE	NONE
7	Output	2	NONE	NONE	NONE

The CNN was constructed with key parameters listed in Table 14.

Table 14. Key parameters of the CNN in this paper.

Parameter	**Activation Function**	**Optimization Algorithm**	**Learning Rate**	**Learning Rate Scheduler**
Value	Leaky ReLU	AdamW	3×10^{-4}	Cosine annealing
Parameter	**Max_Epoch**	**Batch Size**	**Patience**	**Dropout**
Value	100	128	15	0.0 (convolutional layer); 0.5 (fully connected layer)

5.1.4. CNN-SVM

CNN-SVM is constructed by integrating CNN and SVM, combining the strengths of both. Its core workflow is as follows: CNN module processes input data through convolution and pooling operations, enabling multi-level deep feature extraction and generating high-dimensional feature vectors. This process not only preserves critical information but also mitigates the "curse of dimensionality". Subsequently, the feature vectors are fed into SVM, where they are mapped to a higher-dimensional space via kernel functions, and precise classification is achieved by an optimal hyperplane. The training of CNN-SVM follows a two-stage logic of "feature extraction-classification optimization". First, CNN undergoes independent pre-training. As the number of iterations increases, the model's loss function declines, demonstrating continuous optimization in feature learning. After pre-training is completed, the CNN network parameters are fixed, and only the subsequent SVM classifier is trained. The selection of its kernel function and regularization parameters is based on the optimal configuration of an independent SVM model [55].

5.1.5. DBN-MLP

DBN-MLP is a hybrid neural network model constructed by integrating DBN and MLP. DBN consists of multiple stacked Restricted Boltzmann Machines (RBM) and relies on unsupervised learning to achieve hierarchical feature extraction. It can efficiently learn the implicit features of data and progressively optimize them. Its autoencoding capability enables the extraction of high-level abstract features, facilitating effective modeling of complex unlabeled data. MLP centers on supervised learning. It adjusts weights via the backpropagation algorithm and minimizes the loss function to achieve accurate predictions, demonstrating strong performance in complex pattern classification and regression tasks due to its powerful nonlinear mapping ability. The core workflow of DBN-MLP is as follows: DBN extracts deep features from input data in an unsupervised manner, encoding the intrinsic patterns across its layers. The extracted features are fed into the MLP, which

https://doi.org/10.3390/coatings16020207

optimizes its parameters through its multi-layer structure and backpropagation algorithm to accomplish classification or regression tasks [56].

The rational configuration of the number of RBM layers is crucial for balancing model complexity and generalization capability. Too few layers result in insufficient model expressiveness, failing to adequately learn the complex features of landslide data; too many layers increase model complexity, leading not only to higher computational costs and longer training cycles, but also making the model prone to overfitting. This paper adopted a three-layer RBM stacked structure, with neuron counts set to 256, 128 and 64. Each RBM layer aims to learn high-level feature representations of the data. Taking the first RBM layer as an example, its visible layer receives input data from the training set and performs feature transformation by adjusting the connection weights with the hidden layer neurons. The hidden-layer neurons then output abstract representations based on specific activation rules. After the first layer is trained, its hidden layer output is directly used as the input for the second RBM layer. This iterative process achieves gradual abstraction and deep extraction of features. The parameters of the DBN are shown in Table 15.

Table 15. DBN model parameters in this paper.

Parameter	Learning Rate	Training Epochs	Layers	RBM Neuron Counts		
				First Layer	Second Layer	Third Layer
Value	0.01	50	3	256	128	64

MLP comprises two hidden layers, each with the neuron count set to 128, and the output layer is set to five neurons. The ReLU function can effectively address the vanishing gradient problem and accelerate model convergence. When the input value is >0, the output is the input value itself; when the input value is ≤ 0, the output is 0 [57].

5.2. Accuracy Analysis

The five models were trained using training samples. The trained models were then applied to the verification samples (1349 landslide grids and 1349 non-landslide grids), and their performance was evaluated using Accuracy, Precision, Recall, F1-Score, ROC and AUC. The calculation methods are shown in Equations (15)–(19).

$$\text{Accuracy} = \frac{TN + TP}{TN + TP + FP + FN} \tag{15}$$

$$\text{Precision} = \frac{TP}{TP + FP} \tag{16}$$

$$\text{Recall} = \frac{TP}{TP + FN} \tag{17}$$

$$\text{F1} - \text{Score} = 2 \cdot \frac{\text{Recall} \cdot \text{Precision}}{\text{Recall} + \text{Precision}} \tag{18}$$

$$\text{FPR} = \frac{FP}{TN + FP} \tag{19}$$

where: TP means the prediction and actual situation both indicate a landslide, FP means the prediction is a landslide, but the actual situation is a non-landslide, TN means the prediction and actual situation both indicate a non-landslide, FN means the prediction is a non-landslide, but the actual situation is a landslide.

The FPR is the abscissa, and the Recall (TPR) is the ordinate in the ROC, as shown in Figure 9. The calculation results of Accuracy, Precision, Recall, F1-Score and AUC are shown in Table 16. By comprehensively considering Accuracy, Precision, Recall, F1-Score and

https://doi.org/10.3390/coatings16020207

AUC, the rankings of modeling effectiveness for various models and factor combinations are shown in Table 17.

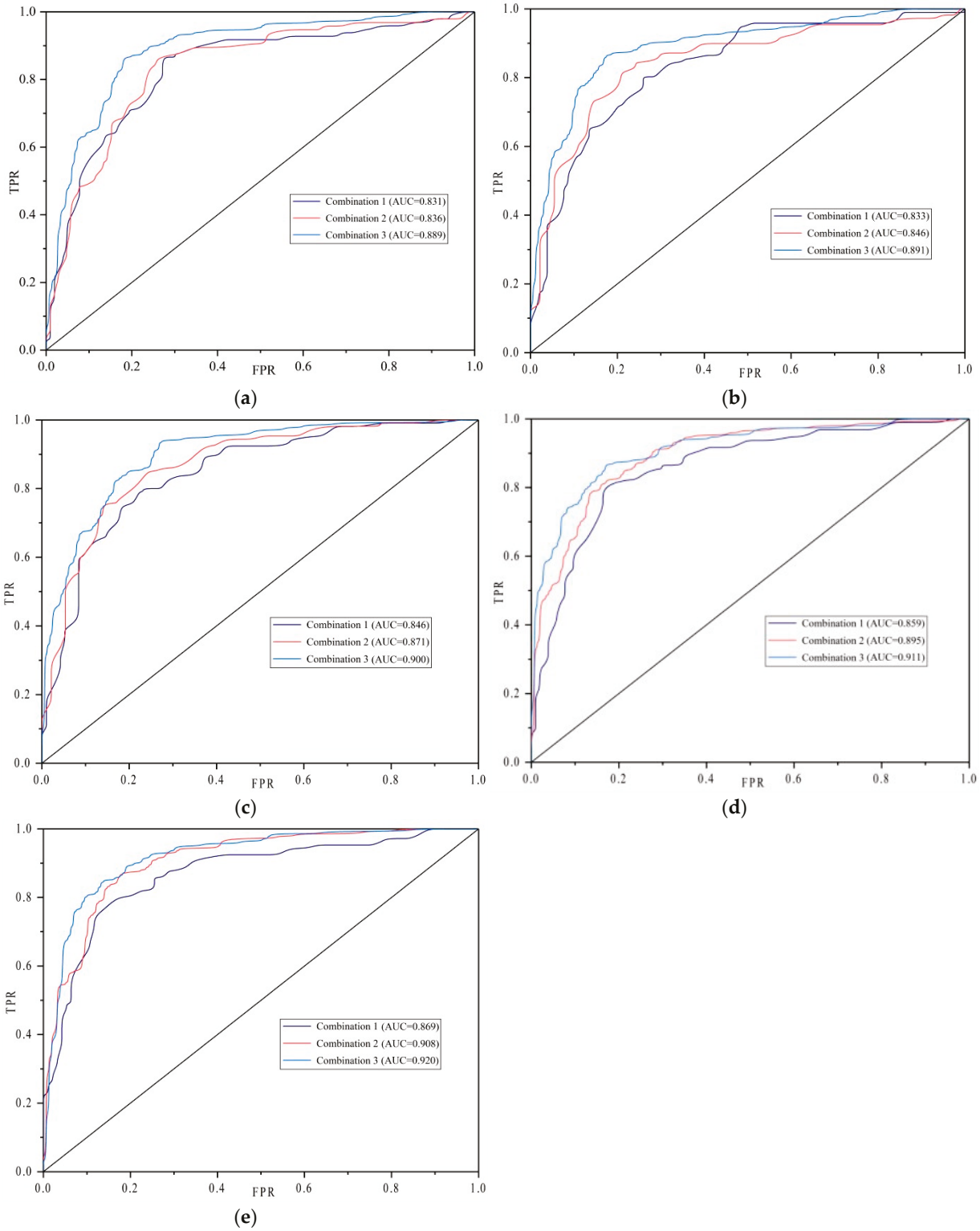

Figure 9. ROC of each combination and model: (**a**) SVM; (**b**) LR; (**c**) RF; (**d**) CNN-SVM; (**e**) DBN-MLP.

Table 16. The calculation results of Accuracy, Precision, Recall, F1-Score and AUC.

Model	Combination														
	No.1					**No.2**					**No.3**				
SVM	TP	FN	FP	TN	AUC	TP	FN	FP	TN	AUC	TP	FN	FP	TN	AUC
	1124	225	254	1095	0.831	1138	211	241	1108	0.836	1191	158	163	1186	0.889
	Accuracy	Precision	Recall	F1-Score	FPR	Accuracy	Precision	Recall	F1-Score	FPR	Accuracy	Precision	Recall	F1-Score	FPR
	0.822	0.815	0.833	0.824	0.188	0.832	0.825	0.843	0.834	0.178	0.881	0.879	0.882	0.881	0.120
RF	TP	FN	FP	TN	AUC	TP	FN	FP	TN	AUC	TP	FN	FP	TN	AUC
	1129	220	250	1099	0.833	1152	197	207	1142	0.846	1203	146	154	1195	0.891
	Accuracy	Precision	Recall	F1-Score	FPR	Accuracy	Precision	Recall	F1-Score	FPR	Accuracy	Precision	Recall	F1-Score	FPR
	0.825	0.818	0.836	0.827	0.185	0.850	0.847	0.853	0.850	0.153	0.888	0.886	0.891	0.889	0.114
CNN	TP	FN	FP	TN	AUC	TP	FN	FP	TN	AUC	TP	FN	FP	TN	AUC
	1150	199	205	1144	0.846	1178	171	171	1178	0.871	1227	122	146	1203	0.900
	Accuracy	Precision	Recall	F1-Score	FPR	Accuracy	Precision	Recall	F1-Score	FPR	Accuracy	Precision	Recall	F1-Score	FPR
	0.850	0.848	0.852	0.850	0.151	0.873	0.873	0.873	0.873	0.126	0.900	0.893	0.909	0.901	0.108
CNN-SVM	TP	FN	FP	TN	AUC	TP	FN	FP	TN	AUC	TP	FN	FP	TN	AUC
	1161	188	184	1165	0.859	1215	134	146	1203	0.895	1251	98	107	1242	0.911
	Accuracy	Precision	Recall	F1-Score	FPR	Accuracy	Precision	Recall	F1-Score	FPR	Accuracy	Precision	Recall	F1-Score	FPR
	0.862	0.863	0.860	0.861	0.136	0.896	0.892	0.900	0.896	0.108	0.924	0.921	0.927	0.924	0.079
DBN-MLP	TP	FN	FP	TN	AUC	TP	FN	FP	TN	AUC	TP	FN	FP	TN	AUC
	1175	174	175	1174	0.869	1231	118	135	1214	0.908	1276	73	85	1264	0.920
	Accuracy	Precision	Recall	F1-Score	FPR	Accuracy	Precision	Recall	F1-Score	FPR	Accuracy	Precision	Recall	F1-Score	FPR
	0.870	0.870	0.871	0.870	0.129	0.906	0.901	0.912	0.906	0.100	0.941	0.937	0.945	0.941	0.063

https://doi.org/10.3390/coatings16020207

Table 17. Rankings of modeling effectiveness for various models and factor combinations.

Model and Combination	**DBN-MLP + No.3**	**CNN-SVM + No.3**	**DBN-MLP + No.2**	**CNN + No.3**	**CNN-SVM + No.2**
Ranking	No.1	No.2	No.3	No.4	No.5
Model and Combination	**RF + No.3**	**SVM + No.3**	**CNN + No.2**	**DBN-MLP + No.1**	**DBN-SVM + No.1**
Ranking	No.6	No.7	No.8	No.9	No.10
Model and Combination	**CNN + No.1**	**RF + No.2**	**SVM + No.2**	**RF + No.1**	**SVM + No.1**
Ranking	No.11	No.12	No.13	No.14	No.15

Among the five models, DBN-MLP yielded the best performance. This can be attributed to the hierarchical feature extraction enabled by its multi-layer network architecture. As network depth increases, the model progressively learns more abstract and global feature representations. In the context of LSM, multi-source data encompassing geological, topographic and meteorological information are inherently high-dimensional and complex. The stacked RBM structure in a DBN allows for progressive abstraction of such data, thereby uncovering deep-seated latent patterns and hazard-related regularities. Specifically, the three-layer RBM stacking employed in this study enables the DBN to gradually extract features from the training samples, from elementary to highly abstract levels, providing more informative and discriminative data representations for subsequent processing.

5.3. LSM Results

LSM results of the DBN-MLP model and combination No.3 were the best, and the landslide susceptible probabilities were divided into five levels: extremely low susceptible areas [0.000, 0.200), low susceptible areas [0.200, 0.400), medium susceptible areas [0.400, 0.600), high susceptible areas [0.600, 0.800) and extremely high susceptible areas [0.800, 1.000]. LSM results based on the DBN-MLP model are shown in Figure 10 and Table 18.

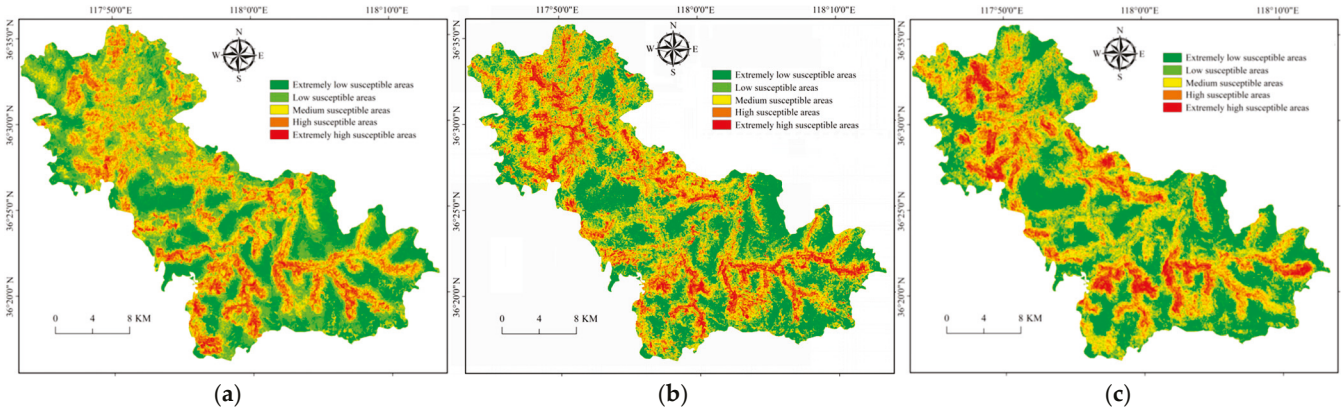

Figure 10. LSM results based on the DBN-MLP model: (**a**) Combination No.1; (**b**) Combination No.2; (**c**) Combination No.3. Source: Geospatial Data Cloud, available online: http://www.gscloud.cn/ (accessed on 10 October 2025).

Table 18. LSM results based on the DBN-MLP model.

Combination	No.1	No.2	No.3	No.1	No.2	No.3	No.1	No.2	No.3	No.1	No.2	No.3
LSM results	Number of partition grids			Proportion of partition grids (%)			Number of landslide grids			Proportion of landslide grids (%)		
Extremely low susceptible areas	247,674	243,794	263,027	31.98	31.47	33.96	24	15	13	1.64	1.03	0.89
Low susceptible areas	164,564	124,699	113,539	21.25	16.10	14.66	27	23	17	1.85	1.58	1.16
Medium susceptible areas	185,914	253,151	233,292	24.00	32.68	30.12	114	71	55	7.81	4.86	3.77
High susceptible areas	124,564	102,652	117,799	16.08	13.25	15.21	268	279	277	18.36	19.11	18.97
Extremely high susceptible areas	51,854	50,274	46,913	6.69	6.50	6.05	1027	1072	1098	70.34	73.42	75.21

The grids of the extremely high susceptible areas account for 6.69%, 6.50% and 6.32% of the total when employing combination No.1, No.2 and No.3, respectively, mainly distributed in the northwest, south and east of Boshan District. The landslide grids distributed in the extremely high susceptible areas account for 70.34%, 73.42% and 75.21% of the total when employing combination No.1, No.2 and No.3, respectively. This indicates that compared with combinations No.1 and No.2, combination No.3 corresponds to the smallest extremely high-susceptibility areas and the highest proportion of landslide grids, which means it achieves the best modeling effect.

6. Discussions

6.1. LSM Results of Different Combinations

The combination No.3 and the DBN-MLP model were used as the benchmark. LSM results of the benchmark were compared with the results of the combinations No.1 and No.2, and the study area was divided into overestimation areas, underestimation areas and the same areas, as shown in Figure 11.

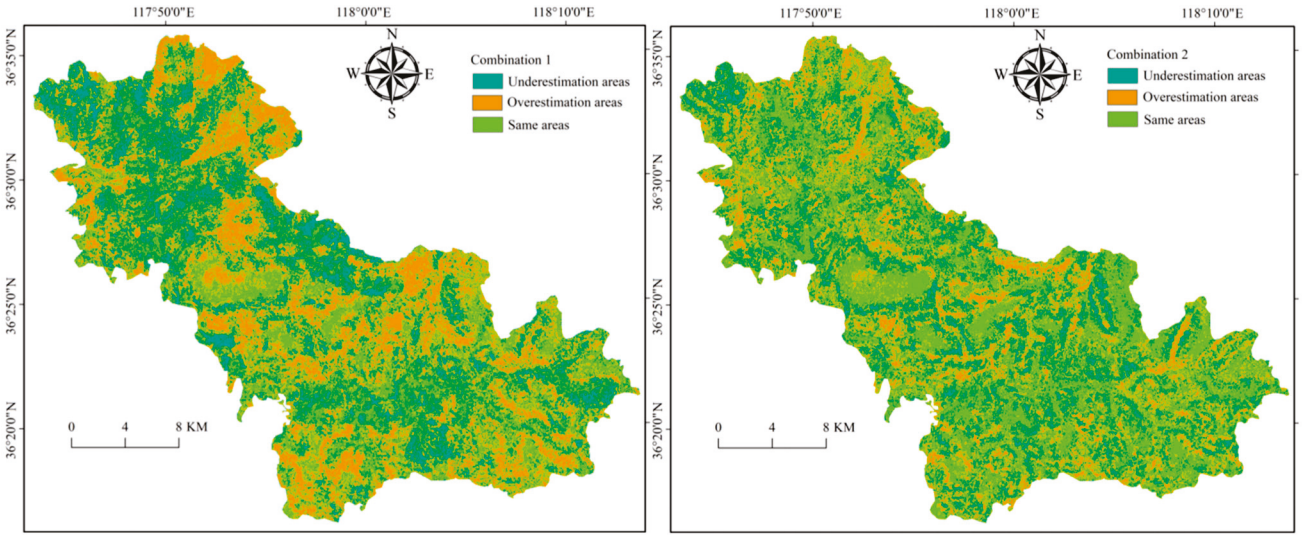

Figure 11. Comparisons of different combinations: (**a**) Comparison of the combinations No.1 and No.3; (**b**) Comparison of the combinations No.2 and No.3. Source: Geospatial Data Cloud, available online: http://www.gscloud.cn/ (accessed on 10 October 2025).

The LSM results of different combinations are quite varied. The overestimation areas are distributed in the south of Boshan District, while the underestimation areas are in the northwest for combination No.1. The overestimation areas are evenly distributed, while the underestimation areas are in the northwest of Boshan District for combination No.2.

The error estimation areas were superimposed with some hazard factors, as shown in Figures 12 and 13.

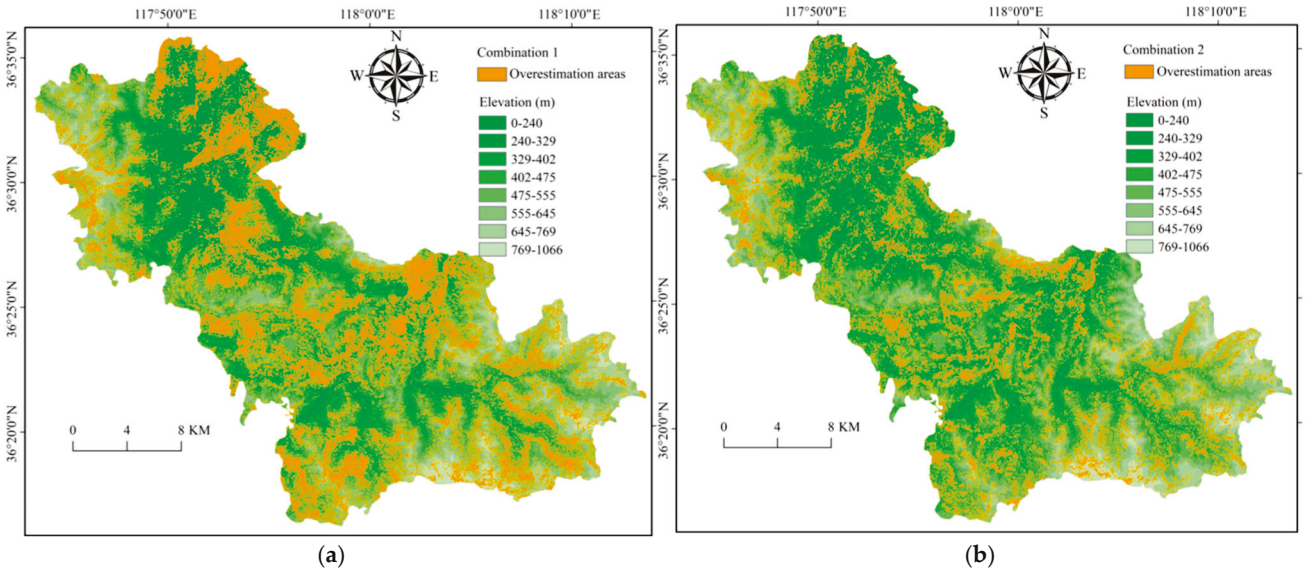

(**a**) (**b**)

Figure 12. Overestimation areas superposed with the elevation: (**a**) Combination No.1; (**b**) Combination No.2. Source: Geospatial Data Cloud, available online: http://www.gscloud.cn/ (accessed on 10 October 2025).

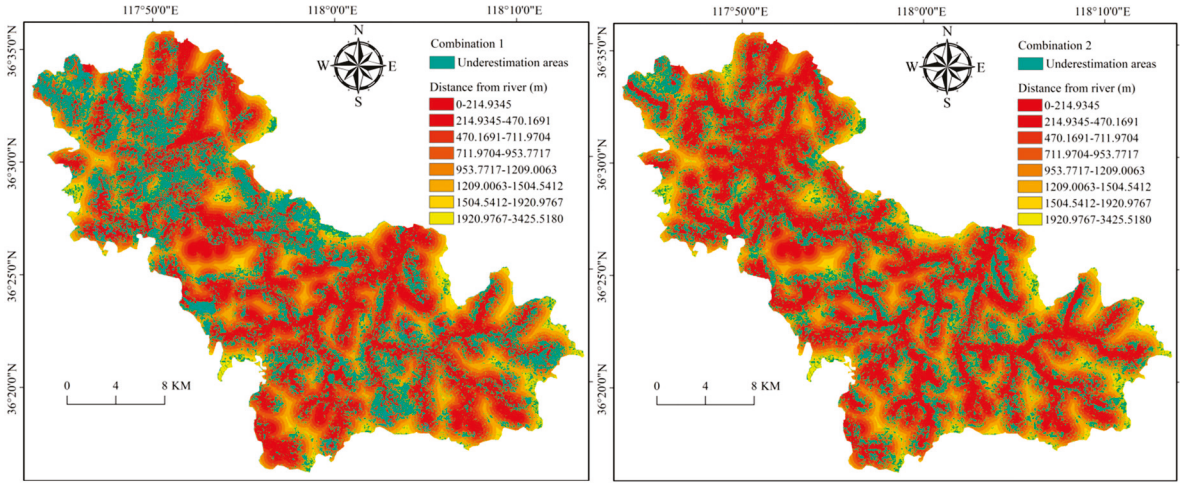

(**a**) (**b**)

Figure 13. Underestimation areas superposed with the distance from the river: (**a**) Combination No.1; (**b**) Combination No.2. Source: Geospatial Data Cloud, available online: http://www.gscloud.cn/ (accessed on 10 October 2025).

The coincidence rate between the overestimated areas and the high-elevation areas is high, and that between the underestimated areas and areas near rivers is also high, indicating that the DBN-MLP for the combinations No.1 and No.2 overestimates the elevation and underestimates the distance from rivers.

6.2. LSM Results Based on Different Models

LSM results of the benchmark were compared with the results of RF, CNN and CNN-SVM, as shown in Figure 14.

https://doi.org/10.3390/coatings16020207

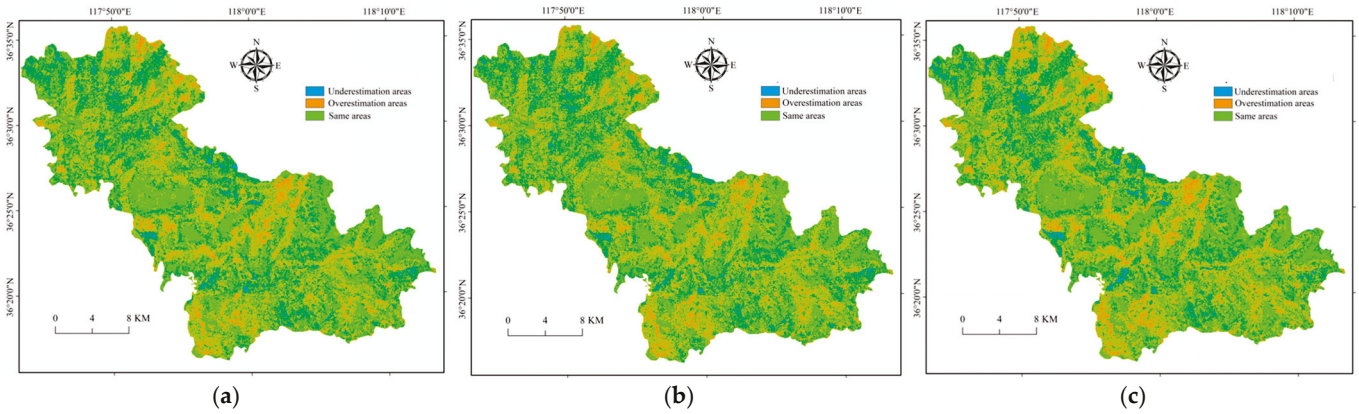

Figure 14. Comparisons of LSM results based on different models: (**a**) Comparison of RF and DBN-MLP; (**b**) Comparison of CNN and DBN-MLP; (**c**) Comparison of CNN-SVM and DBN-MLP. Source: Geospatial Data Cloud, available online: http://www.gscloud.cn/ (accessed on 10 October 2025).

The error-estimation areas based on the CNN show a patchy distribution. The RF has the largest error-estimation areas, which are mostly overestimation and show a scattered distribution. The CNN-SVM has the smallest error estimation areas, which are basically within the error estimation areas of other models. The overestimation areas and underestimation areas of the CNN-SVM were superimposed with some hazard factors, as shown in Figure 15.

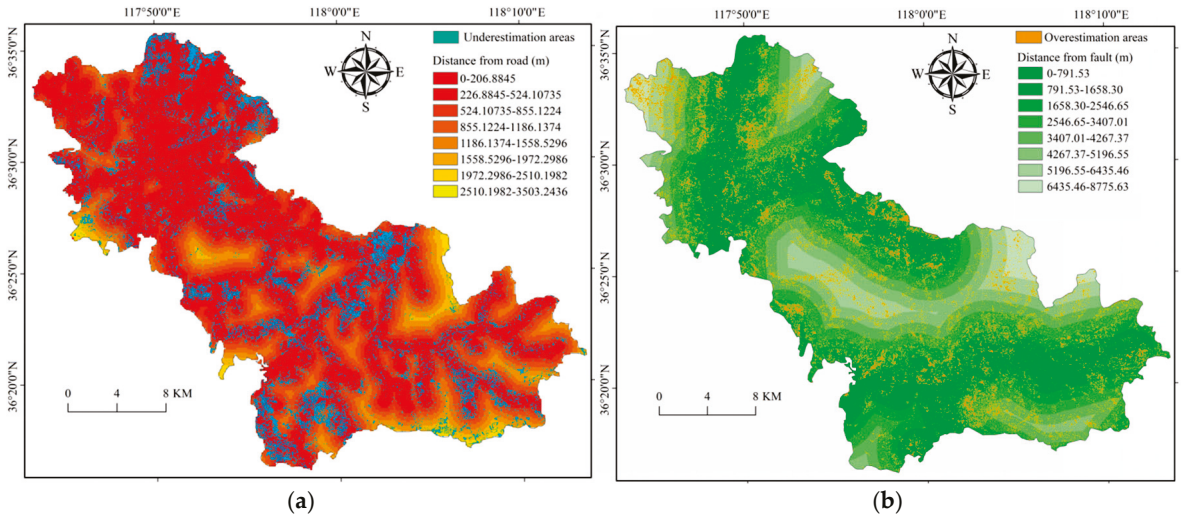

Figure 15. Error estimation areas superposed with hazard factors: (**a**) Underestimation areas superposed with the distance from the road; (**b**) Overestimation areas superposed with the distance from the fault. Source: Geospatial Data Cloud, available online: http://www.gscloud.cn/ (accessed on 10 October 2025).

Underestimation areas are distributed in areas close to roads. The distribution of the overestimation areas is scattered, and the coincidence rate of the underestimation areas and the areas close to the faults is high. Compared with the DBN-MLP, the other models underestimate the distance from the road and overestimate the distance from the fault. In summary, the RF, CNN and CNN-SVM easily discard the feature information of some factors, missing the optimal accuracies of the models. It should be noted that the error estimation areas are primarily described in a descriptive manner. The underlying causes of these errors are likely related to the logical structure and intelligence level of the model, yet

https://doi.org/10.3390/coatings16020207

the specific error-inducing mechanisms have not yet been addressed by researchers. This could serve as a potential topic for future investigation.

7. Conclusions

This study selected the best combination and model through comparative studies and revealed the degree of influence of each hazard factor on landslide susceptibility, greatly improving LSM accuracy, which can provide a scientific basis for land use planning.

(1) Three hazard factor combinations considering time-varying factors (No.1: static factors + values of time-varying factors in 2021; No.2: static factors + annual values of time-varying factors; No.3: static factors + interannual variation values of time-varying factors) were constructed. LSM was conducted based on the SVM, RF, CNN, CNN-SVM, and DBN-MLP. The results show that among the three combinations, the combination No.3 is the best, followed by the combination No.2; among the five models, the DBN-MLP is the best, followed by the CNN-SVM. The extremely high susceptible areas mainly distribute in the northwest, south and east of Boshan District.

(2) The combination No.3 and DBN-MLP were used as the benchmark; the LSM results of different combinations and models were compared. The results show that the extreme tendency of the LSM results of the combinations No.1 and No.2 are strong, and they are easy to produce error estimation areas, which overestimate the elevation and underestimate the distance from river; the LSM results of the CNN-SVM are closer to those of the benchmark, which underestimates the distance from road and overestimates the distance from fault.

(3) Although the DBN-MLP performs well in handling uncertainties, its results can still be influenced by various factors, potentially leading to biased inferences. The study area contains 99 landslide sites, represented by 4498 landslide grid cells. Among these, 3149 cells were used for training and 1349 for validation. While this sample size can generally meet the basic requirements for model training, increasing the number of landslide samples would likely improve predictive performance. When landslide grid cells are limited, pre-training the model with landslide samples from other regions, followed by transfer learning using samples from the study area, can also help achieve optimal modeling results. Furthermore, employing cross-validation for model parameter tuning and constructing hybrid algorithms through ensemble learning can effectively mitigate the inherent randomness and bias of a single model. Future research should continue to address these issues in greater depth.

Author Contributions: Conceptualization, Z.W.; Methodology, C.Y.; Software, J.L.; Validation, Z.W.; Formal analysis, C.Y.; Investigation, J.L.; Resources, Z.W.; Data curation, C.Y.; Writing—original draft, J.L.; Writing—review & editing, Z.W.; Visualization, C.Y.; Supervision, J.L.; Project administration, Z.W.; Funding acquisition, C.Y. All authors have read and agreed to the published version of the manuscript.

Funding: This research was supported by the National Natural Science Foundation of China (Grant No. 51808327) and the Natural Science Foundation of Shandong Province (Grant No. ZR2019PEE016).

Institutional Review Board Statement: Not applicable.

Informed Consent Statement: Not applicable.

Data Availability Statement: The original contributions presented in this study are included in the article. Further inquiries can be directed to the corresponding author.

Conflicts of Interest: The authors declare no conflict of interest.

References

1. Sun, H.Q.; Li, W.Y.; Scaioni, M.; Fu, J.; Guo, X.; Gao, J. Influence of spatial heterogeneity on landslide susceptibility in the transboundary area of the Himalayas. *Geomorphology* **2023**, *433*, 108723. [CrossRef]
2. Hong, H.Y.; Wang, D.S.; Zhu, A.X.; Wang, Y. Landslide susceptibility mapping based on the reliability of landslide and non-landslide sample. *Expert Syst. Appl.* **2024**, *243*, 122933. [CrossRef]
3. Feng, H.; Miao, Z.; Hu, Q. Study on the uncertainty of machine learning model for earthquake-induced landslide susceptibility assessment. *Remote Sens.* **2022**, *14*, 2968. [CrossRef]
4. Thiery, Y.; Kaonga, H.; Mtumbuka, H.; Terrier, M.; Rohmer, J. Landslide hazard assessment and mapping at national scale for Malawi. *J. Afr. Earth Sci.* **2024**, *212*, 105187. [CrossRef]
5. Sharma, N.; Saharia, M.; Ramana, G.V. High resolution landslide susceptibility mapping using ensemble machine learning and geospatial big data. *CATENA* **2024**, *235*, 107653. [CrossRef]
6. Chen, L.; Ma, P.F.; Yu, C.; Zheng, Y.; Zhu, Q.; Ding, Y.L. Landslide susceptibility assessment in multiple urban slope settings with a landslide inventory augmented by InSAR techniques. *Eng. Geol.* **2023**, *327*, 107342. [CrossRef]
7. Li, Y.Y.; Duan, W.H. Decoding vegetation's role in landslide susceptibility mapping: An integrated review of techniques and future directions. *Biogeotechnics* **2024**, *2*, 100056. [CrossRef]
8. Soma, A.S.; Kubota, T. The performance of land use changes causative factor on landslide susceptibility map in upper Ujung-Loe watersheds south Sulawesi, Indonesia. *Geoplanning J. Geomat. Plan.* **2017**, *4*, 157–170. [CrossRef]
9. Alberto, M.M.; Juan, B.A.; Simon, A.; Markus, S. Deforestation controls landslide susceptibility in Far-Western Nepal. *CATENA* **2022**, *219*, 106627. [CrossRef]
10. Jin, B.J.; Zeng, T.R.; Yin, K.L.; Gui, L.; Guo, Z.Z.; Wang, T.F. Dynamic landslide susceptibility mapping based on the PS-InSAR deformation intensity. *Environ. Sci. Pollut. Res.* **2024**, *31*, 7872–7888. [CrossRef]
11. Francis, D.M.; Bryson, L.S. Coupled landslide analyses through dynamic susceptibility and forecastable hazard analysis. *Nat. Hazards* **2025**, *121*, 2971–2999. [CrossRef]
12. Lamichhane, S.; Kansakar, A.R.; Devkota, N.; Dahal, B.K. Integrating dynamic factors for predicting future landslide susceptibility. *Environ. Earth Sci.* **2025**, *84*, 89. [CrossRef]
13. Jia, Y.F.; Yang, H.J.; Zhang, S.J.; Wang, X.Y. Connection methods in landslide susceptibility assessment: Suitability evaluation based on environmental factor type. *J. Mt. Sci.* **2020**, *22*, 2996–3016. [CrossRef]
14. He, Y.F.; Ding, M.T.; Duan, Y.; Zheng, H.; Wu, J.B.; Feng, L. Exploring the dynamic impact of urbanization on landslide susceptibility in Sichuan Province using an explainable XGBoost model. *Eng. Geol.* **2025**, *357*, 108372. [CrossRef]
15. Wang, Z.Q.; Fang, X.W.; Zhang, W.G.; Wang, L.Q.; Wang, K.; Chen, C. Dynamic intelligent prediction approach for landslide displacement based on biological growth models and CNN-LSTM. *J. Mt. Sci.* **2025**, *22*, 71–88. [CrossRef]
16. Huang, F.M.; Yang, Y.; Jiang, B.C.; Chang, Z.L.; Zhou, C.B.; Jiang, S.H.; Huang, J.S.; Catani, F.; Yu, C.S. Effects of different division methods of landslide susceptibility levels on regional landslide susceptibility mapping. *Bull. Eng. Geol. Environ.* **2025**, *84*, 276. [CrossRef]
17. Yang, Z.Q.; Xu, C.; Shao, X.Y.; Ma, S.Y.; Li, L. Landslide susceptibility mapping based on CNN-3D algorithm with attention module embedded. *Bull. Eng. Geol. Environ.* **2022**, *81*, 412. [CrossRef]
18. Chen, K.; Fang, H.L.; Jiang, J. Landslide susceptibility prediction in Lin'an District, China, using ensemble learning with non-landslide sample uncertainty. *Nat. Hazards* **2025**, *121*, 14347–24372. [CrossRef]
19. Zhang, H.; Yin, C.; Wang, S.P.; Guo, P. Landslide susceptibility mapping based on landslide classification and improved Convolutional Neural Networks. *Nat. Hazards* **2022**, *116*, 1931–1971. [CrossRef]
20. Youssef, A.M.; Pradhan, B.; Dikshit, A.; AL-Katheeri, M.M.; Mahdi, A.M. Landslide susceptibility mapping using CNN-1D and 2D deep learning algorithms: Comparison of their performance at Asir Region, KSA. *Bull. Eng. Geol. Environ.* **2022**, *81*, 165–186. [CrossRef]
21. Ge, Y.F.; Liu, G.; Tang, H.M.; Zhao, B.B.; Xiong, C.R. Comparative analysis of five convolutional neural networks for landslide susceptibility assessment. *Bull. Eng. Geol. Environ.* **2023**, *82*, 377. [CrossRef]
22. Wang, Y.; Zhou, C.; Cao, Y.; Meena, S.R.; Feng, Y.; Wang, Y. Utilizing deep learning approach to develop landslide susceptibility mapping considering landslide types. *Bull. Eng. Geol. Environ.* **2024**, *83*, 430. [CrossRef]
23. Bhattacharya, S.; Ali, T.; Chakravortti, S.; Pal, T.; Majee, B.K.; Mondal, A.; Pande, C.B.; Bilal, M.; Rahman, M.T.; Chakrabortty, R. Application of Machine Learning and Deep Learning Algorithms for Landslide Susceptibility Assessment in Landslide Prone Himalayan Region. *Earth Syst. Environ.* **2025**, *9*, 1427–1445. [CrossRef]
24. Zhang, F.F.; Li, C.L.; Wang, Y.W.; Wang, Y.Y. Statistical knowledge-guided multi-classification machine learning modeling scheme for landslide susceptibility levels. *Eng. Geol.* **2026**, *360*, 108458. [CrossRef]
25. Kalantar, B.; Ueda, N.; Saeidi, V.; Ahmadi, K.; Shabani, F. Landslide susceptibility mapping: Machine and ensemble learning based on remote sensing big data. *Remote Sens.* **2020**, *12*, 1737. [CrossRef]

26. Mevoli, F.A.; Borselli, L.; Santangelo, M.; Monte, N.; Lucia, D.; Ugenti, A.; Rossi, M. Landslide susceptibility zoning through physically-based limit equilibrium method modelling. *CATENA* **2026**, *263*, 109726. [CrossRef]
27. Saha, S.; Saha, A.; Hembram, K.T.; Pradhan, B.; Alamri, A. Evaluating the performance of individual and novel ensemble of machine learning and statistical models for landslide susceptibility assessment at Rudraprayag District of Garhwal Himalaya. *Appl. Sci.* **2020**, *10*, 3772. [CrossRef]
28. Ke, C.Y.; Sun, P.; Zhang, S.; Li, R.; Sang, K.Y. Influences of non-landslide sampling strategies on landslide susceptibility mapping: A case of Tianshui city, Northwest of China. *Bull. Eng. Geol. Environ.* **2025**, *84*, 123. [CrossRef]
29. Du, G.L.; Zhang, Y.S.; Javed, I.; Yang, Z.H.; Yao, X. Landslide susceptibility mapping using an integrated model of information value method and logistic regression in the Bailongjiang watershed, Gansu Province, China. *J. Mt. Sci.* **2017**, *14*, 249–268. [CrossRef]
30. Zhang, L.; Qi, W.; Du, T.F.; Zhang, Y. Evaluation of multifunctional land use based on entropy weight method: A case study of Zibo City. *Jiangsu Agric. Sci.* **2020**, *48*, 31–36. (In Chinese) [CrossRef]
31. Yu, S.Y.; Li, L.Y.; Luo, J.J.; Yang, Y.Y. Interseismic slip distribution and locking characteristics of the mid-southern segment of the Tanlu fault zone. *Earthq. Res. Adv.* **2024**, *4*, 100307. [CrossRef]
32. Zhan, J.H.; Wang, M.Z.; Yan, P.F.; Duan, X.F.; Zhang, H.X. Analysis on hydro-geological characteristics of water rich areas in southern mountain area in Zouping City. *Shandong Land Resour.* **2021**, *37*, 52–59. (In Chinese) [CrossRef]
33. Tian, Z.H.; Nutman, A.P. Structural restoration of an Eo-Mesoarchean (3.8–2.9 Ga) terrane, Eastern China, dissected by the Tanlu fault zone. *J. Struct. Geol.* **2022**, *161*, 104629. [CrossRef]
34. Huang, B.; Kusky, T.; Fu, D. Neoarchean accretionary and collisional tectonics in the southern North China Craton: Implications for crustal growth and plate tectonic styles. *Precambrian Res.* **2025**, *420*, 107730. [CrossRef]
35. Jordanova, G.D.; Popović, Z.; Yastika, P.E.; Shimizu, N.; Oštir, K.; Verbovšek, T. SBAS DInSAR and in situ monitoring of the Šumljak landslide (SW Slovenia) dynamics driven by rainfall and piezometric-level fluctuation. *Landslides* **2025**, *22*, 1397–1411. [CrossRef]
36. Li, Q.L.; Li, X.Z.; Zhao, C.C.; Zhang, S.Z. Back analysis key parameters of Scoops3D model using SBAS-InSAR technology for regional landslide hazard assessment. *Landslides* **2025**, *22*, 4097–4112. [CrossRef]
37. Huang, R.Q.; Pei, X.J.; Cui, S.H. Cataclastic characteristics and formation mechanism of rock mass in slidingzone of Daguangbao landslide. *Chin. J. Rock Mech. Eng.* **2016**, *35*, 1–15. (In Chinese) [CrossRef]
38. Yang, S.; Li, D.Y.; Sun, Y.Q.; She, X.J. Effect of landslide spatial representation and raster resolution on the landslide susceptibility assessment. *Environ. Earth Sci.* **2024**, *83*, 132. [CrossRef]
39. Hong, H.Y.; Liu, J.; Bui, D.T.; Pradhan, B.; Acharya, D.T.; Pham, T.B.; Zhu, A.X.; Chen, W.; Ahmad, B.B. Landslide susceptibility mapping using J48 Decision Tree with AdaBoost, Bagging and Rotation Forest ensembles in the Guangchang area (China). *CATENA* **2018**, *163*, 399–413. [CrossRef]
40. Fan, X.; Rossiter, D.G.; Westen, C.V.; Xu, Q.; Görüm, T. Empirical prediction of coseismic landslide dam formation. *Earth Surf. Process. Landf.* **2015**, *39*, 1913–1926. [CrossRef]
41. Yin, C.; Wang, Z.H.; Zhao, X.K. Spatial prediction of highway slope disasters based on convolution neural networks. *Nat. Hazards* **2022**, *113*, 813–831. [CrossRef]
42. Yin, C.; Li, H.R.; Che, F.; Li, Y.; Hu, Z.N.; Liu, D. Susceptibility mapping and zoning of highway landslide disasters in China. *PLoS ONE* **2020**, *15*, e0235780. [CrossRef]
43. Selamat, S.N.; Majid, N.A.; Taha, M.R. Multicollinearity and spatial correlation analysis of landslide conditioning factors in Langat River Basin, Selangor. *Nat. Hazards* **2025**, *121*, 2665–2684. [CrossRef]
44. Qiu, D.; Niu, R.; Zhao, Y.; Wu, X. Risk zoning of earthquake-induced landslides based on slope units: A case study on Lushan earthquake. *J. Jilin Univ.* **2015**, *45*, 1470–1478. (In Chinese) [CrossRef]
45. Saha, S.; Barman, A.; Saha, A.; Hembram, T.K.; Pradhan, B.; Alamri, A. Deep learning algorithms based landslide vulnerability modeling in highly landslide prone areas of Tamil Nadu, India. *Geosci. J.* **2024**, *28*, 1013–1038. [CrossRef]
46. Tan, Z.Y.; Yin, C.; Zhang, X.X.; Ma, X.B.; Liu, X.L.; Li, S.F. Stability assessment of shallow soil landslide and activating rainfall threshold. *Nat. Hazards Rev.* **2024**, *25*, 04024004. [CrossRef]
47. Li, Q.L.; Wei, C.Y.; Xue, X.J.; Zhang, Q.; Liu, S.Y.; Liu, X.N. A method for evaluating ecological quality levels and trends using natural evolution time series. *Environ. Sci. Pollut. Res.* **2021**, *31*, 64314–64388. [CrossRef]
48. Timi, K.; Baba-Hamed, K.; Bouanani, A.; Reghais, A. Analysis of relationships between rainfall, stream flow, and climate indices using the wavelet method: The case of Wadi Khemis, northwestern Algeria. *Dokl. Earth Sci.* **2025**, *525*, 31. [CrossRef]
49. Huan, Y.K.; Song, L.; Khan, U.; Zhang, B.Y. Stacking ensemble of machine learning methods for landslide susceptibility mapping in Zhangjiajie City, Hunan Province, China. *Environ. Earth Sci.* **2023**, *82*, 35. [CrossRef]
50. Barik, M.G.; Adam, J.C.; Barber, M.E.; Muhunthan, B. Improved landslide susceptibility prediction for sustainable forest management in an altered climate. *Eng. Geol.* **2017**, *230*, 104–117. [CrossRef]

51. Bednarik, M.; Yilmaz, I.; Kralovičová, L. Deterministic approach to assess landslide susceptibility and landslide activity in the Central-Western Region of Slovakia. *Bull. Eng. Geol. Environ.* **2024**, *83*, 327. [CrossRef]
52. Zêzere, J.L.; Pereira, S.; Melo, R.; Oliveira, S.C.; Garcia, R.A.C. Mapping landslide susceptibility using data-driven methods. *Sci. Total Environ.* **2017**, *589*, 250–267. [CrossRef] [PubMed]
53. Shu, H.E.; Abudikeyimu, X.; Meng, H.U.; Chen, K. Assessment on landslide susceptibility based on self-organizing feature map network and random forest model: A case study of Dayu County of Jiangxi Province. *Chin. J. Geol. Hazard Control* **2022**, *33*, 132–140.
54. Huang, Z.Y.; Li, P.; Li, S.N.; Liu, Y.; Zhou, S. GIS-based landslide susceptibility mapping in the Longmen Mountain area (China) using three different machine learning algorithms and their comparison. *Environ. Sci. Pollut. Res.* **2023**, *30*, 88612–88626. [CrossRef]
55. Berrich, Y.; Guennoun, Z. EEG-based epilepsy detection using CNN-SVM and DNN-SVM with feature dimensionality reduction by PCA. *Sci. Rep.* **2025**, *15*, 14313. [CrossRef]
56. Li, S.F.; Yin, C.; Li, J.X.; Sun, T.Q. Landslide susceptibility assessment based on remote sensing interpretation and DBN-MLP model: A case study of Yiyuan County, China. *Stoch. Environ. Res. Risk Assess.* **2025**, *39*, 493–508. [CrossRef]
57. Zhao, Q.H.; Wang, F.W.; Wang, W.M.; Zhang, T.X.; Wu, H.D.; Ning, W.J. Research on intrusion detection model based on improved MLP algorithm. *Sci. Rep.* **2025**, *15*, 5159. [CrossRef] [PubMed]

Disclaimer/Publisher's Note: The statements, opinions and data contained in all publications are solely those of the individual author(s) and contributor(s) and not of MDPI and/or the editor(s). MDPI and/or the editor(s) disclaim responsibility for any injury to people or property resulting from any ideas, methods, instructions or products referred to in the content.

coatings

MDPI

Article

Research on the Mechanism of Steel Slag Fine Aggregate Damaging the Volume Stability of Cement-Based Materials

Haoran Zhai [1], Aizhu Liu [2,*], Huiqing Yang [2], Dong Gao [2], Chunguang Liu [2], Wenda Yan [3] and Whengyu Du [4]

[1] School of Civil Engineering and Geomatics, Shandong University of Technology, Zibo 255000, China
[2] Shandong Hi-Speed Urban & Rural Development Group Co., Ltd., Jinan 250014, China
[3] Shandong Provincial Department of Finance, Jinan 250002, China
[4] School of Materials Science and Engineering, Southeast University, Nanjing 211189, China
* Correspondence: aizhuliu11@126.com

Abstract

With the depletion of natural sand and gravel resources and increasing emphasis on environmental protection, natural aggregates suitable for concrete production are becoming increasingly scarce. Steel slag, a by-product of steelmaking, is produced in substantial quantities yet remains underutilized due to its low recycling rate. Owing to the high strength and excellent compatibility of steel slag particles with cementitious materials, they demonstrate significant potential as a replacement for natural river sand in fine aggregate applications. However, the volumetric instability of steel slag has long been a major impediment to its widespread adoption in cement-based composites. This study examines the stability performance of cement mortar containing steel slag aggregate, with the objective of clarifying the mechanisms responsible for dimensional instability resulting from steel slag incorporation. When the replacement level exceeds 40%, the dimensional stability of the mortar deteriorates markedly. The initial contents of free CaO (f-CaO) and free MgO (f-MgO) in the steel slag were determined to be 1.58% and 1.14%, respectively. Following 50 h of hydrothermal treatment, 69.6% of f-CaO and 44.3% of f-MgO had hydrated, causing internal volumetric expansion and subsequent particle fracturing. Under elevated temperature conditions, over-burned lime demonstrated 220% volumetric expansion and completed its reaction within 40 min, consequently impairing early-age stability. In contrast, periclase (dead-burned MgO) exhibited 34% expansion and attained a reaction degree of merely 13.3%, suggesting a more substantial impact on long-term stability. For each mixture, linear expansion measurements were performed on n = 5 independent specimens, and results are reported as mean ± standard deviation.

Keywords: steel slag; volume stability; free calcium oxide; free magnesium oxide; fine aggregate

1. Introduction

Steel slag is a by-product of the steelmaking process, generally accounting for 8%–15% of crude steel production [1]. In 2024, China's steel production reached 840 million tons, steel slag emission was 153 million tons, and the accumulated stockpile was 1.446 billion tons. The utilization rate of steel slag in China is still less than 30% [2], which is far from the 90% utilization rate in developed countries. Steel slag that is not reasonably utilized is often piled up in the open air or buried underground, resulting in a serious waste of land resources [3]. The metal elements in steel slag can leach into soil and waterways, causing

harm to the environment [4]. In addition, steel slag produces a large amount of dust during transportation, which can harm human health if not handled properly [5]. Therefore, it is necessary to implement effective resource utilization strategies to solve the problem of the massive accumulation of steel slag.

Currently, the most widely used metallurgical technologies in China are converter steelmaking and electric furnace steelmaking. The steel slag produced is primarily basic oxygen furnace slag (BOFS) and electric arc furnace slag (EAFS). The main chemical components of steel slag include CaO, SiO_2, FeO, Al_2O_3, MgO, along with trace amounts of MnO, P_2O_5, and other constituents [6]. The primary minerals present in steel slag include C_2S, C_3S, the RO phase (composed of MgO, FeO, and MnO, and characterized by its high hardness and density), as well as f-CaO and f-MgO [7]. Variations in raw materials, smelting technology, and steel types used by different manufacturers result in distinct chemical and mineral compositions of steel slag [8]. Due to its high strength and excellent wear resistance, steel slag can be utilized as a paving material in road construction [9]. Steel slag contains C_2S, C_3S, C_4AF, and other components similar to those found in cement clinker, and it possesses agglutinative properties, making it suitable as a supplementary cementitious material [10]. However, the hydration activity of steel slag is inferior to that of cement clinker, and its high iron content contributes to poor grindability. Certain minerals in steel slag exhibit stability issues, which limit its utilization as a cement material.

With the expanding global infrastructure, concrete and mortar are widely used, leading to over-exploitation of natural sand and gravel. Natural aggregate resources for concrete and mortar are becoming more and more limited in some regions, making it necessary to find a material similar to natural sand as a substitute [11]. The appearance of steel slag is similar to natural fine aggregate. It has high iron content, high hardness, small particle size after crushing, and excellent corrosion resistance. Therefore, it can be used as concrete aggregate or mortar fine aggregate, which alleviates the problem of shortage of natural sand and gravel resources and solves the problem of low utilization of steel slag [12,13]. Goyal et al. [14] showed that replacing natural coarse aggregate in concrete with different proportions of steel slag can improve the compressive and flexural strengths. Wang et al. [15] further demonstrated that with the substitution of fine aggregate by steel slag, the peak strength of concrete can be increased. Moreover, the ratio increases, and the peak stress of concrete increases and then decreases. Abu-Eishah et al. [16] suggested that the use of steel slag aggregate in concrete structures has the potential to improve the mechanical properties of these structures.

The use of steel slag as aggregate creates the problem of poor volume stability. This is mainly due to the presence of f-CaO and f-MgO in steel slag. These react with water to form $Ca(OH)_2$ and $Mg(OH)_2$, resulting in volumetric expansion of 98% and 148% [17], which can lead to cracking or even fracture of the mortar [18]. Xue et al. [19] found that hydration and expansion of steel slag is the main cause of mortar deterioration, which is manifested by volumetric expansion and cracking of the mortar surface. The main reason affecting the expansion of steel slag aggregate is the content of f-CaO and f-MgO. Zhou et al. [20] found that heating accelerates the hydration of free oxides present in the steel slag in the mortar surface layer, which results in high localized expansion stresses in the mortar, leading to mortar damage or fracture damage.

To enhance the engineering applicability of steel slag aggregates, a number of mitigation approaches have been reported in the literature, including (i) natural aging/weathering or hot-water/steam conditioning to promote the pre-hydration of free oxides, (ii) accelerated carbonation (or wet carbonation) to convert $CaO/Ca(OH)_2$ into stable carbonates and to stabilize reactive phases, and (iii) chemical/alkali-based modification to reduce expansion and improve volumetric stability [2,10,21,22]. Despite these advances, the ef-

https://doi.org/10.3390/coatings16010132

fectiveness of each treatment depends strongly on the form, distribution and hydration kinetics of f-CaO and f-MgO within slag particles, which motivates a systematic mechanistic investigation.

Therefore, when using steel slag as fine aggregate in mortar, attention must be paid to the problem of poor volume stability. In this study, steel slag produced by an iron and steel plant in Hebei Province will be analyzed, and its volume stability will be investigated. Although prior studies have recognized that free CaO and free MgO contribute to volumetric instability of steel slag aggregates, quantitative evidence linking time-resolved free-oxide hydration to particle cracking evolution and mortar-scale failure remains limited. In this work, we establish a multi-scale framework combining (i) accelerated boiling expansion tests, (ii) quantitative tracking of particle cracking rate, (iii) titration-based determination of f-CaO and f-MgO consumption with time, and (iv) hydrothermal simulations using over-burnt lime and dead-burnt magnesia to decouple the distinct kinetics and expansion capacities of CaO- and MgO-bearing phases. This integrated approach provides mechanistic insight into why f-CaO dominates early-age instability while f-MgO is more relevant to long-term stability. The 100 °C boiling regime is an accelerated protocol intended to promote rapid hydration of free oxides and enable comparative evaluation within a practical timeframe; accordingly, the measured expansion/damage evolution should be interpreted as a conservative (accelerated) scenario rather than a direct simulation of typical field temperatures.

2. Materials and Methods

2.1. Raw Materials

2.1.1. Steel Slag Aggregate

This study utilizes steel slag produced in Lingshou County, Shijiazhuang City, Hebei Province. This steel slag is basic oxygen furnace slag obtained after magnetic separation and purchased after one year of open storage without any further pretreatment before discharge. It is gray and resembles ordinary natural sand in appearance. The morphology of the steel slag particles is illustrated in Figure 1. Figure 2 shows SEM images of steel slag particles. As can be seen from the figure, the surface pores and cracks of the steel slag particles are relatively few. The dense surface of the steel slag aggregate makes its water absorption rate similar to that of natural sand. The interface transition zone structure and performance of it are not affected by the cement paste. This study investigated BOF steel slag fine aggregate obtained from a single source. Given that the composition and mineralogy of steel slag can vary with feedstock and steelmaking conditions, the quantitative stability thresholds reported herein may not be universally transferable. Future work will include multi-source slag datasets to evaluate variability and improve generalization. To characterize the gradation of the steel slag fine aggregate, sieve analysis was conducted in accordance with ASTM C136/C136M. The particle size distribution is presented in Table 1 (fineness modulus = 2.63). In addition, the apparent density and water absorption reported in Table 2 were determined following ASTM C128.

Table 1. Particle size distribution of steel slag aggregate.

Sieve Size (mm)	Cumulative Passing (%)	Cumulative Retained (%)
4.75	100	0
2.36	86	14
1.18	68	32
0.6	48	52
0.3	26	74

https://doi.org/10.3390/coatings16010132

Table 2. Physical performance index of steel slag.

	Apparent Density (kg/m^3)	Water Absorption (%)
SS	3481	2.6
NA	2600	1.7



Figure 1. Steel slag particles.

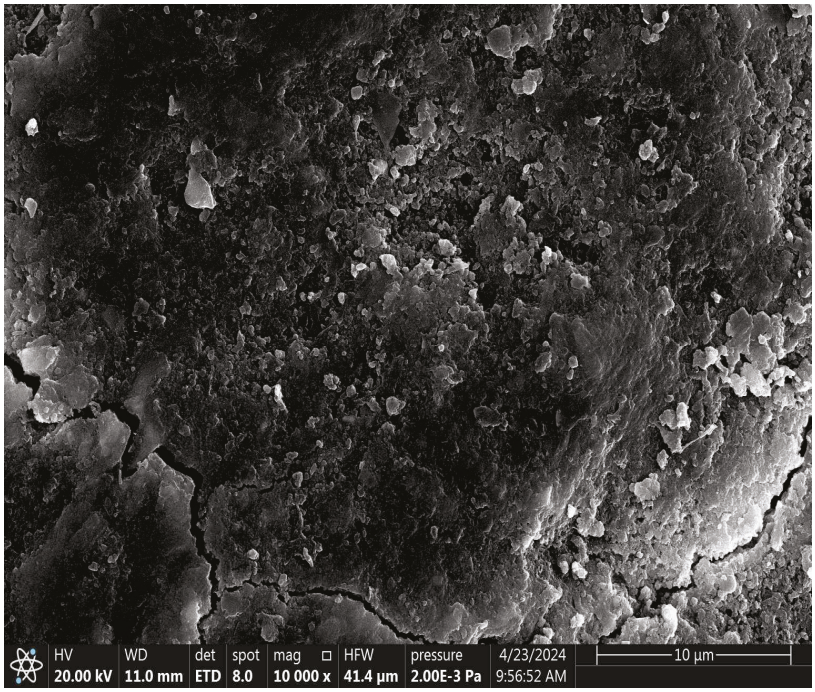

Figure 2. SEM image of the surface of steel slag particles.

https://doi.org/10.3390/coatings16010132

2.1.2. Characterization Methods

The chemical composition of the steel slag was determined by X-ray fluorescence (XRF). Phase composition was analyzed by X-ray diffraction (XRD) using Cu Kα radiation, and the crystalline phases were identified by matching the diffraction patterns with the ICDD PDF database. The morphology and elemental distribution of the steel slag aggregate were examined by scanning electron microscopy equipped with energy-dispersive X-ray spectroscopy (SEM–EDS).

X-ray fluorescence (XRF) analysis was conducted using a wavelength-dispersive XRF spectrometer (ZSX Primus IV, Rigaku, Tokyo, Japan; element range B–Cm). Powder samples were ground to ~200 mesh and prepared as pressed pellets (30 t) and/or fused glass beads (fusion temperature ~1050 °C) depending on the target oxides/elements. The instrument was operated under typical conditions of 40–60 kV and 50–150 mA, with vacuum/He purge selected according to the measured elements. Quantification was performed based on instrument calibration using reference materials with appropriate matrix corrections. SEM observations and EDS microanalyses were conducted using a high-resolution field-emission scanning electron microscope (Apreo S Hi, Thermo Scientific, Waltham, MA, USA) equipped with an EDS detector. Imaging was performed mainly in high-vacuum mode, while low-vacuum/ESEM modes were used when required by sample charging behavior. The nominal spatial resolution of the instrument is 1.0 nm at 30 kV (SE) and 3.0 nm at 1 kV (SE) in high vacuum; 1.4 nm at 30 kV (SE) in low vacuum; and 1.4 nm at 30 kV (SE) in ESEM mode. For SEM imaging, an accelerating voltage of 5–15 kV was typically used, and EDS analyses were acquired at 15–20 kV with a working distance of ~10 mm and a live time of 30–60 s. Prior to observation, samples were mounted on conductive carbon tape and sputter-coated with a thin Au/Pd (or carbon) layer when necessary. X-ray diffraction (XRD) was used to qualitatively identify the mineralogical phases of the steel slag fine aggregates using a polycrystalline X-ray diffractometer (D8-02, Bruker AXS, Ettlingen, Germany). Data were collected over a 2θ range of 5–90° with a step size of 0.02° and a scanning speed of 10°/min; the goniometer accuracy was within ±0.01° (2θ). The diffractometer was operated under standard conditions using Cu Kα radiation (λ = 1.5406 Å) with a tube voltage of 40 kV and tube current of 40 mA. Phase identification was performed by matching the diffraction patterns with standard PDF/ICDD databases.

Table 3 presents the primary oxides and elements of steel slag as analyzed by XRF. The XRF analysis of steel slag reveals that its primary chemical components include CaO, Fe_2O_3, SiO_2, MnO, MgO, along with trace amounts of Al_2O_3, P_2O_5, and other elements.

Table 3. XRF analysis table of steel slag.

Compound	CaO	Fe_2O_3	SiO_2	MnO	MgO	Al_2O_3	P_2O_5	TiO_2	Cr_2O_3	V_2O_5	Others
Wt/%	37.14	37.06	9.84	5.49	2.99	2.33	1.32	1.27	0.91	0.56	1.09

The steel slag was analyzed using X-ray diffraction (XRD) with a D6000 diffractometer. The mineral composition of steel slag fine aggregate was qualitatively analyzed by D8-02 polycrystalline X-ray diffractometer produced by Bruker-AXS company in Germany. The mineral composition of the steel slag was determined using the ICDD international standard PDF card. Figure 3 presents the XRD pattern of steel slag aggregate. The diffraction reflections indicate that steel slag aggregate contains dicalcium silicate (C_2S), tricalcium silicate (C_3S), tricalcium aluminate (C_3A), free calcium oxide (f-CaO), free magnesium oxide (f-MgO), the RO phase (a solid solution of iron, magnesium, and manganese), iron oxides (FeO, Fe_2O_3), and other silicate minerals. RO phase is an inert mineral in steel slag and consists of a solid solution of magnesium, manganese, and iron oxides [21]. The

https://doi.org/10.3390/coatings16010132

presence of iron oxides and RO phase makes the steel slag aggregate denser and harder than natural sand [23]. f-CaO and f-MgO lead to volume expansion of 98% [24] and 148% [25] upon hydration, resulting in cracking of building materials and structural damage [22]. In Figure 3, the most intense reflections of each identified crystalline phase have been labelled explicitly. The minor reflections at approximately 23°, 35°, 40°, and 48° 2θ are attributed to iron oxides and the RO solid-solution phase. No pronounced amorphous hump was detected in the background of the diffraction pattern, indicating that the amorphous content of this slag is relatively low; therefore, only the crystalline phases are discussed in this work.

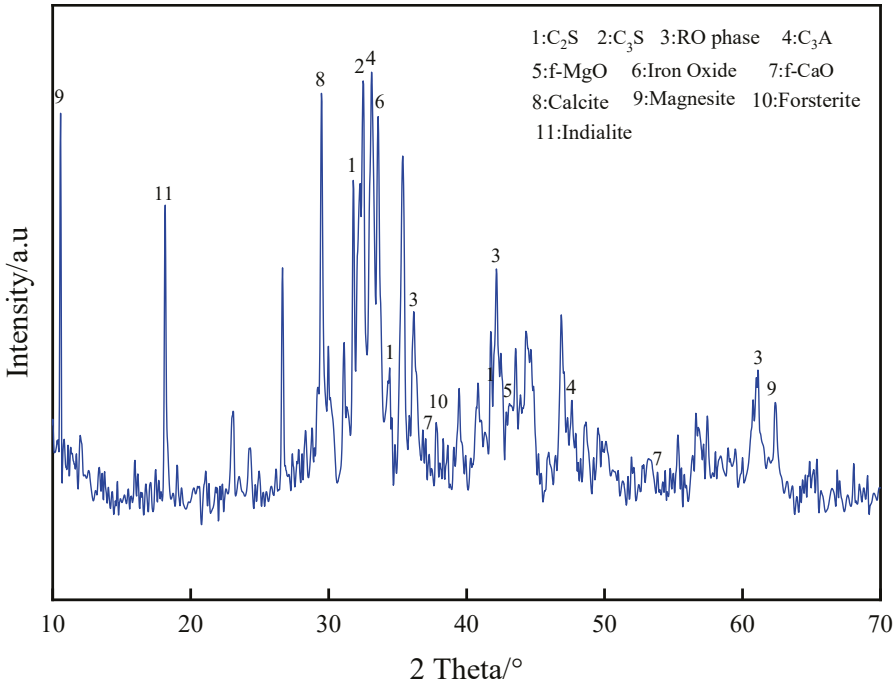

Figure 3. XRD diagram of steel slag.

The physical properties of steel slag are summarized in Table 2. The apparent density of steel slag aggregate is approximately 3481 kg/m^3, which is higher than that of natural aggregates due to the presence of dense iron compounds in steel slag particles [26]. The water absorption of steel slag aggregate is 2.6%, which is higher than that of natural sand. In Table 2, SS and NA denote the mixtures prepared with steel slag aggregate and natural sand, respectively.

2.1.3. Over-Burnt Lime and Dead-Burnt Magnesia

To investigate the destruction of steel slag particles caused by the hydration reactions of free calcium oxide and free magnesia, the interactions of these substances with water in steel slag were simulated using over-burnt lime and dead-burnt magnesia. The XRD of over-burnt lime and dead-burnt magnesia is shown in Figure 4. The crystal spacing of over-burnt lime at (111), (200), and (220) is 2.7707, 2.3995, and 1.6967, and the crystal spacing of dead-burnt magnesia at (111), (200), and (220) is 2.4312, 2.1055, and 1.4888. The over-burnt lime was 97% pure, with traces of incompletely sintered $CaCO_3$, and the dead-burnt magnesia was 99% pure. The relative intensities of the reflections in Figure 4 differ slightly from those in the corresponding PDF cards because of preferred orientation of the crystallites and differences in instrumental conditions. The standard patterns are therefore used only for phase identification and not for quantitative evaluation of phase proportions.

https://doi.org/10.3390/coatings16010132

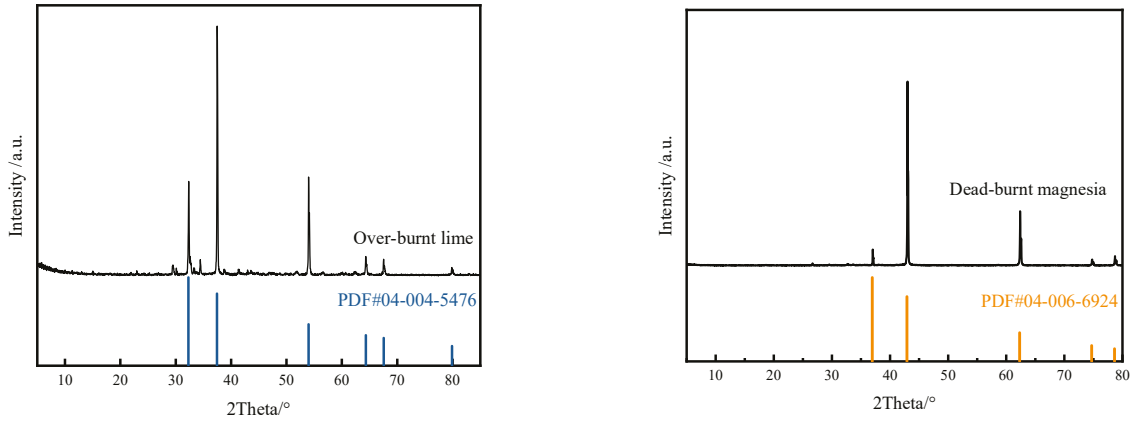

Figure 4. XRD plots of over-burnt lime (**a**) and dead-burnt magnesia (**b**).

2.2. Testing Method

2.2.1. Linear Expansion of Steel Slag Aggregate Mortar

The hydration process of f-CaO and f-MgO is very slow at room temperature but accelerates significantly under heating conditions [27]. Since monitoring the expansion rate of the specimens at ambient temperature would greatly extend the experimental time, boiling was used to accelerate the hydration of f-CaO and f-MgO for stability assessment. The 100 °C boiling regime is used as an accelerated protocol to promote hydration of free oxides within a practical timeframe. Therefore, the measured expansion and damage evolution should be interpreted as accelerated/conservative behavior for comparative assessment and mechanism clarification, rather than a direct replication of typical field thermal histories. For each mixture, linear expansion measurements were performed on n = 5 independent specimens, and results are reported as mean ± SD.

Mortar specimens measuring 25 × 25 × 280 mm were prepared according to the mortar ratios in Table 4. In this table, the groups labelled 100%, 80%, 60%, 40%, and 20% correspond to mixtures in which steel slag fine aggregate replaces 100%, 80%, 60%, 40%, and 20% of the total volume of fine aggregate, respectively, while NA1 is the reference mortar prepared with only natural sand. Because steel slag has a higher density and different packing characteristics than natural sand, the total mass of fine aggregate (steel slag plus natural sand) is not exactly constant among groups, although the aggregate volume was kept comparable. After 7 days of demolding and curing, the lengths were measured using a specific length meter, and the length of the mortar was measured every 5 h of boiling. A total of 10 measurements were taken, and the test procedure is shown in Figure 5. The linear expansion of the mortar was calculated according to Equation (1). In Tables 4 and 5, "Water reducer/%" denotes the dosage of a polycarboxylate-based water-reducing admixture expressed as a mass percentage of cement.

$$L_A = \frac{L_1 - L_0}{280} \times 100 \quad (1)$$

where L_A represents the linear expansion rate (%); l_0 denotes the initial reading (mm); l_1 refers to the reading after boiling (mm); and 280 represents the initial length of the specimen (mm).

Table 4. Mortar mix ratio.

Group	Water/g	Steel Slag Sand/g	Sand/g	Cement/g	Water Reducer/%
100%	157.5	1250	0	315	1
80%	157.5	1000	189	315	0.8
60%	157.5	750	378	315	0.6
40%	157.5	500	567	315	0.4
20%	157.5	250	756	315	0.2
NA1	157.5	0	945	315	0

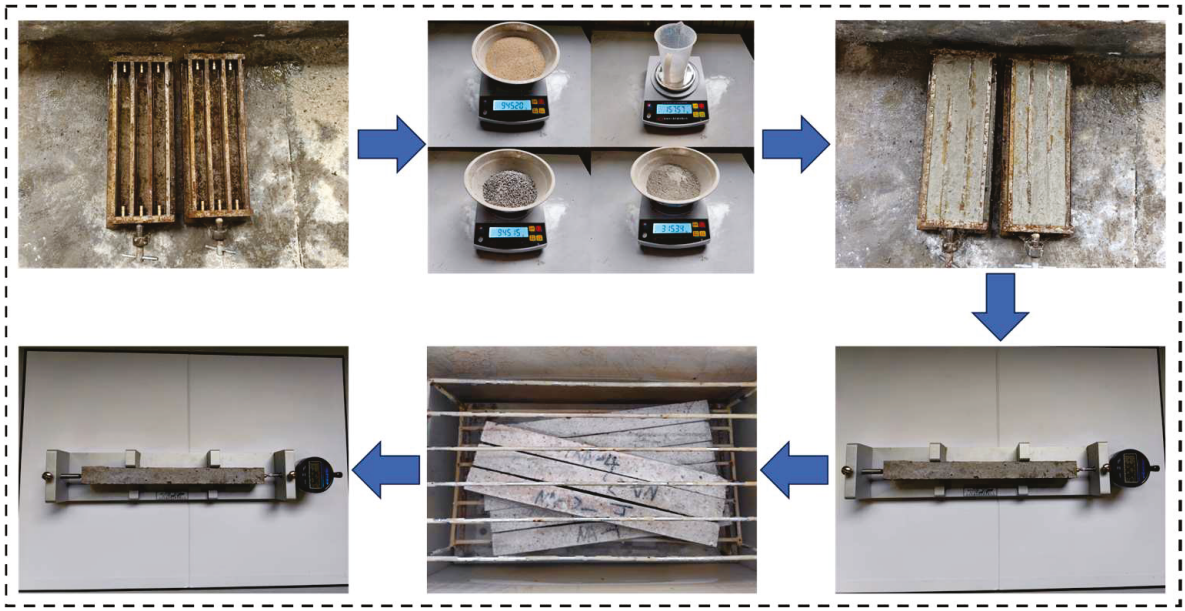

Figure 5. Test process of mortar linear expansion.

Table 5. Mortar mix ratio.

Group	Water/g	Steel Slag Sand/g	Sand/g	Cement/g	Water Reducer/%
SA	225	1786	0	450	1
NA2	225	0	1350	450	0

2.2.2. Compression and Flexure Resistance Test

Make 40 × 40 × 160 mm mortar specimens with the ratios shown in Table 5. Group SA denotes the mortar prepared with steel slag fine aggregate, whereas group NA2 is the corresponding reference mortar prepared with natural sand only. After demolding and curing for 28 days, the specimens were subjected to boiling in water at 100 °C for 0, 10, 20, 30, 40, and 50 h, respectively. After each designated boiling duration, specimens were cooled to room temperature, and then tested for flexural and compressive strengths following the standard procedure. This accelerated protocol was adopted to evaluate the evolution of internal damage induced by slag aggregate expansion. Compressive and flexural strength tests were conducted on n = 5 independent specimens per mixture and age; results are reported as mean ± SD.

2.2.3. Steel Slag Aggregate Particle Cracking Rate

A specific number of steel slag particles were placed in a 100 °C constant-temperature water bath, and the cracking of the particles was observed every 5 h. Particle cracking

https://doi.org/10.3390/coatings16010132

rate was quantified from independent batches (n = 5), and the reported values represent mean ± SD.

2.2.4. Determination of Free Calcium and Magnesium by Titration

The determination of f-CaO and f-MgO in steel slag was carried out by complexometric titration. The experimental procedure is outlined below (Figure 6).

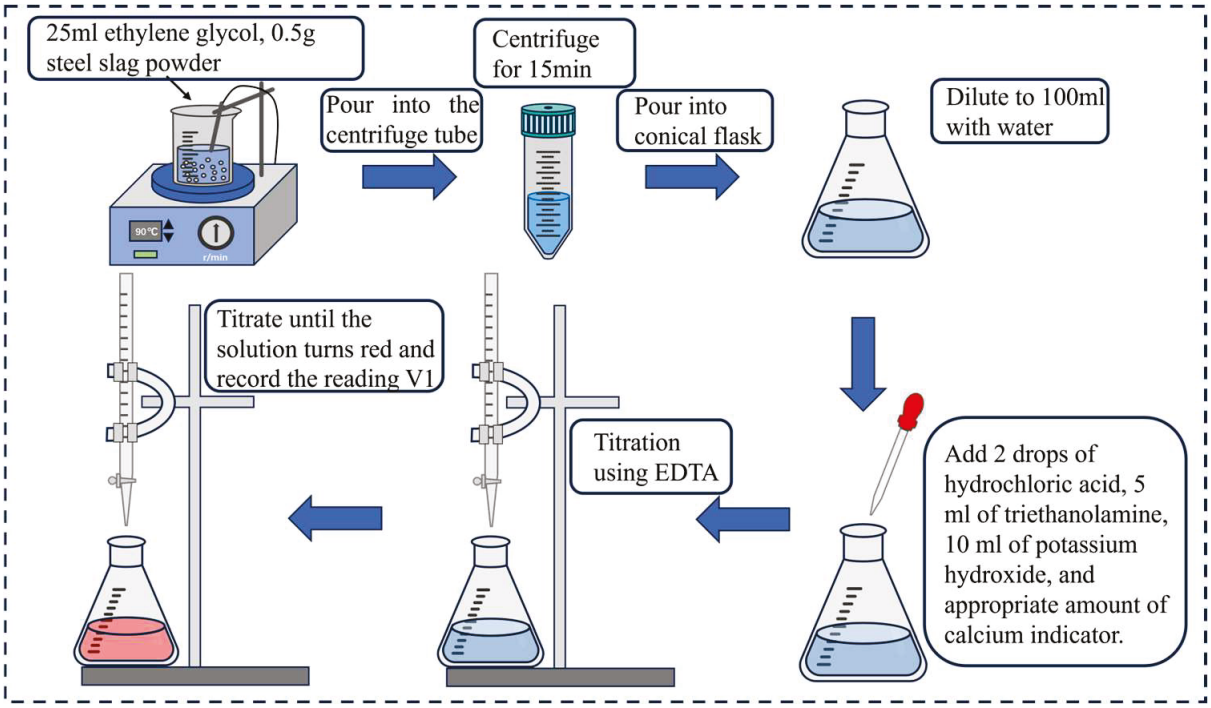

Figure 6. Flow of titrimetric determination of free calcium oxide content.

The method specified in GB/T 38216.3-2023, was used to determine the free calcium oxide content in steel slag [28].

The chemical reactions are shown in reactions (2) to (4).

$$CaO + C_6H_6O_2 \rightarrow (CH_2O)_2Ca + H_2O \quad (2)$$

$$Ca(OH)_2 + C_6H_6O_2 \rightarrow (CH_2O)_2Ca + H_2O \quad (3)$$

$$C_{10}H_{14}N_2NaO_8 + (CH_2O)_2Ca \rightarrow C_{10}H_{14}N_2CaO_8 + HOCH_2CH_2OH \quad (4)$$

The total amount of calcium oxide and calcium hydroxide was calculated using Equation (5).

$$\omega_1 = \frac{T_{CaO} \times V_1}{m \times 1000} \times 100 \quad (5)$$

ω_1 represents the mass fraction of combined free calcium oxide and calcium hydroxide (%); T_{CaO} is the mass equivalent of calcium oxide per milliliter of EDTA standard solution (mg/mL); V_1 is the volume of solution consumed by free total calcium (mL); m is the mass of the sample (g); and 1000 is the unit conversion factor.

The calcium hydroxide content was determined using thermogravimetric analysis. The percentage of mass loss during the weight loss step in the interval from 400 °C to 550 °C on the thermogravimetric curve is denoted as ω_2. The calcium hydroxide content in the steel slag, denoted as ω_3, was calculated using Equation (6):

$$\omega_3 = 4.111 \times 0.7567 \times \omega_2 \quad (6)$$

https://doi.org/10.3390/coatings16010132

The free calcium oxide content in steel slag was calculated using Equation (7):

$$\omega = \omega_1 - \omega_3 \tag{7}$$

ω_1 is the mass fraction (%) of free calcium oxide and calcium hydroxide; ω_3 is the mass fraction (%) of calcium hydroxide (as calcium oxide).

The free magnesium oxide content was determined using EDTA titration, and the test procedure is shown in Figure 7:

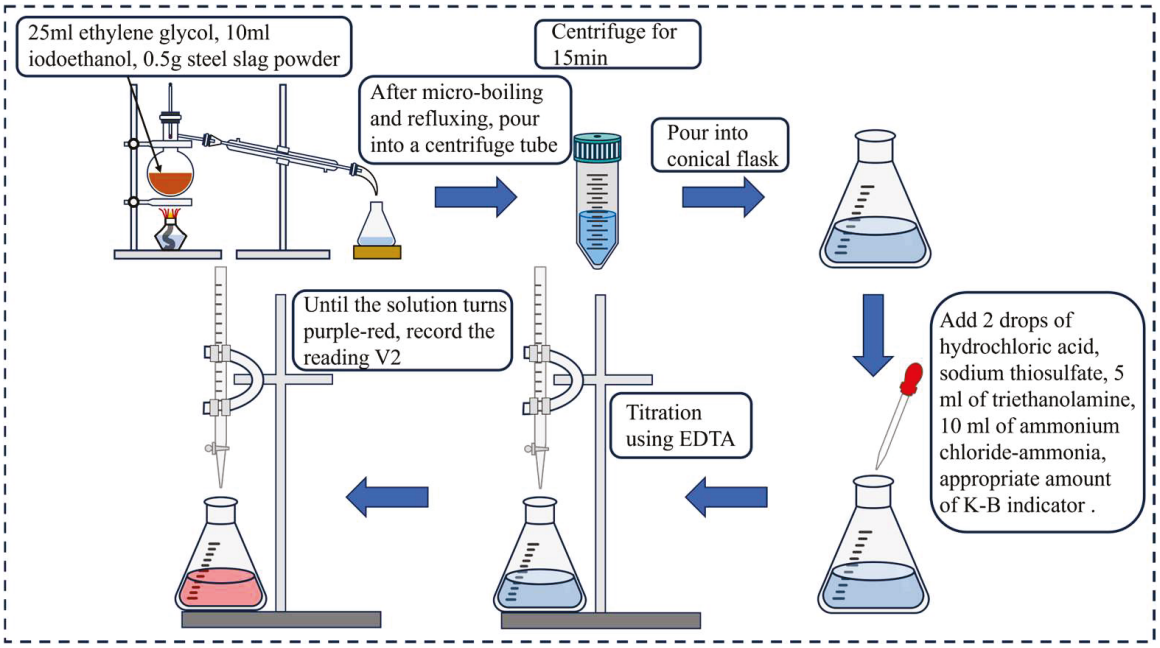

Figure 7. Flow chart of the titrimetric determination of free magnesium oxide content.

The chemical reactions are shown in reactions (8) to (11).

$$CaO + C_6 \rightarrow Ca(CH_2O)_2 + H_2O \tag{8}$$

$$C_{10}H_{14}N_2NaO_8 + (CH_2O)Ca \rightarrow C_{10}H_{14}N_2CaO_8 + HOCH_2CH_2OH \tag{9}$$

$$MgO + C_6H_6O_2 \rightarrow Mg(CH_2O)_2 + H_2O \tag{10}$$

$$C_{10}H_{14}N_2NaO_8 + Mg(CH_2O)_2 \rightarrow C_{10}H_{14}N_2MgO_8 + HOCH_2CH_2OH \tag{11}$$

Finally, the f-MgO content was calculated using Equation (12).

$$\omega_{MgO} = \frac{T_{MgO} \times (V_2 - V_1)}{m \times 1000} \times 100 \tag{12}$$

T_{MgO} is the mass of magnesium oxide equivalent per milliliter of EDTA standard solution ($g \cdot L^{-1}$); m is the sample mass (g); and V_2 is the total volume of solution consumed by calcium and magnesium (mL).

2.2.5. Determination of Hydration Expansion of Over-Burnt Lime and Dead-Burnt Magnesia

Over-burnt lime and dead-burnt magnesia were poured into a 100 mL measuring cylinder and mixed thoroughly at a water to ash ratio of 0.8, and the initial height was measured after settling. Place the measuring cylinder into a 100 °C water bath and measure

https://doi.org/10.3390/coatings16010132

the height of the slurry at intervals until no further change in slurry height is observed. Calculate the volume expansion using Equation (13).

$$L = \frac{V_1 - V_0}{V_0} \times 100 \quad (13)$$

where L is the expansion rate (%), V_1 is the post-reaction volume (mm^2), and V_0 is the initial volume (mm^2).

2.2.6. Data Processing and Statistical Analysis

Unless otherwise stated, all quantitative measurements were conducted using n = 5 independent specimens/batches per condition. Results are reported as mean ± standard deviation (SD), and error bars in figures represent one standard deviation.

3. Results and Discussion

3.1. Mortar Linear Expansion

Figure 8 shows the influence of steel slag aggregate substitution rate on the linear expansion rate of mortar. The NA specimens had the lowest linear expansion of 0.045%, and the natural sand mortar specimens exhibited significant structural integrity after boiling with no cracking. However, the mortar specimens containing 20% steel slag aggregate admixture showed micro-cracks on the surface due to particle expansion.

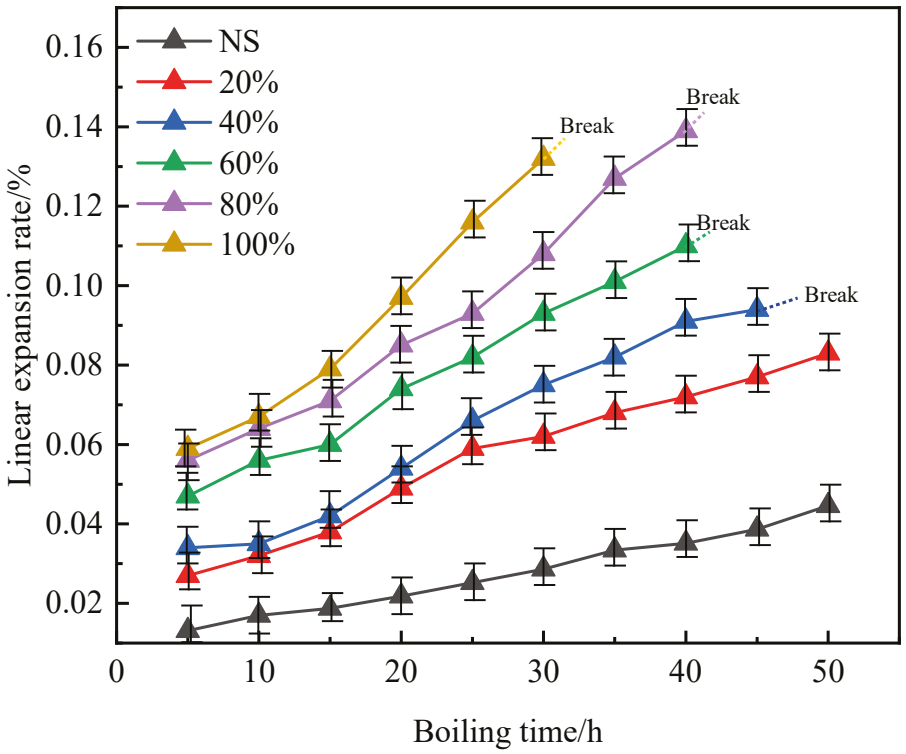

Figure 8. The influence of steel slag aggregate substitution rate on the linear expansion rate of mortar.

The specimens with steel slag aggregate dosage of 40% and higher showed fracture during boiling (Figure 9), and the higher the dosage, the earlier all the specimens fractured. This further illustrates that the use of steel slag aggregate as aggregate creates serious stability problems.



Figure 9. Cracking diagram of specimens with different substitution rates.

Notably, Figures 8 and 9 indicate that the 60% replacement group fractured slightly earlier than the 80% group in this test series. This apparent non-monotonic trend is attributed to specimen-to-specimen variability and the heterogeneous distribution of expansive slag particles (e.g., an expansive particle located close to the surface or near the mid-span can trigger earlier cracking). When considering the overall linear expansion level and the observed damage severity, the deterioration still becomes more pronounced with increasing steel slag replacement. We have clarified this point in Section 3.1 to avoid over-interpreting the fracture time as a sole stability indicator.

The addition of steel slag aggregates to mortar leads to stability problems, mainly in the form of volume expansion, surface deterioration, and fracture. This expansion originates from the hydration of f-CaO and f-MgO, which causes expansion of the steel slag aggregate, leading to expansion and cracking of the mortar.

Crack formation plays a critical role in the observed morphological changes in the mortar strips. When steel slag aggregate is located near the surface, the thinner cementitious layer offers reduced restraint against expansion. This insufficient confinement results in stress concentration at the surface, initiating microcrack development. With continued hydration of f-CaO and f-MgO, steel slag aggregate expansion intensifies, eventually leading to the detachment of the overlying material from the deformed surface region, as illustrated in Figure 10a.

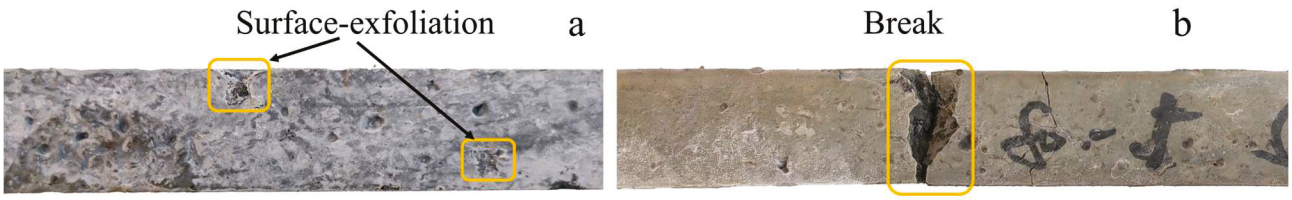

Figure 10. Two forms of damage to specimens by steel slag aggregates: surface spalling (**a**) and fracture (**b**).

When the steel slag aggregate located near the mortar's center interface expands, the surrounding cement matrix develops transverse cracks in response to the expansion forces. With continued expansion, these cracks gradually extend to the entire mortar cross-section, eventually leading to complete fragmentation of the mortar bar [29] (Figure 10b). Examination of the fractured mortar cross-section reveals visible particles of steel slag aggregate, as shown in Figure 11.



Figure 11. Mortar section with cracked steel slag aggregate.

3.2. Compressive Strength of Mortar

The use of linear expansion rates does not adequately reflect the internal damage to the mortar caused by steel slag cracking. Internal cracks in mortar affect its overall strength, but internal cracks are not readily detectable in the mortar's appearance. The steel slag aggregate mortar specimens and natural mortar specimens were made in 40 × 40 × 160 mm molds. The compressive and flexural strengths of natural sand and steel slag aggregate mortars were determined after different boiling times, and the stability of steel slag aggregate was assessed by observing the strength changes. Figure 12 shows the compressive and flexural strengths of steel slag aggregate mortar and natural sand mortar after different boiling times.

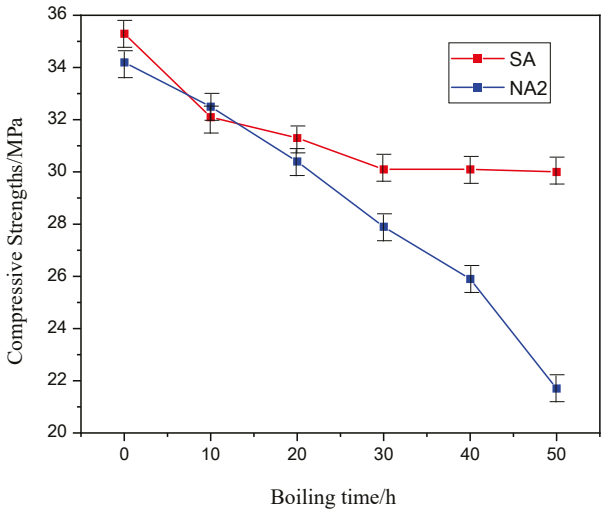

Figure 12. Compressive strength of mortar.

The compressive strength of the steel slag aggregate mortar is slightly better than that of the conventional mortar. Steel slag aggregate has higher hardness than typical mineral admixtures, which increases the resistance to crack extension [30]. The roughness of the steel slag aggregate surface promotes mechanical interlocking within the interfacial transition zone, which results in a stronger bond between the steel slag aggregate and the cement matrix [31]. These combined effects contribute to improved mechanical properties.

The steel slag aggregate mortar maintained a stable compressive strength at the beginning of boiling, but after 50 h, the compressive strength was significantly reduced by 27.5% compared to the conventional mortar. Similarly, the flexural strength also decreased gradually and finally decreased by 59% after 50 h of boiling. The reason for the decrease in strength is the accelerated hydration of the swelling components in the steel slag particles

https://doi.org/10.3390/coatings16010132

under boiling conditions. Upon hydration, these components undergo volume expansion, which leads to cracking and internal stresses in the steel slag aggregate. When these stresses exceed the bearing capacity of the mortar, microcracks appear in the matrix [32]. This fracture process gradually weakens the internal bond structure and eventually leads to a decrease in mechanical properties.

3.3. Cracking of Steel Slag Aggregate Particles

f-CaO and f-MgO cause cracking of steel slag aggregates, which generates stresses and leads to expansion and cracking of the mortar. Therefore, it is essential to analyze the effect of f-CaO and f-MgO hydration and swelling on the particles. Figure 13 show the increasing trend of cracking of steel slag aggregates during the water bath process, with a final cracking rate of 5%. As shown in Figure 14, with the increase in boiling time, the contents of these two substances showed an increasing trend, which proved that more and more f-CaO and f-MgO were involved in the hydration to produce $Ca(OH)_2$ and $Mg(OH)_2$ with the increase in boiling time.

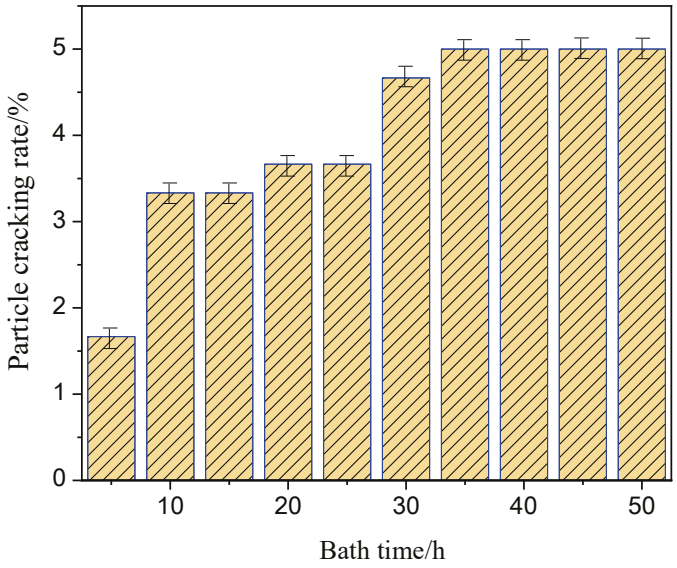

Figure 13. Cracking rate of steel Slag aggregate.

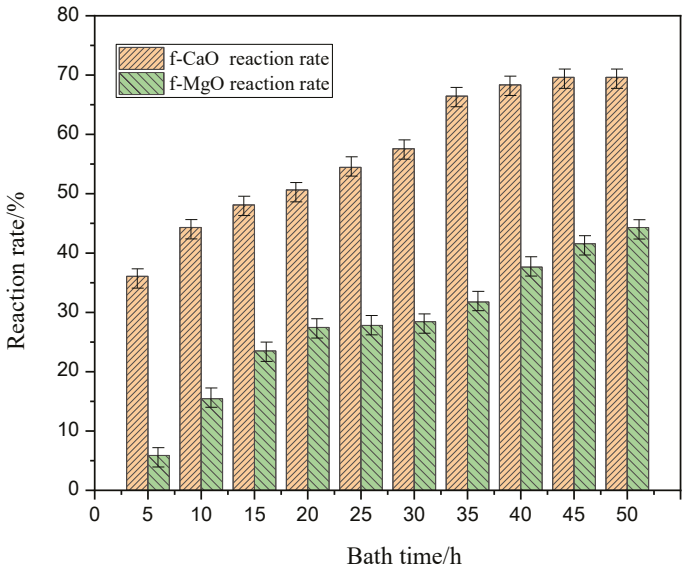

Figure 14. The reaction rate of f-CaO and f-MgO..

Figure 15 and Figure 14 show the changes in f-CaO and f-MgO contents in the steel slag aggregate and the reaction rates of f-CaO and f-MgO in the steel slag aggregate for different water bath times. After 5 h of water bath, 36% of f-CaO and 5.8% of f-MgO were consumed in the steel slag aggregate, at which time cracking phenomenon appeared in the steel slag aggregate, and the number of cracks increased with the time of the water bath, which lasted until 35 h, at which time 66.4% of f-CaO and 31.7% of f-MgO had already been reacted, and the steel slag aggregate did not continue to be cracked. Finally, after 50 h of water bath, the f-CaO content in the steel slag aggregate decreased significantly from the original 1.58% to 0.48%, with a reaction rate of 69.6%, while the f-MgO content decreased from 1.14% to 0.64%, with a reaction rate of 44.3%.

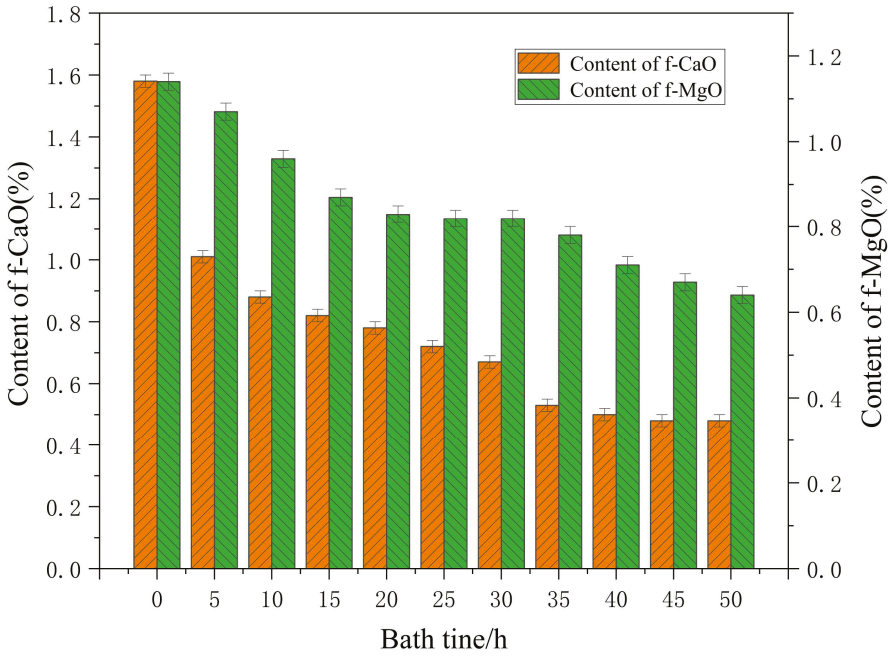

Figure 15. Content of f-CaO and f-MgO in steel slag.

From the reaction rate after the water bath, the hydration activity of f-CaO is stronger, which has a greater impact on the initial stability, while the reaction rate of f-MgO is less than 50% after 50 h of water bath, which has poor hydration activity, and the hydration of f-MgO inside the steel slag aggregate is still difficult, which has a greater impact on the long-term stability.

Figure 16 illustrates the microscopic morphology inside the cracked steel slag aggregate. It can be seen that there are obvious hydration products gathered at the cracks of the particles, which are $Ca(OH)_2$ and $Mg(OH)_2$ formed by the reaction of f-CaO and f-MgO with water. This reaction leads to the cracking of the steel slag particles due to the expansion of their volume.

It should be noted that SEM–EDS provides elemental distribution rather than definitive phase identification. The co-location of Ca (or Mg) and O signals may be associated with Ca-/Mg-bearing phases or hydration products, but EDS alone cannot uniquely distinguish free CaO/free MgO from other Ca-/Mg-containing minerals (e.g., silicates, ferrites) in the complex slag system. Therefore, EDS results in this study are used as supportive spatial evidence and are interpreted together with XRD/titration results and the observed cracking evolution. Elemental analysis via EDS (Figure 17) reveals the chemical composition of different steel slag aggregates. While the slag contains substantial CaO (>30%), most calcium exists in mineral-bound forms rather than as free oxides. The observed spatial correlation between Ca and O signals does not exclusively indicate f-CaO presence.

https://doi.org/10.3390/coatings16010132

Magnesium shows limited distribution in steel slag aggregate minerals, with low overall content, making Mg-O coincident signals more likely to represent f-MgO locations.

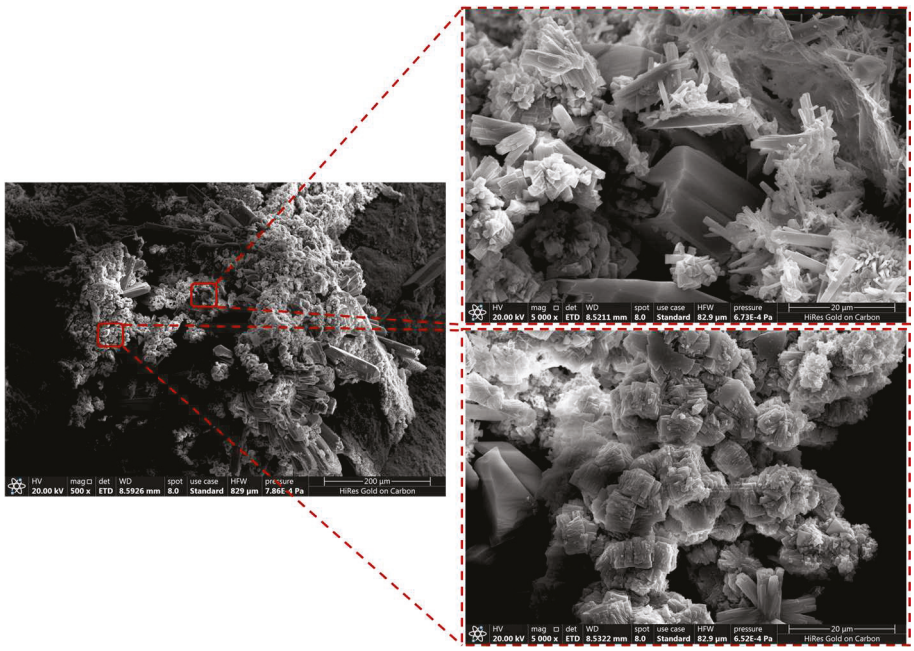

Figure 16. Micro-morphology of cracked steel slag aggregate.

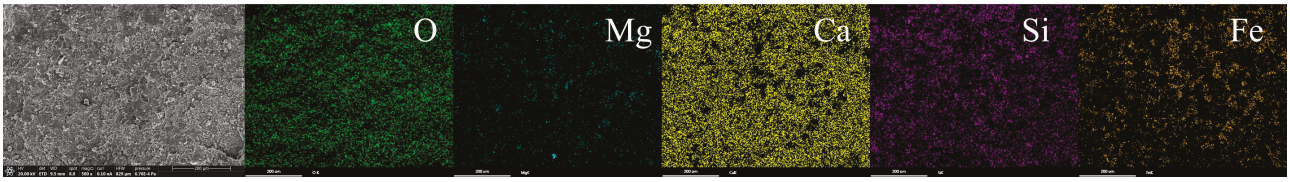

Figure 17. Steel slag aggregate cross-section element distribution.

These findings suggest that the stability problem stems mainly from the localized accumulation of the swelling phases rather than their overall content. Therefore, mitigation strategies should prioritize addressing the uneven distribution of f-CaO and f-MgO rather than focusing only on controlling their overall concentrations.

3.4. Mechanism of Poor Stability of Steel Slag Fine Aggregate

To strengthen the mechanistic interpretation, the present study integrates a multi-scale evidence chain linking macroscopic instability to meso-/micro-scale damage evolution and to the underlying chemical driving forces. Specifically, (i) the boiling expansion response of mortar bars provides a macroscopic manifestation of volumetric instability under accelerated hydration conditions and defines the damage severity and threshold behavior; (ii) the particle cracking rate directly quantifies the evolution of meso-scale damage in steel slag particles, serving as the structural "bridge" between mortar-scale expansion/failure and microstructural cracking; (iii) the titration-based tracking of f-CaO and f-MgO consumption with time offers a quantitative measure of the hydration degree (kinetics) of free oxides, allowing the temporal correspondence between chemical reactions and cracking/expansion to be evaluated; and (iv) the hydrothermal simulations using over-burnt lime and dead-burnt magnesia decouple the contributions of CaO- and MgO-bearing systems under controlled conditions, thereby supporting causal attribution of early-age damage to faster f-CaO hydration while highlighting the potential for residual long-term expansion associated with sluggish f-MgO hydration. By combining these

datasets, the mechanism is not inferred from a single observation but is supported by consistent trends across scales: chemical consumption to localized damage evolution to macroscopic instability.

3.4.1. Expansion and Reaction Rates of f-CaO and f-MgO

To avoid ambiguity, we distinguish the kinetic effect from the total expansion capacity of free oxides. The kinetic effect refers to the hydration rate (i.e., how quickly f-CaO/f-MgO reacts and generates expansive products within a given exposure time), which primarily controls the timing and intensity of early-age damage under accelerated conditions. In contrast, the total expansion capacity denotes the ultimate volumetric expansion potential if hydration proceeds toward completion over a sufficiently long time. Therefore, a phase with fast kinetics (e.g., f-CaO) may dominate early cracking/expansion even if its ultimate capacity is limited, whereas a phase with slow kinetics but considerable capacity (e.g., f-MgO) may contribute less to early-age distress, yet remains a potential source of long-term expansion.

To study the mechanism of mortar damage caused by poor steel slag stability, the reactions of f-CaO and f-MgO in steel slag with water were simulated using over-burnt lime and dead-burnt magnesia.

The volumetric expansion of the hydration reaction of over-burnt lime and dead-burnt magnesia is shown in Figure 18. The reaction expansion of over-burnt lime reached 220% and ceased after 30 min, while the expansion of dead-burnt magnesia reached 35% and stopped increasing after 6 h. Figure 19 shows the change in the physical phase. After 40 min, the diffraction reflection corresponding to f-CaO disappears and only the reflection of calcium hydroxide remains, indicating that the over-burnt lime has completely reacted. Over-burnt lime undergoes a rapid hydration reaction under heating conditions, which can seriously affect stability. The diffraction reflection of f-MgO remains prominent even after 7 h of reaction, while the magnesium hydroxide peak is weak. This suggests that the hydration reaction of dead-burnt magnesia proceeds very slowly in the water bath, leaving most of it unreacted. Additionally, the produced magnesium hydroxide is poorly crystalline and present in low quantities.

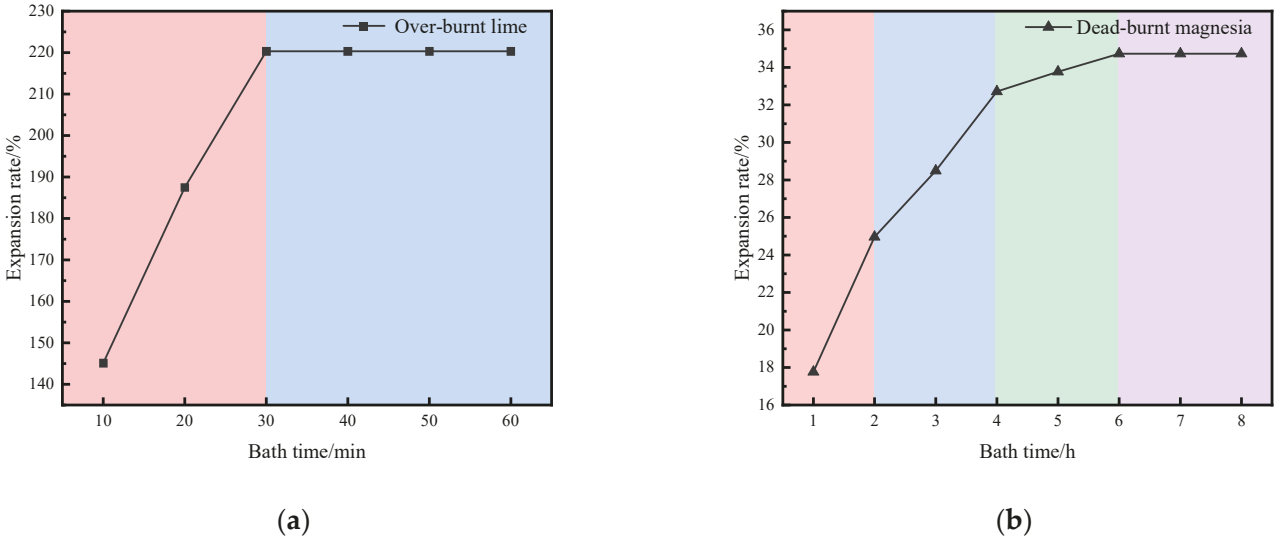

Figure 18. Expansion of over-burnt lime (**a**) and dead-burnt magnesia (**b**) hydration reaction.

https://doi.org/10.3390/coatings16010132

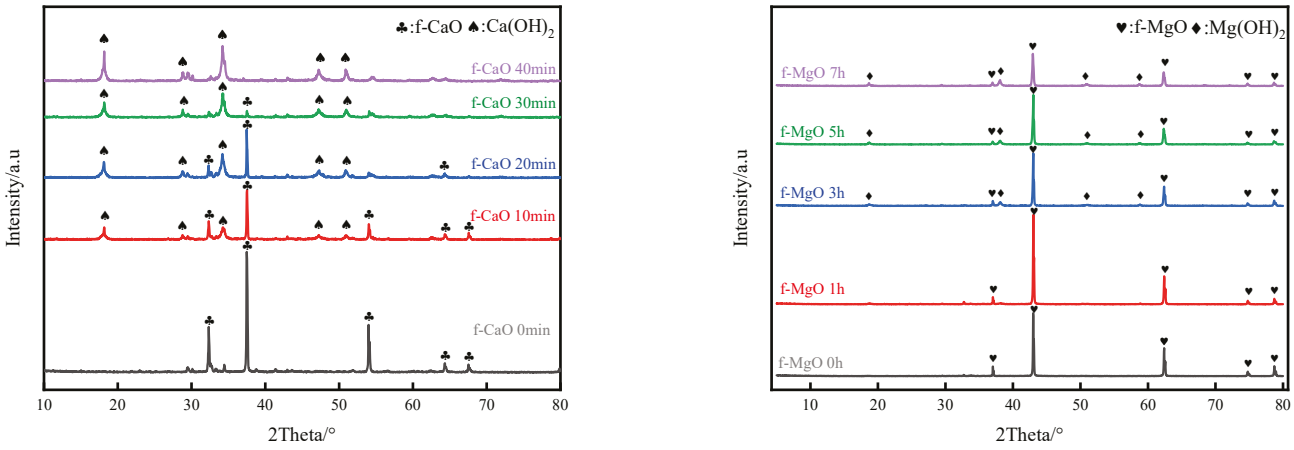

(**a**) (**b**)

Figure 19. Material changes during hydration of over-burnt lime (**a**) and dead-burnt magnesia (**b**).

Figure 20 illustrates the hydration product content of the two substances over time. After heating the reaction for 30 min, the conversion of the over-burnt lime was close to 100%, and the reaction was carried out for 40 min of complete reaction, when the reaction rate reached 100%. While the dead-burnt magnesia in the water bath reaction after 7 h, the sample contained only 19% of the generated Mg $(OH)_2$, 81% of the roasted magnesium is still not reacted, and the reaction rate was only 13.3%. Dead-burnt magnesia does not undergo complete hydration under heating conditions alone.

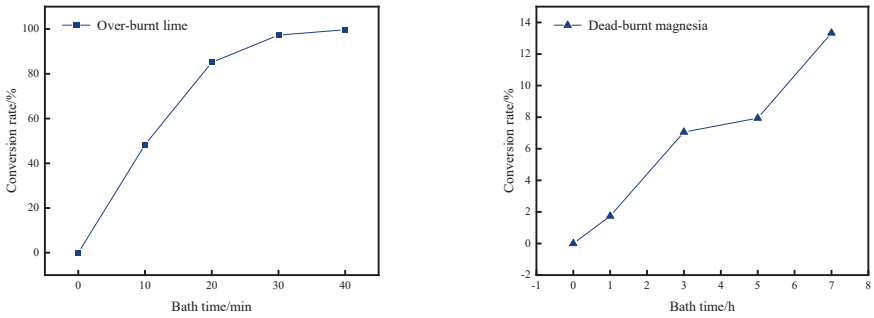

(**a**) (**b**)

Figure 20. Trends in the content of hydration reaction products of over-burnt lime (**a**) and dead-burnt magnesia (**b**).

Dead-burnt magnesia is typically calcined at temperatures between 1450 °C and 2200 °C [33], with the dead-burnt magnesia in this test calcined at 1650 °C. This calcination temperature is similar to that of magnesia formed during the calcination of steel slag. Higher calcination temperatures and longer durations produce larger grains with reduced water reactivity, resulting in a prolonged hydration process. Dead-burnt magnesia calcined at temperatures above 1500 °C exhibits longer hydration times compared to ordinary magnesia. The hydration of f-MgO is a pivotal factor in the long-term stability of steel slag due to the sluggish hydration process of dead burnt magnesia, which can span months or years. The above macroscopic expansion and cracking observations provide the phenomenological basis; in the following, we correlate these damage evolutions with the time-resolved consumption of f-CaO and f-MgO to identify the dominant chemical driving force at each stage.

https://doi.org/10.3390/coatings16010132

3.4.2. Analysis of Hydration Products of f-CaO and f-MgO

Figure 21 shows the microscopic morphology of over-burnt lime at different heating hydration times between 0 and 40 min. As shown in Figure 21a, the observed crystals are f-CaO, with no detectable $Ca(OH)_2$ crystals. In Figure 21b, flaky $Ca(OH)_2$ crystals are visible on the crystal surfaces. Additionally, large, flaky $Ca(OH)_2$ crystals were observed at the bottom, indicating that f-CaO reacted under the heating conditions of the water bath. This reaction produced flaky $Ca(OH)_2$, which deposited on the particle surfaces.

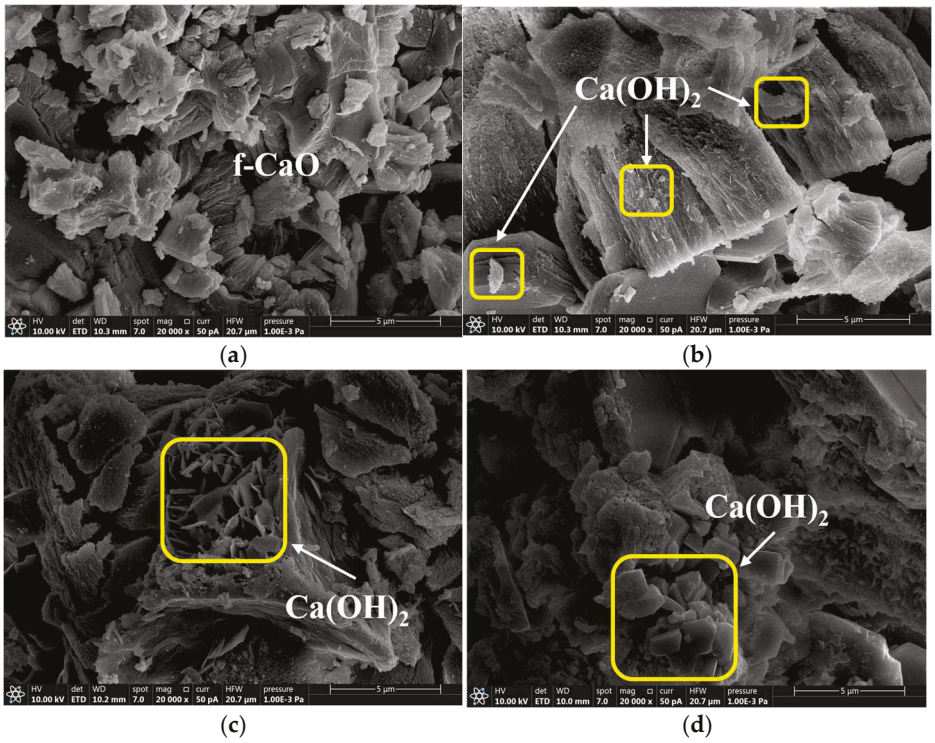

Figure 21. Microscopic morphology evolution of over-burnt lime during heating hydration at 100 °C for (**a**) 0 min, (**b**) 10 min, (**c**) 20 min, and (**d**) 40 min.

In Figure 21c, many $Ca(OH)_2$ crystals grow outward from the interior of the particles, indicating that f-CaO inside the particles is involved in the reaction. A large number of $Ca(OH)_2$ crystals can be seen in Figure 21d. Combined with the XRD image in Figure 19, there is no longer any obvious diffraction reflections associated with f-CaO after 40 min of reaction, indicating that all the f-CaO is hydrated, which can be proved from the conversion of over-burnt lime in Figure 22. F-CaO reacts with water to form $Ca(OH)_2$, which results in the agglomeration of the reaction products, a process that produces porosity and leads to volume expansion.

The evolution of microscopic crystal morphology in dead-burnt magnesia during hydration is presented in Figure 22a–e, showing progressive changes after 0, 1, 3, 5, and 7 h of reaction, respectively. Figure 22a reveals the presence of a prominent f-MgO crystal before hydration. Consistent with established literature [34], elevated calcination temperatures and extended durations promote grain growth in magnesia. The experimental material, calcined at 1650 °C, consequently developed characteristically large f-MgO crystals.

The hydration process reveals distinct morphological changes as observed in Figure 22b,c, where initial plate-like $Mg(OH)_2$ crystals appear and progressively increase in volume. Subsequent stages (Figure 22d,e) show significant surface accumulation of $Mg(OH)_2$ crystals, though their particle size remains relatively small. XRD analysis demonstrates a weak $Mg(OH)_2$ diffraction reflection alongside a dominant diffraction reflection of f-MgO, suggesting both limited crystallization of $Mg(OH)_2$ and incomplete hydration of

https://doi.org/10.3390/coatings16010132

the dead-burnt magnesia. These observations are in agreement with previous findings that f-MgO particles under pressurized conditions show rupture and swelling after 12 h and take 144 h for complete dissolution [35]. This suggests that the hydration kinetics of f-MgO are very slow. While titration quantifies the hydration degree of free oxides in the complex slag system, controlled hydrothermal simulations are further employed to decouple CaO^{-} and MgO-bearing contributions and to rationalize why similar total contents may lead to different damage timings.

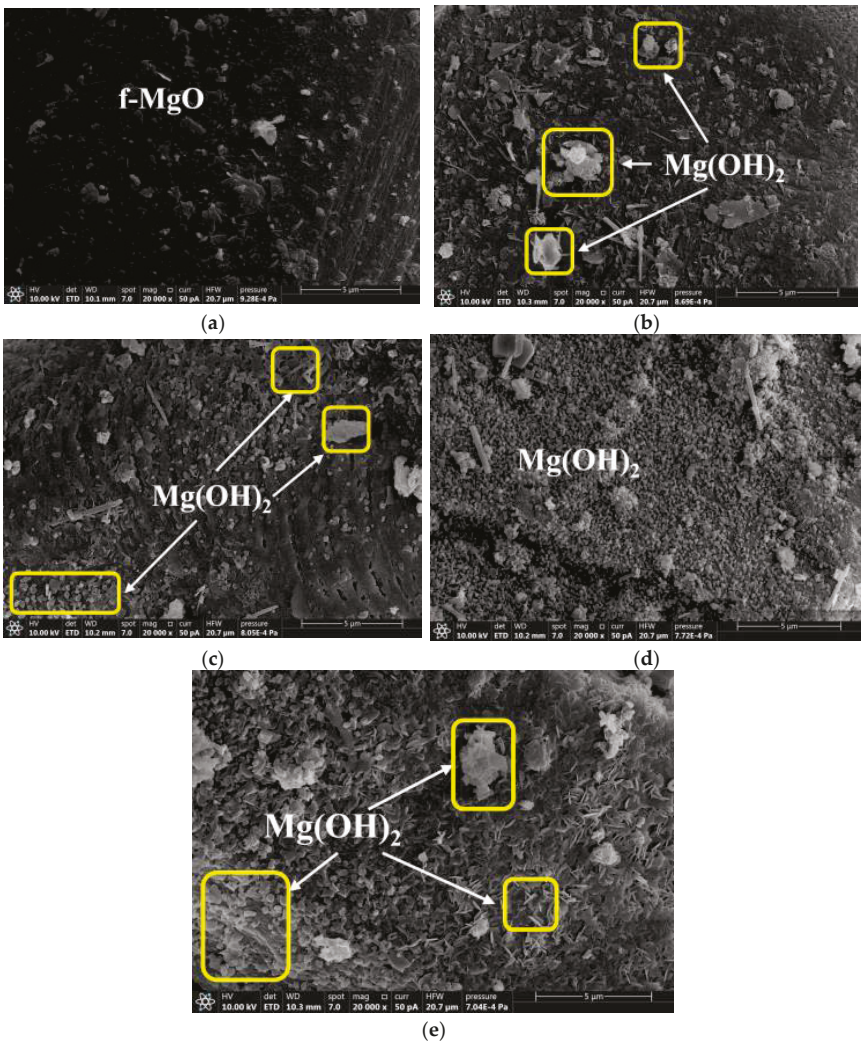

Figure 22. Changes in the microscopic morphology of dead-burnt magnesia during heating hydration at 100 °C for (**a**) 0 h, (**b**) 1 h, (**c**) 3 h, (**d**) 5 h, and (**e**) 7 h.

3.4.3. Mechanistic Explanation

The observation that f-CaO is associated with early-age instability while f-MgO is linked to long-term behavior should be interpreted in terms of timescale-dependent hydration. Under the accelerated boiling regime, f-CaO typically exhibits a higher hydration degree within short durations, leading to rapid accumulation of expansive products and stress concentration near particle defects. Meanwhile, f-MgO hydration is comparatively sluggish; thus, its contribution to expansion may be limited within the early observation window even though its residual expansion capacity may persist. In other words, our results primarily indicate a kinetics-controlled dominance of f-CaO at early ages and a capacity-retaining role of f-MgO at longer timescales, rather than implying that f-MgO is irrelevant to early behavior or that f-CaO has no long-term effect.

https://doi.org/10.3390/coatings16010132

The hydration reaction of f-CaO and f-MgO in steel slag is the key factor leading to the volume expansion and structural damage of mortar. As shown in Figure 23, the hydration reaction of f-CaO and f-MgO in steel slag aggregate starts to occur after contacting with water, and the hydration reaction speed is accelerated with the increase in temperature. According to the reaction rate in Figure 22, the hydration activity of f-CaO is higher, and the hydration reaction is fast in a short time, which leads to early volume expansion and directly destroys the initial structural stability of mortar; the hydration reaction of f-MgO is slower, which needs a longer time to be completely hydrated, and it has a greater impact on the long-term stability problem. With the hydration reaction, the hydration products $Ca(OH)_2$ and $Mg(OH)_2$ are accumulated in the steel slag aggregate, which ultimately leads to the cracking phenomenon of the steel slag aggregate. When steel slag aggregate is mixed into mortar for use, cracking of the aggregate will lead to cracking of the mortar, causing volume stability problems. Therefore, the mechanism is supported by a coherent multi-scale consistency: the reaction kinetics quantified by titration/simulation temporally aligns with the onset of particle cracking, which in turn governs the macroscopic expansion/failure response under accelerated conditions.

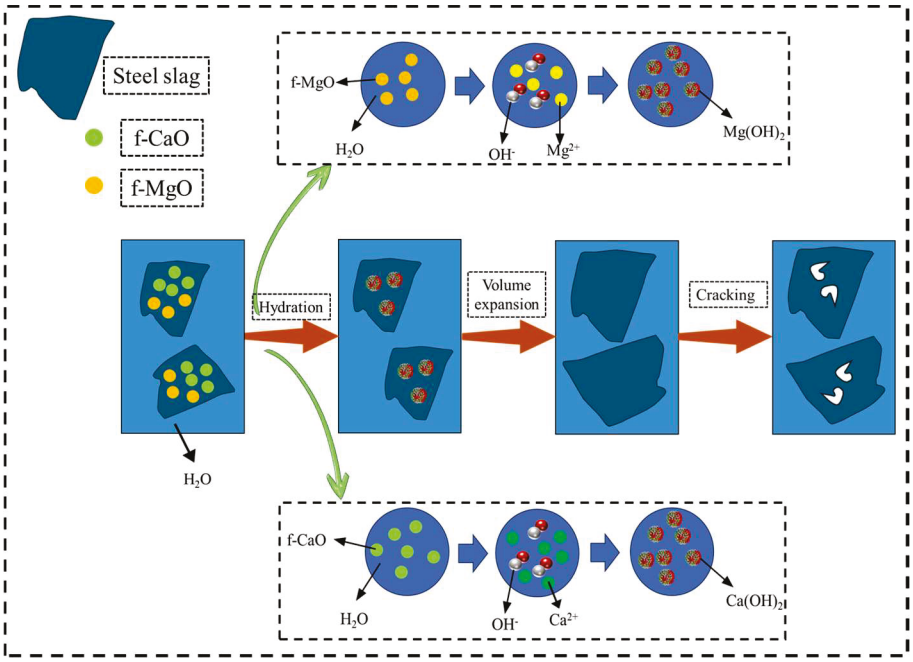

Figure 23. Cracking of steel slag due to hydration products.

4. Conclusions

To optimize the utilization of steel slag, its existing stability issues were investigated, and the stability of steel slag aggregate was evaluated. The reaction expansion, reaction rate, and product changes of over-burnt lime and dead-burnt magnesia were analyzed using a heated water bath. The study reached the following conclusions:

(1) Under the boiling condition of 100 °C, the expansion component in the steel slag aggregate undergoes a hydration reaction, and the mortar specimen mixed with steel slag aggregate has a higher linear expansion rate than the natural sand mortar, and the higher the doping amount of steel slag aggregate, the higher the linear expansion rate. When the dosage of steel slag aggregate reaches or exceeds 40%, the mortar will show different degrees of cracking and fracture.

(2) After boiling, the compressive strength of steel slag aggregate mortar specimens was 27.5% lower, and the flexural strength was 59% lower, compared to NA mortar speci-

https://doi.org/10.3390/coatings16010132

mens. Cracks formed within the boiled steel slag aggregate specimens caused reductions in compressive and flexural strength, highlighting the poor stability of steel slag.

(3) After 50 h of water bath, the cracking rate of steel slag particles was 5%, and the contents of f-CaO and f-MgO in steel slag decreased from 1.58% and 1.14% before boiling to 0.48% and 0.64%. 69.6% of f-CaO and 44.3% of f-MgO were involved in the hydration reaction, and the volumetric expansion led to cracking of the particles, which ultimately led to cracking and fracture of the mortar.

(4) Under heated conditions, over-burnt lime and dead-burnt magnesia accelerate hydration. The over-burnt lime expands by 220% in volume and reacts completely within 40 min, giving a reaction rate of 100%. In contrast, dead-burnt magnesium oxide increases in volume by 34%, and after 7 h, only 19% of the magnesium hydroxide is formed, a reaction rate of 13.3%. Even at high temperatures, the reaction rate of dead burned magnesium remains slow. It can be concluded that f-CaO has a great influence on the pre-stability of steel slag, while f-MgO has a greater influence on the long-term stability of steel slag. More attention should be paid to the long-term stability issues related to f-MgO than to f-CaO.

Under accelerated boiling conditions, mortar containing steel slag fine aggregate exhibited pronounced stability deterioration and even fracture at high replacement levels. Based on the observed damage evolution, a conservative upper limit (e.g., $\leq$20%–30%) is recommended for fine aggregate replacement unless stabilization pretreatments (such as aging, controlled hydration, or carbonation-based treatments) are implemented. The proposed framework combining expansion, cracking evolution, and free-oxide consumption can serve as a rapid screening tool to support mix-design decisions and potential acceptance criteria for steel slag aggregates.

Novelty of this study: (i) the dimensional instability of mortar incorporating unprocessed BOF steel slag fine aggregate was quantified through accelerated boiling expansion and strength degradation; (ii) the reaction degrees of f-CaO and f-MgO were determined and correlated with the cracking of individual slag particles; and (iii) a comparative hydration simulation using over-burnt lime and dead-burnt magnesia clarified the distinct roles of f-CaO (dominant in early-age instability) and f-MgO (dominant in long-term instability).

Future work: (1) investigate practical stabilization/pretreatment routes for steel slag sand (e.g., aging, carbonation, steam/hydrothermal treatment) and establish performance-based acceptance criteria; (2) perform long-term expansion monitoring under ambient curing and realistic service environments to validate the accelerated assessment; and (3) employ 3D techniques (e.g., micro-CT) to track the evolution of internal cracking and its coupling with transport properties and durability.

Author Contributions: H.Z.: Writing—review and editing, Writing—original draft, Visualization, Validation, Software, Methodology, Investigation, Formal analysis, Data curation, Conceptualization. A.L.: Writing—review and editing, Validation, Supervision, Project administration, Resources, Funding acquisition, Methodology, Investigation, Conceptualization. H.Y.: Writing—review and editing, Writing—original draft, Visualization, Validation, Methodology. D.G.: Writing—review and editing, Writing—original draft, Visualization, Validation, Methodology. C.L.: Writing—review and editing, Writing—original draft, Visualization, Validation, Methodology. W.Y.: Formal analysis, Data curation, Conceptualization. W.D.: Writing—review and editing, Writing—original draft, Visualization, Validation, Methodology. All authors have read and agreed to the published version of the manuscript.

Funding: This research received no external funding.

Institutional Review Board Statement: Not applicable.

Informed Consent Statement: Not applicable.

Data Availability Statement: The original contributions presented in this study are included in the article. Further inquiries can be directed to the corresponding author.

Conflicts of Interest: Authors Aizhu Liu, Huiqing Yang, Dong Gao, Chunguang Liu were employed by the company Shandong Hi-Speed Urban & Rural Development Group Co., Ltd. The remaining authors declare that the research was conducted in the absence of any commercial or financial relationships that could be construed as a potential conflict of interest.

References

1. Wang, S.; Kim, J.; Qin, T. Mineral carbonation of iron and steel by-products: State-of-the-art techniques and economic, environmental, and health implications. *J. CO_2 Util.* **2024**, *81*, 102707. [CrossRef]
2. Guo, J.; Bao, Y.; Wang, M. Steel slag in China: Treatment, recycling, and management. *Waste Manag.* **2018**, *78*, 318–330. [CrossRef] [PubMed]
3. Zhu, H.; Ma, M.; He, X.; Zheng, Z.; Su, Y.; Yang, J.; Zhao, H. Effect of wet-grinding steel slag on the properties of Portland cement: An activated method and rheology analysis. *Constr. Build. Mater.* **2021**, *286*, 122823. [CrossRef]
4. Gan, Y.; Li, C.; Zou, J.; Wang, W.; Yu, T. Evaluation of the impact factors on the leaching risk of steel slag and its asphalt mixture. *Case Stud. Constr. Mater.* **2022**, *16*, e01067. [CrossRef]
5. Gao, W.; Zhou, W.; Lyu, X.; Liu, X.; Su, H.; Li, C.; Wang, H. Comprehensive utilization of steel slag: A review. *Powder Technol.* **2023**, *422*, 118449. [CrossRef]
6. Zhang, Z.; Ouyang, J.; Liu, J. Exploration of steel slag by lignin and sodium citrate modification for mechanical properties and stability of steel slag-cement cementitious materials. *J. Clean. Prod.* **2024**, *478*, 143971. [CrossRef]
7. Chen, Z.; Li, R.; Zheng, X.; Liu, J. Carbon sequestration of steel slag and carbonation for activating RO phase. *Cem. Concr. Res.* **2021**, *139*, 106271. [CrossRef]
8. Mombelli, D.; Mapelli, C.; Barella, S.; Di Cecca, C.; Le Saout, G.; Garcia-Diaz, E. The effect of chemical composition on the leaching behaviour of electric arc furnace (EAF) carbon steel slag during a standard leaching test. *J. Environ. Chem. Eng.* **2016**, *4*, 1050–1060. [CrossRef]
9. Aziz, M.M.A.; Hainin, M.R.; Yaacob, H.; Ali, Z.; Chang, F.L.; Adnan, A.M. Characterisation and utilisation of steel slag for the construction of roads and highways. *Mater. Res. Innov.* **2014**, *18*, 255–259. [CrossRef]
10. Rui, Y.; Qian, C.; Zhang, X.; Ma, Z. Different carbon treatments for steel slag powder and their subsequent effects on properties of cement-based materials. *J. Clean. Prod.* **2022**, *362*, 132407. [CrossRef]
11. Kumar, P.; Shukla, S. Utilization of steel slag waste as construction material: A review. *Mater. Today Proc.* **2023**, *78*, 145–152. [CrossRef]
12. Guo, Y.; Xie, J.; Zhao, J.; Zuo, K. Utilization of unprocessed steel slag as fine aggregate in normal- and high-strength concrete. *Constr. Build. Mater.* **2019**, *204*, 41–49. [CrossRef]
13. Chen, H.-B.; Yang, B. Effect of heat treatment on microstructures and mechanical properties of a bulk nanostructured Al-Zn-Mg-Cu alloy. *J. Miner. Metall. Mater. Engl. Ed.* **2009**, *16*, 672–676. [CrossRef]
14. Goyal, P.K.; Mudgal, M.; Ghosh, P.K. Assessing the viability of using BOF steel slag treated with tartaric acid as coarse aggregate in concrete. *Constr. Build. Mater.* **2024**, *436*, 136912. [CrossRef]
15. Wang, C.; Ye, G.; Jin, Q.; Zhou, Z.; Hu, D.; Wei, Y. The uniaxial compressive stress-strain relations of steel slag fine aggregate concrete under steam curing. *Constr. Build. Mater.* **2025**, *459*, 139820. [CrossRef]
16. Abu-Eishah, S.I.; El-Dieb, A.S.; Bedir, M.S. Performance of concrete mixtures made with electric arc furnace (EAF) steel slag aggregate produced in the Arabian Gulf region. *Constr. Build. Mater.* **2012**, *34*, 249–256. [CrossRef]
17. Andrade, H.D.; de Carvalho, J.M.F.; Costa, L.C.B.; Elói, F.P.F.; do Carmo e Silva, K.D.; Peixoto, R.A.F. Mechanical performance and resistance to carbonation of steel slag reinforced concrete. *Constr. Build. Mater.* **2021**, *298*, 123910. [CrossRef]
18. Choi, S.Y.; Yang, E.I. An experimental study on alkali silica reaction of concrete specimen using steel slag as aggregate. *Appl. Sci.* **2020**, *10*, 6699. [CrossRef]
19. Xue, J.-C.; Wang, W.-C.; Wu, C.-H.; Hong, T.-J.; Chen, T.-H.; Huang, C.-Y. Deterioration analysis and expansion behavior prediction of electric arc furnace slag as fine aggregate in mortar. *J. Build. Eng.* **2024**, *85*, 108717. [CrossRef]
20. Zhou, Z.; Jin, Q.; Hu, D.; Zhu, L.; Li, Z.; Su, W. Long-term volume stability of steel slag sand mortar and concrete. *Case Stud. Constr. Mater.* **2025**, *22*, e04197. [CrossRef]
21. Li, W.; Cao, M.; Wang, D.; Zhao, J.; Chang, J. Improving the hydration activity and volume stability of the RO phases in steel slag by combining alkali and wet carbonation treatments. *Cem. Concr. Res.* **2023**, *172*, 107236. [CrossRef]
22. Pang, B.; Zhou, Z.; Xu, H. Utilization of carbonated and granulated steel slag aggregate in concrete. *Constr. Build. Mater.* **2015**, *84*, 454–467. [CrossRef]

23. Yan, J.; Wu, S.; Yang, C.; Zhao, Z.; Xie, J. Influencing mechanisms of RO phase on the cementitious properties of steel slag powder. *Constr. Build. Mater.* **2022**, *350*, 128926. [CrossRef]
24. Zhou, M.; Cheng, X.; Chen, X. Studies on the volumetric stability and mechanical properties of cement-fly-ash-stabilized steel slag. *Materials* **2021**, *14*, 495. [CrossRef]
25. Jiang, Q.; Liu, W.; Wu, S. Analysis on factors affecting moisture stability of steel slag asphalt concrete using grey correlation method. *J. Clean. Prod.* **2023**, *397*, 136490. [CrossRef]
26. Liu, X.; Bao, Y.-P. Separation and extraction of iron resources from hazardous electric arc furnace (EAF) steel slag: Aggregation of Fe-rich layers, magnetic separation, powder characterization. *Process Saf. Environ. Prot.* **2024**, *190*, 420–428. [CrossRef]
27. Wang, Q.; Wang, D.; Zhuang, S. The soundness of steel slag with different free CaO and MgO contents. *Constr. Build. Mater.* **2017**, *151*, 138–146. [CrossRef]
28. *GB/T 38216.3-2023*; Determination of Free Calcium Oxide Content in Steel Slag by EDTA Titration and Thermogravimetric Analysis. State Administration for Market Regulation: Beijing, China, 2023.
29. Albostami, A.S.; Al-Hamd, R.K.S.; Al-Matwari, A.A. Data-driven predictive modeling of steel slag concrete strength for sustainable construction. *Buildings* **2024**, *14*, 2476. [CrossRef]
30. Qiao, C.; Suraneni, P.; Weiss, J. Damage in cement pastes exposed to NaCl solutions. *Constr. Build. Mater.* **2018**, *171*, 120–127. [CrossRef]
31. Skaf, M.; Ortega-López, V.; Fuente-Alonso, J.A.; Santamaría, A.; Manso, J.M. Ladle furnace slag in asphalt mixes. *Constr. Build. Mater.* **2016**, *122*, 488–495. [CrossRef]
32. Yang, C.; Huang, Z.; Wu, S.; He, X.; Su, Y.; Zhao, Z.; Xu, H.; Wang, F.; Zhang, L. Recycling steel slag as aggregate in developing an ultra-thin friction course with high comprehensive road performance. *Constr. Build. Mater.* **2024**, *449*, 138539. [CrossRef]
33. Canterford, J.H. Magnesia—An important industrial mineral: A review of processing options and uses. *Miner. Process. Extr. Metall. Rev.* **2007**, *2*, 57–104. [CrossRef]
34. Ilango, N.K.; Nguyen, H.; German, A.; Winnefeld, F.; Kinnunen, P. Role of magnesium acetate in hydration and carbonation of magnesium oxide-based cements. *Cem. Concr. Res.* **2024**, *175*, 107357. [CrossRef]
35. Park, S.; Ma, J.; Yun, T.S.; Jeon, S.; Byeun, Y.; Kang, D.; Jang, J. Pore-scale swelling mechanism of magnesium oxide granules during hydration. *Constr. Build. Mater.* **2020**, *251*, 119101. [CrossRef]

Disclaimer/Publisher's Note: The statements, opinions and data contained in all publications are solely those of the individual author(s) and contributor(s) and not of MDPI and/or the editor(s). MDPI and/or the editor(s) disclaim responsibility for any injury to people or property resulting from any ideas, methods, instructions or products referred to in the content.

coatings

MDPI

Article

Hierarchical Design of EA ZnCo-LDH/NCS Electrode for Enhanced Electrochemical Performance

Zeyi Liu [1], Huan Wang [1], Xuefeng Chu [1], Wanyue Diao [1], Chao Wang [2], Shiyi Wang [1], Zehao Zhang [1] and Sa Lv [1,*]

[1] Key Laboratory for Architectural Cold Climate Energy Management, Ministry of Education, Jilin Jianzhu University, Changchun 130118, China
[2] Provincial Key Laboratory of Architectural Electricity & Comprehensive Energy Saving, Ministry of Education, Jilin Jianzhu University, Changchun 130118, China
* Correspondence: lvsa@jlju.edu.cn; Tel.: +86-0431-8456-6181

Abstract

Herein, an electrochemically activated zinc–cobalt-layered double hydroxide/nickel–cobalt-sulfide (EA ZnCo-LDH/NCS) hierarchical composite electrode was fabricated in situ via coupled hydrothermal synthesis and electrodeposition. The influence of electrolyte concentration on the activation efficiency was systematically analyzed, and the corresponding effects of electrochemical activation on each component were elucidated. Benefiting from the introduction of the Zn component and subsequent electrochemical activation, the composite electrode exhibits a marked performance enhancement. The EA ZnCo-LDH/NCS electrode achieves a high areal specific capacitance (*Cs*) of 11.39 F cm^{-2} at 4 mA cm^{-2}, maintains 70.15% of this value when the current density is increased ten-fold, and retains 80.05% of its initial capacity after 5000 cycles.

Keywords: composite electrode; electrochemical activation; electrodeposition; hydrothermal synthesis

1. Introduction

The continuously increasing global energy demand underscores the urgency of efficient energy storage technologies. Electrochemical storage devices and their pivotal role in improving energy-utilization efficiency are therefore highlighted. As core components of energy storage devices, electrode materials have consistently attracted extensive research attention [1–3]. Among the various electrode materials, $Co(OH)_2$, a typical pseudocapacitive electrode material, stands out because of its exceptional merits: high theoretical specific capacitance, unique structural characteristics, good conductivity, and cycling stability [4]. Moreover, cobalt-based bimetallic hydroxides/sulfides and their composites have been designed and constructed by optimizing preparation routes such as hydrothermal methods, co-precipitation, and electrodeposition. Various hierarchical or composite structures are thereby obtained, effectively improving the energy storage performance of the electrodes [5–7]. For example, Markhabayeva et al. used a two-step hydrothermal method to prepare a $NiCo_2S_4$ electrode that delivered a specific capacity of 8.1 F cm^{-2} at a discharge current density of 5 mA cm^{-2} [8]. Similarly, Jiang et al. combined electrodeposition with hydrothermal synthesis to fabricate $CoSe_2$@NiCo-LDH composite electrodes that achieved a specific capacity of 6.06 F cm^{-2} at 6 mA cm^{-2} [9].

Recognizing that the composition and preparation methods are the two key factors in breaking through the energy storage limits of electrode materials, researchers have extended

their efforts beyond the aforementioned composite systems. Extensive studies have employed heteroatom doping to modulate the host band structure, thereby enhancing intrinsic conductivity, optimizing charge transfer kinetics, or creating new active sites via dopant-induced lattice defects. For example, Zheng et al. reported Mn-doped Co_9S_8@$Co(OH)_2$ electrodes exhibiting a specific capacity of 5.62 F cm^{-2} at a discharge current density of 1.5 m A cm^{-2} [10].

In view of these considerations and with the aim of mitigating the toxicity and cost of cobalt-based compounds, Zn–Co-layered double hydroxides (ZnCo-LDHs) were prepared by simple hydrothermal synthesis to reduce the overall cobalt content [11,12]. Meanwhile, electrodeposition technology has emerged as an important route for preparing hierarchical composites, offering the unique advantages of controllable stepwise growth with precise layer control, short processing times, high reproducibility, and operational simplicity [13]. Additionally, an electrochemical activation strategy has been implemented to induce controlled compositional and structural transitions that expand ion/electron transport pathways, thereby enhancing the intrinsic electrochemical activity of the electrode material [14,15]. For example, Hong et al. synthesized NiCo-hydroxysulfide and, after activating it in 6 M KOH by cyclic voltammetry, achieved a specific capacity more than twice that obtained with 1 M KOH [16]. Meanwhile, Hong et al. prepared a CoS/NiMn-LDH electrode and subjected it to a 10-cycle charge/discharge activation, yielding about 1.4 times the original specific capacity [17].

Guided by the above analysis and focusing on composition regulation and synthetic methodology as the two pivotal breakthroughs, this study integrates hydrothermal synthesis with electrodeposition to construct a ZnCo-LDH/nickel–cobalt-sulfide (NCS) composite electrode, while systematically evaluating the influence of electrochemical activation on electrode performance. The hierarchical design and activation strategy presented herein provide experimental evidence for the structural and performance modulation of composite electrodes.

2. Materials and Methods

2.1. Materials

Nickel foam (NF, 100 PPI, Kunshan Dessco Co., Ltd., Kunshan, China) substrates (1.0 cm × 1.5 cm) were first sliced and then subjected to sequential washing with dilute HCl, ethanol, and deionized water to remove surface oxides and impurities. All chemicals and reagents employed were of analytical grade and purchased from Sinopharm Chemical Reagent Co., Ltd., Wuhan, China.

2.2. Stepwise Fabrication of EA (ZnCo-LDH/NCS) and EA ZnCo-LDH/NCS Electrodes

The pretreated NF was immersed in a mixed aqueous solution containing 0.05 M $Co(NO_3)_2{\cdot}6H_2O$, 0.025 M $Zn(NO_3)_2{\cdot}6H_2O$, and 0.3 M CH_4N_2O. A hydrothermal reaction was then carried out at 120 °C for 6 h, after which the product ZnCo-LDH was removed and rinsed successively with ethanol and deionized water.

A mixed solution containing 0.05 M $NiCl_2{\cdot}6H_2O$, 0.05 M $CoCl_2{\cdot}6H_2O$, and 0.5 M CH_4N_2S was prepared. A three-electrode system was assembled with the ZnCo-LDH from the previous step as the working electrode, and a platinum foil and a saturated calomel electrode (SCE) acting as the counter and reference electrodes, respectively. A constant potential of −1.1 V was applied for 180 s. After deposition, the resulting zinc–cobalt-layered double hydroxide/nickel–cobalt-sulfide (ZnCo-LDH/NCS) composite electrode was rinsed with deionized water and ethanol, and then dried for characterization. For comparison, single-component ZnCo-LDH and NCS electrodes were also prepared by the same method and are denoted as ZnCo-LDH and NCS, respectively.

https://doi.org/10.3390/coatings16010113

Electrochemical activation (EA) was performed by 25 consecutive cyclic voltammetry cycles at 5 mV s^{-1} in a three-electrode configuration with 1, 3, 5, or 7 M KOH as the electrolyte. After activation, the ZnCo-LDH/NCS composite electrode is designated EA (ZnCo-LDH/NCS); the single-component ZnCo-LDH and NCS electrodes are designated EA ZnCo-LDH and EA NCS, respectively. Depositing the NCS layer onto the activated EA ZnCo-LDH surface gives the composite electrode designated EA ZnCo-LDH/NCS.

2.3. Characterization

The surface morphology and elemental composition of the electrodes were analyzed by scanning electron microscopy (SEM, JSM-7610F 15.0 kV, Tokyo, Japan), X-ray diffractometry (XRD, Cu Kα radiation with λ = 1.5406 Å, Shimadzu Co., Ltd., Kyoto, Japan), and X-ray photoelectron spectroscopy (XPS, ESCALAB 250Xi, ThermoFisher Scientifific Co., Ltd., Waltham, MA, USA, Al Kα as X-ray source). Electrochemical performance was evaluated by cyclic voltammetry (CV), galvanostatic charge–discharge (GCD), electrochemical impedance spectroscopy (EIS), and long-term cycling tests using a CHI760E electrochemical workstation (Shanghai Chenhua Instrument Co., Ltd., Shanghai, China). A three-electrode configuration was employed with the as-prepared ZnCo-LDH/NCS electrode as the working electrode, a Ag/AgCl electrode as the reference, a Pt foil as the counter electrode, and 2 M NaOH as the electrolyte.

3. Results

Figure 1 illustrates the fabrication procedures of the two electrodes. First, ZnCo-LDH nanosheets are grown in situ on NF via a hydrothermal reaction. The process then splits into two routes. In one, a NCS layer is uniformly electrodeposited onto the ZnCo-LDH surface. After the ZnCo-LDH/NCS composite is assembled, electrochemical activation is performed to yield the EA (ZnCo-LDH/NCS) electrode. For comparison, a parallel route carries out the activation before NCS deposition, giving the EA ZnCo-LDH/NCS electrode.

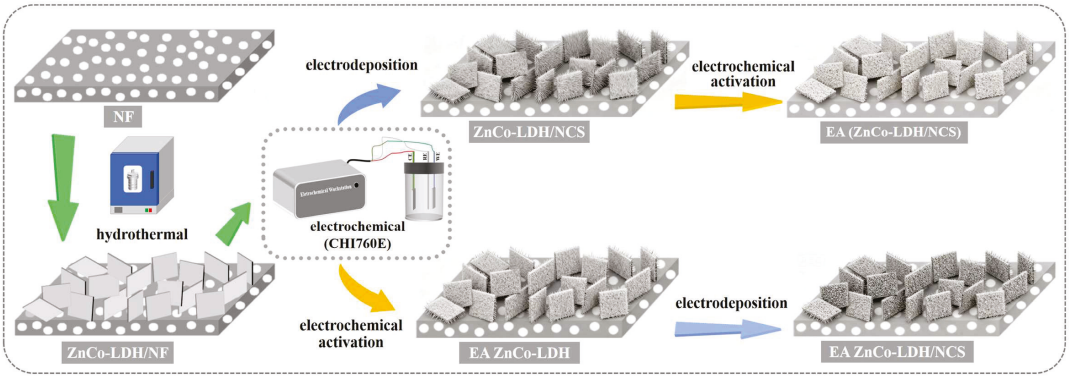

Figure 1. Schematic of the stepwise fabrication processes for the EA (ZnCo-LDH/NCS) and EA ZnCo-LDH/NCS electrodes.

The XRD patterns of ZnCo-LDH, EA ZnCo-LDH, and EA ZnCo-LDH/NCS are presented in Figure S1. The three strongest peaks at 44.6°, 51.9°, and 76.5° arise from the NF substrate. The remaining broad, low-intensity reflections can be indexed to the (003), (012), and (015) planes of the hydrotalcite-like LDH phase, which are in good agreement with the previous report [18,19], indicating that the layered structure is retained after deposition of the NCS layer, albeit with limited crystallinity. Figure 2a presents the XPS survey spectrum of EA ZnCo-LDH/NCS, revealing clear photoelectron signals for Zn 2p, Ni 2p, Co 2p, O 1s, C 1s, and S 2p. In the Zn 2p region (Figure 2b), the signals at 1045.9 and 1021.3 eV are assigned to Zn $2p_{1/2}$ and Zn $2p_{3/2}$, respectively [20]. These two peaks

https://doi.org/10.3390/coatings16010113

are attenuated after the activation treatment. For comparison, Figure S2 displays the Zn 2p spectrum of the hydrothermal reaction without electrochemical activation. The Co 2p spectrum (Figure 2c) exhibits spin–orbit splitting into $2p_{1/2}$ components at 798.49 and 796.94 eV and $2p_{3/2}$ components at 782.64 and 781.09 eV, together with shake-up satellites at around 802.6 and 786.5 eV; this multiplet structure confirms the coexistence of Co^{2+} and Co^{3+} [21]. The Ni 2p region (Figure 2d) shows characteristic peaks at 874.12 eV ($2p_{1/2}$) and 856.42 eV ($2p_{3/2}$), accompanied by satellite peaks at about 880.13 and 862 eV [20]. The O 1s envelope (Figure 2e) is deconvoluted into two components at 532.18 eV (adsorbed H_2O) and 531.15 eV (bound OH^-) [16]. The S 2p spectrum (Figure 2f) is resolved into two doublets: the first at 164.29 eV and 162.47 eV corresponds to $2p_{1/2}$ and $2p_{3/2}$, whereas the second at 169.41 eV ($2p_{1/2}$) and 168.04 eV ($2p_{3/2}$) arises from S-O bonding generated by the reaction of sulfur species with OH^- released during thiourea hydrolysis [22].

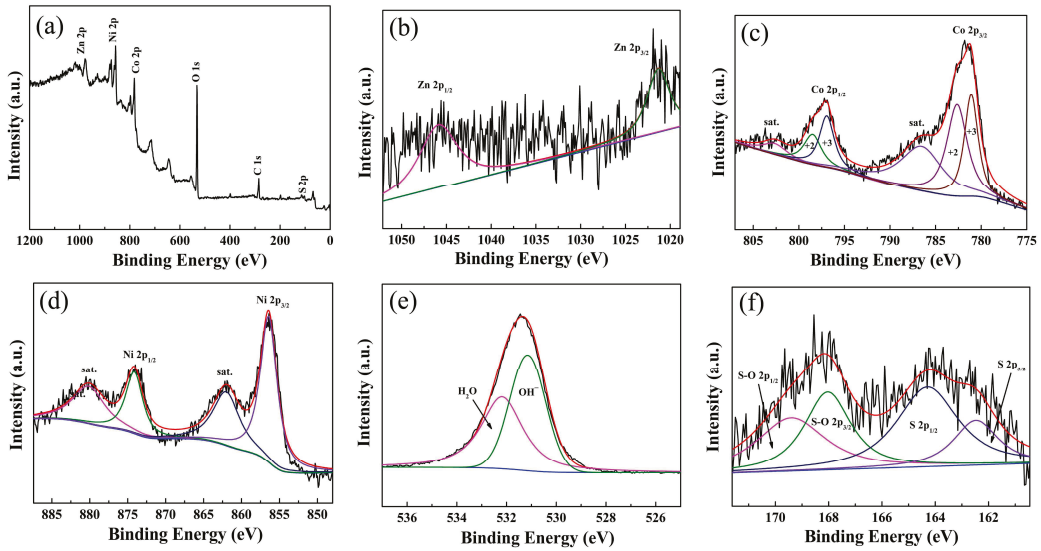

Figure 2. XPS spectra of (**a**) survey scan, (**b**) Zn 2p, (**c**) Co 2p, (**d**) Ni 2p, (**e**) O 1s, and (**f**) S 2p for EA ZnCo-LDH/NCS electrode.

Figure 3a depicts the FE-SEM image of the pristine ZnCo-LDH electrode. Dense ZnCo-LDH nanosheets are uniformly distributed on the NF substrate, and the surface of these nanosheets is relatively smooth and flat, with a thickness of about 18 nm (Figure 3b). Following NCS layer deposition, these nanosheets displayed a substantial thickening and a denser spatial distribution (Figure 3c). At higher magnification, in Figure 3d, the intertwined networks are seen to tightly envelop these nanosheets like a dense layer of burrs.

Figure 4a compares the CV curves (recorded at 5 mV s^{-1} in 2 M NaOH) of the ZnCo-LDH, NCS, and ZnCo-LDH/NCS electrodes. The composite electrode exhibits the strongest current response, substantially exceeding those of the single-component ZnCo-LDH and NCS electrodes, indicating superior energy storage capability. Consistently, GCD tests at 4 mA cm^{-2} (Figure 4b) reveal that the ZnCo-LDH/NCS electrode affords the longest discharge time, followed by ZnCo-LDH, whereas NCS delivers the shortest. The pseudocapacitive behavior is attributed to the following electrochemical reaction [23–25]:

$$Co(OH)_2 + OH^- \leftrightarrow CoOOH + H_2O + e^- \quad (1)$$

$$CoOOH + OH^- \leftrightarrow CoO_2 + H_2O + e^- \quad (2)$$

$$NiS + OH^- \leftrightarrow NiSOH + e^- \quad (3)$$

https://doi.org/10.3390/coatings16010113

$$CoS + OH^- \leftrightarrow CoSOH + e^- \quad (4)$$

$$CoSOH + OH^- \leftrightarrow CoSO + H_2O + e^- \quad (5)$$

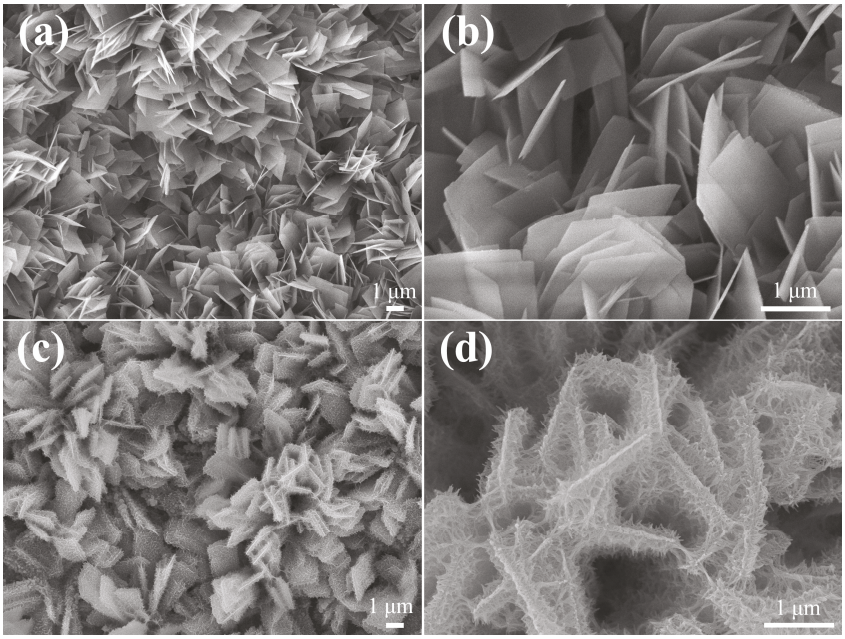

Figure 3. SEM images of (**a**,**b**) ZnCo-LDH and (**c**,**d**) ZnCo-LDH/NCS electrodes recorded at different magnifications.

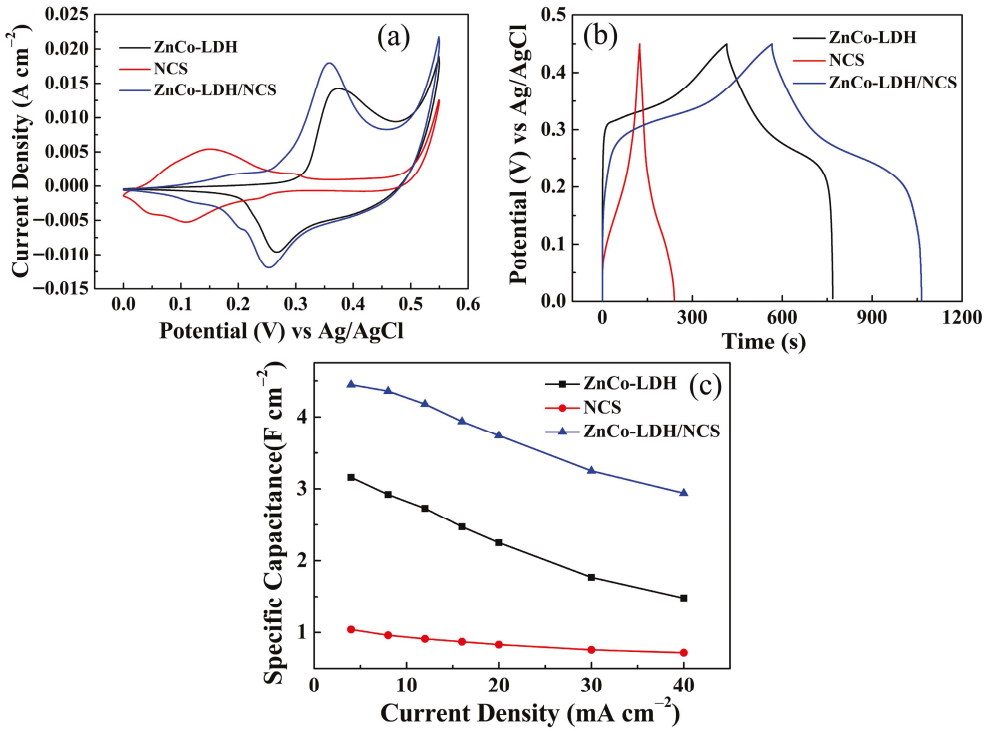

Figure 4. Electrochemical performance comparison of ZnCo-LDH, NCS, and ZnCo-LDH/NCS electrodes: (**a**) CV curves; (**b**) GCD curves; (**c**) Cs at various current densities.

The zinc component hardly participates in the above redox reactions, though it may promote the formation of the Zn-Co composite nanosheet structure. Moreover, $Zn(OH)_2$, as a typical amphoteric hydroxide, acts as a structure-directing agent in our reaction

system, as previously reported [20]. The Cs values of the three electrodes at various current densities are summarized in Figure 4c. The trend is fully consistent with the CV results and corroborates the effectiveness of combining ZnCo-LDH with $Co(OH)_2$.

Remarkably, the ZnCo-LDH/NCS electrode gained an additional performance boost after electrochemical activation in 1 M KOH [designated as EA (ZnCo-LDH/NCS)]. Figure 5 compares the CV and GCD curves before and after this activation. Both the current response (Figure 5a) and the discharge duration (Figure 5b) of the EA (ZnCo-LDH/NCS) electrode increase markedly, demonstrating enhanced energy storage capability.

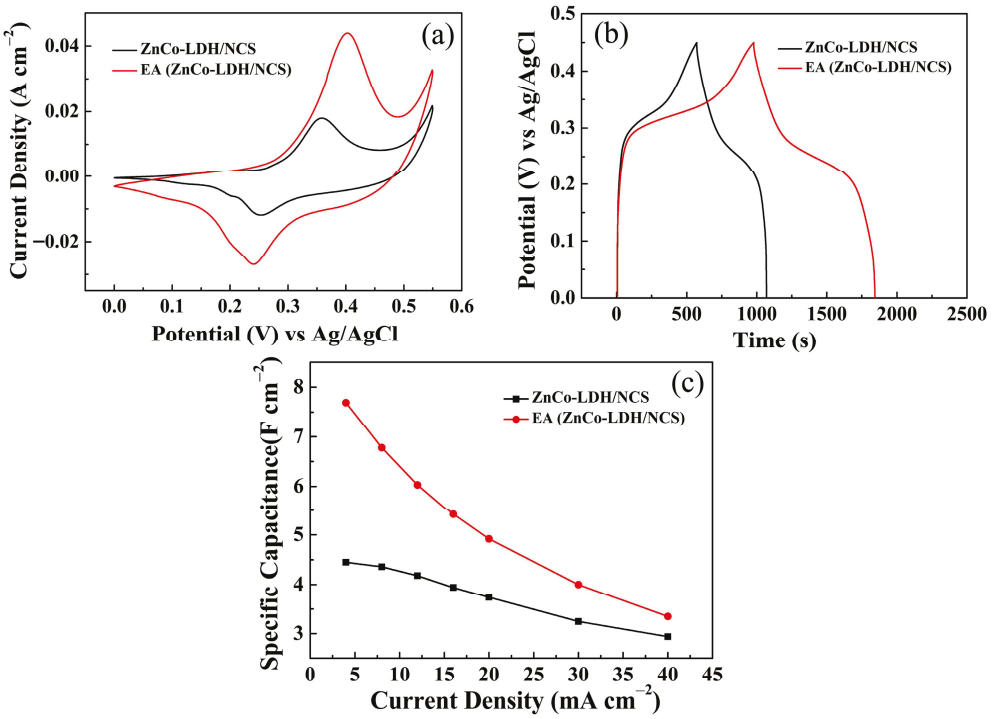

Figure 5. Electrochemical performance comparison of ZnCo-LDH/NCS and EA (ZnCo-LDH/NCS) electrodes: (**a**) CV curves; (**b**) GCD curves; (**c**) *C*s at various current densities.

Figure 6 presents FE-SEM images of the ZnCo-LDH/NCS electrodes after cyclic voltammetry electrochemical activation at different electrolyte concentrations. At a low KOH concentration of 1 M, numerous curved nanoflakes form on the hierarchical surface (Figure 6a,b); these nanoflakes are approximately 20 nm thick and interweave with one another. When the concentration is raised to 3 M (Figure 6c,d), the nanoflakes become markedly denser, and this trend persists as the concentration is increased to 5 M (Figure 6e,f). Further increasing the concentration to 7 M causes excessive stacking of the nanoflakes, destroying the hierarchical architecture and generating numerous cracks.

To further confirm the effectiveness of the activation treatment, composite electrodes were subjected to electrochemical activation in KOH electrolytes of 1, 3, 5, and 7 M. The corresponding activation profiles are displayed in Figure S3. At the same time, post-activation CV (Figure 7a) and GCD (Figure 7b) tests of the four electrodes reveal a progressive enhancement in activation efficiency with increasing electrolyte concentration, reaching an optimum at 5 M and delivering 9.70 F cm^{-2} at 4 mA cm^{-2}. Further elevation to 7 M leads to a performance decline. The C_S values of the four electrodes at various discharge current densities are summarized in Figure 7c. These systematic results corroborate the validity of this strategy and elucidate its concentration-dependent behavior.

https://doi.org/10.3390/coatings16010113

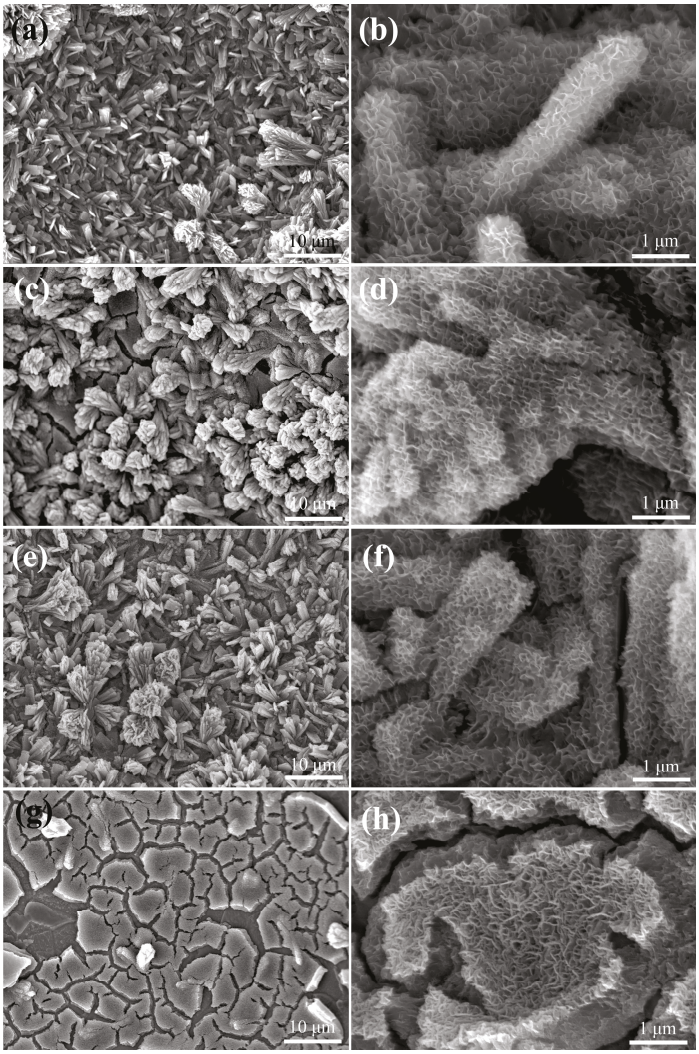

Figure 6. FE-SEM images of EA (ZnCo-LDH/NCS) electrodes activated in different KOH concentrations: (**a**,**b**) 1 M, (**c**,**d**) 3 M, (**e**,**f**) 5 M, and (**g**,**h**) 7 M.

To further clarify the influence of activation treatment on each component, single-component ZnCo-LDH and NCS electrodes and the ZnCo-LDH/NCS composite electrodes were compared after identical activation treatment in 5 M KOH; the activation profiles are displayed in Figure S4. Subsequent CV (Figure 8a) and GCD (Figure 8b) measurements of the three electrodes demonstrate that the composite electrode retains the most pronounced energy storage behavior, which is confirmed in Figure 8c. When the activation responses are evaluated individually, the ZnCo-LDH electrode exhibits a marked increase in current response, whereas the NCS electrode remains almost unchanged, as shown in Figure 9. These observations substantiate that the ZnCo-LDH component is the predominant contributor to the electrochemical activation process.

Figure 10a depicts the SEM image of hydrothermally grown ZnCo-LDH nanosheets after electrochemical activation. These dense nanosheets retain their original alignment on the NF substrate. At higher magnification, their surfaces appear extremely rough, as if short, thick filaments had been drawn out (Figure 10b). After NCS layer deposition (Figure 10c,d), the overall morphology closely matches that shown in Figure 6f.

https://doi.org/10.3390/coatings16010113

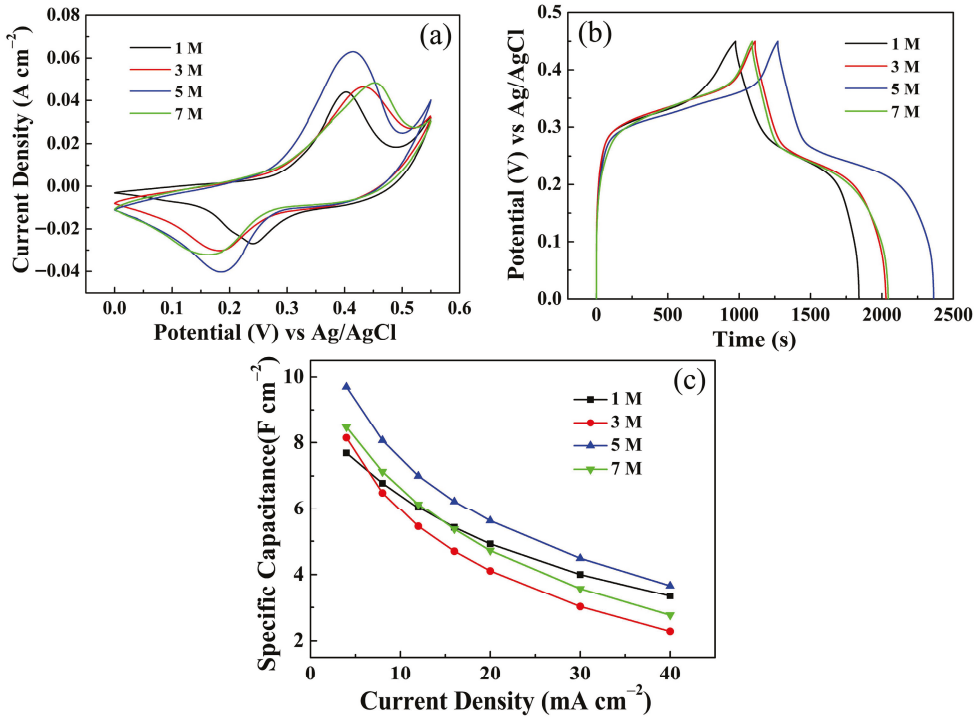

Figure 7. Comparison of the electrochemical performance of ZnCo-LDH/NCS electrodes activated with four different electrolyte concentrations: (**a**) CV curves; (**b**) GCD curves; (**c**) Cs at various current densities.

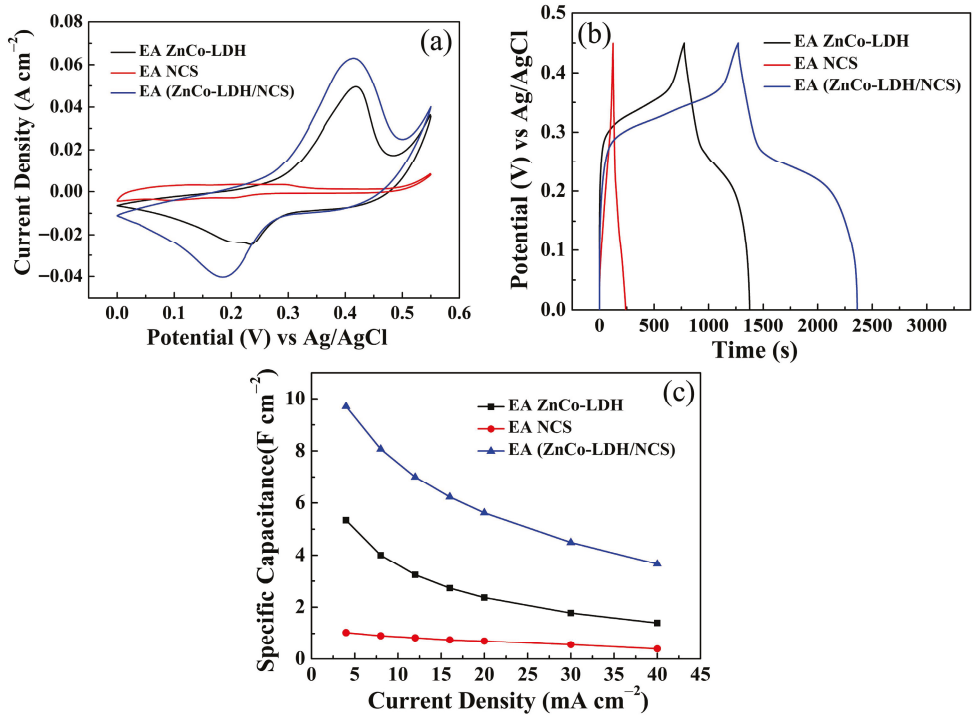

Figure 8. Electrochemical performance comparison of EA ZnCo-LDH, EA NCS, and EA (ZnCo-LDH/NCS) electrodes: (**a**) CV curves; (**b**) GCD curves; (**c**) Cs at various current densities.

Based on the preceding analysis, a ZnCo-LDH/NCS electrode in which only the ZnCo-LDH layer was electrochemically activated was fabricated and denoted EA ZnCo-LDH/NCS. Its energy storage performance was compared with that of the EA (ZnCo-LDH/NCS) electrode. Both CV (Figure 11a) and GCD (Figure 11b) data consistently reveal the superior characteristics of EA ZnCo-LDH/NCS, thus confirming that elec-

https://doi.org/10.3390/coatings16010113

trochemical activation of ZnCo-LDH provides the primary contribution to the specific capacity. In addition, the EIS spectra of the EA ZnCo-LDH, NCS, and EA ZnCo-LDH/NCS electrodes are compared in Figure S5. The results demonstrate that the *R*ct of the EA ZnCo-LDH/NCS composite electrode is smaller than that of the single-component EA ZnCo-LDH and NCS, confirming accelerated interfacial ion diffusion and thereby facilitating electrochemical reactions [20,21].

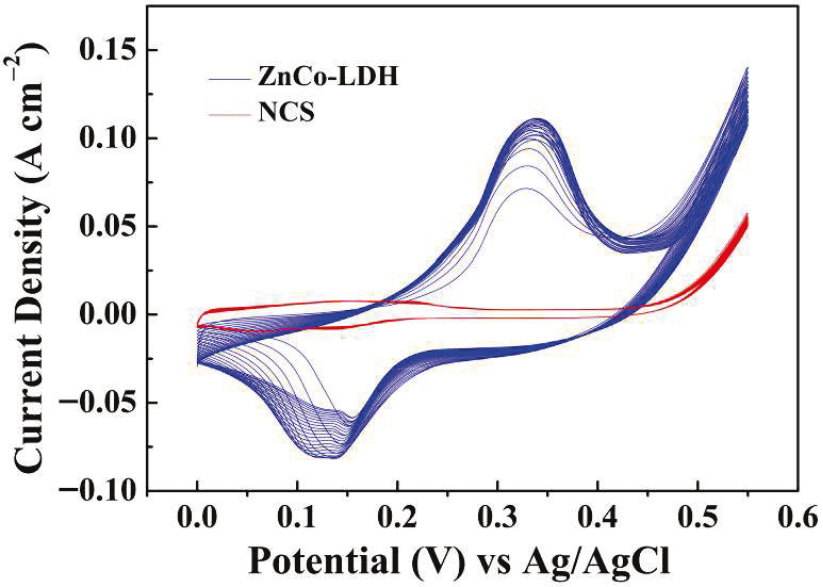

Figure 9. Electrochemical activation curves of ZnCo-LDH and NCS electrodes.

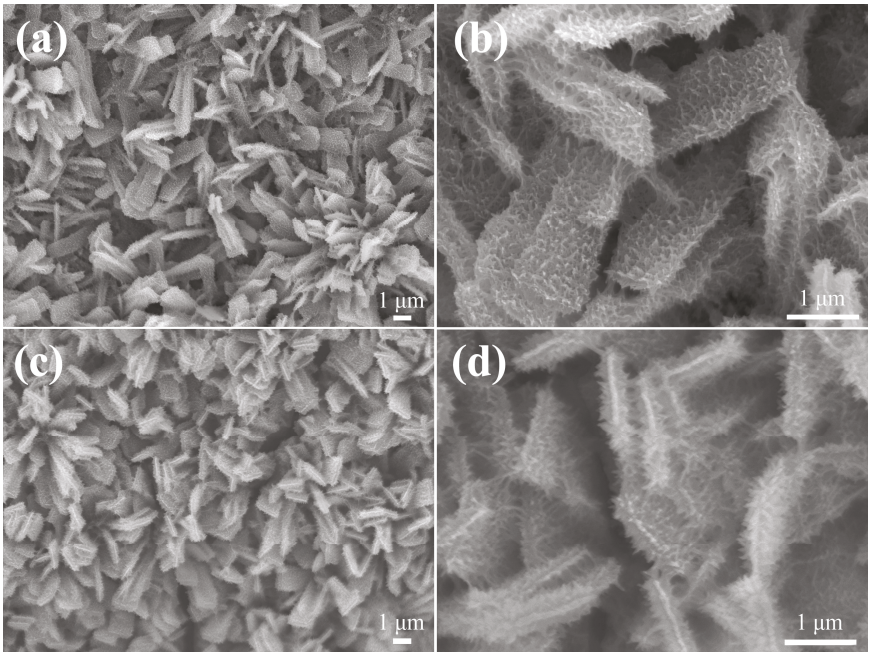

Figure 10. FE-SEM images of (**a**,**b**) EA ZnCo-LDH and (**c**,**d**) EA ZnCo-LDH/NCS electrodes at different magnifications.

Therefore, the energy storage characteristics of the EA ZnCo-LDH/NCS electrode were systematically investigated. Figure 12a presents the CV curves recorded at various scan rates. Within a potential window of 0–0.55 V, the profile of the CV response remained essentially unchanged. As the scan rate increased, the peak positions shifted toward the edges of the window and the absolute value of current response progressively increased.

https://doi.org/10.3390/coatings16010113

In fact, lower scan rates allow for more extensive contact between the electrochemically active sites and the OH^- in the electrolyte, thereby enabling a more complete electrochemical reaction [26]. The GCD curves recorded at various current densities are presented in Figure 12b. The results show that the electrode discharge time increases monotonically with decreasing current density. At a current density of 4 mA cm^{-2}, the discharge duration reaches 1281 s, yielding a high *C*s of 11.39 F cm^{-2} as calculated by the standard formula [27,28] (see Supplementary Materials). At 40 mA cm^{-2}, the discharge duration is 90 s and the *C*s is 7.99 F cm^{-2}. This suggests that, at lower current densities, the prolonged residence time of OH^- at the electrochemically active sites drives the redox reactions to completion, thereby enhancing charge storage utilization [29]. Figure 12c reveals the dependence of *C*s on current density. Upon a ten-fold increase in current density, the *C*s decays by only 29.85%. In addition, the voltage drop curve was plotted from the GCD test data, and the average R_{ESR} calculated using the inserted equation was 0.95 Ω cm^{-2} [24,27] (see Supplementary Materials).

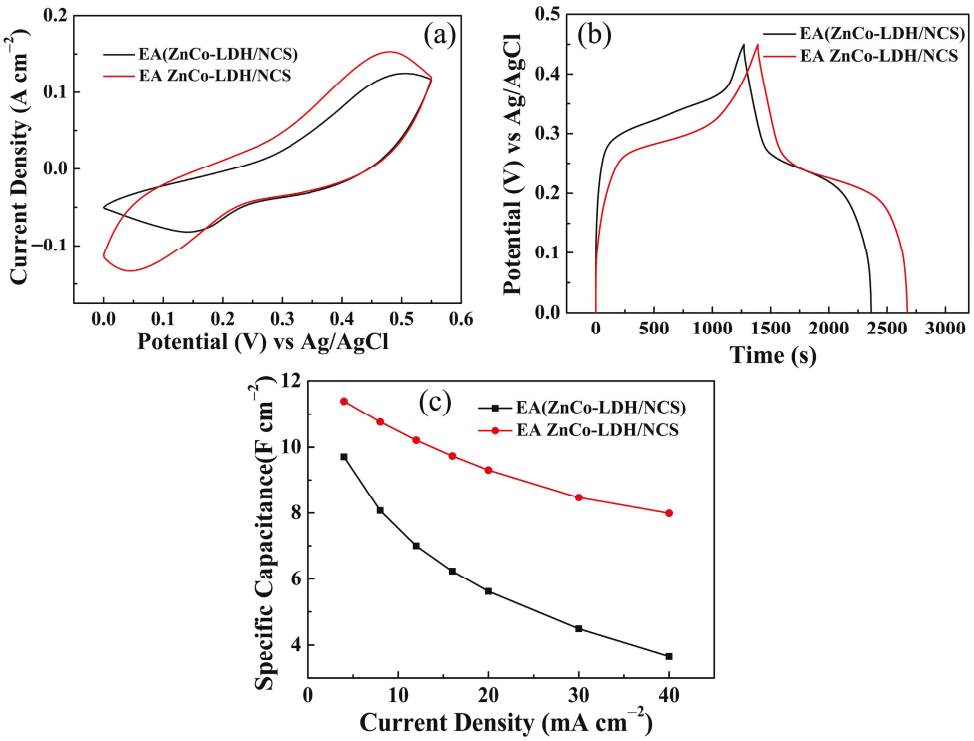

Figure 11. Electrochemical performance comparison of EA (ZnCo-LDH/NCS) and EA ZnCo-LDH/NCS electrodes: (**a**) CV curves; (**b**) GCD curves; (**c**) *C*s at various current densities.

Figure 13 depicts the long-term cycling stability of the EA ZnCo-LDH/NCS electrode evaluated over 5000 consecutive charge–discharge tests. After 2900 cycles, the Cs stabilizes at approximately 80.05% of its initial value and thereafter shows negligible further decay. The observed *C*s fade can be attributed to the partial irreversible internal structural collapse of the activated electrode during prolonged charge–discharge cycling, which reduces the accessible electrochemically active sites. The inset shows an SEM image of the EA ZnCo-LDH/NCS electrode after electrochemical testing, which confirms that the overall hierarchical structure remains essentially unchanged, although partial cross-linking is observed within the NCS layer.

https://doi.org/10.3390/coatings16010113

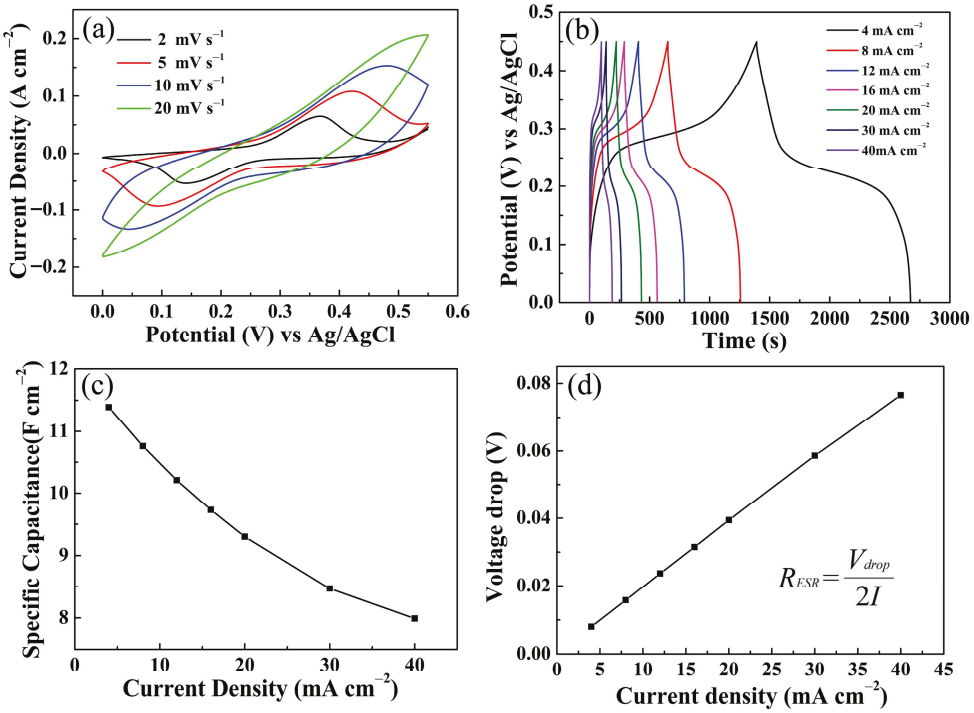

Figure 12. Electrochemical performance of EA ZnCo-LDH/NCS electrode: (**a**) CV curves; (**b**) GCD curves; (**c**) *Cs*; and (**d**) voltage drops at various current densities.

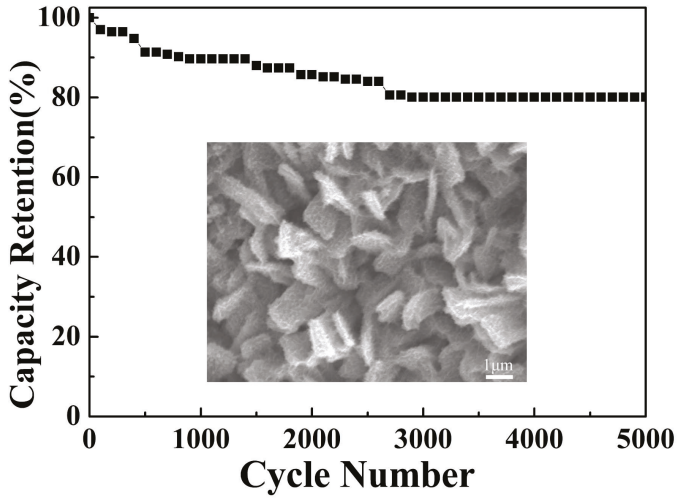

Figure 13. Cycling stability of the EA ZnCo-LDH/NCS electrode; the inset shows the post-test FE-SEM image.

Table 1 summarizes the test conditions and Cs values of representative electrodes reported in the literature. The EA-ZnCo-LDH/NCS electrode fabricated in this study demonstrates superior capacitive performance. This enhancement can be rationalized by the following aspects: (1) Expedient and precisely tunable fabrication. The hydrothermal synthesis step ensures the crystallinity and preferred orientation of ZnCo-LDH nanosheets, whereas the subsequent electrodeposition step allows precise, room-temperature tuning of the active-layer thickness and mass loading without the need for high-temperature annealing or polymeric binders [18,30,31]. (2) Compositional synergy. The partial substitution of Co by Zn to form the ZnCo-LDH electrode markedly reduces cobalt content and its inherent toxicity, while the dynamic dissolution–redeposition reconstruction mechanism of Zn in alkaline media continuously regenerates electrochemically active sites and thereby increases the Cs [11]. (3) Electrochemical activation that engenders lattice defects and cation

vacancies within the ZnCo-LDH framework synchronously optimizes the density of effective active sites and the ionic/electronic transport pathways, and thus markedly enhances the Cs and rate performance of the electrode [12,32–35]. (4) Activation efficacy was systematically evaluated by comparing the overall composite electrode under KOH concentrations of 1, 3, 5, and 7 M, while parallel tests were conducted on EA ZnCo-LDH and EA NCS electrodes. This systematic comparison established the optimal activation condition and corroborated that the synergistic combination of composite architecture and controlled electrochemical activation is essential for the observed performance enhancement.

Table 1. *C*s evaluation of representative electrodes.

Electrode	Substrate	Electrolyte	Current Density (mA cm^{-2})	*Cs* (F cm^{-2})	Ref.
$Co(OH)_2/Ni_3S_2$	Ni foam	2 M NaOH	2	5.73	[36]
$NiCo_2S_4$	Ni foam	3M KOH	5	8.1	[8]
$CoSe_2$@NiCo-LDH	Ni foam	KOH	6	6.06	[9]
Mn-doped Co_9S_8@$Co(OH)_2$	Ni foam	3 M KOH	1.5	5.62	[10]
Se–NiCoS	Ni foam	3 M KOH	1	2.00	[37]
NCS/CNT	Carbonized Wood	6 M KOH	5	8.62	[38]
Ni/Co-oxyhydroxides	carbon cloth	6 M KOH	5	8.87	[39]
NiCo-MOFs	Ni foam	1M KOH	1	5.84	[40]
Co@CPE	Pleurotus eryngii (PE)	6 M KOH	2	5.04	[41]
EA ZnCo-LDH/NCS	Ni foam	2 M NaOH	4	11.39	this work

4. Conclusions

In the present system, ZnCo-LDH was first grown in situ on NF substrates via a hydrothermal route, followed by electrodeposition of a NCS layer to yield the ZnCo-LDH/NCS composite electrode. On the one hand, ZnCo-LDH/NCS was electrochemically activated in electrolytes of different concentrations to obtain the EA (ZnCo-LDH/NCS) electrode. The impact of activation concentration was systematically compared and analyzed, and at 5 M, the electrode reached 9.70 F cm^{-2} at 4 mA cm^{-2}. On the other hand, the composite electrode obtained by depositing a NCS layer onto pre-electrochemically activated ZnCo-LDH, designated EA ZnCo-LDH/NCS, exhibited the most favorable energy storage performance, delivering a Cs of 11.39 F cm^{-2} at 4 mA cm^{-2} and retaining 80.05% of its initial capacity after 5000 cycles. This electrochemical activation strategy is readily extendable to the rational design of other hierarchical composite electrodes.

Supplementary Materials: The following supporting information can be downloaded at https://www.mdpi.com/article/10.3390/coatings16010113/s1. Figure S1: XRD patterns of ZnCo-LDH, EA ZnCo-LDH, and EA ZnCo-LDH/NCS. Figure S2: XPS spectra of Zn 2p for ZnCo-LDH electrode. Figure S3: Electrochemical activation curves of ZnCo-LDH/NCS electrode with four different electrolyte concentrations: (a) 1 M; (b) 3 M; (c) 5 M; (d) 7 M. Figure S4. Electrochemical activation curves of (a) ZnCo-LDH, (b) NCS, and (c) ZnCo-LDH/NCS electrodes. Figure S5. EIS spectra of EA ZnCo-LDH, NCS. and EA ZnCo-LDH/NCS electrodes; formula for calculating the *C*s and R_{ESR}.

Author Contributions: Conceptualization, H.W.; methodology, W.D.; software, S.W.; formal analysis, X.C.; investigation, Z.L., and Z.Z.; writing—original draft prepartion, Z.L.; writing—review and editing, S.L.; supervision, C.W.; funding acquisition, S.L. All authors have read and agreed to the published version of the manuscript.

Funding: This research was funded by The Scientific and Technology Development Project of Jilin Province, China (Grant No. YDZJ202501ZYTS326).

Institutional Review Board Statement: Not applicable.

Informed Consent Statement: Not applicable.

Data Availability Statement: The original contributions presented in this study are included in the article/Supplementary Materials. Further inquiries can be directed to the corresponding author.

Conflicts of Interest: The authors declare no conflicts of interest.

References

1. Ke, J.Q.; Zhang, Y.F.; Wen, Z.P.; Huang, S.; Ye, M.H.; Tang, Y.C.; Liu, X.Q.; Li, C.C. Designing strategies of advanced electrode materials for high-rate rechargeable batteries. *J. Mater. Chem. A* **2023**, *11*, 4428–4457. [CrossRef]
2. Liang, C.; Wang, S.Z.; Sha, S.Y.; Lv, S.Y.; Wang, G.D.; Wang, B.F.; Li, Q.B.; Yu, J.X.; Xu, X.G.; Zhang, L. Novel semiconductor materials for advanced supercapacitors. *J. Mater. Chem. C* **2023**, *11*, 4288–4317. [CrossRef]
3. Li, X.; Ren, J.N.; Sridhar, D.; Xu, B.B.; Algadi, H.; El-Bahy, Z.M.; Ma, Y.; Li, T.X.; Guo, Z.H. Progress of layered double hydroxide-based materials for supercapacitors. *Mater. Chem. Front.* **2023**, *7*, 1520–1561. [CrossRef]
4. Guo, J.H.; Feng, X.Q.; Wang, S.R.; Wu, Q.K.; Lv, S.S.; Zhou, Y.; Li, H.; Chen, Z.; Zhang, Y.Z. Facile synthesis of hexagonal α-$Co(OH)_2$ nanosheets and their superior activity in the selective reduction of nitro compounds. *Dalton Trans.* **2021**, *50*, 18061–18068.
5. Arishi, M. Morphologically engineered mixed metal oxides on carbon fibers as a binder-free electrode for diffusion capacitance-dominated hybrid supercapacitors. *Rare Metals* **2025**, *44*, 8548–8564.
6. Li, Z.L.; Ning, S.L.; Xu, J.C.; Zhu, J.M.; Yuan, Z.X.; Wu, Y.L.; Chen, J.; Xie, F.Y.; Jin, Y.S.; Wang, N.; et al. In situ electrochemical activation of $Co(OH)_2$@$Ni(OH)_2$ heterostructures for efficient ethanol electrooxidation reforming and innovative zinc-ethanol-air batteries. *Energy Environ. Sci.* **2022**, *15*, 5300–5312.
7. Xu, Z.H.; Li, X.L.; Li, Q.W.; Lv, K.; Liu, J.S.; Hang, X.K.; Bayaguud, A. Mechanism research progress on transition metal compound electrode materials for supercapacitors. *Rare Metals* **2024**, *43*, 4076–4098. [CrossRef]
8. Markhabayeva, A.A.; Anarova, A.S.; Abdullin, K.A.; Kalkozova, Z.K.; Tulegenova, A.T.; Nuraje, N. A hybrid supercapacitor from nickel cobalt sulfide and activated carbon for energy storage application. *Phys. Status Solidi RRL* **2024**, *18*, 2300211.
9. Gao, Y.; Jiang, Y.; Cai, B.; Gu, H.; Xu, R.X.; Sun, Y.X.; Zhou, J.W.; Yu, F. Growing magnetic NiCo-LDH nanosheets on the Ni@$CoSe_2$ surface to enhance energy storage capacity in asymmetric supercapacitors. *ACS Appl. Energy Mater.* **2025**, *8*, 1671–1682.
10. Zheng, L.; Ye, W.; Yang, P.; Song, J.; Shi, X.; Zheng, H. Manganese doping to boost the capacitance performance of hierarchical Co_9S_8@$Co(OH)_2$ nanosheet arrays. *Green Energy Environ.* **2022**, *7*, 1289–1297. [CrossRef]
11. Wang, C.W.; Han, L.; Yang, S.; Liu, Z.L.; Liu, M.; Li, B. Nanosheet-structured ZnCo-LDH microsphere as active material for rechargeable zinc batteries. *J. Colloid Interface Sci.* **2024**, *659*, 119–126.
12. Jiang, H.Y.; Wang, H.W.; Li, D.B.; Hong, X.D.; Wang, X.L. Electrochemical activation of Zn-doped NiCoO for improving the electrochemical performance. *J. Alloys Compd.* **2025**, *1026*, 180500.
13. Jadhav, S.L.; Jadhav, A.L.; Mandlekar, B.K.; Sarawade, P.B.; Kadam, A.V. Influence of deposition current and different electrolytes on charge storage performance of Co_3O_4 electrode material. *J. Phys. Chem. Solids* **2023**, *180*, 111422. [CrossRef]
14. Hong, X.D.; He, J.H.; Duan, C.X.; Wang, G.J.; Liang, B. Recent advance in electrochemically activated supercapacitors: Activation mechanisms, electrode materials and prospects. *Renew. Sust. Energy Rev.* **2025**, *209*, 115134.
15. Liu, G.C.; Song, X.Z.; Hao, Y.C.; Feng, Z.F.; Hu, R.Y.; Wang, X.F.; Meng, Y.L.; Tan, Z.Q. In situ growth and electrochemical activation of copper-based nickel-cobalt hydroxide for high-performance energy storage devices. *ACS Appl. Energy Mater.* **2021**, *4*, 9460–9469.
16. Deng, C.Y.; He, J.H.; Wang, G.J.; Hong, X.D.; Liang, B. Electrochemical activation of NiCo-hydroxysulfides in high-concentration KOH for constructing ultra-high capacitance electrodes. *Electrochim. Acta* **2023**, *463*, 142815.
17. He, J.H.; Deng, C.Y.; Wang, G.J.; Duan, C.X.; Hong, X.D.; Liang, B. Charge/discharge activation of CoS/NiMn-hydroxide composite for enhancing the electrochemical performance. *Ceram. Int.* **2023**, *49*, 38585–38592.
18. Wang, C.W.; Wu, W.L.; Zhao, C.H.; Liu, T.T.; Wang, L.; Zhu, J.F. Rational design of 2D/1D ZnCo-LDH hierarchical structure with high rate performance as advanced symmetric supercapacitors. *J. Colloid Interface Sci.* **2021**, *602*, 177–186. [PubMed]
19. Dai, M.Z.; Zhao, D.P.; Liu, H.Q.; Zhu, X.F.; Wu, X.; Wang, B. Nanohybridization of Ni-Co-S Nanosheets with $ZnCo_2O_4$ Nanowires as Supercapacitor Electrodes with Long Cycling Stabilities. *ACS Appl. Energy Mater.* **2021**, *4*, 2637–2643.
20. Vahedizadeh, F.; Moraveji, S.; Fotouhi, L.; Zirak, M.; Shahrokhian, S. Hierarchical core@shell ZnCo LDH@NiS_2 on nickel foam for high-performance asymmetric supercapacitors. *J. Energy Storage* **2024**, *94*, 112460. [CrossRef]
21. Xu, Z.Y.; Du, C.C.; Yang, H.K.; Huang, J.L.; Zhang, X.H.; Chen, J.H. NiCoP@CoS tree-like core-shell nanoarrays on nickel foam as battery-type electrodes for supercapacitors. *Chem. Eng. J.* **2021**, *421*, 127871. [CrossRef]

22. Anuratha, K.S.; Su, Y.Z.; Wang, P.J.; Hasin, P.; Wu, J.H.; Hsieh, C.K.; Chang, J.K.; Lin, J.Y. Free-standing 3D core-shell architecture of Ni_3S_2@NiCoP as an efficient cathode material for hybrid supercapacitors. *J. Colloid Interface Sci.* **2022**, *625*, 565–575.
23. Cong, Y.; Jiang, T.T.; Dai, Y.M.; Wu, X.F.; Lv, X.F.; Chen, M.T.; Ye, T.W.; Wu, Q. 3D network structure of $Co(OH)_2$ nanoflakes/Ag dendrites via a one-step electrodeposition for high-performance supercapacitors. *Mater. Res. Bull.* **2023**, *157*, 112013.
24. He, D.; Wan, J.N.; Liu, G.L.; Suo, H.; Zhao, C. Design and construction of hierarchical α-$Co(OH)_2$-coated ultra-thin ZnO flower nanostructures on nickel foam for high-performance supercapacitors. *J. Alloys Compd.* **2020**, *838*, 155556.
25. Ma, F.; Dai, X.Q.; Jin, J.; Tie, N.; Dai, Y.T. Hierarchical core-shell hollow $CoMoS_4$@Ni-Co-S nanotubes hybrid arrays as advanced electrode material for supercapacitors. *Electrochim. Acta* **2020**, *331*, 135459. [CrossRef]
26. Wang, L.; You, J.H.; Zhao, Y.; Bao, W.T. Core-shell CuO@NiCoMn-LDH supported by copper foam for high-performance supercapacitors. *Dalton Trans.* **2022**, *51*, 3314–3322. [PubMed]
27. Liu, G.L.; He, X.; He, D.; Cui, B.Y.; Zhu, L.; Suo, H.; Zhao, C. Construction of CuO@Ni-Fe layered double hydroxide hierarchical core-shell nanorod arrays on copper foam for high-performance supercapacitors. *J. Mater. Sci. Mater. Electron.* **2019**, *30*, 2080–2088.
28. Tan, Z.C.; Fan, J.C.; Huang, T.; Hu, R.S.; Fang, Y.F.; Liu, H.O.; Luo, W.B.; Chao, Z.S. Asymmetric supercapacitors based on Co_9S_8–ZnCo-layered double hydroxide nanocomposite electrodes. *ACS Appl. Nano Mater.* **2024**, *7*, 21617–21627. [CrossRef]
29. Chen, J.M.; Zhang, H.L.; Peng, X.; Shao, X.; Chai, Y.F.; Ma, M.; Li, Z.L.; Liu, S.D.; Ding, B. Heterostructure engineering of transition metal dichalcogenides for high-performance supercapacitors. *Rare Metals* **2025**, *44*, 8198–8236. [CrossRef]
30. Fang, Z.; Peng, C.; Zhou, Q.L.; Liu, Z. Electrocatalytic hydrogen peroxide production: Advances, challenges and future perspectives. *Chem. Rec.* **2025**, *25*, e202500066. [CrossRef] [PubMed]
31. Chen, Q.; Zuo, H.C.; Wang, H.; Chen, S. Rapid room-temperature synthesis of porous sulfur-doped nickel-chromium-layered double hydroxide for oxygen evolution catalysis in seawater splitting. *Int. J. Electrochem. Sci.* **2023**, *18*, 100402. [CrossRef]
32. Zhang, G.N.; Wu, X.Y.; Xu, Y.H.; Cao, Y.Y.; Luo, Y.Y.; Yang, H.J.; Wang, J.J.; Li, W.B.; Li, X.F. Modulating electronic and interface structure of CuO/CoNi-LDH via electrochemical activation for high areal-performance supercapacitors. *J. Energy Storage* **2024**, *83*, 110426. [CrossRef]
33. Yan, J.; Cen, M.X.; Guo, Y.B.; Wang, B.Y.; Tian, Y.; Song, Z.L.; Peng, X.S.; Lian, J.B.; Ng, D.H.L. Highly sulfur-doped porous carbon enhances sodium-ion storage with superior rate capability and long cycling stability. *J. Mater. Sci.* **2025**, *60*, 19883–19895. [CrossRef]
34. Li, J.M.; Chang, L.H.; Chen, B.M.; Huang, H.; Guo, Z.C. Electrochemistry behavior and corrosion resistance of Al-Mn alloy prepared by recovering 1070-Al and Al-Mn alloys in $ZnSO_4$ solutions. *Int. J. Electrochem. Sci.* **2023**, *18*, 45–52.
35. Song, L.; Zhong, X.H.; Wang, F.L.; Huang, Z.H.; Hong, Z.; Gao, Y.F.; Wang, H.D.; Ren, J.W.; Peng, S.J.; Li, L. Convenient room-temperature synthesis of sulfur and nitrogen co-doped NiCo-LDH coupled with CNTs on NiCo foam as battery-type electrode for high performance hybrid supercapacitor. *Rare Metals* **2024**, *43*, 4286–4301.
36. Lv, S.; Shang, W.S.; Chi, Y.D.; Wang, H.; Chu, X.F.; Geng, P.Y.; Wang, C.; Yang, J.; Cheng, Z.F.; Yang, X.T. Hierarchical Design of $Co(OH)_2/Ni_3S_2$ Heterostructure on Nickel Foam for Energy Storage. *Processes* **2022**, *10*, 1255. [CrossRef]
37. Zhou, A.; Chi, R.T.; Liu, R.; Shi, Y.J.; Zhang, Z.X.; Che, H.W.; Wang, G.S.; Mu, J.B.; Wang, Y.M.; Zhang, X.R. Se-doped nickel-cobalt sulfide nanotube arrays with 3D networks for high-performance hybrid supercapacitor. *Ceram. Int.* **2022**, *48*, 30536–30545.
38. Wang, X.; Deng, Y.; Wang, Z.; Li, Z.; Wang, L.; Ouyang, J.; Zhou, C.; Luo, Y. Sophora-like nickel–cobalt sulfide and carbon nanotube composites in carbonized wood slice electrodes for all-solid-state supercapacitors. *ACS Appl. Energy Mater.* **2022**, *5*, 7400–7407.
39. Pan, M.H.; Zeng, W.L.; Quan, H.Y.; Cui, J.M.; Guo, Y.; Wang, Y.Y.; Chen, D.Z. Low-crystalline Ni/Co-oxyhydroxides nanoarrays on carbon cloth with high mass loading and hierarchical structure as cathode for supercapacitors. *Electrochim. Acta* **2020**, *357*, 136886. [CrossRef]
40. Huang, S.; Shi, X.-R.; Sun, C.; Zhang, X.; Huang, M.; Liu, R.; Wang, H.; Xu, S. Template-controlled in-situ growing of NiCo-MOF nanosheets on Ni foam with mixed linkers for high performance asymmetric supercapacitors. *Appl. Surf. Sci.* **2022**, *572*, 151344. [CrossRef]
41. Wei, Z.; Zhang, Z.; Wang, F.; Min, S. Monolithic porous carbon membrane-based hybrid electrodes with ultrahigh mass loading carbon-encapsulated Co nanoparticles for high-performance supercapacitors. *New J. Chem.* **2024**, *48*, 3403. [CrossRef]

Disclaimer/Publisher's Note: The statements, opinions and data contained in all publications are solely those of the individual author(s) and contributor(s) and not of MDPI and/or the editor(s). MDPI and/or the editor(s) disclaim responsibility for any injury to people or property resulting from any ideas, methods, instructions or products referred to in the content.

coatings

MDPI

Article

Analysis of Failure Characteristics and Mechanisms of Asphalt Pavements for Municipal Landscape Roads

Lei Zhang [1,*], Xinxin Cao [2], Xuefeng Mei [3], Xinhui Fu [1] and Huanhuan Zhang [1]

[1] School of Horticulture and Landscape Architecture, Fujian Vocational College of Agriculture, Fuzhou 350007, China; 13003833143@163.com (X.F.); 19862533143@163.com (H.Z.)
[2] Department of Road and Urban Railway Engineering, Beijing University of Technology, Beijing 100124, China; caoxinxin@sdut.edu.cn
[3] College of Civil Engineering, Inner Mongolia University of Science and Technology, Baotou 014010, China; xfmei@my.swjtu.edu.cn
* Correspondence: t1778456358@163.com

Abstract

With the acceleration of urbanization, municipal landscape roads play a crucial role in urban public spaces. This study focuses on the distress detection and aging characteristics of asphalt pavements in municipal landscape roads. Firstly, a novel method is proposed based on the SpA-Former shadow removal network, which effectively addresses the interference caused by tree shadows and significantly improves the accuracy of automated distress identification. Distress detection results indicate that transverse cracks are the most common type of distress, primarily influenced by environmental factors such as asphalt material aging, temperature fluctuations, and freeze-thaw cycles—these factors induce asphalt embrittlement and a substantial decline in crack resistance. Subsequently, accelerated aging experiments were conducted to simulate the aging process of asphalt materials. It was found that as aging time extends, asphalt stiffness increases significantly; while this enhances deformation resistance, it also makes the material more prone to cracking under low-temperature conditions. Low-temperature crack resistance tests reveal that asphalt aged for more than six years exhibits a sharp deterioration in low-temperature crack resistance, showing distinct brittle characteristics. Furthermore, freeze-thaw cycle experiments demonstrate that the coupling effect of asphalt aging and freeze-thaw action significantly impairs its freeze-thaw resistance—particularly for asphalt aged over six years, which nearly loses its freeze-thaw resistance. In summary, the coupling effect of asphalt aging and environmental factors is the primary cause of pavement damage in municipal landscape roads. This study divides 2542 images into three mutually exclusive subsets: a training set of 2123 images, a validation set of 209 images, and a test set of 210 images. The research provides new theoretical references and technical support for the maintenance and management of landscape roads, especially demonstrating practical significance in distress detection and the analysis of material aging mechanisms.

Keywords: municipal landscape roads; distress detection; transverse cracks; asphalt aging; environmental factors

1. Introduction

With the deepening of urbanization, municipal landscape roads, as an important component of urban public spaces, have seen their functional orientation shift from traditional

traffic bearing to a focus dominated by ecology, aesthetics, and recreation [1]. Fundamentally different from conventional vehicular roads, landscape roads primarily serve pedestrians and slow-moving traffic, and are almost free from the repeated action of vehicle loads. This distinct characteristic leads to an essential difference in failure modes and causative mechanisms compared to conventional roads: the occurrence and development of distresses in landscape roads are primarily governed by the coupling effects of material aging and complex environmental factors, rather than traditional fatigue damage [2].

However, this very ecological and aesthetic positioning paradoxically presents severe challenges to their long-term durability. The dense trees lining the roads, while creating a pleasant environment, also produce extensive dynamic and dappled shadows that severely interfere with the automated detection of surface distresses based on machine vision [3]. The uneven illumination, reduced contrast, and feature occlusion caused by shadows lead to a sharp decline in the accuracy of traditional image processing algorithms and general deep learning models, resulting in numerous missed detections and false positives [4]. Research indicates that variations in lighting conditions, particularly the presence of shadowed areas, significantly impact color fidelity and feature discernibility in images, thereby reducing the reliability of distress recognition systems [5]. For instance, Tedeschi et al. developed a real-time automatic crack and pothole recognition system for Android devices utilizing the OpenCV library for image processing, yet it did not adequately account for the disruptive effects of shadows [6]. This issue forces maintenance management to still rely on inefficient and subjective manual inspections, becoming a bottleneck for achieving intelligent maintenance.

Regarding shadow processing, although numerous image enhancement and specialized shadow removal algorithms (such as ST-CGAN and DC-ShadowNet) exist, they are primarily designed for natural scenes or satellite imagery. These methods often lack sufficient specificity for the distinctive low-illumination textures created by leaf gaps in landscape roads. Furthermore, their multi-stage workflows are prone to error accumulation, making it challenging to meet the accuracy and efficiency requirements for engineering-grade applications [7]. Duan et al. proposed a shadow-aware image colorization method that pays particular attention to the accuracy of shadow areas, which is significant for identifying pavement distress under complex lighting conditions [5]. Therefore, developing an end-to-end shadow removal method capable of effectively handling complex tree shadow interference has become a crucial prerequisite for enhancing the accuracy of distress identification in landscape roads.

In recent years, deep learning technologies have achieved remarkable progress in pavement distress identification. Lv et al. designed a pavement distress recognition model based on Mask R-CNN, which achieved a test accuracy of 99% on different datasets [8]. Sheng et al. proposed an improved model named SMG-YOLOv8 based on the YOLOv8s framework; this model demonstrated excellent performance in recognizing multiple types of pavement distress, particularly under varying lighting conditions [9]. Generative Adversarial Networks (GANs) have also been applied to pavement distress recognition. Liu et al. introduced a GAN-based data augmentation algorithm incorporating a self-attention mechanism, which effectively mitigates the blurring artifacts that can occur during the training of traditional DCGANs [4]. Boateng et al. developed the PaveGAN method, which achieves real-time pavement distress recognition and pixel-level annotation, with a recognition accuracy of 84% under different illumination conditions [10]. Furthermore, Light Detection and Ranging (LiDAR) technology offers a novel solution for distress identification. Khan et al. utilized LiDAR data to generate Digital Elevation Models (DEMs) and hill-shade maps for identifying and assessing pavement distresses [11].

https://doi.org/10.3390/coatings16010028

While computer vision technologies have made significant strides in pavement inspection, their application in municipal landscape roads faces unique challenges due to the specific environmental conditions. More critically, in the absence of vehicular fatigue factors, material aging and environmental erosion emerge as the dominant mechanisms leading to performance deterioration [12]. These landscape roads are consistently exposed to a particular microenvironment characterized by abundant moisture and significant fluctuations in temperature and humidity. Persistent factors such as freeze-thaw cycles, moisture variations from root systems, and ultraviolet radiation constitute the primary threats to their long-term durability [13]. Research by Goli et al. indicated that moisture intrusion significantly accelerates the fatigue and cracking behavior of Warm Mix Asphalt (WMA) containing Reclaimed Asphalt Pavement (RAP) [14]. Furthermore, Jiang et al., utilizing digital image processing techniques, analyzed the cracking behavior of asphalt concrete pavements under different temperature conditions, revealing the considerable impact of temperature fluctuations on pavement performance [15].

Preliminary investigations indicate that transverse cracks represent the most prevalent and typical distress form in such roads. While it is generally speculated that their causes are related to thermal stress and reflection from the base layer, systematic experimental evidence remains scarce [16]. Krami et al. employed electrical resistivity tomography to study the environmental factors influencing asphalt pavement cracking on different road sections in Morocco, finding that the winter season significantly affects soil resistivity and asphalt pavement cracking [17]. Particularly, the intrinsic mechanisms through which the aging behavior of asphalt binder over prolonged service leads to a transition from flexibility to brittleness, and how this aging synergistically interacts with environmental factors in this specific context to ultimately accelerate cracking and failure, remains a significant gap in current research [18].

Zhang et al. investigated the impact of climate change on fatigue cracking in road asphalt pavements, revealing that temperature fluctuations and the migration of freeze-thaw zones significantly influence fatigue cracking [19]. Furthermore, Rys et al., through field investigations, analyzed factors affecting low-temperature cracking of pavements and found that asphalt aging and environmental factors such as temperature variations have a pronounced effect [2]. In a review of low-temperature cracking and its mitigation methods for asphalt pavements in cold regions, Ma et al. also highlighted the significant impact of asphalt aging and environmental factors like temperature changes [20]. While these studies provide crucial references for further elucidating the distress mechanisms in landscape roads, there remains a lack of in-depth, systematic analysis dedicated to the pure aging-environment coupling mechanism under traffic-free conditions.

Therefore, this study aims to conduct a systematic investigation of municipal landscape roads as non-load-bearing facilities, progressing from a "breakthrough in intelligent surface detection technology" to an "in-depth analysis of the intrinsic aging-environment coupling mechanism." First, an end-to-end shadow removal network, capable of efficiently handling complex tree-shadow scenarios, will be developed to overcome the primary obstacle for accurate distress identification. Subsequently, based on high-precision detection results, the types and spatial distribution characteristics of distresses will be statistically analyzed to identify the predominant failure modes. Finally, by simulating various aging states of the material and systematically testing its performance evolution patterns under simulated service environments (e.g., freeze-thaw cycles, moisture-thermal conditions), this research seeks to fundamentally elucidate the initiation and progression mechanisms of characteristic distresses dominated by environmental aging. The findings are expected to provide a theoretical foundation and technical support for the scientific design, precise maintenance, and long-term management of these pavements. The research is helpful

https://doi.org/10.3390/coatings16010028

for clarifying the causes of cracking in non-load-bearing pavements and guiding efforts to extend pavement service life, which can conserve construction resources and reduce carbon emissions.

2. Research Methods

2.1. Pavement Distress Data Collection and Preprocessing

This study employed an automated detection vehicle equipped with a standardized mobile measurement system for pavement image collection on municipal landscape roads. All pavement image data were collected from a landscape road in Weifang, Shandong Province, China. This region has a mean annual temperature of approximately 12.5 °C and an average annual precipitation of 600–800 mm, characteristic of a temperate monsoon climate. The road is located in a plain area, and data collection was conducted during autumn. Autumn is marked by significant diurnal temperature variations and a high incidence of cracking. Further analysis of pavement distress characteristics in other seasons is required in future studies. A global shutter industrial camera (e.g., Daheng Imaging MER2-1220-32U3M, Beijing, China) was mounted inside the windshield at a height of approximately 1.5 m above ground, with a lens depression angle of about 15 degrees, ensuring a stable and clear field of view covering the road surface 5–7 m ahead. Data acquisition was conducted over a total distance of approximately 10 km, spanning multiple independent road segments to ensure diversity. To minimize interference from traffic and achieve consistent lighting conditions, collection was scheduled on weekdays during spring and early summer, specifically between 9:00–11:00 a.m. and 2:00–4:00 p.m., resulting in 2542 valid distress images with a resolution of 1920 × 1080 pixels.

To address challenges inherent to landscape roads, such as uneven illumination, shadows, and complex textures, the original images underwent a standardized preprocessing pipeline. This included histogram equalization, brightness normalization, and noise filtering to enhance overall image quality and feature consistency, as illustrated in Figure 1.

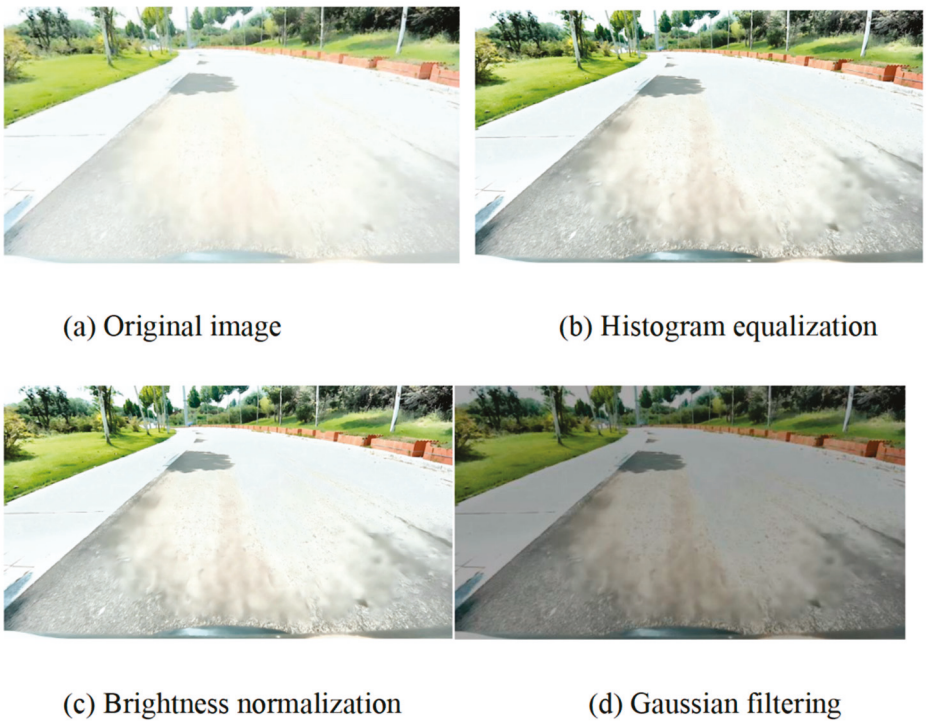

Figure 1. The standardized preprocessing pipeline.

A detailed annotation protocol was established, defining four major distress types: longitudinal cracks, transverse cracks, alligator cracks, and potholes. Three trained annotators then independently performed pixel-level mask annotation using the Labelme tool. To ensure label quality and consistency, 10% of the images (254 images) were co-annotated by all annotators. The inter-annotator agreement, measured by the mean Intersection over Union (mIoU), exceeded 0.85, demonstrating high annotation reliability. All annotations were subsequently reviewed and refined by an expert.

To ensure a statistically robust evaluation of model performance, this study adopted a stratified data partitioning strategy instead of a simple random split. The entire dataset of 2542 images was divided into three mutually exclusive subsets: a training set containing 2123 images for model optimization, a validation set of 209 images for hyperparameter tuning, and a final test set of 210 images for unbiased performance evaluation. This rigorous partitioning maximizes data utility while guaranteeing the fairness of the evaluation and the reliability of the conclusions.

To tackle the problem of tree shadow interference, the SpA-Former end-to-end shadow detection and removal network was employed to process all 2542 valid images. This network integrates shadow detection and removal into a single stage, eliminating the need for separate detection steps or post-processing adjustments [21]. The specific workflow is illustrated in Figure 2 and detailed as follows:

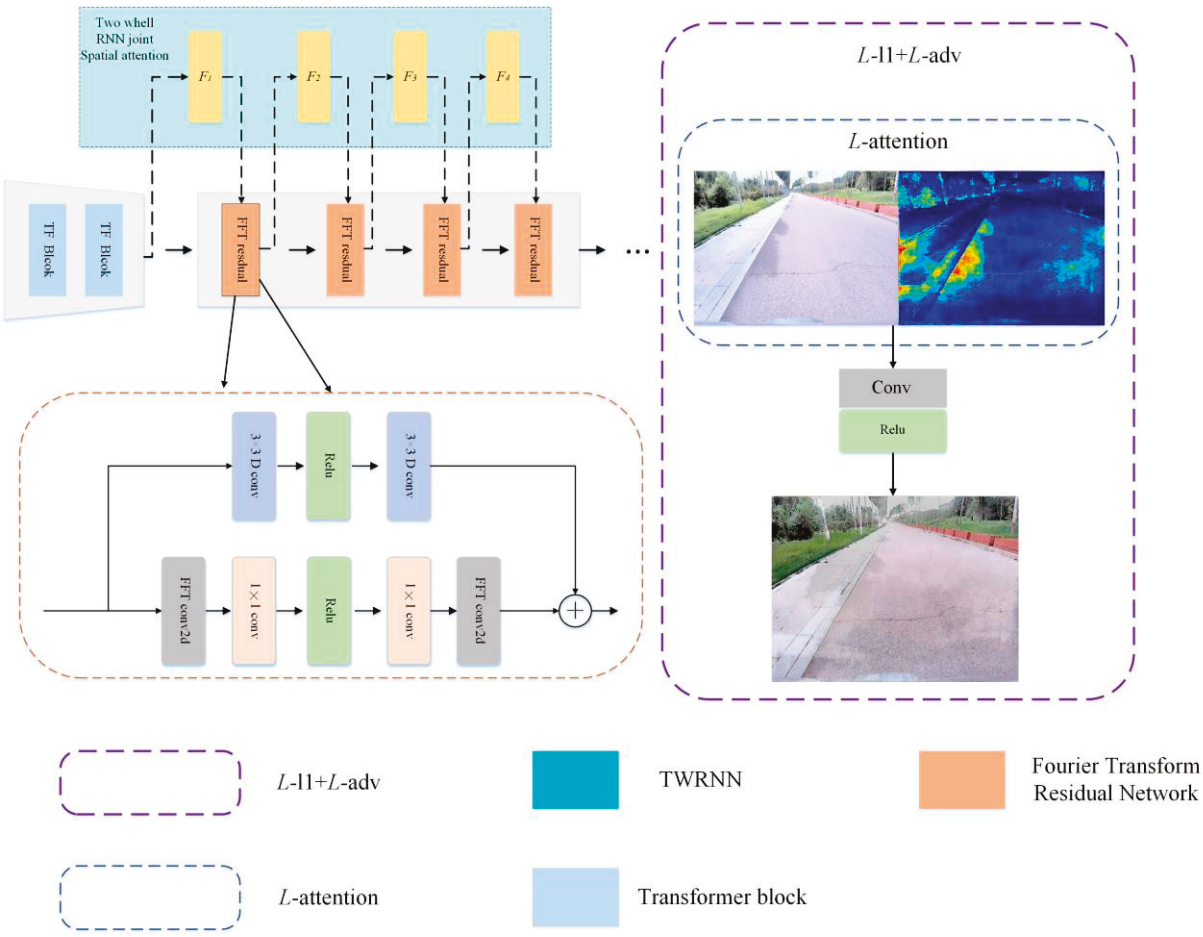

Figure 2. Flowchart of tree shadow interference removal via SpA-Former.

Image Patching and Encoding: The original 1920 × 1080-pixel images were resized to 640 × 480 pixels (with the original scale restored during the inference stage) and segmented into 160 × 120 non-overlapping patches using a 4 × 4 convolution operation with a stride

of 4. Each patch was then transformed into a 768-dimensional token via linear projection. Learnable absolute positional encodings were incorporated into these tokens to inject spatial information. Concurrently, at the patch level, internal multi-layer transformations were applied to adaptively correct low-order illumination variations caused by tree shadows, thereby mitigating the interference of redundant low-frequency information on subsequent feature computation.

Global Feature Extraction via Transformer Encoder: The Transformer encoder layer in SpA-Former plays a critical role in capturing long-range dependencies within the image by leveraging the self-attention mechanism to model global information. By dividing the image into patches and converting them into a sequence, the encoder computes relationships between different image regions, effectively integrating contextual information. This global modeling capability is essential for understanding the complex relationships between shadowed areas and normally lit surrounding regions, aiding the network in maintaining overall image consistency and semantic coherence during the shadow removal process. SpA-Former employs an 8-layer Transformer encoder to progressively refine the token sequence. Each layer first applies layer normalization, followed by 16-head self-attention that computes global contextual relationships. Through the scaled dot-product attention mechanism, each token interacts with all other tokens in the sequence, efficiently establishing a global receptive field and capturing complex correspondences between shadowed regions and normally illuminated areas across the entire image. The feed-forward network (FFN) uses a GELU activation function, initially expanding the dimension from 768 to 3072 before projecting it back to 768. Residual connections are incorporated to stabilize the training process, ensuring effective propagation of global illumination and semantic information. This process establishes a "whole-image" level prior without requiring downsampling, enabling the network to consistently perceive the correspondence between shadowed regions and distant normally lit areas.

Multi-Domain Fusion with Joint Fourier Transform Residual Block: The 160 $\times$ 120 $\times$ 768 feature maps output by the encoder are processed in parallel along three distinct pathways: ① Spatial Domain Path: A spatial 3 $\times$ 3 depthwise separable convolution extracts local features such as pavement crack edges. ② Frequency Domain Path: The features are transformed into the frequency domain via a Fast Fourier Transform (FFT). A learnable, point-wise multiplication is applied to the low-frequency components to correct global color casts caused by shadows. ③ Frequency Refinement Path: The frequency representation is decomposed into magnitude and phase components. Each is modulated using 1 $\times$ 1 convolutions before being transformed back to the spatial domain via an Inverse FFT (IFFT), thereby enhancing high-frequency information related to pavement textures, such as potholes. The outputs from these three paths are fused using learnable weights. The combined features are subsequently recalibrated by a Squeeze-and-Excitation (SE) channel attention mechanism to emphasize the most informative channels. This design achieves multi-scale coupling between the spatial and frequency domains, enabling precise shadow removal while completely preserving critical distress details.

Dual-Round Joint Spatial Attention Optimization and Decoder Output: In the first round, max-average pooling is applied along the channel axis, followed by a 7 $\times$ 7 grouped convolution to generate an initial shadow confidence map. In the second round, the feature map is divided into 8 $\times$ 8 windows, and the inter-pixel covariance matrix within each window is computed. A lightweight Transformer block is then employed to perform non-local similarity matching between shadow edges and adjacent normally lit regions. The attention maps from both rounds are multiplied element-wise to produce a fine-grained shadow mask. This mask is used to perform channel-wise multiplication and addition with the original features, thereby amplifying illumination discrepancy features in shadowed

https://doi.org/10.3390/coatings16010028

areas. Finally, a 4-stage residual decoder with upsampling restores the spatial resolution to 256 × 256. A 1 × 1 convolutional layer at the network output predicts a residual image containing the required illumination and color corrections. This residual is added pixel-wise to the original input image to generate the final shadow-free image. The entire network is trained under a joint loss function combining L1 loss, VGG perceptual loss, and FFT consistency loss. During inference, only a single forward pass is required for processing. The proposed method achieves a shadow removal rate of over 98% on processed images, with a 40%–60% improvement in grayscale contrast within distress regions.

Model Implementation and Training Details: Since obtaining pixel-aligned pairs of shadowed and shadow-free images in real-world scenarios is challenging, we constructed a synthetic dataset for training by selecting 200 high-quality, shadow-free pavement images from the collected dataset to serve as ground truth. To simulate realistic tree shadows, irregular shadow masks were generated using Perlin noise to mimic the complexity of leaf gaps and branch structures, which were then superimposed onto the clean images using a linear illumination decay model to create paired input data. The model was implemented in PyTorch(version 2.0.1) and trained on a workstation equipped with a single NVIDIA RTX 4060 GPU, utilizing the AdamW optimizer with a batch size of 4 and an initial learning rate of 1×10^{-4} for 100 epochs, with loss weight coefficients set to $\lambda_1 = 1.0$, $\lambda_{\text{per}} = 0.1$, and $\lambda_{\text{fft}} = 0.05$. To quantitatively evaluate the performance, we defined the "shadow removal rate" (η) based on the reduction of the Root Mean Square Error (RMSE) between the shadow regions of the output and the ground truth, calculated as $\eta = (1 - \frac{\text{RMSE}_{\text{output}}}{\text{RMSE}_{\text{input}}}) \times 100\%$, achieving an average rate of over 98%. Furthermore, to address the concern of false positive removal (i.e., erroneously erasing real distress features), we computed the Structural Similarity Index (SSIM) specifically within the distress regions; the resulting high SSIM score (>0.92) confirms that the topological structure and texture details of the pavement cracks are effectively preserved while only the illumination inconsistency is removed, as visually demonstrated in Figure 3.

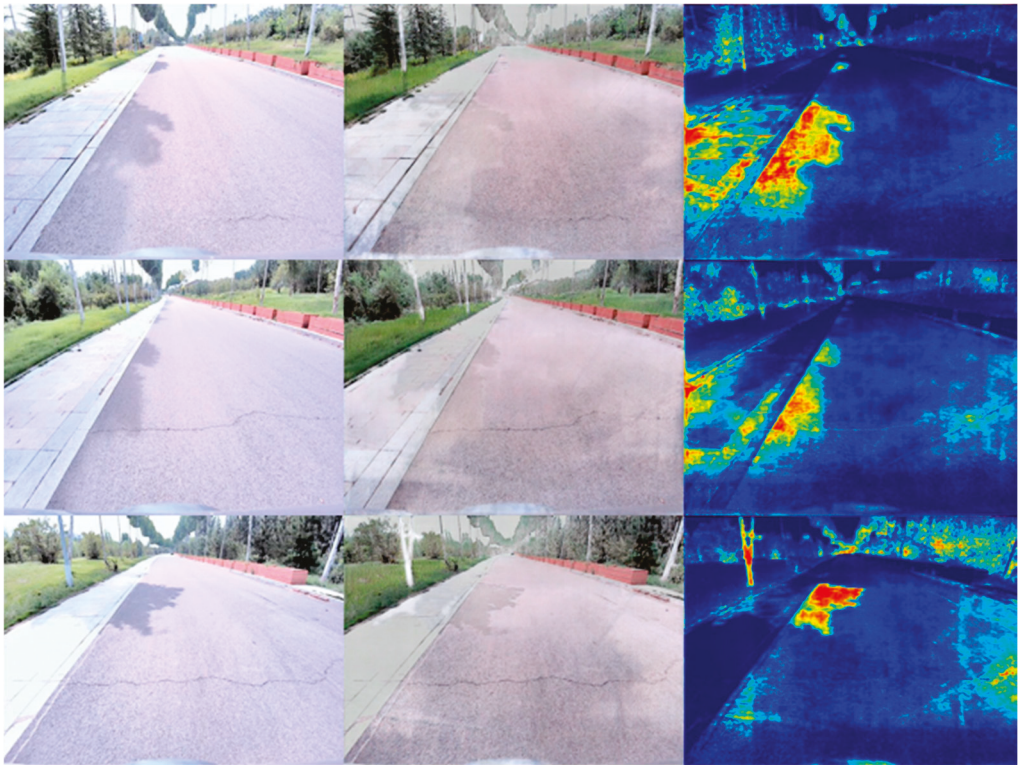

Figure 3. Shadow removal results using the proposed SpA-Former network.

https://doi.org/10.3390/coatings16010028

2.2. Pavement Distress Identification Methods

A dataset for asphalt pavement distress identification was constructed from 2542 original images. To ensure rigorous evaluation, these images were stratified into a training set (2123 images), a validation set (209 images), and a test set (210 images). All images were annotated using the Labelme tool, focusing on crack types and potholes. To ensure the reliability of the ground truth, 10% of the data was cross-annotated, achieving a mean Intersection over Union (mIoU) of over 0.85 among annotators. Sample annotations of the targeted distress characteristics are illustrated in Figure 4.



Figure 4. Illustrates sample annotations of the targeted distress characteristics.

YOLOv8-seg is an instance segmentation model developed based on the YOLOv8 framework. According to the depth and width of the model, it can be divided into five scale variants: n, s, m, l, and x. The number of parameters in these five scales increases sequentially. Users can select the optimal model according to specific application scenarios. The YOLOv8-seg algorithm consists of five components: input preprocessing, backbone network, feature fusion network (neck), prediction head, and postprocessing [22]. The original image is first preprocessed to obtain the model input image. The role of the backbone network is to extract features at different scales from the input image. The feature fusion network then integrates the multi-scale features extracted by the backbone to produce three final feature maps used for prediction. Subsequently, the prediction head utilizes these three sets of multi-scale features from the fusion network to generate prediction results at their respective scales. Finally, during postprocessing, the results from multiple scales are restored to the original image dimensions, and redundant predictions are eliminated using the Non-Maximum Suppression (NMS) algorithm.

The attention mechanism is a widely used method for enhancing the performance of convolutional neural networks (CNNs). Conventional models often process a substantial amount of redundant information during feature extraction, which reduces feature effectiveness and creates performance bottlenecks. Introducing an attention mechanism at appropriate locations within the model enables it to focus on more critical information for recognition from the vast feature information, thereby improving the effectiveness of feature extraction and overcoming these performance limitations. In recent years, the Convolutional Block Attention Module (CBAM) has been extensively adopted by researchers due to its high efficiency. The core of CBAM consists of two sequential sub-modules: channel attention and spatial attention. The input features pass through these modules successively, which recalibrate the feature map by emphasizing informative features along the channel and spatial dimensions, respectively [23]. A schematic diagram of the CBAM structure is shown in Figure 5.

https://doi.org/10.3390/coatings16010028

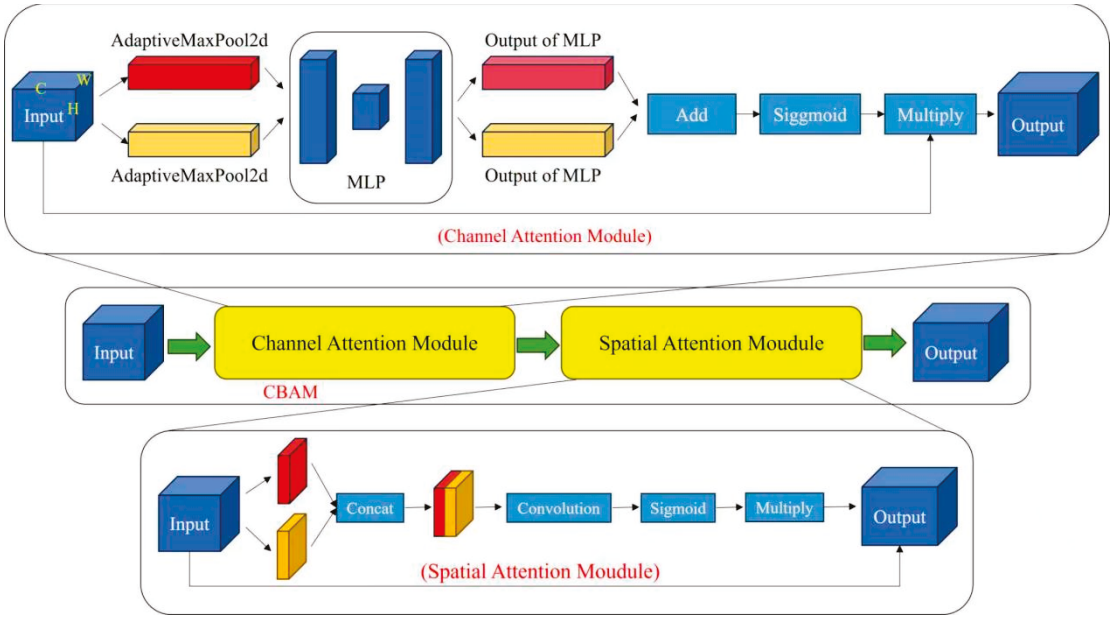

Figure 5. Schematic diagram of the Convolutional Block Attention Module (CBAM) structure.

In the channel attention module, the input features first undergo separate adaptive max pooling and adaptive average pooling operations to generate two distinct feature sets that preserve channel-specific information. These two sets of features are then processed by a shared Multi-Layer Perceptron (MLP) to integrate their information. The outputs of the MLP are summed element-wise, and a Sigmoid activation function is applied to generate weight coefficients for each channel, constrained to the range [0, 1]. Finally, the original input features are multiplied by these channel weight coefficients to produce the module's output. In the spatial attention module, the input features are subjected to separate max pooling and average pooling operations along the channel dimension to produce two feature maps that retain spatial information. These two feature maps are then concatenated along the channel dimension. The concatenated result is processed by a convolutional layer to integrate the information, followed by a Sigmoid activation function to generate a spatial weight map with values between 0 and 1, representing the importance of each spatial location. This spatial weight map is subsequently multiplied by the original input features to yield the final output of the module.

This paper introduces the CBAM (Convolutional Block Attention Module) attention mechanism into the YOLOv8-seg model to enhance its performance [24]. The location of the incorporation and the structure of the modified YOLOv8-seg model are illustrated in Figure 6.

Different from the shadow removal network, the detection model requires specific optimization strategies. The improved YOLOv8s-seg model was implemented in the PyTorch framework and trained on a workstation equipped with an NVIDIA RTX 4060 GPU. We utilized the SGD optimizer, which is suitable for CNN-based detection tasks, with a momentum of 0.937 and a weight decay of 0.0005. The model weights were initialized using parameters pretrained on the COCO dataset to accelerate convergence. During training, the input image size was standardized to 640 × 640 pixels. Given the memory efficiency of YOLO compared to the Transformer model, the batch size was set to 16. The training spanned 300 epochs with an initial learning rate of 0.01, employing a cosine annealing schedule and an early stopping patience of 50 epochs to prevent overfitting. Standard data augmentation strategies, including Mosaic augmentation, random HSV

adjustments, and horizontal flipping, were applied to enhance the model's robustness against environmental variations.

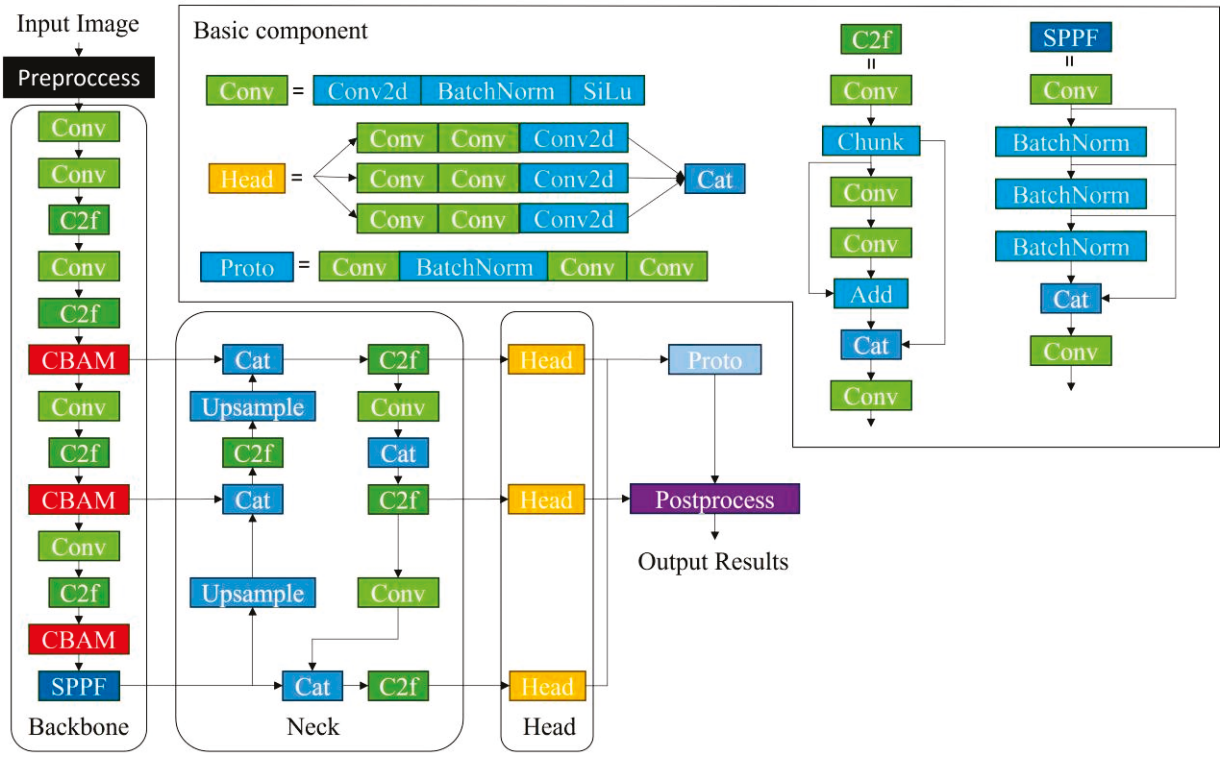

Figure 6. Schematic diagram of the improved YOLOv8-seg architecture.

2.3. Materials and Aging Simulation

This study employed penetration grade 70# base asphalt as the binder material, with all its fundamental performance indicators meeting the technical requirements specified in the "Technical Specifications for Construction of Highway Asphalt Pavements" (JTG F40-2004). The base asphalt was sourced from Shandong Chambroad Petrochemicals Co., Ltd. (Binzhou, China), with a penetration of 63.6 (0.1 mm) and a softening point of 48.5 °C. The aggregate used was limestone, and the mineral filler was produced by grinding limestone. The AC-13 median gradation was selected to prepare asphalt mixtures, simulating the material combinations and structural types commonly used in actual engineering projects. To simulate the long-term in-service aging state of asphalt mixtures in landscape roads, this study utilized laboratory accelerated aging test methods. Short-term aging, simulating aging during the construction phase, was conducted by placing the asphalt sample in a Rolling Thin Film Oven (RTFO) at 163 °C for 85 min while introducing air at a specified flow rate. This process forms a uniform thin film of asphalt on the inner wall of the rotating bottle, subjecting it to thermal oxidation. Long-term aging was performed using a Pressure Aging Vessel (PAV) in accordance with the AASHTO R30 standard. Different PAV aging durations (0, 20, 40, 60, and 80 h) were set to correspond approximately to actual pavement service ages of 0, 2, 4, 6, and 8 years, respectively. The asphalt film thickness in the RTFO test is approximately 1.25 mm, and in the PAV test, it is approximately 3.2 mm. This method effectively simulates the oxidative aging process of asphalt during its service life and is a widely accepted international accelerated aging test, providing samples with varying aging states for subsequent performance testing.

https://doi.org/10.3390/coatings16010028

2.4. Materials Testing Methods

To comprehensively evaluate the performance degradation patterns of asphalt binders and their mixtures at different aging degrees, the following test methods were adopted in this study:

2.4.1. Rheological Performance Tests of Asphalt Binder

To fully assess the changes in the high-temperature and low-temperature rheological properties of the asphalt binder during the aging process, systematic tests were conducted using a Dynamic Shear Rheometer (DSR) and a Bending Beam Rheometer (BBR).

The Dynamic Shear Rheometer (DSR) test was employed to characterize the high-temperature rheological properties of the asphalt. Asphalt samples were fabricated into specimens of specified dimensions and placed between parallel plate fixtures. An oscillatory shear load was applied over a defined temperature range to measure parameters such as the complex shear modulus ($|G^*|$) and phase angle (δ). In the DSR test, the measurement was conducted at a temperature of 60 °C with a scanning frequency of 10 rad/s. A 25 mm diameter parallel plate geometry with a 1 mm gap was used, and a scanning strain of 0.1% was applied, which falls within the linear viscoelastic range of the asphalt. The high-temperature rutting factor ($G^*/\sin\delta$) was calculated to evaluate the binder's resistance to permanent deformation. The test was conducted in accordance with the AASHTO T315 standard.

The Bending Beam Rheometer (BBR) test was utilized to evaluate the low-temperature cracking resistance of the asphalt. In the BBR test, the specimen used was a small beam with dimensions of 127 mm in length, 12.7 mm in width, and 6.35 mm in height. The test was conducted at a temperature of -12 °C, with a standard temperature conditioning time of 60 ± 5 min. The test was repeated three times for reproducibility. Their creep deformation behavior was monitored to obtain two key parameters: creep stiffness (S) and creep rate (m-value). The S-value indicates the stiffness of the asphalt at low temperatures, while the m-value characterizes its stress relaxation capability. The test was conducted according to the AASHTO T313 standard, with reference to the Superpave performance grading specifications for low-temperature performance, which stipulate that the S-value should not exceed 300 MPa and the m-value should not be less than 0.30.

The combination of DSR and BBR tests comprehensively reveals the performance evolution patterns of asphalt under both high- and low-temperature conditions from a rheological perspective, providing a critical basis for analyzing the impact of aging on asphalt pavement failure.

2.4.2. Low-Temperature Cracking Resistance Test of Asphalt Mixtures

Three-Point Bending (3PB) Test: The test was performed by applying mid-span loading at a rate of 50 mm/min to beam specimens measuring 250 mm (length) × 30 mm (width) × 35 mm (height) in a low-temperature environment (e.g., -10 °C). The maximum tensile strain and failure stiffness modulus were measured to evaluate the low-temperature deformation capacity of the mixture.

Semi-Circular Bending (SCB) Test: Cylindrical specimens measuring Φ150 mm × 25 mm were cut into semi-circular shapes with a prefabricated notch. The notched specimens were subjected to three-point loading at low temperatures, and the fracture energy was calculated to evaluate the mixture's resistance to crack propagation.

2.4.3. Freeze-Thaw Durability Test of Asphalt Mixtures

The freeze-thaw resistance of asphalt mixtures was evaluated using the Indirect Tensile Test (IDT), strictly following the T0729 procedure outlined in the Chinese specification

https://doi.org/10.3390/coatings16010028

Test Methods of Bitumen and Bituminous Mixtures for Highway Engineering (JTG E20-2011). Cylindrical specimens measuring Φ101.6 mm × 63.5 mm were saturated with water and subsequently subjected to predetermined freeze-thaw cycles. Each cycle consisted of freezing at −18 °C for 16 h followed by thawing in a 60 °C water bath for 24 h. The number of freeze-thaw cycles applied was 0, 3, 5, and 10, respectively. Indirect tensile strength tests were conducted on each group of specimens. The Tensile Strength Ratio (TSR), defined as the percentage of the indirect tensile strength of conditioned specimens to that of unconditioned specimens, served as the key performance indicator. This ratio scientifically characterizes the moisture susceptibility and freeze-thaw damage resistance of the asphalt mixture.

3. Results and Analysis

3.1. Distress Identification Accuracy and Distribution Characteristics

To precisely quantify the contribution of the SpA-Former shadow removal module to the downstream distress detection task, a comparative ablation study was conducted. The YOLOv8-seg model was evaluated on two datasets: the original dataset containing tree shadows and the processed dataset where shadows were removed. As shown in Table 1, the presence of shadows in the original images severely hindered feature extraction, resulting in a Mean Average Precision (mAP@0.5) of only 86.5%. Shadows were frequently misidentified as cracks (false positives) or obscured real distresses (false negatives). After applying the proposed shadow removal method, the mAP@0.5 significantly improved to 96.2%, representing a net gain of 9.7%. Notably, the Recall rate increased by 10.5%, indicating that the shadow removal algorithm effectively recovered distress details previously hidden by shadows, thereby drastically reducing missed detections. This quantitative comparison demonstrates a robust positive correlation between shadow removal quality and distress detection accuracy.

Table 1. Comparison of distress detection performance with and without shadow removal.

Input Data Type	Precision (%)	Recall (%)	mAP@0.5 (%)	Improvement (mAP)
Original mages (with shadows)	88.2	85.8	86.5	-
Processed mages (Shadow Removal)	97.1	96.3	96.2	+9.7%

Figure 7 presents the precision analysis results of distress identification on municipal landscape road asphalt pavements using the YOLOv8-seg model, including core evaluation metrics such as Precision, Recall, and F1-score. The results provide a comprehensive quantification of the model's performance across various distress types, highlighting its practical utility. Precision (P) represents the proportion of correctly identified distress areas among all regions predicted as distress by the model. Recall (R) indicates the proportion of actual distress areas successfully detected by the model. These two metrics collectively evaluate the model's reliability and comprehensiveness in distress identification. The F1-score, which integrates both Precision and Recall, offers a more balanced assessment of the model's performance, particularly when handling imbalanced datasets. Furthermore, the model demonstrates efficient detection of fine cracks (with widths less than 2 mm), highlighting its strong capability in identifying small-scale distresses. For pothole-type distresses, the model also exhibits outstanding identification performance, achieving a precision of 94.8%, recall of 93.5%, and an F1-score exceeding 94%. As distresses with distinct morphological features, potholes present noticeable edge characteristics that

https://doi.org/10.3390/coatings16010028

the YOLOv8-seg model effectively captures through multi-scale feature fusion, ensuring efficient detection. Although the detection accuracy for potholes is slightly lower compared to crack-type distresses, the overall performance remains excellent, indicating the model's strong adaptability in identifying complex road distresses. In summary, the results presented in Figure 7 confirm that the YOLOv8-seg model achieves high accuracy and reliability in detecting distresses on municipal landscape road asphalt pavements, particularly in identifying cracks and potholes. These precision metrics not only validate the model's effectiveness of the model in distress detection tasks but also establish a foundation for its implementation in engineering-level applications. Future research could focus on further optimizing the model to enhance its accuracy in identifying other types of distresses, especially under challenging lighting conditions or shadow interference.

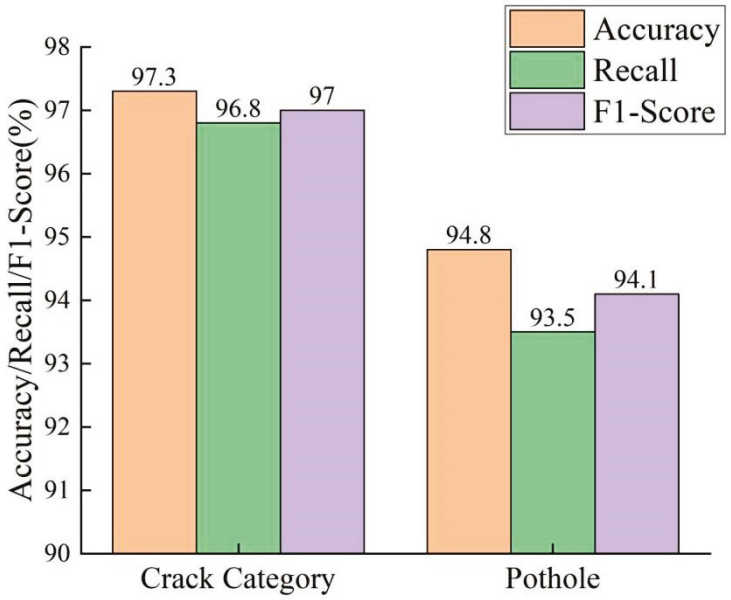

Figure 7. Distress identification accuracy.

Figure 8 presents the quantity and proportion of different distress types identified in the asphalt pavement of municipal landscape roads. Transverse cracks were the most prevalent distress type, with a total of 521 occurrences, significantly outnumbering all other categories. This indicates that transverse cracking is the most common distress form in municipal landscape roads. Longitudinal cracks were observed 58 times, substantially fewer than transverse cracks, suggesting a lower frequency of occurrence potentially related to factors such as subgrade settlement or construction quality. Alligator cracking and potholes, representing more severe distress modes, were recorded 24 and 12 times respectively. Although these distress types occurred less frequently, their presence typically indicates more critical underlying issues including asphalt fatigue, material aging, or poor freeze-thaw resistance, which may accelerate pavement deterioration. In summary, transverse cracks constitute the primary distress type in municipal landscape roads. While longitudinal cracks, alligator cracking, and potholes occur less frequently, they warrant careful attention due to their significant implications for pavement structural integrity.

https://doi.org/10.3390/coatings16010028

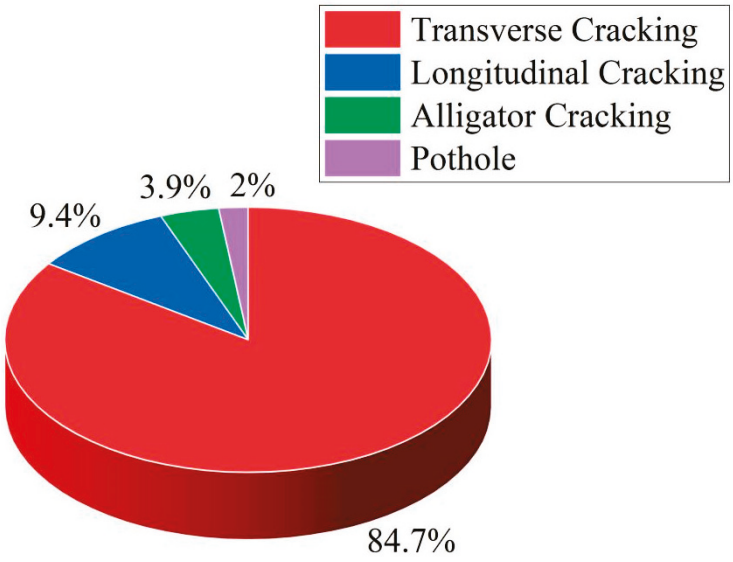

Figure 8. Number and Proportions of Different distress Types.

The aforementioned analysis reveals that transverse cracks constitute the primary distress in landscape asphalt pavements. The initiation and propagation of transverse cracks are closely associated with the aging of asphalt materials and complex environmental factors, representing the combined effect of both mechanisms. As an organic binder, asphalt inevitably undergoes aging during long-term service, primarily manifested through the volatilization of light components and oxidative hardening, leading to reduced flexibility and increased brittleness. This degradation of material properties diminishes the ability of asphalt mixtures to resist deformation and stress, creating an inherent predisposition for crack formation. Studies indicate that pavements incorporating Reclaimed Asphalt Pavement (RAP) are particularly susceptible to accelerated brittleness, as the asphalt binder in RAP has already undergone prior aging. Improper recycling techniques can further exacerbate pavement embrittlement, influencing both crack spacing and propagation patterns [25]. Environmental factors serve as critical external conditions that trigger and accelerate the formation of transverse cracks. Among these, temperature fluctuation exerts the most significant influence. In regions with substantial daily or seasonal temperature variations, the asphalt surface layer and the underlying semi-rigid base course undergo considerable volume changes due to thermal expansion and contraction. When temperatures drop, the pavement structure contracts. However, restrained by interlayer friction and boundary conditions, tensile stress develops within the material. When this tensile stress exceeds the tensile strength of the already aged and embrittled asphalt mixture, regular transverse cracking occurs [26]. Furthermore, moisture that infiltrates fine cracks or interlayer gaps within the pavement structure freezes and expands in volume, generating substantial frost-heave pressure. Upon thawing, the bearing capacity drops abruptly. This repeated freeze-thaw cycle significantly accelerates crack propagation and causes structural deterioration of the pavement [27]. Prolonged environmental exposure, including ultraviolet radiation and rainwater erosion, continuously accelerates asphalt aging, establishing a vicious cycle. Moreover, the presence of transverse cracks exacerbates environmental damage to the pavement. These cracks provide pathways for moisture and air to penetrate the pavement structure, which not only weakens interlayer bonding but also accelerates the deterioration of base course materials and further aging of the asphalt. Studies have shown that when back-calculating the modulus of pavement structural layers using non-destructive testing data such as deflection basins, transverse cracks significantly affect the accuracy of the results. This underscores the profound impact of cracking on the overall

structural performance of the pavement [28]. Therefore, asphalt aging and environmental factors exhibit an interconnected and mutually reinforcing coupling relationship. The following section analyzes the mechanical properties of asphalt under combined aging and environmental effects through experimental investigation.

3.2. Rheological Properties of Asphalt After Aging

To systematically evaluate the comprehensive impact of the aging process on the performance of asphalt, the variation patterns of its rheological properties under different aging durations were analyzed using key parameters, including the complex shear modulus (|G|), high-temperature rutting factor (G/sinδ), stiffness modulus (S), and m-value. The results are presented in Figures 9–12.

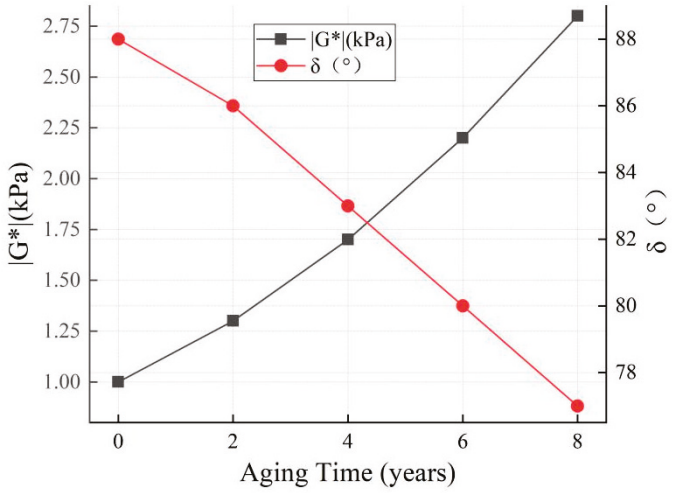

Figure 9. Relationship between complex shear modulus, phase angle, and aging duration.

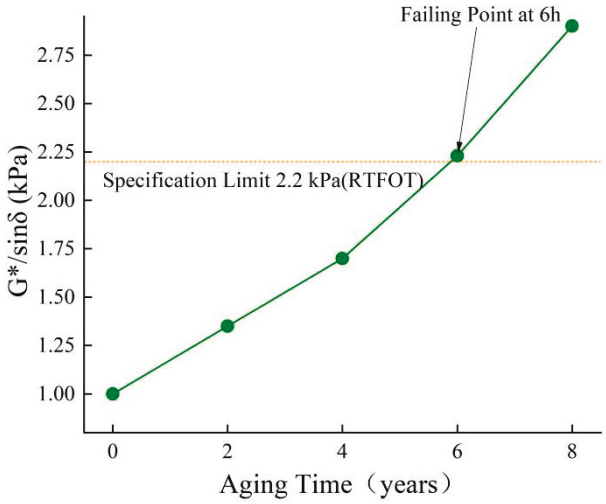

Figure 10. Relationship between High-Temperature Rutting Factor and Aging Duration.

Figure 9 illustrates the variation of the complex shear modulus (|G*|) of asphalt with different aging durations. As can be observed from the figure, the complex shear modulus increases significantly with the extension of aging duration. Specifically, at 0 years of aging, the |G*| value is approximately 1.00 kPa; when the aging duration reaches 2 years, the |G*| increases to about 1.50 kPa; at 4 years of aging, it is 1.80 kPa; at 6 years of aging, it reaches 2.30 kPa; and at 8 years of aging, it approaches 2.50 kPa. This phenomenon indicates that asphalt materials gradually harden during the aging process: their deformation resistance is enhanced, while their flexibility decreases, rendering the

materials more brittle and prone to cracking. In particular, after 6 years of aging, the complex shear modulus increases remarkably, making the asphalt hard and brittle, and its crack resistance at low temperatures decreases significantly. The overall trend presents a linear annual growth, which further confirms that the hardening process of asphalt is one of the main causes for the formation of transverse cracks.

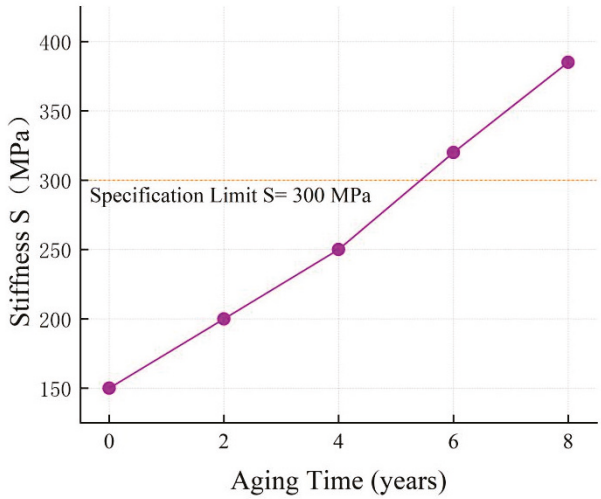

Figure 11. Relationship between Stiffness (S) and Aging Duration.

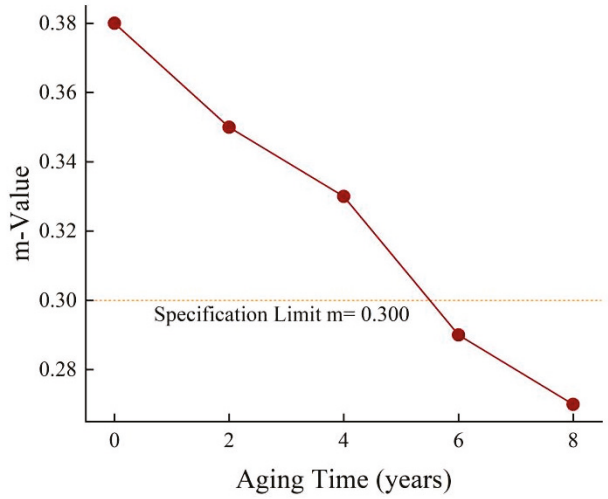

Figure 12. Relationship between m Value and Aging Duration.

Figure 10 illustrates the variation of the high-temperature rutting factor (G*/sinδ) with aging duration. As can be seen from the figure, the rutting factor increases gradually with the extension of asphalt aging duration. Specifically, it rises from approximately 1.50 kPa at 0 years of aging to about 1.75 kPa after 2 years of aging, reaches roughly 2.00 kPa after 4 years, climbs to 2.30 kPa after 6 years, and finally approaches 2.50 kPa at 8 years of aging. This increasing trend indicates that as the asphalt ages, its rutting resistance is enhanced; however, such hardening also leads to increased brittleness of the asphalt, resulting in deteriorated low-temperature crack resistance. The increase in the rutting factor reflects the improved deformation resistance of asphalt under high-temperature conditions, but due to the hardening caused by aging, the asphalt becomes more prone to transverse cracking in low-temperature environments. The overall trend of annual increase further exacerbates the risk of low-temperature cracking.

As shown in Figure 11, the stiffness (S) of asphalt increases significantly with the extension of aging duration. Specifically, the stiffness is approximately 50 MPa at 0 years of

https://doi.org/10.3390/coatings16010028

aging, about 80 MPa after 2 years of aging, roughly 120 MPa after 4 years of aging, and approaches 200 MPa after 6 years of aging. When the aging duration reaches 8 years, the stiffness has climbed to 320 MPa, which clearly exceeds the standard limit of 300 MPa. This increasing trend indicates that as aging progresses, asphalt gradually hardens and its deformation resistance improves. However, such hardening also causes asphalt to lose its original flexibility—especially under low-temperature conditions, the brittleness of the asphalt material is intensified, making it prone to cracking. The linear increase in stiffness directly leads to the brittle fracture of asphalt under the action of thermal expansion and contraction stress. Therefore, with the increase in aging duration, the occurrence probability of transverse cracks rises significantly.

Figure 12 illustrates the variation of the asphalt's m Value with aging duration. As can be observed from the figure, the m Value decreases significantly as the aging duration extends. Specifically, it drops from approximately 0.35 at 0 years of aging to 0.30 after 2 years of aging, further decreases to 0.25 after 4 years, reaches 0.22 after 6 years, and only remains at 0.18 after 8 years of aging. The m Value serves as a key indicator for evaluating the low-temperature crack resistance of asphalt. This decrease in the m Value indicates that the asphalt's low-temperature crack resistance gradually deteriorates. With the increase in aging duration, the brittleness of the asphalt material increases, making it more likely to crack under low-temperature conditions. In particular, after 8 years of aging, the m Value is far below 0.30, which suggests that the asphalt's low-temperature crack resistance has almost been lost. This trend demonstrates that as the asphalt ages, the material becomes more fragile and prone to cracking under low-temperature conditions—especially in winter when there are large temperature differences.

3.3. Low-Temperature Crack Resistance of Asphalt Mixtures with Different Aging Degrees

As indicated by the preceding analysis of rheological parameters, asphalt aging leads to material hardening and embrittlement. To validate how this change is reflected in the macroscopic performance of asphalt mixtures, the low-temperature crack resistance of mixtures with different aging degrees was further evaluated through low-temperature bending tests. The results are shown in Figure 13.

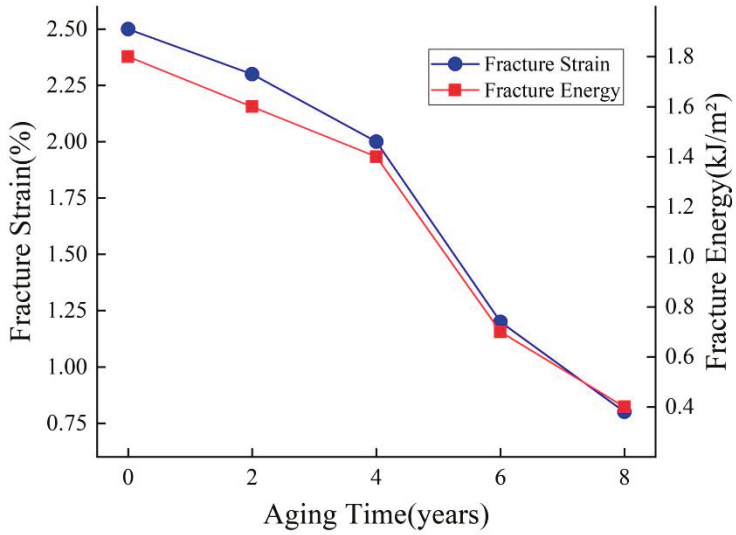

Figure 13. Low-Temperature Crack Resistance of Asphalt Mixtures with Different Aging Degrees.

Figure 13 illustrates the low-temperature crack resistance of asphalt mixtures with different aging durations under low-temperature conditions, which is specifically evaluated by two indicators: Fracture Strain and Fracture Energy. The data in the figure reveals that

https://doi.org/10.3390/coatings16010028

as the aging duration of asphalt increases, the low-temperature crack resistance of the material decreases significantly. Initially (at 0 years of aging), the fracture strain of the asphalt mixture under low temperature is approximately 2.5%, indicating that the material exhibits good ductility at low temperatures and can withstand a certain amount of tensile strain without brittle fracture. However, with the extension of aging duration, the fracture strain decreases gradually: it has dropped to approximately 1.0% after 6 years of aging, and further falls to nearly 0.5% after 8 years of aging. This decrease indicates that as the asphalt ages, the ductility of the material gradually weakens, making it more prone to brittle fracture. Especially in low-temperature environments, the formation of cracks becomes much easier.

On the other hand, the Fracture Energy also decreases gradually with the extension of aging duration. Initially (at 0 years of aging), the Fracture Energy is approximately 1.8 kJ/m^2, indicating that the asphalt material can withstand a relatively large amount of energy without cracking under low-temperature conditions. As the aging duration prolongs, the Fracture Energy decreases step by step: it drops to about 0.8 kJ/m^2 after 6 years of aging, and only reaches 0.4 kJ/m^2 after 8 years of aging—this phenomenon indicates a significant decline in the asphalt's crack resistance. This decrease in Fracture Energy means that when the asphalt is subjected to low-temperature stress, the external force it can withstand is reduced, making the fracture of the material much more likely to occur.

Taken together, the data in Figure 12 clearly reflects that with the extension of aging duration, the low-temperature crack resistance of asphalt gradually decreases, and the material's ductility and energy absorption capacity are significantly weakened. This change indicates that the aging process gradually renders the asphalt material more brittle, making it more prone to cracking especially under low-temperature conditions. Therefore, for asphalt pavements in long-term service, special attention must be paid to their low-temperature performance, and timely maintenance and repair should be carried out to prevent the further propagation of low-temperature cracks and ensure the long-term stability of the pavement.

3.4. Freeze-Thaw Cycle Performance of Asphalt with Different Aging Degrees

In addition to low-temperature crack resistance, the freeze-thaw durability of asphalt mixtures is another critical factor affecting the long-term service performance of pavements in cold regions. To evaluate the impact of aging on the frost resistance of the mixtures, this study further tested the variations in Indirect Tensile Strength (IDT) and Tensile Strength Ratio (TSR) of specimens with different aging durations under the action of freeze-thaw cycles. The results are shown in Figures 14 and 15, respectively.

Figure 14 illustrates the variation of Indirect Tensile Strength (IDT) of asphalt mixtures with different aging durations under the action of freeze-thaw cycles. IDT strength is a key indicator for evaluating the freeze-thaw resistance of asphalt mixtures: the higher the IDT strength, the stronger the freeze-thaw resistance. Specifically, for asphalt with 0 years of aging, its IDT strength is relatively high (approximately 1.80 MPa) without undergoing freeze-thaw cycles; even after 10 freeze-thaw cycles, the IDT strength still remains at around 1.60 MPa. This indicates that fresh asphalt mixtures possess good freeze-thaw durability. For asphalt with 2 years of aging, the IDT strength is also high without freeze-thaw cycles; however, after 5 freeze-thaw cycles, the IDT strength drops to approximately 1.40 MPa, showing a slight decline in freeze-thaw resistance. With the further increase in aging duration, the IDT strength of asphalt with 4 years of aging is about 1.20 MPa, and it decreases further after 5 freeze-thaw cycles—this demonstrates that the aging process gradually weakens the ductility and strength of asphalt. For asphalt with

https://doi.org/10.3390/coatings16010028

6 years of aging, the IDT strength drops further to 0.80 MPa after 3 freeze-thaw cycles, exhibiting a significant reduction in freeze-thaw damage resistance. The variation trend in the figure clearly shows that as the aging duration increases, the freeze-thaw resistance of asphalt gradually weakens, and the damage caused by freeze-thaw cycles becomes increasingly significant. Especially when the asphalt aging exceeds 6 years, its structural damage is very significant.

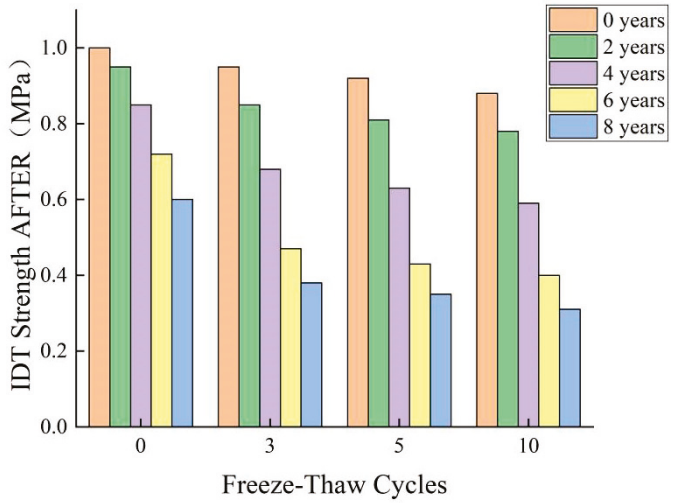

Figure 14. Analysis of Variation in IDT Strength of Asphalt Mixtures with Different Aging Durations.

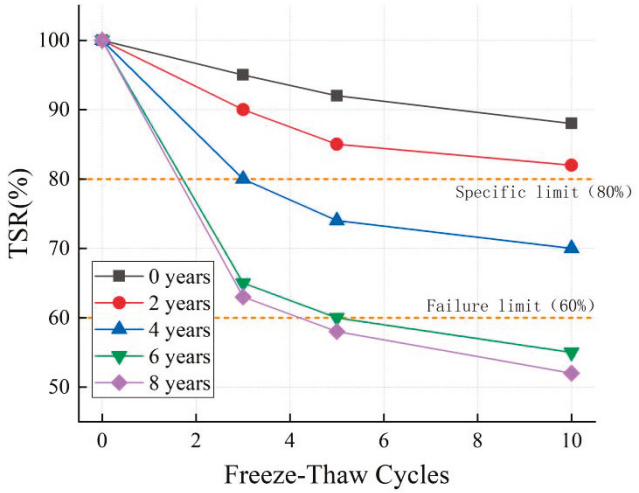

Figure 15. Analysis of Variation in TSR of Asphalt Mixtures with Different Aging Durations.

Figure 15 illustrates the variation of the Tensile Strength Ratio (TSR) of asphalt mixtures with different aging durations during freeze-thaw cycles. The TSR value reflects the freeze-thaw resistance of asphalt mixtures: a higher TSR value indicates better water stability and stronger resistance to freeze-thaw damage. Specifically, for asphalt with 0 years of aging, the TSR remains above 80% even after 10 freeze-thaw cycles, demonstrating strong freeze-thaw resistance. For asphalt with 2 years of aging, the TSR is slightly reduced after 10 freeze-thaw cycles but still maintained at approximately 80%, indicating that the asphalt has just begun to be affected by aging yet can still resist freeze-thaw effects relatively well. As the aging duration increases, the TSR of asphalt with 4 years of aging drops to around 75% after 5 freeze-thaw cycles. For asphalt with 6 years of aging, the TSR plummets to below 60% even after only 3 freeze-thaw cycles, showing obvious performance degradation. In particular, the TSR of asphalt with 8 years of aging has fallen to below 60% after 3 freeze-thaw cycles, indicating that the material has become embrittled and almost

lost its freeze-thaw resistance. These data reveal that asphalt aging leads to a gradual decline in its water stability and freeze-thaw resistance, and the impact of freeze-thaw cycles becomes increasingly significant. Especially for asphalt aged for 6 years or more, its resistance to freeze-thaw damage is significantly weakened, which can easily lead to pavement damage and failure.

4. Conclusions and Future Work

This study, through in-depth analysis of the distress characteristics of asphalt pavements for municipal landscape roads, the aging process of asphalt materials, low-temperature crack resistance, and the impact of freeze-thaw cycles, reveals the significant impacts of asphalt aging and environmental factors on pavement performance. The research results provide a theoretical basis and technical support for the intelligent detection and maintenance management of municipal landscape road pavements, and the optimized design of materials. The main conclusions are as follows:

1. Through the identification and analysis of distresses in asphalt pavements of municipal landscape roads, this study found that transverse cracks are the most common type of pavement distress. The formation of transverse cracks is closely related to environmental factors such as asphalt aging, temperature fluctuations, and moisture intrusion. Specifically, asphalt aging causes the material to harden and become brittle, leading to a significant decrease in its low-temperature crack resistance. Meanwhile, temperature differences and freeze-thaw action further accelerate the propagation of cracks. The study shows that transverse cracks account for 72% of the total number of cracks, making them the most common and most destructive type of distress in municipal landscape road pavements.
2. Tree shadows on landscape roads are a key factor affecting the accuracy of pavement distress identification. To address this issue, the SpA-Former shadow removal network was proposed in this study, which effectively eliminates tree shadow interference in images and significantly enhances the contrast of distress areas. It is shown by the experimental results that after applying this technology, the grayscale contrast of distress areas is improved by 40%–60%, which enhances the accuracy of distress detection and provides effective technical support for intelligent distress detection.
3. Through indoor aging simulation experiments, it was found in this study that the low-temperature crack resistance of asphalt decreases significantly during the aging process. Specifically, the fracture strain decreases from 2.5% to 0.5%, and the fracture energy drops from 1.8 kJ/m^2 to 0.4 kJ/m^2. As the asphalt ages, its ductility decreases and brittleness increases, causing it to be more prone to cracking in low-temperature environments. This aging process gradually makes the asphalt lose its flexibility. Especially under low-temperature conditions, the probability of cracking increases significantly.
4. It is shown by the study that the stiffness of asphalt increases significantly as the aging duration extends. Specifically, the stiffness increases from 50 MPa at 0 years of aging to 320 MPa at 8 years of aging, which far exceeds the standard limit of 300 MPa. The increase in asphalt stiffness enhances its deformation resistance; however, it also makes the asphalt material more brittle in low-temperature environments, rendering it prone to cracking. During the aging process, the asphalt gradually hardens and loses its original flexibility. As a result, it is more likely to undergo brittle fracture under stresses such as thermal expansion and contraction, which further accelerates the formation of transverse cracks.
5. The impact of freeze-thaw cycles on the freeze-thaw resistance of asphalt mixtures with different aging durations was analyzed in this study. Results show that as the

https://doi.org/10.3390/coatings16010028

aging duration of asphalt increases, its freeze-thaw resistance decreases significantly. Specifically, for unaged asphalt (0 years of aging), the TSR (Tensile Strength Ratio) remains above 80% even after 10 freeze-thaw cycles. In contrast, for asphalt aged for 6 and 8 years, the TSR drops to below 60% after only 3 freeze-thaw cycles, showing a significant reduction in freeze-thaw resistance. Meanwhile, the IDT (Indirect Tensile Strength) also decreases gradually with the increase in the number of freeze-thaw cycles. Especially for asphalt aged for more than 6 years, its freeze-thaw resistance is almost lost, indicating that the performance of the asphalt material has severely degraded and its resistance to freeze-thaw damage has been greatly weakened.

6. As the starting point of a series of studies, future work will deepen along three directions: First, expanding to the structural scale by constructing composite pavement specimens incorporating different base layers (e.g., semi-rigid, flexible) and considering interlayer bonding, to quantify the influence of base restraint and structural integrity on cracking behavior through mechanical testing and simulation. Second, broadening the spectrum of influencing factors by systematically studying the interactive effects of variable traffic loads, extreme climatic conditions, and different asphalt chemical compositions (e.g., modified asphalt, high RAP content) on aging pathways and failure modes, based on the established temperate climate benchmark, to enhance the universality of the conclusions. Third, promoting engineering application validation by conducting long-term performance monitoring and full-scale testing for the proposed preventive maintenance window (years 5–6) and the use of softer asphalt (e.g., penetration grade 90). Through comparative road section studies, the actual benefits of delaying cracking and extending service life will be quantified, ultimately forming operable design and maintenance guidelines to translate material mechanism discoveries into engineering practice.

Author Contributions: Conceptualization, L.Z.; Methodology, L.Z. and X.M.; Software, X.C.; Validation, X.C.; Formal analysis, L.Z.; Investigation, H.Z.; Data curation, X.M.; Writing—original draft, L.Z.; Writing—review & editing, X.M., X.F. and H.Z.; Visualization, H.Z.; Supervision, L.Z., X.C. and X.F.; Project administration, X.F. All authors have read and agreed to the published version of the manuscript.

Funding: This research was funded by the Fujian Vocational and Technical College of Agriculture's project to take the lead grant number 2024JS009.

Institutional Review Board Statement: Not applicable.

Informed Consent Statement: Not applicable.

Data Availability Statement: Data are contained within the article.

Conflicts of Interest: The authors declare no conflict of interest.

References

1. Yang, S.; Park, H.; Baek, C. Fatigue Cracking Characteristics of Asphalt Pavement Structure under Aging and Moisture Damage. *Sustainability* **2023**, *15*, 5210. [CrossRef]
2. Rys, D.; Jaczewski, M.; Pszczola, M.; Kamedulska, A.; Kamedulski, B. Factors affecting low-temperature cracking of asphalt pavements: Analysis of field observations using the ordered logistic model. *Int. J. Pavement Eng.* **2023**, *24*, 215–228. [CrossRef]
3. Picos, K.; DiazRamírez, V.H.; Tapia, J.J. A roadmap to global illumination in 3D scenes: Solutions for GPU object recognition applications. In Proceedings of the SPIE Optical Engineering + Applications, San Diego, CA, USA, 17–21 August 2014.
4. Liu, C.; Yao, Y.; Li, J.; Qian, J.; Liu, L. Research on lightweight GPR road surface distress image recognition and data expansion algorithm based on YOLO and GAN. *Case Stud. Constr. Mater.* **2024**, *20*, e02789.
5. Duan, X.; Cao, Y.; Zhang, R.; Wang, X.; Li, P. Shadow-aware image colorization. *Vis. Comput.* **2024**, *40*, 4969–4979. [CrossRef]
6. Tedeschi, A.; Benedetto, J.F. A real-time automatic pavement crack and pothole recognition system for mobile Android-based devices. *Adv. Eng. Inform.* **2017**, *33*, 306–315. [CrossRef]

7. Xu, J.; Zhang, J.; Sun, W. Recognition of the Typical Distress in Concrete Pavement Based on GPR and 1D-CNN. *Remote Sens.* **2021**, *13*, 2356. [CrossRef]
8. Lv, Z.; Cheng, C.; Lv, H. Automatic identification of pavement cracks in public roads using an optimized deep convolutional neural network model. *Philos. Trans. R. Soc. A* **2023**, *381*, 20220147. [CrossRef]
9. Sheng, Z.; Bei, Z.; Ling, T.; Chen, Q.; Zhang, L. Research on high-precision recognition model for multi-scene asphalt pavement distresses based on deep learning. *Sci. Rep.* **2024**, *14*, 25416.
10. Boateng, M.A.; Gyamfi, Y.A. Generative adversarial network for real-time identification and pixel-level annotation of highway pavement distresses. *Autom. Constr.* **2025**, *158*, 105213.
11. Khan, N.H.R.; Kumar, S.V. Terrestrial LiDAR derived 3D point cloud model, digital elevation model (DEM) and hillshade map for identification and evaluation of pavement distresses. *Results Eng.* **2024**, *22*, 101876. [CrossRef]
12. Mivehchi, M.; Wen, H.; Wen, Y.; Wang, L. Study of Measures to Design Asphalt Mixes Including High Percentages of Recycled Asphalt Pavement and Recycled Asphalt Shingles. *Transp. Res. Rec.* **2023**, *2677*, 678–690. [CrossRef]
13. Jiang, L.; Gong, M.; Xiong, Z.; Liu, S.; Fan, J.; Xu, Z.; Hong, J. In situ mechanical response characteristics of Autonomous Rail Rapid Transit (ART) applied to semi-flexible asphalt pavements. *Road Mater. Pavement Des.* **2024**, *25*, 2644–2663. [CrossRef]
14. Goli, H.; Latifi, M.; Sadeghian, M. Comparing the Effect of Moisture on Different Fatigue and Cracking Behaviors of RAP-WMA. *J. Transp. Eng. Part B Pavements* **2023**, *149*, 04023034. [CrossRef]
15. Jiang, J.; Xu, K.; Song, Y.; Gao, L.; Zhang, J. Investigation of cracking behavior in asphalt pavement using digital image processing technology. *Front. Built Environ.* **2025**, *11*, 1324567. [CrossRef]
16. Xing, M.; Yang, H.; Zhao, Z.; Yu, T. Effect of Asphalt Pavement Base Layers on Transverse Shrinkage Cracking Characteristics. *Sustainability* **2023**, *15*, 7568. [CrossRef]
17. Krami, K.; Benamara, A.; Radouani, M.; Ettayeb, M.; Tarik, L. Study of Asphalt Pavement Cracking in Different Road Sections of Morocco Using Electrical Resistivity Tomography. *Int. J. Geophys.* **2024**, *2024*, 6683254. [CrossRef]
18. Meng, G.; Yao, X.; Du, X. Low temperature cracking behavior of asphalt binders and mixtures: A review. *J. Road Eng.* **2023**, *3*, 329–347. [CrossRef]
19. Zhang, Q.; Yang, S.; Zhu, L.; Liu, T. Temperature variations and frozen zone migration: Assessing the influence of climate change on fatigue cracking in roadway asphalt pavements. *Road Mater. Pavement Des.* **2025**, *26*, 1105–1121. [CrossRef]
20. Ma, R.; Li, Y.; Cheng, P.; Chen, X.; Cheng, A. Low-Temperature Cracking and Improvement Methods for Asphalt Pavement in Cold Regions: A Review. *Buildings* **2024**, *14*, 3652. [CrossRef]
21. Zhang, X.; Zhao, Y.; Gu, C.; Lu, C.; Zhu, S. SpA-Former: An Effective and lightweight Transformer for image shadow removal. In Proceedings of the International Conference on Neural Networks (IJCNN), Gold Coast, Australia, 18–23 June 2023; pp. 1–8.
22. Tang, Y.; Zhao, S.; Qin, H.; Ming, P.; Fang, T.; Zeng, J. An End-to-End Particle Gradation Detection Method for EarthRockfill Dams from Images Using an Enhanced YOLOv8-Seg Model. *Sensors* **2025**, *25*, 4797. [CrossRef]
23. Ma, J.; Zhao, Y.; Fan, W.; Liu, J. An Improved YOLOv8 Model for Lotus Seedpod Instance Segmentation in the Lotus Pond Environment. *Agronomy* **2024**, *14*, 1325. [CrossRef]
24. Xu, W.; Zhou, J.L.; Qian, X.; Fu, S. Method for Identifying the Severity of Wheat Scab in the Field Based on AR Glasses and Improved YOLOv8m-seg. *J. Agric. Big Data* **2024**, *6*, 497–508.
25. Hu, Z.; Zhang, W.; Peng, T. Transverse crack patterns of long-term field asphalt pavement constructed with semi-rigid base. *Int. J. Pavement Res. Technol.* **2024**, *17*, 353–365. [CrossRef]
26. Shi, S.; Tong, J.; Zhang, Y.; Ma, T.; Zhang, J. Numerical analysis of the initiation cause of the surface transverse cracks in semirigid asphalt pavement. *J. Transp. Eng. Part B Pavements* **2023**, *149*, 04023034. [CrossRef]
27. Zhang, C.; Wang, H.; Yang, X.; You, Z. A combinational prediction model for transverse crack of asphalt pavement. *KSCE J. Civ. Eng.* **2018**, *22*, 2051–2060. [CrossRef]
28. Fu, G.; Zhao, Y.; Ong, G.P.; Wang, Y.; Lu, J. Effects of transverse cracks on the backcalculated layer properties of asphalt pavements from non-destructive testing data. *J. Nondestruct. Eval.* **2023**, *42*, 58. [CrossRef]

Disclaimer/Publisher's Note: The statements, opinions and data contained in all publications are solely those of the individual author(s) and contributor(s) and not of MDPI and/or the editor(s). MDPI and/or the editor(s) disclaim responsibility for any injury to people or property resulting from any ideas, methods, instructions or products referred to in the content.

coatings

MDPI

Article

Synthesis and Performance of Triisopropanolamine-Modified Polycarboxylate Cement Grinding Aid

Sanan Song [1,2], Yan Yan [1,3], Yu Liu [4], Chao Wang [1,2], Liyan Wang [3], Liping Zhang [5] and Huan Wang [1,2,*]

[1] Key Laboratory for Comprehensive Energy Saving of Cold Regions Architecture, Ministry of Education, Jilin Jianzhu University, Changchun 130118, China; songsanan@jlju.edu.cn (S.S.); yy97784143@163.com (Y.Y.); wangchao@jlju.edu.cn (C.W.)
[2] Jilin Provincial Key Laboratory of Architectural Electricity & Comprehensive Energy Saving, Jilin Jianzhu University, Changchun 130118, China
[3] Department of Materials Science, Jilin Jianzhu University, Changchun 130118, China; wly@jlju.edu.cn
[4] Jilin Xipu Cement Grinding Aid Co., Ltd., Changchun 130114, China; 13844141389@163.com
[5] Baotou Steel North-West Pioneer Construction Co., Ltd., Baotou 014010, China; 13847226050@163.com
* Correspondence: wanghuan@jlju.edu.cn; Tel.: +86-0431-84566327

Abstract

In this study, a triisopropanolamine (TIPA)-modified polycarboxylate cement grinding aid was synthesized via a free radical polymerization reaction, and its effects on cement properties were investigated. The synthesized grinding aid was evaluated through cement grinding experiments, by comparing cement samples with and without the additive. The influences on particle size distribution, specific surface area, residue content, setting behavior, flowability, and mechanical strength were systematically evaluated. The results demonstrated that the modified polycarboxylate cement grinding aid significantly refined size distribution of particles, enlarged the specific surface area to 4900 cm^2/g (27.9% increase), decreased 45 μm residue content to 0.8%, accelerated setting, and improved the flowability of the cement paste. Strength tests of cement mortar indicated that the additive improved both early and late compressive strength, with 3d and 28d strengths increasing by 6.5 MPa and 5.7 MPa, respectively, compared to the blank sample, providing strong theoretical support for its potential use in industrial cement production.

Keywords: cement grinding aid; modified polycarboxylate; grinding efficiency

1. Introduction

Cement is an indispensable component of the modern construction industry, and its production scale and technological level directly influence the quality and efficiency of national infrastructure development. Although China's cement production has declined slightly in recent years, it still remains the largest producer globally, with significant challenges such as high energy and resource consumption and severe environmental pollution [1–3]. Among the various production stages, grinding is a critical and energy-intensive step, accounting for 30%–40% of total energy consumption [4–6]. Therefore, improving grinding efficiency and reducing energy consumption while maintaining or enhancing cement performance are key challenges.

Since the 1930s, grinding aids have been widely applied in cement production as efficient chemical additives. By adsorbing onto particle surfaces, they reduce agglomeration, enhance grinding efficiency, optimize particle distribution, and improve powder flowability [7,8].

According to differences in chemical composition and mechanism of action, cement grinding aids can be divided into various types, each with different technical characteristics and application limitations, as shown in Table 1. Conventional grinding aids generally consist of low-molecular-weight compounds like, organic grinding acids, inorganic grinding aids, or composite grinding aids [9–17]. Organic grinding aids rely on polar groups (-OH, -NH_2) adsorbing onto particle surfaces to reduce surface energy. They prevent agglomeration through steric hindrance or electrostatic repulsion. However, they are not only relatively expensive but also have limited contribution to the later strength development of some cements. Among them, triethanolamine (TEA) is known to increase the degree of the hydration of C_3A, promote the formation of ettringite (Aft), and hinder the hydration of C_3S. Its effect strongly depends on dosage: at 0.02% it acts as an accelerator, at 0.5% as a retarder, and at 1% as an accelerator again [18]. Triisopropanolamine (TIPA), however, exhibits poor compatibility with other admixtures, often resulting in reduced workability of concrete [19]. Inorganic grinding aids mainly improve grinding efficiency by introducing ions (such as Na^+, Cl^-, $SO_4{}^{2-}$) to alter particle surface properties and the slurry environment. However, they have a single function, only serving as grinding aids, and their effectiveness is inferior to that of organic grinding aids. In addition, the introduced chloride salts (Cl^-) can corrode steel bars, so they need to be strictly controlled. Composite grinding aids, on the other hand, are mixtures where each component performs its own role: organic components provide adsorption and dispersion, while inorganic components offer ion activation or lattice interference. However, there may be antagonism between components, requiring a large number of experiments to optimize the ratio and dosage. Polycarboxylate-based grinding aids have recently drawn attention due to their tunable molecular structure, high dispersing efficiency, and environmental compatibility [20–22]. Their molecular design allows introduction of hydroxyl, carboxyl, amino, and ether groups to improve dispersion, reduce agglomeration, and enhance hydration activity. As a result, both grinding efficiency and cement strength can be improved simultaneously.

Table 1. Types, core components, mechanisms and key performance characteristics of cement grinding aid.

Classification	Organic Grinding Aids	Inorganic Grinding Aids	Composite Grinding Aids	Our Work
Core components	Triethanolamine (TEA), triisopropanolamine (TIPA), acetamide, fatty acids, ethylene glycol	Inorganic salts, coal, graphite, coke, gypsum	Organic mixtures, inorganic mixtures, organic-inorganic hybrid mixtures	Acryloyl chloride-modified triisopropanolamine (ACTA), acrylic acid, TPEG
Mechanism	Polar groups (-OH, -NH_2) adsorb on particle surfaces, reduce surface energy, prevent agglomeration through steric hindrance or electrostatic repulsion	Introduction of ions (e.g., Na^+, Cl^-, $SO_4{}^{2-}$) alters particle surface properties and slurry environment, thereby improving grinding efficiency	Organic components provide adsorption and dispersion, and inorganic components provide ionic activation or lattice interference	Polar groups (-OH, -COOH, ether chains) work synergistically to prevent agglomeration through steric hindrance and electrostatic repulsion, while ACTA components promote hydration
Specific surface area	Increase: 15%–25%	Increase: +5%–15%	Increase: 20%–30%	4900 cm^2/g (increased 27.9%)
Compressive strength	3d: +5–11 MPa 28d: +3–14 MPa	3d: +4–6 MPa 28d: +2–7 MPa	3d: +2–6 MPa 28d: +5–10 MPa	3d: +6.5 MPa 28d: +5.7 MPa

Although polycarboxylate-based grinding aids have attracted attention due to their structural adjustability, existing research has mostly focused on the regulation of groups such as carboxyl and ether groups. There is less research on introducing TIPA into the polycarboxylate molecular chain to synergistically improve grinding efficiency and hydration activity. Additionally, the problem of poor compatibility of TIPA when used alone with other admixtures has not been effectively solved through molecular structure modification. This study addresses this gap by designing and synthesizing TIPA-modified polycarboxylate-based grinding aids to enhance their polarity, exploring the correlation

between their structure and performance, and providing a new approach for developing efficient and environmentally friendly cement grinding aids.

2. Materials and Experimental Methods

2.1. Materials

Triisopropanolamine (TIPA), acryloyl chloride, acrylic acid (AA), isopentenol polyoxyethylene ether (TPEG-2400), N,N-dimethylformamide (DMF), diethyl ether, ascorbic acid (VC), hydrogen peroxide (H_2O_2), triethylamine, 3-mercaptopropionic acid, sodium hydroxide (NaOH), and gypsum were obtained from Shanghai Macklin Biochemical Technology Co., Ltd. (Shanghai, China). The composition of the Portland cement clinker was analyzed using X-ray fluorescence (XRF) (AXIOS, PANalytical, Eindhoven, Netherlands), and the results are presented in Table 2.

Table 2. Chemical composition of cement clinker (%).

CaO	SiO_2	Al_2O_3	Fe_2O_3	SO_3	MgO	K_2O	TiO_2	NaO	Loss
62.1	20.5	5.2	4.3	3.5	1.2	0.8	0.3	0.2	1.9

2.2. Synthesis Process

2.2.1. Synthesis of Acryloyl Chloride-Modified Triisopropanolamine Derivative

Triisopropanolamine (20 g) was dissolved in N,N-dimethylformamide (DMF, 80 mL), after which 10 mL of triethylamine was introduced as an acid-binding agent. The mixture was stirred at 0 °C under a nitrogen atmosphere to remove residual moisture. Then, a separate solution of 15 mL acryloyl chloride in DMF (50 mL) was added dropwise to the TIPA–DMF solution. Following the addition, the ice bath was withdrawn, and the reaction proceeded for 6 h at ambient temperature with continuous stirring.

Next, the mixture was filtered to eliminate the triethylamine salt by-products, and the filtrate was subjected to reduced-pressure distillation at 65 °C for 2 h to remove most of the DMF solvent. The resulting solution was then slowly added to an ice-cooled diethyl ether solution under stirring. Following thorough mixing, the organic phase was decanted, and the precipitate was repeatedly washed with diethyl ether (three times). The final product was dried in a vacuum oven to obtain the acryloyl chloride-modified triisopropanolamine derivative (ACTA), the schematic structure of which is illustrated in Figure 1.

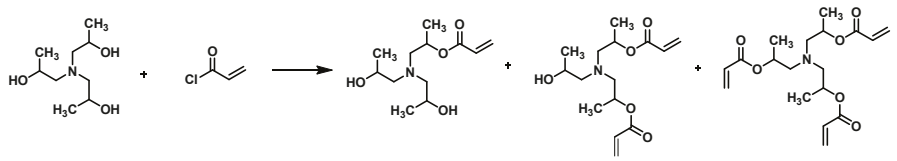

Figure 1. Schematic illustration of the preparation of the acryloyl chloride-modified triisopropanolamine derivative.

2.2.2. Synthesis of the Modified Polycarboxylate Cement Grinding Aid

A typical synthesis procedure was as follows:

Acrylic acid (4.3 g) and the modified triisopropanolamine intermediate (1.8 g) were dissolved in 10 mL of deionized water to obtain Solution A. Separately, ascorbic acid (6.32 g) and 3-mercaptopropionic acid (14.74 g) were dissolved in 20 mL of deionized water to obtain Solution B.

TPEG-2400 (36 g) was introduced into a three-necked flask with 40 mL of deionized water and stirred until fully dissolved. Hydrogen peroxide (42.1 g, H_2O_2) was then added to the solution. Under continuous stirring, Solutions A and B were successively added

dropwise to the flask over 3 h and 3.5 h, respectively. Upon completion of the additions, the mixture was kept at constant temperature and stirred for an additional 1 h to complete the reaction.

The reaction mixture was then tuned to pH 7 using a 40 wt% NaOH aqueous solution, yielding the target product, designated as grinding aid 1 (GA1). By varying the molar ratios of acrylic acid (AA), acryloyl chloride-modified triisopropanolamine derivative (ACTA), and TPEG as 3.5:1:1, 3:1.5:1, and 2.5:2:1, three additional products were synthesized and denoted as GA2, GA3, and GA4, respectively.

2.3. Experimental Methods

2.3.1. FTIR Spectra

FTIR spectra were obtained on a Nicolet 67 (Thermo Nicolet, Madison, WI, USA) spectrometer. About 1 mg of sample was thoroughly blended with 100 mg of spectroscopic-grade KBr, and the uniform mixture was pressed into a transparent pellet prior to spectral acquisition.

2.3.2. NMR Spectra

The ^{1}H NMR spectrum of liquid hydrogen was measured using a 400 MHz superconducting nuclear magnetic resonance spectrometer (AVANCE NEO 400, Bruker, Rheinstetten, Germany), with DMSO-d6 as the solvent.

2.3.3. GPC

The molecular weight of hyperbranched GA1-GA4 was measured by GPC apparatus (LC-20AD, Shimadzu, Kyoto, Japan).

2.3.4. Cement Grinding Experiment

A control mixture containing 95 wt% clinker and 5 wt% gypsum was prepared for the grinding experiments. Before grinding, clinker and gypsum were both crushed to a particle size less than 6–7 mm. Cement grinding experiments were conducted in the laboratory using a φ500 mm × 500 mm ball mill manufactured by Shanghai Jianyuan Instrument Factory (Shanghai, China). Steel balls served as the grinding medium with a rotational speed of 180 rpm and a grinding time of 30 min.

For each grinding test, a total feed of 5 kg was used, and the grinding duration was fixed at 30 min for all samples. The resulting cement samples included the blank cement (C-Blank) and those prepared with the four grinding aids, denoted as C-GA1, C-GA2, C-GA3, and C-GA4. All experiments were conducted in triplicate.

2.3.5. Cement Characterization Methods

The fineness of cement was determined according to GB/T 1345-2005 [23], and the specific surface area was measured following GB/T 8074-2008 [24]. The standard consistency water requirement and setting times were tested according to GB/T 1346-2024 [25], whereas the flowability of cement mortar was evaluated in compliance with GB/T 2419-2005 [26]. Mechanical properties, including flexural and compressive strengths, were tested after curing 3 and 28 days based on GB/T 17671-2021 [27]. Particle size distribution was characterized using a Microtrac S3500 laser particle size analyzer (Microtrac Inc., Montgomeryville, PA, USA; 780 nm laser).

2.3.6. Hydration Heat Measurement

TAM AIR-08 multi-channel isothermal calorimeter (Waters Corporation, New Castle, DE, USA) was conducted to investigate the hydration heat of cement with GA. The test was conducted under controlled environmental conditions of (20 ± 1) °C and a relative

humidity of not less than 90%. 1 g cement and deionized water (w/c = 0.5) were mixed and poured into a specific container under stirring. The heat release curve of cement hydration was calculated by computer.

2.3.7. SEM

The morphology of cement particles was investigated via field-emission scanning electron microscopy (FE-SEM, JSM-7610F, JEOL, Tokyo, Japan).

3. Results and Discussion

The FTIR spectrum of the acryloyl chloride-modified triisopropanolamine derivative (Figure 2) exhibits characteristic absorption bands at 3325 cm^{-1}, corresponding to O–H stretching, and at 2976 cm^{-1} and 2929 cm^{-1}, which are ascribed to the asymmetric stretching vibrations of CH_3 and CH_2 groups within the isopropyl chain. A strong peak at 1724 cm^{-1} represents the C=O vibration, while the band at 1650 cm^{-1} is assigned to C=C stretching. Additional absorptions at 1458 cm^{-1} and 1380 cm^{-1} arise from CH_2 bending and CH_3 symmetric deformation, respectively. The peak at 1138 cm^{-1} attributes to the C–O vibration.

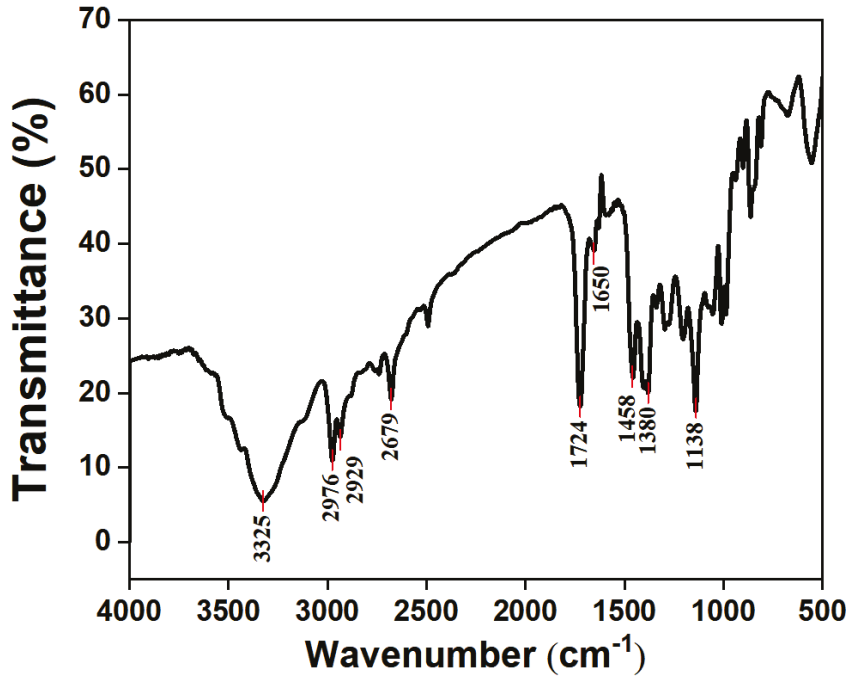

Figure 2. FTIR spectra of the acryloyl chloride-modified triisopropanolamine derivative.

The simultaneous presence of pronounced C=O and C=C bands confirms the formation of an ester bond between acryloyl chloride and triisopropanolamine, demonstrating the successful incorporation of the vinyl group into the triisopropanolamine framework [1,10]. These spectral features collectively substantiate the successful synthesis of the acryloyl chloride-modified triisopropanolamine derivative.

Figure 3 presents the FTIR spectra of the four synthesized grinding aids (GA1–GA4). The main spectral features are comparable among the samples. Taking GA1 as an example: the absorption peak at 3432 cm^{-1} corresponds to O–H stretching, indicating the presence of residual hydroxyl groups derived from the triisopropanolamine intermediate. The peaks at 2916 cm^{-1} and 2873 cm^{-1} arise from asymmetric stretching vibrations of CH_3 and CH_2 groups, typical of alkyl chains. The peak at 1724 cm^{-1} is ascribed to C=O stretching

vibration, and the band at 1644 cm^{-1} corresponds to the C=C stretching mode, suggesting that some double bonds remain unreacted.

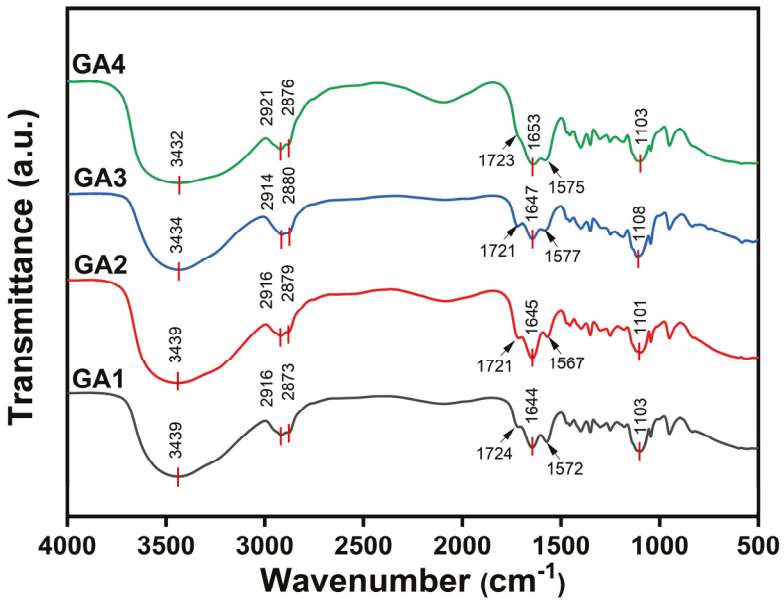

Figure 3. FTIR spectra of the synthesized grinding aids GA1–GA4.

The band observed at 1572 cm^{-1} is characteristic of the asymmetric stretching of the carboxylate group (COO^-), while the prominent absorption at 1103 cm^{-1} is ascribed to C–O–C vibrations associated with the polyether segments of TPEG. In the magnified spectra (Figure 4, 1000–1200 cm^{-1} region), the weaker C–O stretching peak near 1138 cm^{-1} suggests partial overlap with the strong ether absorption of TPEG, indicating successful incorporation of ester and ether functionalities within the polymer backbone.

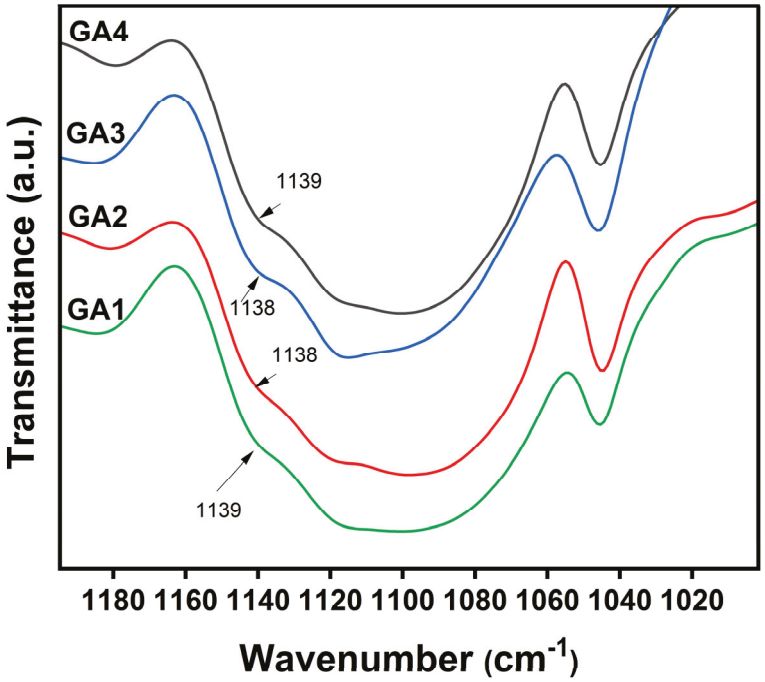

Figure 4. Enlarged FTIR spectra of GA1–GA4 in the 1000–1200 cm^{-1} region.

The presence of key characteristic peaks corresponding to C=O (ester), C–O–C (ether), and residual O–H groups confirms the successful synthesis of the target polycarboxylate-based grinding aids.

The structural characteristics of the synthesized triisopropanolamine-modified polycarboxylate cement grinding aid were further confirmed by 1H NMR, with GA3 taken as an example for explanation. As shown in Figure 5, δ = 0.97–1.07 ppm, the peak is assigned to the methyl group (-CH(CH_3)$_2$) of the isopropyl group in the ACTA unit; δ = 1.87 ppm, the peak is assigned to the methyl group (-C-CH_3) of the main chain of TPEG; δ = 2.26–2.31 ppm, the peak is assigned to the α-CH of the acrylic acid unit (-CH(COOH)-); δ = 2.39–2.45 ppm, the peak is assigned to the -CH_2- of the TPEG unit (connecting the main chain and PEO) and the N-CH_2- of the ACTA unit; δ = 2.60–2.65 ppm, the peak is assigned to the α-CH of ACTA (-CH-COO-); δ = 2.84 ppm, the peak is assigned to the methylene group CH of the isopropyl group in ACTA (-CH(CH_3)$_2$); δ = 3.33 ppm, the peak is assigned to the residual water peak; δ = 3.50–3.60 ppm, the peak is assigned to the PEO chain (-OCH_2CH_2-)n of TPEG.

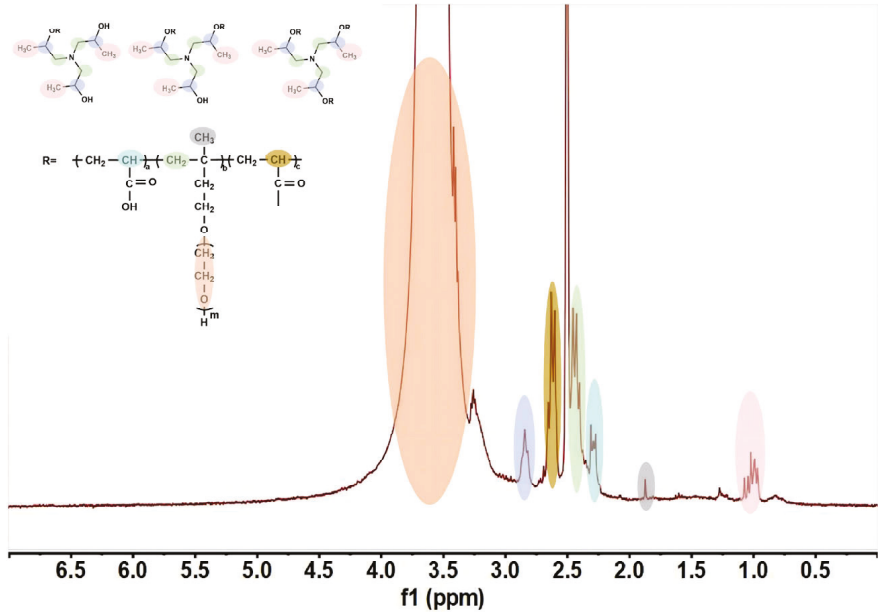

Figure 5. ^{1}H NMR spectroscopy of GA3.

The molecular weight and molecular weight distribution of GA1–GA4 were determined by gel permeation chromatography (GPC). The monomer ratio, molecular weight, and polydispersity index of GA1–GA4 are shown in Table 3. GA 1–GA 4 are all polymers, with actual GPC measured values ranging from 15,000 to 21,000. The molecular weight distribution is relatively narrow, between 1.29 and 1.39. This is due to the addition of chain transfer agents in the polymerization reaction, which enhances the chain transfer effect and narrows the molecular weight distribution. In addition, the branched structure of ACTA and the macromonomer characteristics of TPEG make the polymer chain length tend to be uniform. The reason why the molecular weight of GA4 is lower than that of GA3 may be due to the different radical polymerization reactivity ratios of AA, ACTA, and TPEG. The double bond activity of AA is higher than that of ACTA. In GA4, the proportion of AA decreases while the proportion of ACTA increases, leading to a reduction in the ratio of active monomers in the polymerization system. This weakens the driving force for chain growth reactions, making it difficult for molecular chains to extend sufficiently, and ultimately resulting in a lower degree of polymerization compared to GA3. ACTA molecules contain isopropyl branches, which create significant steric hindrance. Excess

ACTA during polymerization hinders the migration and collision of free radicals, increasing the probability of chain termination reactions and limiting molecular chain length. In contrast, GA3 has a moderate proportion of ACTA, allowing the steric hindrance effect to be controlled, thus enabling more complete chain growth.

Table 3. The ratio of monomer units, molecular weight and polydispersity index of grinding aids GA1–GA4.

Type	AA:ACTA:TPEG (mol/mol)	Molecular Weight (g/mol)	Polydispersity Index
GA1	4:0.5:1	16,095	1.34
GA2	3.5:1:1	15,343	1.39
GA3	3:1.5:1	20,457	1.38
GA4	2.5:2:1	18,429	1.29

The cement clinker, gypsum, and synthesized grinding aids were co-ground for 30 min, and the results were compared with those of the blank cement sample (without any additive) to evaluate the effects of the grinding aids on cement fineness and size distribution of particle. The selected dosage of the grinding aid (0.3%) aligned with our previous research on concrete admixtures, thereby facilitating direct comparison of related formulations [28]. As shown in Table 4, the residue on the 45 μm sieve significantly decreased after the addition of grinding aids, indicating a substantial reduction in coarse particles. Among the samples, the cement containing grinding aid GA-3 exhibited the lowest residue (0.8%), confirming that the additive effectively reduced the content of larger particles. Furthermore, the specific surface area of the cement is markedly increased with the addition of grinding aids, demonstrating their ability to enhance the degree of grinding. The specific surface area of GA-3 sample reached 4900 $cm^2 \cdot g^{-1}$, representing a 27.9% increase compared with the blank cement. These results collectively demonstrate that the synthesized polycarboxylate-based grinding aids significantly improve the grinding efficiency of cement.

Table 4. Effect of different grinding aids on cement fineness.

Cement Type	Grinding Duration (min)	Ratio (%)	Specific Surface Area (cm^2/g)	Growth Rate of Specific Surface Area (%)	Remaining Material 45 μm (%)
C-blank	30	0	3830 ± 52	0	8.2 ± 0.3
C-GA1	30	0.3%	4830 ± 45	26.1	1.6 ± 0.2
C-GA2	30	0.3%	4850 ± 38	26.6	1.5 ± 0.2
C-GA3	30	0.3%	4900 ± 41	27.9	0.8 ± 0.1
C-GA4	30	0.3%	4720 ± 50	23.2	1.9 ± 0.2

The size distributions of the five cement samples are summarized in Table 5. Since particle size distribution reflects the proportion of particles across different size ranges, it provides a more accurate measure of grinding efficiency than fineness or specific surface area alone. Previous studies have shown that particles in the 3–32 μm range have the most significant influence on cement hydration and performance [29,30]. As seen in Table 5, the proportion of fine particles (3–32 μm) in C-GA3 is the highest among all samples—36.1% higher than that of the blank cement—while its average particle size decreases by 12.76 μm. In contrast, the blank cement contains the largest proportion of coarse particles (>45 μm), whereas C-GA3 exhibits a substantial reduction in this fraction. These findings demonstrate

that GA3 exhibits the highest grinding efficiency, producing finer and more uniformly distributed cement particles compared with other formulations.

Table 5. Particle size distribution of cement powders.

Serial Number	Particle Size Distribution (wt%)				Average Particle Size (μm)
	<3 μm	3–32 μm	32–45 μm	>45 μm	
C-blank	0.93 ± 0.08	54.37 ± 1.25	15.79 ± 0.82	27.00 ± 1.15	33.89 ± 1.2
C-GA1	1.94 ± 0.12	71.35 ± 1.50	9.48 ± 0.55	12.44 ± 0.78	25.96 ± 0.92
C-GA2	1.93 ± 0.10	71.53 ± 1.32	11.50 ± 0.63	10.43 ± 0.65	24.34 ± 0.78
C-GA3	2.03 ± 0.11	73.65 ± 1.48	11.45 ± 0.58	7.50 ± 0.42	21.13 ± 0.85
C-GA4	1.91 ± 0.09	69.55 ± 1.62	11.08 ± 0.71	12.55 ± 0.80	26.03 ± 1.05

By combining cement grinding fineness and particle size distribution, it can be known that GA3 performs best. Although GA4 has an increased ACTA content, its performance shows a deteriorating trend. This difference may be due to the synergistic or imbalanced effects of the ratio of functional groups and chain structure of the grinding aids. In the GA3 structure, carboxyl groups chelate with Ca^{2+} on the cement surface to inhibit particle agglomeration, while the hydrophilic nature of the carboxyl groups ensures the dispersibility of the polymer in the cement paste. Excessive hydrophilicity of the molecular chain can lead to adsorption saturation, which weakens the steric hindrance effect. The hydroxyl groups on the ACTA in its structure form hydrogen bonds with active sites on the cement mineral surface, enhancing the polymer's adsorption to particles. Meanwhile, ACTA can also promote hydration. However, GA4, due to an excess of ACTA, has a reduced number of carboxyl groups in the molecular chain, resulting in insufficient chelation ability with Ca^{2+} on the cement particle surface and weakened electrostatic repulsion. Therefore, even though the adsorption effect of the ACTA group is enhanced, it cannot compensate for the weakened dispersing effect of the carboxylic acid. In addition, an increased amount of ACTA reduces the overall hydrophilicity of the polymer. The ACTA molecule has many polar groups; excessive addition leads to a sharp increase in the branching degree of the polymer main chain, intensify molecular chain entanglement, thereby reducing the dispersing effect.

The setting time, water demand, and flowability of the cement pastes were evaluated, and the relevant results are given in Table 6. As shown, all cements containing grinding aids (C-GA1–C-GA4) exhibited shorter initial and final setting times than the blank cement, confirming that the additives promoted cement hydration. The C-GA3 sample showed the most pronounced effect, reducing the initial and final setting times by 33 and 46 min, respectively. This behavior is attributed to the alkanolamine functionalities in the grinding aid, which enhance the cement minerals' reactivity and accelerate hydration reactions, thus expediting the setting process.

Table 6. Effect of grinding aids on the physical properties of cement.

Cement Type	Setting Time (min)		Water Requirement of Normal Consistency (% *w*/*w*)	Fluidity/mm
	Initial	Final		
C-blank	188 ± 5	246 ± 6	27.4 ± 0.2	224 ± 3
C-GA1	174 ± 4	230 ± 5	27.2 ± 0.3	235 ± 4
C-GA2	173 ± 4	230 ± 5	27 ± 0.2	238 ± 3
C-GA3	155 ± 3	200 ± 4	27.2 ± 0.1	232 ± 4
C-GA4	181 ± 5	242 ± 5	27 ± 0.2	230 ± 3

The water requirement for standard consistency of the GA-containing cements was slightly lower than that of the blank sample, suggesting that the synthesized modified polycarboxylate grinding aids effectively adsorbed onto cement particle surfaces. This adsorption enhances particle dispersion and introduces steric hindrance effects, which prevent particle agglomeration [31].

Furthermore, the fluidity of all cements containing grinding aids was higher than that of the blank cement. Although the addition of grinding aids increased the specific surface area and shortened setting time—factors that might otherwise raise water demand—the polycarboxylate-based GAs exhibited excellent dispersibility. By adsorbing on the cement surface and inducing electrostatic repulsion between particles, they minimized aggregation. The balance between these effects led to a notable improvement in mortar flowability, demonstrating that the modified grinding aids contribute positively to the workability of cement systems.

The flexural and compressive strength results of the five cement mortars after 3-day and 28-day curing periods are presented in Table 7. As shown, all cements containing grinding aids (C-GA1–C-GA4) exhibited higher strengths than the blank cement at both ages. Among them, C-GA3 demonstrated the most significant improvement, with 3-day compressive strength increased by 6.5 MPa and the 28-day compressive strength increased by 5.7 MPa compared with the blank sample.

Table 7. Effect of grinding aids on the mechanical properties of cement mortar.

Cement Type	Flexural Strength (MPa)		Compressive Strength (MPa)	
	3d	28d	3d	28d
C-blank	5.6 ± 0.3	9.3 ± 0.4	18.0 ± 0.6	43.2 ± 1.1
C-GA1	7.1 ± 0.4	9.9 ± 0.3	20.6 ± 0.7	46.8 ± 1.0
C-GA2	7.0 ± 0.3	10.3 ± 0.4	22.9 ± 0.9	47.2 ± 1.2
C-GA3	7.4 ± 0.3	10.6 ± 0.3	24.5 ± 0.8	48.9 ± 1.0
C-GA4	6.8 ± 0.3	9.7 ± 0.3	21.2 ± 0.9	46.5 ± 1.1

This enhancement is considered to be attributed to the larger specific surface area of the GA3-modified cement, which facilitates more efficient contact between cement particles and water. The increased surface reactivity accelerates the hydration process, resulting in faster formation of hydration products and improved early strength development. Consequently, the modified polycarboxylate grinding aid GA3 not only enhances grinding efficiency but also contributes to both early and long-term mechanical performance of cement.

Cement hydration is a complex physicochemical process, and the energy changes during this process can be intuitively presented through hydration heat detection. Given the close relationship between the rate of hydration heat release and hydration kinetics, this indicator can directly reveal the time nodes, heat release intensity, and total heat of hydration peaks (induction period, acceleration period). These thermodynamic parameters are closely related to the setting time and early strength development of cement. Based on this, this study measured the heat flow and heat of hydration using a TAM-Air isothermal calorimeter. As shown in Figure 6a, it can be seen that blank cement exhibits a distinct exothermic peak during the initial hydration stage (approximately 0–10 h), followed by a gradual decline, indicating that the hydration reaction is more intense initially and then becomes milder. In contrast, cement with the grinding aid GA3 shows a more pronounced exothermic peak and a higher peak value during the initial stage (approximately 0–10 h), suggesting that GA3 accelerates the early hydration reaction of cement. Subsequently, the rate of decline is similar to that of blank cement, but the overall rate remains slightly higher. As shown in Figure 6b, with the passage of time, the cumulative hydration heat of blank cement gradually increases and eventually stabilizes. This indicates that the hydration

reaction of cement is a continuous process, but the reaction rate gradually slows down over time. Meanwhile, cement with the grinding aid GA3 shows faster growth in cumulative hydration heat during the initial stage (approximately 0–20 h), demonstrating that GA3 promotes the early hydration reaction. Thereafter, the trend of cumulative hydration heat growth is similar to that of blank cement, but the total cumulative amount is slightly higher. Based on the test results of hydration heat, the addition of grinding aid GA3 significantly accelerates the early hydration reaction of cement, as evidenced by the significant increase in heat release rate and cumulative hydration heat during the initial stage. However, as time progresses, the hydration reaction trends of both become consistent, indicating that the grinding aid mainly affects the early hydration process.

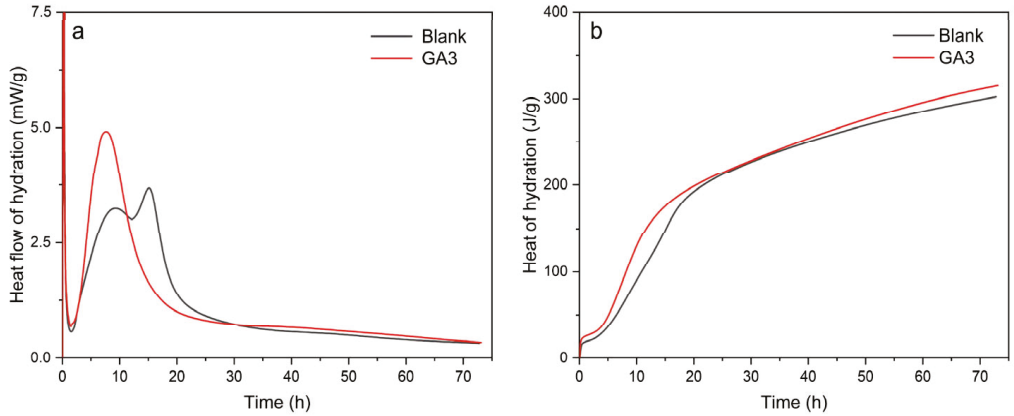

Figure 6. Heat flow and heat release of cement hydration. (**a**) Hydration heat release rate curve. (**b**) Hydration heat release curve.

Figure 7 indicates the SEM results of cement samples (a–e) and their corresponding particle size distribution histograms (f–j). The blank cement without the modified polycarboxylate grinding aid exhibits large and irregularly distributed particles in its SEM image (a), and its particle size distribution (f) shows a relatively broad range—collectively indicating poor dispersion. In contrast, the cements incorporating the modified grinding aids (C-GA1–C-GA4, corresponding to b-e, respectively) display finer and more uniformly distributed particles in their SEM images; meanwhile, their particle size distributions (g–j) present narrower peaks, which reflects better size uniformity. Among them, C-GA3 presents the most homogeneous and refined particle morphology in SEM image (e), and its particle size distribution (j) shows the most concentrated peak, confirming the optimal dispersion effect. This improvement is mainly attributed to the carboxyl (-COOH) groups in the modified polycarboxylate molecules, which can chelate with Ca^{2+} ions on the surface of cement particles to form a stable double electric layer structure. The resulting electrostatic repulsion effectively inhibits particle agglomeration. Meanwhile, the long polyether chains of TPEG provide an additional steric hindrance effect, further enhancing particle dispersion [20]. These combined mechanisms confirm that all synthesized grinding aids improved the size distribution of particle and uniformity of cement, with GA3 showing the most pronounced effect.

To further investigate the effect of C-GA3 on the distribution of cement chemical phases, EDS area scan analysis was conducted (Figure 8b–i). The results show that the distribution of major elements such as Ca, Si, and Al exhibits high uniformity. The elemental signals are continuously distributed throughout the field of view, with no obvious element segregation or enrichment clusters observed. This uniform elemental distribution characteristic indicates that the C-GA3 grinding aid promotes the dispersion and mixing of different mineral phases at the microscale through its surface activity. Combining SEM and mapping

results, it can be known that C-GA3 molecules adsorb on the particle surface, reducing the particle surface energy. This not only prevents the re-agglomeration of fine powders (thus obtaining finer particles) but also makes the components distribute more uniformly in space, which is conducive to the uniform progress of subsequent hydration reactions.

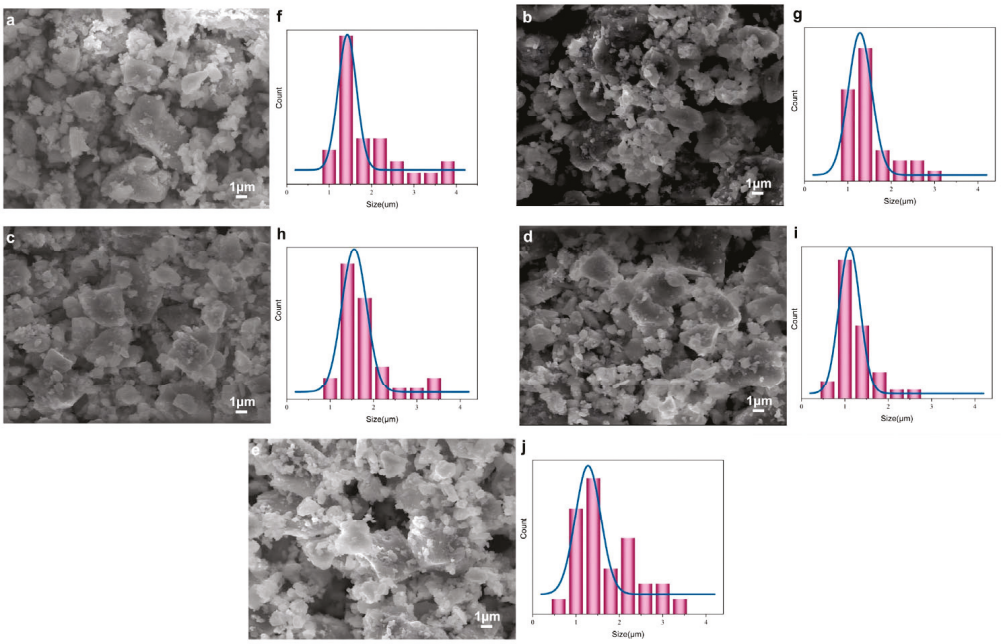

Figure 7. SEM images and corresponding particle size distribution histograms of cement samples: (**a**,**f**) blank cement; (**b**,**g**) C-GA1; (**c**,**h**) C-GA2; (**d**,**i**) C-GA3; (**e**,**j**) C-GA4.

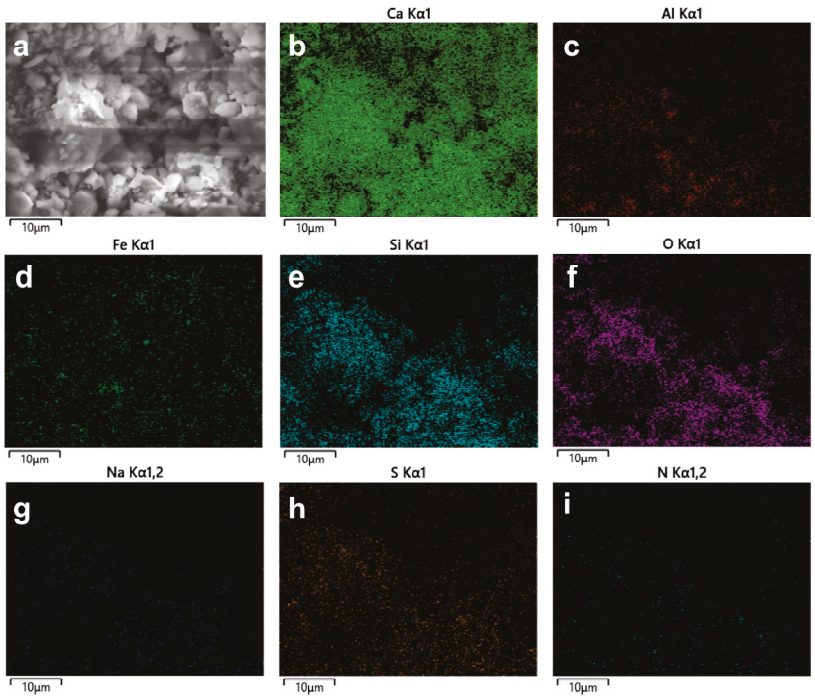

Figure 8. SEM images of (**a**) C-GA3, (**b**) Ca elemental mapping images of C-GA3, (**c**) Al elemental mapping images of C-GA3, (**d**) Fe elemental mapping images of C-GA3, (**e**) Si elemental mapping images of C-GA3, (**f**) O elemental mapping images of C-GA3, (**g**) Na elemental mapping images of C-GA3, (**h**) S elemental mapping images of C-GA3 and (**i**) N elemental mapping images of C-GA3.

4. Conclusions

Based on the results and discussions above, the following conclusions can be drawn:

(1) A modified polycarboxylate grinding aid was successfully synthesized via a free-radical polymerization reaction, and its performance in cement grinding was systematically investigated.
(2) The addition of modified polycarboxylate grinding aid significantly improved the grinding efficiency of cement. Compared with the blank cement, the optimal sample GA-3 (with AA:ACTA:TPEG molar ratio of 3:1.5:1) reduced the residue on the 45 μm sieve to 0.8%, increased the specific surface area by 27.9% (reaching 4900 cm^2/g), and increased the proportion of particles in the beneficial size range of 3–32 μm by 36.1%.
(3) The grinding aid optimized the particle size distribution of cement. SEM and particle size analysis showed finer and more uniform particles. It also improved cement paste properties, with a slight reduction in water requirement for standard consistency, increased fluidity, and significantly shortened setting times (GA-3 reduced initial and final setting times by 33 and 46 min, respectively).
(4) Mechanical property tests showed that all cement samples containing grinding aids exhibited higher strengths at both 3-day and 28-day ages compared to the blank sample. GA-3 performed best, with 3-day and 28-day compressive strengths increased by 6.5 MPa and 5.7 MPa, respectively, confirming the dual functions of this grinding aid in both grinding efficiency improvement and strength enhancement.
(5) In this study, triisopropanolamine was modified with acryloyl chloride and introduced into the polycarboxylate molecular chain, successfully resolving the poor compatibility issue of TIPA when used alone, while synergistically enhancing grinding efficiency and hydration activity. This provides theoretical and technical support for developing high-performance and environmentally friendly cement grinding aids.

This study is basic research conducted under laboratory conditions, aiming to verify the fundamental principles and potential application value of new compounds, and to provide theoretical support for industrial applications. However, the synthesis process of this grinding aid is complex and requires strict process control, which may restrict large-scale production. The next key task is to carry out pilot-scale amplification and factory site testing. Under the premise of ensuring stable product performance, process amplification issues need to be addressed to promote the transformation of laboratory achievements into industrial applications.

Author Contributions: Writing—original draft, Y.Y. and S.S.; writing—review and editing, L.W., Y.L. and L.Z.; supervision, H.W. and C.W. All authors have read and agreed to the published version of the manuscript.

Funding: This research was funded by the science and technology development project of Jilin province, China (No. 20230508059RC).

Data Availability Statement: The data presented in this study are available on request from the corresponding author.

Acknowledgments: The authors gratefully acknowledge the technical support provided by Jilin Xipu Cement Grinding Aid Co., Ltd., & Baotou Steel North-West Pioneer Construction Co., Ltd.

Conflicts of Interest: Yu Liu was employed by Jilin Xipu Cement Grinding Aid Co., Ltd. and was employed by Jilin Xipu Cement Grinding Aid Co., Ltd. Liping Zhang was employed byBaotou Steel North-West Pioneer Construction Co., Ltd. The remaining authors declare that the research was conducted in the absence of any commercial or financial relationships that could be construed as a potential conflict of interest.

Abbreviations

The following abbreviations are used in this manuscript:

TIPA	triisopropanolamine
TEA	triethanolamine
Aft	ettringite
AA	acrylic acid
TPEG	isopentenol polyoxyethylene
DMF	N,N-dimethylformamide
VC	ascorbic acid
H_2O_2	hydrogen peroxide
NaOH	sodium hydroxide
GA	grinding aid
GPC	gel permeation chromatography
NMR	Nuclear Magnetic Resonance Spectra
SEM	Scanning electron microscope

References

1. Zhang, T.; Gao, J.; Hu, J. Preparation of polymer-based cement grinding aid and their performance on grindability. *Constr. Build. Mater.* **2015**, *75*, 163–168. [CrossRef]
2. Kaya, Y.; Kobya, V.; Mardani, A. Evaluation of fresh state, rheological properties, and compressive strength performance of cementitious system with grinding aids. *J. Appl. Polym. Sci.* **2024**, *141*, e55212. [CrossRef]
3. Zan, S.; Ishak, K. A study of different grinding aids for low-energy cement clinker production. *J. S. Afr. Inst. Min. Metall.* **2023**, *123*, 471–478. [CrossRef] [PubMed]
4. Altun, O. Energy and cement quality optimization of a cement grinding circuit. *Adv. Powder Technol.* **2018**, *29*, 1713–1723. [CrossRef]
5. Ghiasvand, E.; Ramezanianpour, A. Effect of grinding method and particle size distribution on long term properties of binary and ternary cements. *Constr. Build. Mater.* **2017**, *134*, 75–82. [CrossRef]
6. Tsakalakis, K.G.; Stamboltzis, G.A. Correlation of the Blaine value and the d80 size of the cement particle size distribution. *ZKG Int.* **2008**, *61*, 60.
7. Zhang, X.; Hu, H. Preparation and analysis of a polyacrylate grinding aid for grinding calcium carbonate (GCC) in an ultrafine wet grinding process. *Powder Technol.* **2014**, *254*, 470–479. [CrossRef]
8. Paramasivam, R.; Vedaraman, R. Effects of the physical properties of liquid additives on dry grinding. *Powder Technol.* **1992**, *70*, 43–50. [CrossRef]
9. Prziwara, P.; Kwade, A. Grinding aid additives for dry fine grinding processes–Part II: Continuous and industrial grinding. *Powder Technol.* **2021**, *394*, 207–213. [CrossRef]
10. Yang, J.; Li, G.; Yang, W. Effect of polycarboxylic grinding aid on cement chemistry and properties. *Polymers* **2022**, *14*, 3905. [CrossRef]
11. Zhou, Y.; Wang, J.; Song, Y. Study on structure-performance relationship and action mechanism of organic chemicals in cement grinding aids. *Mater. Lett.* **2024**, *364*, 136365. [CrossRef]
12. Mishra, R.K.; Weibel, M.; Müller, T. Energy-effective grinding of inorganic solids using organic additives. *Chimia* **2017**, *71*, 451–460. [CrossRef] [PubMed]
13. Njiru, N.E.; Muthengia, W.J.; Munyao, M.O. Review of the Effect of Grinding Aids and Admixtures on the Performance of Cements. *Adv. Civ. Eng.* **2023**, *2023*, 6697842. [CrossRef]
14. Katsioti, M.; Tsakiridis, P.E.; Giannatos, P. Characterization of various cement grinding aids and their impact on grindability and cement performance. *Constr. Build. Mater.* **2009**, *23*, 1954–1959. [CrossRef]
15. Мирюк, O.A. Phase composition of belite cements of increased hydraulic activity. *Mag. Civ. Eng.* **2022**, *112*, 11201.
16. Wang, C.; Wang, Y.; Pan, Y. The fractal characteristics of cement-based materials with grinding aid via BSE image analysis. *Sci. Rep.* **2025**, *15*, 37717. [CrossRef]
17. Zhao, J.; Wang, D.; Yan, P.; Zhao, S.; Zhang, D. Particle characteristics and hydration activity of ground granulated blast furnace slag powder containing industrial crude glycerol-based grinding aids. *Constr. Build. Mater.* **2016**, *104*, 134–141. [CrossRef]
18. Han, J.; Wang, K.; Shi, J.; Wang, Y. Mechanism of triethanolamine on Portland cement hydration process and microstructure characteristics. *Constr. Build. Mater.* **2015**, *93*, 457–462. [CrossRef]
19. He, Y.; Zhang, X.; Wu, G.; Shi, P. Effects of polycarboxylate-based grinding aid on the performance of grinded cement. *J. Wuhan Univ. Technol.-Mater. Sci. Ed.* **2021**, *36*, 682–688. [CrossRef]

20. Yang, H.; Plank, J.; Sun, Z. Investigation on the optimal chemical structure of methacrylate ester based polycarboxylate superplasticizers to be used as cement grinding aid under laboratory conditions: Effect of anionicity, side chain length and dosage on grinding efficiency, mortar workability and strength development. *Constr. Build. Mater.* **2019**, *224*, 1018–1025. [CrossRef]
21. He, Y.; Liu, S.; Luo, Q.; Liu, W.; Xu, M. Influence of PCE-type GA on cement hydration performances. *Constr. Build. Mater.* **2021**, *302*, 124432. [CrossRef]
22. Kaya, Y.; Şahin, H.G.; Mardani, N.; Mardani, A. Influence of Grinding Aids on the Grinding Performance and Rheological Properties of Cementitious Systems. *Materials* **2024**, *17*, 5328. [CrossRef]
23. *GB/T 1345-2005*; The Testing Sieving Method for Fineness of Cement. Standardization Administration of PRC: Beijing, China, 2005.
24. *GB/T 8074-2008*; Testing Method for Specific Surface of Cement-Blaine Method. Standardization Administration of PRC: Beijing, China, 2008.
25. *GB/T 1346-2024*; Test Methods for Water Requirement of Standard Consistency, Setting Time and Soundness of the Portland Cement. Standardization Administration of PRC: Beijing, China, 2024.
26. *GB/T 2419-2005*; Test Method for Fluidity of Cement Mortar. Standardization Administration of PRC: Beijing, China, 2005.
27. *GB/T 17671-2021*; Test Method of Cement Mortar Strength (ISO Method). Standardization Administration of PRC: Beijing, China, 2021.
28. Wang, H.; Zhao, W.; Wang, S.; Wang, C.; Du, Q.; Yan, Y. Maltitol-Derived Sacrificial Agent for Enhancing the Compatibility between PCE and Cement Paste. *Materials* **2023**, *16*, 7515. [CrossRef]
29. Kobya, V.; Kaya, Y.; Mardani-Aghabaglou, A. Effect of amine and glycol-based grinding aids utilization rate on grinding efficiency and rheological properties of cementitious systems. *J. Build. Eng.* **2022**, *47*, 103917. [CrossRef]
30. Sun, Z.; Yang, H.; Shui, L.; Liu, Y.; Yang, X.; Ji, Y.; Hu, K.; Luo, Q. Preparation of polycarboxylate-based grinding aid and its influence on cement properties under laboratory condition. *Constr. Build. Mater.* **2016**, *127*, 363–368. [CrossRef]
31. Uchikawa, H.; Hanehara, S.; Sawaki, D. The role of steric repulsive force in the dispersion of cement particles in fresh paste prepared with organic admixture. *Cem. Concr. Res.* **1997**, *27*, 37–50. [CrossRef]

Disclaimer/Publisher's Note: The statements, opinions and data contained in all publications are solely those of the individual author(s) and contributor(s) and not of MDPI and/or the editor(s). MDPI and/or the editor(s) disclaim responsibility for any injury to people or property resulting from any ideas, methods, instructions or products referred to in the content.

coatings

MDPI

Review

Research Progress on the Preparation and Performance of Recycled Mortars Using Solid Waste-Based Cementitious Materials

Yanjiao Gao [1], Jiale Chen [2], Qing Li [3,*], Tian Su [1,4,*], Meng Li [1], Bangxiang Li [1] and Xuefeng Mei [5]

[1] Department of Civil Engineering, School of Civil Engineering and Geomatics, Shandong University of Technology, Zibo 255000, China
[2] School of Architectural and Hydraulic Engineering, Jiujiang Polytechnic University of Science and Technology, Jiujiang 332020, China
[3] Department of Architecture, School of Civil Engineering and Architecture, Hebei University of Engineering Science, Shijiazhuang 050091, China
[4] Department of Engineering and Management, International College, Krirk University, No. 3 Soi Ramintra 1, Ramintra Road, Anusaowaree, Bangkok 10220, Thailand
[5] Department of Architectural Engineering, School of Civil Engineering, Inner Mongolia University of Science and Technology, 7 Alding Street, Baotou 014010, China
* Correspondence: liqing278761715@126.com (Q.L.); sutian@sdut.edu.cn (T.S.)

Abstract

Solid waste-based cementitious materials (SWCMs) represent an innovative class of binders derived mainly from construction and demolition waste as well as industrial byproducts. Their application in recycled mortar offers a promising pathway to partially replace conventional cement, thereby advancing resource recycling and facilitating a low-carbon transition in the cement industry. This review systematically examines the properties, activation techniques, strength development, and corrosion resistance of recycled mortar prepared with SWCMs. Recycled powder (RP) and industrial solid waste have gelation potential, but their low reactivity requires activation treatment to enhance utilization efficiency. Activation methods, including thermal activation, carbonation, and alkali activation, effectively enhance reactivity and promote the formation of dense gel structures (e.g., C-(A)-S-H, N-A-S-H). While low replacement ratios optimize pore structure via the microfiller effect, higher ratios introduce excessive inert components, impairing mechanical properties. SWCMs demonstrate superior resistance to sulfate and chloride attacks, but their acid resistance is relatively limited. They also have excellent freeze–thaw resistance. SWCMs represent a viable and sustainable alternative to conventional cement, exhibiting commendable mechanical and durability properties when properly activated and formulated, thereby contributing to resource recycling and environmental sustainability in the cement industry.

Keywords: industrial solid waste; construction solid waste; recycled mortar; activation technology

1. Introduction

The advancement of economic globalization has accelerated the rapid development of industries worldwide, yet it has also resulted in substantial resource consumption and increased greenhouse gas emissions. Statistics indicate that the construction sector accounts for approximately 40% of the natural resources used in industrial production. In addition to emitting greenhouse gases during production and construction, this sector

generates enormous amounts of construction and demolition waste [1]. Cement, as one of the most essential building materials, is responsible for approximately 40% of CO_2 emissions during its production process while also consuming significant amounts of natural resources. Moreover, the total volume of solid waste generated from construction and demolition activities has reached 3.5 billion tons [2], constituting 30% to 50% of the global solid waste stream [3,4]. Simultaneously, industrial by-products such as fly ash, slag, and desulfurization gypsum, which are produced by metallurgical, chemical, and other industries, have also accumulated on a massive scale. Collectively, these materials exert considerable environmental pressure [5]. Currently, the resource utilization rate of such solid wastes remains relatively low, with a large proportion ultimately disposed of in landfills or stockpiles. This not only occupies valuable land resources but also causes complex pollution of soil, water, and the atmosphere, emerging as a critical bottleneck to sustainable urban development.

Among construction waste materials, waste concrete and waste clay bricks constitute the two predominant components. In recent years, beyond merely crushing and sieving these materials for use as recycled aggregates, further grinding them into recycled powder for application as cementitious materials has emerged as a cutting-edge research direction aimed at achieving high-value recycling of construction waste [6]. This approach seeks to transform waste from a simple physical filler into a key component that participates in cementitious reactions and is regarded as one of the core pathways to advance construction waste recycling from "downcycling" to "upcycling." However, recycled powder often contains stabilized hydration products (such as C-S-H gel and $Ca(OH)_2$) or high-temperature sintered inert phases (e.g., quartz and mullite), which generally lead to inherent drawbacks such as a low content of active components, high chemical inertness, irregular particle morphology, and high water demand [7]. As a result, composite cementitious systems incorporating recycled powder as a partial replacement for cement often suffer from slow hydration rates, insufficient early-age strength development, and poor microstructural densification. When used as a source of aluminosilicates in geopolymer synthesis, recycled powder presents challenges such as low reactivity, rapid consumption of alkaline species in solution, and the formation of loosely structured polymerization products [8,9]. These fundamental limitations in material activity severely restrict the high-volume application of recycled powder in structural materials, posing significant challenges to its widespread adoption in practical engineering.

Moreover, the disposal of industrial solid waste has become an equally pressing issue. Byproducts such as fly ash from coal-fired power plants, blast furnace slag from iron and steel smelting, and desulfurization gypsum and red mud have accumulated in massive quantities, posing serious environmental threats. In recent years, the advanced utilization of industrial solid waste has become a leading research direction for achieving high-value recycling. This approach moves beyond conventional applications, such as road base materials or cement blends, instead of using these wastes as essential raw materials for green construction materials, including geopolymers and alkali-activated binders [10–12]. This approach aims to transform industrial solid waste from an "environmental burden" into a strategic resource that supports the development of "zero-waste cities" and low-carbon building solutions, representing a shift from low-end disposal toward value-added creation [13–15]. However, owing to differences in sources and production processes, these wastes often present inherent drawbacks, such as significant variability in chemical composition, complex active phase constituents, and diverse physical characteristics [16]. These limitations make it challenging to precisely control reaction pathways, workability, and long-term volume stability when such wastes are used as sole or primary precursors in alkali-activated systems [17]. Furthermore, the design of blended systems and process-

ing strategies for performance optimization is complicated by unclear structure-activity relationships among reaction mechanisms, resultant phases, and macroscopic properties, largely due to the heterogeneity and complexity of solid wastes [18,19]. These fundamental bottlenecks at both the material utilization and engineering application levels severely restrict the reliable, large-scale use of industrial solid waste-based cementitious materials in structural engineering, resulting in considerable challenges in industrialization.

Promoting the systematic integration and synergistic utilization of construction waste and industrial solid waste in the field of cementitious materials is crucial for achieving both high-performance and low-carbon objectives. By combining the use of recycled powder with alkali activation technology for industrial solid waste, it is possible not only to leverage their complementary advantages and enhance the overall performance and stability of the cementitious system but also to significantly reduce reliance on conventional cement [20,21], thereby substantially decreasing energy consumption and carbon emissions at the source.

Given the above considerations, there is a pressing need to systematically review, consolidate, and critically assess research progress in the field of solid waste-based cementitious materials for recycled mortar. This review specifically addresses a critical gap by establishing a comprehensive framework for solid waste-based cementitious materials, which synergistically utilize recycled powder derived from construction and demolition waste (CDW) and industrial solid wastes. It systematically elucidates how various activation methods, such as thermal activation, carbonation, and alkali activation treatments, relate to material properties. The review systematically links these activation mechanisms to the resulting material performance, particularly mechanical strength and resistance to diverse aggressive environments, including sulfate attack, acid corrosion, chloride penetration, and freeze–thaw cycles. By providing a comparative analysis of degradation mechanisms under different aggressive conditions and correlating them with gel chemistry and microstructure, this work offers novel insights for designing high-performance, low-carbon binders with enhanced durability. Thus, it bridges the knowledge gap between isolated activation studies and the practical, durable application of fully waste-based mortars.

2. Methodology Adopted for the Review

To ensure systematicity, representativeness, and relevance in selecting references for this review, a dynamic, evolutionary, and layered in-depth search and screening strategy was employed. The retrieval databases included the Web of Science (WoS) Core Collection (encompassing sub-databases such as SCI, SSCI and AHCI) and the China National Knowledge Infrastructure (CNKI) (including core databases of Peking University Chinese and CSCD), ensuring comprehensive coverage of internationally authoritative literature and important domestic research achievements. The determination of keywords was a gradual process, refined and expanded as research and understanding deepened. Initially, "recycled mortar" served as the entry point, which was then extended to material system keywords such as "polymer mortar" and "alkali-activated cementitious materials". After clarifying the basic reaction mechanisms, the scope was further broadened to preparation methods such as "thermally activated mortar" and "carbonized mortar". The focus shifted to material properties, introducing evaluation terms such as "corrosion resistance", "freeze-thaw resistance", "sulfate resistance", and "acid corrosion resistance". Based on this principle, the study constructed a multi-level keyword system comprising core concepts and their synonym clusters. These elements were strategically combined with Boolean operators including AND and OR, which enabled an optimal balance between recall and precision throughout the retrieval process and laid a reliable foundation for the review. After the initial literature acquisition, clear inclusion and exclusion criteria were defined: priority was given to original research articles and authoritative peer-reviewed reviews,

while unreviewed conference abstracts, news reports, and literature for which the full text could not be obtained were excluded. Through this structured process, the study aimed to build a comprehensive and precise literature base, thereby supporting the reliability and relevance of the review's arguments.

3. Feasibility of Solid Waste-Based Cementitious Materials for Recycled Mortars

Solid waste-based recycled mortar is an environmentally sustainable construction material made from solid wastes, including construction and demolition debris and industrial by-products. It is produced through the partial or complete replacement of conventional natural aggregates and cementitious materials via physical, chemical, or hybrid processing techniques according to specific mixture formulations. This approach seeks to valorize solid wastes as valuable resources, thereby reducing the consumption of natural resources, mitigating environmental pollution, and fostering the development of a circular economy.

3.1. Material Characteristics

3.1.1. Construction Solid Waste Materials

Recycled powder (RP) is an ultrafine powder (particle size < 0.16 mm) primarily produced from construction and demolition waste, such as waste concrete, bricks, and masonry, through a series of processing steps, including screening, crushing, and grinding. The raw materials are diverse in origin and are derived mainly from waste concrete and clay bricks generated during demolition projects, as well as from construction residues and laboratory waste. The physicochemical properties of RP, including its reactivity index and particle size distribution, exhibit considerable heterogeneity. This stems from significant variations in the source materials, such as building type, service life, and original composition. During production, the raw materials undergo meticulous processing involving crushing, sorting, drying, and high-precision grinding to meet standardized specifications [22]. Consequently, RP particles are characterized by rough surfaces, irregular and angular morphologies, and porous structures, as shown in Figure 1 [23,24]. The irregular particle shape increases interparticle friction, which adversely affects mortar fluidity, whereas the porous structure elevates water demand, thereby influencing rheological performance. However, the angular and rough surfaces of the particles provide a larger reactive area that promotes hydration, and the porous texture facilitates internal curing by absorbing and retaining water [25].

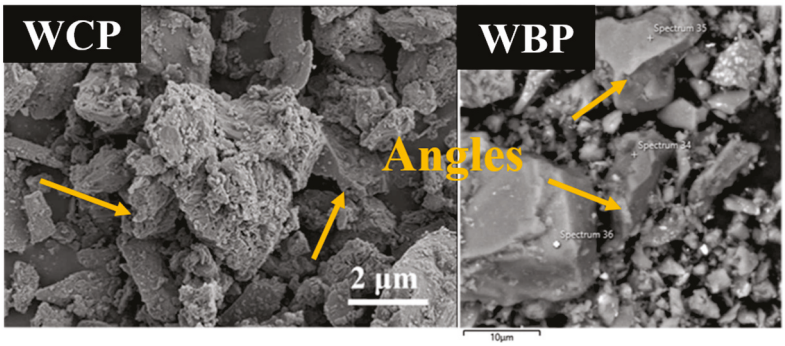

Figure 1. SEM images of recycled concrete powder and recycled brick powder [23,24].

Owing to variations in raw material sources, the composition of RP can vary significantly. Waste concrete powder (WCP) primarily consists of both crystalline and amorphous phases, including quartz (SiO_2), calcite ($CaCO_3$), dolomite ($CaMg(CO_3)_2$), C-S-H gel, and ettringite, and unhydrated clinker phases, such as C_2S, C_3S, and C_4AF, as illustrated in Figure 2a [23]. Quartz and dolomite originate from fine and coarse aggregates, respectively,

introduced during the concrete crushing process. Calcite results from the carbonation of both the aggregate and the concrete. As shown in Figure 2b, the major chemical constituents of WCP are SiO_2, CaO, Fe_2O_3, Al_2O_3, and MgO. Among these, SiO_2 is the most abundant component, followed by CaO. In contrast, waste brick powder (WBP) has a distinctly different composition, characterized by high contents of SiO_2 and Al_2O_3, as indicated in Figure 3b. The X-ray diffraction (XRD) pattern of WBP confirms that quartz is the predominant crystalline phase, as shown in Figure 3a [24]. The high concentrations of key oxides, such as CaO, SiO_2, and Al_2O_3, in RP indicate its potential pozzolanic reactivity [26]. The presence of amorphous SiO_2 and Al_2O_3 particles may promote the reaction of volcanic ash. However, CaO exists in the form of calcium carbonate, which prevents it from participating in new hydration reactions.

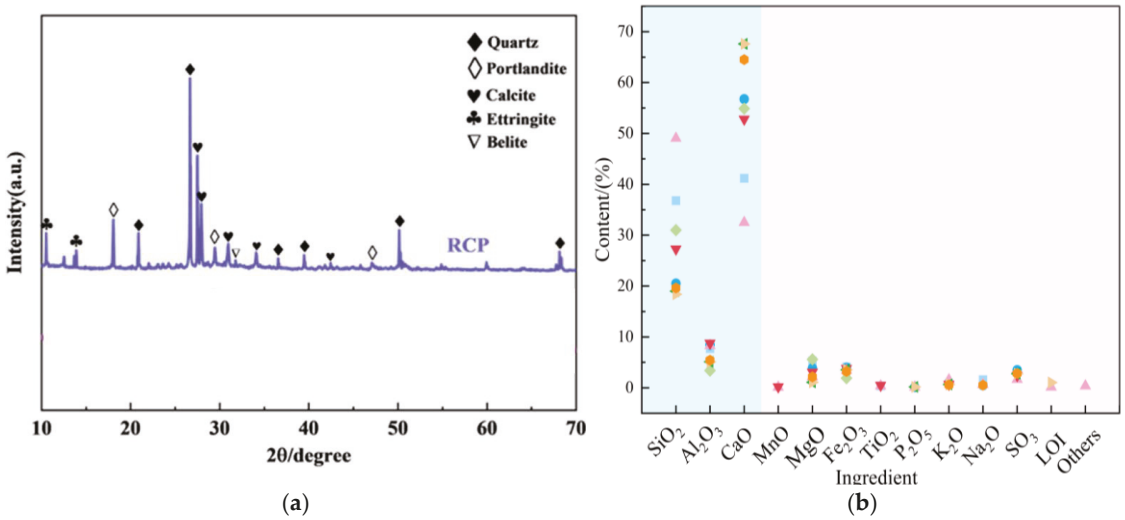

(**a**) (**b**)

Figure 2. XRD pattern (**a**) and main chemical composition (**b**) of waste concrete powder [25,27–34].

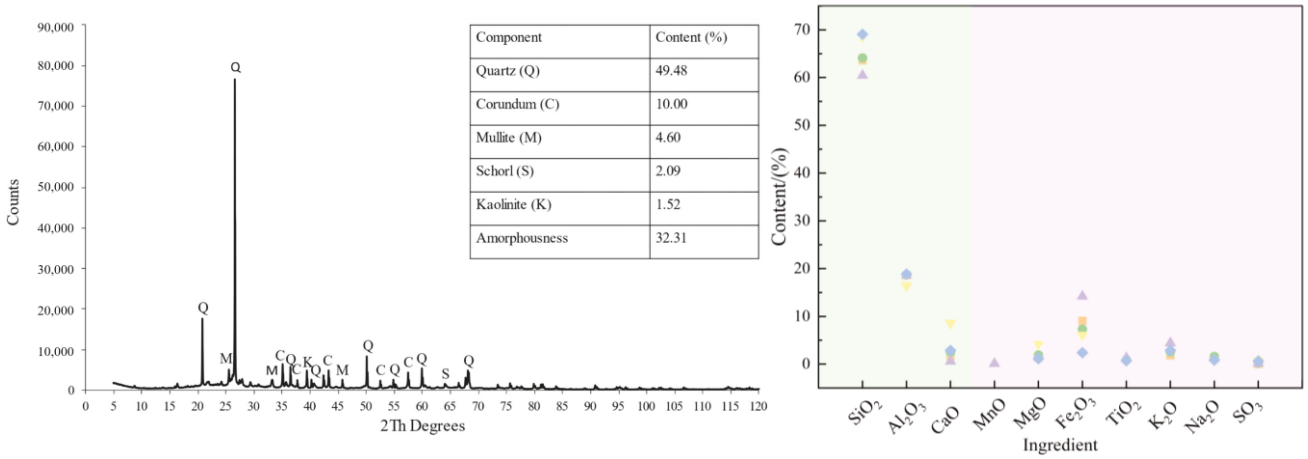

(**a**) (**b**)

Figure 3. XRD pattern (**a**) and main chemical composition (**b**) of waste brick powder [24,35–39].

3.1.2. Industrial Solid Waste

Industrial solid wastes, such as slag and fly ash, present inherent advantages for developing alkali-activated materials because of their high contents of silicon and aluminum components, which are readily soluble in alkaline environments. By directly activating the silicoaluminate component in the precursor with an alkaline activator, depolymerization and reconstruction of the active components in solid waste can be achieved. This process overcomes the traditional cement's reliance on C_3S and C_2S minerals, providing a more

efficient reaction pathway. Owing to their low-carbon characteristics, these systems have attracted widespread attention.

Compared with ordinary Portland cement, alkali-activated materials exhibit lower energy consumption, higher mechanical strength, and superior durability, making them promising alternatives to traditional cement [29,40]. The chemical compositions of two commonly used precursors, fly ash and slag, are presented in Figure 4. Although variations exist depending on the raw material sources, the main components of both are concentrated in three oxides, namely, SiO_2, CaO, and Al_2O_3. Fly ash and slag represent two typical systems. As shown in Figure 4a, fly ash is a low-calcium system dominated by silica and alumina (SiO_2 and Al_2O_3). Slag is a high-calcium system rich in silica and calcium oxides (SiO_2 and CaO), as indicated in Figure 4b. The proportions of Si, Ca, and Al significantly influence the performance of the resulting hardened mortar [41].

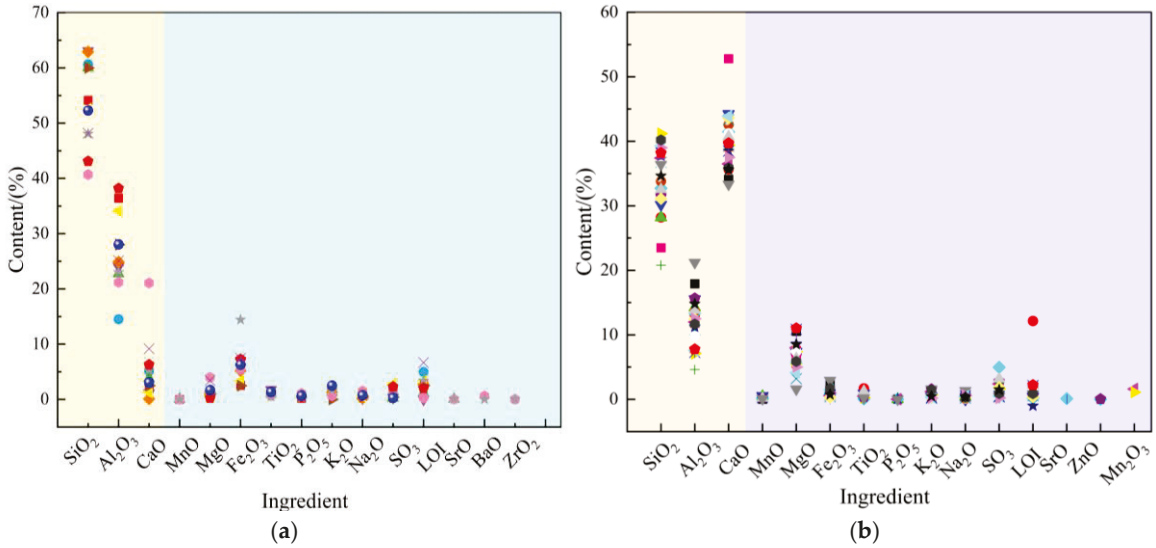

Figure 4. The main chemical components of fly ash (**a**) and slag powder (**b**) [42–66].

Fly ash (FA), one of the most prevalent industrial byproducts, is a fine powder collected from flue gas following the combustion of bituminous coal in coal-fired power plants. It typically exhibits gray to dark gray coloration, occasionally appearing light gray, depending on the unburned carbon content and mineral composition. Generally, higher carbon levels result in darker shades. Most FA particles range from 1–100 μm in size and have a high specific surface area [42,45]. Class F fly ash, also known as low-calcium FA, is typically derived from anthracite or bituminous coal, whereas Class C (high-calcium) FA is produced from lignite or subbituminous coal. Compared with high-calcium FA, low-calcium FA is richer in SiO_2 and Al_2O_3, with a CaO content generally less than 15%, whereas the CaO content of high-calcium FA is between 15% and 30% [43]. As shown in Figure 5a, the FA particles are predominantly spherical and consist largely of an amorphous glass phase, along with minor crystalline phases such as quartz, mullite, and magnetite, as evidenced by the XRD pattern in Figure 5b [67]. Although fly ash is widely used as an alkali-activated precursor, the large-scale closure of coal-fired power plants and the transition of the power industry towards a more environmentally sustainable model are expected to significantly reduce its production in the future. Moreover, the extensive application of fly ash as a supplementary cementitious material in conventional building materials has generated significant competitive demand. This demand may hinder its large-scale development and utilization as an alkali-activated precursor for other applications.

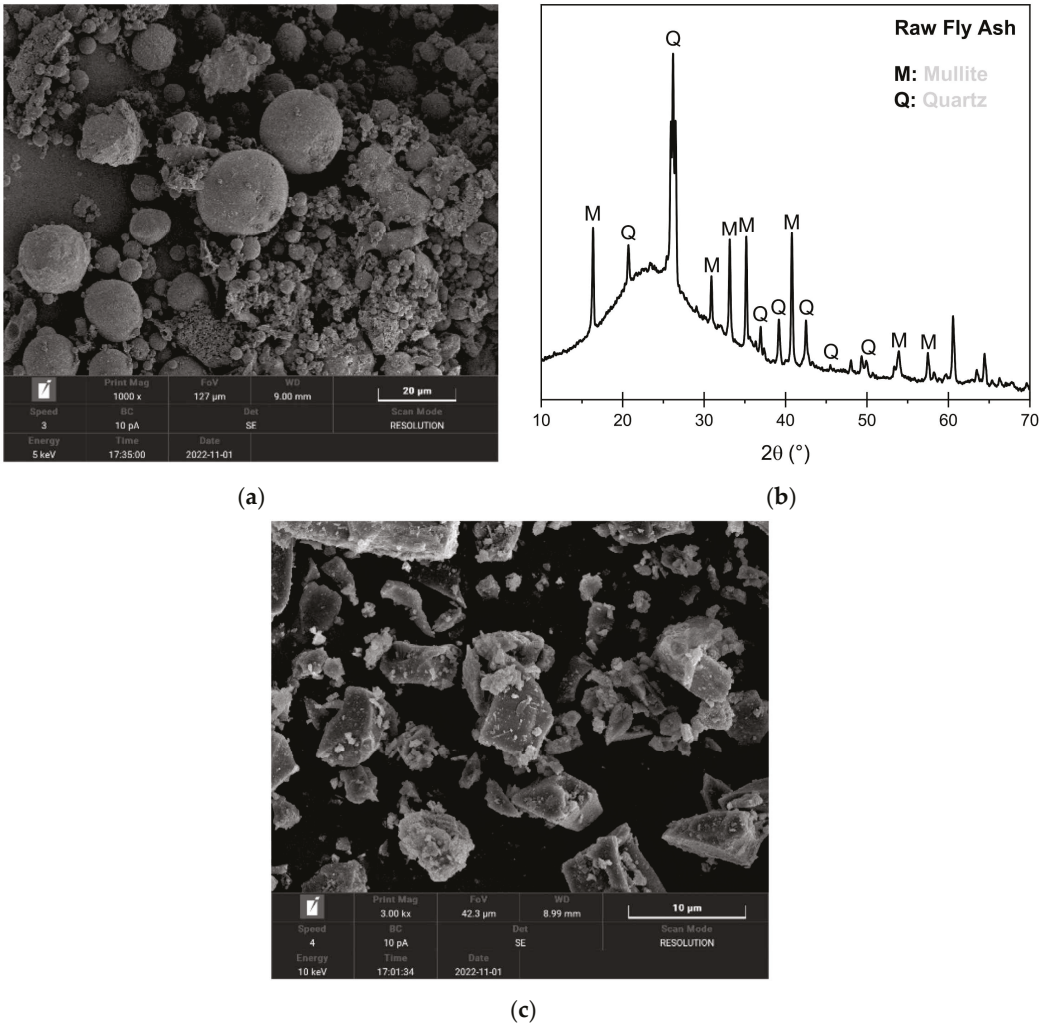

Figure 5. SEM images of fly ash (**a**) and XRD patterns of fly ash (**b**) and SEM images of ground granulated blast furnace slag (**c**) [67,68].

Ground granulated blast furnace slag (GGBS) is a significant by-product generated during the iron-making process in blast furnaces and is widely utilized as an industrial solid waste material. As illustrated in Figure 5c, GGBS particles exhibit an angular and irregular morphology, with colors ranging from white to light gray. Its chemical composition predominantly consists of CaO, SiO_2, Al_2O_3, and MgO. Upon rapid cooling from the molten state, GGBS solidifies into a primarily amorphous glassy phase. This metastable glassy structure imparts latent hydraulic activity, which is essential for its application as a cementitious material [28,46–48].

Silica fume (SF), also known as microsilica, is an ultrafine gray powder collected from flue gases during the production of silicon or ferrosilicon alloys. As illustrated in Figure 6, the SF particles are predominantly spherical and exhibit an amorphous structure. With an average particle size of approximately 0.1 µm, silica fume is approximately two orders of magnitude finer than cement particles are, classifying it as a nanoscale material. It is characterized by an exceptionally high SiO_2 content, generally no less than 85%, along with minor oxides such as Al_2O_3, Fe_2O_3, CaO, and MgO. The silica in SF is almost entirely amorphous, which endows it with high chemical reactivity and significant pozzolanic activity [69].

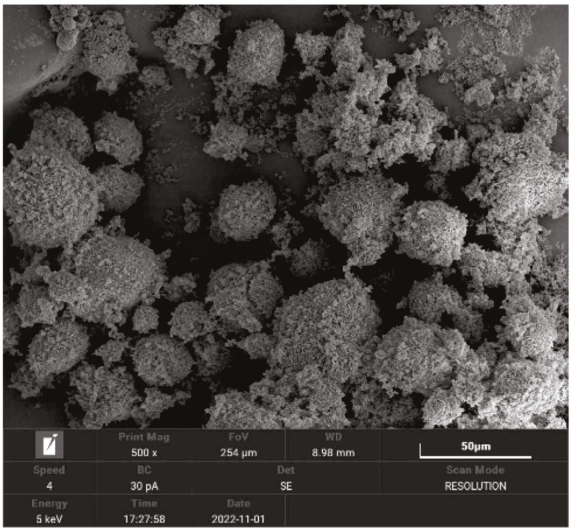

Figure 6. SEM images of silica fume [67].

Red mud (RM) is a highly alkaline solid residue generated during the extraction of alumina (Al_2O_3) from bauxite ore. It is a characteristic reddish-brown color due to its high iron oxide content. As shown in Figure 7a, the microstructure of the RM predominantly consists of irregular platelets, along with some spherical beads and porous agglomerates. The pH value of red mud ranges from 10.5–13.5, indicating strong alkalinity. Its chemical composition includes Fe_2O_3, Al_2O_3, SiO_2, TiO_2, CaO, Na_2O, and other oxides, which contribute to its potential suitability for use in alkali-activated systems. The main crystalline phases identified by XRD (Figure 7b) include hematite, goethite, calcite, katoite, and cancrinite. However, the presence of heavy metals such as Cr, V, and As, as well as naturally occurring radionuclides such as uranium-238 (^{238}U), thorium-232 (^{232}Th), and radium-226 (^{226}Ra), may limit their widespread application [45,47].

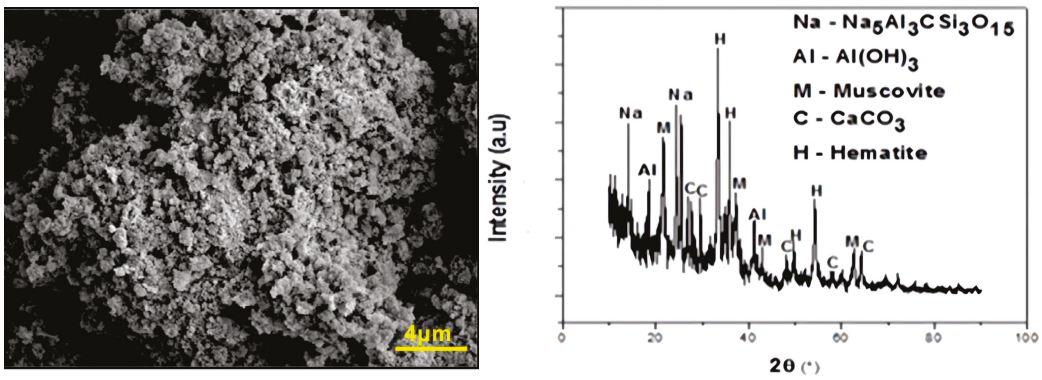

(**a**) (**b**)

Figure 7. SEM images (**a**) and XRD patterns (**b**) of Red Mud [70,71].

Desulfurization gypsum (DG) is an industrial byproduct generated during the flue gas purification process via limestone–gypsum wet desulfurization technology in coal-fired power plants and steel mills. Compared with natural gypsum, desulfurization gypsum appears grayish-white or light yellow in color, with a microscopic morphology characterized by short columnar or plate-like crystals, as shown in Figure 8a. Its main component is calcium sulfate dihydrate ($CaSO_4 \cdot 2H_2O$), although it may contain small amounts of soluble salts such as chloride ions and magnesium oxide [46]. After drying treatment, this material exhibited excellent cementitious properties.

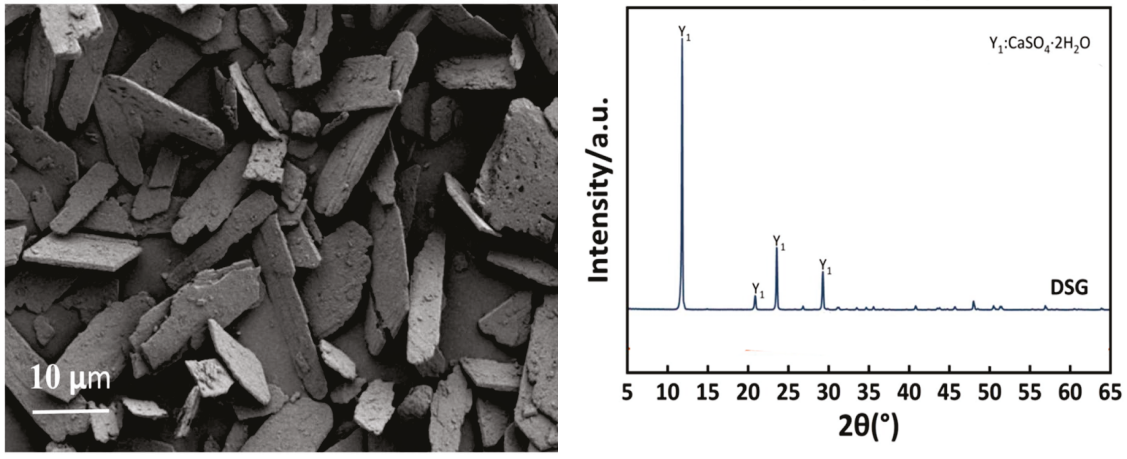

(**a**) (**b**)

Figure 8. SEM images (**a**) and XRD patterns (**b**) of Desulfurization Gypsum [46].

3.2. Activation Methods for Solid Waste-Based Cementitious Materials

Owing to the generally low reactivity of solid waste materials, their use as cementitious components is limited. However, certain potentially active constituents in solid waste, including amorphous silicoaluminates and substances within the glassy silicon-aluminum phase, can be activated. Through specific methods, these materials are transformed into highly reactive cementitious components, which enables efficient solid waste utilization.

3.2.1. Thermal Activation

Subjecting WCP to elevated temperatures significantly alters its physical and chemical properties, thereby affecting the performance of the mortar prepared with it. At high temperatures (>500 °C), dehydration and decomposition occur in hydration products, such as calcium silicate hydrate (C-S-H) and calcium carbonate ($CaCO_3$). At high temperatures, $CaCO_3$ undergoes thermal decomposition reactions, directly releasing CO_2 gas and generating CaO. As the temperature increases, the C-S-H gel initially loses adsorbed water and some bound water, and its structure will gradually be damaged. With further temperature rises, its amorphous structure undergoes reconstruction, and calcium silicate minerals such as β-C_2S and C_3S crystallize through atomic rearrangement, as shown in reaction Equations (1) and (2). The common characteristic of these decomposition products is their relatively high reactivity [69].

As the temperature rises, the phase composition undergoes significant changes. The XRD pattern of the thermally activated WCP is shown in Figure 9, where mineral phases such as quartz and dolomite ($CaMg(CO_3)_2$) can still be identified within the temperature range of room temperature to 600 °C. When the temperature rises from 600 °C to 800 °C, a diffraction peak of CaO appears at $2\theta \approx 37.5°$, indicating the decomposition of calcite ($CaCO_3$) at high temperatures. In addition, diffraction peaks of C_2S and C_3S are detected, which result from the decomposition of C-S-H at high temperatures. Since C-S-H gel is an amorphous mineral phase, it cannot be detected by XRD. All these decomposition products have potential pozzolanic activity. When the temperature continues to rise to 1000 °C, the diffraction peaks of CaO, C_2S and C_3S become significantly more intense, indicating ongoing decomposition [40]. At 1200 °C, diffraction peaks of gypsum are detected [31]. Furthermore, existing studies have shown that ettringite decomposes between 350 °C and 400 °C, while calcium hydroxide (CH) remains stable [72]. AFt gradually dehydrates within the range of 75 °C to 300 °C. Around 150 °C, AFt is almost completely dehydrated and can form Al_2O_3 and CaO, which possess certain gelling abilities [30].

$$CaCO_3 \rightarrow CaO + CO_2 \quad (1)$$

$$C\text{-}S\text{-}H \rightarrow \beta\text{-}C_2S + C_3S \quad (2)$$

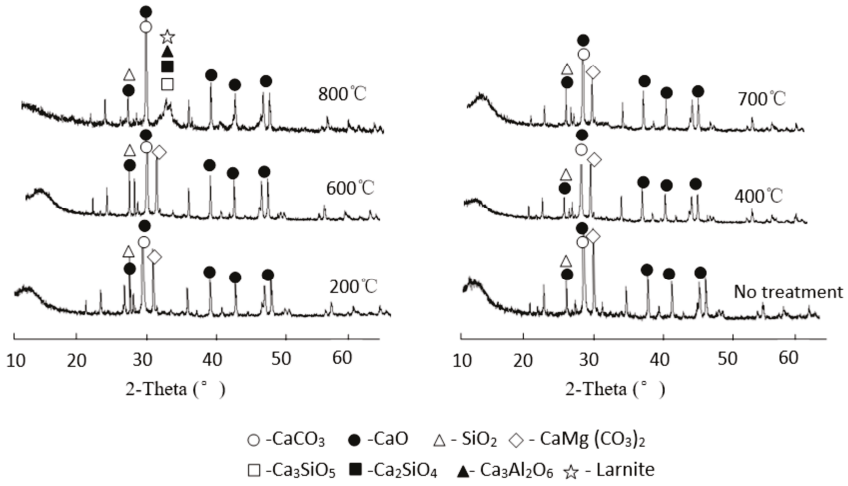

Figure 9. XRD patterns of thermally activated WCP [28].

Furthermore, thermal activation significantly altered the microstructural characteristics of WCP. Unlike untreated WCP, the matrix has a denser microstructure within the temperature range of 300–400 °C because of the decomposition of hydration products (CH and C-S-H) and partial calcite [73]. At temperatures between 400 °C and 1000 °C, the particles exhibit increased density, which is attributed to the interlinking of newly formed hydration products on their surfaces [28]. However, when the temperature reaches 1200 °C, the WCP particles soften, and nearly all the hydration products decompose [74]. While this enhances particle flowability, it simultaneously weakens their nucleation effect. The microstructural evolution of WCP under different thermal activation temperatures is illustrated in Figure 10 [28]. As the temperature increases, the particles become finer and more rounded. However, above 750 °C, the finer particles gradually coalesce, leading to a reduction in the reactive surface area of the WCP particles [72]. Therefore, when conducting thermal activation treatment on raw materials, precise temperature control must be maintained to achieve the required performance.

Thermal activation treatment involves drying and calcining raw materials at specific temperatures and durations. This process requires external energy input, resulting in additional energy consumption. Table 1 presents the energy consumption of cement, untreated RP, and thermally activated RP, with the energy consumption of thermally activated waste powder calculated based on previous studies [75]. The results indicate that although the energy consumption for thermal activation of RP is higher than that of untreated RP, it remains relatively low compared to that of cement. Thermal activation enhances the activity and microstructure of RP, enabling it to replace cement to a greater extent. Future research should focus on expanding its applications to promote the recycling and utilization of solid waste more broadly. Therefore, thermally activating RP and applying it is both feasible and promising. Additionally, it is advisable to utilize clean energy sources such as wind, solar, and nuclear energy during the thermal activation process. This approach will further reduce energy consumption and make the process more low-carbon and environmentally friendly.

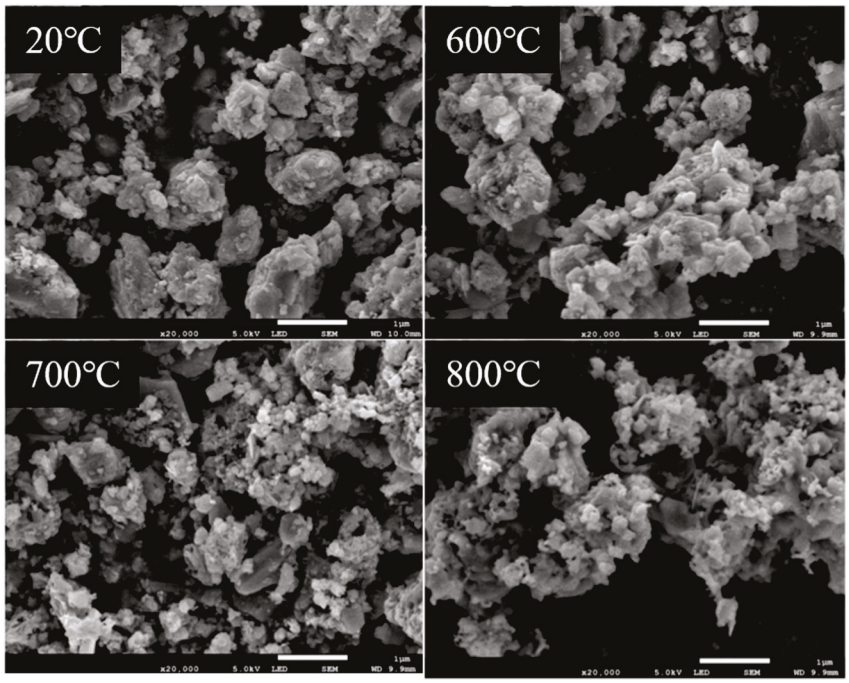

Figure 10. SEM image of a thermally treated WCP [28].

Table 1. Energy consumption of cement, untreated RP and heat-activated RP.

RP		OPC	Ref.
Before thermal activation After thermal activation	18 kwh/t 70.5 kwh/t	105 kwh/t	[8]
Before thermal activation After thermal activation	0.1–1.2 MJ/Kg 2.85–3.95 MJ/Kg	5.5 MJ/Kg	[76]

Research shows that the thermal activation of WCP enhances its reactivity and microstructure. By improving these properties, this method enables a higher cement replacement ratio and unlocks the material's full utilization potential. However, thermal activation involves increased energy consumption, as achieving the required calcination temperature still depends on fossil fuels and electricity. Additionally, it requires precise control over the calcination parameters, including the temperature, duration, and cooling methods, which makes it relatively complex. Consequently, achieving efficient and low-carbon applications of thermal activation remains a critical challenge for future research.

3.2.2. Carbonation

Previous studies have confirmed that key components in solid waste materials, such as CH, C_2S, and C_3S, undergo carbonation when exposed to CO_2. Existing research indicates that upon introducing CO_2 gas, the components in solid waste materials (such as CH, C_2S and C_3S) undergo carbonation reactions with CO_2. The essence of this reaction is "decalcification followed by re-precipitation". For example, CH is directly carbonized to form $CaCO_3$. Under the synergistic effect of CO_2 and H_2O, calcium ions from C_2S and C_3S precipitate as $CaCO_3$, while the silicon-oxygen framework in the original structure reorganizes, primarily generating amorphous C-S-H gel. Therefore, the main products of the carbonation reaction are $CaCO_3$ and C-S-H, which improve the material composition and optimize the microstructure, thereby enhancing the performance of the mortar. The carbonation reactions are represented by the following equations:

$$Ca(OH)_2 + CO_2 \rightarrow CaCO_3 + H_2O \quad (3)$$

$$3CaO \cdot 2SiO_2 \cdot 3H_2O + 3CO_2 \rightarrow 3CaCO_3 \cdot 2SiO_2 \cdot 3H_2O \quad (4)$$

$$3(3CaO \cdot 2SiO_2) + (3 - x)CO_2 + yH_2O \rightarrow xCaO \cdot 2SiO_2 \cdot yH_2O + (3 - x)CaCO_3 \quad (5)$$

$$2(3CaO \cdot SiO_2) + (2 - x)CO_2 + yH_2O \rightarrow xCaO \cdot 2SiO_2 \cdot yH_2O + (2 - x)CaCO_3 \quad (6)$$

As noted in Section 3.1, untreated WCP, with quartz and calcite as the primary mineral phases, also contains a certain amount of CH, AFt, and partially hydrated C_2S, C_3S, and other compounds. XRD analysis (Figure 11) [29] revealed that after carbonation treatment, quartz and calcite remained the dominant crystalline phases, while the diffraction peak intensity of dolomite ($CaO{\cdot}MgO{\cdot}2CO_2$) was markedly enhanced. In contrast, the characteristic peaks of phases such as CH, AFt, C_2S, and C_3S are significantly diminished or have disappeared. These observations indicate that the reactive phases mentioned above participate in carbonation reactions with CO_2, leading to the formation of new products, predominantly $CaCO_3$.

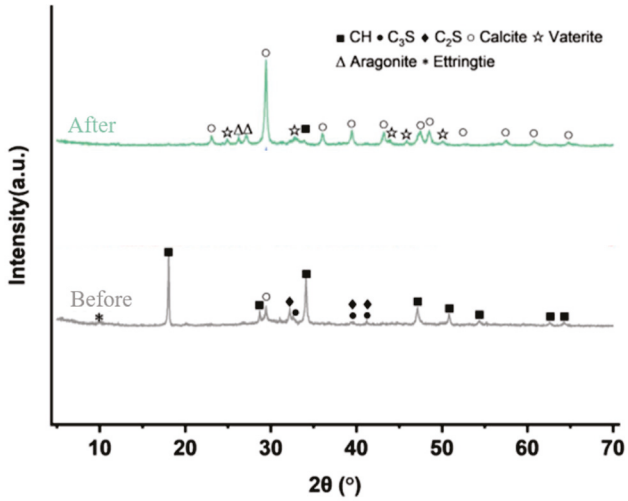

Figure 11. XRD patterns of WCP before and after carbonation [77].

The carbonation reaction significantly influences the microstructure and macroscopic properties of the material. The precipitated $CaCO_3$ and silica-based gels deposit and accumulate on particle surfaces and within pores, markedly refining the microstructural morphology. The microstructure of the carbonized WCP is shown in Figure 12 [30]. The carbonated WCP sample exhibited reduced porosity and a more regular pore morphology, with characteristic rhombohedral calcite crystals appearing on the surface. Previous studies have indicated that well-formed, fine calcite crystal precipitates facilitate nucleation and promote the growth of hydration products in cementitious composites [30], thereby contributing to the increased strength of the mortar. However, in large-scale processing, it is not guaranteed that all materials will achieve the desired carbonation effect. Uneven reactions can result in localized over-carbonation or under-carbonation, which may introduce new stress concentration points or weak areas within the material. Furthermore, carbonation improved the granulometric properties of WCP. The particle size analysis results before and after carbonation are presented in Figure 13. The median particle size of the samples after carbonation is generally larger than that before carbonation. This indicates that the carbonation reaction not only alters the phase composition but also increases particle size and enhances overall uniformity. This improvement is achieved through the deposition of newly formed fine $CaCO_3$ crystals on the particle surfaces, which effectively fill the pores [29]. However, excessive carbonation may cause the carbonation products

to block the pores, which instead hinders the further diffusion of CO_2 and creating a self-inhibitory effect.

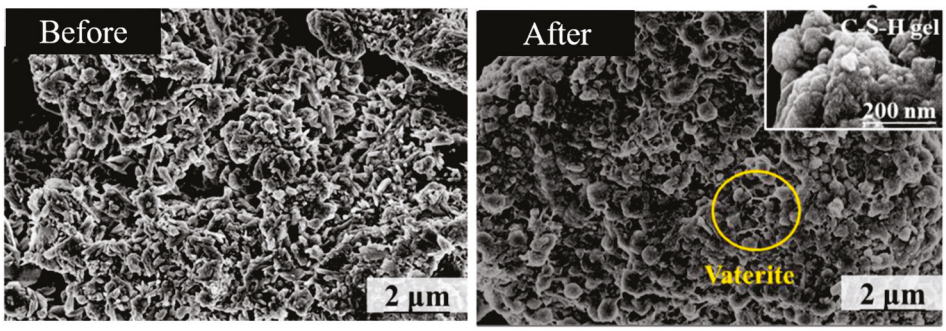

Figure 12. SEM images of the WCP before and after carbonation [78].

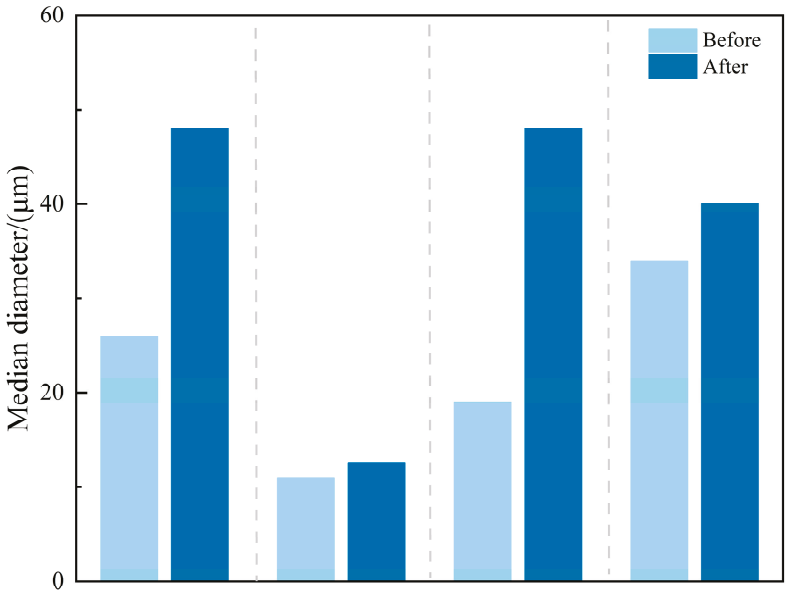

Figure 13. Median diameter of the WCP before and after carbonation [29,40,41,79].

Carbonation treatment is a process that utilizes CO_2-rich gas to treat solid waste under controlled conditions, such as temperature and relative humidity, converting CO_2 into thermodynamically stable carbonates that can be permanently stored [80,81]. This process not only enhances material performance but also enables the storage of CO_2 gas. Compared to traditional improved technologies, carbonation treatment is a green and sustainable technology. The amount of CO_2 absorbed serves as a measure of the potential for carbon sequestration. Table 2 presents the amount of CO_2 absorbed after carbonation. The data indicate that selecting appropriate carbonation conditions can maximize the carbon sequestration potential of the material. Therefore, future research should focus on optimizing carbonation conditions to improve the performance of carbonized materials, increase the carbon sequestration capacity, and reduce energy consumption and costs associated with CO_2 capture and transportation. This will help achieve an optimal balance among performance, environmental protection, and cost in carbonation treatment.

In summary, carbonation treatment of RP effectively modifies the composition, microstructure, and particle size distribution of solid waste materials. By increasing their reactivity, carbonation increases the utilization rate of RP, reduces the cement demand, and simultaneously sequesters CO_2, thereby lowering greenhouse gas emissions. Moreover, this process does not require high-temperature calcination, resulting in low energy consumption. However, variability in powder composition, including low CaO content, can

lead to inconsistent carbonation efficiency. Additionally, the high costs associated with CO_2 capture and purification, along with potential long-term stability issues caused by volumetric changes in carbonation products, present significant challenges. Therefore, achieving large-scale application of carbonation treatment remains a critical research priority.

Table 2. Absorption of CO_2 after carbonation.

Materials	Carbonation Conditions			Temperature	Absorption Capacity	Ref.
	Relative Humidity	Carbonation Time	CO_2 Concentration			
Cement paste powder	60 ± 5%	-	99%	20 ± 1 °C	47.5%	[82]
50% OPC + 50% FA	65%	-	0.04%	20 ± 1 °C	1.74	[83]
50% OPC + 50% GGBS					1.82	
50% OPC + 50% FA	65%	28 d	20%		19.68	
50% OPC + 50% GGBS					28.41	
Recycled concrete fines	5–10%	30 min	>99%	20	2.76	[34]
				60	10.86	
				100	21.65	
				140	12.11	
Recycled concrete fines	70 ± 5%	12 d	20 ± 3%	20 ± 2	44	[41]

3.2.3. Alkali Activation

The latent reactive components in solid waste materials can be effectively activated by alkaline activators to form a dense three-dimensional network structure. This reaction process does not depend on the C_3S and C_2S minerals found in traditional Portland cement. The performance of the resulting material can be compared with or even better than that of traditional cement materials. Therefore, it has the potential to be used as an alternative to traditional cement.

In such systems, the type and modulus of the activator, along with the reactivity of the precursor, jointly regulate the kinetics of gel formation and the densification of the microstructure. This synergy not only facilitates rapid development of early-age strength but also enables continuous polymerization, which enhances long-term mechanical performance. This unique reaction characteristic offers a novel approach to overcoming the inherent limitations of recycled micropowder in traditional cement. It also underscores the flexibility and potential of alkali-activated systems in material design and performance regulation.

The alkali-activated elements Ca, Si and Al in cementitious materials work synergistically to regulate the reaction process and the formation of final products, thereby influencing the macroscopic properties of the materials. When the Ca content is relatively high, it is a high-calcium aluminosilicate system, which typically reacts efficiently at ambient temperature, primarily forming a C-A-S-H gel as the reaction product. The second type is a low-calcium aluminosilicate system, which often requires elevated temperatures and longer curing periods, with N-A-S-H gel as the main resulting phase [84]. The activation mechanism of high-calcium alkali-activated systems is illustrated in Figure 14. Under the influence of alkaline activators such as NaOH or Na_2SiO_3, elements such as Si, Ca, and Al are released from calcium silicate or aluminosilicate sources, forming soluble ionic species or hydroxyl compounds such as $Si(OH)_4^-$, $Al(OH)_3^-$, and $Ca(OH)_2$. These dissolved species further react in an alkaline environment to produce amorphous calcium silicate hydrate (C-S-H) and calcium aluminate hydrate (C-A-H) gels [85]. In an environment rich in calcium elements, the reaction rate accelerates, promoting the rapid formation of a denser C-A-S-H gel, thereby enhancing the material with higher early strength [86]. In

contrast, the reaction of low-calcium alkali-activated materials involves three main stages: (1) dissolution of aluminosilicate raw materials under strong alkali, releasing reactive aluminate and silicate tetrahedral units; (2) polycondensation of these active units, where silicate and aluminate tetrahedra connect via shared oxygen atoms, forming Si-O-Si and Si-O-Al bonds, leading to a three-dimensional gel network; and (3) continuous growth and cross-linking of the gel phase, resulting in final hardening [87–89], as depicted in Figure 15. The three-dimensional N-A-S-H gel network, composed of Si and Al, provides excellent long-term strength development and structural stability [90], thereby enhancing the material with better durability.

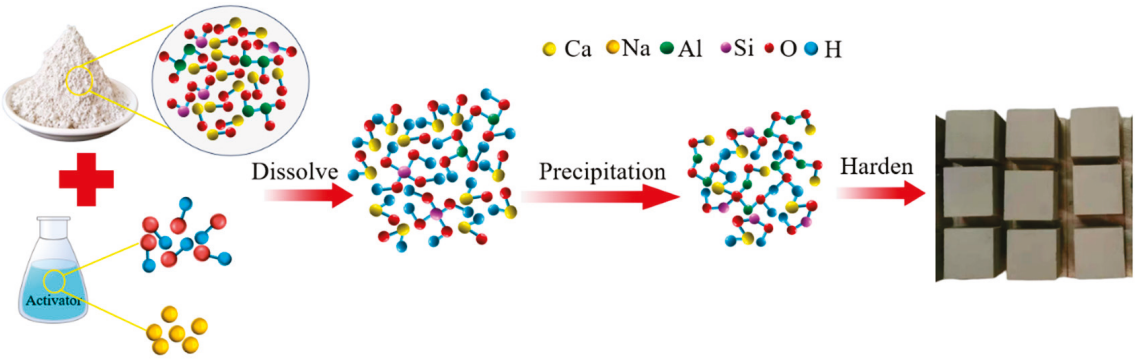

Figure 14. Reaction mechanism of high-calcium alkali-activated materials.

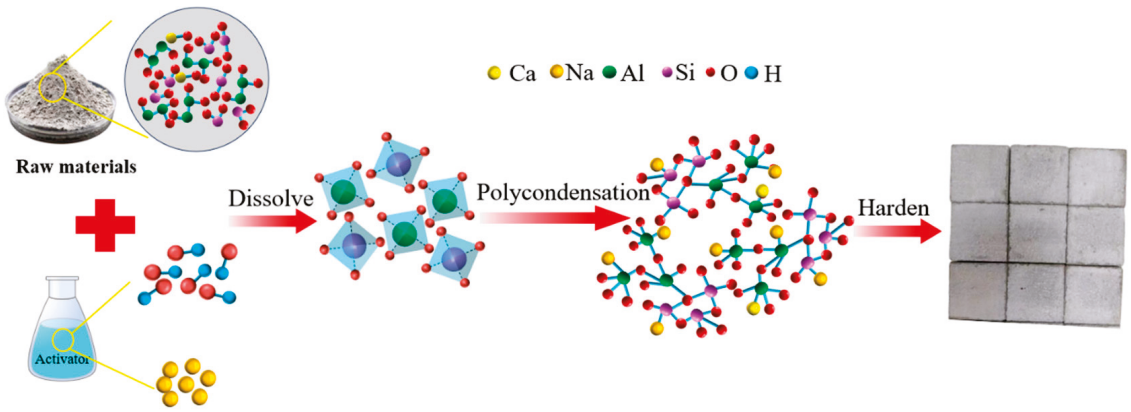

Figure 15. Reaction process of low-calcium alkali-activated systems.

Alkaline activators stimulate the amorphous aluminosilicate components in solid waste materials to form cementitious reaction products. The type of activator influences mortar performance by modulating reaction pathways, gel phase composition, and microstructural development. For example, sodium-based base activators are used. The main function of NaOH is to provide a high-pH environment. OH^- destroys the glassy structure of raw materials, which releases active SiO_2 and Al_2O_3 monomers and forms silicate ($[SiO_4]^{4-}$) and aluminate ($[AlO_4]^{5-}$) ions. Additionally, the Na^+ ions supplied by NaOH not only maintain charge balance within the system but also catalyze polycondensation reactions. The dissolution rate is governed by both the NaOH concentration and the duration of the dissolution process. On the other hand, sodium silicate provides both OH^- and SiO_3^{2-} ions. While OH^- contributes to the alkaline environment and facilitates the release of Si and Al species, SiO_3^{2-} directly participates in the formation of the gel network. Owing to its higher silicon content, sodium silicate promotes the development of a more stable aluminosilicate network during the reaction, thereby increasing the mechanical strength [48].

The molar ratio of SiO_2 to Na_2O is known as the silicate modulus (denoted as M). It is a critical parameter influencing the performance of alkali-activated systems. By quantitatively regulating the alkalinity of the activator, the silicate modulus controls the composition and structure of the resulting gel phases, thereby ultimately determining the material properties. In current practice, composite activators comprising strong alkalis and silicate compounds are commonly used. Strong alkalis provide a high-pH environment that promotes the dissolution of Si and Al from the precursor, whereas silicate sources supply reactive silica that facilitates cross-linking within the gel network. By adjusting the proportions of alkali and silicate, the silicate modulus can be precisely controlled [49]. Research indicates that the optimal range of M varies with the type of precursor. For low-calcium systems, the modulus should generally not exceed 2 [91], as sufficient OH^- is required to break down the Al-O-Si networks. In contrast, for high-calcium systems, the modulus should not fall below 2, since although Ca^{2+} promotes the formation of C-S-H gel, adequate silicate ions are necessary to support the reorganization of aluminosilicate species. However, unreacted bases may remain in this system, and these alkaline substances can serve as potential internal alkali sources. This significantly increases the risk of alkali-aggregate reactions and severely compromises the long-term volumetric stability and durability of the material.

Furthermore, the type of alkali metal cation significantly influences the reaction process, gel structure, and final properties of the activated mortar. As shown in Figure 16a [52], the microstructure of the potassium-based activator (PS)-activated mortar exhibited a dense and homogeneous morphology with no obvious unreacted particles. The reaction products are uniformly distributed and compact, displaying minimal pores or cracks, along with a dense interfacial transition zone between the paste and fine aggregates. This indicates that the larger ionic radius and lower charge density of K^+ result in slower migration rates, which moderate the dissolution kinetics of aluminosilicate precursors. The consequently more controlled reaction progression leads to homogeneous gel formation, reduced chemical shrinkage, and a strong bonding capacity with silicate tetrahedra ($SiO_4{}^{4-}$) [50]. The resulting C-(K)-A-S-H gel possesses a stable structure with fewer microdefects, such as pores and cracks. Its chain-like configuration is more flexible than that of the C-(N)-A-S-H gel, contributing to a uniform pore structure [92]. As presented in Figure 16b, the microstructure of the sodium-based activator (SS)-activated mortar shows a more porous and cracked morphology. It has a microstructure with numerous pores and cracks, and many unreacted particles can be observed. Moreover, there are many cracks between the slurry and fine aggregates, and the interface transition zone is relatively weak [93]. This can be attributed to the smaller ionic radius and higher charge density of Na^+, which accelerates the dissolution of aluminosilicate phases and leads to rapid early-age hydration. The resulting C-(N)-A-S-H gel tends to encapsulate unreacted particles, hindering further hydration, while the rapid reaction often induces localized shrinkage stress concentrations, resulting in microcracking. Moreover, the C-(N)-A-S-H gel is more rigid [50].

However, when solid waste undergoes alkaline activation treatment, self-shrinkage tends to occur, leading to the formation of structural cracks that compromise the performance of the mortar. Self-drying is the primary cause of mortar shrinkage [94]. The capillary pressure generated by water evaporation leads to drying shrinkage within the mortar. The drying shrinkage of AAM mortar is significantly greater than that of OPC mortar. This drying shrinkage in AAM mortar gradually develops after the final setting, with the shrinkage value increasing over time [95]. In the AAM system, this factor is not the sole dominant influence; the characteristics of the C-A-S-H gel also have a significant impact. The hydration product of AAM, C-A-S-H gel, should not be considered a continuous porous material. It is more like a gel-like or granular material containing micro-defects. Its chemical shrinkage during drying is associated with the rearrangement and redistribution

of C-A-S-H nanoparticles [96]. Moreover, the contractions caused by both mechanisms are irreversible [92]. Therefore, mitigating mortar shrinkage requires addressing both of these aspects. Relative humidity (RH) significantly influences shrinkage by regulating capillary stress and surface free energy. At high RH levels (>50%), the rearrangement and reorganization of the C-A-S-H microstructure result in pronounced viscous behavior. This rearrangement causes the collapse of gel pores and refinement of the pore structure [97]. Conversely, at low RH levels (<40–50%), the direction, magnitude, and location of stresses induced by surface free energy differ, promoting the densification of the particles themselves [98,99]. Therefore, addressing shrinkage and cracking in alkali-activated material (AAM) mortar requires attention to both material design and curing conditions. Optimizing the mix ratio and activator parameters can produce a denser, more stable gel. Additionally, incorporating components that generate an appropriate amount of expansive hydration products (such as ettringite) during the early stages can induce compensatory expansion, offsetting some chemical and drying shrinkage. However, the dosage of these expansive components must be carefully controlled to prevent excessive expansion, which could cause greater damage. Finally, establishing a scientific curing regime and maintaining appropriate humidity levels are essential for effective shrinkage control.

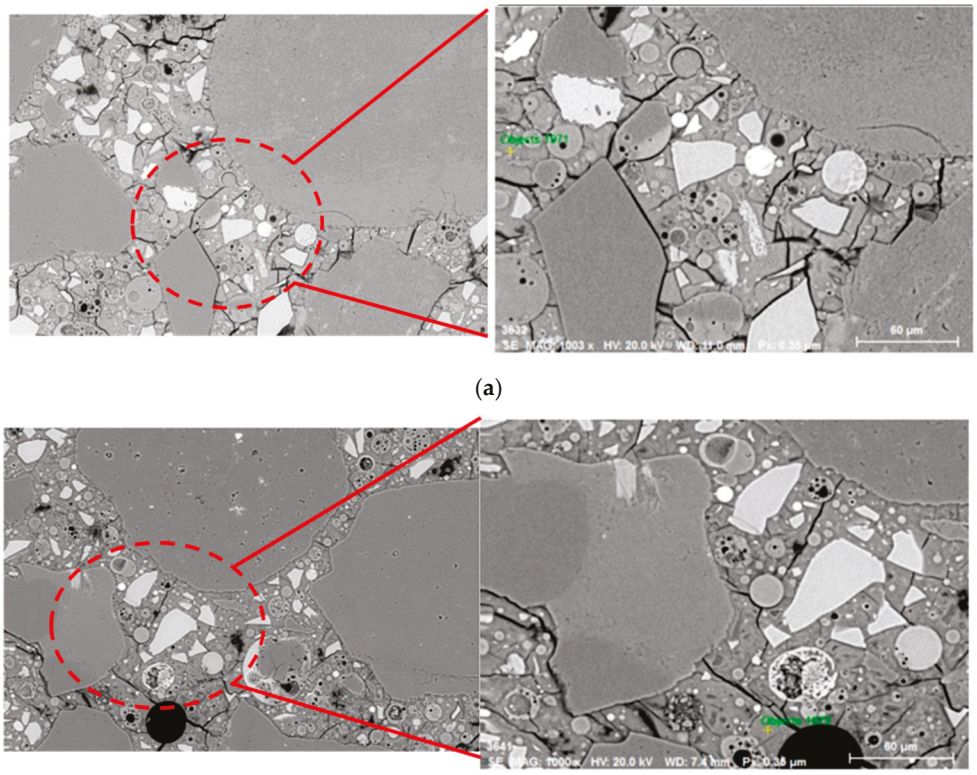

(**a**)

(**b**)

Figure 16. SEM images of the mortars produced with potassium silicate (**a**) and sodium silicate (**b**) [52].

Alkaline activation treatment of solid waste materials enables their efficient utilization by allowing the use of all solid waste cementitious materials, thereby addressing the high carbon emissions associated with traditional cement production. However, the dosage and modulus of alkali must be precisely controlled. Prolonged exposure can lead to alkali–aggregate reactions or carbonation shrinkage, which may compromise the service life of the structure. Additionally, the use of strong alkalis increases health and safety risks and complicates construction operations.

By replacing conventional cement, solid waste-based cementitious materials offer a viable route for significantly reducing resource consumption and carbon emissions. These materials incorporate construction solid wastes, such as discarded concrete and brick powder, as well as industrial solid wastes, such as slag and fly ash. The potential cementitious properties of these materials can be effectively activated through various treatment methods. These processes include thermal activation to break down the glassy structure, carbonation to capture CO_2 and form strength-enhancing calcium carbonate, and alkali activation to depolymerize silico aluminate phases and reconstruct a three-dimensional gel network. However, it faces challenges such as low activation efficiency, high energy consumption, and significant contraction. Future efforts should focus on the development and application of solid waste materials [100] to achieve diverse application scenarios [101,102]. Additionally, future efforts should prioritize the development of low-carbon activation technologies, such as efficient carbonation and low-temperature alkali activation. Additionally, the synergistic effects of multiple solid wastes should be optimized, and long-term durability studies should be conducted. These measures are critical for overcoming technical bottlenecks and advancing the large-scale application of solid waste recycled mortar, thereby contributing to a circular economy.

4. Mechanical Strength of Solid Waste-Based Cementitious Recycled Mortars

In the engineering application of materials, their mechanical behavior in practical use is crucial in addition to their basic properties. As a core component of building structures, the strength of mortar is a key indicator for measuring its mechanical properties, which directly determines the safety and stability of the structure. Therefore, in-depth research on how replacing cement with solid waste affects mortar strength is essential. This research not only further verifies the effectiveness of using solid waste materials but also provides a necessary foundation for promoting the engineering application of recycled solid waste mortar.

4.1. Effect of the Solid Waste Replacement Ratio on Mortar Strength

Compared with that of conventional cement mortar, the incorporation of recycled powder (RP) generally leads to a reduction in mortar performance. This decline is attributed primarily to the dilution of the main reactive phases in the cement, namely, C_2S and C_3S, combined with the inherently low reactivity of RP, which has a limited capacity to participate in hydration reactions. Consequently, the formation of hydration products decreases, and the microstructural compactness is reduced, thereby compromising the overall mechanical properties of the mortar.

Studies have shown that when waste concrete powder (WCP) is used to partially replace ordinary Portland cement, the development trend of compressive strength follows the pattern illustrated in Figure 17. The compressive strength of the mortar decreases as the WCP replacement ratio increases. Under conditions of a low substitution rate, WCP has a distinct “microaggregate effect”. Its particles optimize the graded composition of the cementitious system, fill internal pores, block water migration channels, and thereby inhibit the self-shrinkage behavior of the mortar. Furthermore, the porous structure of the WCP can adsorb part of the free water, helping to maintain internal humidity and promote continued cement hydration, which contributes to increased compactness, reduced drying shrinkage, and an improved interfacial transition zone (ITZ) structure. Although the incorporation of WCP dilutes the active components in cement, leading to a reduction in the total amount of hydration products [103], the surfaces of WCP particles can serve as nucleation sites for hydration products, accelerating the cement hydration process. Additionally, unhydrated

cement particles and active components (such as SiO_2 and Al_2O_3) in WCP can undergo secondary hydration reactions, generating additional C-(A)-S-H gel, which partially compensates for the performance loss caused by the reduced cement content. Consequently, the impact on mortar strength remains relatively limited at low replacement ratios. At higher replacement levels, the dilution effect of WCP increases the proportion of inert components, which not only significantly reduces the amount of cementitious hydration products in the system but also retards the hydration process due to the adsorption of substantial free water [104]. This leads to pore coarsening, increased connectivity, and exacerbation of both autogenous and drying shrinkage, ultimately resulting in deterioration of the ITZ, reduced compactness, and decreased mortar strength.

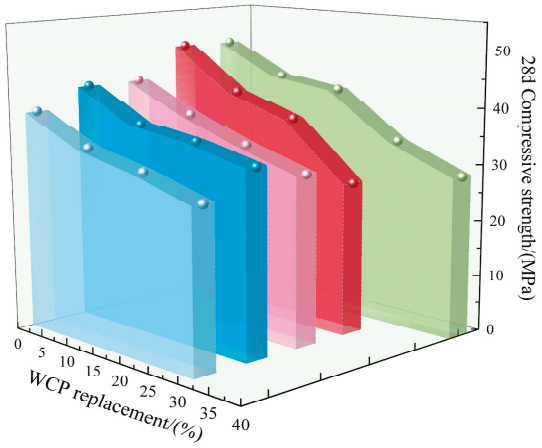

Figure 17. Compressive strength of the mortars with different WCP substitution rates [36,105–108].

The use of RP with higher reactivity can lead to certain improvements in mortar performance. Waste brick powder (WBP), which contains a greater proportion of amorphous aluminosilicates capable of undergoing pozzolanic reactions, is more reactive than WCP. Consequently, when WBP is used to partially replace cement, the resulting mortar demonstrates greater strength than WCP-modified mortar at the same replacement ratio, as shown in Figures 17 and 18. When the dosage ranges from 15% to 20%, the mortar can achieve its highest strength. This improvement is not only attributed to the previously mentioned volcanic ash reaction [109], but also because WBP exhibits a "micro-aggregate effect" similar to that of WCP, effectively filling the pores of the slurry [110]. This dual action comprehensively enhances the strength of the mortar. However, when the dosage exceeds this optimal range, the dilution effect of WBP becomes dominant, reducing the relative content of effective cementitious components in the system and subsequently causing a decline in macroscopic strength. Regarding the XRD patterns of pastes, different replacement levels of WBP are presented in Figure 19 [111]. In WCP-blended pastes, the diffraction peaks of CH are noticeably reduced, whereas those of $CaCO_3$ and SiO_2 increase significantly [72]. This indicates that the incorporation of WCP not only reduces the formation of cement hydration products but also introduces inert phases, such as quartz (SiO_2) from aggregate minerals and calcite ($CaCO_3$). Consequently, the overall reactivity and degree of hydration decrease. These factors contribute to the formation of a loose and porous microstructure, as illustrated in Figure 20a [112]. In contrast, WBP-modified pastes clearly exhibit a decrease in the diffraction peaks of CH and $CaCO_3$, accompanied by a significant increase in the SiO_2 peak. This indicates that WBP reduces the content of CH and $CaCO_3$ in the binder system. Since WBP contains no hydrated phases, it initially decreases the total amount of hydration products. However, the SiO_2 in WBP is predominantly present as amorphous silica with pozzolanic activity, which can further react with CH to form additional C-S-H gel [25]. This reaction refines the pore structure, resulting in a matrix with fewer capillary pores

and cracks and greater compactness than WCP blends do, as shown in Figure 20b [113]. The abundant presence of C-S-H in the microstructure of the WBP paste indicates that, unlike WCP, the incorporation of WBP enhances the overall degree of hydration in the cementitious system.

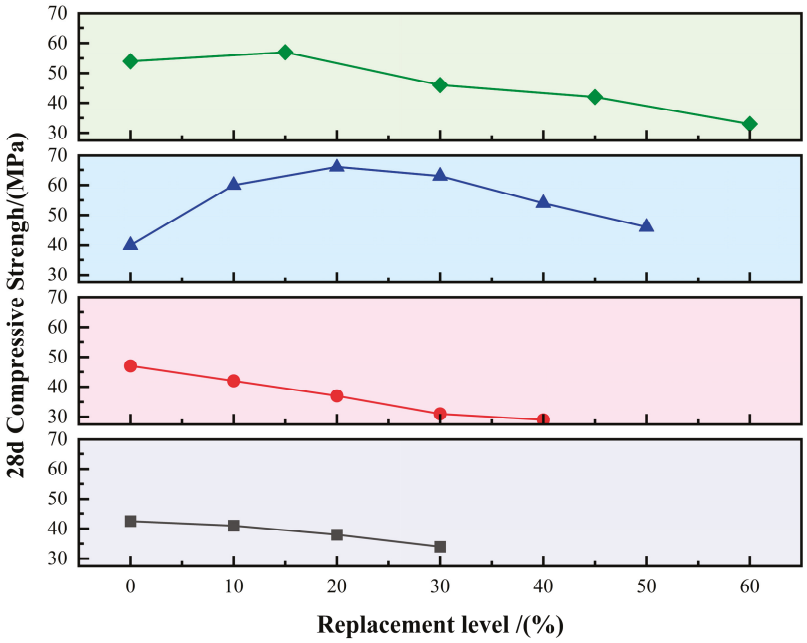

Figure 18. Compressive strength of mortar containing WBP [37–39,108].

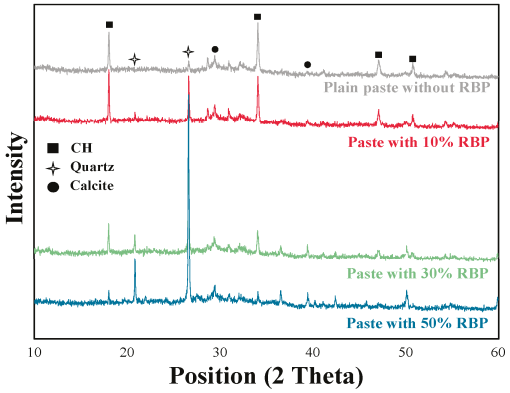

Figure 19. XRD patterns of the different WBP substitution rates [111].

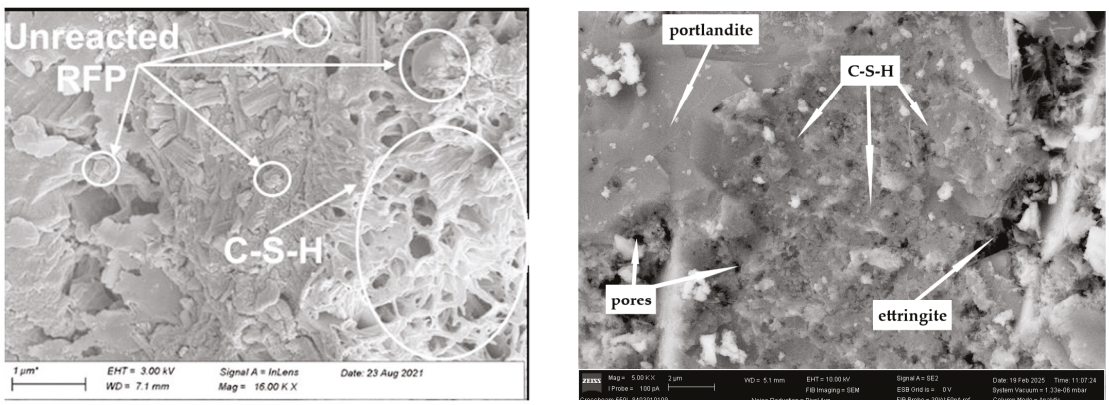

(**a**) (**b**)

Figure 20. SEM images of paste with WCP (**a**) and WBP (**b**) [112,113].

4.2. Effects of Various Activation Methods on the Mortar Strength

4.2.1. The Influence of Thermal Activation on the Mortar Strength

Compared with mortar containing untreated RP, the use of thermally activated RP significantly enhances the mechanical performance. This improvement is attributed primarily to changes in the phase composition and microstructure of the RPs induced by the thermal treatment. On the one hand, the original cement hydration products, such as CH and C-S-H gel, undergo dehydration and decomposition, transforming into more reactive phases, including C_2S, C_3S, Al_2O_3, and CaO. On the other hand, the internal porosity and specific surface area of RP particles increase [31,72,73,114]. These modifications not only provide abundant nucleation sites that accelerate early-age hydration kinetics but also enable the activated components to participate in secondary pozzolanic reactions, generating additional C-S-H gels. Consequently, the microstructure of the paste is refined, resulting in improved mechanical properties.

The thermal activation temperature is a critical parameter governing the pozzolanic activity of RP. As shown in Figure 21, the compressive and flexural strengths of the mortar initially increase and then decrease with increasing activation temperature, reaching a maximum at approximately 800 °C, which corresponds to the peak pozzolanic reactivity of RP under different thermal treatment conditions. Studies indicate that within the temperature range of 750–800 °C, RP attains an optimal reactive state. Under thermal activation, portlandite ($Ca(OH)_2$) fully decomposes, and the C-S-H gel is largely converted into an active amorphous phase, whereas the decomposition of calcite ($CaCO_3$) remains limited. This limitation mitigates the potential volume instability caused by excessive free CaO [115], thereby contributing to strength enhancement. However, when the temperature exceeds 800 °C, some amorphous phases undergo sintering and crystallization, forming low-reactivity crystalline phases such as wollastonite ($CaSiO_3$) and gehlenite ($Ca_2Al_2SiO_7$), as evidenced by the distinct diffraction peaks in the XRD patterns (Figure 22) [116]. Owing to their chemical stability and low reactivity, the formation of these crystalline phases significantly diminishes the pozzolanic effect, thereby restricting further development of mechanical properties. At temperatures above 1000 °C, the gypsum ($CaSO_4 \cdot 2H_2O$) potentially present in RP decomposes into soluble anhydrite ($CaSO_4$) [117], which can rapidly rehydrate upon contact with water, disrupting normal hydration processes and adversely affecting the final mortar strength.

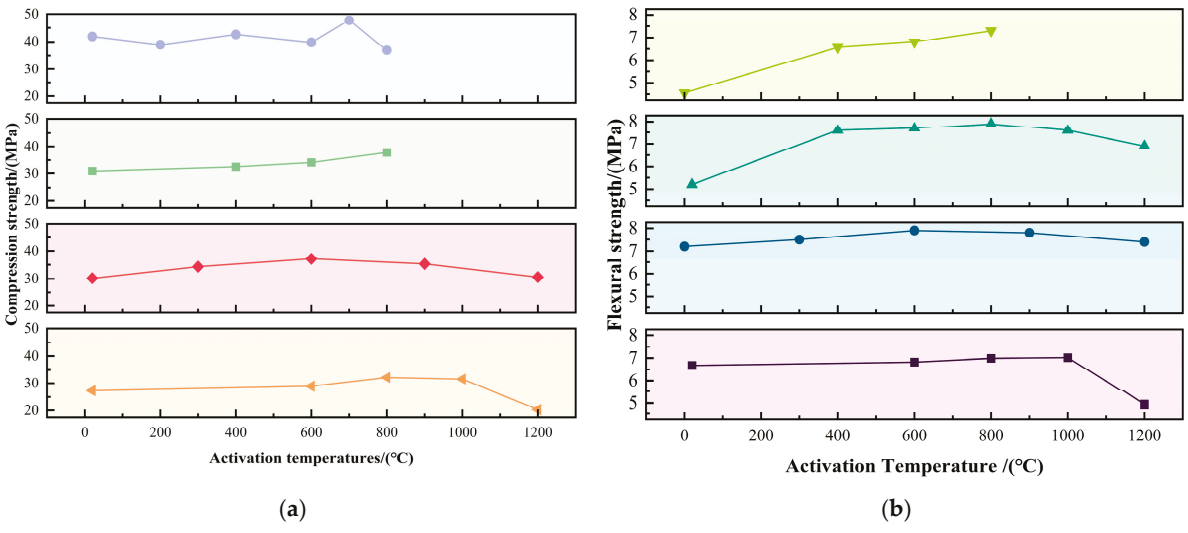

Figure 21. 28 d Compressive strength (**a**) and flexural strength (**b**) of mortar at different thermal activation temperatures containing 30% WCP [28,31,32,72,74,75].

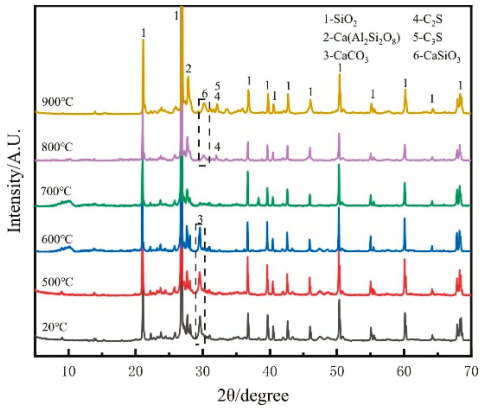

Figure 22. XRD patterns of thermally activated RP [116].

4.2.2. The Influence of Carbonation on the Mortar Strength

After carbonation treatment, the strength of the mortar significantly improves. As shown in Figure 23, the compressive strength of the carbonized mortar at both 7 d and 28 d is higher than that of the non-carbonized group. This improvement is attributed to the formation of dense calcite microcrystals on the surface of WCP following carbonation [118]. These microcrystals possess a high specific surface area and active surfaces, which serve as nucleation sites for the C-S-H gel, thereby promoting early-age cement hydration. Furthermore, $CaCO_3$ can guide the ordered growth of C-S-H gel, contributing to early strength development. The influence of the carbonation treatment on the mortar strength is illustrated in Figure 23. Additionally, $CaCO_3$ reacts with aluminate phases such as C_3A in cement to form needle-like monocarboaluminate ($Ca_4Al_2(CO_3)(OH)_{12}\cdot 5H_2O$). This reaction product not only enhances matrix densification but also consumes free water during its formation, reducing overall porosity [66]. Simultaneously, the precipitation of $CaCO_3$ fills the capillary pores within the WCP, helping mitigate internal defects. As mentioned in Section 3.2.2, carbonation treatment increases the WCP particle size and optimizes the particle size distribution, which improves the ITZ between the aggregates and the cement paste, thereby refining the microstructure and mechanical performance of the mortar. Moreover, carbonated WCP retains partially unhydrated reactive components such as $Ca(OH)_2$, C_2S, and C_3S [119]. With prolonged curing, these components continue to hydrate, generating additional C-S-H gel, which contributes to the favorable long-term mechanical performance of the mortar.

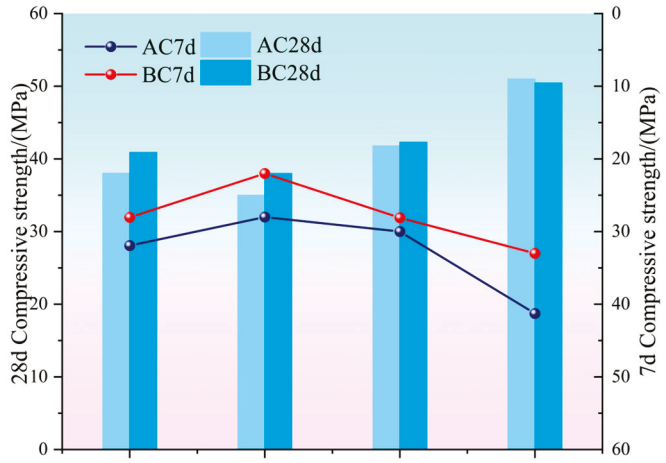

Figure 23. 7-day and 28-day compressive strengths of mortar containing 20% WCP before and after carbonation [27,29,30,33].

The carbonation temperature serves as a pivotal factor in regulating the polymorph of $CaCO_3$ crystals, thereby influencing the microstructure and resultant strength of mortar. The microstructural evolution of WCP carbonized at different temperatures is presented in Figure 24 [78]. At 20 °C, spherical vaterite constituted the primary carbonation product. As the temperature increased, the proportion of cubic calcite gradually increased. By 140 °C, vaterite is almost entirely replaced, and the calcite crystals exhibit larger dimensions than those formed at 100 °C. At 60 °C, carbonation predominantly yields vaterite, which has a high specific surface area and a fine particle size. Its high surface activity provides effective nucleation sites for cement hydration, accelerating the early hydration of C_3S and C_3A [120] and promoting the formation of hydration products, thereby increasing early strength. However, owing to its metastable nature, vaterite tends to dissolve readily [121], which limits the extent of early strength improvement. When the temperature exceeds 100 °C, vaterite transforms into more stable calcite through a dissolution–reprecipitation process [122]. Calcite crystals are dense and stable; although their nucleation effect is relatively weaker in the early stages, their stability helps retard the decomposition of hydration products at later ages. Through pore filling and reinforcement of the ITZ, calcite compensates for some of the strength loss resulting from reduced cement content. A temperature of 100 °C promotes CO_2 diffusion and ion migration, thereby improving the carbonation efficiency. However, beyond 140 °C, moisture evaporation reduces the relative humidity in the system, inhibiting the carbonation reaction [34]. Under such conditions, although the calcite content increases, its larger particle size may weaken the nucleation effect. In addition, insufficient encapsulation by $CaCO_3$ leaves unreacted siliceous gels, which can lead to a decline in long-term strength.

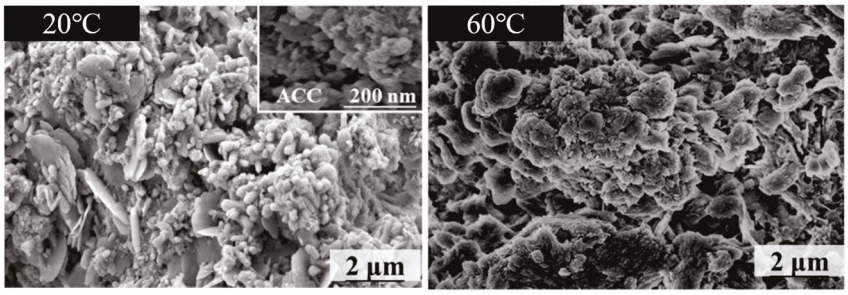

Figure 24. SEM images of WCP after carbonation at different temperatures [78].

4.2.3. The Influence of Alkaline Activation on the Mortar Strength

The type of alkaline activator significantly influences the strength development and microstructure formation of mortar. Sodium-based activators create a highly alkaline environment that rapidly dissolves Si and Al from the raw materials, accelerating early gel formation and resulting in high early-age strength. However, this rapid reaction alters the internal moisture distribution through the fast consumption and migration of water, leading to structural stress imbalances and inducing shrinkage. In contrast, potassium-based activators promote a more moderate reaction process with different moisture retention and migration behaviors, avoiding significant structural stress changes at early stages and thus resulting in negligible shrinkage. Compared with that of sodium-based systems, the resulting gel structure is more homogeneous, contributing to a denser microstructure and consequently better strength development [105]. As shown in Figure 25 [51–53], the compressive strength of mortar activated with either sodium- or potassium-based activators at 28 days is significantly greater than that at 7 days, indicating a continuous reaction and stable microstructural development in both systems at later ages. Notably, the 28-day compressive strength of the K^+-activated mortar is consistently greater than that of the Na^+-

activated samples. This confirms that the denser microstructure guided by K^+ ultimately results in superior macroscopic mechanical performance.

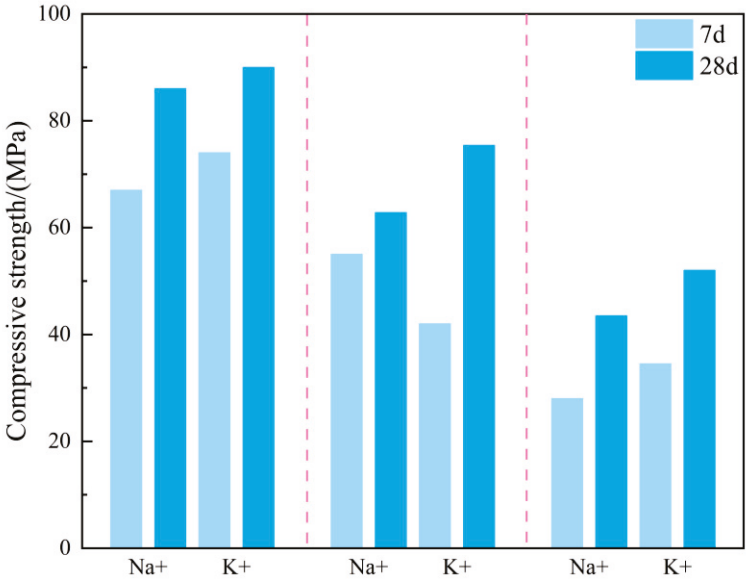

Figure 25. Compressive strengths of sodium-based and potassium-based activators [51–53]. Note: Due to differences in materials and moduli, the compressive strength data are not directly comparable. The integration of these data aims to qualitatively assess and verify the feasibility of using different activators.

The silicate modulus of the alkali activator is a critical parameter influencing the mechanical performance of mortar. As shown in Figure 26 [49,54,55,123,124], the effect of the modulus on the compressive strength generally tends to initially increase but then decreases. At lower moduli, the relatively high Na_2O content in the activator rapidly elevates the pH of the system, promoting the breakage of Si-O and Al-O bonds in the precursor and accelerating the release of reactive aluminosilicate monomers. This facilitates the early formation and cross-linking of the gel phase, thereby enhancing early strength. Within the optimal modulus range, a balanced ratio of SiO_2 to Na_2O in the activator maintains sufficient alkalinity while supplying adequate silicate species for polycondensations [125]. The resulting gel phase exhibited a high degree of polymerization, significantly reduced microporosity, and a dense matrix structure. The reduction in strength observed at a lower modulus is attributed to the high alkali concentration in the mixture. This high alkalinity systematically shortens the silicate chain length, hindering the polymerization of alkali-activated materials and consequently compromising the mortar's durability and stability. An appropriately modulated activator can enhance the interfacial bonding between the cementitious matrix and aggregates, reducing microcracking at the interface and consequently improving the overall compressive strength. However, when the modulus is too high, the significantly increased SiO_2 proportion in the silicate activator increases the system's viscosity and reduces the OH^- concentration [56]. This slows the dissolution rate of the precursor, limits the release of reactive aluminosilicate monomers, and leads to an incomplete reaction. Unreacted SiO_2 may remain in a free state, creating structural defects. Excessive SiO_2 can also interfere with the polycondensation process of the gel, resulting in a loose gel structure and increased porosity. Furthermore, an insufficient Na^+ concentration in high-modulus systems may lead to dealkalization of the gel phase, reducing the matrix density and consequently diminishing the strength.

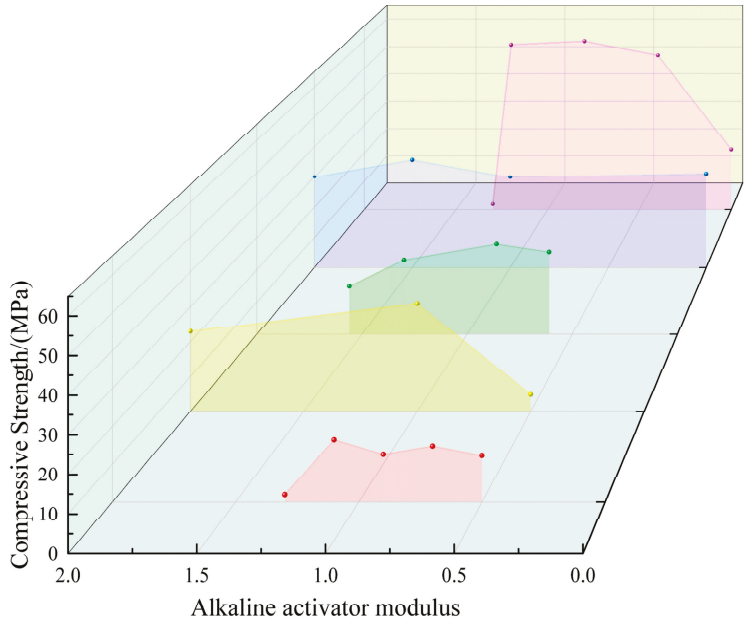

Figure 26. Effects of the alkaline activator modulus on the compressive strength [49,54,55,123,124]. Note: Due to the different types of materials and activators, the compressive strength data are not directly comparable. The purpose of integrating these data is to qualitatively assess and verify the feasibility of using different moduli.

The influence of solid waste as a cement substitute on mortar strength is complex and variable. At low replacement ratios, the "microaggregate effect" contributes to structural refinement, resulting in only a marginal reduction in strength. However, at high replacement levels, the predominance of inert components and insufficient hydration lead to a significant decline in strength. Activation methods such as thermal treatment, carbonation, and alkali activation can enhance the mechanical performance. To clearly present the strength development patterns of solid waste-based recycled mortar under various research conditions, the key findings of this section are summarized in Table 3. Nevertheless, the large-scale application of these materials continues to face multiple constraints. These include the high energy consumption of thermal activation, the elevated cost and inconsistent efficiency of carbonation, as well as the stringent control requirements and long-term reaction risks related to alkali activation. Future research should prioritize the development of green activation technologies, such as low-temperature alkali activation and biocatalyzed carbonation, to reduce energy consumption and carbon emissions. Additionally, further investigations are needed to explore the synergistic "complementary Ca-Si-Al mechanism" through blending construction and industrial solid wastes, establish accelerated aging models to clarify long-term strength degradation patterns, and incorporate internal curing materials to balance strength development and shrinkage.

Table 3. The influence of different factors on the strength of recycled mortar made from solid waste-based cementitious materials.

Categories of Influencing Factors	Specific Conditions	Trend or Range of Compressive Strength Variation	Ref.
Solid waste substitution rate	Waste concrete powder, low substitution rate (<20%)	The intensity is slightly reduced (approximately 85–95% of that in the control group)	[36,105–108]

Table 3. *Cont.*

Categories of Influencing Factors	Specific Conditions		Trend or Range of Compressive Strength Variation	Ref.
Solid waste substitution rate	Waste concrete powder, high substitution rate (≥30%)		The intensity decreases significantly (approximately 50–80% of that in the control group)	[36,105–108]
	Waste brick powder, with the same substitution rate		The strength is generally higher than that of the WCP system	[37–39,108]
Activation method	Thermal activation	Temperature	The intensity has increased significantly and reached its peak.	[28,31,32,72,74,75]
		Excessively high temperature (>1000 °C)	The strength has decreased significantly.	[28,31,32,72,74,75]
	Carbonation	Carbonation	The strength of both 7 d and 28 d has been enhanced.	[27,29,30,33]
		Carbonation temperature	Regulate early and long-term strength development by influencing the crystal type.	[34,78,122]
	Alkali activation	Cationic type of alkaline activator	The strength of the K^+ system at 28 d is usually higher.	[51–53]
		Modulus of alkali activator	The intensity initially increases with the modulus, then decreases, indicating the presence of an optimal range.	[49,54,55,123,124]

5. Durability of Solid Waste-Based Cementitious Recycled Mortars Against Chemical Attacks

In practical engineering applications, mortar is often subjected to complex and variable service environments, such as normal, marine, or industrial settings. When used in structures exposed to contaminants, the intrusion of corrosive media can significantly compromise structural durability. Therefore, investigating the corrosion resistance of solid waste-based mortar is not only essential for enhancing its overall performance but also a necessary prerequisite for promoting its application in harsh environments. This chapter focuses on typical corrosive scenarios, including sulfate attack, acid corrosion, and chloride ion ingress, and analyses the corrosion resistance mechanisms, performance variations, and influencing factors of solid waste-based mortar.

5.1. Corrosion Resistance

5.1.1. Sulfate Attack

Sulfate ions represent one of the most common anions in aqueous environments. During sulfate attack, sulfate ions (SO_4^{2-}) first penetrate the cementitious matrix, where they react with portlandite (CH) to form gypsum ($CaSO_4 \cdot 2H_2O$). The gypsum subsequently reacts with aluminum-containing phases (e.g., C-A-H) in the cement paste to generate ettringite (AFt). Under specific conditions such as low temperatures, SO_4^{2-} can also interact with C-S-H and carbonates to form thaumasite, as illustrated by the following reaction equations. The formation of these products can induce substantial internal stresses, leading to cracking and degradation, which explains the generally poor sulfate resistance of conventional cement-based materials. In contrast, alkali-activated cementitious materials prepared from industrial solid wastes, such as slag and fly ash, exhibit improved resistance to sulfate attack to a certain extent.

$$Ca(OH)_2 + SO_4^{2-} + 2H_2O \rightarrow CaSO_4 \cdot 2H_2O + 2OH^- \quad (7)$$

$$3CaO \cdot Al_2O_3 \cdot 6H_2O + 3Ca(OH)_2 + 3SO_4^{2-} + 25H_2O \rightarrow 3CaO \cdot Al_2O_3 \cdot 3CaSO_4 \cdot 31H_2O + 6OH^- \quad (8)$$

$$CaSi_2O_7 \cdot 3H_2O + 2CaSO_4 \cdot 2H_2O + 2CaCO_3 + 24H_2O \rightarrow Ca_6[Si(OH)_6](CO_3)_2(SO_4)_2 \cdot 24H_2O + Ca(OH)_2 \quad (9)$$

Sulfate attack on cement-based materials involves a complex combination of physicochemical processes. When sulfate ions (SO_4^{2-}) penetrate the paste, chemical attack is initiated as SO_4^{2-} reacts with the C-(A)-S-H gel, leading to its decalcification. The released calcium ions dissolve into the pore mixture, where they combine with water and SO_4^{2-} to form gypsum and ettringite (AFt) [57]. In the initial stage, an appropriate amount of gypsum can promote the formation of well-developed and stable AFt crystals. The precipitation of AFt helps fill pores and microcracks, thereby increasing the compactness of the mortar and temporarily mitigating further sulfate ingress. However, as the attack continues, excessive gypsum leads to a high sulfate ion concentration in the matrix. Under these conditions, AFt continues to grow and crystallize, generating a crystallization pressure that induces internal microcracks and porosity [126]. At this stage, physical damage begins to dominate the degradation process, establishing a cyclic "ingress–damage–accelerated ingress" feedback loop that ultimately results in structural failure [127]. When the attacking medium is magnesium sulfate ($MgSO_4$), the deterioration mechanism becomes even more severe. Because Mg^{2+} is more reactive than Ca^{2+}, it displaces Ca^{2+} in cement hydration products such as CH and C-S-H, forming noncementitious $Mg(OH)_2$ and low-strength M-S-H [128], as shown in the following equations. This process not only consumes the key cementitious phase in the system but also leads to disintegration of the cementitious structure and a sudden drop in strength. Moreover, the released SO_4^{2-} continues to participate in the abovementioned sulfate erosion cycle, exacerbating the deterioration of the material.

$$Ca(OH)_2 + MgSO_4 \rightarrow Mg(OH)_2 + CaSO_4 \quad (10)$$

$$C\text{-}S\text{-}H + MgSO_4 \rightarrow M\text{-}S\text{-}H + CaSO_4 \quad (11)$$

The composition of raw materials significantly influences the mechanical properties and sulfate resistance of alkali-activated materials by determining the types of hydration products formed. In alkali-activated slag-fly ash systems, as the slag content gradually decreases, the dominant gel phase transitions from calcium-rich C-A-S-H to sodium-containing C-(N)-A-S-H. With further reduction in slag content, the system primarily forms N-A-S-H gel. This phase evolution is attributed to the decreasing Ca^{2+} concentration resulting from the reduced addition of high-CaO slag. The mechanical strength of the mortar varies with these changes in gel type. A decrease in slag content leads to a gradual reduction in strength, which can be explained by the dense layered structure of the C-A-S-H gel, which minimizes structural defects. However, the three-dimensional network of the N-A-S-H gel tends to contain more micropores [129], resulting in a comparatively lower strength. Thus, variations in the hydration product content substantially affect the mechanical performance of the matrix.

Under sulfate attack conditions, the degradation mechanisms and resistance of different gel structures exhibit distinct behaviors. As the immersion time in the Na_2SO_4 solution increased, all the mortar samples experienced progressive strength loss. In the case of the C-A-S-H gel, SO_4^{2-} ions induce decalcification through ion exchange reactions, leading to disintegration of the gel framework. This process is accompanied by the formation of expansive products such as gypsum and ettringite (AFt), which significantly

increase internal porosity and microcracking, resulting in rapid strength deterioration. As shown in Figure 27 [130–133], mortar formulations with higher slag contents exhibit more pronounced strength loss in the later stages of sulfate exposure. In contrast, although the N-A-S-H gel undergoes dealumination [134], this reaction typically does not cause complete breakdown of the gel network. The three-dimensional aluminosilicate framework remains largely intact. Moreover, the XRD pattern of sulfate erosion (Figure 28) shows that the peak intensity of the corrosion product ettringite decreases or even disappears at low slag ratios. This phenomenon may be attributed to the reduced slag content, which lowers the Ca/Si ratio. Consequently, the hydration products gradually transform from C-A-S-H to N-A-S-H gel, with the Al used for ettringite formation being redirected to generate N-A-S-H gel. Therefore, the strength degradation rate of low-calcium materials is slower, demonstrating superior long-term resistance.

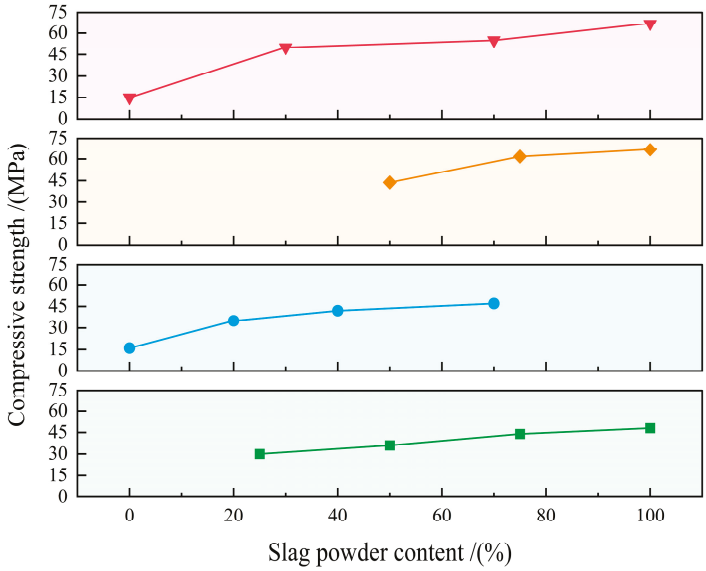

Figure 27. Compressive strength of different slag powder contents under sulfate attack [130–133]. Note: Due to variations in materials, the compressive strength data are not directly comparable. The purpose of integrating these data is to qualitatively assess and verify the feasibility of using different slag powder contents to resist sulfate corrosion.

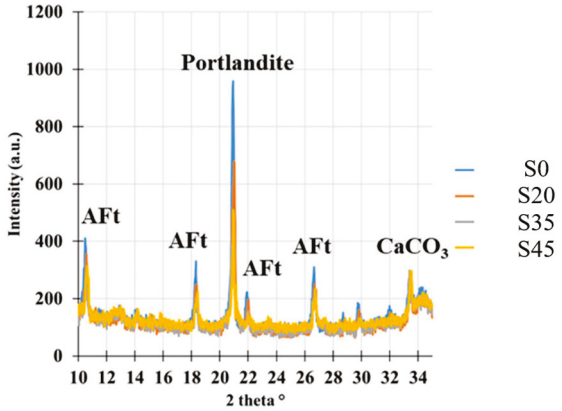

Figure 28. XRD patterns of mortar samples with different slag/fly ash ratios in 5% Na_2SO_4 solutions [135].

Studies on the durability of alkali-activated cementitious materials in sulfate environments have revealed significantly lower resistance to $MgSO_4$ attack than Na_2SO_4 exposure [44,136,137]. The erosion mechanism of sodium sulfate and magnesium sulfate

on mortar is shown in Figure 29. This difference stems from the high charge density of Mg^{2+}, which replaces Ca^{2+} in the C-A-S-H gel, leading to the formation of gypsum and AFt. It can further substitute for Al^{3+} in the gel network, resulting in depolymerization of the three-dimensional framework composed of silicon (aluminum) oxygen tetrahedra [138]. Concurrently, H^+ ions generated by the hydrolysis of $MgSO_4$ decrease the pH of the system, accelerating gel decomposition [58]. The XRD patterns of the mortar samples under magnesium sulfate attack are shown in Figure 30. Under the exposure of magnesium sulfate, the diffraction peaks of C-A-S-H gradually diminished, whereas those of gypsum and brucite became more pronounced. Notably, AFt does not exhibit clear diffraction peaks in the XRD patterns, as it becomes unstable at pH values below 10.7 [139]. From a microstructural perspective [58,59], all mortar samples after sulfate attack exhibit noticeable pores and cracks caused by crystallization pressure from expansive products, ultimately forming interconnected microcracks and significantly reducing the density of the ITZ. Compared with the samples exposed to Na_2SO_4, those subjected to $MgSO_4$ presented a more porous and loose microstructure, indicating a greater degree of deterioration and a faster rate of performance degradation.

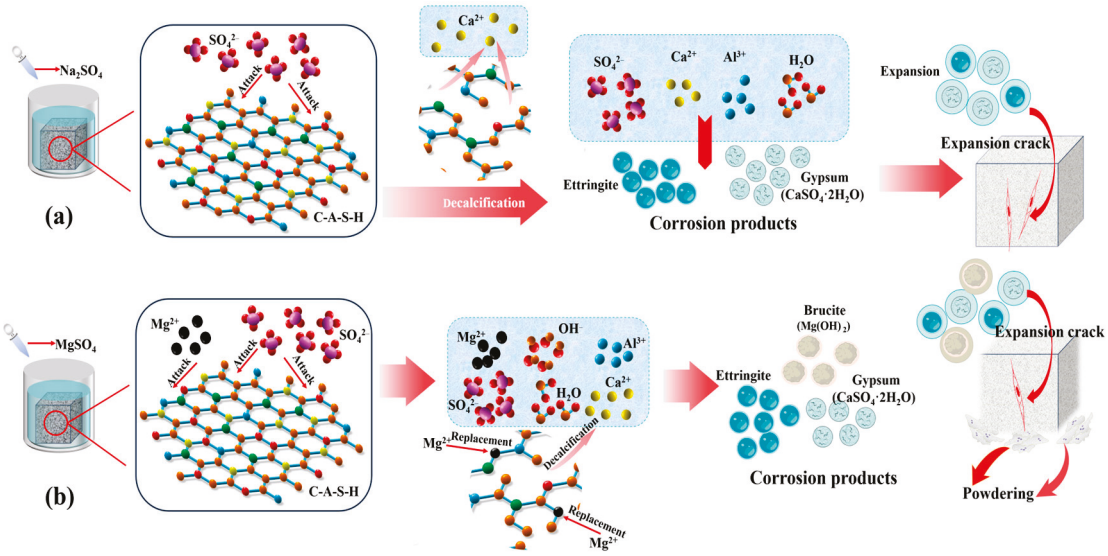

Figure 29. Erosion mechanisms of sodium sulfate (**a**) and magnesium sulfate (**b**).

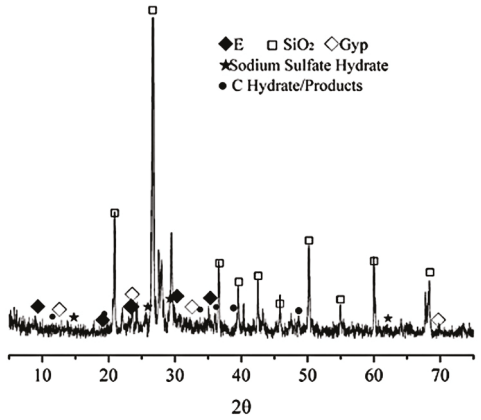

Figure 30. XRD patterns of mortar samples in $MgSO_4$ solutions: [140].

5.1.2. Acid Corrosion

When the surface of traditional Portland cement building structures comes into contact with acid rain or other acidic media, H^+ ions initially undergo a neutralization reaction

with $Ca(OH)_2$ in the structure. This process causes the dissolution of solid-phase hydrated silicates and hydrated aluminate salts, thereby reducing the alkalinity of the structure. The H^+ ions further attack the Ca^{2+} in C-S-H, forming a noncementitious silica gel ($SiO_2 \cdot nH_2O$), as represented in reaction Equations (12) and (13). This process degrades the cementitious framework and leads to a decrease in mortar strength. Notably, H^+ corrosion often occurs in conjunction with sulfate attack and carbonation, which collectively accelerate the deterioration process.

$$Ca(OH)_2 + 2H^+ \rightarrow Ca^{2+} + 2H_2O \quad (12)$$

$$C\text{-}S\text{-}H + nH^+ \rightarrow Ca^{2+} + SiO_2 \cdot nH_2O \quad (13)$$

In contrast to ordinary Portland cement systems, alkali-activated materials derived from industrial solid wastes primarily form a three-dimensional network-structured aluminosilicate gel (N-A-S-H). The superior acid resistance of these systems can be attributed to their distinct chemical compositions and microstructures. On the one hand, the three-dimensional framework composed of $[SiO_4]^{4-}$ and $[AlO_4]^{5-}$ tetrahedra exhibits better resistance to acid attack than the C-S-H gel in conventional cement [122]. The absence of $Ca(OH)_2$ as a vulnerable phase for acid reactions further enhances the overall chemical stability. On the other hand, since calcium is the primary target during acid corrosion and tends to form soluble salts such as $CaCl_2$ or $CaSO_4$, the C-(A)-S-H gel formed in industrial waste-based systems generally has a low Ca/Si ratio. Compared with the high Ca/Si C-S-H in OPC, the low-Ca C-(A)-S-H releases fewer Ca^{2+} ions under H^+ attack, thereby reducing gypsum formation and avoiding the expansion caused by AFt and internal cracking due to gypsum precipitation [90]. Furthermore, the alkali activation process leads to the formation of a highly dense microstructure characterized by low porosity and poor pore connectivity, effectively hindering the penetration and diffusion of acidic media. Compared with traditional Portland cement systems, alkali-activated materials derived from industrial solid waste generally exhibit better acid resistance.

In alkali-activated systems, H^+ ions initially undergo ion exchange with cations (e.g., Na^+, K^+, and Ca^{2+}) in the gel network. This constitutes the primary degradation mechanism at the early stage, which elevates the pH of the pore solution [60] and induces weight gain due to water absorption after cation leaching. As the acid concentration increases or is prolonged, H^+ begins to attack and breakdown the Si-O-Al and Si-O-Si network structures [61], triggering dealumination and desilication reactions that ultimately dissolve the gel framework. This process represents the fundamental cause of severe material deterioration.

The chemical composition of raw materials fundamentally governs the acid resistance of mortar, with the calcium content and silicon-to-aluminum (Si/Al) ratio being particularly influential in determining the acid degradation mechanism. From the perspective of phase composition, the calcium content of the system directly dictates the type of dominant gel phase and its stability under acidic conditions. High-calcium systems such as slag-based materials primarily form C-A-S-H gels. This gel is prone to calcium leaching during acid attack, which leads to structural disintegration and loss of cohesion. Consequently, these systems exhibit relatively poor acid resistance [141]. In contrast, low-calcium systems such as fly ash-based materials primarily form a three-dimensional N-A-S-H-dominated network. Owing to the lower content of exchangeable calcium ions that can be replaced by H^+, the aluminosilicate framework remains more stable in acidic environments, resulting in superior durability [142]. Furthermore, from the perspective of chemical bond stability, the Si/Al ratio of the raw material directly affects the degree of polymerization and hydrolytic stability of the gel network. Since the bond energy of Si-O is significantly greater than that of Al-O, a higher Si/Al ratio implies a greater proportion of more hydrolysis-resistant

Si-O-Si bonds and a lower proportion of more acid-vulnerable Si-O-Al and Al-O-Al bonds within the gel structure. Therefore, increasing the Si/Al ratio effectively enhances the resistance of a material to acid attack [138].

Furthermore, the deterioration mechanisms of alkali-activated cementitious materials in hydrochloric acid (HCl) and sulfuric acid (H_2SO_4) environments are fundamentally distinct. This is primarily manifested in the differences in attack mechanisms, reaction products, and failure modes. Figure 31 shows the change ratios of the compressive strength of mortar after corrosion by sulfuric acid and hydrochloric acid, respectively. It is evident that the reduction in compressive strength after sulfuric acid exposure is less pronounced than that after hydrochloric acid exposure. The microstructures of the mortar samples after exposure to sulfuric and hydrochloric acid are compared in Figure 32 [143]. The corrosion mechanism in HCl is predominantly governed by H^+ attack, leading to dissolution-based degradation. Chloride ions do not participate directly in chemical reactions but accelerate H^+ penetration through ion exchange. The resulting corrosion products (e.g., chlorides) are highly soluble and can be continuously leached away by the acid solution, constantly exposing fresh surfaces and allowing the corrosion front to progress inwards [144]. In contrast, sulfuric acid attack involves a dual degradation mechanism. In addition to the direct damage to the gel network caused by H^+, it is accompanied by sulfate-related reactions [145], which constitute the key difference between the two acids. SO_4^{2-} reacts with Ca^{2+} and Al^{3+} in the system to form low-solubility precipitates such as gypsum and ettringite. These products may initially block capillary pores and slow acid ingress; however, as the reaction continues, their continued precipitation generates increasing crystallization pressure, leading to internal stress accumulation, microcrack propagation, and eventual surface spalling. Consequently, mortar exposed to HCl exposure exhibits a relatively linear strength loss due to progressive dissolution, whereas H_2SO_4 attack causes expansion and cracking, which often leads to sudden failure, reflected in a more abrupt, nonlinear decline in strength.

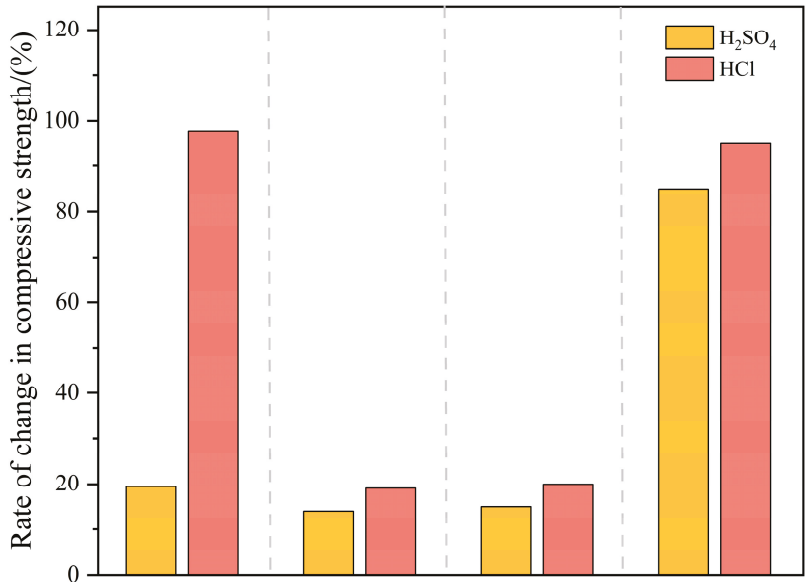

Figure 31. The change ratio of compressive strength of mortar after different types of acid corrosion [146–149]. Note: Due to differences in materials, the compressive strength data are not directly comparable. The integration of these data is intended to qualitatively assess and verify the feasibility of the acid resistance of mortar.

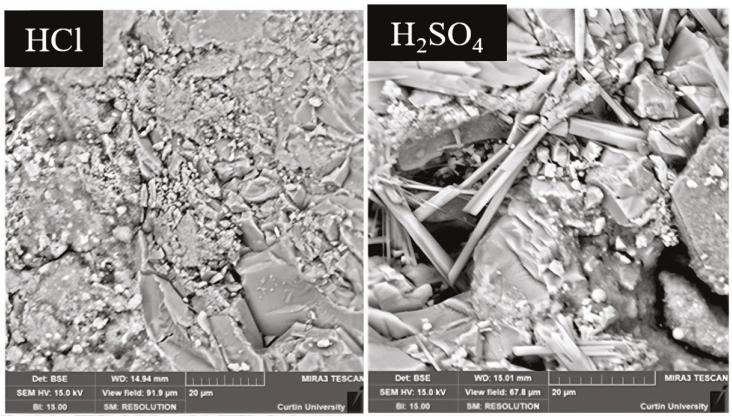

Figure 32. SEM images of mortar immersed in 0.31 mol/L solution. [143].

5.1.3. Chloride Ion Ingress

Chloride ion ingress is one of the primary causes of deterioration in the durability of reinforced concrete structures, posing a particularly severe threat to constructions in coastal or saline soil environments. Although chloride ions do not corrode the cement paste or coarse aggregates in concrete, they induce corrosion of the steel reinforcement. This corrosion generates expansion stress, leading to cracking along the reinforcement, a reduction in the bond strength between the steel and the concrete, and eventual spalling of the concrete cover. These processes further accelerate chloride penetration, ultimately resulting in structural deterioration. Therefore, the porosity and water absorption capacity of a material are critical indicators of its resistance to chloride ion attack.

After chloride ions (Cl^-) penetrate cement-based materials via capillary action, they initiate a series of physicochemical processes. Upon entering the matrix through capillary pores, Cl^- reacts with C_3A to form Friedel's salt, as shown in Equation (14). This low-solubility product can initially bind chlorides and slow the ingress process. However, in later stages, the expansion associated with Friedel's salt generates internal stress [62], inducing microcracks that facilitate further chloride penetration. Simultaneously, Cl^- reacts with portlandite (CH) to form highly soluble $CaCl_2$ [63], as indicated in Equation (15). This process continuously consumes the CH phase, which is essential for maintaining high alkalinity, and significantly reduces the pore solution pH. It also diminishes the contribution of CH to the strength framework, thereby destabilizing the chemical environment required for C-S-H gel stability. In addition, Cl^- can adsorb onto the surface of C-S-H gel [150], where it interacts with Ca^{2+} to form soluble $CaCl_2$. This leads to depolymerization of the gel network, increased gel porosity, and enhanced permeability, collectively accelerating chloride ingress.

$$2C_3A + Ca^{2+} + 2Cl^- + 10H_2O \rightarrow 3CaO \cdot Al_2O_3 \cdot CaCl_2 \cdot 10H_2O \quad (14)$$

$$Ca(OH)_2 + 2Cl^- \rightarrow CaCl_2 + 2OH^- \quad (15)$$

In contrast to ordinary Portland cement (OPC), the main hydration products of alkali-activated materials (AAMs) derived from solid wastes are aluminosilicate gels with low calcium-to-silicon ratios, such as N-A-S-H or C-A-S-H. These gels generally form a denser and more homogeneous microstructure than do the high Ca/Si and C-S-H gels in OPC systems [151]. At the microscale, this compact structure creates tortuous transport paths that significantly hinder the diffusion of chloride ions in the pore solution. Moreover, the refined pore system with reduced connectivity further restricted Cl^- migration. Unlike OPC, AAMs contain little or no free CH, which fundamentally minimizes the formation of expansive phases such as Friedel's salt, thereby avoiding the associated crystallization

pressure and microcrack propagation [152]. The low-calcium nature of AAM gels limits not only the total amount of Ca^{2+} available for reaction with Cl^- but also the tendency to form expansive products [153]. However, more importantly, under corrosive conditions, the limited leachable calcium helps preserve the structural integrity of the main silicate-aluminate framework, which is composed of $[SiO_4]^{4-}$ and $[AlO_4]^{5-}$ tetrahedral units. This considerably slows the gel depolymerization caused by calcium leaching [154]. Consequently, AAMs establish multiple protective mechanisms through their dense microstructure, optimized phase composition, and stable chemical bonding, collectively contributing to their superior resistance to chloride ion penetration compared with that of conventional OPC systems.

The composition of raw materials in solid wastes significantly influences the chloride resistance of mortar. In high-calcium systems, Ca^{2+} promotes the formation of the C-(A)-S-H gel [155], which develops a dense microstructure during early hydration. This not only enhances early-age strength but also establishes an effective physical barrier by reducing pore connectivity, thereby significantly hindering chloride transport and diffusion. Moreover, the resulting Friedel's salt exhibited excellent chloride-binding capacity, contributing to the immobilization of chloride ions [156]. In addition, aluminum and silicon, as essential elements in the aluminosilicate gel network, play a vital role in forming a dense binding framework. A lower Si/Al ratio facilitates the formation of highly cross-linked N-A-S-H or C-N-A-S-H gels [157]. In such structures, the increased proportion of $[AlO_4]^{5-}$ tetrahedra promotes a more compact three-dimensional network, which reduces the overall porosity and suppresses potential chloride penetration pathways, thereby achieving an efficient physical blocking effect against Cl^- ingress.

The corrosion behavior of different chloride salts in mortar is notably different. Owing to their smaller ionic radius, monovalent cationic chlorides (e.g., NaCl and KCl) exhibit greater mobility in the pore solution, which may facilitate faster diffusion of Cl^- into the mortar. In contrast, divalent cationic chlorides, characterized by larger ionic radii and higher charge densities, migrate more slowly, potentially slowing the overall Cl^- penetration rate [158]. More importantly, divalent cations such as Ca^{2+} and Mg^{2+} contribute to the formation of Friedel's salt, brucite, and minor calcium chloride hydrate ($CaCl_2 \cdot 6H_2O$) [64], which can partially fill pores and refine the pore structure, thereby mitigating the chloride ingress rate. However, compared with $CaCl_2$, $MgCl_2$ is more destructive to mortar. The underlying mechanism lies in the direct degradation of the gel network by Mg^{2+}, leading to the formation of weakly cementitious M-S-H and crystalline $Mg(OH)_2$. Although these products may initially fill pores to some extent, the resulting M-S-H phase has very low strength. Furthermore, this cation exchange process directly disrupts the chemical structure and binding capacity of the primary gel phases, ultimately causing significant deterioration in mortar strength, as shown in Figure 33.

Solid waste-based cementitious materials have remarkable advantages in terms of corrosion resistance. Their low-calcium aluminosilicate gels (e.g., N-A-S-H) possess a dense microstructure and high chemical stability, providing effective resistance against sulfate, acid, and chloride ion attack. Compared with conventional cement, low-calcium systems exhibit superior resistance to Na_2SO_4 exposure, although their performance against $MgSO_4$ remains relatively limited. Under acid corrosion, systems with high Si/Al ratios exhibit increased durability due to the stability of Si-O-Si bonds. In the case of chloride ingress, the dense gel matrix acts as a physical barrier, whereas Friedel's salt contributes to chemical binding, synergistically inhibiting chloride penetration. However, the current understanding of the degradation mechanisms under combined multi-ion corrosion conditions remains insufficient, and variability in solid waste composition may pose long-term environmental risks. Future efforts should prioritize the development of multifactor corrosion models,

optimize the gel composition through blending diverse solid wastes, and strengthen engineering validation in aggressive environments such as marine and saline–alkali areas. These advances are essential for promoting the large-scale application of solid waste-based mortar in high-durability green construction.

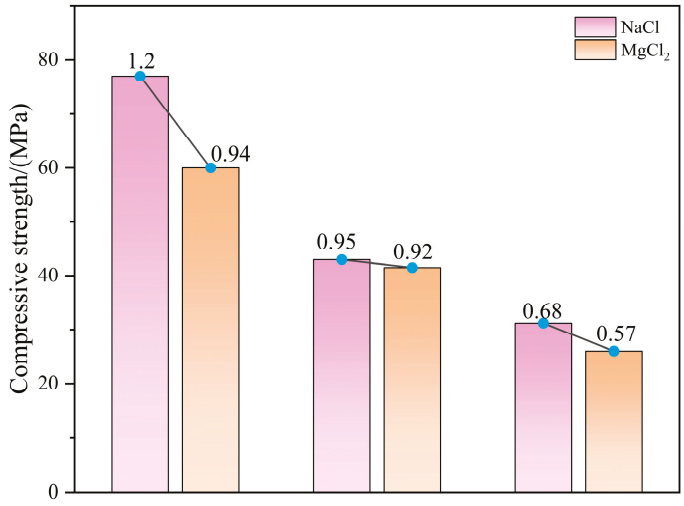

Figure 33. The ratio of compressive strength to residual strength of mortar after corrosion by different types of chlorides [159–161]. Note: Due to differences in materials, the compressive strength data are not directly comparable. The purpose of integrating these data is to qualitatively assess and verify the mortar's resistance to chloride corrosion.

5.2. Freeze–Thaw Resistance

Freeze–thaw damage is one of the most significant forms of deterioration affecting building structures in cold regions, including walls, floors, water conservancy projects, bridges, and culverts. Freeze–thaw failure is a complex physical fatigue process. It mainly occurs when water penetrates the internal pores of a structure and freezes at low temperatures. This freezing causes the pore volume to expand, resulting in the formation of microcracks. As the temperature rises, water gradually seeps deeper into the structure through these pores and cracks. Under repeated cycles of expansion pressure and water osmotic pressure, the surface of the structure shows a peeling process, progressing layer by layer from the outside inward. Consequently, the microcracks and pores within the structure increase and expand, leading to a loss of quality and deterioration in structural strength [162].

Compared to ordinary Portland cement, industrial solid wastes such as fly ash, mineral powder and silica fume have smaller particle sizes and a slower hydration rate. These characteristics enable them to effectively fill the voids within cement-based materials, thereby enhancing structural density [11,91]. Calcium hydroxide, a primary hydration product of cement, possesses a loose and fragile microstructure with large pore diameters. Through the pozzolanic reaction, solid wastes consume calcium hydroxide, producing additional C-S-H and C-A-S-H gels. The newly formed gels deposit within existing capillary pores and macropores, dividing them into smaller, more closed pores [163]. This significantly reduces the number of harmful pores (>50 nm) while increasing the number of harmless pores (<20 nm). This denser and more refined pore structure effectively hinders the intrusion of external moisture and significantly reduces the total amount of internal frozen water and its migration ability. Therefore, solid waste systems typically demonstrate superior freeze–thaw resistance compared to OPC, as shown in Figure 34 [164,165]. However, due to the relatively slow hydration reaction rate of solid waste materials, their early strength development is relatively sluggish [11,25]. Exposure to freeze–thaw cycles during the early

stages can cause more severe structural damage. Additionally, solid waste particles are small and possess a large specific surface area, which increases water demand. Excessive water demand may lead to a higher water-to-binder ratio, thereby increasing the system's porosity [166] and adversely affecting freeze–thaw resistance.

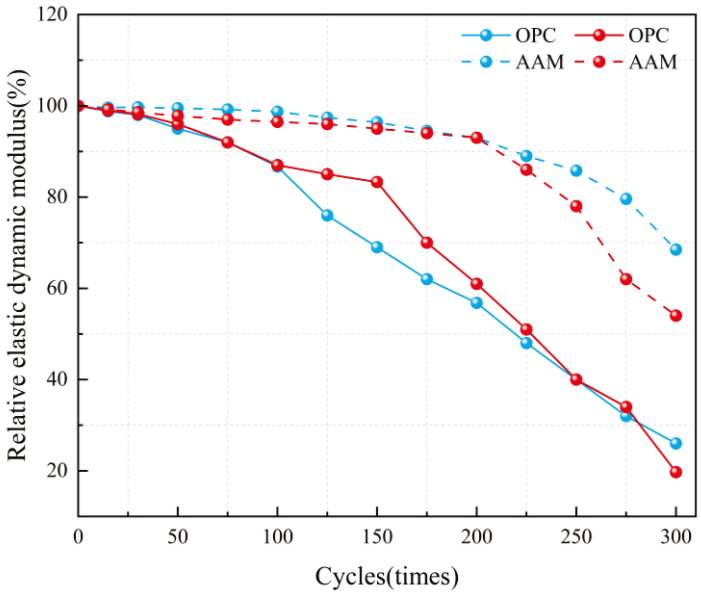

Figure 34. The relative dynamic elastic modulus of mortar after freeze–thaw [164,165]. Note: Due to differences in materials, the data on relative dynamic elastic modulus are not directly comparable. Their integration aims to qualitatively assess and verify the feasibility of the freeze–thaw resistance of solid waste mortar.

Pore structure is a key factor affecting the freeze–thaw resistance of mortar. High porosity indicates that, in a saturated state, the mortar contains more freezable water. When freezing occurs, the volume expansion potential is greater, resulting in stronger destructive forces. However, total porosity alone is not a decisive indicator; pore size distribution is more critical. Generally, pores with diameters greater than 50 μm are classified as harmful pores, while those exceeding 200 μm are considered highly harmful pores [165]. These pores are the primary sites of freeze–thaw damage because they facilitate rapid water penetration and migration and serve as main reservoirs for free water. Their abundance directly determines the quality of the freeze–thaw resistance of the mortar. With the increase of the number of freeze–thaw cycles, the number of pores within the mortar also rises, causing cumulative damage until the material's performance deteriorates completely [164,167,168].

Based on the above, solid waste-based cementitious materials have demonstrated significant advantages in freeze–thaw resistance. These solid waste materials enhance the density of mortar by refining its pore structure, thereby optimizing its microstructure and further improving its freeze–thaw resistance. Although the use of solid waste materials may result in slower early strength development and an increased risk of early freeze–thaw damage, their ongoing secondary hydration reactions continuously optimize the pore structure over time. Consequently, the frost resistance of these materials improves with age, exhibiting a long-term durability advantage compared to traditional cement mortar.

6. Future Prospects

Future research should prioritize three key directions to advance the field:

(1) Develop a synergistic utilization strategy for multi-component solid waste systems to achieve complementary effects in chemistry and microstructure. In the future, this approach will lead to the creation of high-performance, multifunctional, and recyclable

advanced building material systems. Furthermore, the application of solid waste materials should not be limited to building materials alone. For example, copper slag and zinc slag inherently provide antibacterial metal ions [169]. Future developments could include sustained-release antibacterial coatings for use in environments with stringent hygiene requirements, such as hospitals and schools. By leveraging the alkaline properties of steel slag, mine slag, red mud and other materials, along with the various metal oxides they contain [170], non-toxic anti-rust coating pigments can be produced to gradually replace traditional heavy metal-based anti-corrosion pigments, such as those containing chromium and lead. The application of solid waste materials offers new sustainable development pathways for the construction, industrial and household sectors.

(2) The focus is shifting from the activation of a single type of solid waste to the coordinated activation of multiple solid wastes. By scientifically designing the proportions of different solid wastes and leveraging the solid-phase reactions that occur during the heat treatment process, new highly active phases are generated, achieving a synergistic enhancement of the activation effect. Non-traditional thermal activation methods, such as microwave and infrared radiation activation, are being developed. These technologies utilize the selective coupling of electromagnetic waves with materials to achieve internal heating, significantly enhancing thermal efficiency and potentially generating more active phases. Future carbonation technologies will evolve from merely treating solid waste to manufacturing value-added products. By precisely controlling process parameters such as temperature, humidity and CO_2 concentration, the crystal form, morphology, and particle size of calcium carbonate can be directionally regulated to produce specialized calcium carbonate suitable for high-value industrial applications, including plastics, coatings, and papermaking, thereby maximizing value. Additionally, solid activators based on industrial by-products (such as complex alkali salts) are being developed to address issues related to the strong corrosiveness and inconvenient transportation of liquid activators. Through precise regulation of proportions and processes, alkali-activated materials with intelligent properties, such as self-repair, self-sensing, moisture regulation, and antibacterial are prepared, greatly enhancing their added value. Furthermore, innovative low-carbon activation approaches are being pursued to minimize energy consumption and environmental impact while maintaining performance.

(3) Establish a reliable long-term durability model based on on-site performance under actual usage conditions. These efforts aim to transform laboratory-scale achievements into structurally feasible and environmentally sustainable applications. In future developments, solid waste materials will become advanced engineering materials characterized by longer lifespans, enhanced safety, and reduced maintenance requirements in harsh environments. This will be achieved through mechanism-driven material design and performance improvement through the integration of multiple technologies. Develop pH-sensitive coatings based on solid waste that change color when an internal corrosive environment is initiated, providing a visual early warning of corrosion. Combine solid waste carriers with phase change materials. When the temperature drops, the phase change material solidifies and releases heat, mitigating sudden temperature declines within the mortar. This process delays the formation of ice crystals and reduces freeze–thaw damage.

7. Conclusions

This review provides a systematic analysis of solid waste-based cementitious materials for recycled mortar, focusing on raw material properties, activation methods, mechanical strength, and corrosion resistance. The main conclusions are as follows:

(1) By analyzing the composition, mineral composition and microscopic morphology of solid waste, it has been found that construction solid waste (such as discarded concrete

powder and brick powder) and industrial solid waste (such as slag and fly ash) possess the technical feasibility to partially or fully replace cement in the preparation of recycled mortar due to their high content of active SiO_2, Al_2O_3 and CaO components. However, their inherent inertness limits direct utilization efficiency, and their active ingredients must be activated through specific methods.

(2) Activated solid waste materials exhibit a higher utilization rate. Thermal activation can significantly enhance material reactivity; however, it is limited by high energy consumption and process complexity. Carbonation technology, which fixes CO_2 and generates calcite, offers both environmental protection and structural enhancement benefits. However, its efficiency is significantly affected by variations in raw material composition. Alkali-activated systems are most effective in forming high-strength and high-density gels, but require precise control of the activator modulus and alkali content, as well as management of potential alkali-aggregate reactions and long-term shrinkage risks. Future efforts should focus on the coordinated optimization of multiple activation methods and the development of low-energy, environmentally friendly activation pathways.

(3) The solid waste substitution rate significantly impacts the strength of mortar. At low substitution levels, the "micro-aggregate effect" predominates, resulting in limited strength loss. However, a high substitution rate causes a significant decrease in strength due to the dilution of cementitious components and insufficient hydration. Activation treatments can improve strength to varying degrees, with alkaline activation showing particularly notable effects. Future research should further explore the synergistic effects of multi-source solid waste to promote the precision of mix proportion design.

(4) Solid waste-based mortar generally outperforms traditional cement in terms of corrosion resistance. Its dense low-calcium silicoaluminate gel structure significantly enhances resistance to acid attack and chloride ion penetration. Specifically, it exhibits superior resistance to Na_2SO_4 erosion but is more susceptible to damage from $MgSO_4$. The mortar remains stable against HCl erosion; however, exposure to H_2SO_4 can lead to gypsum-induced expansion failure. Chloride ion erosion is inhibited through the combined effects of the gel's physical barrier and chemical curing. Additionally, solid waste particles refine the pore structure, reduce the amount of freeze–thaw water, and enhance frost resistance. However, caution is required regarding the potential risk of early freeze–thaw damage due to the slow development of early strength.

Through systematic analysis, this review demonstrates that solid waste-based recycled mortar is technically feasible. Its mechanical properties and durability can be effectively enhanced through activation methods.

Author Contributions: Y.G.: investigation, conceptualization, writing—original draft. J.C. and M.L.: data curation, formal analysis, writing—original draft. Q.L.: software. B.L.: data curation, funding acquisition. T.S. and X.M.: conceptualization, funding acquisition, supervision, writing—review and editing. All authors have read and agreed to the published version of the manuscript.

Funding: This work was supported by the National Natural Science Foundation of China (52309137 (Bangxiang Li)), the Natural Science Foundation of Shandong Province (ZR2025MS802 (Tian Su); ZR2024QE218 (Bangxiang Li)), and the Natural Science Foundation of Inner Mongolia Autonomous Region (2025MS05007 (Xuefeng Mei)).

Institutional Review Board Statement: Not applicable.

Informed Consent Statement: Not applicable.

Conflicts of Interest: The authors declare no conflicts of interest.

References

1. Bilal, M.; Khan, K.I.A.; Thaheem, M.J.; Nasir, A.R. Current state and barriers to the circular economy in the building sector: Towards a mitigation framework. *J. Clean. Prod.* **2020**, *276*, 123250. [CrossRef]
2. GEP Research. Global and China Construction and Demolition Waste Industry Market Research Report. 2025. Available online: https://www.gepresearch.com/ (accessed on 26 July 2025).
3. Hamilton, I.; Rapf, O.; Kockat, D.J.; Kockat, D.J.; Zuhaib, D.S.; Abergel, T.; Oppermann, M.; Otto, M.; Loran, S.; Fagotto, I.; et al. *2020 Global Status Report for Buildings and Construction*; United Nations Environmental Programme: Nairobi, Kenya, 2020.
4. Akhtar, A.; Sarmah, A.K. Construction and demolition waste generation and properties of recycled aggregate concrete: A global perspective. *J. Clean. Prod.* **2018**, *186*, 262–281. [CrossRef]
5. Rissman, J.; Bataille, C.; Masanet, E.; Aden, N.; Morrow III, W.R.; Zhou, N.; Elliott, N.; Dell, R.; Heeren, N.; Huckestein, B.; et al. Technologies and policies to decarbonize global industry: Review and assessment of mitigation drivers through 2070. *Appl. Energy* **2020**, *266*, 114848. [CrossRef]
6. Soto-Paz, J.; Arroyo, O.; Torres-Guevara, L.E.; Parra-Orobio, B.A.; Casallas-Ojeda, M. The circular economy in the construction and demolition waste management: A comparative analysis in emerging and developed countries. *J. Build. Eng.* **2023**, *78*, 107724. [CrossRef]
7. Ma, S.; Yin, J.; Wu, W.; Zeng, Q.; Zhao, Y. Review on Alkali-Activated Cementitious Materials Based on Recycled Fine Powder from Construction Waste. *Concrete* **2023**, 170–174+180. [CrossRef]
8. Xiao, J.; Ma, Z.; Sui, T.; Akbarnezhad, A.; Duan, Z. Mechanical properties of concrete mixed with recycled powder produced from construction and demolition waste. *J. Clean. Prod.* **2018**, *188*, 720–731. [CrossRef]
9. Provis, J.L.; Bernal, S.A. Geopolymers and related alkali-activated materials. *Annu. Rev. Mater. Res.* **2014**, *44*, 299–327. [CrossRef]
10. Zheng, W.; Zou, M.; Wang, Y. Research Progress on Alkali-Activated Cementitious Materials. *J. Build. Struct.* **2019**, *40*, 28–39.
11. Zhang, P.; Zheng, Y.; Wang, K.; Zhang, J. A review on properties of fresh and hardened geopolymer mortar. *Compos. Part B Eng.* **2018**, *152*, 79–95. [CrossRef]
12. Zhang, J.; Shi, C.; Zhang, Z.; Ou, Z. Durability of alkali-activated materials in aggressive environments: A review on recent studies. *Constr. Build. Mater.* **2017**, *152*, 598–613. [CrossRef]
13. Almutairi, A.L.; Tayeh, B.A.; Adesina, A.; Isleem, H.F.; Zeyad, A.M. Potential applications of geopolymer concrete in construction: A review. *Case Stud. Constr. Mater.* **2021**, *15*, e00733. [CrossRef]
14. Rashad, A.M. Metakaolin as cementitious material: History, scours, production and composition—A comprehensive overview. *Constr. Build. Mater.* **2013**, *41*, 303–318. [CrossRef]
15. Rashad, A.M. A comprehensive overview about the influence of different admixtures and additives on the properties of alkali-activated fly ash. *Mater. Des.* **2014**, *53*, 1005–1025. [CrossRef]
16. Kong, Y.K.; Kurumisawa, K. Fresh properties and characteristic testing methods for alkali-activated materials: A review. *J. Build. Eng.* **2023**, *75*, 106830. [CrossRef]
17. Chen, B.; Perumal, P.; Aghabeyk, F.; Adediran, A.; Illikainen, M.; Ye, G. Advances in using municipal solid waste incineration (MSWI) bottom ash as precursor for alkali-activated materials: A critical review. *Resour. Conserv. Recycl.* **2024**, *204*, 107516. [CrossRef]
18. Sun, Y.; Mohan, M.K.; Tao, Y.; Zhang, Y.; Van Tittelboom, K.; Ye, G.; De Schutter, G. A conceptual design of two-stream alkali-activated materials. *Cem. Concr. Compos.* **2024**, *148*, 105485. [CrossRef]
19. Yusslee, E.; Beskhyroun, S. Performance evaluation of hybrid one-Part Alkali activated materials (AAMs) for concrete structural repair. *Buildings* **2022**, *12*, 2025. [CrossRef]
20. Liu, J.; Tian, Y.; Ge, X.; Liu, B.; Liu, K.; Song, G. Experimental study on MgO-Na2CO3 combined excitation recycled fine-powder-slag cementitious system and modification. *Buildings* **2024**, *14*, 592. [CrossRef]
21. Li, Q.; Li, J.; Zhang, S.; Huang, X.; Wang, X.; Wang, Y.; Ni, W. Research progress of low-carbon cementitious materials based on synergistic industrial wastes. *Energies* **2023**, *16*, 2376. [CrossRef]
22. Alibeigibeni, A.; Stochino, F.; Zucca, M.; Gayarre, F.L. Enhancing concrete sustainability: A critical review of the performance of recycled concrete aggregates (RCAs) in structural concrete. *Buildings* **2025**, *15*, 1361. [CrossRef]
23. Zou, Z.; Li, J.; Li, J.; Gao, H.; Zhang, Y.; Yu, Y.; Zhang, C. Effect of high-volume recycled concrete powder on microstructure and mechanical performance of alkali-activated slag mortar using response surface approach. *Structures* **2025**, *79*, 109515. [CrossRef]
24. Sharmin, S.; Sarker, P.K.; Biswas, W.K.; Abousnina, R.M.; Javed, U. Characterization of waste clay brick powder and its effect on the mechanical properties and microstructure of geopolymer mortar. *Constr. Build. Mater.* **2024**, *412*, 134848. [CrossRef]
25. Sallı Bideci, Ö.; Bideci, A.; Ashour, A. Utilization of recycled brick powder as supplementary cementitious materials—A comprehensive review. *Materials* **2024**, *17*, 637. [CrossRef]
26. Shi, C.; Day, R.L. Early strength development and hydration of alkali-activated blast furnace slag/fly ash blends. *Adv. Cem. Res.* **1999**, *11*, 189–196. [CrossRef]

27. Peng, L.; Jiang, Y.; Ban, J.; Shen, Y.; Ma, Z.; Zhao, Y.; Shen, P.; Poon, C.S. Mechanism underlying early hydration kinetics of carbonated recycled concrete fines-ordinary portland cement (CRCF-OPC) paste. *Cem. Concr. Compos.* **2023**, *144*, 105275. [CrossRef]
28. Sui, Y.; Ou, C.; Liu, S.; Zhang, J.; Tian, Q. Study on properties of waste concrete powder by thermal treatment and application in mortar. *Appl. Sci.* **2020**, *10*, 998. [CrossRef]
29. Kaliyavaradhan, S.K.; Li, L.; Ling, T.C. Response surface methodology for the optimization of CO2 uptake using waste concrete powder. *Constr. Build. Mater.* **2022**, *340*, 127758. [CrossRef]
30. Kaliyavaradhan, S.K.; Ling, T.C.; Mo, K.H. CO_2 sequestration of fresh concrete slurry waste: Optimization of CO2 uptake and feasible use as a potential cement binder. *J. CO_2 Util.* **2020**, *42*, 101330. [CrossRef]
31. Zhang, D.; Zhang, S.; Huang, B.; Yang, Q.; Li, J. Comparison of mechanical, chemical, and thermal activation methods on the utilisation of recycled concrete powder from construction and demolition waste. *J. Build. Eng.* **2022**, *61*, 105295. [CrossRef]
32. Hu, R.; Wang, C.; Shen, J.; Ma, Z. Chloride transport and thermoactivated modification of sustainable cement-based materials with high-content waste concrete powder. *J. Mater. Res. Technol.* **2023**, *23*, 4012–4031. [CrossRef]
33. Zhao, Y.; Cui, K.; He, J.; Zheng, Y.; Shen, P.; Poon, C.S.; Peng, G.; Guo, R.; Xia, D. Highly reactive carbonated recycled concrete fines prepared via mechanochemical carbonation: Influence on the early performance of cement composites. *Cem. Concr. Compos.* **2024**, *152*, 105636. [CrossRef]
34. Wu, Y.; Mehdizadeh, H.; Mo, K.H.; Ling, T.C. High-temperature CO2 for accelerating the carbonation of recycled concrete fines. *J. Build. Eng.* **2022**, *52*, 104526. [CrossRef]
35. Shao, J.; Gao, J.; Zhao, Y.; Chen, X. Study on the pozzolanic reaction of clay brick powder in blended cement pastes. *Constr. Build. Mater.* **2019**, *213*, 209–215. [CrossRef]
36. Duan, Z.; Hou, S.; Xiao, J.; Li, B. Study on the essential properties of recycled powders from construction and demolition waste. *J. Clean. Prod.* **2020**, *253*, 119865. [CrossRef]
37. Lam, M.N.T.; Nguyen, D.T.; Nguyen, D.L. Potential use of clay brick waste powder and ceramic waste aggregate in mortar. *Constr. Build. Mater.* **2021**, *313*, 125516. [CrossRef]
38. Mansoor, S.S.; Hama, S.M.; Hamdullah, D.N. Effectiveness of replacing cement partially with waste brick powder in mortar. *J. King Saud Univ.-Eng. Sci.* **2024**, *36*, 524–532. [CrossRef]
39. Wang, X.; Zhang, T.; Chen, P.; Xu, G.; Guo, Y.; Wei, J.; Yu, Q. Hydration mechanism and microstructure evolution of recycled brick powder blended cement toward low-carbon and cleaner production. *Constr. Build. Mater.* **2024**, *438*, 137097. [CrossRef]
40. Wu, H.; Liang, C.; Xiao, J.; Ma, Z. Properties and CO_2-curing enhancement of cement-based materials containing various sources of waste hardened cement paste powder. *J. Build. Eng.* **2021**, *44*, 102677. [CrossRef]
41. Ouyang, X.; Wang, L.; Xu, S.; Ma, Y.; Ye, G. Surface characterization of carbonated recycled concrete fines and its effect on the rheology, hydration and strength development of cement paste. *Cem. Concr. Compos.* **2020**, *114*, 103809. [CrossRef]
42. Wang, T.; Fan, X.; Gao, C. Strength, pore characteristics, and characterization of fly ash-slag-based geopolymer mortar modified with silica fume. *Structures* **2024**, *69*, 107525. [CrossRef]
43. Khan, M.N.N.; Kuri, J.C.; Sarker, P.K. Effect of waste glass powder as a partial precursor in ambient cured alkali activated fly ash and fly ash-GGBFS mortars. *J. Build. Eng.* **2021**, *34*, 101934. [CrossRef]
44. Zhang, J.; Shi, C.; Zhang, Z.; Hu, X. Reaction mechanism of sulfate attack on alkali-activated slag/fly ash cements. *Constr. Build. Mater.* **2022**, *318*, 126052. [CrossRef]
45. Xiaoshuang, S.; Yanpeng, S.; Jinqian, L.; Yuhao, Z.; Ruihan, H. Preparation and performance optimization of fly ash-slag-red mud based geopolymer mortar: Simplex-centroid experimental design method. *Constr. Build. Mater.* **2024**, *450*, 138573. [CrossRef]
46. Xue, L.; Ni, Z.; Zhou, Z.; Zhang, Z.; Xiong, H.; Wang, H.; Zhuge, X.; Liu, H. Effects of desulfurized gypsum on shrinkage behavior of alkali-activated slag (AAS) and hybrid alkali-activated cement (HAC). *Case Stud. Constr. Mater.* **2025**, *22*, e04320. [CrossRef]
47. Wan, X.; Wang, B.; Jin, Z.; Li, S.; Yu, Q.; Cao, J. Solidification of chloride ion in alkali-activated slag-red mud. *Constr. Build. Mater.* **2024**, *451*, 138838. [CrossRef]
48. Haha, M.B.; Le Saout, G.; Winnefeld, F.; Lothenbach, B. Influence of activator type on hydration kinetics, hydrate assemblage and microstructural development of alkali activated blast-furnace slags. *Cem. Concr. Res.* **2011**, *41*, 301–310. [CrossRef]
49. Aydın, S.; Baradan, B. Effect of activator type and content on properties of alkali-activated slag mortars. *Compos. Part B Eng.* **2014**, *57*, 166–172. [CrossRef]
50. Palacios, M.; Gismera, S.; Alonso, M.D.M.; De Lacaillerie, J.D.E.; Lothenbach, B.; Favier, A.; Brumaud, C.; Puertas, F. Early reactivity of sodium silicate-activated slag pastes and its impact on rheological properties. *Cem. Concr. Res.* **2021**, *140*, 106302. [CrossRef]
51. Wang, W.; Noguchi, T.; Maruyama, I. Effects of alkali cations from silicate activators and exposure conditions on the alkali-silica reaction in alkali-activated slag mortars. *Constr. Build. Mater.* **2024**, *451*, 138929. [CrossRef]
52. Sitarz, M.; Castro-Gomes, J.; Hager, I. Strength and microstructure characteristics of blended fly ash and ground granulated blast furnace slag geopolymer mortars with Na and K silicate solution. *Materials* **2021**, *15*, 211. [CrossRef]

53. Omur, T.; Kabay, N.; Miyan, N.; Özkan, H.; Özkan, Ç. The effect of alkaline activators and sand ratio on the physico-mechanical properties of blast furnace slag based mortars. *J. Build. Eng.* **2022**, *58*, 104998. [CrossRef]
54. Guo, Y.; Xu, X.; Guo, W. Effect of alkaline activator on SIOT-GGBS-MK based alkali-activated mortar. *Constr. Build. Mater.* **2025**, *467*, 140322. [CrossRef]
55. Wang, D.; Zou, K.; Zhu, S.; Guo, L. Optimization of Mix Proportions and Mechanical Properties of Coal Gangue-Based Multi-Solid-Waste Geopolymer Mortars. *Case Stud. Constr. Mater.* **2025**, *23*, e05134. [CrossRef]
56. De Vargas, A.S.; Dal Molin, D.C.C.; Vilela, A.C.F.; Da Silva, F.J.; Pavao, B.; Veit, H. The effects of Na2O/SiO2 molar ratio, curing temperature and age on compressive strength, morphology and microstructure of alkali-activated fly ash-based geopolymers. *Cem. Concr. Compos.* **2011**, *33*, 653–660. [CrossRef]
57. Al-Dulaijan, S.U.; Maslehuddin, M.; Al-Zahrani, M.M.; Sharif, A.M.; Shameem, M.; Ibrahim, M. Sulfate resistance of plain and blended cements exposed to varying concentrations of sodium sulfate. *Cem. Concr. Compos.* **2003**, *25*, 429–437. [CrossRef]
58. Elyamany, H.E.; Abd Elmoaty, M.; Elshaboury, A.M. Magnesium sulfate resistance of geopolymer mortar. *Constr. Build. Mater.* **2018**, *184*, 111–127. [CrossRef]
59. Komljenović, M.; Baščarević, Z.; Marjanović, N.; Nikolić, V. External sulfate attack on alkali-activated slag. *Constr. Build. Mater.* **2013**, *49*, 31–39. [CrossRef]
60. Komljenović, M.M.; Baščarević, Z.; Marjanović, N.; Nikolić, V. Decalcification resistance of alkali-activated slag. *J. Hazard. Mater.* **2012**, *233*, 112–121. [CrossRef]
61. Deir, E.; Gebregziabiher, B.S.; Peethamparan, S. Influence of starting material on the early age hydration kinetics, microstructure and composition of binding gel in alkali activated binder systems. *Cem. Concr. Compos.* **2014**, *48*, 108–117. [CrossRef]
62. Geng, J.; Easterbrook, D.; Li, L.Y.; Mo, L.W. The stability of bound chlorides in cement paste with sulfate attack. *Cem. Concr. Res.* **2015**, *68*, 211–222. [CrossRef]
63. Maes, M.; De Belie, N. Resistance of concrete and mortar against combined attack of chloride and sodium sulphate. *Cem. Concr. Compos.* **2014**, *53*, 59–72. [CrossRef]
64. Chen, Z.; Ye, H. Understanding the impact of main seawater ions and leaching on the chloride transport in alkali-activated slag and Portland cement. *Cem. Concr. Res.* **2023**, *164*, 107063. [CrossRef]
65. Jiang, L.; Niu, Y.; Jin, W.; Gao, H.; Chen, L. Influence of chloride salt type on chloride ion diffusion performance of alkali-activated slag mortar. *Constr. Build. Mater.* **2022**, *351*, 128930. [CrossRef]
66. Xu, R.; Kong, F.; Yang, R.; Wang, H.; Hong, T. Influences of silicate modulus and alkali content on macroscopic properties and microstructure of alkali-activated blast furnace slag-copper slag. *Constr. Build. Mater.* **2024**, *442*, 137622. [CrossRef]
67. Yu, M.; Wang, T.; Chi, Y.; Li, D.; Li, L.Y.; Shi, F. Residual mechanical properties of GGBS-FA-SF blended geopolymer concrete after exposed to elevated temperatures. *Constr. Build. Mater.* **2024**, *411*, 134378. [CrossRef]
68. Jia, R.; Ran, B.; Lv, T.; Yu, Y.; Hu, X.; Xu, L. Synergistic effect of waste concrete powder and traditional SCMs in preparing clinker-free cement: Hydration and microstructure evolution. *Constr. Build. Mater.* **2025**, *491*, 142798. [CrossRef]
69. Yön, M.Ş. Mechanical, durability and microstructure properties of eco-friendly self-compacting mortars with addition of volcanic scoria, silica fume and boron waste as cement replacement. *Constr. Build. Mater.* **2025**, *462*, 139894.
70. Li, Z.; Gao, M.; Lei, Z.; Tong, L.; Sun, J.; Wang, Y.; Wang, X.; Jiang, X. Ternary cementless composite based on red mud, ultra-fine fly ash, and GGBS: Synergistic utilization and geopolymerization mechanism. *Case Stud. Constr. Mater.* **2023**, *19*, e02410. [CrossRef]
71. Sun, D.M.; Beulah, M.; Saji, J. Sustainable synergies: Performance evaluation of cement mortar with red mud and industrial by-products. *Next Mater.* **2026**, *10*, 101479. [CrossRef]
72. Bogas, J.A.; Carriço, A.; Pereira, M.F.C. Mechanical characterization of thermal activated low-carbon recycled cement mortars. *J. Clean. Prod.* **2019**, *218*, 377–389. [CrossRef]
73. Wu, H.; Yang, D.; Ma, Z. Micro-structure, mechanical and transport properties of cementitious materials with high-volume waste concrete powder and thermal modification. *Constr. Build. Mater.* **2021**, *313*, 125477. [CrossRef]
74. Ma, Z.; Shen, J.; Wu, H.; Zhang, P. Properties and activation modification of eco-friendly cementitious materials incorporating high-volume hydrated cement powder from construction waste. *Constr. Build. Mater.* **2022**, *316*, 125788. [CrossRef]
75. Wu, H.; Xu, J.; Yang, D.; Ma, Z. Utilizing thermal activation treatment to improve the properties of waste cementitious powder and its newmade cementitious materials. *J. Clean. Prod.* **2021**, *322*, 129074. [CrossRef]
76. Zhao, Y.; Gao, J.; Liu, C.; Chen, X.; Xu, Z. The particle-size effect of waste clay brick powder on its pozzolanic activity and properties of blended cement. *J. Clean. Prod.* **2020**, *242*, 118521. [CrossRef]
77. Shao, Z.; Fang, Z.; Sakai, Y. Enhancement of compacted hardened cement paste powder through carbonation: Evolution of CO2 diffusion, phase assemblage and pore structure. *Case Stud. Constr. Mater.* **2025**, *23*, e05293. [CrossRef]
78. Huang, J.; Chen, Y.; Yu, Q. Amorphous calcium carbonate formation from carbonated recycled cement powder: A novel carbonation-activated cementitious material. *Compos. Part B Eng.* **2025**, *297*, 112336. [CrossRef]
79. Kong, X.; Yao, Y.; Kai, M.; Guan, Y.; Ding, X.; Gu, Z.; Liu, J. The assessment of the mechanical and durability properties of mortar prepared with carbon dioxide-treated recycled concrete-brick powder. *Constr. Build. Mater.* **2025**, *466*, 140305. [CrossRef]

80. Kaliyavaradhan, S.K.; Ling, T.C. Potential of CO_2 sequestration through construction and demolition (C&D) waste—An overview. *J. CO_2 Util.* **2017**, *20*, 234–242.
81. Pan, S.Y.; Chen, Y.H.; Fan, L.S.; Fan, L.S.; Kim, H.; Gao, X.; Ling, T.C.; Chiang, P.C.; Gu, G. CO2 mineralization and utilization by alkaline solid wastes for potential carbon reduction. *Nat. Sustain.* **2020**, *3*, 399–405. [CrossRef]
82. Lu, B.; Shi, C.; Zhang, J.; Wang, J. Effects of carbonated hardened cement paste powder on hydration and microstructure of Portland cement. *Constr. Build. Mater.* **2018**, *186*, 699–708. [CrossRef]
83. Mehdizadeh, H.; Cheng, X.; Mo, K.H.; Ling, T.C. Upcycling of waste hydrated cement paste containing high-volume supplementary cementitious materials via CO_2 pre-treatment. *J. Build. Eng.* **2022**, *52*, 104396. [CrossRef]
84. Zhang, Y.; Yang, M.; Kang, L.; Zhang, L.; Zhang, K. Research progress on catalysts for a new type of alkali-activated cementitious materials. *J. Inorg. Mater.* **2016**, *31*, 225–233.
85. Purdon, A.O. The action of alkalis on blast-furnace slag. *Soc. Chem. Ind.* **1940**, *59*, 191–202.
86. Puligilla, S.; Chen, X.; Mondal, P. Understanding the role of silicate concentration on the early-age reaction kinetics of a calcium containing geopolymeric binder. *Constr. Build. Mater.* **2018**, *191*, 206–215. [CrossRef]
87. Davidovits, J. Geopolymers and geopolymeric materials. *J. Therm. Anal.* **1989**, *35*, 429–441. [CrossRef]
88. Buchwald, A.; Schulz, M. Alkali-activated binders by use of industrial by-products. *Cem. Concr. Res.* **2005**, *35*, 968–973. [CrossRef]
89. Duxson, P.; Fernández-Jiménez, A.; Provis, J.L.; Lukey, G.C.; Palomo, A.; van Deventer, J.S. Geopolymer technology: The current state of the art. *J. Mater. Sci.* **2007**, *42*, 2917–2933. [CrossRef]
90. Chen, Y.; de Lima, L.M.; Li, Z.; Ma, B.; Lothenbach, B.; Yin, S.; Yu, Q.; Ye, G. Synthesis, solubility and thermodynamic properties of NASH gels with various target Si/Al ratios. *Cem. Concr. Res.* **2024**, *180*, 107484. [CrossRef]
91. Venkatesan, G.; Alengaram, U.J.; Ibrahim, S.; Ibrahim, M.S.I. Effect of Fly Ash characteristics, sodium-based alkaline activators, and process variables on the compressive strength of siliceous Fly Ash geopolymers with microstructural properties: A comprehensive review. *Constr. Build. Mater.* **2024**, *437*, 136808. [CrossRef]
92. da Silva Rocha, T.; Dias, D.P.; França, F.C.C.; de Salles Guerra, R.R.; de Oliveira, L.R.D.C. Metakaolin-based geopolymer mortars with different alkaline activators (Na+ and K+). *Constr. Build. Mater.* **2018**, *178*, 453–461. [CrossRef]
93. Ye, H.; Radlińska, A. A Review and Comparative Study of Existing Shrinkage Prediction Models for Portland and Non-Portland Cementitious Materials. *Adv. Mater. Sci. Eng.* **2016**, *2016*, 2418219. [CrossRef]
94. Zhao, L.; Ma, X.; Song, S.; You, P.; Wu, H. Activating effect of potassium silicate solution in low portland cement binder. *Constr. Build. Mater.* **2022**, *319*, 126091. [CrossRef]
95. Tian, L.; Chen, X.; Liu, X.; Li, H.; Ge, Y. Mechanisms of recycled fine brick aggregate in autogenous shrinkage mitigation, mechanical properties enhancement and microstructure improvement of alkali-activated slag-fly ash mortar. *Constr. Build. Mater.* **2023**, *373*, 130755. [CrossRef]
96. Ye, H. Creep mechanisms of calcium–silicate–hydrate: An overview of recent advances and challenges. *Int. J. Concr. Struct. Mater.* **2015**, *9*, 453–462. [CrossRef]
97. Ye, H.; Radlińska, A. Shrinkage mechanisms of alkali-activated slag. *Cem. Concr. Res.* **2016**, *88*, 126–135. [CrossRef]
98. Maruyama, I.; Nishioka, Y.; Igarashi, G.; Matsui, K. Microstructural and bulk property changes in hardened cement paste during the first drying process. *Cem. Concr. Res.* **2014**, *58*, 20–34. [CrossRef]
99. Kovler, K.; Zhutovsky, S. Overview and future trends of shrinkage research. *Mater. Struct.* **2006**, *39*, 827–847. [CrossRef]
100. Ma, X.; Zheng, Y.; Xu, L.; Cai, J.; Zhang, Z.; Pan, J. Enhancing post-fire performance of CFST columns using novel solid waste-based coating: Experiments, Simulation and Design. *J. Build. Eng.* **2025**, *115*, 114548. [CrossRef]
101. Verma, J.; Aliasghari, S.; Ameli, N.; Irungu, B.M.; Aleem, E.; Gaur, G.; Shishkin, A.; Matthews, A.; Goel, S. Towards Net-Zero Architecture: Functional Coatings from Fly Ash Waste for Energy-Efficient and Hygienic Building Surfaces. *J. Build. Eng.* **2025**, *116*, 114461. [CrossRef]
102. Fayed, E.K.; El-Khayatt, A.M.; El-Hosiny, F.I.; Ghareb, M.; Abd El-Gawad, W.M.; Sabik, A.; Al-Jabri, K.; Abdel-Gawwad, H.A. Alkali-activated concrete waste powder-based coating: Preparation, performance, and electrochemical resistance. *Dev. Built Environ.* **2025**, *23*, 100714. [CrossRef]
103. Li, L.; Joseph, P.; Zhang, X.; Zhang, L. A study of some relevant properties of concrete incorporating waste ceramic powder as a cement replacement agent. *J. Build. Eng.* **2024**, *87*, 109106. [CrossRef]
104. Raini, I.; Mesrar, L.; Touache, A.; Raini, I.; Jabrane, R. Performance evaluation of cement mortar containing construction and demolition waste as supplementary cement materials. *Ceram. Silik* **2022**, *66*, 407–418. [CrossRef]
105. Ma, Z.; Liu, X.; Hu, R.; Ba, G.; Wang, C. Using recycled aggregate and powder from high-strength mortar waste for durable cement-based materials: Microstructure and chloride transport. *J. Clean. Prod.* **2023**, *417*, 137998. [CrossRef]
106. Zhao, G.Y. Basic Properties of Recycled Concrete Micronized Powder and Its Activation Technology. Master's Thesis, China University of Mining and Technology, Beijing, China, 2014.
107. Zhao, L.; Zhou, W.J.; Duan, P.X. Research on the Basic Properties and Application of Recycled Construction Waste Micronized Powder. Master's Thesis, Beijing University of Architecture, Beijing, China, 2019.

108. Wu, H.; Liang, C.; Wang, C.; Ma, Z. Properties of green mortar blended with waste concrete-brick powder at various components, replacement ratios and particle sizes. *Constr. Build. Mater.* **2022**, *342*, 128050. [CrossRef]
109. Ayaz Khan, M.N.; Liaqat, N.; Ahmed, I.; Basit, A.; Umar, M.; Khan, M.A. Effect of brick dust on strength and workability of concrete. *IOP Conf. Ser. Mater. Sci. Eng.* **2018**, *414*, 012005. [CrossRef]
110. O'farrell, M.; Wild, S.; Sabir, B.B. Pore size distribution and compressive strength of waste clay brick mortar. *Cem. Concr. Compos.* **2001**, *23*, 81–91. [CrossRef]
111. Wu, H.; Xiao, J.; Liang, C.; Ma, Z. Properties of cementitious materials with recycled aggregate and powder both from clay brick waste. *Buildings* **2021**, *11*, 119. [CrossRef]
112. Bian, Y.; Qiu, X.; Zhao, J.; Li, Z.; Ouyang, J. Influence of Recycled Concrete Fine Powder on Durability of Cement Mortar. *Fluid Dyn. Mater. Process.* **2024**, *20*, 45–58. [CrossRef]
113. Kryzhanovskyi, V.; Orlowsky, J.; Skocek, J.; Macias Barrientos, M. Utilization of Brick Powder in Blended Cement Compositions: Rheological, Mechanical, and Microstructural Properties. *Materials* **2025**, *18*, 5120. [CrossRef]
114. Tian, Q.; Qu, M.; Zhang, M.; Wu, J.; Cai, J. Research Progress on Activation Methods of Recycled Micro-powder from Waste Concrete. *Bull. Silic. Ind.* **2020**, *39*, 2476–2485.
115. Medina, G.; Del Bosque, I.F.S.; Frías, M.; De Rojas, M.S.; Medina, C. Mineralogical study of granite waste in a pozzolan/Ca (OH)2 system: Influence of the activation process. *Appl. Clay Sci.* **2017**, *135*, 362–371. [CrossRef]
116. Chen, L.; Wei, M.; Lei, N.; Li, H. Effect of chemical–thermal activation on the properties of recycled fine powder cementitious materials. *Case Stud. Constr. Mater.* **2024**, *20*, e02956. [CrossRef]
117. Lin, K.L.; Chen, B.Y.; Chiou, C.S.; Cheng, A. Waste brick's potential for use as a pozzolan in blended Portland cement. *Waste Manag. Res.* **2010**, *28*, 647–652. [CrossRef]
118. Rostami, V.; Shao, Y.; Boyd, A.J.; He, Z. Microstructure of cement paste subject to early carbonation curing. *Cem. Concr. Res.* **2012**, *42*, 186–193. [CrossRef]
119. Zhang, D.; Ghouleh, Z.; Shao, Y. Review on carbonation curing of cement-based materials. *J. CO_2 Util.* **2017**, *21*, 119–131. [CrossRef]
120. Mehdizadeh, H.; Ling, T.C. Hydration and strength of cement paste containing metastable vaterite derived from recycled concrete fines and CO_2. *Cem. Concr. Res.* **2025**, *194*, 107891. [CrossRef]
121. de Leeuw, N.H.; Parker, S.C. Surface structure and morphology of calcium carbonate polymorphs calcite, aragonite, and vaterite: An atomistic approach. *J. Phys. Chem. B* **1998**, *102*, 2914–2922. [CrossRef]
122. Rodriguez-Blanco, J.D.; Shaw, S.; Benning, L.G. The kinetics and mechanisms of amorphous calcium carbonate (ACC) crystallization to calcite, via vaterite. *Nanoscale* **2011**, *3*, 265–271. [CrossRef] [PubMed]
123. García-Díaz, A.; Delgado-Plana, P.; Bueno-Rodríguez, S.; Eliche-Quesada, D. Investigation of waste clay brick (chamotte) addition and activator modulus in the properties of alkaline activation cements based on construction and demolition waste. *J. Build. Eng.* **2024**, *84*, 108568. [CrossRef]
124. Che, J.; Yang, R.; Wang, J.; Liu, H.; Hu, Y.; Doh, S.I. Research on basic mechanical properties of different modulus alkaline excited ECC. *Phys. Chem. Earth Parts A/B/C* **2022**, *128*, 103233. [CrossRef]
125. Duxson, P.; Provis, J.L.; Lukey, G.C.; Mallicoat, S.W.; Kriven, W.M.; Van Deventer, J.S. Understanding the relationship between geopolymer composition, microstructure and mechanical properties. *Colloids Surf. A Physicochem. Eng. Asp.* **2005**, *269*, 47–58. [CrossRef]
126. Santhanam, M.; Cohen, M.D.; Olek, J. Effects of gypsum formation on the performance of cement mortars during external sulfate attack. *Cem. Concr. Res.* **2003**, *33*, 325–332. [CrossRef]
127. Chen, J.; Jiang, M. Long-term evolution of delayed ettringite and gypsum in Portland cement mortars under sulfate erosion. *Constr. Build. Mater.* **2009**, *23*, 812–816. [CrossRef]
128. Sotiriadis, K.; Mazur, A.S.; Tolstoy, P.M.; Mácová, P.; Viani, A. External magnesium sulfate attack on hydrated Portland-limestone cements: Effect of the concurrent presence of sodium chloride in the corrosive environment and metakaolin admixture in the binder. *Cem. Concr. Compos.* **2024**, *151*, 105614. [CrossRef]
129. Bernal, S.A.; Provis, J.L.; Walkley, B.; San Nicolas, R.; Gehman, J.D.; Brice, D.G.; Kilcullen, A.R.; Duxson, P.; Van Deventer, J.S. Gel nanostructure in alkali-activated binders based on slag and fly ash, and effects of accelerated carbonation. *Cem. Concr. Res.* **2013**, *53*, 127–144. [CrossRef]
130. Zhou, S.; Ma, C.; Long, G.; Xie, Y. A novel non-Portland cementitious material: Mechanical properties, durability and characterization. *Constr. Build. Mater.* **2020**, *238*, 117671. [CrossRef]
131. Aiken, T.A.; Kwasny, J.; Sha, W.; Soutsos, M.N. Effect of slag content and activator dosage on the resistance of fly ash geopolymer binders to sulfuric acid attack. *Cem. Concr. Res.* **2018**, *111*, 23–40. [CrossRef]
132. Mohamed, O.A.; Al Khattab, R. Fresh properties and sulfuric acid resistance of sustainable mortar using alkali-activated GGBS/fly ash binder. *Polymers* **2022**, *14*, 591. [CrossRef] [PubMed]

133. Zhang, W.; Yao, X.; Yang, T.; Zhang, Z. The degradation mechanisms of alkali-activated fly ash/slag blend cements exposed to sulphuric acid. *Constr. Build. Mater.* **2018**, *186*, 1177–1187. [CrossRef]
134. Wang, Y.; Cao, Y.; Zhang, Z.; Zhang, P.; Ma, Y.; Wang, A.; Wang, H. Intrinsic sulfuric acid resistance of C-(N)-ASH and NASH gels produced by alkali-activation of synthetic calcium aluminosilicate precursors. *Cem. Concr. Res.* **2023**, *165*, 107068. [CrossRef]
135. El Inaty, F.; Marchetti, M.; Quiertant, M.; Metalssi, O.O. Effect of curing on the coupled attack of sulfate and chloride ions on low-carbon cementitious materials including slag, fly ash, and metakaolin. *Constr. Build. Mater.* **2024**, *438*, 137307. [CrossRef]
136. Jia, R.; Wang, Q.; Luo, T. Mechanisms and differences between sodium and magnesium sulfate attacks on alkali-activated phosphorus slag. *Constr. Build. Mater.* **2023**, *403*, 133117. [CrossRef]
137. Lou, Y.; Kang, S.; Wu, W.; Wang, X.; Sun, H.; Chen, F.; Xu, M. Sulfate resistance of recycled powder-slag-based geopolymers under different erosive environments. *Constr. Build. Mater.* **2025**, *462*, 139950. [CrossRef]
138. Andersen, M.D.; Jakobsen, H.J.; Skibsted, J. Incorporation of aluminum in the calcium silicate hydrate (C-S-H) of hydrated Portland cements: A high-field 27Al and 29Si MAS NMR investigation. *Inorg. Chem.* **2003**, *42*, 2280–2287. [CrossRef]
139. Gong, K.; White, C.E. Nanoscale chemical degradation mechanisms of sulfate attack in alkali-activated slag. *J. Phys. Chem. C* **2018**, *122*, 5992–6004. [CrossRef]
140. Zhao, G.; Hu, Y.; Li, S.; Wang, Z.; Guo, M.; Han, F.; Wang, H. Degradation mechanisms of chloride contaminated cast-in-situ concrete partially exposed to magnesium-sulfate combined environment. *KSCE J. Civ. Eng.* **2023**, *27*, 618–629. [CrossRef]
141. Yang, J.; Ding, Q.; Zhang, G.; Hou, D.; Zhao, M.; Cao, J. Effect of sulfate attack on the composition and micro-mechanical properties of CASH gel in cement-slag paste: A combined study of nanoindentation and SEM-EDS. *Constr. Build. Mater.* **2022**, *345*, 128275. [CrossRef]
142. García-Lodeiro, I.; Palomo, A.; Fernández-Jiménez, A.; Macphee, D.E. Compatibility studies between NASH and CASH gels. Study in the ternary diagram Na_2O-CaO-Al_2O_3-SiO_2-H_2O. *Cem. Concr. Res.* **2011**, *41*, 923–931. [CrossRef]
143. Javed, U.; Shaikh, F.U.A.; Sarker, P.K. Corrosive effect of HCl and H2SO4 exposure on the strength and microstructure of lithium slag geopolymer mortars. *Constr. Build. Mater.* **2024**, *411*, 134588. [CrossRef]
144. Huo, R.; Li, S.; Ding, Y. Experimental study on physicochemical and mechanical properties of mortar subjected to acid corrosion. *Adv. Mater. Sci. Eng.* **2018**, *2018*, 3283907. [CrossRef]
145. Al-Amoudi, O.S.B.; Maslehuddin, M.; Abdul-Al, Y.A.B. Role of chloride ions on expansion and strength reduction in plain and blended cements in sulfate environments. *Constr. Build. Mater.* **1995**, *9*, 25–33. [CrossRef]
146. Xu, H.; Zhang, W.; Liu, S.; Jiang, P.; Liu, S.; Zhang, N. Study on the degradation mechanism of lithium slag-gypsum-based geopolymers in sulfuric acid, hydrochloric acid, and acetic acid environments. *Constr. Build. Mater.* **2025**, *494*, 143272. [CrossRef]
147. Mohapatra, A.K.; Pradhan, B. Evaluation of extent of corrosion degradation and deterioration mechanism of hybrid alkali-activated mortar subjected to sulfuric acid and hydrochloric acid solutions. *Constr. Build. Mater.* **2025**, *470*, 140506. [CrossRef]
148. Hu, Y. Study on the Acid Resistance of Alkali-Activated Cementitious Materials. Ph.D. Thesis, Xi'an University of Architecture and Technology, Xi'an, China, 2019.
149. Zheng, Y. Performance and Degradation Mechanism of Geopolymers Under Sulfate and Acid Environments. Ph.D. Thesis, Anhui University of Architecture, Hefei, China, 2020.
150. Lothenbach, B.; Nonat, A. Calcium silicate hydrates: Solid and liquid phase composition. *Cem. Concr. Res.* **2015**, *78*, 57–70. [CrossRef]
151. Provis, J.L.; Palomo, A.; Shi, C. Advances in understanding alkali-activated materials. *Cem. Concr. Res.* **2015**, *78*, 110–125. [CrossRef]
152. Fan, X.; Wang, Y.; Yu, Q.; Gao, X.; Ye, J.; Zhang, Y. Improving the chloride binding capacity of alkali activated slag by calcium and aluminum enriched minerals. *J. Build. Eng.* **2023**, *70*, 106384. [CrossRef]
153. Ye, H.; Huang, L.; Chen, Z. Influence of activator composition on the chloride binding capacity of alkali-activated slag. *Cem. Concr. Compos.* **2019**, *104*, 103368. [CrossRef]
154. Wang, A.; Zheng, Y.; Zhang, Z.; Liu, K.; Li, Y.; Shi, L.; Sun, D. The durability of alkali-activated materials in comparison with ordinary Portland cements and concretes: A review. *Engineering* **2020**, *6*, 695–706. [CrossRef]
155. García-Lodeiro, I.; Fernández-Jiménez, A.; Palomo, A.; Macphee, D.E. Effect of calcium additions on N-A-S-H cementitious gels. *J. Am. Ceram. Soc.* **2010**, *93*, 1934–1940. [CrossRef]
156. Matschei, T.; Lothenbach, B.; Glasser, F.P. The AFm phase in Portland cement. *Cem. Concr. Res.* **2007**, *37*, 118–130. [CrossRef]
157. Chen, Y.; Dolado, J.S.; Li, Z.; Yin, S.; Yu, Q.; Kostiuchenko, A.; Ye, G. A molecular dynamics study of N-A-S-H gel with various Si/Al ratios. *J. Am. Ceram. Soc.* **2022**, *105*, 6462–6474. [CrossRef]
158. Song, Z.; Jiang, L.; Chu, H.; Xiong, C.; Liu, R.; You, L. Modeling of chloride diffusion in concrete immersed in CaCl2 and NaCl solutions with account of multi-phase reactions and ionic interactions. *Constr. Build. Mater.* **2014**, *66*, 1–9. [CrossRef]
159. Wang, W.; Li, Q.; Xing, G.; Xu, S. Comparative study on the durability of ultra-high toughness cementitious composites and mortar under salt attacks. *J. Clean. Prod.* **2025**, *494*, 144844. [CrossRef]

160. Yang, G.; Na, B.; Jin, W.; Zhi, F.; Zhang, J.; Zhang, L.; Jiang, L. Effect of chloride salt types on corrosion resistance of reinforcing steel in cement mortar mixed with DNA primer inhibitor. *Cem. Concr. Compos.* **2024**, *148*, 105454. [CrossRef]
161. Liu, L.; Chen, X.; Pang, K.; Neupane, A.; Xie, L.; Shen, D. Degradation of alkali-activated slag pastes exposed to high-concentration chloride, sulfate and magnesium multi-salt solutions. *Constr. Build. Mater.* **2025**, *464*, 140182. [CrossRef]
162. Zheng, X.; Wang, Y.; Zhang, S.; Xu, F.; Zhu, X.; Jiang, X.; Zhou, L.; Shen, Y.; Chen, Q.; Yan, Z.; et al. Research progress of the thermophysical and mechanical properties of concrete subjected to freeze-thaw cycles. *Constr. Build. Mater.* **2022**, *330*, 127254. [CrossRef]
163. Liu, L.; Yuan, M.; Zheng, X.; Wu, J. One-Part Alkali-Activated Slag/Fly Ash for Soft Soil Stabilization: Freeze-Thaw Durability Assessment and Mechanism Elucidation. *Buildings* **2025**, *15*, 2386. [CrossRef]
164. Wu, S.; Liang, Y.; Zhang, S.; Sun, H.; Ji, T.; Li, J. Damage mechanics of CaO-Na2CO3-Slag cement mortar under freeze-thaw in water and sulfate solution. *J. Build. Eng.* **2025**, *111*, 113621. [CrossRef]
165. Wang, X.; Li, F.; Gao, F.; Wang, Y.; Li, M.; Wang, J.; Guo, X.; Nikolayevich, K.A.; Nikolaevich, L.S. Characteristics of alkali-activated slag mortar under combined freeze-thaw cycles and sulfate exposure: Microstructural and mechanical insights. *Constr. Build. Mater.* **2025**, *493*, 143087. [CrossRef]
166. Hlobil, M.; Kumpová, I.; Hlobilová, A. Surface area and size distribution of cement particles in hydrating paste as indicators for the conceptualization of a cement paste representative volume element. *Cem. Concr. Compos.* **2022**, *134*, 104798. [CrossRef]
167. Zhang, S.; Fan, Y.; Li, N. Pore structure and freezing resistance of nanoclay modified cement based materials. *Mater. Res. Innov.* **2014**, *18*, S2-358–S2-362. [CrossRef]
168. Jiao, Z.; Li, X.; Yu, Q. Effect of curing conditions on freeze-thaw resistance of geopolymer mortars containing various calcium resources. *Constr. Build. Mater.* **2021**, *313*, 125507. [CrossRef]
169. Jordán, M.M.; Rincón López, J.M.; Almendro-Candel, M.B.; Navarro-Pedreño, J. Technological and environmental behaviour of traditional ceramic bodies obtained by recycling of two types of residues. *Coatings* **2022**, *12*, 221. [CrossRef]
170. Li, B.; Xu, F.; Ding, Y.; Zheng, F.; Zou, J. Integrated Utilization Strategies for Red Mud: Iron Extraction, Sintered Brick Production, and Non-Calcined Cementitious Binder Development for Environmental Sustainability. *Coatings* **2025**, *15*, 522. [CrossRef]

Disclaimer/Publisher's Note: The statements, opinions and data contained in all publications are solely those of the individual author(s) and contributor(s) and not of MDPI and/or the editor(s). MDPI and/or the editor(s) disclaim responsibility for any injury to people or property resulting from any ideas, methods, instructions or products referred to in the content.

coatings

MDPI

Article

Sustainable Biomass Functional Monomer-Modified Polycarboxylate Superplasticizers Enable the Creation of High-Performance Cement Pastes

Yu Yan [1,2], Qifei Du [2], Wanyue Diao [1,3], Chao Wang [1,3], Liyan Wang [2], Sa Lv [1,3], Lingwei Kong [2], Liping Zhang [4], Yuanzhang Xi [5] and Huan Wang [1,3,*]

[1] Key Laboratory for Comprehensive Energy Saving of Cold Regions Architecture, Ministry of Education, Jilin Jianzhu University, Changchun 130118, China; 15042068204@163.com (Y.Y.); diaowy@jlju.edu.cn (W.D.); wangchao@jlju.edu.cn (C.W.); lvsa82@163.com (S.L.)
[2] Department of Materials Science, Jilin Jianzhu University, Changchun 130118, China; 15908060514@163.com (Q.D.); wly@jlju.edu.cn (L.W.); kong-lingwei@126.com (L.K.)
[3] Jilin Provincial Key Laboratory of Architectural Electricity & Comprehensive Energy Saving, Jilin Jianzhu University, Changchun 130118, China
[4] Baotou Steel North-West Pioneer Construction Co., Ltd., Baotou 014010, China; 13847226050@163.com
[5] Institute of Civil Engineering, Jilin Province Economic Management Cardre College, Changchun 130012, China; xyzhero9999@163.com
* Correspondence: wanghuan@jlju.edu.cn; Tel.: +86-0431-84566327

Abstract

In this work, a complex and eco-friendly biomass raffinose monomer-modified polycarboxylate superplasticizer (RAF-PCE) was designed and synthesized via the free radical polymerization technique to simultaneously improve paste fluidity and delay fluidity loss in concrete applications. The adsorption, fluidity, and early hydration behaviors of cementitious systems after the introduction of RAF-PCE have been systematically investigated. Experimental results demonstrate that the hydroxy group in raffinose promotes the adsorption of RAF-PCE on the cement particles, thereby elevating the dispersion characteristic of cement paste through electrostatic repulsion, enabling excellent initial fluidity (310 mm). Additionally, its steric hindrance effect has also been identified to play a role in improving paste fluidity and reducing the slump loss of cement slurry. Detailed analyses unveil that RAF-PCE can reduce the concentration of free Ca^{2+} in the pore solution through complexation with Ca^{2+}, which prevents the early precipitation of hydration products and realizes a delayed effect on cement hydration, ultimately evolving into a homogeneous and compact microstructure for superior compressive tensile strength of the cement mortar. The 28-day compressive strength of cement incorporating RAF-PCE reached 79.2 MPa, representing a 5.5% enhancement over conventional PCE systems. Our work provides novel insights into the promotion of innovative and green development in the concrete industry by utilizing renewable biomass resources for high-performance materials.

Keywords: polycarboxylate superplasticizer; raffinose; paste fluidity; biomass; hydration

1. Introduction

Polycarboxylate superplasticizer (PCE) has been regarded as the most extensively utilized admixture for cement and concrete owing to its benefits of high water reduction rate, strong molecular structure design, good adaptability, and environmental friendliness compared to traditional superplasticizers [1]. PCE contains negatively charged (-COO^-)

groups in its backbone, enabling easy adsorption onto the positively charged cement particle surface. Additionally, its polyethylene glycol (PEG) side chains inhibit cement particle aggregation via steric hindrance [2], thereby significantly enhancing the superplasticizer's dispersion capacity and water reduction efficiency and the rheological properties of cement slurry [3]. However, super-high-rise pumping and long-term transportation of PCE result in an excessive slump loss in concrete, thereby significantly diminishing the workability of the concrete in real construction engineering [4–6].

Recently, tremendous efforts have been made to scrutinize functional monomers for PCE structural design in attempts to address the slump loss of concrete cement [7]. For example, Yang et al. (2024) introduced trimethylolpropane triacrylate as a trifunctional crosslinking agent into PCE to achieve excellent initial fluidity and workability of mortar [8]. Zhang et al. (2026) proposed a controlled-release PCE with high slump retention by introducing unsaturated ester; this design significantly enhances the slow-release slump retention performance of concrete slurry [9]. Despite these successful attempts, excessive addition of PCE containing slow-release components prolongs the setting time [10]. This leads to severe retardation and significantly reduces concrete quality. Furthermore, when employing compound PCE, the time and temperature conditions of use are also pivotal [11] and therefore create a complex fabrication process and high cost, which further reduces the practical applicability of the utilization of PCE [12–15]. Hence, a rational design of PCE through the straightforward synthetic method to enhance slump retention while simultaneously controlling the setting time and retardation effect is still in high demand in the cement industry [16,17]. Therefore, designing a PCE that can enhance slump retention without excessively delaying setting remains a key challenge.

To better clarify the correlation between the molecular structure and performance of polycarboxylate superplasticizers (PCE), Table 1 summarizes the characteristic groups, water-reducing rate, retarding effect, and compressive strength data of traditional PCEs, with the biomass raffinose modified PCE (RAF-PCE) developed in this paper introduced as a comparison. The data show that polyester/polyether-type PCEs achieve dispersion through carboxyl (-COO^-) groups and long polyester/polyether side chains, with water-reducing rates of 25%–35% and 25%–40%, respectively. However, their retarding effect is relatively weak, and polyester-type PCEs have limited later strength development [18,19]. This is because ester bonds undergo alkaline hydrolysis to release carboxyl groups, enhancing initial dispersion but resulting in poor long-term stability. Meanwhile, polyether side chains form a thick hydration layer on cement particle surfaces, effectively preventing particle aggregation. Although ether bonds are stable, they tend to desorb at high temperatures, leading to reduced slump retention. In contrast, amide/imide-type PCEs have advantages in retarding performance and later strength. This is because amide groups (-CONH-) can form coordinate bonds with Ca^{2+} on cement surfaces, leading to stronger adsorption. However, they have obvious drawbacks: the multi-step synthesis process results in higher costs [20]. Zwitterionic PCEs carry both positive and negative charges, forming an 'ion pair' adsorption layer on cement particle surfaces, which enhances adsorption capacity. However, strong electrostatic interactions make molecular structure regulation complex, resulting in only moderate retarding effects. They also face issues of high cost and complex synthesis processes [21,22]. These limitations highlight the bottlenecks of traditional PCEs in the synergistic optimization of dispersibility, retarding performance, and strength development.

Table 1. Types and key performance characteristics of polycarboxylate superplasticizers.

Classification	Characteristic Functional Groups	Water Reduction Rate	Retardation Effect	Compressive Strength
Polyester-type	Carboxylate (-COO^-), Ester bond (-COO^-) The backbone incorporates both anionic (carboxylate) and cationic monomer units.	25%–35%	Relatively weak or slightly promotes coagulation	Significant enhancement of early-age strength
Polyether-type	Carboxylate (-COO^-), Ether bond (-C-O-C-), Poly(ethylene oxide) (PEO) side chains Amide/imide groups on the backbone or side chains allow precise control over side-chain density and length.	25%–40%	Neutral or extremely slight delay in coagulation	Significant strength enhancement at all stages with balanced development
Amide/Imide-type	Amide (-CONH-) or Imide (-CO-N-CO-) backbone (e.g., polyacrylate) grafted with polyether long side chains.	20%–30%	Significant delay in coagulation	Stable and continuous strength growth in later stages
Zwitterionic-type	Carboxylate (-COO^-), Cationic group Backbone (e.g., polymaleic anhydride) grafted with polyester long side chains.	20%–30%	A significant effect in delaying coagulation	Steady strength enhancement at all stages
Our work	Carboxyl group (-COO^-), ether bond (-C-O-C-), sugar ring hydroxyl group (-OH)	25%–31%	A significant effect in delaying coagulation: the initial setting time extended by 2.92 h and the final setting time extended by 4.95 h	3-day average compressive strength 51.9 MPa; 7-day average compressive strength 67.2 MPa; 28-day average compressive strength 79.2 MPa

In order to break through this bottleneck, this study focuses on natural biomass materials with renewable and environmentally friendly properties, selecting them as sustainable functional monomers to modify the molecular structure of PCE for the preparation of high-performance concrete [23]. Raffinose, a functional trisaccharide originating from natural plants, is mainly composed of galactose, fructose, and glucose, which possess an abundance of hydroxyl groups [24–27]. Leveraging these properties, the RAF-PCE we prepared achieves a balanced performance: it prolongs final setting time by 4.95 h while delivering compressive strengths of 51.9 MPa (3 days), 67.2 MPa (7 days), and 79.2 MPa (28 days). Herein, we clearly state that our work is the first to incorporate raffinose trisaccharide as a functional monomer in PCE synthesis, creating a unique molecular architecture with multiple hydroxyl groups that provide balanced dispersion and retardation properties without compromising early strength development. This specific innovation distinguishes our work from previous studies. Further detailed investigations and in-depth analysis were employed to elucidate the influence of raffinose-incorporated PCE on cement hydration behavior. It is expected that the current work will contribute to the theoretical foundation

for innovative structural design and further boost the development of PCE with superior performance.

2. Experimental Section

2.1. Materials

The cement used in this study is P.O 42.5 cement as stipulated in GB/T 8076-2008 [28], with A specific surface area of $\geq$300 m^2/kg. The particle size distribution is residue on an 80 μm sieve $\leq$5%, and the mineral composition distribution is $C_3A \leq 8\%$, $SO_3 \leq 3.5\%$. It was purchased from Changchun Yatai Cement Co., Ltd. (Changchun, China). Isopentenol polyoxyethylene ether (TPEG) with a molecular weight (Mw) of 2400 was provided by Shandong Yousuo Chemical Technology Co., Ltd. (Qingdao, China). Acrylic acid (AA, 99%) and hydrogen peroxide (HP) were purchased from Xilong Scientific Co., Ltd. (Guangdong, China). Ascorbic acid (VC, 98%), 3-mercaptopropionic (MPA, 98%), and sodium hydroxide (NaOH, 99%) were bought from Shanghai Macklin Biochemical Technology Co., Ltd. (Shanghai, China). Triethylamine (TEA, 98%) and N,N-Dimethylformamide (DMF, 99%) were obtained from Tianjin Xinbote Chemical Co., Ltd. (Tianjin, China). Acryloyl chloride (AC, 99%) was purchased from Shanghai Aladdin Biochemical Technology Co., Ltd. (Shanghai, China).

2.2. Synthesis Process

Figure 1 illustrates the synthesis strategies of two polymers and the preparation and transformation process of the key intermediate RA through clear experimental setup diagrams and reaction processes. Part a shows the synthesis process of conventional PCE. It depicts the entire process where TPEG in a 25 °C aqueous solution reacts with HP, AA, VC, and TEA in a three-necked flask for 2 h, and finally PCE is obtained by adjusting the pH to 7 with NaOH. Part b illustrates the preparation of the RA intermediate. It shows that raffinose (RA) intermediate is obtained by dissolving raffinose and TEA in DMF, then adding the AC solution dropwise under ice bath conditions, followed by reaction, filtration, vacuum distillation, ether precipitation, and drying. Part c depicts that TPEG undergoes copolymerization at 50 °C in a three-necked flask with HP, solution C containing RA, and solution D containing VC/MPA, and finally the RAF-PCE product is obtained by adjusting the pH to 7 with 40% NaOH.

2.2.1. Synthesis of PCE

Then, 20 g TPEG was dissolved in deionized water in a three-neck flask under vigorous stirring at 25 °C, followed by adding a few drops of HP. Then, AA, VC, and TEA were slowly added to the above mixture. The obtained solution was further kept at 25 °C for 2 h with stirring. Finally, the pH of the solution was adjusted to 7 with NaOH (40 wt%) to obtain PCE for further use.

2.2.2. Synthesis of RA

Raffinose (7.6 g) and TEA (3.0 g) were dissolved in DMF (200 mL) at ambient temperature to obtain solution A. Subsequently, AC (4.6 g) in 100 mL DMF was slowly added to solution A within 3 h with an ice water bath under vigorous stirring, followed by further reacting for 6 h at 25 °C. Then, filtration and vacuum distillation were applied to the obtained mixture to remove TEA and DMF. After that, the purified product was added to 150 mL of ice-cooled ethyl ether under vigorous stirring in a dropwise manner. Finally, the obtained yellow viscous liquid was rinsed with ether several times and then dried in a vacuum oven. The dried intermediate was sealed and stored for further use. The schematic diagram of the reaction process is shown in Figure 2.

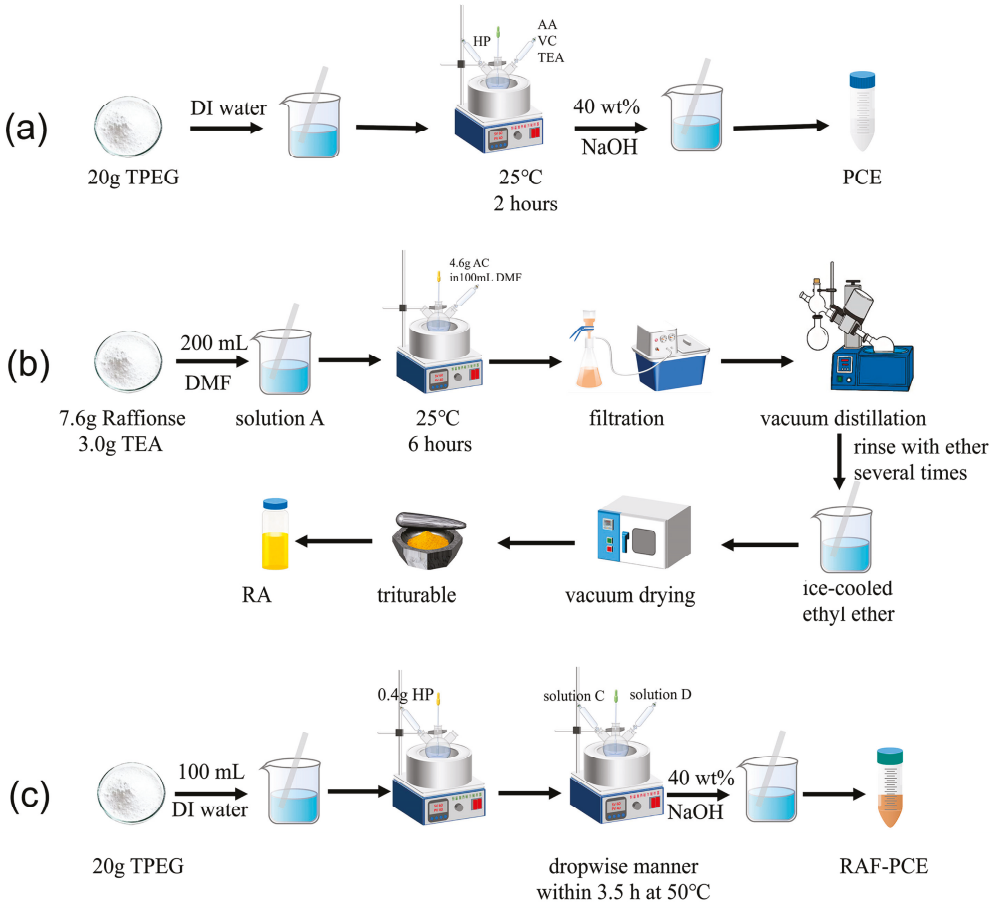

Figure 1. Schematic diagram of the synthesis of (**a**) PCE, (**b**) RA, (**c**) RAF-PCE.

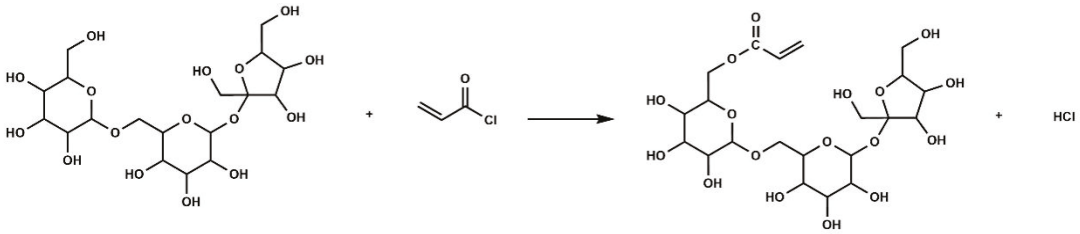

Figure 2. Schematic diagram of the reaction process for RA.

2.2.3. Synthesis of RAF-PCE

Then, 20 g TPEG was added to a three-neck flask (250 mL) with 100 mL deionized water (DI). Vigorous stirring and heating were applied to dissolve TPEG; at this point, HP (0.4 g) was slowly added within 5 min. Subsequently, solution C (2.4 g AA and 0.5 g RA in 10 mL DI water) and solution D (0.4 g VC and 0.06 g MPA in 10 mL DI water) were simultaneously added in a dropwise manner within 3.5 h at 50 °C. After cooling down to room temperature, the PH was adjusted to 7 with NaOH (40 wt%) to obtain the modified PCE with 40% raffinose. The relevant synthesis reaction was shown in Figure 3 [29].

2.3. Testing and Characterization

2.3.1. FTIR

FTIR was characterized using a Nicolet 67 (Thermo Nicolet, Madison, WI, USA) spectrometer. The water reducer after dialysis was mixed with KBr and then pressed into

flakes. Spectra were recorded over a spectral range from 400 to 4000 cm^{-1} at a resolution of 4 cm^{-1} using 32 scans.

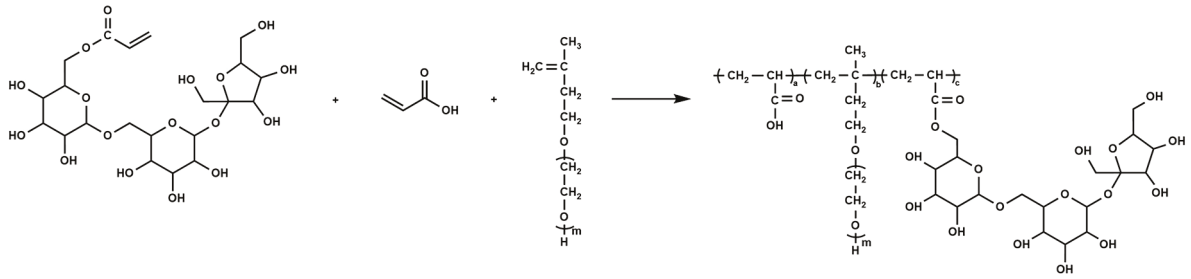

Figure 3. Schematic diagram of the reaction process modified RAF-PCE.

2.3.2. Fluidity Test

The fluidity of the cement slurries was determined in accordance with the GB/T 8077-2023 [30] Concrete Admixture Homogeneity Test Method. The pastes containing 0.16% PCE were prepared by mixing cement with water (w/c ratio of 0.29). The w/c = 0.29 strictly complies with the standard requirements of GB/T 8077-2023, which can effectively distinguish the dispersing performance of different water-reducing agents, ensuring the comparability and authority of the test results. Both the deionized water and the ambient environment were maintained at a temperature of 20 ± 2 °C throughout the testing. The fluidity of cement paste was tested at 0, 30, 60, 90, and 120 min, respectively. Three parallel measurements according to GB/T 8077-2023.

2.3.3. Water Reduction Rate Test

The water reduction ratios of PCE in mortar were tested according to the national standard GB/T 8077-2023 method. All measurements were performed in triplicate.

2.3.4. Gel Permeation Chromatography

The molecular weight of hyperbranched PCE was measured using a GPC apparatus (LC-20AD, Shimadzu, Kyoto, Japan).

2.3.5. Adsorption Capacity Test

The adsorption capacity of the water reducer was measured by the depletion method using a total organic carbon (TOC) analyzer (Multi N/C3100, Analytik Jena, Jena, Germany). The amount of PCE adsorbed on the cement was calculated based on the difference between the total amount of PCE in the initial solution and the residual amount in the interstitial solution of cement pastes. All measurements were performed in triplicate.

2.3.6. Zeta-Potential Measurement

Zeta-potential measurements were realized by micro-electrophoresis using Zeta Probe Analyzer TM zeta-potential analyzer (Colloidal Dynamics, Pawtucket, RI, USA).

2.3.7. Hydration Heat Measurement

A TAM AIR-08 multi-channel isothermal calorimeter (Waters Corporation, New Castle, DE, USA) was used to investigate the hydration heat of cement with PCE. The test was conducted under controlled environmental conditions of (20 ± 1) °C and a relative humidity of not less than 90%. Then, 1 g of cement, deionized water (w/c = 0.4), and PCE were mixed and poured into a specific container under stirring. The heat release curve of cement hydration was calculated by a computer.

2.3.8. Flexural Strength and Compressive Strength

The mechanical properties of cement mortar were tested in accordance with the GB/T 17671-2021 [31] standard method using 40 × 40 × 160 mm prismatic mortar specimens, with each group containing 3 specimens. The strengths of cement mortar at 3 days, 7 days, and 28 days are measured.

2.3.9. X-Ray Diffraction Analysis

XRD was performed on the D/Max IIIA XRD instrument (Rigaku Corporation, Tokyo, Japan) equipped with Cu Kα-radiation at a speed of 10°/min and a step of 0.02° in the range from 10 to 70°.

2.3.10. SEM Test

The samples were characterized by scanning electron microscopy (JSM-7610F, Beijing, China).

3. Results and Discussion

3.1. FTIR Analysis

To verify the successful chemical grafting of raffinose onto the polycarboxylate superplasticizer backbone, FTIR spectroscopy was used to characterize the functional groups of monomer a (raffinose), intermediate b (raffinose acrylate), and modified water-reducing agent c (RAF-PCE). As shown in Figure 4, the peaks at 3352, 2916, and 1047 cm^{-1} could be assigned to the stretching vibration peak of -OH, C-H, and C-O-C in the raffinose monomer, respectively. The characteristic C=O stretching vibration peak of ester carbonyl at 1723 cm^{-1} and the C=C stretching vibration peak of 1655 cm^{-1} were also detected in intermediate b, indicating that polymerizable double bonds were successfully introduced into the raffinose structure via an esterification reaction. For RAF-PCE, the peaks at 3435, 2877, 1724, and 1104 cm^{-1} could be assigned to the stretching of -OH, C-H, C=O, and C-O-C, respectively, representing the combined functional groups from both the polymer backbone and the raffinose side chains. Notably, the 1724 cm^{-1} peak originates from the ester groups introduced during intermediate b synthesis; the other peaks reflect the complete RAF-PCE molecular structure. More importantly, the disappearance of characteristic peaks of C=C at 1655 cm^{-1} indicates that RAF-PCE was successfully synthesized and the monomers were completely consumed during polymerization.

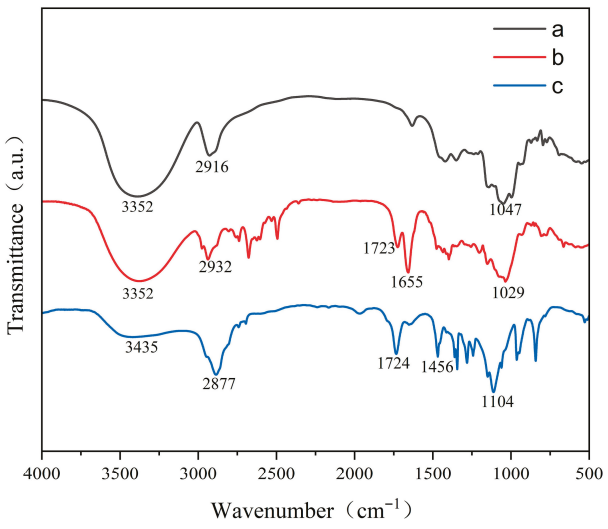

Figure 4. FTIR spectroscopy of monomer (a), intermediate (b), RAF-PCE (c).

3.2. Fluidity of Cement Paste

The raffinose acrylate dosage, reaction temperature, reaction time, and initiator dosage were investigated to optimize the synthetic conditions and determine the most significant factors. As indicated in Figure 5, the maximum flowability of cement slurry can reach 305 mm, and the flowability loss of cement slurry is relatively low, almost unchanged within one hour, and slightly decreased after one hour under the conditions of the molar ratio of monomer AA:TPEG:RA at 1:4:0.1; MPA at 0.5%, rection time at 4 h, and reaction temperature 50 °C.

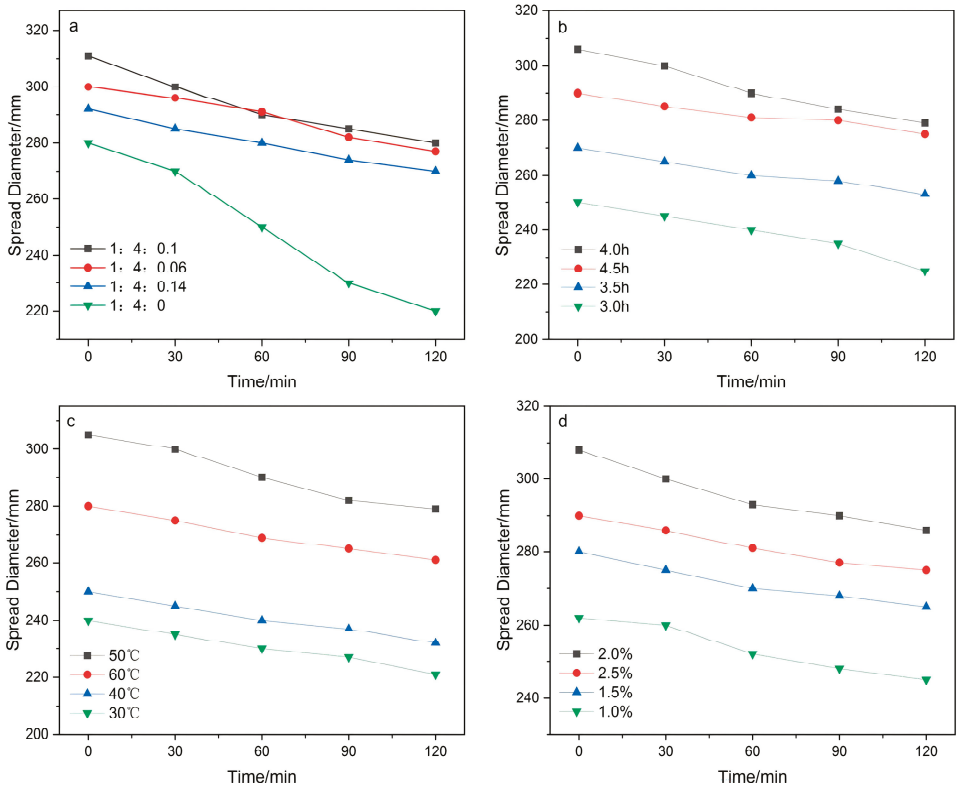

Figure 5. The influence of different conditions on the fluidity of cement paste ((**a**) the amount of raffinose acrylate; (**b**) reaction time; (**c**) reaction temperature; (**d**) amount of initiator).

The fluidity of the PCE grafted with acrylic raffinose ester is significantly improved due to the introduction of hydroxyl groups by the raffinose molecule, which makes the surface of cement particles tend to adsorb water molecules through hydrogen bonds and van der Waals forces. This could effectively hinder the aggregation between cement particles and slowly release water locked in the flocculated structure. Hence, the dispersion and slump retention performance of cement paste was improved. In addition, the steric hindrance effect of raffinose molecules significantly prevents cement particles from aggregating, thus contributing to significant improvements in fluidity. Meanwhile, raffinose will be gradually hydrolyzed and provide more carboxylic anion groups, which will produce obvious electrostatic repulsion between cement grains, thus improving the dispersity of cement and preventing slump loss. Benefiting from the continuous hydrolysis process, the retention performance of cement could also be enhanced.

The molecular weight of the polymer superplasticizer molecules can be readily controlled by adjusting the initiator dosage. With the increase in initiator dosage, the molecular weight of RAF-PCE is gradually decreased (Table 2), which probably originates from the high initial concentration-induced acceleration of the polymerization reaction rate and

generation of more polymerized fragments. Control experiments unveil that the water reduction rate of RAF-PCE 3 (31%) is obviously higher than that of the superplasticizer.

Table 2. Molecular weight, water reduction rate, and flowability of cement slurry with a dosage of 0.3% for RAF modified PCE prepared with different initiator dosages.

Type	Dosage of Initiator	Molecular Weight (g/mol)	Initial Fluidity (mm)	Water Reduction Ration (%)
RAF-PCE 1	1.0%	34,122	250	25%
RAF-PCE 2	1.5%	32,135	270	27%
RAF-PCE 3	2.0%	28,063	310	31%
RAF-PCE 4	2.5%	25,054	300	30%
RAF-PCE 5	3.0%	24,976	280	28%

3.3. Adsorption Capacity

The adsorption capacity of polycarboxylate superplasticizers on cement particles directly determines their dispersion performance, as higher adsorption typically leads to stronger electrostatic repulsion and steric hindrance, thereby improving cement paste fluidity. The adsorption capacity of PCE of cement particles was explored by the TOC analyzer. As exhibited in Figure 6, the adsorbed amounts of PCE and RAF-PCE increase linearly as a function of water-reducing agent dosage at the initial stage. This is due to the deposition of hydration products on the surface of the cement particle, which decreases the number of water reducer molecules in solution. As the water-reducing agent dosage exceeds 0.6 mg/g, the adsorption amount of PCE and RAF-PCE tends to be stable. It is noted that the adsorption capacity of the RAF-PCE is higher than that of the PCE. This was attributed to the stronger adsorption of hydroxyl groups in the RAF-PCE for cement grains.

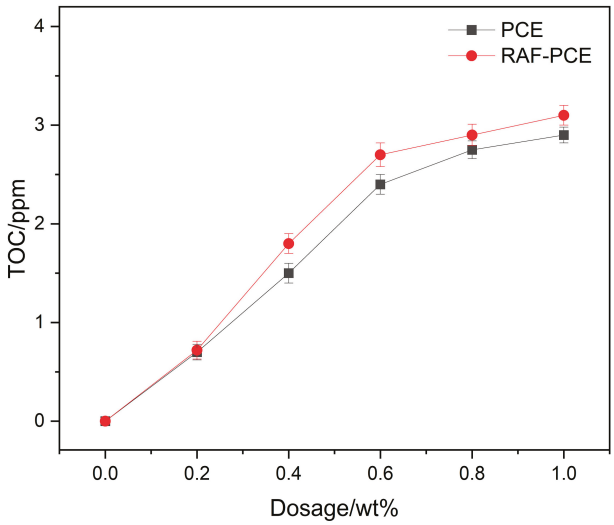

Figure 6. The adsorption capacity of PCE and RAF-PCE.

3.4. Zeta-Potential Test

The zeta-potential of cement particles in the presence of polycarboxylate superplasticizers reflects their surface charge status; a more negative zeta-potential indicates stronger electrostatic repulsion between particles, helping prevent aggregation and improve dispersion. To study the influence of RAF-PCE on cementitious systems, the zeta-potential of cement paste with various water reducer dosages was measured. Here, the surface charge property of the cement particle is highly dependent on the anionic groups of the

modified water reducer. As indicated in Figure 7, the zeta-potential decreases with the increase in RAF-PCE content when the dosages of superplasticizer are less than 0.2%. This was caused by the adsorption of negative ionization groups on the surface of the cement particle. Once the relevant dosages exceed 0.2%, the surface of cement particles is saturated by superplasticizer; hence, the relevant zeta-potential reaches the plateau region (~8.5 mV), implying the superior adsorption ability of superplasticizer and excellent flowability of cement slurry [32,33].

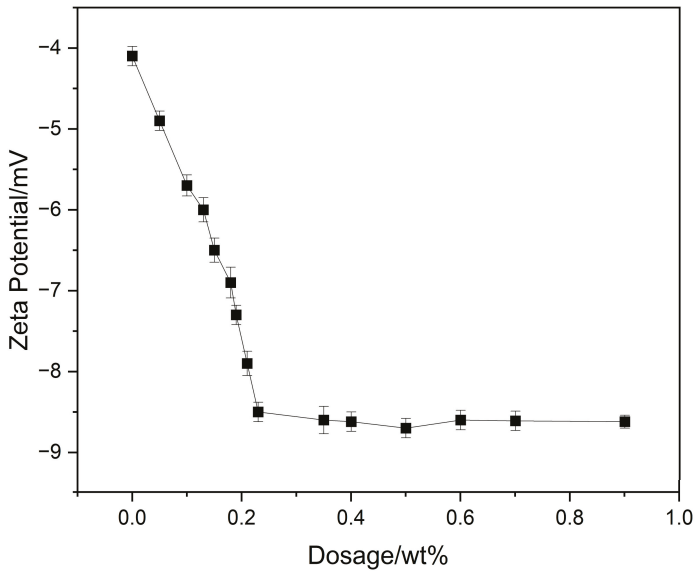

Figure 7. The zeta-potential of supernatant under different dosages.

3.5. Hydration Heat Test

Hydration heat is a critical indicator of cement hydration kinetics which directly reflects the timing of hydration exothermic peaks (induction period, acceleration period), the intensity of heat release, and the total heat generated, all of which are closely linked to cement setting time, early strength development, and potential thermal cracking in mass concrete. To systematically investigate the effect of water reducer on the hydration process, the heat flow and heat release were evaluated using a multi-channel isothermal calorimeter. Compared with the blank sample, the hydration exothermic peak of cement pastes with RAF-PCE and PCE reflects different degrees of delay (Figure 8a), indicating that the addition of superplasticizer can prolong the hydration of cement. Interestingly, the hydration heat of cement pastes containing RAF-PCE exhibits a lower and wider peak than that of PCE. The above results are probably attributed to the increase in adhesion of polymer molecules and the dense hydrates generated on the surface of the cement particles, which effectively impede the dissolution rate and delay cement hydration. In addition, the anion functional group of the water reducer could complex with Ca^{2+} in the cement, and therefore suppresses the nucleation and growth of the hydration mineral [34–36], which prolongs the induction period of the cement hydration. Figure 8b is the hydration heat release curve. As indicated, the cement pastes with RAF-PCE exhibit the smallest hydration heat release, which is consistent with the law of hydration heat flow.

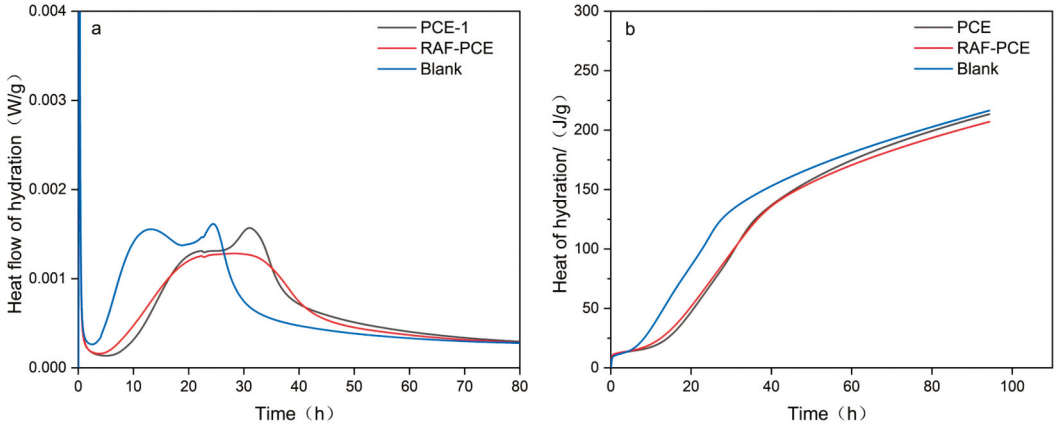

Figure 8. Heat flow and heat release of cement hydration. (**a**) Hydration heat release rate curve, (**b**) hydration heat release curve.

3.6. Setting Time

Next, the influence of the RAF-PCE on the setting time of cement paste was studied. The initial and final setting times of the cement paste are defined as the times at the initial solidification and subsequent hardening, respectively [29,37]. As shown in Table 3, the initial and final setting times of cement pastes with RAF-PCE are longer than those of PCE and the blank sample, signifying that RAF-PCE displays a superior retarding effect compared to the others. This result stems from that the hydrophilic hydroxyl and carboxyl groups in the modified superplasticizer can not only adsorb on the surface of cement grains and combine with hydration products via hydrogen bond [38,39], but also interact with the Ca^{2+} in the cement system to form various calcium chelates, reducing hydration reaction rate of cement slurry, thus delaying the setting time [40].

Table 3. The setting time of cement pastes with blank, PCE, and RAF-PCE.

	Initial		Final		
	Initial Time (h)	**Change in Initial Setting Time (h)**	**Final Times (h)**	**Change in Final Setting Time (h)**	**Interval Time (h)**
Blank	2.91 ± 0.12	0	5.03 ± 0.18	0	2.12 ± 0.09
PCE	4.15 ± 0.15	+1.24	7.20 ± 0.21	+2.17	3.05 ± 0.12
RAF-PCE	5.83 ± 0.21	+2.92	9.98 ± 0.32	+4.95	4.15 ± 0.15

3.7. Strength of Cement Mortar

It is worth mentioning that according to the national standard GB/T 8077-2023 Test Methods for Homogeneity of Concrete Admixtures, the maximum allowable initial setting extension for retarding superplasticizers is ≤3 h. Our RAF-PCE extends the initial setting time by 2.92 h (from 2.91 h to 5.83 h), which strictly complies with this standard. This retardation effect is particularly suitable for high-rise concrete pumping and long-distance transportation (2–3 h), as it maintains workability without delaying construction schedules. Importantly, early strength development remains uncompromised (3 d compressive strength: 51.9 MPa, accounting for 65.5% of 28 d strength), fully meeting the requirements of precast component production and on-site construction.

The mechanical property of hardened mortar is a crucial reference index for assessing the modified PCE [41]. The flexural strength and compressive strength results of cement mortar with different PCE samples at 3, 7, and 28 days are presented in Table 4. As shown, for all the samples, the mortar strength increased with increasing curing time. Clearly, the

compressive strength of cement mortar containing RAF-PCE is higher than that of PCE and the blank sample at different curing times, which is beneficial for prefabricated components requiring strength development. We attribute this result to the excellent dispersion and retention properties of RAF-PCE, which promote the hydration degree and crystal structure formation in the cement system. This will result in the compact structure of cement mortar and therefore ultimately improve the strength of hardened slurry. Regarding flexural strength, the cement mortar with RAF-PCE displays superior flexural strength compared to other samples. This could be ascribed to the dense structure of cement mortar with RAF-PCE, hence resulting in the reduction in cracks and delay of the crack development, which effectively restrains concrete damage and enhances the flexural strength of the hardened mortar.

Table 4. Flexural strength and compressive strength results.

Samples	Flexural Strength/MPa			Compressive Strength/MPa		
	3 d	**7 d**	**28 d**	**3 d**	**7 d**	**28 d**
Blank	5.5 ± 0.3	6.7 ± 0.2	8.2 ± 0.4	37.1 ± 1.5	49.4 ± 1.8	65.6 ± 2.1
PCE	6.7 ± 0.2	8.4 ± 0.3	9.7 ± 0.3	50.5 ± 1.6	60.1 ± 1.7	75.1 ± 2.0
RAF-PCE	6.9 ± 0.3	8.9 ± 0.2	10.3 ± 0.4	51.9 ± 1.2	67.2 ± 1.5	79.2 ± 1.8

3.8. XRD

The evolution of hydration cement mineral phases with different superplasticizers was determined by XRD. As exhibited in Figure 9, the mineral chemical composition of minerals in the hardened slurry was mainly composed of calcium hydroxide (CH), C-S-H gel, ettringite (AFt), and unhydrated cement phase, including tricalcium silicate (C_3S), dicalcium silicate (C_2S), tricalcium aluminate (C_3A), and tetracalcium ferroaluminate (C_4AF). Apparently, no new peak could be observed in the cement slurry with PCE and RAF-PCE, suggesting that the addition of superplasticizers would not change the crystal structure of cement hydration products. From the above diagram, it can be seen that the C_3S and other minerals in cement were gradually consumed with the continued hydration process, while the hydration products of CH and the amorphous phase are gradually increased. Compared with the blank sample, the diffraction peak intensities of AFt and CH in cement paste with PCE and RAF-PCE are lower than those of the blank group before 1 d, while the contents of unhydrated minerals such as C_3S and C_2S are significantly higher than those in the blank group. The results indicate induction period in the cement hydration process would be extended through the introduction of a water reducer, which weakens the cement hydration degree in the initial stage. It is proposed that such a phenomenon could be ascribed to the adsorption of PCE onto the surface of cement grain and the chelation of carboxylate and hydroxy groups with Ca^{2+}, which is well consistent with the results of hydration heat. Additionally, as the hydration time increases to 7 d, the RAF-PCE exhibits the higher intensity peak of CH and a weaker intensity peak of unhydrated minerals such as C_3S and C_2S than other samples. This indicates that the modified water-reducing agent has minimal influence on the subsequent stage of cement hydration. The incorporation of RAF-PCE improves the dispersion capacity of cement particles and the degree of hydration, which is beneficial for adequate hydration of cement at a later stage.

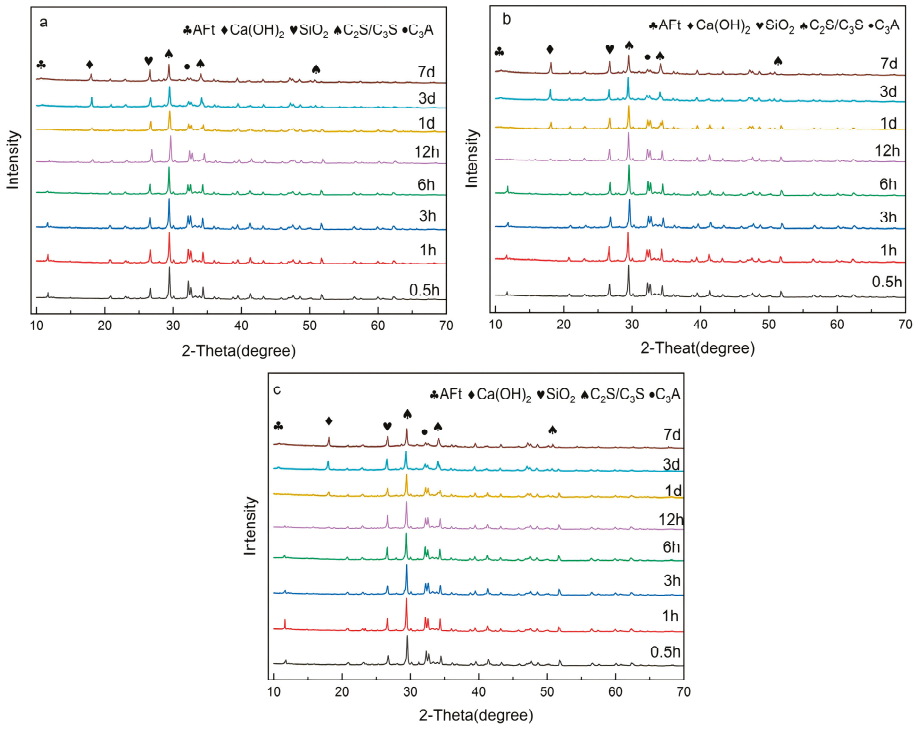

Figure 9. The XRD patterns of cement paste with blank (**a**), PCE (**b**), and RAF-PCE (**c**), respectively.

3.9. SEM

The microstructure evolution of the hardened cement-based material during the hydration process was observed by SEM measurements. As shown Figure 10, in the initial hydration stage of 12 h and 1 d (Figure 10a–f), the blank sample (Figure 10a,d) presents numerous acicular ettringite (AFt) crystals and flocculent C-S-H gel, while no apparent hydration products appear for the sample with PCE (Figure 10b,e) and RAF-PCE (Figure 10c,f), verifying the obvious inhibitory effect of water reducer in the induction period of cement hydration. By increasing hydration time to 3 d, the surface of hardened cement particles containing RAF-PCE (Figure 10i) is surrounded by a large number of C-S-H and AFt crystals. After 7 d of hydration, the AFt and C-S-H gel in the blank sample (Figure 10j) evolves into chaotic clusters and forms a loose structure with plenty of holes and cracks. Furthermore, although the relatively dense structure can be observed after the introduction of PCE, holes and cracks in the sample still existed. Interestingly, after the introduction of RAF-PCE, the hydration products become closely overlapped with each other and connect with the plate structures to form a homogeneous and compact microstructure, which facilitates the development of cement paste strength [42,43].

3.10. Environmental and Sustainability Assessment

(1) Raffinose is extracted from agricultural by-products (such as beet molasses and cottonseed), which reduces reliance on fossil-derived monomers, promotes high-value utilization of waste resources, and reflects the sustainability of raw materials.

(2) The synthesis process of RAF-PCE is green and environmentally friendly. Esterification and free radical polymerization reactions are carried out at low temperatures ($\leq$50 °C) without toxic catalysts. Compared with traditional PCE chemical modification methods, energy consumption can be effectively reduced.

(3) Cement is the cornerstone of buildings and public infrastructure, and its manufacturing process is characterized by energy-intensive and high carbon dioxide (CO_2) emissions, estimated to account for 7.5% of global emissions [44]. The RAF-PCE in

this paper has a high water reduction rate (31%), which can greatly reduce the amount of cement used while ensuring strength. In other words, the use of polycarboxylate superplasticizer with high water reduction rate can indirectly reduce In other words, using polycarboxylate superplasticizers with high water-reducing efficiency can indirectly reduce carbon dioxide emissions by reducing cement consumption, thereby helping to achieve the global "dual carbon" goals.

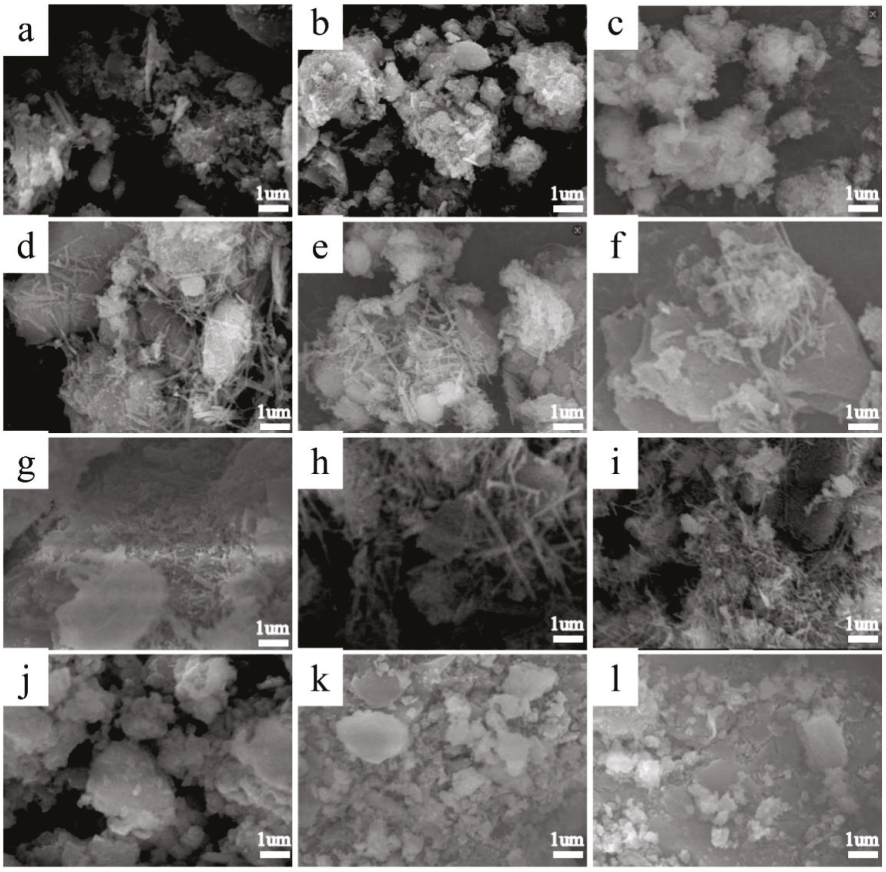

Figure 10. SEM images of the hardened cement with blank (**a**,**d**,**g**,**j**), PCE (**b**,**e**,**h**,**k**), and RAF-PCE (**c**,**f**,**i**,**l**) after 12 h, 1 d, 3 d, and 7 d.

4. Conclusions

Based on the results and discussions above, the conclusions can be drawn as follows:

(1) A novel biomass-based polycarboxylate superplasticizer (RAF-PCE) was successfully synthesized by incorporating a raffinose-derived monomer. RAF-PCE exhibits superior dispersing ability and significantly improves the fluidity retention of cement paste compared to conventional PCE, effectively addressing the issue of rapid slump loss.

(2) RAF-PCE effectively delays cement hydration, as evidenced by calorimetry and setting time measurements. This retarding effect is attributed to the combined action of the strong adsorption of its hydroxyl groups onto cement particles and the complexation of its functional groups with Ca^{2+} ions in the pore solution, which inhibits the nucleation and growth of early hydration products.

(3) The incorporation of RAF-PCE promotes the formation of a more homogeneous and compact microstructure in hardened cement paste, with reduced porosity and fewer cracks. This microstructural refinement directly translates to enhanced mechanical properties, resulting in higher compressive and flexural strength at all curing ages. The 28-day compressive strength reaches 79.2 MPa.

(4) This research presents a feasible and eco-friendly strategy for developing high-performance superplasticizers by utilizing renewable biomass resources. RAF-PCE not only delivers excellent comprehensive performance but also paves the way for the green and sustainable development of the concrete industry.

Author Contributions: Writing—original draft, Y.Y., Q.D., and W.D.; writing—review and editing, L.W., S.L., L.K., and L.Z.; supervision, Y.X., L.W., C.W., and H.W. All authors have read and agreed to the published version of the manuscript.

Funding: This research was funded by the science and technology development project of Jilin province, China (No. 20230508059RC), and the financial support from the Key Laboratory for Comprehensive Energy Saving of Cold Regions Architecture of the Ministry of Education.

Institutional Review Board Statement: Not applicable.

Informed Consent Statement: Not applicable.

Data Availability Statement: The data presented in this study are available upon request from the corresponding author.

Acknowledgments: The authors gratefully acknowledge the technical support provided by Baotou Steel North-West Pioneer Construction Co., Ltd.

Conflicts of Interest: Author Liping Zhang was employed by the company Baotou Steel North-West Pioneer Construction Co., Ltd. The remaining authors declare that the research was conducted in the absence of any commercial or financial relationships that could be construed as a potential conflict of interest.

Abbreviations

The following abbreviations are used in this manuscript:

PCE	polycarboxylate superplasticizer
RAF-PCE	raffinose monomer modified polycarboxylate superplasticizer
PEG	polyethylene glycol
TPEG	isopentenol polyoxyethylene ether
Mw	molecular weight
AA	acrylic acid
HP	hydrogen peroxide
VC	ascorbic acid
MPA	3-mercaptopropionic
NaOH	sodium hydroxide
TEA	triethylamine
DMF	N,N-Dimethylformamide
RA	synthesis of raffinose acrylate
AC	acryloyl chloride
DI	deionized
FTIR	Fourier transform infrared spectroscopy
TOC	total organic carbon
GPC	gel permeation chromatography
XRD	X-ray diffraction
SEM	scanning electron microscope
CH	calcium hydroxide
AFt	ettringite
C_3S	tricalcium silicate
C_2S	dicalcium silicate
C_3A	tricalcium aluminate
C_4AF	tetracalcium ferroaluminate

References

1. Huang, H.; Qian, C.; Zhao, F.; Qu, J.; Guo, J.; Danzinger, M. Improvement on microstructure of concrete by polycarboxylate superplasticizer (PCE) and its influence on durability of concrete. *Constr. Build. Mater.* **2016**, *110*, 293–299. [CrossRef]
2. Tutal, A.; Partschefeld, S.; Schneider, J.; Osburg, A. Effects of bio-based plasticizers, made from starch, on the properties of fresh and hardened metakaolin-geopolymer mortar: Basic investigations. *Clays Clay Miner.* **2020**, *68*, 413–427. [CrossRef]
3. Li, X.; Peng, Z.; Feng, Q.; Zheng, Y.; Zhang, X.; Zhang, H.; Long, Y.; Zhang, Y.; Zhou, J. Preparation of Zwitterionic Polycarboxylate Dispersant and its Influence on Rheological Properties and Dispersion Mechanism of Oil Well Cement. *Silicon* **2025**, *17*, 3355–3374. [CrossRef]
4. Hwang, C.-L.; Lee, L.-S. Future Research Trends in High-performance Concrete: Cost-effective Considerations. *Transp. Res. Rec.* **1997**, *1574*, 49–55. [CrossRef]
5. Kulkarni, V.R. High performance concrete for high-rise buildings: Some crucial issues. *Int. J. Res. Eng. Technol.* **2016**, *5*, 26–33. [CrossRef]
6. Feng, P.; Zhang, G.; Zhang, W.; Cui, H.; Xin, T. Comparison of ester-based slow-release polycarboxylate superplasticizers with their polycarboxylate counterparts. *Colloids Surf. A* **2022**, *633*, 127878. [CrossRef]
7. Plank, J.; Sakai, E.; Miao, C.; Yu, C.; Hong, J. Chemical admixtures—Chemistry, applications and their impact on concrete microstructure and durability. *Cem. Concr. Res.* **2015**, *78*, 81–99. [CrossRef]
8. Yang, Y.; Tan, Y.; Li, Z.; Zhou, G.; Yu, X.; Xu, D.; Yong, Q.; Zhao, H.; Xie, Z. Interaction mechanisms between polycarboxylate superplasticizers and cement, and the influence of functional groups on superplasticizer performance: A review. *Polym. Bull.* **2024**, *81*, 10415–10438. [CrossRef]
9. Zhang, Y.; Feng, P.; Chan, H.K.; Han, Z.; Liu, B.; Lei, L. Design of a Novel Starch-Modified MPEG PCE for Enhanced Slump Retention in Alkali-Activated Slag Binder. *Cem. Concr. Compos.* **2026**, *165*, 106358. [CrossRef]
10. Sun, Y.; Yu, R.; Shui, Z.; Wang, X.; Qian, D.; Rao, B.; Huang, J.; He, Y. Understanding the porous aggregates carrier effect on reducing autogenous shrinkage of Ultra-High Performance Concrete (UHPC) based on response surface method. *Constr. Build. Mater.* **2019**, *222*, 130–141. [CrossRef]
11. Zhang, M.; Gao, W.; Zhang, F.; Mi, Y.; Wang, W.; An, Q.; Wang, J.; Ma, X.; Miao, J.; Hu, Z. Efficient ternary non-fullerene polymer solar cells with PCE of 11.92% and FF of 76.5%. *Energy Environ. Sci.* **2018**, *11*, 841–849. [CrossRef]
12. Yang, D.; Yang, R.; Priya, S.; Liu, S. Recent advances in flexible perovskite solar cells: Fabrication and applications. *Angew. Chem. Int. Ed.* **2019**, *58*, 4466–4483. [CrossRef] [PubMed]
13. Yun, S.; Qin, Y.; Uhl, A.R.; Vlachopoulos, N.; Yin, M.; Li, D.; Han, X.; Hagfeldt, A. New-generation integrated devices based on dye-sensitized and perovskite solar cells. *Energy Environ. Sci.* **2018**, *11*, 476–526. [CrossRef]
14. Li, Z.; Klein, T.R.; Kim, D.H.; Yang, M.; Berry, J.J.; Van Hest, M.F.; Zhu, K. Scalable fabrication of perovskite solar cells. *Nat. Rev. Mater.* **2018**, *3*, 18017. [CrossRef]
15. Huang, F.; Li, M.; Siffalovic, P.; Cao, G.; Tian, J. From scalable solution fabrication of perovskite films towards commercialization of solar cells. *Energy Environ. Sci.* **2019**, *12*, 518–549. [CrossRef]
16. Zhang, L.; Miao, X.; Kong, X.; Zhou, S. Retardation effect of PCE superplasticizers with different architectures and their impacts on early strength of cement mortar. *Cem. Concr. Compos.* **2019**, *104*, 103369. [CrossRef]
17. Gao, Y.; Liu, Y.; Wang, G.; Liu, J.; Cao, Z.; Yong, Q.; Zhao, H. Interaction Between Polycarboxylate Superplasticizer and Clay in Cement and Its Sensitivity Inhibition Mechanism: A Review. *Materials.* **2025**, *18*, 2662. [CrossRef]
18. Arzu, S. Organizational commitment turnover intentions and the influence of cultural values. *J. Occup. Organ. Psychol.* **2010**, *76*, 303–321.
19. Tian, H.; Kong, X.; Su, T.; Wang, D. Comparative study of two PCE superplasticizers with varied charge density in Portland cement and sulfoaluminate cement systems. *Cem. Concr. Res.* **2019**, *115*, 43–58. [CrossRef]
20. Allcock, H.; Morozowich, R. Bioerodible polyphospha zenes and their medical potential. *Polym. Chem.* **2012**, *3*, 57–58. [CrossRef]
21. Maki, H.; Tsujito, M.; Yamada, T. Intrinsic 31P NMR Chemical Shifts and the Basicities of Phosphate Groups in a Short-Chain Imino Polyphosphate. *J. Solut. Chem.* **2013**, *42*, 27–43. [CrossRef]
22. Miao, C.; Ran, Q.; Liu, J.; Mao, Y.; Shang, Y.; Sha, J. New generation amphoteric comb-like copolymer superplasticizer and its properties. *Polym. Polym. Compos.* **2011**, *19*, 1–8. [CrossRef]
23. Chen, M.; Ma, J.; Feng, Y.; Yuan, Q.; Wu, Y.; Liu, Y.; Hu, G.; Liu, X. Advancing aqueous zinc-ion batteries with carbon dots: A comprehensive review. *EcoEnergy* **2025**, *3*, 254–295. [CrossRef]
24. Vandamme, E.; Soetaert, W. Biotechnical modification of carbohydrates. *FEMS Microbiol. Rev.* **1995**, *16*, 163–186. [CrossRef]
25. Webster, C.D.; Lim, C. Introduction to fish nutrition. In *Nutrient Requirements and Feeding of Finfish for Aquaculture*; CABI Publishing: Wallingford, UK, 2002; pp. 1–27.
26. Rodén, L. Biosynthesis of acidic glycosaminoglycans (mucopolysaccharides). *Metab. Conjug. Metab. Hydrolys.* **1970**, *2*, 345–442.
27. Wigglesworth, V. Digestion and nutrition. In *The Principles of Insect Physiology*; Springer: Berlin/Heidelberg, Germany, 1972; pp. 476–552.

28. *GB/T 8076-2008*; Concrete Admixtures. Standardization Administration of PRC: Beijing, China, 2008.
29. Benzaazoua, M.; Fall, M.; Belem, T. A contribution to understanding the hardening process of cemented pastefill. *Miner. Eng.* **2004**, *17*, 141–152. [CrossRef]
30. *GB/T 8077-2023*; Methods for Testing Uniformity of Concrete Admixtures. State Administration for Market Regulation, China National Standardization Administration: Beijing, China, 2023.
31. *GB/T 17671-2021*; Test Method of Cement Mortar Strength (ISO Method). Standardization Administration of the People's Republic of China: Beijing, China, 2021.
32. Plank, J.; Hirsch, C. Impact of zeta potential of early cement hydration phases on superplasticizer adsorption. *Cem. Concr. Res.* **2007**, *37*, 537–542. [CrossRef]
33. Zhang, Q.; Shu, X.; Yang, Y.; Wang, X.; Liu, J.; Ran, Q. Preferential adsorption of superplasticizer on cement/silica fume and its effect on rheological properties of UHPC. *Constr. Build. Mater.* **2022**, *359*, 129519. [CrossRef]
34. John, E.; Lothenbach, B. Cement hydration mechanisms through time—A review. *J. Mater. Sci.* **2023**, *58*, 9805–9833. [CrossRef]
35. Cheung, J.; Jeknavorian, A.; Roberts, L.; Silva, D. Impact of admixtures on the hydration kinetics of Portland cement. *Cem. Concr. Res.* **2011**, *41*, 1289–1309. [CrossRef]
36. Beaudoin, J.; Odler, I. Hydration, setting and hardening. In *Lea's Chemistry of Cement and Concrete*; Elsevier: Amsterdam, The Netherlands, 2019; p. 157.
37. Glasser, F. Fundamental aspects of cement solidification and stabilisation. *J. Hazard. Mater.* **1997**, *52*, 151–170. [CrossRef]
38. Sha, S.; Wang, M.; Shi, C.; Xiao, Y. Influence of the structures of polycarboxylate superplasticizer on its performance in cement-based materials-A review. *Constr. Build. Mater.* **2020**, *233*, 117257. [CrossRef]
39. Zhao, L.; Guo, X.; Liu, Y.; Ge, C.; Guo, L.; Shu, X.; Liu, J. Synergistic effects of silica nanoparticles/polycarboxylate superplasticizer modified graphene oxide on mechanical behavior and hydration process of cement composites. *RSC Adv.* **2017**, *7*, 16688–16702. [CrossRef]
40. Zhang, C.; Jin, J.; Xu, W.; Yang, J.; Li, M. Synthesis and characterization of SSS/MA/NVCL copolymer as high temperature oil well cement retarder. *J. Dispers. Sci. Technol.* **2022**, *43*, 1405–1415. [CrossRef]
41. Abdel–Aty, Y.Y.; Mahmoud, H.S.; Al-Zahrani, A.A. Experimental evaluation of consolidation techniques of fossiliferous limestone in masonry walls of heritage buildings at historic Jeddah, Kingdom of Saudi Arabia. *Adv. Res. Conserv. Sci.* **2020**, *1*, 16–33. [CrossRef]
42. Wu, Z.; Deng, Y.; Liu, S.; Liu, Q.; Chen, Y.; Zha, F. Strength and micro-structure evolution of compacted soils modified by admixtures of cement and metakaolin. *Appl. Clay Sci.* **2016**, *127*, 44–51. [CrossRef]
43. Balonis, M.; Glasser, F.P. The density of cement phases. *Cem. Concr. Res.* **2009**, *39*, 733–739. [CrossRef]
44. Liu, Z.; Lu, R.; Ma, Y.; Hu, Y.; Zhang, X.; Wang, Y.; Li, W. Carbon emission reduction in cement production catalyzed by steel solid waste. *Natl. Sci. Rev.* **2025**, *12*, nwaf109. [CrossRef]

Disclaimer/Publisher's Note: The statements, opinions and data contained in all publications are solely those of the individual author(s) and contributor(s) and not of MDPI and/or the editor(s). MDPI and/or the editor(s) disclaim responsibility for any injury to people or property resulting from any ideas, methods, instructions or products referred to in the content.

coatings

MDPI

Article

Influence of Cellulose Ether on Properties of Premixed Mortar Based on Orthogonal Test Method

Yun Lin [1], Qin Hu [2,*], Shuzeng Shen [3], Mo Zhou [4], Jintuan Zhang [2], Siqing Zhang [3], Guimeng Ban [2] and Zne-Jung Lee [5]

[1] School of Intelligent Construction, Fuzhou University of International Studies and Trade, Fuzhou 350202, China
[2] College of Architecture and Electrical Engineering, Hezhou University, Hezhou 542899, China; zhangjt@hzxy.edu.cn (J.Z.); 15907886612@163.com (G.B.)
[3] School of Architecture and Design Art, Shaoxing Vocational & Technical College, Shaoxing 312000, China
[4] College of Architectural Engineering, Tianjin University, Tianjin 300072, China
[5] Department of Electronic and Information Engineering, School of Advanced Manufacturing, Fuzhou University, Quanzhou 362200, China; johnlee@fzu.edu.cn
* Correspondence: huqin051@hzxy.edu.cn

Abstract

To promote energy efficiency, emission reduction, and green low-carbon development, this study investigates the influence of cellulose ether (CE) content and its interactions with supplementary materials, including stone powder (SP), manufactured sand (MS), polyvinyl alcohol (PVA), and bentonite (BT), on the performance of premixed mortar using an L16(4^5) orthogonal experimental design. The effects of five factors at four levels were analyzed, focusing on mortar workability and compressive strength. Results showed that CE content significantly affected consistency, water retention, and compressive strength ($p < 0.01$). A 60% increase in CE led to a 4.7% reduction in flowability, a 2.05% improvement in water retention, and an 18.49% decrease in compressive strength. Response surface methodology identified optimal compositions for each property. The CE-BT interaction influenced consistency ($R^2 = 0.6894$), while CE-PVA interactions affected water retention ($R^2 = 0.9336$). A ternary model for compressive strength (CE-SP-MS) showed that SP and MS replacements had significant negative effects, with optimal SP replacement at 10%. PVA at 0.04% effectively inhibited plastic shrinkage cracking. The study provides predictive models for mortar performance, aiding in the optimization of premixed mortar formulations.

Keywords: cellulose ether; mechanical properties; orthogonal experiment; premixed mortar

1. Introduction

Premixed mortar, as a pivotal material in modern construction industrialization, has emerged as the predominant trend in building mortar development due to its consistent quality, enhanced construction efficiency, and environmental benefits. However, compared to traditional site-mixed mortar, premixed mortar is required to possess superior workability, stability, and durability to meet the demands of mechanical application and long-term service life. To achieve these performance characteristics, various mineral admixtures and chemical additives are widely employed. Among them, cellulose ether (CE) serves as a crucial water-retaining agent, playing a vital role in determining the comprehensive properties of mortar [1–4].

Cellulose ether, a water-soluble polymer obtained by etherifying cellulose, significantly enhances the water retention of mortar. This property prevents premature water

evaporation or absorption by the substrate, ensuring the proper hydration of the cement and supporting the normal development of mortar strength [5]. Moreover, cellulose ether improves the lubrication, viscosity, anti-slump, and overall workability of the mortar. However, studies have shown that while increasing cellulose ether content significantly affects the workability and mechanical properties of mortar, excessive amounts may lead to a decrease in compressive strength and wet density [6,7]. This balance between performance enhancements needs to be carefully considered in formulation design.

Similarly to cellulose ether, stone powder, a byproduct of manufactured sand production, can effectively improve the pore structure of mortar through its micro filling effect and pozzolanic activity, enhancing both the compactness and crack resistance of the mortar [8,9]. The addition of stone powder not only helps reduce environmental pollution but also partially replaces cement, improving the physical properties of mortar. Additionally, manufactured sand, as an alternative to natural river sand, plays a positive role in improving the mechanical properties of mortar, especially its compressive strength, due to its unique particle shape and grading characteristics [10].

Furthermore, Polyvinyl Alcohol (PVA) and bentonite are commonly used admixtures that further enhance mortar performance by reducing plastic shrinkage cracking, improving toughness and crack resistance, and improving water retention and thickening properties [11–13]. When combined with cellulose ether, these materials create a synergistic effect, improving the workability of the mortar while enhancing its crack resistance and durability [14,15].

Although existing research provides insights into the individual effects of these materials, most studies focus on single-factor influences and fail to comprehensively address the interactions among multiple components. In practical applications, premixed mortars typically contain various admixtures and additives, where complex synergistic effects exist. Consequently, findings from single-factor studies often lack direct applicability for guiding industrial production [16–20].

The orthogonal experimental design is an efficient method for investigating multi-factor and multi-level systems. By selecting a representative set of test points, it significantly reduces the number of required experiments while yielding reliable conclusions. For instance, Wang et al. [21] used an L16(4^3) orthogonal array and showed that tartaric acid (TA) exerted the strongest adverse effect on the flowability of self-leveling mortars, whereas polycarboxylate ether (PCE) and cellulose ether (CE) increased flowability. Brachaczek et al. [22] applied a Taguchi L8 orthogonal design to evaluate the influence of an air-entraining agent (AEA), cement, polymer additives, cellulose ether and perlite on the air content and porosity of repair mortars, and concluded that AEA dominated air content, while perlite and polymer additives mainly governed porosity, with cement and cellulose ether playing secondary roles. Likewise, Qingxuan Li et al., Junran Liu et al., and Chengbin Yuan et al. similarly utilized a three-factor, three-level orthogonal array design [L9(3^3)] to examine the key factors and their significance levels for different modified mortars [23–25]. In contrast to these studies, the present work integrates L16(4^3) orthogonal experimental design with response surface methodology (RSM) and employs repeated tests and residual analysis to validate the predictive models. This approach enables a systematic quantification of the main and interactive effects of CE dosage and other key variables (stone powder-to-cement replacement ratio, manufactured-sand-to-river-sand replacement ratio, PVA dosage and bentonite dosage) on the properties of premixed mortars, thereby providing a scientific basis for formula optimization.

2. Experimental Program

2.1. Raw Materials

Ordinary Portland cement (P·O 42.5), conforming to the Chinese standard GB 175-2007, was used as the primary cementitious material. Its technical properties are summarized in Table 1. Natural river sand and manufactured sand served as fine aggregates. The river sand, with a fineness modulus of 2.4, was classified as medium sand in Zone II. The manufactured sand, produced by crushing limestone and tuff, had a fineness modulus of 2.7. Key properties of both sands, tested according to GB/T 14684-2022, are presented in Table 2.

Table 1. Technical specifications of P·O 42.5 ordinary Portland cement.

Density/ g/cm^3	Standard Consistency Water Content/%	Fineness/ %	Specific Surface Area/ m^2/kg	Stability	Compressive Strength/MPa		Flexural Strength/MPa		Condensation Time/min	
					3 d	28 d	3 d	28 d	Initial Setting	Final Setting
3.10	25	4.1	450	Qualified	28.9	51.2	5.5	8.2	165	290

Table 2. Test results of the main properties of manufactured sand and river sand.

Type of Sand	Loose Bulk Density/kg/m^3	Apparent Density/kg/m^3	Fineness Modulus
Manufactured Sand	1560	2580	2.7
River Sand	1505	2600	2.4

Stone powder, a by-product collected during the production of manufactured sand, was utilized after drying and sieving. Its primary characteristics, evaluated against the specifications of GB/T 35164-2017 and JGJ/T 318-2014, are listed in Table 3. Fineness refers to the particle size distribution of stone powder, typically expressed as a percentage of material passing through a sieve of a specific aperture. The determination of fineness is conducted through sieve analysis utilizing a standard sieve. The methylene blue value serves as an overall indicator to ascertain the presence of expansive clay minerals (such as clay powder) within the stone powder and to quantify their content. This is achieved by progressively adding methylene blue solution to a suspension created by mixing aggregates with water, observing for the emergence of a light blue halo indicating free methylene blue, which reflects the adsorption characteristics of the aggregate towards the dye solution. The activity index indicates the content of reactive components within the stone powder that can participate in the hydration reaction of cement, thereby influencing the performance of the pre-mixed mortar. The activity index is determined through chemical analysis. Hydroxypropyl methyl cellulose ether (HPMC), complying with the JC/T 2190-2013 standard and with a viscosity of 40,000 MPa·s, was employed as the cellulose ether. Polyvinyl alcohol (PVA) fibers had a tensile strength $\geq$ 1200 MPa, a length of 6 mm, and a diameter of 18–25 μm. Sodium bentonite, with a montmorillonite content $\geq$ 85% and a swelling capacity $\geq$ 15 mL/g, was also used.

Table 3. Results of stone powder performance tests.

Type of Stone Powder	Active Index/%		Fineness	Mobility Ratio/%	Calcium Carbonate Content/%	Methylene Blue Value
	7 d	28 d				
Tuff Powder	52.3	53.4	13.5	92	60.20	0.92
Limestone Powder	60.9	63.3	13.8	96	80.29	0.96

2.2. Apparatus

The main instruments and equipment utilized in the experiments include the JJ-5 planetary cement mortar mixer (compliant with JC/T 681-2022 standards), the NYL-300 compression testing machine, the KZJ-500 electric flexural testing machine, and a standard curing chamber (maintaining a temperature of 20 ± 2 °C and a relative humidity of over 95%), provided by Zhejiang Huannan Instrument Equipment Co., Ltd., established on 25 March 2005, is located in Qianshang Village, Daoxu Subdistrict, Shangyu District, Shaoxing, Zhejiang Province, China. Additionally, the mortar consistency meter SC-145, the mortar setting time tester ZKS-100, and the drying shrinkage measurement device JG/170 were supplied by Shaoxing Jiaoche Instrument Equipment Co., Ltd., established on 7 June 2016, is located in No. 10, Tunbei Wujiazhuang, Xintunnan Village, Daoxu Subdistrict, Shangyu District, Shaoxing, Zhejiang Province, China. The water retention measurement device 100 × 25 was provided by Shaoxing QianNeng Instrument Equipment Co., Ltd., established on 29 September 2012, is located in No. 69, Zhongxing Road, Daoxu Subdistrict, Shangyu District, Shaoxing, Zhejiang Province, China. Furthermore, the microcomputer-controlled electronic universal testing machine (used for tensile bond strength testing) DN-W50KN was sourced from Shandong Jinan KJ Instrument Equipment Co., Ltd., established on 30 September 2019, is located in Room 301, Unit 3, Building 6, Meili Xincju Second District, Huaiyin District, Jinan, Shandong Province, China. and the rapid freeze–thaw testing machine TDR-9 was provided by Shanghai Luda Experimental Instrument Co., Ltd., established on 25 April 2000, is located in No. 32, Xinxin Road, Shedun Town, Songjiang District, Shanghai, China.

2.3. Experimental Design

Based on the 'Specification for the Design of Mortar Mix Proportions' (JGJ/T 98-2010) and referring to the theoretical mix proportions outlined in the 'Specification for the Design of Premixed Mortar Proportions' (DBJ33/T1314-2024), preliminary tests were conducted to validate the applicability of different materials and additives at varying levels in the premixed mortar. An orthogonal array testing design was adopted, specifically an L16 (4^5) layout involving five factors at four levels each [21,22]. The five factors considered were: cellulose ether content (CE), stone powder replacement ratio for cement (SP), manufactured sand replacement ratio for river sand (MS), PVA content (PVA), and bentonite content (BT). The levels for each factor, defined as the percentage by mass of the respective material, are detailed in Table 4. The contents of PVA, bentonite, stone powder, and CE are expressed as a percentage of the total cementitious material mass. The manufactured sand content is given as a percentage of the total fine aggregate mass. The total mass of stone powder and cement was fixed at 150 g, the total mass of river sand and manufactured sand was fixed at 850 g, and the water content was fixed at 165 g. The experimental matrix was constructed based on the principles of orthogonal design [26].

Table 4. Factor level table.

Level	Factor				
	CE/%	SP/%	MS/%	PVA/%	BT/%
1	0.0125	10	20	0.035	0.9
2	0.015	20	30	0.04	1.0
3	0.0175	30	40	0.045	1.1
4	0.02	40	50	0.05	1.2

Following the technical standards for application of premixed mortar, the key fresh properties assessed for masonry and plastering mortars were consistency (Note: Mea-

sured as the penetration depth of a standard cone; a greater depth indicates higher fluidity/consistency) and water retention. The primary hardened property evaluated was the 28-day compressive strength. Accordingly, the orthogonal experiments were designed to measure these three performance indicators: consistency, water retention, and compressive strength [27].

3. Results and Discussion

3.1. Orthogonal Test Results

The results for orthogonal test groups are presented in Table 5, where the constituent materials are reported in parts by weight. Orthogonal analysis was employed to investigate the influence of five factors—cellulose ether content (CE), stone powder replacement ratio for cement (SP), manufactured sand replacement ratio for river sand (MS), PVA content (PVA), and bentonite content (BT)—on the consistency, water retention, and 28-day compressive strength of the premixed mortar.

Table 5. Orthogonal test results of premixed mortar performance.

Serial Number	CE/%	SP/%	MS/%	PVA/%	BT/%	Consistency/mm	Water Retention Rate/%	28 d Compressive Strength/MPa
1	0.0125	10	20	0.035	0.9	95	91.5	13.5
2	0.0125	20	30	0.04	1	98	91.6	10.5
3	0.0125	30	40	0.045	1.1	96	91.2	8.2
4	0.0125	40	50	0.05	1.2	94	91.7	6.2
5	0.015	10	30	0.045	1.2	93	92	9.8
6	0.015	20	20	0.05	1.1	94	92.2	10.3
7	0.015	30	50	0.035	1	97	91.8	7.5
8	0.015	40	40	0.04	0.9	93	92.1	6
9	0.0175	10	40	0.05	1	94	92.5	8
10	0.0175	20	50	0.045	0.9	96	92.3	7.2
11	0.0175	30	20	0.04	1.2	90	93	10
12	0.0175	40	30	0.035	1.1	92	92.8	6.5
13	0.02	10	50	0.04	1.1	91	93.5	7
14	0.02	20	40	0.035	1.2	90	93.8	8.5
15	0.02	30	30	0.05	0.9	93	93.2	9
16	0.02	40	20	0.045	1	91	93	6.8

3.2. Analysis of Mean and Range

3.2.1. Consistency Analysis

Table 6 presents the mean values and range analysis for consistency. The order of factor significance affecting consistence was: CE > BT > SP ≈ MS > PVA. Thus, CE was the most influential factor, followed by BT. The mean values indicate that increasing the CE significantly reduced mortar consistency (i.e., decreased fluidity). This phenomenon is attributed to the hydrophilic, long-chain polymer structure of CE molecules. Their ether and hydroxyl groups form strong hydrogen bonds with water molecules, converting substantial free water into bound water associated with the polymer chains. This markedly increases the apparent viscosity and internal cohesion of the paste, impairing particle mobility and thus reducing fluidity. Furthermore, at higher dosages, the dissolved CE chains entangle and connect, forming a continuous, weak three-dimensional gel network throughout the system. This network encapsulates and immobilizes cement particles and other solid components, necessitating the disruption of this structure for flow to initiate, thereby significantly decreasing fluidity. The optimal mix proportion for achieving the

highest consistency was determined as: CE (Level 1), SP (Level 2), MS (Level 4), PVA (Level 3), BT (Level 2).

Table 6. Analysis of mean and range of consistency.

Level	Factor				
	CE/%	SP/%	MS/%	PVA/%	BT/%
1	95.75	93.25	92.5	93.5	94.25
2	94.25	94.5	94	93	95
3	93	94	93.25	94	93.25
4	91.25	92.5	94.5	93.75	91.75
Extreme Value Sort	4.5(1)	2(3)	2(3)	1(4)	3.25(2)

Figure 1 illustrates the trend of mortar consistency with varying CE and BT. As shown, consistency exhibits a declining trend with increasing CE dosage. An increase in CE by 60% resulted in a 4.7% reduction in mortar consistency.

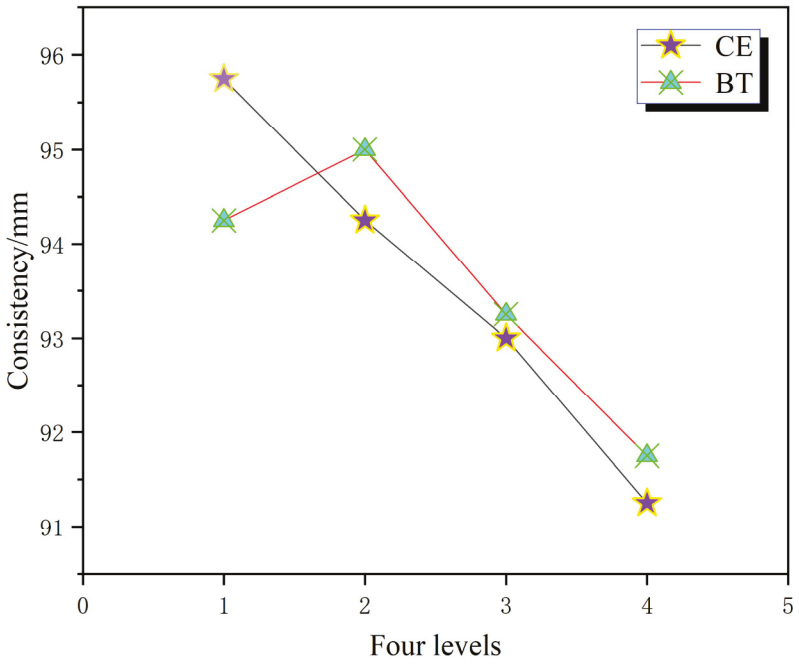

Figure 1. Trend chart of the consistency of premixed mortar.

3.2.2. Water Retention Analysis

The mean values and range analysis for water retention are shown in Table 7. The significance ranking for water retention was: CE > PVA > BT > SP > MS, identifying CE and PVA as the primary factors. An increase in CE substantially enhances water retention through the physicochemical action of its polymer chains. The hydrophilic functional groups (e.g., hydroxyl, ether) on the CE chains form an extensive hydrogen-bonding network with water molecules, effectively converting free water into bound water and reducing the driving force for evaporation. The dissolved CE significantly increases the viscosity of the pore solution, and its long-chain structure establishes a three-dimensional network within the mortar. This network imposes considerable kinetic hindrance to water migration, drastically slowing the rate of water penetration into substrates and evaporation to the environment. Additionally, the air-entraining and foam-stabilizing effects of CE introduce fine, closed air bubbles that disrupt capillary connectivity, altering the pore

structure and providing an additional physical barrier to moisture movement. Consequently, with increasing CE content, this synergistic water-retention effect—combining chemical adsorption, physical obstruction, and rheological modification—becomes more pronounced, leading to an approximately linear improvement in water retention. The optimal mix proportion for maximum water retention was: CE (Level 4), SP (Level 2), MS (Level 1), PVA (Level 2), BT (Level 4).

Table 7. Analysis of mean and range of water retention rate.

Level	Factor				
	CE/%	SP/%	MS/%	PVA/%	BT/%
1	91.5	92.375	92.425	92.475	92.275
2	92.025	92.475	92.4	92.55	92.225
3	92.65	92.3	92.4	92.125	92.425
4	93.375	92.4	92.325	92.4	92.625
Extreme Value Sort	1.875(1)	0.175(4)	0.1(5)	0.425(2)	0.4(3)

Figure 2 depicts the variation in water retention with CE and PVA. Water retention shows an increasing trend with higher CE. Specifically, a 60% increase in CE content led to a 2.05% rise in water retention.

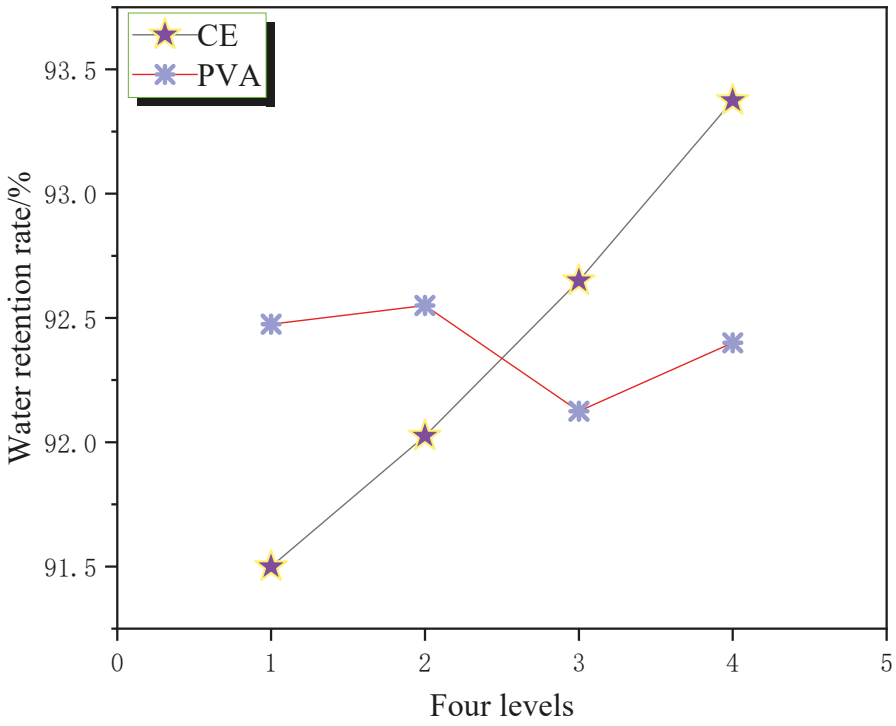

Figure 2. Trend chart of water retention rate of premixed mortar.

3.2.3. Compressive Strength Analysis

Table 8 displays the mean values and range analysis for compressive strength. The factor significance for strength was SP > MS > CE > PVA > BT, highlighting the predominance of the replacement materials. The observed strength reduction associated with increased stone powder and manufactured sand replacement levels stems from the combined negative effects on the compositional structure and the Interfacial Transition Zone (ITZ) within the cementitious matrix. Stone powder, acting largely as an inert filler, substantially reduces the total amount of reactive cementitious material when replacing cement. This

leads to a decreased absolute volume of hydration products (e.g., C-S-H gel), weakening the binding capacity and driving force for matrix densification. Concurrently, the angular particle shape and potentially unfavorable gradation of manufactured sand increase internal friction and create more interfacial weak zones, hindering the achievement of dense particle packing. Critically, the fine particles in both stone powder and manufactured sand can exacerbate flocculation and competitively adsorb a portion of the mixing water. This effectively increases the water-to-cement ratio locally, leading to higher inherent porosity and micro-crack concentration in the hardened state. These factors collectively degrade the structure and mechanical properties of the ITZ, making it a preferential path for stress concentration and crack propagation, ultimately manifesting as a systematic decline in compressive strength.

Table 8. Analysis of the mean and range of compressive strength.

Level	Factor				
	CE/%	**SP/%**	**MS/%**	**PVA/%**	**BT/%**
1	9.6	9.575	10.150	9.000	8.925
2	8.400	9.125	8.950	8.375	8.200
3	7.925	8.675	7.675	8.000	8.000
4	7.825	6.375	6.975	8.375	8.625
Extreme Value Sort	1.775(3)	3.2(1)	3.175(2)	1.0(4)	0.925(5)

The strength reduction associated with increased CE primarily arises from physical mechanisms. Firstly, its air-entraining effect introduces numerous stable, fine air bubbles into the matrix. These pores act as stress concentration points and reduce the effective load-bearing area. Secondly, the strong water adsorption and network formation by the polymer chains can retard the hydration kinetics of cement minerals and potentially interfere with the spatial arrangement and densification of hydration products due to steric hindrance. However, the magnitude of its impact is notably weaker compared to the replacement effects of stone powder and manufactured sand. Fundamentally, replacing cement with stone powder directly and irreversibly dilutes the volume of the active cementitious phase, fundamentally reducing the primary source of strength—the C-S-H gel. The harsh morphology of manufactured sand severely compromises the structure and density of the ITZ, introducing numerous inherent micro-defects. In contrast, while CE introduces porosity, the flexible three-dimensional network it forms causes limited structural disruption at low dosages, and its water-retaining effect might even promote prolonged hydration. Therefore, the influence of CE can be viewed as a 'weakening modification' of the formed structure, whereas the replacement by stone powder and manufactured sand constitutes a 'fundamental weakening' of the material's foundational structure, explaining their more pronounced negative impact on macroscopic compressive strength. The optimal mix proportion for achieving the highest compressive strength was: CE (Level 1), SP (Level 1), MS (Level 1), PVA (Level 1), BT (Level 1).

Figure 3 shows the variation in compressive strength with CE, SP, and MS. Compressive strength decreased with increasing CE dosage. A 60% increase in CE content led to an 18.49% reduction in compressive strength.

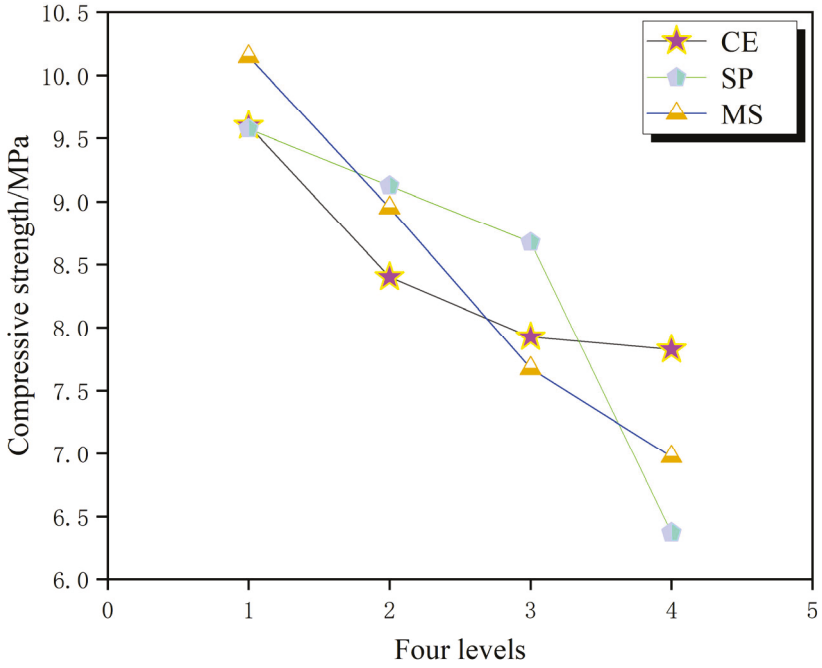

Figure 3. Trend chart of compressive strength of premixed mortar.

3.3. Analysis of Variance

While range analysis can intuitively determine the primary and secondary order of factor influence on the test indicators, it cannot assess whether these influences are statistically significant [28,29]. To ensure data accuracy, triplicate measurements were taken for each experimental trial. An Analysis of Variance (ANOVA) was subsequently performed on the results to quantify the degree of influence exerted by each factor; the results are summarized in Tables 9–11.

Table 9. Variance analysis of consistency.

Source of Variance	Sum of Squared Deviation	Degree of Freedom	Mean Square	F-Value	Significant
A	131.896	3	43.965	47.962	$p < 0.01$
B	22.396	3	7.465	8.144	$p < 0.01$
C	26.062	3	8.687	9.477	$p < 0.01$
D	5.396	3	1.799	1.962	$p = 0.140$
E	79.896	3	26.632	29.053	$p < 0.01$
Error	29.333	32	0.917		

Table 10. Variance analysis of water retention rate.

Source of Variance	Sum of Squared Deviation	Degree of Freedom	Mean Square	F-Value	Significant
A	23.486	3	7.829	200.947	$p < 0.01$
B	0.191	3	0.064	1.631	$p = 0.202$
C	0.071	3	0.024	0.604	$p = 0.617$
D	1.271	3	0.424	10.872	$p < 0.01$
E	1.141	3	0.380	9.759	$p < 0.01$
Error	1.247	32	0.039		

Table 11. Variance analysis of compressive strength.

Source of Variance	Sum of Squared Deviation	Degree of Freedom	Mean Square	F-Value	Significant
A	23.887	3	7.962	199.062	$p < 0.01$
B	72.922	3	24.307	607.687	$p < 0.01$
C	70.987	3	23.662	591.562	$p < 0.01$
D	6.187	3	2.062	51.563	$p < 0.01$
E	6.248	3	2.083	52.063	$p < 0.01$
Error	1.280	32	0.040		

The threshold of the F-test used in this study are as follows: F0.05(3,32) = 2.9; F0.025(3,32) = 3.56; F0.01(3,32) = 4.46; F0.005(3,32) = 5.17; F0.0025(3,32) = 5.91; F0.001(3,32) = 6.94. According to the F-values in Table 9: F(D) = 1.962 is less than F0.05(3,32) = 2.9, and its significance probability (p = 0.140) > 0.05. This indicates that variations in Factor D (PVA) have no significant effect on mortar consistency. In contrast, F(A) = 47.962, F(E) = 26.632, F(C) = 9.477, and F(B) = 8.144 all exceed F0.001(3,32) = 6.94, confirming their significant impacts on consistency. The order of significance is A (CE) > E (BT) > C (MS) > B (SP).

From the F-values in Table 10: F(C) = 0.604 and F(B) = 1.631 are both below F0.05(3,32) = 2.9, with p-values of 0.617 and 0.202, respectively (both > 0.05). This demonstrates that Factors B (SP) and C (MS) do not significantly affect the water retention of the mortar. Conversely, F(A) = 200.947, F(D) = 10.872, F(E) = 9.759 all show F-values greater than F0.001(3,32) = 6.94, establishing their highly significant effects on water retention. Their order of significance is A (CE) > D (PVA) > E (BT).

The F-values presented in Table 11 reveal that all five factors—A (CE), B (SP), C (MS), D (PVA), and (BT)—possess F-values greater than the critical value, with associated p-values < 0.01. Therefore, all five factors exert a statistically significant influence on the compressive strength of the premixed mortar. The order of their significance is B (SP) > C (MS) > A (CE) > E (BT) > D (PVA).

3.4. Regression Analysis

3.4.1. Consistency Fitting

While range and ANOVA can identify a relatively optimal factor combination within the predefined levels, they cannot locate the absolute optimum within the tested ranges. In contrast, regression analysis based on the experimental data enables effective prediction and optimization of the results [30–35]. Therefore, regression analysis was applied to the experimental findings in this study using Design-Expert 13 software.

As the prior ANOVA indicated that Factor D (PVA) had no significant effect on consistency, the regression analysis incorporated only the significant factors. The two most influential factors, A (CE) and E (BT), were used to develop a first-order regression model with consistence as the response.

$$Y = 93.5625 - 2.2125\,CE - 1.3875\,BT \quad (1)$$

The relationship between the experimental data and the values predicted by the fitted Equation (1) is shown in Figure 4. A coefficient of determination (R^2 = 0.6894) confirms that Equation (1) accurately represents the relationship between the consistence of premixed mortar and the contents of CE and bentonite.

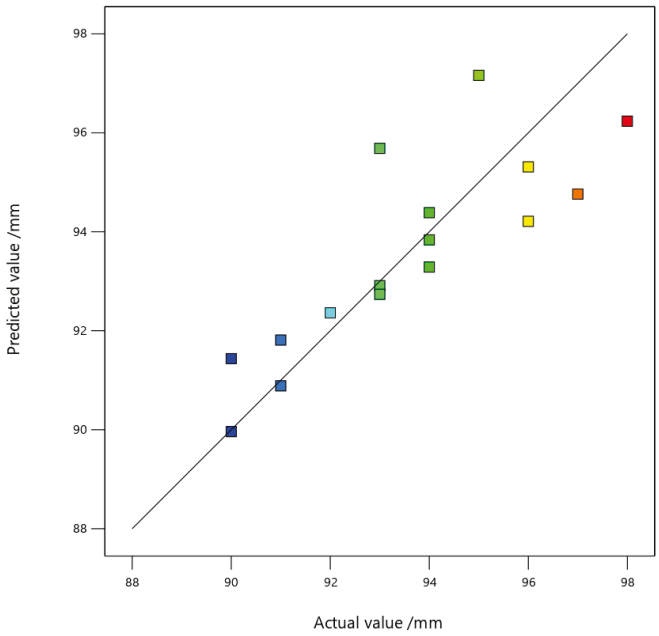

Figure 4. Relationship between the measured and predicted values of the consistency.

Figure 4 shows a close agreement between the predicted values from the model and the experimental data, validating the model's accuracy in describing the correlation between the factors and the response. Therefore, the developed model reliably represents the true parameter relationships and can be used for predicting and analyzing the consistency of premixed mortar. Figure 5 presents the residual normal distribution of the consistency of the premixed mortar, where all data points closely align along a single line, indicating that the fitting error of the regression model for the consistency of the premixed mortar is relatively small. A response surface plot for the significant factors (CE and BT) versus consistency, generated using Design-Expert software, is provided in Figure 6.

As shown in Figure 6, the consistency of premixed mortar decreases with increasing contents of both CE and BT within a certain range. However, the rate of reduction associated with BT is less steep compared to that caused by CE. Furthermore, a simultaneous increase in both CE and BT can effectively suppress the consistency of the mortar.

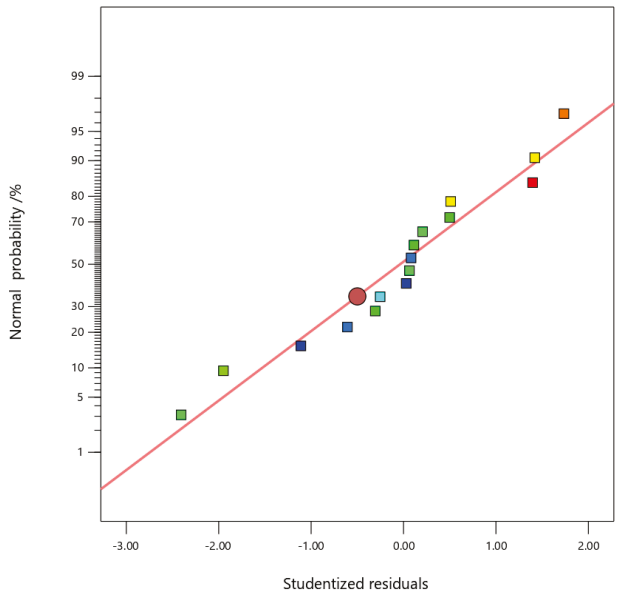

Figure 5. Residual analysis of the consistency.

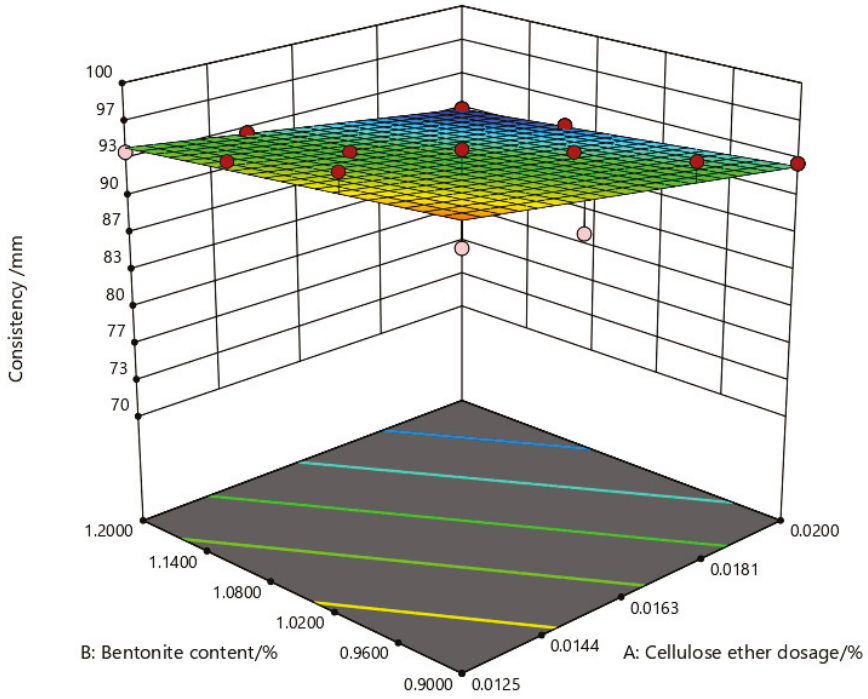

Figure 6. Consistency response diagram of premixed mortar.

3.4.2. Water Retention Rate Fitting

Since the prior ANOVA revealed that Factors C (MS) and B (SP) had no significant effect on water retention, the regression analysis considered only the significant factors. The two most influential factors, A (CE) and D (PVA), were selected. A multiple regression analysis was subsequently performed, establishing a first-order model with water retention as the response variable.

$$Y = 92.3875 + 0.9375\,CE - 0.0975\,PVA \quad (2)$$

The correlation between the experimental values and those predicted by the fitted Equation (2) is presented in Figure 6. The coefficient of determination (R^2 =0.9336) confirms that Equation (2) effectively represents the relationship between the water retention of premixed mortar and the contents of CE and PVA.

Figure 7 demonstrates a close agreement between the predicted values from the developed model and the experimental data, indicating the model's suitability for characterizing the relationship between the experimental factors and the response. Consequently, the model accurately reflects the underlying relationships among the parameters and can be reliably used for predicting and analyzing the water retention of premixed mortar. Figure 8 presents the residual normal distribution of water retention of the premixed mortar, where all data points closely align along a single line, indicating that the fitting error of the regression model for the water retention of the premixed mortar is relatively small. A response surface plot illustrating the relationship between the significant factors—cellulose ether (CE) content and PVA content—and the response variable (water retention) was generated using Design-Expert software, as shown in Figure 9.

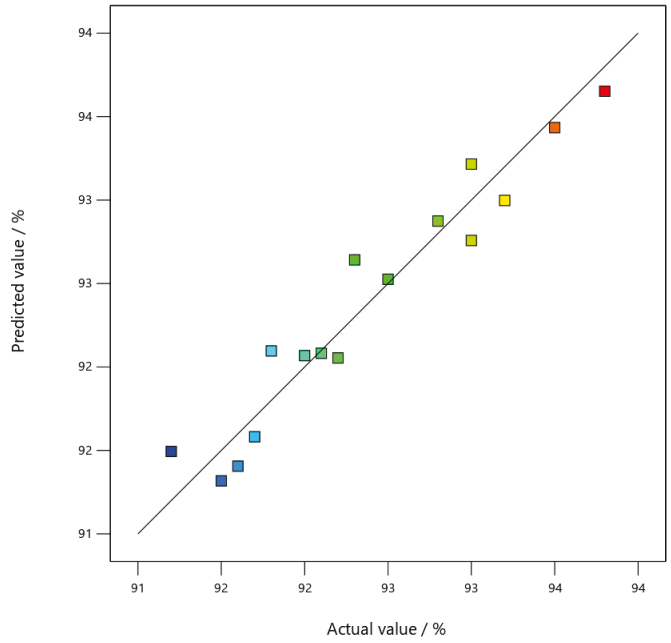

Figure 7. Relationship between the water retention test values and predicted values.

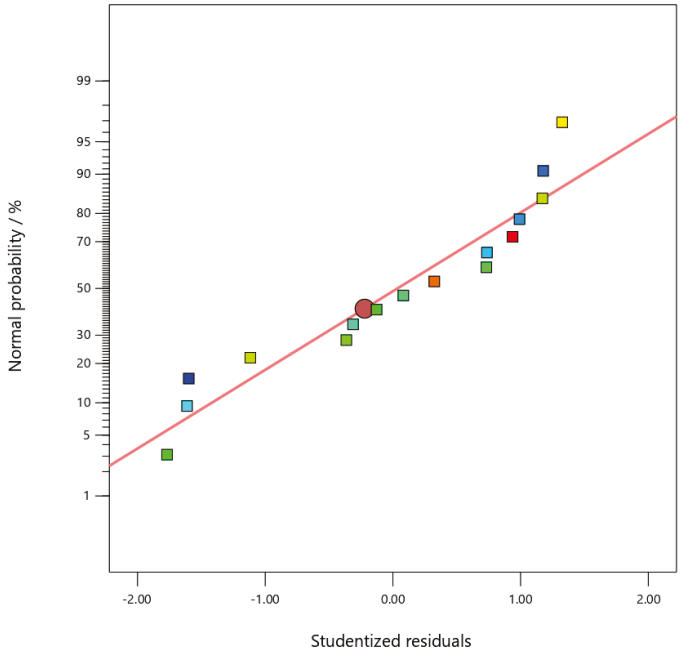

Figure 8. Residual analysis of the water retention.

Based on Figure 9, it can be concluded that within a certain range, the water retention of premixed mortar increases with higher cellulose ether content but decreases with increased PVA content. However, the declining trend associated with PVA content is more gradual compared to the increasing trend promoted by CE. Furthermore, simultaneously increasing the CE while appropriately reducing the PVA can effectively enhance the water retention capacity of the premixed mortar.

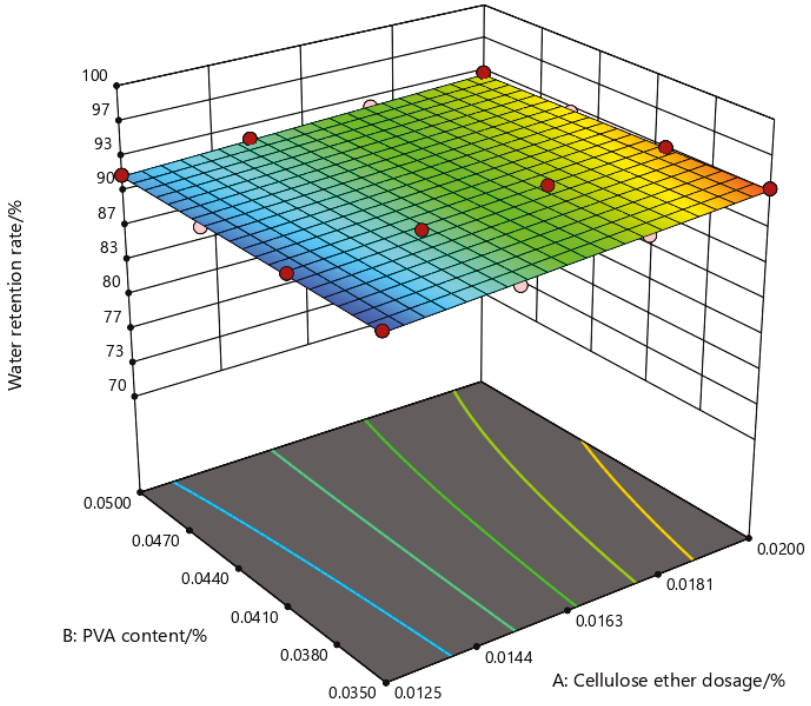

Figure 9. Water retention rate response curve of premixed mortar.

3.4.3. Compressive Strength Fitting

Since the prior analysis of variance confirmed that all five factors—CE (A), SP (B), MS (C), PVA (D) and BT (E)—significantly affect the compressive strength, the three most influential factors (B, C, and A) were selected for regression analysis. A multiple regression analysis was performed on the experimental data, establishing a first-order model with compressive strength as the response variable.

$$Y = 8.51 - 0.9117\,CE - 1.63\,SP - 1.67\,MS \quad (3)$$

The relationship between the experimental values and those calculated by the fitted Equation (3) is shown in Figure 8. The coefficient of determination ($R^2 = 0.8561$) indicates that the relationship between the compressive strength of premixed mortar and the three factors—CE, SP, and MS—can be effectively represented by Equation (3).

As shown in Figure 10, the predicted values obtained from the established model demonstrate close agreement with the experimental values, indicating the model's suitability for characterizing the correlation between the experimental factors and the response. Consequently, the developed model accurately reflects the intrinsic relationships among the parameters and can be reliably employed for predicting and analyzing the compressive strength of premixed mortar. Figure 11 presents the residual normal distribution of compressive strength of the premixed mortar, where all data points closely align along a single line, indicating that the fitting error of the regression model for the compressive strength of the premixed mortar is relatively small. Using Design-Expert software, a response surface plot was generated to visualize the relationship between the key experimental factors (CE, SP, and MS) and the response variable (compressive strength of premixed mortar), as presented in Figure 12.

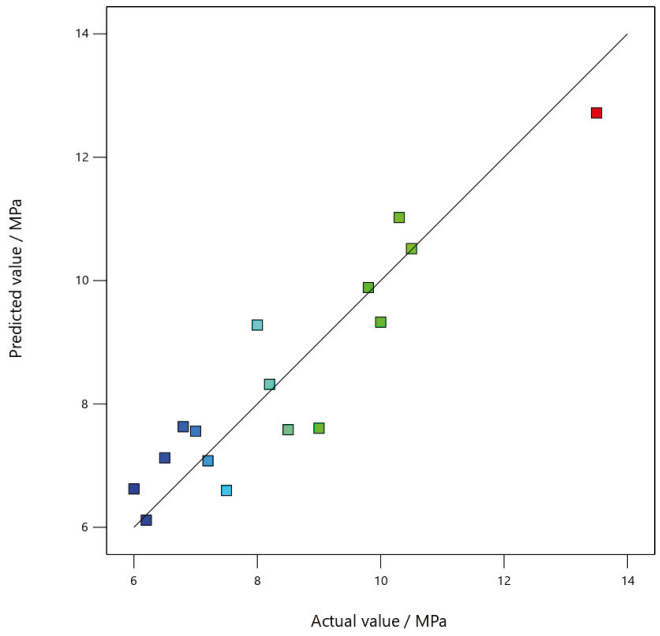

Figure 10. Relationship between the compressive strength test values and predicted values.

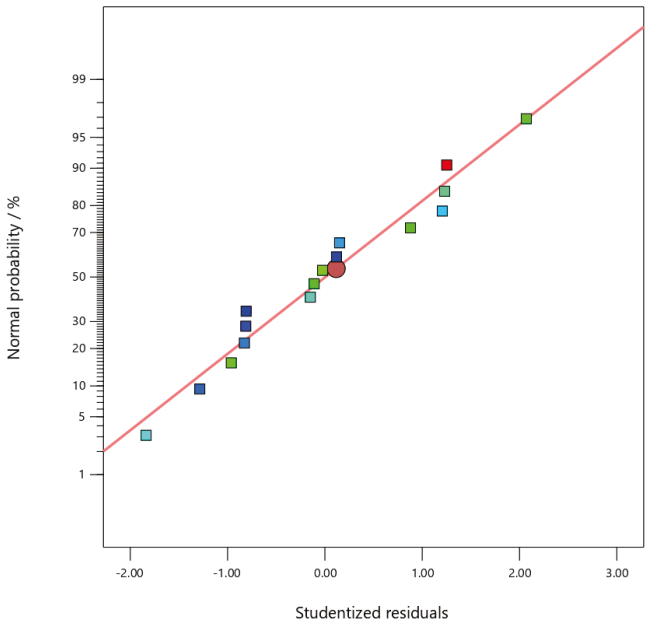

Figure 11. Residual analysis of compressives strength.

Based on the results presented in Figure 12, the compressive strength of the premixed mortar decreases with increasing CE, SP, and MS. However, the declining trend associated with the CE is less pronounced compared to the reduction caused by the SP.

Furthermore, to enhance the water retention capacity without compromising the compressive strength, modification of the CE's physicochemical properties—such as its particle size, morphology, and chemical functionality—is a promising avenue for future research and development.

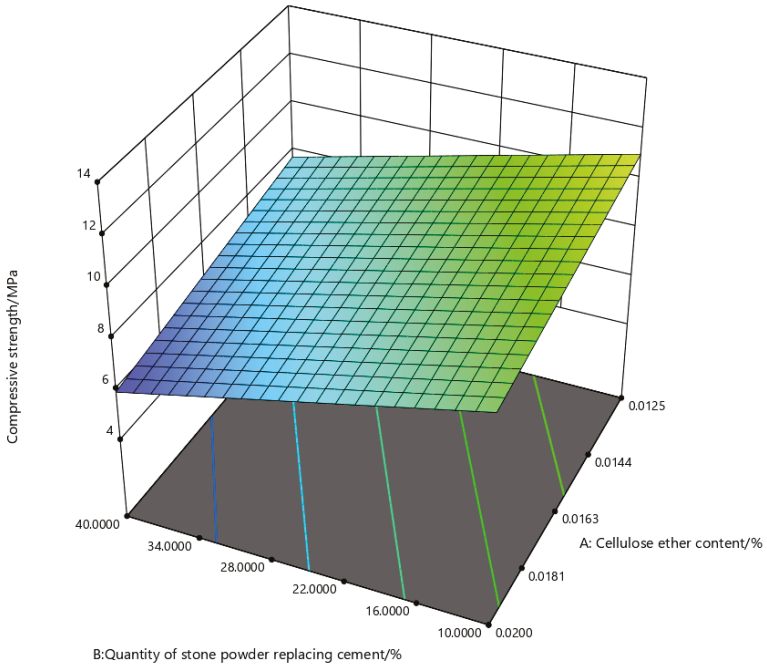

Figure 12. Compressive strength response diagram of premixed mortar.

4. Conclusions

This study investigates the influence of cellulose ether (CE) content and its interactions with supplementary materials—including stone powder (SP), manufactured sand (MS), polyvinyl alcohol (PVA), and bentonite (BT)—on the performance of premixed mortar using an orthogonal experimental design. Performed mean and range analysis, variance analysis, and regression fitting analysis. The key conclusions are as follows:

1. The optimal fluidity (consistency) was achieved with specific mix proportions (CE: 0.0175, SP: 20%, MS: 50%, PVA: 0.045%, BT: 1%). The order of factor significance affecting fluidity was: CE > BT > SP ≈ MS> PVA. Thus, CE was the most influential factor, followed by BT.
2. The maximum water retention was obtained with a different mix combination (CE: 0.02%, SP: 20%, MS: 20%, PVA: 0.04%, BT: 1.2%). The significance ranking for water retention was CE > PVA > BT > SP > MS, identifying CE and PVA as the primary factors.
3. The highest compressive strength was observed with another set of parameters (CE: 0.0125%, SP: 10%, MS: 20%, PVA: 0.035%, BT: 0.9%). The factor significance for compressive strength was SP > MS > CE > PVA > BT, highlighting the predominance of the replacement materials.
4. Variations in PVA showed no significant effect on mortar fluidity, whereas the other four factors had significant impacts. The replacement levels of MS and SP did not significantly affect the water retention rate, in contrast to the three other factors which did. All five factors—CE, SP, MS, PVA, and BT—exerted significant influences on the compressive strength of the mortar.
5. The combined effect of CE and BT on fluidity was fitted using a linear regression model. The trend indicated a decrease in fluidity with increasing dosages of both CE and BT. The influence of CE and PVA on water retention was also described by a linear regression. The model suggested that within a certain range, water retention increases with higher CE but decreases with increasing PVA. A multiple linear regression model fitted the relationship between compressive strength and CE, SP, and MS. The results revealed a declining trend in compressive strength with increases in these three factors. Overall, this study quantitatively revealed the coupled effects of organic

and inorganic admixtures in premixed mortar and established predictive models for key performance indicators, providing a scientific basis for mix design optimization and offering significant theoretical and practical value for achieving performance balance and green, low-carbon mortar design.

Author Contributions: Methodology, J.Z.; Investigation, S.S.; Resources, Y.L. and S.S.; Data curation, Y.L., S.S. and S.Z.; Writing—original draft, Y.L., Q.H., S.S. and G.B.; Writing—review & editing, Y.L., M.Z. and J.Z.; Project administration, Y.L.; Funding acquisition, Y.L., Q.H., J.Z. and Z.-J.L.; Supervision, Z.-J.L. All authors have read and agreed to the published version of the manuscript.

Funding: The authors gratefully acknowledge the financial support from the Fujian Provincial Natural Science Foundation Project (2024J08236), Hezhou University Professor Research Start-up Fund (2025JSQD04), the Science and Technology Program of the Guangxi Department of Housing and Urban-Rural Development (R&D, 2024), the Special Project in Key Fields of the Guangdong Provincial Department of Education (No. 2023ZDX3106), and the Guangxi Program for Fostering Research Capacity of Young University Faculty (No. 2025KY0792).

Institutional Review Board Statement: Not applicable.

Informed Consent Statement: Not applicable.

Data Availability Statement: The original contributions presented in this study are included in the article. Further inquiries can be directed to the corresponding author.

Acknowledgments: Sincere appreciation is extended to all supporting institutions and funding agencies.

Conflicts of Interest: The authors declare that they have no known competing financial interests or personal relationships that could have appeared to influence the work reported in this paper.

References

1. Zerig, T.; Belachia, M.; Aidoud, A.; Meftah, N.; Djedid, T.; Abbas, M. Statistical analysis using the RSM approach of the physical behavior of green polymerized eco-mortar. *J. Clean. Prod.* **2024**, *450*, 141858. [CrossRef]
2. Rami Reddy, C.R.; Rao, H.S.; Ghorpade, V. Mechanical and Microstructural Behavior of Foamed Concrete with Polypropylene Fibers and Mineral Admixtures. *Procedia Struct. Integr.* **2025**, *70*, 223–230. [CrossRef]
3. Lara, R.C.; de Castro Xavier, G.; Canela, M.C.; Carvalho, J.A.; Alexandre, J.; de Azevedo, A.R.G. Characterization and photocatalytic performance of cement mortars with incorporation of TiO_2 and mineral admixtures. *Environ. Sci. Pollut. Res.* **2023**, *30*, 95537–95549. [CrossRef]
4. Şahmaran, M.; Christianto, H.A.; Yaman, İ.Ö. The effect of chemical admixtures and mineral additives on the properties of self-compacting mortars. *Cem. Concr. Compos.* **2006**, *28*, 432–440. [CrossRef]
5. Zhou, S.-C.; Lv, H.-L.; Li, N.; Zhang, J. Effects of Chemical Admixtures on the Working and Mechanical Properties of Ordinary Dry-Mixed Mortar. *Adv. Mater. Sci. Eng.* **2019**, *2019*, 5978089. [CrossRef]
6. Jenni, A.; Zurbriggen, R.; Holzer, L.; Herwegh, M. Changes in microstructures and physical properties of polymer-modified mortars during wet storage. *Cem. Concr. Res.* **2006**, *36*, 79–90. [CrossRef]
7. De Gasparo, A.; Herwegh, M.; Zurbriggen, R.; Scrivener, K. Quantitative distribution patterns of additives in self-leveling flooring compounds (underlayments) as function of application, formulation and climatic conditions. *Cem. Concr. Res.* **2009**, *39*, 313–323. [CrossRef]
8. Ye, F.; Qiao, H.; Feng, Q.; Tian, Y.; Su, L.; Fu, Y. Study on multi-performance optimization of basalt stone powder supplementary cementitious materials. *J. Build. Eng.* **2023**, *80*, 108018. [CrossRef]
9. Tang, Y.; Qiu, W.; Liu, D.; Zhang, W.; Zhang, R. Experimental Study on the Properties of Mortar and Concrete Made with Tunnel Slag Machine-Made Sand. *Materials* **2022**, *15*, 4817. [CrossRef] [PubMed]
10. De Almeida, J.; Delboni, H.; Jr Bento, R.; Reggio, A.; Cremonese, E. Performance Analysis of HRCTM HPGR in Manufactured Sand Production. *Minerals* **2023**, *13*, 222. [CrossRef]
11. Zhang, Y.; Zheng, Y.; Du, C.; Hu, S.; Wang, Z. Hybrid effects of basalt and polyvinyl alcohol fibers on the mechanical properties and macro-microscopic analysis of low-heat portland cement concrete. *J. Mater. Res. Technol.* **2023**, *25*, 608–632. [CrossRef]
12. Su, J.; Zhang, P.; Guo, J.; Zheng, Y. Effect of PVA fibers on durability of nano-SiO_2-reinforced cement-based composites subjected to wet-thermal and chloride salt-coupled environment. *Nanotechnol. Rev.* **2023**, *12*, 20230140. [CrossRef]

13. Basak, S.; Shakyawar, D.B.; Samanta, K.K.; Kumar, N.; Bhowmick, M.; Debnath, S.; Ghosh, R.K.; Manjunatha, B.S.; Ghosh, S.; Mustafa, I.; et al. Cellulose-protein blended sustainable biodegradable flexible composite: A step towards a leather alternative. *Cellulose* **2023**, *30*, 11087–11112. [CrossRef]
14. Martin, C.; Nourian, A.; Babaie, M.; Nasr, G.G. Innovative drilling fluid containing sand grafted with a cationic surfactant capable of drilling high pressure and high temperature geothermal and petroleum wells. *Geoenergy Sci. Eng.* **2024**, *237*, 212767. [CrossRef]
15. Cui, S.-L.; Zhang, H.-Y.; Zhang, M. Swelling characteristics of compacted GMZ bentonite–sand mixtures as a buffer/backfill material in China. *Eng. Geol.* **2012**, *141–142*, 65–73. [CrossRef]
16. Zhang, J.; Lv, T.; Zhu, Y.; Hou, D. Damage mechanism of engineered cementitious composites after exposed to elevated temperatures: Experimental and molecular dynamics study. *Cem. Concr. Compos.* **2022**, *129*, 104507. [CrossRef]
17. Wu, H.; Liu, J.; Zhang, X. Feasibility study on use of cellular concrete for air convection embankment on permafrost foundations in Fairbanks, Alaska. *Transp. Geotech.* **2020**, *22*, 100317. [CrossRef]
18. Cao, Y.; Mihardjo, L.W.W.; Parikhani, T. Thermal performance, parametric analysis, and multi-objective optimization of a direct-expansion solar-assisted heat pump water heater using NSGA-II and decision makings. *Appl. Therm. Eng.* **2020**, *181*, 115892. [CrossRef]
19. Koyuncu, D.D.E.; Okur, M. Investigation of dye removal ability and reusability of green and sustainable silica and carbon-silica hybrid aerogels prepared from paddy waste ash. *Colloids Surf. A Physicochem. Eng. Asp.* **2021**, *628*, 127370. [CrossRef]
20. Pyo, S.; Abate, S.Y.; Kim, H.-K. Abrasion resistance of ultra high performance concrete incorporating coarser aggregate. *Constr. Build. Mater.* **2018**, *165*, 11–16. [CrossRef]
21. Wang, Y.; Wu, J.; Su, L.; Zhang, Z.; Wang, Z.; Lei, T.; Lu, X.; Ye, Z. Effect of Chemical Admixtures on the Working Performance and Mechanical Properties of Cement-Based Self-Leveling Mortar. *Buildings* **2023**, *13*, 2248. [CrossRef]
22. Brachaczek, W. Study of the Properties of Renovation Plasters as a Function of Air Content and Porosity Using an Orthogonal Design of Experiment. *Period. Polytech. Civ. Eng.* **2018**, *62*, 1007–1014. [CrossRef]
23. Li, Q.; Zhang, S.; Zhang, Z. Experimental preparation and mechanical properties enhancement of polymer mortar in industrial solid waste base. *J. Phys. Conf. Ser.* **2025**, *3068*, 012126. [CrossRef]
24. Liu, J.; Yang, N.; Chen, H. Study on the mechanical properties and microstructural simulation of alkali-activated mineral powder-based mortar. *Eur. J. Environ. Civ. Eng.* **2025**, 1–21. [CrossRef]
25. Yuan, C.; Cai, Y.; Gu, Q.; Sang, D. Research on Modified High-performance Cement Mortar of Prefabricated Buildings Based on Orthogonal Test. *Int. J. Concr. Struct. Mater.* **2022**, *16*, 50. [CrossRef]
26. Liu, Y.; Li, Y.; Jiang, G. Orthogonal experiment on performance of mortar made with dune sand. *Constr. Build. Mater.* **2020**, *264*, 120254. [CrossRef]
27. Lu, B.; Zhang, Z.; Zhu, H.; Liu, K.; Zhang, Y.; Chen, W. Optimization design of recycled powder mortar mix ratio based on orthogonal test. *Constr. Build. Mater.* **2025**, *474*, 141145. [CrossRef]
28. Liu, L.; Lei, M.; Gong, C.; Gan, S.; Yang, Z.; Kang, L.; Jia, C. A robust mix design method for self-compacting concrete. *Constr. Build. Mater.* **2022**, *352*, 128927. [CrossRef]
29. Liu, M.; Yang, D.; Chen, L.; Chen, G.; Ma, Z. Effect of silicate modulus and alkali content on the microstructure and macroscopic properties of alkali-activated recycled powder mortar. *Constr. Build. Mater.* **2023**, *397*, 132365. [CrossRef]
30. Ren, F.; Zhou, C.; Zeng, Q.; Ding, Z.; Xing, F.; Wang, W. The dependence of capillary sorptivity and gas permeability on initial water content for unsaturated cement mortars. *Cem. Concr. Compos.* **2019**, *104*, 103356. [CrossRef]
31. Jin, C.; Qian, Y.; Khan, K.; Ahmad, A.; Amin, M.N.; Althoey, F.; Nawaz, R. Predicting the damage to cementitious composites due to acid attack and evaluating the effectiveness of eggshell powder using interpretable artificial intelligence models. *Mater. Today Commun.* **2023**, *37*, 107333. [CrossRef]
32. Qin, J.; Pang, X.; Cheng, G.; Bu, Y.; Liu, H. Influences of different admixtures on the properties of oil well cement systems at HPHT conditions. *Cem. Concr. Compos.* **2021**, *123*, 104202. [CrossRef]
33. Shaheen, K.; Shah, Z.; Arshad, T.; Khan, S.B.; Guo, J.; Khan, M.N.; Suo, H. Electrical conductance, dielectric properties and photodegradation ability of aluminum based Heterogeneous nanoparticles. *Mater. Chem. Phys.* **2020**, *254*, 123546. [CrossRef]
34. Wang, S.; Xia, P.; Gong, F.; Zeng, Q.; Chen, K.; Zhao, Y. Multi objective optimization of recycled aggregate concrete based on explainable machine learning. *J. Clean. Prod.* **2024**, *445*, 141045. [CrossRef]
35. Geng, S.-Y.; Luo, Q.-L.; Cheng, B.-Y.; Li, L.-X.; Wen, D.-C.; Long, W.-J. Intelligent multi-objective optimization of 3D printing low-carbon concrete for multi-scenario requirements. *J. Clean. Prod.* **2024**, *445*, 141361. [CrossRef]

Disclaimer/Publisher's Note: The statements, opinions and data contained in all publications are solely those of the individual author(s) and contributor(s) and not of MDPI and/or the editor(s). MDPI and/or the editor(s) disclaim responsibility for any injury to people or property resulting from any ideas, methods, instructions or products referred to in the content.

coatings

MDPI

Article

Seismic Damage Risk Assessment of Reinforced Concrete Bridges Considering Structural Parameter Uncertainties

Jiagu Chen, Chao Yin *, Tianqi Sun and Jiaxu Li

School of Civil Engineering and Geomatics, Shandong University of Technology, Zibo 255049, China; 13665526992@163.com (J.C.); 24507030901@stumail.sdut.edu.cn (T.S.); 24507030902@stumail.sdut.edu.cn (J.L.)
* Correspondence: yinchao1987611@163.com

Abstract

To accurately assess the seismic risk of bridges, this study systematically conducted probabilistic seismic hazard–fragility–risk assessments using a reinforced concrete continuous girder bridge as a case study. First, the CPSHA method from China's fifth-generation seismic zoning framework was employed to calculate the Peak Ground Acceleration (PGA) with 2%, 10%, and 63% exceedance probabilities over 50 years as 171.16 gal, 98.10 gal, and 28.61 gal, respectively, classifying the site as being with 0.10 g zone (basic intensity VII). Second, by innovatively integrating the Response Surface Method with Monte Carlo simulation, the study efficiently quantified the coupled effects of structural parameter and ground motion uncertainties, a finite element model was established based on OpenSees, and the seismic fragility curves were plotted. Finally, the risk probability of seismic damage was calculated based on the seismic hazard curve method. The results demonstrate that the study area encompasses 46 potential seismic sources according to China's fifth-generation zoning. The seismic fragility curves clearly show that side piers and their bearings are generally more susceptible to damage than middle piers and their bearings. Over 50 years, the pier risk probabilities for the intact, slight, moderate, severe damage, and collapse are 68.90%, 6.22%, 15.75%, 7.86%, and 1.27%, while the corresponding probabilities of bearing are 3.54%, 44.11%, 25.64%, 7.74%, and 18.97%, indicating significantly higher bearing risks at the moderate damage and collapse levels. The method proposed in this study is applicable to various types of bridges and has high promotion and application value.

Keywords: bridge; seismic hazard assessment; OpenSees; Response Surface Method; seismic fragility assessment; structural uncertainty; probability risk assessment

1. Introduction

China is located at the intersection of the Circum-Pacific Seismic Zone and the Eurasian Seismic Zone, making it one of the countries most severely affected by earthquake disasters globally [1]. The 1976 Tangshan earthquake nearly destroyed all highway and railway bridges in Tangshan City. The 2008 Wenchuan earthquake caused severe damage or collapse to 25 highway bridges in Sichuan Province. Notably, the G213 Baihua Bridge, located approximately 1.0 km from the Longmenshan active fault, experienced the collapse of its fifth span, with 90% of the remaining piers exhibiting crushing failures [2]. With the arrival of active cycles, future earthquakes may cause even more severe bridge damage. Therefore, systematically analyzing the failure mechanisms and damage degrees of bridges under different ground motions is crucial for improving seismic capacity of bridges and ability of regional disaster mitigation.

The degree of bridge seismic damage depends on two aspects. First, the intensity and probability of seismics at the bridge site (study site), which belongs to seismic hazard assessment. Factors such as seismic zones, distribution of potential seismic source zones, historical seismic records and site conditions may affect seismic hazards. Second, the seismic performance of the bridge itself, characterized by the probability of exceeding various damage levels under a given ground motion, which belongs to seismic fragility assessment, may affect seismic hazards. Factors such as bridge structural form, construction quality and protective measures influence seismic fragility. The probability of bridge seismic risk, which represents the probability of a specific bridge exceeding various damage levels over a certain period [3], is derived from the integration of seismic hazard and fragility assessments by analyzing their coupled characteristics.

Numerous scholars have made significant contributions to the field of structural seismic risk assessment. In the field of seismic hazard assessment, Cornell proposed the Probabilistic Seismic Hazard Analysis (PSHA) [4]. China's current seismic hazard assessment methodology (CPSHA) was developed based on PSHA [5]. The third to fifth generations of China's seismic ground motion zonation schemes were formulated by CPSHA [6]. For seismic fragility assessment, Vamvatsikos and Cornell introduced the Incremental Dynamic Analysis (IDA), which has since become the most widely adopted method [7]. Wang et al. proposed a fragility assessment approach that incorporated multi-dimensional performance limit states and pioneered fragility curves for multi-span continuous concrete girder bridges, explicitly accounting for pier ductility and lateral deformation [8]. Li et al. established the probability density evolution theory and applied it to nonlinear dynamic response analysis, thereby quantifying the variability in physical parameters of engineering structures [9]. In seismic risk assessment, Yin et al. and Che et al. employed the Monte Carlo method and seismic hazard curve method to assess seismic risks for a highway embankment and proposed a risk management method based on risk acceptability theory [10,11]. Abeysiriwardena et al. developed a seismic risk analysis method for RC frame structures considering aftershock effects [12]. Their work involved convolving mainshock–aftershock fragility functions with hazard functions, extending the traditional risk integral formula to a bivariate domain, and deriving demand risk functions incorporate aftershock impacts.

Structural uncertainties are inherent in the design, construction and operation of bridges. A critical technical challenge lies in characterizing the coupled effects of structural parameter and ground motion uncertainties on bridge seismic performance. Although Chinese seismic design philosophy for bridges adheres to the principle of "no damage under minor seismic events, repairable damage under moderate seismic events, and no collapse under major seismic events" [13], clear definitions are lacking for the corresponding seismic intensity indicators ("minor", "moderate" "major" and damage states ("no damage", "repairable" "no collapse"); this ambiguity significantly limits the practical application of the philosophy. To address these issues, primary contributions of this study are twofold: (1) to develop an integrated probabilistic framework for bridge seismic risk assessment; (2) to introduce a novel, computationally efficient methodology that integrates the Response Surface Method with Monte Carlo simulation to effectively quantify the coupled effects of structural and ground motion uncertainties. This integrated approach thereby provides a practical and theoretically sound tool for performance-based seismic design and decision-making. The study flowchart is shown in Figure 1.

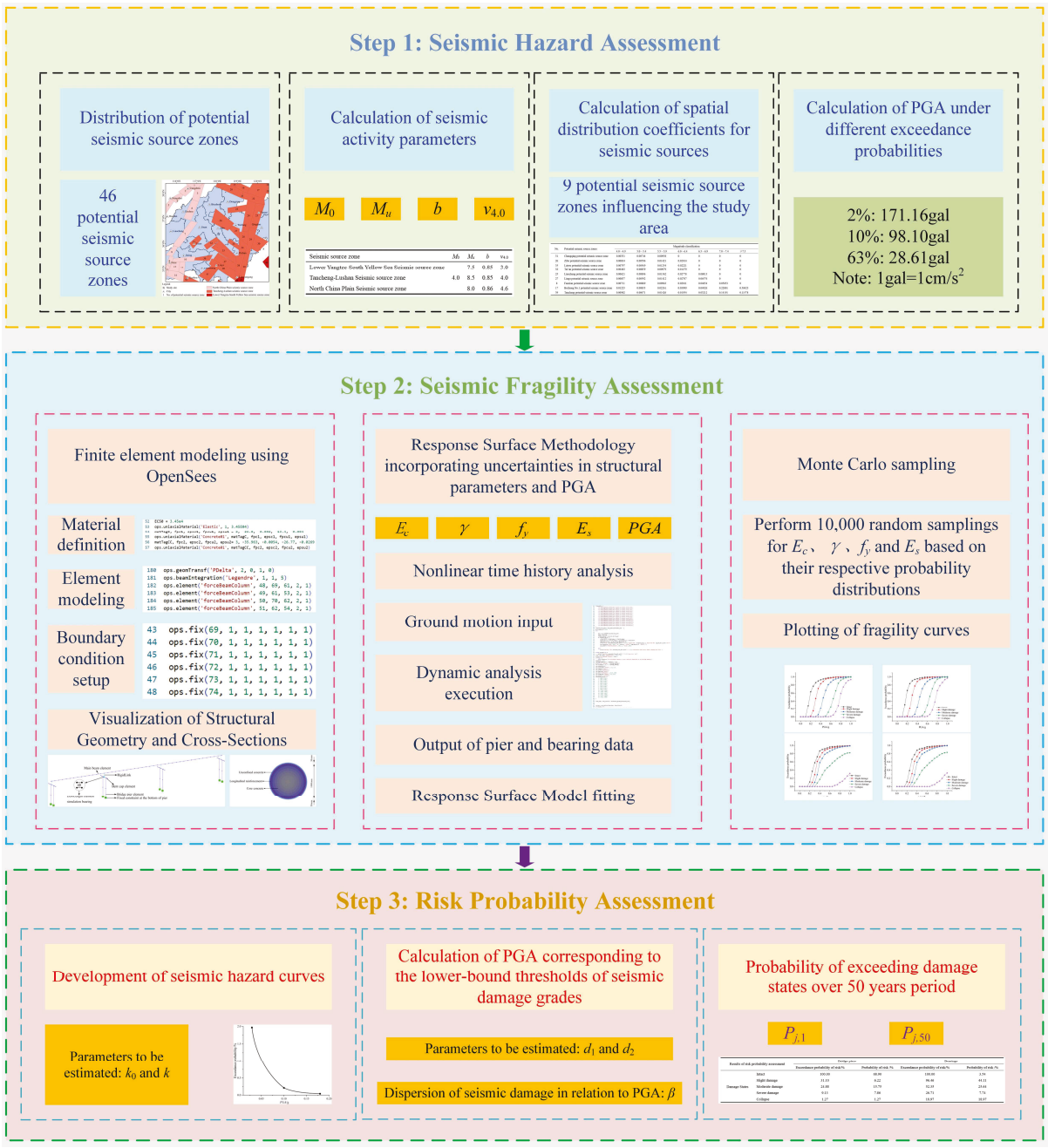

Figure 1. Study flowchart.

2. Finite Element Model Development of the Study Object

The bridge studied is located in Boshan District, Zibo City, Shandong Province, China, with a span arrangement of 3 × 30 m. The main beam was constructed with C50 concrete (The 28-day compressive strength of the concrete is 50 MPa), while the bridge piers and bent caps were constructed using C40 concrete (the 28-day compressive strength of the concrete is 40 MPa). HRB400 steel (the tensile strength of the reinforcing steel is 400 MPa.) was adopted for reinforcement, and pot rubber bearings were employed as supports. In the finite element modeling using OpenSees (Open System for Earthquake Engineering Simulation), the main beam and bent caps were modeled with elastic beam-column elements, the bearings were simulated using zero-length elements, the bridge piers were represented by force-based beam-column elements with fixed bases at the foundation. Given that the bridge site is characterized by stiff soil (Site Class II), where soil–structure interaction effects

are known to be minimal, this fixed-base assumption is considered appropriate, allowing the analysis to focus on the uncertainty and performance of the superstructure components. Concrete in the bridge piers was modeled with the Concrete01 material, and reinforcing steel was characterized by the Steel02 material [14–16]. The constitutive relationships of the Concrete01 and Steel02 materials are shown in Figure 2. Figure 2 is cited from the official OpenSees website at: https://opensees.berkeley.edu/ (accessed on 27 April 2024)

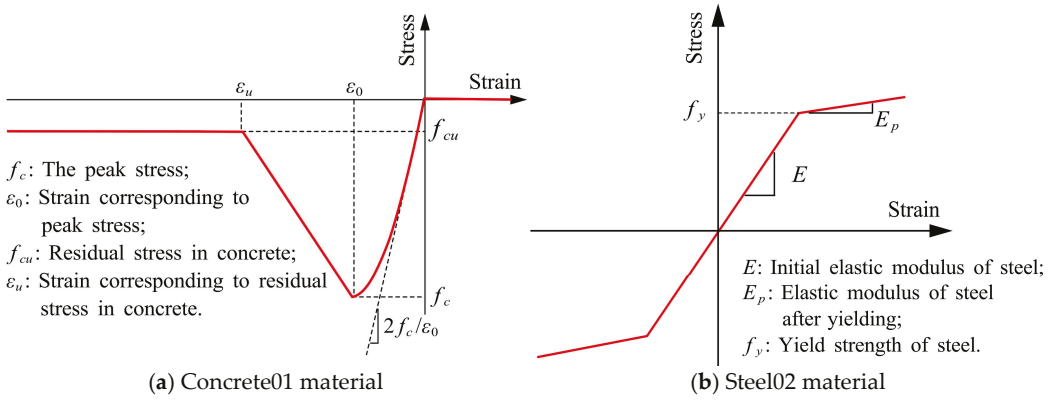

(**a**) Concrete01 material (**b**) Steel02 material

Figure 2. Constitutive relationships of material.

The piers were discretized into fiber elements, which were partitioned using Legendre integration. Each element was divided into five integration points along its longitudinal axis, with each integration point having the same cross-section. The five Legendre integration points along the longitudinal direction of the pier and the division of fibers at their cross-sections are shown in Figure 3.

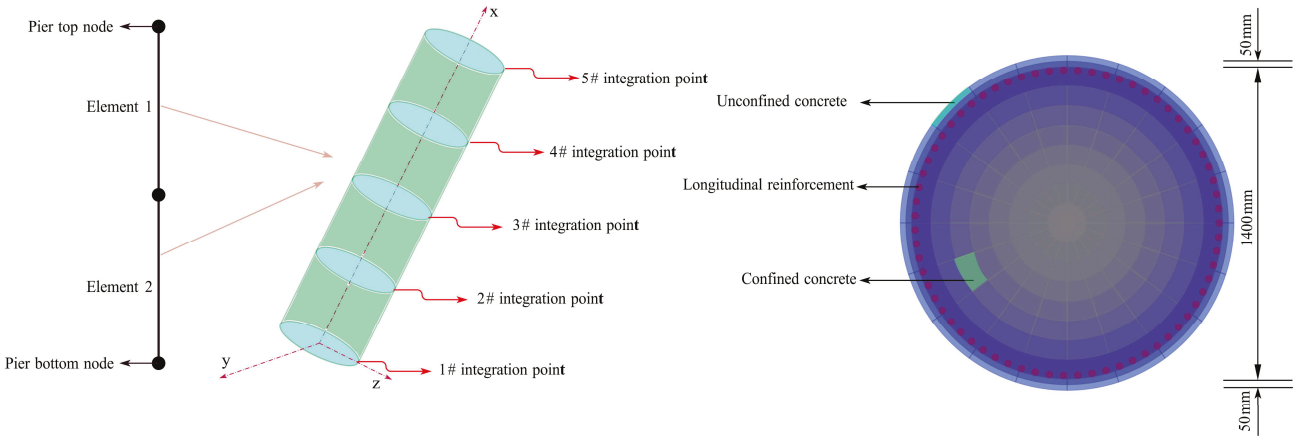

Figure 3. Legendre integration points and the fiber division of their cross-sections.

The Midas and Opensees finite element models are shown in Figures 4 and 5, respectively.

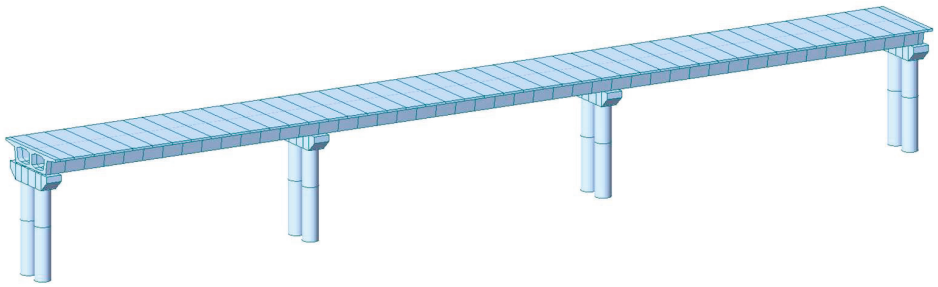

Figure 4. Midas finite element model of bridge.

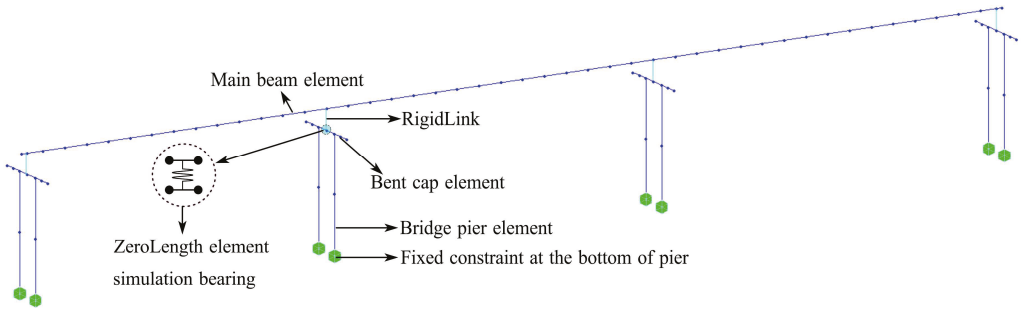

Figure 5. OpenSees finite element model of bridge.

3. Classification of Bridge Seismic Damage Levels and Selection of Damage Parameters

3.1. Classification of Bridge Seismic Damage Levels

The Standard for Classification Seismic Damage to Buildings and Structures (GB/T 24335-2009) [17] classify the seismic damage into five levels: intact, slight damage, moderate damage, severe damage and collapse [18]. This study adopts this classification for bridge and provides qualitative descriptions for each damage level, as summarized in Table 1.

Table 1. Qualitative descriptions of bridge seismic damage levels.

Seismic Damage Levels	Damage Description
Intact	The bridge components remain undamaged, and normal operation is maintained.
Slight damage	Surface-level concrete spalling or cracks are observed, normal operation can resume after minor repairs.
Moderate damage	Significant longitudinal or lateral displacement occurs, normal operation is achievable following emergency repairs.
Severe damage	Through cracks develop in the structure, partial operation can be restored with temporary reinforcement.
Collapse	Girder collapse or pier failure occurs, resulting in complete functional loss and operational shutdown.

3.2. Seismic Damage Parameters for Bridges

Bridge piers and bearings are the primary components susceptible to seismic damage. Accordingly, separate damage parameters were selected for each to assess their performance independently.

3.2.1. Seismic Damage Parameters of Bridge Piers

Due to their nonlinear response characteristics, which are mainly governed by flexural damage [19], the displacement ductility ratio was selected as the seismic damage parameter for bridge piers in this study [20]. The calculation method is shown in Equation (1).

$$\mu_d = \frac{\Delta_d}{\Delta_{cy1}} \tag{1}$$

where μ_d is the displacement ductility ratio of the pier, Δ_d is the relative displacement of the pier top, and Δ_{cy1} is the relative displacement at the pier top when the outermost longitudinal reinforcement steel first yields. The relationship between the bridge seismic levels and μ_d is summarized in Table 2.

Table 2. Relationship between bridge seismic damage levels and $\mu_{d.}$

Seismic Damage Levels	Intact	Slight Damage	Moderate Damage	Severe Damage	Collapse
μ_d	$0 \le \mu_d < \mu_{cy1}$	$\mu_{cy1} \le \mu_d < \mu_{cy}$	$\mu_{cy} \le \mu_d < \mu_{c4}$	$\mu_{c4} \le \mu_d < \mu_{c\max}$	$\mu_d \ge \mu_{c\max}$

Where μ_{cy1} is the displacement ductility ratio at the first yield of the outermost longitudinal reinforcement in the bridge pier. μ_{cy} is the equivalent displacement ductility ratio, defined as the ratio of the ultimate displacement to the yield displacement of the bridge pier, where a higher value indicates superior ductility. μ_{c4} represent the displacement ductility ratio when the compressive strain of the cover concrete reaches 0.004, which corresponds to the stage of complete spalling of cover concrete and initiation of crake in the core concrete region. Finally, $\mu_{c\max}$ is the maximum ductility ratio, attained when the core concrete crushes, the longitudinal reinforcing steel yields, and the stirrups fracture. Since μ_{cy1} only accounts for the initial yield and ignores the subsequent nonlinear deformations, it is defined as $\mu_{cy1} = 1$. The calculation methods for μ_{cy}, μ_{c4} and $\mu_{c\max}$ are shown in Equation (2)–(4) [21].

$$\mu_{cy} = \frac{\Delta_{cy}}{\Delta_{cy1}} = \frac{\varphi_{y2}}{\varphi_{y1}} \tag{2}$$

$$\mu_{c4} = \frac{\Delta_{cy} + \left(\frac{0.08 \cdot L + 0.022 \cdot f_y \cdot d_s}{2}\right) \cdot (\varphi_{c4} - \varphi_{y2}) \cdot \left(L - \frac{0.08 \cdot L + 0.022 \cdot f_y \cdot d_s}{2}\right)}{\Delta_{cy1}} \tag{3}$$

$$\mu_{c\max} = \mu_{c4} + 3 \tag{4}$$

where φ_{y1} denotes the curvature at the first yield of the outermost longitudinal reinforcing steel in the bridge pier. φ_{y2} is the equivalent yield curvature, and φ_{c4} is the curvature when the compressive strain of the cover concrete reaches 0.004. L denotes the height of the bridge pier. f_y is the yield strength of the reinforcement steel. d_s is the diameter of the steel. This study adopted the following parameter values: $\varphi_{y1} = 8.164 \times 10^{-4}$ rad/m, $\varphi_{y2} = 9.233 \times 10^{-4}$ rad/m, $\varphi_{c4} = 3.421 \times 10^{-3}$ rad/m, $L = 10$ m, $f_y = 400$ MPa and $d_s = 0.03$ m. Based on these calculations, Table 2 was converted to Table 3.

Table 3. Relationship between bridge seismic damage levels and $\mu_{d.}$

Seismic Damage Levels	Intact	Slight Damage	Moderate Damage	Severe Damage	Collapse
μ_d	$0 \le \mu_d < 1$	$1 \le \mu_d < 1.132$	$1.132 \le \mu_d < 1.893$	$1.893 \le \mu_d < 4.893$	$\mu_d \ge 4.893$

3.2.2. Seismic Damage Parameters of Bearings

Due to the relatively low horizontal displacement threshold of pot rubber bearings, this study selected the shear deformation d as the seismic damage parameter for bearings, following the research by Zhong et al. [22]. The relationship between bridge seismic damage level and d is shown in Table 4.

Table 4. Relationship between bridge seismic damage levels and d.

Seismic Damage Levels	Intact	Slight Damage	Moderate Damage	Severe Damage	Collapse
d/mm	$0 \le d < 25$	$25 \le d < 50$	$50 \le d < 75$	$75 \le d < 90$	$d \ge 90$

4. Probabilistic Seismic Hazard Assessment of the Study Site

4.1. Overview of the CPSHA Method

(1) The methodology adopted the principle of three-level potential seismic source zone division and constructed the corresponding seismic activity model. This model comprises seismic statistical zones (seismic zones) and potential seismic source zones of background seismic activity (background sources), and potential seismic source zones of tectonic structures (tectonic sources), which are spatially superimposed [23]. The seismic statistical zone serves as the bottom layer and the statistical unit for seismic activity parameters. The background source, as the middle layer, reflects the characteristics of background seismic activity within the seismic zones and differences in seismic tectonic models. The tectonic source, as the top layer, reflects the characteristics of moderate-to-strong seismic activities associated with local tectonic structures. The representation of spatial inhomogeneity in seismic activity varies across different magnitude ranges: for small-to-moderate magnitudes, it is jointly represented by tectonic sources and background sources, whereas for moderate-to-strong magnitudes, it is represented solely by tectonic sources.

(2) The seismic magnitudes in seismic zone follow the Gutenberg–Richter relationship, as shown in Equation (5) [24].

$$\lg N = a - b \cdot M (M_0 \le M \le M_u) \tag{5}$$

where N is the number of earthquakes with magnitudes greater than or equal to M, M is the seismic magnitude; M_0 is the threshold magnitude, defined as the minimum magnitude that causing damage; M_u is the magnitude upper limit, which is the maximum possible seismic magnitude; a and b are statistical parameters, where a reflects the level of seismic activity over a specific period, and b reflects the proportional relationship between large and small earthquakes. The probability density function of the magnitude distribution in seismic zones can be derived from Equation (5), as shown in Equation (6) [25].

$$f(M) = \frac{\beta \cdot e^{-\beta \cdot (M - M_0)}}{1 - e^{-\beta \cdot (M_u - M_0)}} (M_0 \le M \le M_u) \tag{6}$$

where $\beta = b \cdot \ln 10$.

(3) The seismic activity in a seismic zone over a period follows a Poisson distribution, implying that the probabilistic characteristics of seismic activity in the zone can be determined by a parameter v. The two-state Poisson model assumes that seismic activity in the seismic zone has "active" and "inactive" states, making it more consistent with the actual occurrence pattern of earthquakes. The probability P_K of K earthquakes occurring in the seismic zone over the next T years as shown in Equation (7) [26].

$$P_K = \frac{(v \cdot T)^K}{K!} \cdot e^{-v \cdot T} \tag{7}$$

(4) Seismic activity within a seismic zone is non-uniformly distributed, whereas it is uniformly distributed within a potential seismic source zone. The probability that an earthquake in magnitude bin m_j occurs in the i-th potential seismic source zone is denoted as $f_{i,mj}$. Given that the area of the i-th potential seismic source zone is A_i, the probability $P(m_j \mid i)$ of an earthquake in magnitude bin m_j occurring at any point within the i-th potential seismic source zone as shown in Equation (8) [27].

$$P(m_j | i) = f_{i,m_j} / A_i \tag{8}$$

(5) Equation (9) was derived based on Equation (5) to Equation (8).

$$P(m_j) = \frac{2}{\beta} \cdot f_m(m_j) \cdot \mathrm{sh}(\beta \cdot \Delta m/2) = \frac{2 \cdot e^{-\beta \cdot (m_j - M_0)}}{1 - e^{-\beta \cdot (M_u - M_0)}} \cdot \mathrm{sh}(\beta \cdot \Delta m/2) \tag{9}$$

where $P(m_j)$ is the probability that an earthquake within the seismic zone lies within the magnitude bin $m_j \pm 0.5\Delta m$, and sh($\beta \cdot \Delta m/2$) denoted the hyperbolic function with $\beta \cdot \Delta m/2$ as its argument. Assuming that an earthquake of magnitude m_j occurs randomly in the k-th seismic zone, the probability of generating a PGA $\geq y_q$ at a given site is expressed by Equation (10).

$$\begin{aligned} P(\mathrm{PGA} \geq y_q)_k = & \sum_{j=1}^{N_m} \sum_{i=1}^{N_{ks}} \int \int P\left(\mathrm{PGA} \geq y_q \middle| m_j, (x,y)_{ki}\right) \\ & \cdot \frac{2 \cdot e^{-\beta_k \cdot (m_j - M_0)}}{1 - e^{-\beta_k \cdot (M_u - M_0)}} \cdot \frac{f_{ki,m_j}}{A_{ki}} \cdot \mathrm{sh}\left(-\frac{\beta_k}{2} \cdot \Delta m\right) \mathrm{d}x\mathrm{d}y \end{aligned} \tag{10}$$

where N_m is the total number of magnitude bins, N_{ks} is the number of potential seismic source zones in the k-th seismic zone, y_q is the specified PGA value, and dxdy is the cell area of the gridded potential seismic source zones. By integrating the effects of N_z seismic zones in the area using the total probability formula, the seismic hazard probability can be calculated using Equation (11).

$$\begin{aligned} P(\mathrm{PGA} \geq y_q) = 1 - \exp\Bigg[& -\sum_{j=1}^{N_m} \sum_{i=1}^{N_{ks}} \sum_{k=1}^{N_z} \int \int P\left(\mathrm{PGA} \geq y_q \middle| m_j, (x,y)_{ki}\right) \\ & \cdot \frac{2 \cdot e^{-\beta_k \cdot (m_j - M_0)}}{1 - e^{-\beta_k \cdot (M_u - M_0)}} \cdot \frac{f_{ki,m_j}}{A_{ki}} \cdot \mathrm{sh}\left(-\frac{\beta_k}{2} \cdot \Delta m\right) \mathrm{d}x\mathrm{d}y \Bigg] \end{aligned} \tag{11}$$

(6) The PGA attenuation relationship shown in Equation (12) is adopted [28].

$$\lg \mathrm{PGA} = A + B \cdot M + C \cdot \lg\left(R + D \cdot e^{E \cdot M}\right) \tag{12}$$

where M is the surface wave magnitude, R is the epicentral distance, and A, B, C, D and E are coefficients, with values shown in Table 5.

Table 5. Coefficients of the PGA attenuation relationship.

Direction	*A*		*B*		*C*	*D*	*E*
	$M \geq 6.5$	$M < 6.5$	$M \geq 6.5$	$M < 6.5$			
Long axis	−0.363	1.437	0.791	0.513	−2.103	2.088	0.399
Short axis	−1.147	0.712	0.788	0.502	−1.825	0.944	0.447

Where the Long axis refers to the principal direction in the spatial distribution of ground motion parameters, along which these parameters vary gradually and exhibit a wider zone of influence. That is, ground motion parameter attenuation along the Long Axis occurs at relatively low gradient with increasing distance from the seismic source. In contrast, the Short axis represents the principal direction in which ground motion parameters change more rapidly and have a narrow influence range. Along the Short axis, the values decay more sharply with increasing distance from the seismic source.

(7) According to the conversion coefficient method of the fifth-generation seismic ground motion parameter zoning scheme, Equation (13) is adopted to convert bedrock PGA to site class II PGA [29].

$$\mathrm{PGA}_{II} = F_a \cdot \mathrm{PGA}_J \tag{13}$$

where PGA_J is the bedrock PGA, PGA_{II} is the PGA for class II sites, F_a is the conversion coefficient, which is calculated using Equation (14) [30].

$$F_a = \begin{cases} 1.25 & PGA_J \leq 62.5gal \\ 1.25 - (PGA_J - 62.5)/1250 & 62.5gal < PGA_J \leq 375gal \\ 1 & PGA_J > 375gal \end{cases} \quad (14)$$

where 1 gal = 1 cm/s^2.

4.2. Case Study

Based on the fifth-generation seismic ground motion parameter zoning scheme, the study area (extended 200 km from the study site) was influenced by the Tancheng–Lushan seismic source zone, the Lower Yangtze–South Yellow Sea seismic source zone, and the North China Plain seismic source zone. These three source zones encompass 28, 4 and 14 potential seismic source zones, respectively, totaling 46 potential seismic source zones, as shown in Figure 6.

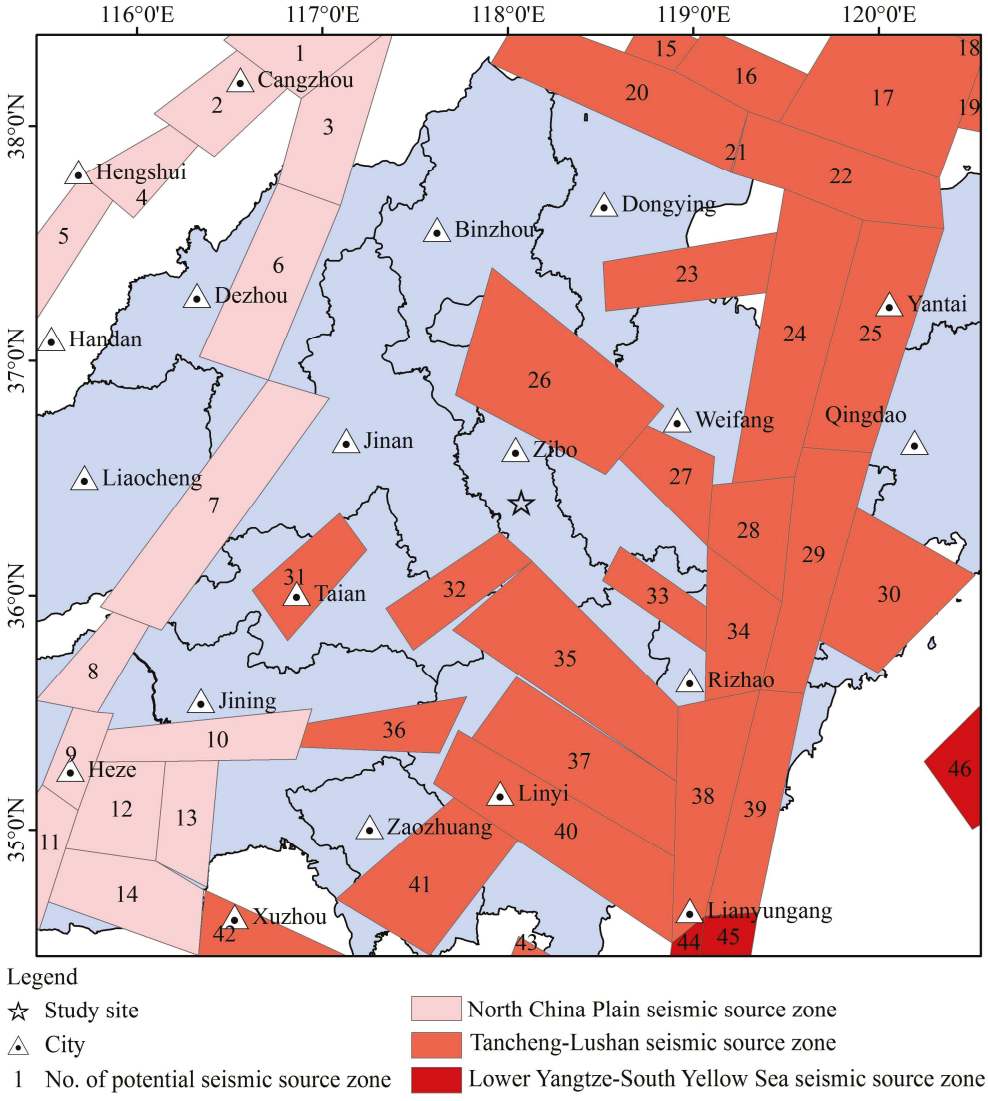

Figure 6. Distribution of seismic zones and potential seismic source areas.

According to the fifth-generation seismic ground motion parameter zoning scheme, the values of M_0, M_u, b and the annual average occurrence rate $v_{4.0}$ for earthquakes above magnitude 4.0 in each seismic zone are shown in Table 6.

Table 6. Seismic activity parameters.

Seismic Source Zone	M_0	M_u	b	$v_{4.0}$
Lower Yangtze–South Yellow Sea seismic source zone	4.0	7.5	0.85	3.0
Tancheng–Lushan seismic source zone		8.5	0.85	4.0
North China Plain seismic source zone		8.0	0.86	4.6

There are 9 potential seismic source zones affecting the seismic hazard of the study area, and their seismic spatial distribution coefficients are shown in Table 7.

Table 7. Seismic spatial distribution coefficients.

No.	Potential Source Zones	Magnitude Classification						
		[4.0, 4.9]	[5.0, 5.4]	[5.5, 5.9]	[6.0, 6.4]	[6.5, 6.9]	[7.0, 7.4]	≥7.5
31	Changqing potential seismic source zone	0.00331	0.00744	0.00958	0	0	0	0
26	Zibo potential seismic source zone	0.00834	0.00596	0.01421	0.02014	0	0	0
35	Laiwu potential seismic source zone	0.00797	0.00569	0.01254	0.02221	0	0	0
32	Tai'an potential seismic source zone	0.00463	0.00859	0.00979	0.01279	0	0	0
25	Liaocheng potential seismic source zone	0.00621	0.00896	0.01362	0.02778	0.08013	0	0
27	Linqu potential seismic source zone	0.00837	0.00592	0.01412	0.02707	0.06576	0	0
8	Fanxian potential seismic source zone	0.00711	0.00889	0.00963	0.02011	0.04854	0.05853	0
17	Bozhong No.1 potential seismic source zone	0.01225	0.00855	0.02261	0.03999	0.04926	0.22801	0.58423
39	Tancheng potential seismic source zone	0.00982	0.00671	0.01426	0.01934	0.03212	0.14191	0.11578

The fifth-generation seismic ground motion parameter zoning scheme specifies the PGA with a 10% probability of exceedance over 50 years as the design basis earthquake for general structures. Using the seismic safety assessment software SECR2019, the PGA values for the study site corresponding to 2%, 10% and 63% probabilities of exceedance over 50 years are calculated as 171.16 gal, 98.10 gal and 28.61 gal, respectively. These results place the study site within the 0.10 g zone, which corresponds to basic seismic intensity zone VII.

5. Seismic Fragility Assessment of the Study Object Based on the Monte Carlo Method and Response Surface Method

5.1. Uncertainty Analysis of Structural-Seismic Motion Samples

5.1.1. Probability Distribution and Normalization of Random Variables

In seismic analysis, uncertainties in bridge structures primarily arise from variations in material properties, geometric characteristics, and construction practices. Furthermore, ground motion intensity significantly influences structural responses [31]. Therefore, this study selected five random variables for fragility assessment: concrete elastic modulus E_c, damping ratio γ, steel yield strength f_y, steel elastic modulus E_s, and PGA. Among them, E_c, f_y and E_s follow log-normal distributions [32–34], whereas γ follows a normal distribution [35].

The Central Composite Design (CCD) method is a widely used approach for constructing response surface models due to its simplicity, efficiency, and reasonable number of required trials [36]. The random variables were normalized using the CCD method as shown in Equation (15). The probability distributions and corresponding statistical parameters of these random variables are summarized in Table 8.

$$x_i = \frac{\xi_i - (\xi_{i,\max} + \xi_{i,\min})/2}{(\xi_{i,\max} + \xi_{i,\min})/2} \tag{15}$$

where ξ_i, $\xi_{i,\min}$ and $\xi_{i,\max}$ denote the value, minimum value and maximum value of the i-th random variable, respectively; x_i is the normalized value of the i-th random variable, where $x_i = 1$, 0 and -1 represent ξ_i taking the maximum value, mean value and minimum value, respectively. $i = 1$, 2, 3, 4 and 5 represents the variables E_c, γ, f_y, E_s and PGA, respectively.

Table 8. Probability distributions and statistical parameters of random variables.

Random Variables	Probability Distribution	Variables Before and After Normalization	Minimum Value	Mean Value	Maximum Value	Standard Deviation	Coefficient of Variation
E_c/MPa	Log-normal distribution	ξ_1	2.99×10^4	3.25×10^4	3.51×10^4	2600	0.080
		x_1	-1	0	1		
γ	Normal distribution	ξ_2	0.035	0.05	0.065	0.015	0.300
		x_2	-1	0	1		
f_y/MPa	Log-normal distribution	ξ_3	372	400	428	28	0.070
		x_3	-1	0	1		
E_s/MPa	Log-normal distribution	ξ_4	1.94×10^4	2.00×10^4	2.06×10^4	6000	0.030
		x_4	-1	0	1		
PGA/g		ξ_5	0.2	0.6	1.0		
		x_5	-1	0	1		

5.1.2. Selection of Ground Motion Inputs

Due to the high lateral stiffness of the bridge, this study only considered longitudinal ground motion input. Fifteen measured ground motions were selected based on the target response spectrum, as listed in Table 9, with their acceleration response spectrum shown in Figure 7. These ground motions were carefully selected to be representative of the seismic hazard at the site, encompassing a range of magnitudes and source-to-site distances. The PGA of the measured ground motions was adjusted to 20 groups with intervals of 0.05 g, ranging from a minimum of 0 to a maximum of 1.0 g. The natural ground motions are amplitude-scaled to these values, resulting in a total of 300 ground motion records.

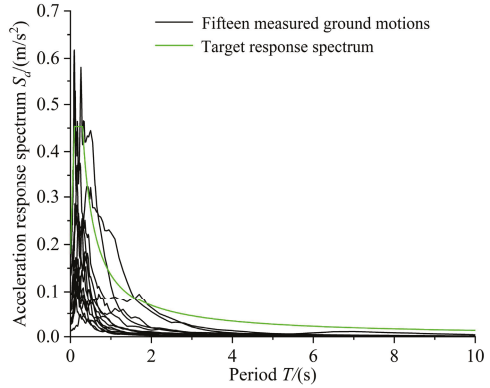

Figure 7. Acceleration response spectrum.

Table 9. Measured ground motion information.

No.	Earthquake	Year	Station Name	*M*	*R*/km	v_{s30}/m·s^{-1}
1	Imperial Valley-04	1953	El Centro Array #9	5.50	15.11	213.44
2	Lytle Creek	1970	Castaic-Old Ridge Route	5.33	103.23	450.28
3	Lytle Creek	1970	Cedar Springs Pumphouse	5.33	21.33	477.22
4	Lytle Creek	1970	Lake Hughes #1	5.33	90.25	425.34
5	Lytle Creek	1970	Puddingstone Dam (Abutment)	5.33	29.49	421.44
6	Lytle Creek	1970	Santa Anita Dam	5.33	42.14	667.13
7	Lytle Creek	1970	Wrightwood-6074 Park Dr	5.33	10.70	486.00
8	San Fernando	1971	Cedar Springs Pumphouse	6.61	92.25	477.22
9	San Fernando"	1971	Colton-So Cal Edison	6.61	96.81	301.95
10	San Fernando	1971	Fort Tejon	6.61	59.52	394.18
11	San Fernando	1971	Gormon-Oso Pump Plant	6.61	43.95	308.35
12	San Fernando	1971	Tehachapi Pump	6.61	61.75	669.48
13	San Fernando	1971	Wrightwood-6074 Park Dr	6.61	61.64	486.00
14	Point Mugu	1973	Port Hueneme	5.65	15.48	248.98
15	Hollister-03	1974	Gilroy Array #1	5.14	9.99	1428.14

Note, v_{s30} is the average shear wave velocity within 30 m below ground.

5.2. Development of Response Surface Model

5.2.1. Introduction to Response Surface Model

The Response Surface Method is a statistical approach used to analyze the relationship between response variables and multiple input variables [37,38]. Owing to the nonlinear response of bridges under seismic action, a quadratic polynomial is typically selected as the response surface function [39,40], as expressed in Equation (16).

$$\hat{y} = a_0 + \sum_{i=0}^{k} a_i \cdot x_i + \sum_{i=1}^{k-1} \sum_{j>1}^{k} a_{ij} \cdot x_i \cdot x_j + \sum_{i=1}^{k} a_{ii} \cdot {x_i}^2 + \varepsilon \tag{16}$$

where k is the number of input variables, x_i, and x_j represent the values of input variables, a_0, a_i, a_{ii} and a_{ij} are undetermined coefficients estimated using the CCD method, and ε is the error term, which follows a normal distribution with a mean of zero.

For the finite element model of the bridge, conducting $N = 2^k + 2k + 1$ times of IDA yields a system of linear equations for the unknow coefficients a_0, a_i, a_{ii} and a_{ij}. Using the least squares method to obtain the unbiased estimates of these undetermined coefficients, and validate the resulting response surface model using the coefficient of determination R^2 and the adjusted coefficient of determination ${R_a}^2$. Following common practice in response surface modeling, at least one of R^2 and ${R_a}^2$ is required to exceed 0.9 [41], as defined in Equations (17) and (18).

$$R^2 = \frac{\alpha^T X^T Y - (E^T Y)^2 / N}{Y^T Y - (E^T Y)^2 / N} \tag{17}$$

$${R_a}^2 = 1 - \frac{(1 - R^2)(N - 1)}{(N - k)} \tag{18}$$

where α denotes the vector of undetermined coefficients, X represents the design matrix of variable, Y is the true response vector, E is the unit vector.

5.2.2. IDA Analysis Based on the CCD Method

This study selected $k = 5$, so the CCD method was used to design $N = 43$ groups of IDA. Each group comprised 15 ground records, yielding a total of 645 analyses. The mean values and standard deviations of the seismic damage parameters for the side piers, middle piers, and their corresponding bearings in each group were recorded, as summarized in Table 10.

Table 10. Results of IDA.

No.	x_1	x_2	x_3	x_4	x_5	Bridge Piers				Bearings			
						μ_d of Side Piers		μ_d of Middle Piers		*d* of Side Pier Bearings/mm		*d* of Middle Pier Bearings/mm	
						Mean Value	Standard Deviation	Mean Value	Standard Deviation	Mean Value	Standard Deviation	Mean Value	Standard Deviation
1	−1	−1	−1	−1	−1	0.24	0.22	0.24	0.22	27.33	25.07	26.51	24.39
2	−1	−1	−1	−1	1	1.10	1.01	1.08	0.99	103.75	95.29	102.16	93.87
3	−1	−1	−1	1	−1	0.22	0.20	0.22	0.20	23.97	21.95	21.55	19.80
4	−1	−1	−1	1	1	1.08	0.99	1.07	0.98	99.46	91.30	98.45	90.41
5	−1	−1	1	−1	−1	0.22	0.22	0.22	0.22	24.05	22.06	21.30	19.60
6	−1	−1	1	−1	1	1.08	1.00	1.06	0.98	99.87	91.73	99.33	91.27
7	−1	−1	1	1	−1	0.20	0.18	0.20	0.19	19.30	17.68	18.10	16.63
8	−1	−1	1	1	1	1.05	0.97	1.04	0.95	97.57	89.56	96.36	88.49
9	−1	1	−1	−1	−1	0.20	0.19	0.20	0.19	24.33	22.29	20.94	19.24
10	−1	1	−1	−1	1	1.08	0.99	1.07	0.98	100.16	91.82	99.01	90.76
11	−1	1	−1	1	−1	0.20	0.18	0.20	0.18	19.74	18.07	18.45	16.90
12	−1	1	−1	1	1	1.06	0.97	1.03	0.95	97.89	89.66	96.43	88.35
13	−1	1	1	−1	−1	0.20	0.19	0.20	0.18	20.08	18.40	17.96	16.48
14	−1	1	1	−1	1	1.05	0.96	1.04	0.95	98.11	89.94	96.84	88.77
15	−1	1	1	1	−1	0.18	0.17	0.18	0.17	16.52	15.10	14.82	13.58
16	−1	1	1	1	1	1.02	0.94	0.99	0.91	94.96	86.98	94.63	86.70
17	1	−1	−1	−1	−1	0.22	0.20	0.21	0.20	23.81	21.84	20.84	19.18
18	1	−1	−1	−1	1	1.08	0.99	1.07	0.98	100.33	92.15	98.87	90.85
19	1	−1	−1	1	−1	0.20	0.18	0.20	0.18	20.56	18.83	17.73	16.29
20	1	−1	−1	1	1	1.05	0.96	1.03	0.95	98.41	90.34	96.94	89.03
21	1	−1	1	−1	−1	0.20	0.18	0.20	0.19	20.06	18.40	17.81	16.39
22	1	−1	1	−1	1	1.05	0.96	1.04	0.95	98.11	90.14	96.51	88.68
23	1	−1	1	1	−1	0.19	0.17	0.18	0.17	15.63	14.32	15.17	13.94
24	1	−1	1	1	1	1.00	0.92	1.00	0.92	95.46	87.63	94.52	86.80
25	1	1	−1	−1	−1	0.20	0.18	0.19	0.18	20.03	18.35	17.93	16.46
26	1	1	−1	−1	1	1.05	0.97	1.04	0.95	97.92	89.76	96.54	88.49
27	1	1	−1	1	−1	0.20	0.18	0.19	0.18	16.17	14.78	14.30	13.09
28	1	1	−1	1	1	1.02	0.94	1.00	0.91	95.61	87.58	93.92	86.05
29	1	1	1	−1	−1	0.18	0.17	0.18	0.17	15.85	14.52	14.95	13.72
30	1	1	1	−1	1	1.02	0.93	1.00	0.92	95.10	87.18	94.31	86.45
31	1	1	1	1	−1	0.15	0.13	0.16	0.15	11.96	10.93	11.57	10.60
32	1	1	1	1	1	0.99	0.91	0.98	0.90	93.54	85.68	92.03	84.32
33	1	0	0	0	0	0.65	0.59	0.64	0.59	56.09	51.46	54.89	50.38
34	−1	0	0	0	0	0.67	0.62	0.66	0.60	57.40	52.66	55.74	51.16
35	0	1	0	0	0	0.66	0.60	0.64	0.59	56.21	51.51	54.71	50.14
36	0	−1	0	0	0	0.67	0.61	0.66	0.60	57.59	52.87	56.12	51.56
37	0	0	1	0	0	0.66	0.60	0.65	0.60	56.12	51.49	54.65	50.16
38	0	0	−1	0	0	0.67	0.62	0.66	0.61	57.48	52.74	56.03	51.43
39	0	0	0	1	0	0.66	0.60	0.65	0.60	55.96	51.31	54.47	49.97
40	0	0	0	−1	0	0.67	0.62	0.66	0.61	57.53	52.81	56.08	51.50
41	0	0	0	0	1	1.05	0.96	1.03	0.95	98.07	89.96	96.53	88.57
42	0	0	0	0	−1	0.20	0.18	0.20	0.19	20.13	18.44	17.92	16.46
43	0	0	0	0	0	0.66	0.61	0.66	0.61	56.63	51.95	55.94	51.07

The R^2 and ${R_a}^2$ values of the mean and standard deviation of the seismic damage parameters of the side piers, middle piers, and their corresponding bearings were calculated using Equations (17) and (18), as shown in Table 11.

Table 11. Calculation results of R^2 and ${R_a}^2$.

Parameters	Bridge Piers				Bearings			
	μ_d of Side Piers		μ_d of Middle Piers		*d* of Side Pier Bearings/mm		*d* of Middle Pier Bearings/mm	
	Mean Value	Standard Deviation	Mean Value	Standard Deviation	Mean Value	Standard Deviation	Mean Value	Standard Deviation
R^2	0.9998	0.9998	0.9998	0.9997	0.9998	0.9998	0.9998	0.9998
${R_a}^2$	0.9997	0.9997	0.9995	0.9995	0.9997	0.9997	0.9997	0.9997

From Table 11, both R^2 and ${R_a}^2$ exceed 0.9, confirming that the CCD method effectively captures trends in the simulation data and accurately reflects the influence of each random variable on the seismic damage of the bridge.

5.2.3. Solution of Response Surface Model

By integrating the data from Table 10 with Equation (16), the response surface model was solved. The response surface functions for the mean and standard deviation of the displacement ductility ratio u_d of side piers are shown in Equation (19) and Equation (20), respectively.

$$\begin{aligned} u_{d,m} &= 0.663 - 0.018x_1 - 0.011x_2 - 0.013x_3 - 0.011x_4 + 0.424x_5 \\ &-0.004{x_1}^2 + 0.001{x_2}^2 + 0.001{x_3}^2 + 0.001{x_4}^2 - 0.039{x_5}^2 \\ &+0.001x_1x_2 - 0.002x_1x_3 - 0.001x_1x_4 - 0.004x_1x_5 \\ &-0.001x_2x_3 + 0.001x_2x_4 - 0.001x_2x_5 \\ &-0.003x_3x_4 - 0.003x_3x_5 - 0.004x_4x_5 \end{aligned} \tag{19}$$

$$\begin{aligned} u_{d,\sigma} &= 0.607 - 1.294 \times 10^{-2}x_1 - 1.059 \times 10^{-2}x_2 - 1.088 \times 10^{-2}x_3 - 1.147 \times 10^{-2}x_4 + 3.897 \times 10^{-1}x_5 \\ &-1.737 \times 10^{-3}{x_1}^2 - 1.737 \times 10^{-3}{x_2}^2 + 3.263 \times 10^{-3}{x_3}^2 + 3.263 \times 10^{-3}{x_4}^2 - 3.674 \times 10^{-2}{x_5}^2 \\ &+1.563 \times 10^{-3}x_1x_2 - 3.438 \times 10^{-3}x_1x_3 - 3.125 \times 10^{-4}x_1x_4 - 2.813 \times 10^{-3}x_1x_5 \\ &-1.563 \times 10^{-3}x_2x_3 + 1.563 \times 10^{-3}x_2x_4 - 9.375 \times 10^{-4}x_2x_5 \\ &-2.188 \times 10^{-3}x_3x_4 - 3.438 \times 10^{-3}x_3x_5 - 1.563 \times 10^{-3}x_4x_5 \end{aligned} \tag{20}$$

The response surface functions for the mean and standard deviation of the displacement ductility ratio u_d of middle piers are shown in Equation (21) and Equation (22), respectively.

$$\begin{aligned} u_{d,m} &= 0.653 - 1.147 \times 10^{-2}x_1 - 1.265 \times 10^{-2}x_2 - 1.118 \times 10^{-2}x_3 - 1.118 \times 10^{-2}x_4 + 4.176 \times 10^{-1}x_5 \\ &-2.487 \times 10^{-3}{x_1}^2 - 2.487 \times 10^{-3}{x_2}^2 + 2.513 \times 10^{-3}{x_3}^2 + 2.513 \times 10^{-3}{x_4}^2 - 3.749 \times 10^{-2}{x_5}^2 \\ &+9.375 \times 10^{-4}x_1x_2 - 3.125 \times 10^{-4}x_1x_3 - 3.125 \times 10^{-4}x_1x_4 - 2.188 \times 10^{-3}x_1x_5 \\ &-3.125 \times 10^{-4}x_2x_3 - 3.125 \times 10^{-4}x_2x_4 - 2.188 \times 10^{-3}x_2x_5 \\ &-1.563 \times 10^{-3}x_3x_4 - 3.438 \times 10^{-3}x_3x_5 - 4.688 \times 10^{-3}x_4x_5 \end{aligned} \tag{21}$$

$$\begin{aligned} u_{d,\sigma} &= 0.602 - 1.029 \times 10^{-2}x_1 - 1.206 \times 10^{-2}x_2 - 9.118 \times 10^{-3}x_3 - 1.088 \times 10^{-2}x_4 + 3.812 \times 10^{-1}x_5 \\ &-6.046 \times 10^{-3}{x_1}^2 - 6.046 \times 10^{-3}{x_2}^2 + 3.954 \times 10^{-3}{x_3}^2 + 3.954 \times 10^{-3}{x_4}^2 - 3.105 \times 10^{-2}{x_5}^2 \\ &+1.250 \times 10^{-3}x_1x_2 - 6.250 \times 10^{-4}x_1x_3 - 3.908 \times 10^{-17}x_1x_4 - 2.500 \times 10^{-3}x_1x_5 \\ &-1.250 \times 10^{-3}x_2x_3 + 6.250 \times 10^{-4}x_2x_4 - 1.875 \times 10^{-3}x_2x_5 \\ &-1.250 \times 10^{-3}x_3x_4 - 3.750 \times 10^{-3}x_3x_5 - 3.125 \times 10^{-3}x_4x_5 \end{aligned} \tag{22}$$

The response surface functions for the mean and standard deviation of the shear deformation d of side pier bearings are shown in Equation (23) and Equation (24), respectively.

$$\begin{aligned} d_\mu &= 56.812 - 1.466x_1 - 1.502x_2 - 1.608x_3 - 1.580x_4 + 38.965x_5 \\ &-8.989 \times 10^{-2}{x_1}^2 + 6.511 \times 10^{-2}{x_2}^2 - 3.489 \times 10^{-2}{x_3}^2 - 8.989 \times 10^{-2}{x_4}^2 + 2.265{x_5}^2 \\ &-8.375 \times 10^{-2}x_1x_2 - 3.000 \times 10^{-2}x_1x_3 + 1.375 \times 10^{-1}x_1x_4 + 4.363 \times 10^{-1}x_1x_5 \\ &+5.750 \times 10^{-2}x_2x_3 + 5.500 \times 10^{-2}x_2x_4 + 3.238 \times 10^{-1}x_2x_5 \\ &-1.375 \times 10^{-2}x_3x_4 + 3.650 \times 10^{-1}x_3x_5 + 3.513 \times 10^{-1}x_4x_5 \end{aligned} \tag{23}$$

$$\begin{aligned} d_\sigma &= 52.119 - 1.343x_1 - 1.430x_2 - 1.473x_3 - 1.472x_4 + 35.755x_5 \\ &-8.024 \times 10^{-2}{x_1}^2 + 4.976 \times 10^{-2}{x_2}^2 - 2.524 \times 10^{-2}{x_3}^2 - 8.024 \times 10^{-2}{x_4}^2 + 2.060{x_5}^2 \\ &-7.781 \times 10^{-2}x_1x_2 - 2.594 \times 10^{-2}x_1x_3 + 1.266 \times 10^{-1}x_1x_4 + 4.009 \times 10^{-1}x_1x_5 \\ &+5.219 \times 10^{-2}x_2x_3 + 4.969 \times 10^{-2}x_2x_4 + 2.553 \times 10^{-1}x_2x_5 \\ &-1.344 \times 10^{-2}x_3x_4 + 3.347 \times 10^{-1}x_3x_5 + 3.122 \times 10^{-1}x_4x_5 \end{aligned} \tag{24}$$

The response surface functions for the mean and standard deviation of the shear deformation d of middle pier bearings are shown in Equation (25) and Equation (26), respectively.

$$
\begin{aligned}
d_\mu = {} & 55.381 - 1.463x_1 - 1.439x_2 - 1.345x_3 - 1.425x_4 + 39.280x_5 \\
& + 3.786 \times 10^{-3}{x_1}^2 + 1.038 \times 10^{-1}{x_2}^2 + 2.879 \times 10^{-2}{x_3}^2 - 3.621 \times 10^{-2}{x_4}^2 + 1.914{x_5}^2 \\
& + 5.750 \times 10^{-2}x_1x_2 + 1.238 \times 10^{-1}x_1x_3 + 1.150 \times 10^{-1}x_1x_4 + 3.050 \times 10^{-1}x_1x_5 \\
& + 1.106 \times 10^{-1}x_2x_3 + 6.813 \times 10^{-2}x_2x_4 + 2.706 \times 10^{-1}x_2x_5 \\
& + 1.006 \times 10^{-1}x_3x_4 + 2.744 \times 10^{-1}x_3x_5 + 1.956 \times 10^{-1}x_4x_5
\end{aligned} \tag{25}
$$

$$
\begin{aligned}
d_\sigma = {} & 50.792 - 1.344x_1 - 1.385x_2 - 1.236x_3 - 1.328x_4 + 36.033x_5 \\
& + 1.310 \times 10^{-2}{x_1}^2 + 9.310 \times 10^{-2}{x_2}^2 + 3.810 \times 10^{-2}{x_3}^2 - 2.190 \times 10^{-2}{x_4}^2 + 1.758{x_5}^2 \\
& + 5.313 \times 10^{-2}x_1x_2 + 1.144 \times 10^{-1}x_1x_3 + 1.069 \times 10^{-1}x_1x_4 + 2.813 \times 10^{-1}x_1x_5 \\
& + 1.031 \times 10^{-1}x_2x_3 + 6.438 \times 10^{-2}x_2x_4 + 2.075 \times 10^{-1}x_2x_5 \\
& + 9.438 \times 10^{-2}x_3x_4 + 2.525 \times 10^{-1}x_3x_5 + 1.763 \times 10^{-1}x_4x_5
\end{aligned} \tag{26}
$$

5.3. Plotting of Seismic Fragility Curves for the Research Object

5.3.1. Calculation of Seismic Exceedance Probability Based on Monte Carlo Method

Using the probability distributions of E_c, γ, f_y and E_s, 10,000 bridge samples were generated via the Monte Carlo Simulation. The PGA range was divided into 20 intensity levels from 0 to 1.0 g with an interval of 0.05 g. By inputting the 10,000 bridge samples across those 20 PGA levels through Equations (19) to (26), the corresponding seismic damage parameter values were obtained [42].

Combining Tables 3 and 4, the number of bridge samples that reached and exceeded each seismic damage level under different PGA intensity levels, along with the corresponding exceedance probabilities were calculated using the method shown in Equation (27) [43].

$$P_f = N\left(\mu \geq LS_f\right)/10,000 \tag{27}$$

where P_f denotes the exceedance probability of each level of seismic damage under different PGA intensity, where f = 1, 2, 3, 4 and 5 representing the intact, slight damage, moderate damage, severe damage and collapse states, respectively $N(\mu \geq LS_f)$, represents the number of bridge samples reaching or exceeding the f-th level of seismic damage.

The calculated exceedance probability for each seismic damage level of the bridge piers and pier bearings is shown in Tables 12–15, respectively.

Table 12. Exceedance probabilities of various seismic damage levels for side piers of the research object.

PGA/g	P_1 of Side Piers	P_2 of Side Piers	P_3 of Side Piers	P_4 of Side Piers	P_5 of Side Piers
0.00	0	0	0	0	0
0.05	0	0	0	0	0
0.10	0	0	0	0	0
0.15	0.0008	0	0	0	0
0.20	0.1154	0.0003	0	0	0
0.25	0.3887	0.1028	0.0004	0	0
0.30	0.6621	0.3119	0.1017	0.0003	0
0.35	0.7752	0.6144	0.2891	0.0892	0
0.40	0.8821	0.7282	0.5881	0.1778	0
0.45	0.9122	0.8267	0.6892	0.2871	0
0.50	0.9282	0.8861	0.7902	0.3901	0
0.55	0.9428	0.9122	0.8236	0.4578	0
0.60	0.9661	0.9318	0.8618	0.5129	0
0.65	0.9707	0.9459	0.8891	0.5782	0.0004
0.70	0.9788	0.9577	0.9208	0.6278	0.0278
0.75	0.9826	0.9681	0.9418	0.6839	0.0472
0.80	0.9878	0.9781	0.9565	0.7208	0.0987

Table 12. *Cont.*

PGA/g	P_1 of Side Piers	P_2 of Side Piers	P_3 of Side Piers	P_4 of Side Piers	P_5 of Side Piers
0.85	0.9918	0.9819	0.9708	0.7677	0.132
0.90	0.9926	0.9912	0.9812	0.8001	0.197
0.95	0.9938	0.9933	0.9911	0.8219	0.277
1.00	0.9968	0.9948	0.9922	0.8302	0.329

Table 13. Exceedance probabilities of various seismic damage levels for middle piers of the research object.

PGA/g	P_1 of Middle Piers	P_2 of Middle Piers	P_3 of Middle Piers	P_4 of Middle Piers	P_5 of Middle Piers
0.00	0	0	0	0	0
0.05	0	0	0	0	0
0.10	0	0	0	0	0
0.15	0.0008	0	0	0	0
0.20	0.1108	0.0003	0	0	0
0.25	0.3711	0.1011	0.0004	0	0
0.30	0.5782	0.2881	0.1011	0.0003	0
0.35	0.7231	0.6101	0.2871	0.0873	0
0.40	0.8652	0.7218	0.5822	0.1725	0
0.45	0.9016	0.8211	0.6865	0.2842	0
0.50	0.9188	0.8812	0.7842	0.3881	0
0.55	0.9392	0.9082	0.8202	0.4566	0
0.60	0.9612	0.9288	0.8588	0.5019	0
0.65	0.9684	0.9415	0.8878	0.5725	0.0004
0.70	0.9721	0.9566	0.9181	0.6225	0.0255
0.75	0.9811	0.9623	0.9402	0.6811	0.0461
0.80	0.9821	0.9702	0.9556	0.7188	0.0977
0.85	0.9861	0.9735	0.9661	0.7608	0.129
0.90	0.9877	0.9821	0.9772	0.7942	0.188
0.95	0.9901	0.9877	0.9812	0.8128	0.256
1.00	0.9912	0.9901	0.9892	0.8218	0.318

Table 14. Exceedance probabilities of various seismic damage levels for side pier bearings of the research object.

PGA/g	P_1 of Side Pier Bearings	P_2 of Side Pier Bearings	P_3 of Side Pier Bearings	P_4 of Side Pier Bearings	P_5 of Side Pier Bearings
0.00	0	0	0	0	0
0.05	0.0021	0	0	0	0
0.10	0.0028	0	0	0	0
0.15	0.3122	0.0004	0	0	0
0.20	0.6651	0.0181	0	0	0
0.25	0.8342	0.2118	0.0003	0	0
0.30	0.9028	0.5542	0.0074	0	0
0.35	0.9374	0.7758	0.0618	0.0001	0
0.40	0.9529	0.8869	0.2529	0.0006	0
0.45	0.9708	0.9328	0.5081	0.0038	0
0.50	0.9823	0.9544	0.7118	0.0296	0.008
0.55	0.9914	0.9682	0.8215	0.1172	0.0032
0.60	0.9933	0.9732	0.8891	0.3028	0.0129
0.65	0.9951	0.9838	0.9322	0.5182	0.0571
0.70	0.9968	0.9907	0.9588	0.7088	0.1682
0.75	0.9978	0.9958	0.9762	0.8618	0.3822
0.80	0.9987	0.9986	0.9881	0.9442	0.6621
0.85	0.9994	0.9991	0.9916	0.9731	0.7824
0.90	1	0.9999	0.9982	0.9918	0.8627
0.95	1	1	0.9997	0.9926	0.9318
1.00	1	1	1	0.9965	0.9688

Table 15. Exceedance probabilities of various seismic damage levels for middle pier bearings of the research object.

PGA/g	P_1 of Middle Pier Bearings	P_2 of Middle Pier Bearings	P_3 of Middle Pier Bearings	P_4 of Middle Pier Bearings	P_5 of Middle Pier Bearings
0.00	0	0	0	0	0
0.05	0.0011	0	0	0	0
0.10	0.0019	0	0	0	0
0.15	0.2871	0.0003	0	0	0
0.20	0.6341	0.0168	0	0	0
0.25	0.7711	0.1475	0.0002	0	0
0.30	0.8574	0.4682	0.0058	0	0
0.35	0.8991	0.7147	0.0521	0.0001	0
0.40	0.9288	0.8318	0.2177	0.0005	0
0.45	0.9481	0.8874	0.4838	0.0021	0
0.50	0.9618	0.9478	0.6688	0.0189	0.0007
0.55	0.9786	0.9608	0.8081	0.1098	0.0025
0.60	0.9824	0.9728	0.8691	0.2575	0.0118
0.65	0.9902	0.9811	0.9219	0.4671	0.0451
0.70	0.9936	0.9901	0.9489	0.6577	0.1287
0.75	0.9974	0.9948	0.9681	0.8429	0.2881
0.80	0.9988	0.9977	0.9779	0.9177	0.5908
0.85	0.9999	0.9991	0.9862	0.9528	0.7521
0.90	1	0.9997	0.9972	0.9762	0.8489
0.95	1	0.9999	0.9995	0.9914	0.9118
1.00	1	1	0.9999	0.9948	0.9337

5.3.2. Seismic Fragility Curves of Bridge Piers

The seismic fragility curves of the side piers and middle piers were plotted, respectively, with the PGA on the horizontal axis and the exceedance probabilities of different seismic damage levels on the vertical axis, as shown in Figures 8 and 9.

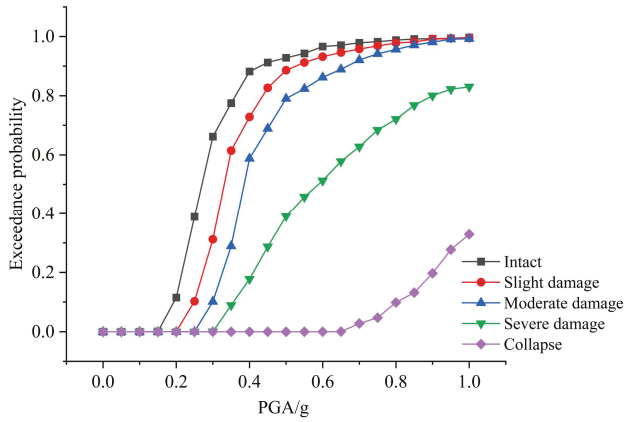

Figure 8. Seismic fragility curves of side piers.

From Figures 8 and 9 show that as PGA increases, the exceedance probabilities of side piers and middle piers developing from intact state to collapse gradually rise, indicating a continuous increase in the fragility of bridge piers. At low PGA levels, the probability of slight damage is nearly zero, confirming minimal seismic effects on bridge piers. For slight and moderate damage states, the probability of damage increases rapidly until the PGA reaches approximately 0.3 g, beyond this value, the growth rate slows down and stabilizes. The fragility curves for slight and moderate damage are very close, which is attributed to the small difference in load-carrying capacity between these states, reflecting similar yield and equivalent yield curvatures in the pier reinforcement.

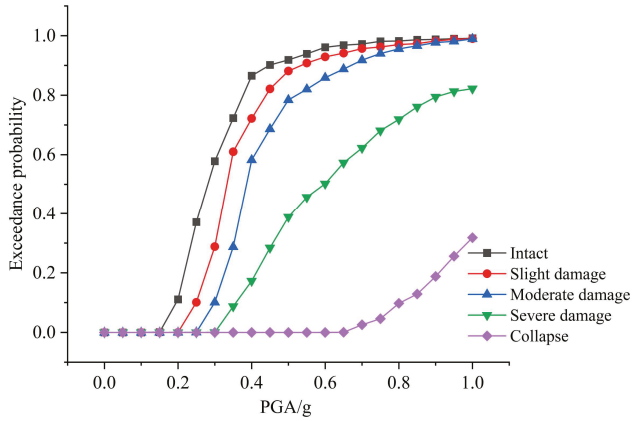

Figure 9. Seismic fragility curves of middle piers.

When the PGA gradually increases to about 0.5 g, severe damage begins to become distinctly apparent. The gap between the curves for moderate and severe damage indicates that the piers have a ductile behavior during this transition, which reduces the probability of severe damage and indicates a substantial difference between the curvature at equivalent yield and that at concrete crushing. Only when the PGA increases further do the piers begin to show complete collapse, and at the same PGA level, the exceedance probability of complete collapse is much lower than that of slight, moderate, or severe damage.

5.3.3. Seismic Fragility Curves of Bearings

Taking PGA as the horizontal axis and the exceedance probabilities of different seismic damage levels as the vertical axis, the seismic fragility curves for the side pier bearings and middle pier bearings of the research object were, respectively, plotted, as shown in Figures 10 and 11.

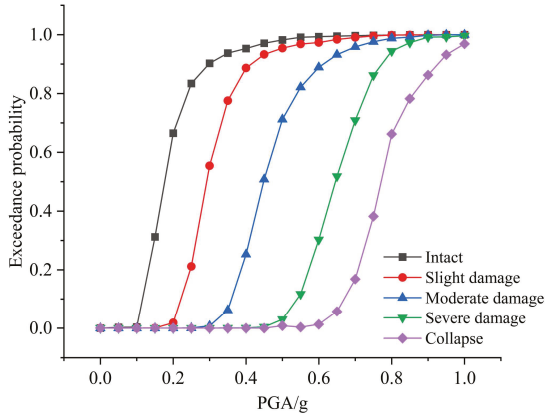

Figure 10. Seismic fragility curves of side pier bearings.

From Figures 10 and 11, as PGA increase, the exceedance probabilities of bearings developing from an intact state to slight, moderate, severe damage, and collapse gradually rise, indicating growing fragility of bearings. At low PGA, the probability of slight damage is nearly zero, suggesting negligible seismic demands on the bearings. For slight and moderate damage, the probability of damage rises rapidly until the PGA reaches approximately 0.4 g; beyond which the rate increase slows and stabilizes. The fragility curves of slight and moderate damage lie close together, due to the small difference in load-carrying capacity between these damage states, indicating only minor changes in mechanical properties.

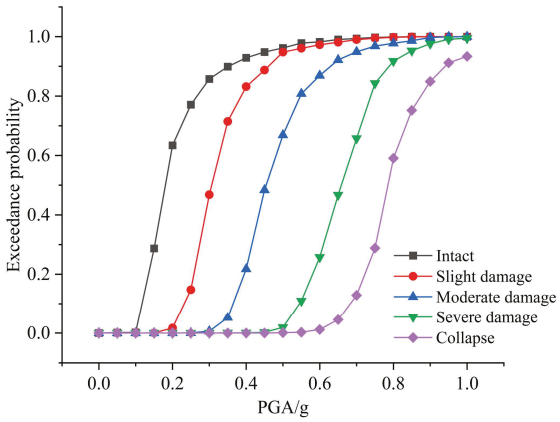

Figure 11. Seismic fragility curves of middle pier bearings.

When the PGA increases to about 0.6 g, severe damage begins to appear. The notable separation between the moderate and severe damage curves, primarily the bearings, has a ductile behavior during this transition, which substantially reduces the probability of severe damage and indicates significant changes in mechanical properties between these damage stages. Only when the PGA further increases does the bearing exhibit collapse, and at the same PGA level, the exceedance probability of collapse is much lower than that of the other damage states.

5.4. Comparative Analysis and Methodological Enhancement

Conventional seismic fragility analyses often simplify or omit the explicit treatment of parametric uncertainties, which can lead to an incomplete assessment of structural fragility. For instance, the fragility assessment of RC frames by Abeysiriwardena et al. did not incorporate the uncertainties in key structural properties [12]. In contrast, the method proposed in this study provides a significant enhancement by systematically quantifying the coupled effects of uncertainties from four structural parameters and PGA. This is achieved by the integration of the Response Surface Method with large-scale Monte Carlo simulation, resulting in fragility curves that offer a more realistic and reliable representation of seismic performance, thereby establishing a more robust basis for risk assessment.

6. Seismic Probability Risk Assessment of the Research Object Based on Seismic Hazard Curve Method

6.1. Basic Theory

The seismic risk probability is mathematically defined as the convolution of seismic hazard and fragility, representing the integrated probability of exceeding each level of seismic damage under all seismic events over the next t years, as shown in Equation (28) [44].

$$P_{j,t} = \sum_{\text{all } x_i} P(R_{j-} \leq S | \text{PGA} = x_i) \cdot P_t(\text{PGA} = x_i) \tag{28}$$

where $P_{j,t}$ is the risk probability of exceeding the j-th damage level over the next t years; $R_{j\text{-}}$ represent the value of the seismic damage parameter corresponding to the j-th damage level; S is the value of the seismic damage parameter of the bridge under seismic action; x_i is the PGA that the research site may encounter over the next t years. Due to the continuity of PGA values, Equation (28) can be rewritten as Equation (29).

$$P_{j,t} = \int P(R_{j-} \leq S | \text{PGA} = x_i) \cdot f(x) \mathrm{d}x \tag{29}$$

where $f(x)$ is the probability density function of PGA at the site over t years. The risk probability that the bridge will exceed the j-th level of seismic damage in the next 1 year as shown in Equation (30).

$$P_{j,1} = \int P(R_{j-} \leq S|\text{PGA} = x_i)\text{d}H(x) \tag{30}$$

where $H(x)$ is the annual distribution function of PGA at the site, whose shape is the seismic hazard curve, as shown in Equation (31) [45].

$$H(x) = P(\text{PGA} \geq x) \approx k_0 \cdot x^{-k} \tag{31}$$

where k_0 and k are parameters derived from the seismic hazard assessment results.

Based on the results of seismic fragility assessment, Equations (32) and (33) can be obtained.

$$P_{j,1}(R_{j-} \leq S|\text{PGA} = x_i) = \phi\left[\frac{\ln(S/R_{j-})}{\beta}\right] = 1 - \phi\left[\frac{\ln(R_{j-}/S)}{\beta}\right] \tag{32}$$

$$S_i = d_1 \cdot {x_i}^{d_2} \tag{33}$$

where β is the dispersion parameter relating seismic damage to ground motion intensity; d_1 and d_2 are undetermined coefficients.

Equation (30) can be rewritten as Equation (34).

$$P_{j,1} = \int P(R_{j-} \leq S|\text{PGA} = x_i)\text{d}H(x) = \int \left[1 - \phi\left(\frac{\ln(R_{j-}/d_1 \cdot x^{d_2})}{\beta}\right)\right]\text{d}H(x) \tag{34}$$

By performing integral transformation on Equation (34), Equation (35) can be obtained.

$$P_{j,1} = \int \frac{\text{d}\left\{1 - \phi\left\{\frac{\ln\left[R_{j-}/(d_1 \cdot x^{d_2})\right]}{\beta}\right\}\right\}}{\text{d}x} \cdot H(x)\text{d}x \tag{35}$$

The standard normal cumulative distribution function yields Equation (36).

$$\frac{\text{d}\left\{1 - \phi\left\{\frac{\ln\left[R_{j-}/(d_1 \cdot x^{d_2})\right]}{\beta}\right\}\right\}}{\text{d}x} = \frac{d_2}{x \cdot \beta} \cdot \phi\left\{\frac{\ln\left[R_{j-}/(d_1 \cdot x^{d_2})\right]}{\beta}\right\} \tag{36}$$

Then, Equation (35) can be further rewritten as Equation (37).

$$\begin{aligned} &P_{j,1} = \int \frac{d_2}{x \cdot \beta} \cdot \phi\left\{\frac{\ln\left[R_{j-}/(d_1 \cdot x^{d_2})\right]}{\beta}\right\} \cdot H(x)\text{d}x = \\ &\int_0^\infty \frac{d_2}{x \cdot \beta} \cdot \frac{1}{\sqrt{2\pi}} \cdot \exp\left[\frac{1}{2} \cdot \left(\frac{\ln R_{j-} - \ln d_1 - d_2 \ln x}{\beta}\right)^2\right] \cdot k_0 \cdot x^{-k}\text{d}x \end{aligned} \tag{37}$$

Simplifying Equation (37) yields Equation (38).

$$P_{j,1} = k_0 \cdot \left(\frac{R_{j-}}{d_1}\right)^{-\frac{k}{d_2}} \cdot \exp\left(\frac{k^2 \cdot \beta^2}{2 \cdot {d_2}^2}\right) \tag{38}$$

From Equation (33), Equation (39) is derived.

$$\mathrm{PGA}_{j-} = \left(\frac{R_{j-}}{d_1}\right)^{\frac{1}{d_2}} \tag{39}$$

where PGA_{j-} is the critical PGA corresponding to R_{j-}, substituting Equation (39) into Equation (38) gives Equation (40).

$$P_{j,1} = k_0 \cdot \left(\mathrm{PGA}_{j-}\right)^{-k} \cdot \exp\left(\frac{k^2 \cdot \beta^2}{2 \cdot {d_2}^2}\right) \tag{40}$$

Referring to Equation (37), Equation (40) can be transformed into Equation (41).

$$P_{j,1} = H(\mathrm{PGA}_{j-}) \cdot \exp\left(\frac{k^2 \cdot \beta^2}{2 \cdot {d_2}^2}\right) \tag{41}$$

6.2. Case Analysis

As shown in Tables 12–15, under the same PGA levels, the seismic damage of the side piers is more severe than middle piers. Therefore, only the side piers and their bearings were considered in the probability risk assessment. According to the results of the IDA, for the bridge piers, the parameters are β = 0.8567, d_1 = 1.082 and d_2 = 0.995, for the bearings, the parameters are β = 0.8353, d_1 = 76.853, and d_2 = 0.99.

According to the results of seismic hazard assessment, the PGA values with different exceedance probabilities for the research site over the next 1 year are shown in Table 16.

Table 16. PGA with different exceedance probabilities over 1 year.

Exceedance Probability Over 1 Year/%	**0.0404**	**0.2105**	**1.9689**
PGA/g	0.1747	0.1001	0.0292

Using Equation (31) and Table 16, the seismic hazard curve was plotted, as shown in Figure 12 and Equation (42).

$$H(x) = 0.0012 \cdot x^{-2.113} \tag{42}$$

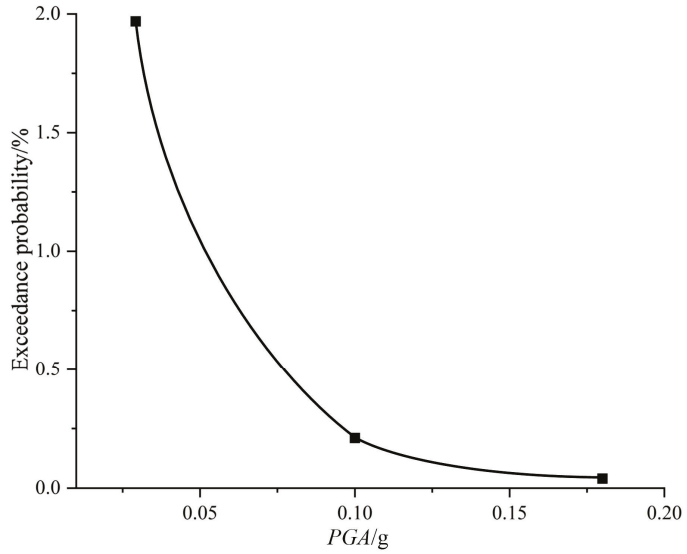

Figure 12. Seismic hazard curve.

Using Equation (39) and Tables 3 and 4, $PGA_{j\text{-}}$ was calculated, as shown in Tables 17 and 18.

Table 17. $PGA_{j\text{-}}$ corresponding to $\mu_{d,\max}$.

$\mu_{d,\max}$	1.000	1.132	1.893	4.893
$PGA_{j\text{-}}$	0.9238	1.0464	1.7545	4.5566

Table 18. $PGA_{j\text{-}}$ corresponding to $d_{\max}$.

$d_{\max}$/mm	25	50	75	90
$PGA_{j\text{-}}$	0.3216	0.6478	0.9756	1.1729

Combining Equation (41) and (42), the risk probabilities of the bridge piers exceeding each level of seismic damage over 1 year are calculated as follows, slight damage $P_{2,1}$ = 0.007424, moderate damage $P_{3,1}$ = 0.005705, severe damage $P_{4,1}$ = 0.001914 and collapse $P_{5,1}$ = 0.000255. For the bearings, the probabilities are: slight damage $P_{2,1}$ = 0.064627, moderate damage $P_{3,1}$ = 0.014716, severe damage $P_{4,1}$ = 0.006195 and collapse $P_{5,1}$ = 0.004198.

Based on the Poisson distribution, a seismic occurrence probability prediction model is constructed. According to the assumptions of the Poisson distribution, it is considered that the probability of seismic events occurring each year and their impacts are independent of each other. The conversion method for the risk probabilities of the bridge piers and bearings exceeding each level of seismic damage over 1 year and over 50 years is shown in Equation (43).

$$P_{j,50} = 1 - \left(1 - P_{j,1}\right)^{50} \tag{43}$$

Following calculations, the risk probabilities of the bridge piers and bearings exceeding each level of seismic damage over 50 years are shown in Table 19.

Table 19. Assessment results of seismic damage risk probability for the research object.

Results of Probability Risk Assessment		Bridge Piers		Bearings	
		Probability of Exceedance Risk/%	Risk Probability/%	Probability of Exceedance Risk/%	Risk Probability/%
Damage States	Intact	100.00	68.90	100.00	3.54
	Slight damage	31.10	6.22	96.46	44.11
	Moderate damage	24.88	15.75	52.35	25.64
	Severe damage	9.13	7.86	26.71	7.74
	Collapse	1.27	1.27	18.97	18.97

7. Conclusions

This study systematically conducted seismic hazard, seismic fragility, and probability risk assessments using a reinforced concrete continuous girder bridge as a case study. First, the PGA with different exceedance probabilities at the study site was calculated using the CPSHA method from the fifth-generation seismic ground motion parameter zoning scheme. Second, the Monte Carlo method and Response Surface Method were integrated to characterize uncertainties in bridge structural parameters and PGA, and seismic fragility curves were plotted. Third, the risk probability was calculated based on the seismic hazard curve method, providing a theoretical basis for bridge seismic design and performance assessment. The research results were as follows.

(1) The study area is influenced by the Tancheng–Lushan, the Lower Yangtze–South Yellow Sea, and the North China Plain seismic source zones, involving a total of 46 potential seismic source zones. The PGAs with 2%, 10%, and 63% exceedance probabilities over the next 50 years at the site are 171.16 gal, 98.10 gal, and 28.61 gal, respectively, indicating that the site in the 0.10 g seismic intensity zone corresponds to basic intensity zone VII.

(2) As PGA increases, both side piers and middle piers show clear pattern of progression from an intact state to slight, moderate, severe, and eventually collapse. The exceedance probabilities for all levels of damage rise consistently with increasing PGA, strongly confirming that the intensity of ground motion is the core factor determining the extent of bridge pier damage. At the same PGA level, the exceedance probabilities for slight, moderate, severe, and collapse damage in side piers are generally higher than those in middle piers, confirming their higher seismic fragility. When the PGA is in the range of 0.4–0.6 g, the exceedance probability of moderate damage in side piers is significantly higher than that in middle piers, reflecting that side piers are more prone to moderate damage under moderate-intensity earthquakes. At high PGA levels (>0.8 g), the exceedance probability of collapse for side piers is also notably greater than for middle piers, indicating that side piers face a higher collapse risk. Based on these findings, seismic design for bridges should prioritize enhancing the seismic performance of side piers, using measures such as optimizing the structural configuration of side piers, strengthening anti-sliding and anti-fall beam measures at bearings, and reasonably installing seismic restraint devices to improve overall bridge seismic reliability.

Similarly, as PGA increases, both side and middle pier bearings exhibit progression from intact to slight, moderate, severe damage, and collapse, with the exceedance probabilities for all damage levels increasing with PGA. This fully demonstrates that ground motion intensity is the key factor affecting bearing damage. At the same PGA level, the exceedance probabilities for all damage levels in side pier bearings are generally higher than those in middle pier bearings, and their fragility curves lie above those of middle pier bearings. This indicates that side pier bearings are more susceptible to earthquake damage and show a more significant trend of damage escalation as PGA increases. In the range of 0.4–0.6 g, the exceedance probabilities of moderate damage for side pier bearings are significantly higher, and at PGA > 0.8 g, their collapse probabilities are also significantly greater.

(3) Over the next 50 years, the risk probabilities for the bridge piers to remain intact suffer slight, moderate, severe damage and collapse, at 68.90%, 6.22%, 15.75%, 7.86% and 1.27%, respectively. For the bearings, the corresponding probabilities are 3.54%, 44.11%, 25.64%, 7.74% and 18.97%, indicating that the overall seismic damage risk of bearings is higher than that of piers, especially for moderate damage and collapse. The high seismic risk of bearings necessitates targeted mitigation methods: (a) optimize design by adopting high-capacity isolation bearings and strengthening anti-unseating devices; (b) enhance inspection by incorporating bearings into routine and post-earthquake monitoring programs; and (c) promote retrofitting by installing external dampers or replacing conventional bearings with isolation or damping systems to improve overall resilience.

(4) The proposed seismic hazard–fragility–probability risk assessment system is applicable to various bridge structures and has high promotional and application value. While the specific risk probabilities are case-sensitive, the overall framework is generalizable to various bridge structures. Its application requires tailoring the finite element model and damage criteria to the specific structural system under investigation. However, there are still limitations: (a) omission of soil–structure interaction, potentially underestimate local risk; (b) lack of refined modeling bearing anchor bolts and stirrup spacing in plastic hinge regions, and unquantified impacts of construction quality variations; (c) only horizontal

seismic motion input is used, ignoring multi-dimensional seismic motion effects on bearing shear deformation and pier flexural-shear failure; and (d) the validity of the finite element model relies on well-established modeling techniques rather than direct validation against experimental data from a physically identical bridge test. While the constitutive models and element formulations used have been extensively validated in the literature, future work should include a comprehensive experimental comparison to further corroborate the findings.

Author Contributions: Conceptualization, J.C.; Methodology, J.C. and C.Y.; Software, J.C. and C.Y.; Validation, J.C.; Resources, C.Y.; Data curation, J.C. and C.Y.; Writing—original draft, J.C.; Writing—review & editing, J.C., C.Y., T.S. and J.L.; Visualization, J.C.; Project administration, C.Y.; Funding acquisition, C.Y. All authors have read and agreed to the published version of the manuscript.

Funding: This research was supported by the National Natural Science Foundation of China (Grant No. 51808327) and the Natural Science Foundation of Shandong Province (Grant No. ZR2019PEE016).

Institutional Review Board Statement: Not applicable.

Informed Consent Statement: Not applicable.

Data Availability Statement: The data, models, and codes supporting the findings of this study are available from the corresponding author upon reasonable request.

Conflicts of Interest: The authors declare no conflict of interest.

References

1. Han, Y.Y.; Zang, Y.; Meng, L.Y.; Wang, Y.; Deng, S.; Ma, Y.; Xie, M. A summary of seismic activities in and around China in 2021. *Earthq. Res. Adv.* **2022**, *2*, 100157. [CrossRef]
2. Liu, J.L.; Jia, H.X.; Lin, J.Q.; Hu, H. Seismic Damage Rapid Assessment of Road Networks considering Individual Road Damage State and Reliability of Road Networks in Emergency Conditions. *Adv. Civ. Eng.* **2020**, *2020*, 9631804. [CrossRef]
3. Ozsarac, V.; Monteiro, R.; Calvi, G.M. Probabilistic seismic assessment of reinforced concrete bridges using simulated records. *Struct. Infrastruct. Eng.* **2023**, *19*, 554–574. [CrossRef]
4. Cornell, C.A. Engineering seismic risk analysis. *Bull. Seismol. Soc. Am.* **1968**, *58*, 1583–1606. [CrossRef]
5. Pan, H.; Jin, Y.; Hu, Y.X. Discussion about the relationship between seismic belt and seismic statistical zone. *Acta Seismol. Sin.* **2003**, *16*, 323–329. [CrossRef]
6. Bi, J.M.; Song, C.; Cao, F.Y. Declustering characteristics of the North China Plain seismic belt and its effect on probabilistic seismic hazard analysis. *Sci. Rep.* **2024**, *14*, 22170. [CrossRef] [PubMed]
7. Vamvatsikos, D.; Cornell, C.A. Developing efficient scalar and vector intensity measures for IDA capacity estimation by incorporating elastic spectral shape information. *Earthq. Eng. Struct. Dyn.* **2005**, *34*, 1573–1600. [CrossRef]
8. Wang, Q.A.; Wu, Z.Y.; Liu, S.K. Seismic fragility analysis of highway bridges considering multi dimensional performance limit state. *Earthq. Eng. Eng. Vib.* **2012**, *11*, 185–193. [CrossRef]
9. Li, J.; Chen, J.B.; Sun, W.L.; Peng, Y.B. Advances of the probability density evolution method for nonlinear stochastic systems. *Probabilistic Eng. Mech.* **2012**, *28*, 132–142. [CrossRef]
10. Yin, C.; Li, Y.; Liu, F.F. Probability risk assessment and management of embankment seismic damages based on CPSHA-PSDA. *Iran. J. Sci. Technol. Trans. A Sci.* **2019**, *43*, 1563–1574. [CrossRef]
11. Che, F.; Yin, C.; Zhang, H.; Tang, G.T.; Hu, Z.N.; Liu, D.; Li, Y.; Huang, Z.F. Assessing the risk probability of the embankment seismic damage using Monte Carlo method. *Adv. Civ. Eng.* **2020**, *2020*, 8839400. [CrossRef]
12. Abeysiriwardena, T.M.; Wijesundara, K.K.; Nascimbene, R. Seismic risk assessment of typical reinforced concrete frame school buildings in Sri Lanka. *Buildings* **2023**, *13*, 2662. [CrossRef]
13. Cheng, X.L.; Li, Q.Q.; Hai, R.; He, X.F. Study on seismic vulnerability analysis of the interaction system between saturated soft soil and subway station structures. *Sci. Rep.* **2023**, *13*, 7410. [CrossRef] [PubMed]
14. Zhou, X.H.; Zhou, Z.; Gan, D. Modeling of cyclically loaded square thin-walled CSFT columns stiffened by diagonal ribs using OpenSees. *Thin-Walled Struct.* **2023**, *187*, 110736. [CrossRef]
15. Tatar, A.; Baker, A.M.; Dowden, D.M. A generalized method for numerical modeling of seismically resilient friction dampers using flat slider bearing element. *Eng. Struct.* **2023**, *275*, 115248. [CrossRef]
16. Guan, M.S.; Hang, X.R.; Wang, M.S.; Zhao, H.Y.; Liang, Q.Q.; Wang, Y. Development and implementation of shear wall finite element in OpenSees. *Eng. Struct.* **2024**, *304*, 117639. [CrossRef]

17. *GB/T 24335-2009*; Classification of Earthquake Damage to Buildings and Special Structures. National Technical Committee for Seismological Standardization: Beijing, China, 2009.
18. Bhatta, S.; Dang, J. Seismic damage prediction of RC buildings using machine learning. *Earthq. Eng. Struct. Dyn.* **2023**, *52*, 3504–3527. [CrossRef]
19. Yamaguchi, T.; Mizutani, T. A Physics-Informed Neural Network for the Nonlinear Damage Identification in a Reinforced Concrete Bridge Pier Using Seismic Responses. *Struct. Control Health Monit.* **2024**, *2024*, 5532909. [CrossRef]
20. Qiu, W.H.; Wang, K.H.; Guo, W.Z. Seismic Performance of the Wall Pier of Covered Bridge in the Weak Direction. *Iran. J. Sci. Technol. Trans. Civ. Eng.* **2024**, *48*, 4183–4200. [CrossRef]
21. Song, S.; Qian, Y.J.; Liu, J.; Xie, X.R.; Wu, G. Time-variant fragility analysis of the bridge system considering time-varying dependence among typical component seismic demands. *Earthq. Eng. Eng. Vib.* **2019**, *18*, 363–377. [CrossRef]
22. Zhong, H.Q.; Yuan, W.C.; Dang, X.Z.; Deng, X.W. Seismic performance of composite rubber bearings for highway bridges: Bearing test and numerical parametric study. *Eng. Struct.* **2022**, *253*, 113680. [CrossRef]
23. Xu, W.J.; Wu, J.; Gao, M.T. Seismic hazard analysis of China's mainland based on a new seismicity model. *Int. J. Disaster Risk Sci.* **2023**, *14*, 280–297. [CrossRef]
24. Iwata, D.; Nanjo, K.Z. Adaptive estimation of the Gutenberg–Richter b value using a state space model and particle filtering. *Sci. Rep.* **2024**, *14*, 4630. [CrossRef] [PubMed]
25. Cao, X.Y.; Feng, D.C.; Beer, M. Consistent seismic hazard and fragility analysis considering combined capacity-demand uncertainties via probability density evolution method. *Struct. Saf.* **2023**, *103*, 102330. [CrossRef]
26. Pei, W.L.; Zhou, S.Y.; Zhuang, J.C.; Xiong, Z.Y.; Piao, J. Application and discussion of statistical seismology in probabilistic seismic hazard assessment studies. *Sci. China (Earth Sci.)* **2022**, *65*, 257–268. [CrossRef]
27. Han, S.C.; Sun, J.Z.; Xiong, F. Analysis for site seismic hazard probability considering the orientation distribution of potential seismic sources. *Nat. Hazards* **2024**, *121*, 2433–2464. [CrossRef]
28. Vandana; Dadhich, H.K.; Mittal, H.; Mishra, O.P. Ground motion prediction equation for NW Himalaya and its surrounding region. *Quat. Sci. Adv.* **2024**, *13*, 100136. [CrossRef]
29. Eskandarinejad, A.; Shiau, J.; Keawsawasvong, S. Effect of Depth-Dependent Shear Wave Velocity Profiles on Site Amplification. *Transp. Infrastruct. Geotechnol.* **2022**, *10*, 1255–1283. [CrossRef]
30. Zhong, Z.L.; Shen, Y.Y.; Zhao, M.; Li, L.Y.; Du, X.L. Seismic performance evaluation of two-story and three-span subway station in different engineering sites. *J. Earthq. Eng.* **2022**, *26*, 7505–7535. [CrossRef]
31. Yin, K.S.; Xu, Y.; Li, J.Z.; Zhou, X. Gaussian process regression driven rapid life-cycle based seismic fragility and risk assessment of laminated rubber bearings supported highway bridges subjected to multiple uncertainty sources. *Eng. Struct.* **2024**, *316*, 118615. [CrossRef]
32. Liu, Y.Y.; Chen, J.B.; Li, J. The modified mesoscopic stochastic fracture model incorporating the random field of Young's modulus for the uniaxial constitutive law of concrete. *Probabilistic Eng. Mech.* **2024**, *75*, 103585. [CrossRef]
33. Chen, Y.X.; Zhang, J.Y.; Ma, J.C.; Zhou, S.L.; Liu, Y.S.; Zheng, Z.X. Tensile strength and fracture toughness of steel fiber reinforced concrete measured from small notched beams. *Case Stud. Constr. Mater.* **2022**, *17*, e01401. [CrossRef]
34. Ge, F.W.; Tong, M.N.; Zhao, Y.G. A structural demand model for seismic fragility analysis based on three-parameter lognormal distribution. *Soil Dyn. Earthq. Eng.* **2021**, *147*, 106770. [CrossRef]
35. Hu, X.N.; Fang, G.S.; Ge, Y.J. Uncertainty propagation of flutter derivatives and structural damping in buffeting fragility analysis of long-span bridges using surrogate models. *Struct. Saf.* **2024**, *106*, 102410. [CrossRef]
36. Xiang, Z.; Zhu, Z.W. Multi-objective optimization of a composite orthotropic bridge with RSM and NSGA-II algorithm. *J. Constr. Steel Res.* **2022**, *188*, 106938. [CrossRef]
37. Sun, D.L.; Wang, J.; Wen, H.J.; Ding, Y.K.; Mi, C.L. Landslide susceptibility mapping (LSM) based on different boosting and hyperparameter optimization algorithms: A case of Wanzhou District, China. *J. Rock Mech. Geotech. Eng.* **2024**, *16*, 3221–3232. [CrossRef]
38. Kong, D.H.; Luo, Q.; Zhang, W.S.; Jiang, L.W.; Zhang, L. Reliability analysis approach for railway embankment slopes using response surface method based Monte Carlo simulation. *Geotech. Geol. Eng.* **2022**, *40*, 4529–4538. [CrossRef]
39. Pang, Y.T.; Meng, R.; Li, C.D.; Li, C. A probabilistic approach for performance-based assessment of highway bridges under post-earthquake induced landslides. *Soil Dyn. Earthq. Eng.* **2022**, *155*, 107207. [CrossRef]
40. Liu, Y.; Meng, X.L.; Hu, L.L.; Bao, Y.; Hancock, C. Application of Response Surface-Corrected Finite Element Model and Bayesian Neural Networks to Predict the Dynamic Response of Forth Road Bridges under Strong Winds. *Sensors* **2024**, *24*, 2091. [CrossRef]
41. Huang, J.; Qiu, S.Q.; Rodrigue, D. Parameters estimation and fatigue life prediction of sisal fibre reinforced foam concrete. *J. Mater. Res. Technol.* **2022**, *20*, 381–396. [CrossRef]
42. Cabanzo, C.; Mendes, N.; Akiyama, M.; Lourenço, P.B.; Matos, J.C. Probabilistic framework for seismic performance assessment of a multi-span masonry arch bridge employing surrogate modeling techniques. *Eng. Struct.* **2025**, *325*, 119399. [CrossRef]

43. Ashrafifar, J.; Estekanchi, H. Life-cycle seismic fragility and resilience assessment of aging bridges using the endurance time method. *Soil Dyn. Earthq. Eng.* **2023**, *164*, 107524. [CrossRef]
44. Li, S.Q.; Gardoni, P. Seismic loss assessment for regional building portfolios considering empirical seismic vulnerability functions. *Bull. Earthq. Eng.* **2024**, *22*, 487–517. [CrossRef]
45. Kan, C.Y.; Tsai, C.C.; Chen, C.J. Simple method for probabilistic seismic landslide hazard analysis based on seismic hazard curve and incorporating uncertainty of strength parameters. *Eng. Geol.* **2023**, *314*, 107002. [CrossRef]

Disclaimer/Publisher's Note: The statements, opinions and data contained in all publications are solely those of the individual author(s) and contributor(s) and not of MDPI and/or the editor(s). MDPI and/or the editor(s) disclaim responsibility for any injury to people or property resulting from any ideas, methods, instructions or products referred to in the content.

coatings

MDPI

Article

Frost Resistance and Damage Mechanism of Recycled Aggregate Concrete

Meng Li [1], Huaiqin Liu [1], Bangxiang Li [1], Shangwei Gong [1], Changgui Xu [2,*], Tian Su [1,3,*], Xuefeng Mei [4] and Sheng Xu [4]

[1] Department of Civil Engineering, School of Civil Engineering and Geomatics, Shandong University of Technology, Zibo 255000, China; 17888312603@163.com (H.L.)
[2] Department of Landscape Architecture, School of Civil Engineering and Architecture, Hebei University of Engineering Science, Shijiazhuang 050011, China
[3] Department of Engineering and Management, International College, Krirk University, No. 3 Soi Ramintra 1, Ramintra Road, Anusaowaree, Bangkhen, Bangkok 10220, Thailand
[4] Department of Architectural Engineering, School of Civil Engineering, Inner Mongolia University of Science and Technology, 7 Alding Street, Baotou 014010, China
* Correspondence: changguixu123@163.com (C.X.); sutiancivil@foxmail.com (T.S.)

Abstract

This study systematically evaluates the influence of the recycled coarse aggregate (RCA) replacement rate and the number of freeze–thaw cycles (FTCs) on the frost damage of recycled aggregate concrete (RAC) through rapid freeze–thaw tests, and delves into the underlying damage mechanisms. The findings demonstrate that the incorporation of recycled aggregates deteriorates the frost resistance of concrete to a certain extent, primarily manifested by increased apparent damage with rising FTC numbers and RCA content. Specimens with an RCA replacement rate exceeding 50% exhibited extensive mortar spalling and aggregate exposure after 50 FTCs. The mass loss rate initially decreased in the early freezing-thawing stage, then began to increase after approximately 20 cycles, reaching a maximum of 5.09%. The relative dynamic elasticity modulus (RDEM) decreased with an increase in both FTCs and RCA content, dropping to a minimum of 71.99%. Furthermore, based on the relative dynamic elastic modulus, this study developed a GM(1, 1) freeze–thaw damage prediction model applicable to a full replacement range of 0%–100% RCA with a precision level of Grade I. Microstructural analysis revealed that microcracks and pores within the interfacial transition zones (ITZs) and the surrounding matrix of both NCA and RCA are critical for the initiation and propagation of freeze–thaw damage, thereby elucidating the damage mechanism in RAC.

Keywords: recycled coarse aggregate concrete; freeze–thaw cycle; freeze–thaw damage prediction model; damage mechanism

1. Introduction

The global acceleration of urbanization has led to a massive generation of construction and demolition waste, a significant portion of which is waste concrete, polluting the environment and occupying land, and has increased sharply [1]. Moreover, the large amount of concrete consumed leads to the depletion of natural sand and gravel resources, causing severe damage to the ecological environment [2]. RAC uses crushed and screened waste concrete to replace natural aggregate, which can avoid excessive mining of sand and gravel resources, achieve resource utilization of construction waste, reduce carbon emissions, and

have both environmental protection and economic value [3]. Nevertheless, due to the adherence of RCA to residual mortar and the presence of internal microcracks, RCA exhibits increased porosity, elevated water absorption, and reduced mechanical strength relative to natural coarse aggregate (NCA) [4,5]. These limitations hinder the extensive utilization of recycled concrete in construction applications. In addition, after the concrete is subjected to freezing, the internal microcracks further propagate, causing a certain degree of damage to the structure. When subjected to freezing and thawing, progressive detachment occurred between the aggregate and the mortar matrix; the structure gradually becomes loose, and the bearing capacity decreases significantly, thereby reducing its safety and stability [6]. Concrete structure buildings that have reached the freeze–thaw limit are extremely difficult and expensive to repair. Therefore, ensuring excellent mechanical performance and durability, particularly under the freeze–thaw (F-T) conditions, is paramount for the widespread adoption of RAC.

The mechanical properties of RAC are influenced by multiple factors, including the RCA replacement ratio, water-to-cement ratio, and sand ratio. Through orthogonal experiments, Zhang et al. [7] reported that among the many factors affecting RAC, the RCA substitution ratio has the greatest effect on its mechanical properties. At present, it is generally believed that when the replacement ratio of RCAs does not exceed 30%, their effect on the mechanical strength of concrete is insignificant [8]. Omidinasab et al. [9] reported a 4.4% reduction in cubic compressive strength at a 25% RCA replacement rate, escalating to a 20% decrease at 100% replacement. When RAC was subjected to bending loading, a replacement ratio of up to 50% had a relatively insignificant effect on its flexural strength. Ahmed et al. [10] observed a 3.53% decrease in flexural strength at 50% replacement, which surged to 26.67% at full replacement. RAC is a brittle material, and its tensile strength is far lower than its compressive strength, causing the RCA substitution ratio to have a more significant effect on the tensile strength of concrete. Xue et al. [11] noted tensile strength reductions of 31.39% and 34.14% at 40% and 100% replacement rates, respectively. This behavior is often attributed to the expansion of the defect zone (encompassing microcracks and the ITZ) with higher RCA content, promoting stress concentration during loading and leading to premature failure [12,13].

The distinct pore structure and higher porosity of RAC compared to natural aggregate concrete (NAC) result in inferior frost resistance [14]. Numerous studies confirm that the F-T durability of RAC deteriorates as the RCA replacement rate increases [15,16]. Niu et al. [17] documented compressive strength losses of 10.39%, 14.59%, and 21.09% after 100 F-T cycles for RAC with 0%, 50%, and 100% RCA, respectively. Accurately predicting F-T damage is thus essential. Deng et al. [18] and Liu et al. [19] proposed gray system theory in connection with uncertainty systems with incomplete small data and poor information. Liu et al. [20], Feng et al. [21] and Gao et al. [22] used the GM model to predict the freeze–thaw damage of concrete, which highlights the versatility of the GM model in the analysis process.

For conventional concrete, the F-T damage mechanism has been relatively well explained based on the hydrostatic pressure and osmotic pressure theories proposed by Powers [23,24]. However, the inherent and more complex microscopic defects and weak areas within RCA prevent the direct application of these classical theories to the RAC system. Many scholars have conducted extensive research on the theory that the durability of concrete continuously decreases during FTCs [25,26]. With the development of RAC technology, Kong et al. [27], Qiu et al. [28], and Bai et al. [29] proposed F-T damage mechanisms for RAC based on classical freeze–thaw damage theories. However, the micro-mechanisms underpinning these theoretical frameworks remain inadequately elucidated, and existing studies have not sufficiently addressed the interactive effects of RCA replacement rates

and the frequency of FTCs. Moreover, there is a notable absence of predictive models capable of accurately forecasting the F-T durability of concrete across the entire spectrum of RCA replacement ratios (0%–100%). Consequently, it is imperative to further investigate the intrinsic F-T damage mechanisms in RAC. This research systematically examines the combined influence of the full range of RCA replacement rates (0%–100%) and the number of FTCs to develop a high-precision GM model for predicting F-T damage, and provides an in-depth analysis and clarification of the F-T damage mechanism of RAC through microscopic tests.

Although existing studies have explored the frost resistance of RAC, research on high-precision service life prediction based on the Grey Model (GM) remains scarce. Specifically, there is an absence of F-T damage models for concrete incorporating RCA at replacement levels spanning from 0% to 100%. Furthermore, the internal mechanisms underlying F-T damage in RAC have not been systematically or comprehensively elucidated. Based on this, the present study investigates the influence of the RCA replacement rate and the number of FTCs on the frost resistance of RAC through rapid freeze–thaw tests. A highly accurate GM(1, 1) predictive model for F-T damage in RAC, encompassing replacement rates ranging from 0% to 100%, has been developed. This model is founded on the variations observed in the RDEM of RAC subjected to F-T conditions. Furthermore, the internal F-T damage mechanism of RAC is systematically elucidated through microstructural analysis.

2. Test Materials and Methods

2.1. Test Materials

P.O 42.5 ordinary Portland cement, conforming to Chinese standard GB/T 39698-2020 [30], was used. Its physical properties and chemical composition are detailed in Tables 1 and 2, respectively. Both NCA and RCA were sourced from Xintiansheng Concrete Co., Ltd. (Zibo, China), meeting the specifications of JGJ 52-2006 [31]. Their physical properties and particle size distribution are presented in Table 3 and Figure 1. Natural river sand, employed as fine aggregate following JGJ 52-2006 [31], had a grading curve shown in Figure 2.

Table 1. Physical properties of cement.

	Initial Setting/min	Final Setting/min	Compressive Strength (MPa)		Flexural Strength (MPa)		Stability
			3 d	28 d	3 d	28 d	
P.O.42.5	179	247	22.2	47.2	4.8	7.9	qualified

Table 2. Chemical composition of the cement.

Chemical Composition	CaO	SiO_2	Al_2O_3	Fe_2O_3	MgO	Na_2O	K_2O
Content	61.91	21.65	5.32	3.22	2.51	0.21	0.16

Table 3. Physical properties of the NCA and RCA samples.

Physical Property	NCA	RCA
Water absorption (%)	1.1	3.2
Apparent density (kg/m^3)	2635	2541
Crushing index (%)	7.5	16
Flaky and particle content (%)	7.7	8.6
Mud content (%)	0.5	1.5
Maximum particle size (mm)	26.5	26.5

Note: When the mud content was equivalent, the performance of NCA remained superior to that of RCA, suggesting that the influence of aggregate mud content on the experimental results was negligible [32,33].

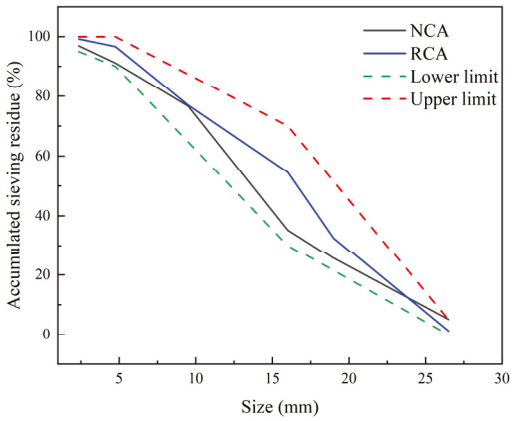

Figure 1. Grading curves of NCA and RCA.

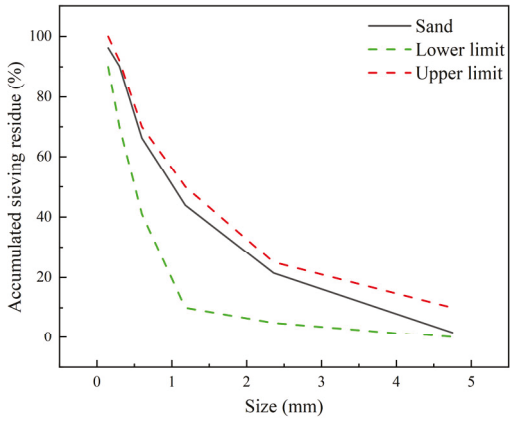

Figure 2. Grading curve of sand.

2.2. Mix Ratio

In accordance with JGJ 55-2019 [34], the concrete mix design was carried out in this test, as shown in Table 4. The number of ordinary concretes prepared with natural aggregate is "NC", and the number of recycled concretes prepared with recycled aggregate is "R + recycled Coarse aggregate volume fraction". Five mix proportions were designed in this study, with a constant water–cement ratio of 0.45. Prior to concrete casting, the aggregates were pre-wetted and maintained in a saturated surface-dry condition during casting to eliminate the influence of aggregate absorption on the effective water–cement ratio [32,33]. In accordance with established research practices [35,36], the equal volume replacement method was used to replace NCA with RCA to ensure that the compactness of the concrete was not affected by the volume change in the aggregate.

Table 4. Concrete mix proportions.

Type	NCA (%)	RCA (%)	Sand (kg/m^3)	Water (kg/m^3)	Cement (kg/m^3)
NC	100	0	580.66	205	455.56
R30	70	30	580.66	205	455.56
R50	50	50	580.66	205	455.56
R70	30	70	580.66	205	455.56
R100	0	100	580.66	205	455.56

2.3. Test Methods

2.3.1. Freeze Resistance Test

In accordance with GB/T 50082-2009 [37], the rapid freeze–thaw test was conducted to evaluate the frost resistance of RAC. A TDR-9 rapid freeze–thaw testing machine and a DT-10W dynamic modulus tester (Tianjin Luda Construction Instrument Co., Ltd., Tianjin,

China) were employed (Figure 3). To simulate the damage induced by alternating positive and negative temperatures in water-saturated concrete under natural conditions [37–40], this experiment stipulates that each FTC shall not exceed 4 h, and the thawing time shall not exceed one-quarter of the total cycle duration. The temperature regime was set as follows: maximum temperature +5 ± 2 °C, minimum temperature −18 ± 2 °C, and transition time ≤10 min. After every 10 FTCs, specimens were removed, surface-dried, and measured for lateral fundamental frequency and mass. Every five cycles, specimens were repositioned to ensure uniform exposure. The test was terminated when the RDEM fell below 60% or the mass loss exceeded 5%.



(**a**) (**b**)

Figure 3. Frost resistance test apparatus: (**a**) Rapid freeze–thaw testing machine; and (**b**) RDEM instrument.

In this study, three specimens were prepared for each mix proportion, and the final result was taken as the average of the test results from these three specimens. The mass loss rate and RDEM of the concrete specimens after FTCs were calculated using the following equations, respectively:

$$\begin{aligned} \Delta W_{ni} &= \frac{W_{0i} - W_{ni}}{W_{0i}} \times 100 \\ \Delta W_{ni} &= \frac{\sum_{i=1}^{3} \Delta W_{ni}}{3} \end{aligned} \quad (1)$$

where ΔW_{ni} is the mass loss rate (%) of sample i after n FTCs, W_{0i} is the mass loss of test piece i without an FTC (mm), W_{ni} is the mass loss rate of sample i after n FTCs (mm), and ΔW_n denotes the average mass loss rate (%) of specimens with the same mix proportion after n FTCs.

$$\begin{aligned} P_i &= \frac{f_{0i} - f_{ni}}{f_{0i}} \times 100 \\ P_n &= \frac{\sum_{i=1}^{3} P_i}{3} \end{aligned} \quad (2)$$

where P_i is the RDEM of sample i after n FTCs (%), f_{0i} is the lateral fundamental frequency of sample i without FTCs (Hz), f_{ni} is the freeze–thaw cycle frequency of sample i and the horizontal fundamental frequency after n FTCs (Hz), and P_n denotes the average RDEM (%) of specimens with the same mix proportion after n FTCs.

2.3.2. Microscopic Tests

The morphological characteristics of the cement stone samples at the microscopic level were observed via field emission environmental scanning electron microscopy (SEM) (Thermo Scientific, Waltham, MA, USA) and USB digital microscopy (DMD) (Yusen, Suzhou, China), as shown in Figure 4. Prior to SEM observation, the samples were oven-dried, fractured to expose fresh surfaces, and sputter-coated with a thin layer of gold to enhance conductivity. Observations were conducted under high vacuum conditions at an accelerating voltage of 10 kV. The DMD examination was performed on the samples' as-cast surfaces to document macroscopic features without any pre-treatment.

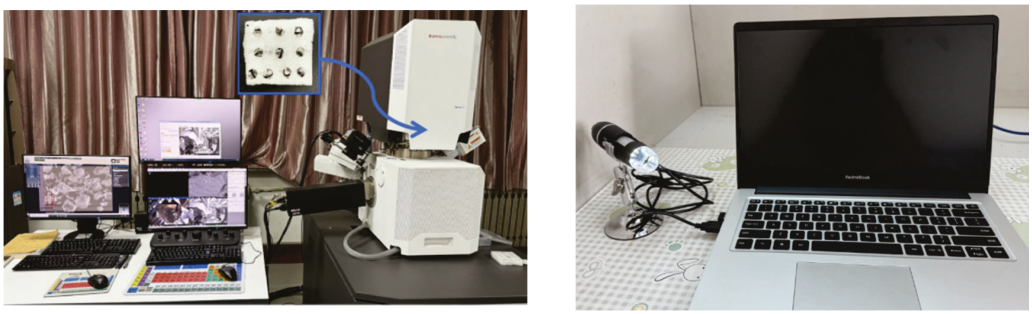

(**a**) (**b**)

Figure 4. Microscopic test set: (**a**) SEM; and (**b**) DMD.

3. Results and Discussion

3.1. Frost Resistance Performance

3.1.1. Appearance

The surface characteristics of RAC following FTCs are illustrated in Figure 5. After 10 FTCs, the surfaces displayed pitting and minor erosion, with the severity of surface deterioration increasing in proportion to the RCA replacement ratio (Figure 5a). Upon completion of 30 FTCs, micro-pores merged to form larger cavities, resulting in a markedly rougher surface texture; notably, corner spalling of coarse aggregates was observed, especially in mixtures with elevated RCA content (Figure 5b). After 50 FTCs, extensive spalling of the surface mortar occurred, exposing certain coarse aggregates (Figure 5c). In the advanced stages of freeze–thaw exposure, the extent of exposed and spalled coarse aggregate areas on the specimen surface progressively increased with higher RCA replacement rates [41,42]. In summary, throughout the FTC process, the RCA substitution rate exerted a significant influence on the degree of visible damage to the specimens, with higher RCA proportions correlating with increased levels of surface deterioration [43].

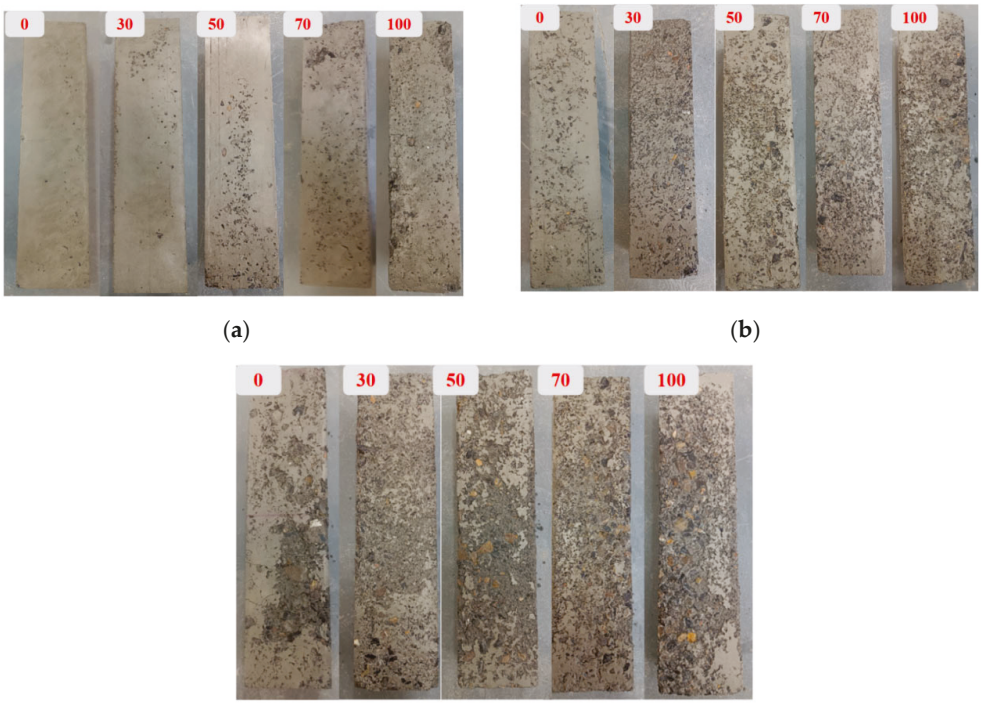

(**a**) (**b**)

(**c**)

Figure 5. Appearances of the RCA concrete after FTCs: (**a**) 10 times; (**b**) 30 times; and (**c**) 50 times [32]. (Note: The numbers (0, 30, 50, 70, 100) in the figure denote the RCA replacement ratios).

3.1.2. Mass Loss

The variation in mass of RAC during F-T cycling is plotted in Figure 6. With the increase in the number of FTCs, the mass of the RAC test piece initially increased but then decreased. The increasing stage of test sample quality was mainly concentrated in the 10–20 FTCs, and the decreasing stage of test sample quality was mainly concentrated in the 20–50 FTCs. These findings indicate that cracks in RAC develop rapidly during the early and middle-term FTCs and that bone–pulp separation is most severe during the middle and late stages of the FTC. There are two reasons for the quality change of the test piece [44,45]. First, the mortar undergoes frost heave and F-T splitting under the action of FTCs, causing cracks to form inside the mortar, which reduces the mass of the test sample; second, the mortar undergoes FTCs. After the thawing cycle, the cracks developed inside the concrete, and the independent closed pores that were connected with each other under the action of the FTC opened up spaces for the infiltration of water, resulting in an increase in the mass of the test piece.

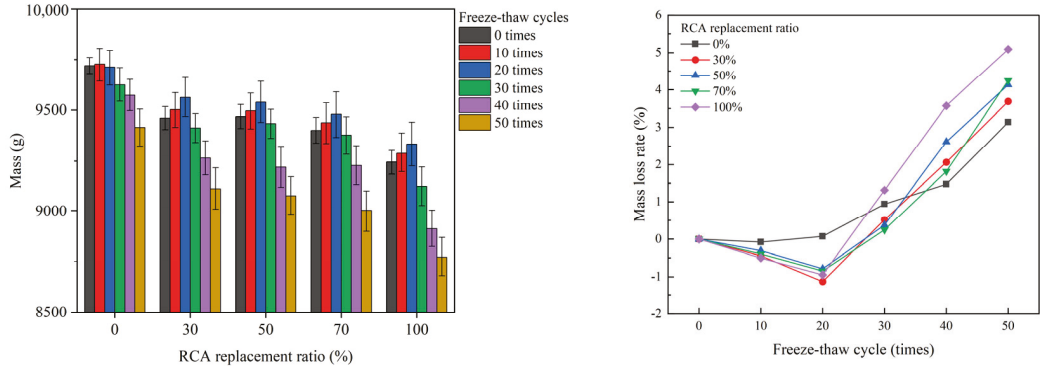

Figure 6. Mass change of RCA concrete: (**a**) Mass; (**b**) Mass loss rate.

With an increasing number of FTCs, the mass of the concrete specimen, measured in its water-saturated state, initially exhibits an increase followed by a subsequent decrease. Concurrently, the rate of mass loss demonstrates an initial decline before rising. A negative mass loss rate signifies a net mass gain attributable to water absorption, whereas a positive mass loss rate reflects material degradation resulting from surface scaling.

Compared to the initial mass, during the early stages of FTCs (10–20 times), the mass of the NAC specimens and the average mass of the RAC specimens increased by 7.8 g and 86.8 g, respectively (corresponding to the nadir of the mass loss rate for NAC and the average mass loss rate for RAC, reaching -0.08% and -0.92%, respectively). In the later stages (50 times), the mass of the NAC specimens and the average mass of the RAC specimens decreased by 305.2 g and 402.4 g, respectively (corresponding to the peak mass loss rate for NAC and the average mass loss rate for RAC, reaching 3.14% and 4.29%, respectively). The significant difference in these data arises because, compared to NCA, RCA possesses more internal pores, which provide greater space for water ingress during the initial FTCs. Consequently, the mass gain of RAC specimens is more pronounced initially. This also establishes the necessary conditions for more severe water ingress and mass loss in the later stages. The macroscopic scaling (i.e., the actual mass loss) observed on the concrete specimen surfaces in the later stages is the ultimate result of the cumulative internal damage process.

The fitting models of the number of FTCs (n), RCA replacement rate (r) and mass loss rate (ΔW_{ni}) of the RAC are shown in Figure 7, and the fitting models are as follows:

$$\Delta W_{ni} = Z_0 + an + bn + cr^2 + dr^2 \quad (3)$$

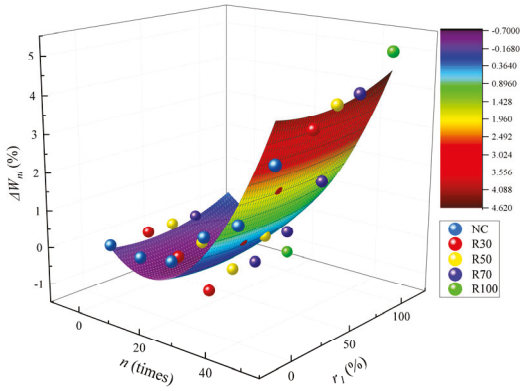

Figure 7. Fitting model of the number of FTCs, RCA replacement ratio and mass loss rate.

Table 5 shows the fitting parameters of n, r, and ΔW_{ni} The fitting correlation coefficient R^2 was 0.9253, indicating that the fitted model could better predict the mass loss rate of RAC after FTCs.

Table 5. Fitting parameters between n, r and ΔW_{ni}.

ΔW_{ni}	z_0	a	b	c	d	R^2
RAC	−0.08272	−0.08065	−0.00763	0.00331	1.21316×10^{-4}	0.9253

3.1.3. Relative Dynamic Elastic Modulus

The changes in the RDEM (P_n) of the RAC in the freeze–thaw environment are shown in Figure 8. In general, the resonant frequency of an object is related to its density. During the FTC, the resonance frequency of the test piece is measured via dynamic ballast to accurately determine the development status of fractures [46]. With an increasing number of FTCs, the RDEM of the concrete samples with different RCA substitution ratios tended to decrease. After 50 FTCs, the RDEM of the RAC decreased to 71.99%–80.78%. In addition, under different numbers of FTCs, the RDEM of the concrete with an RCA replacement rate of 100% was the lowest, and the RDEM of the RAC decreased with increasing RCA replacement rate.

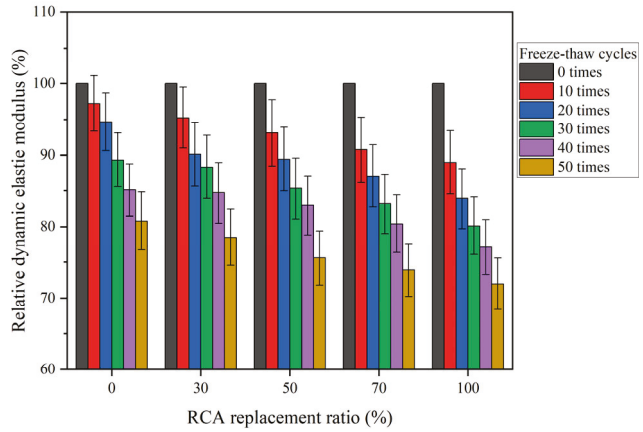

Figure 8. RDEM of the RCA concrete.

The fitting models of RAC n, r, and P_n are shown in Figure 9. The fitted models are as follows:

$$P_n = 102.59688 - 0.44581n - 0.7709r \quad (4)$$

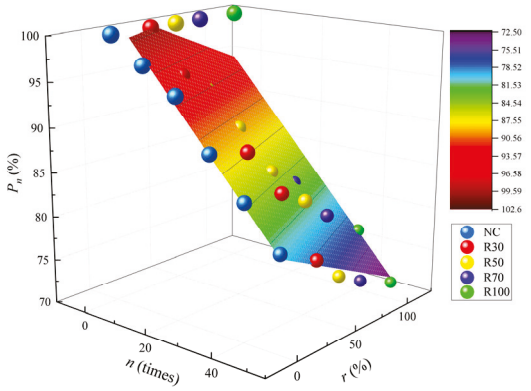

Figure 9. Fitting model of the number of FTCs, RCA replacement ratio, and RDEM.

The fitted correlation coefficient R^2 of 0.9621 indicates that the model provides a highly accurate prediction of the RDEM of RAC after FTCs.

3.2. Freeze–Thaw Damage Model

Owing to the changes in positive and negative temperatures, the aqueous solution alternates back and forth between the liquid phase and the solid phase; as a result, cracks inside the concrete are gradually generated and developed, and the performance of the concrete is gradually reduced. The degree of damage is a variable that represents the internal damage state of the material and can be used to describe the damage evolution process of concrete during the FTC [22,47]. On the basis of damage mechanics theory, concrete before FTCs is considered a nondestructive material composed of countless microelements, and the degree of damage is defined as the ratio of the number of microelements damaged after FTCs to the number of microelements damaged before FTCs [48]. In this study, the RDEM of the concrete was used to represent the change in the number of microelements in the concrete before and after freeze–thawing [26,49]. On the basis of the strain equivalence assumption proposed by Lematire [50], the degree of damage D_N is defined as follows:

$$D_N = 1 - \frac{E_N}{E_0} \tag{5}$$

where D_N represents the freeze–thaw damage value of the concrete sample, E_N represents the dynamic elastic modulus of the concrete sample after N cycles of freeze–thaw, E_0 represents the dynamic modulus of elasticity of the concrete sample without freeze–thaw, and N represents the number of FTCs of the test sample.

3.2.1. Construction of GM(1, 1) Model

Various prediction models for freeze–thaw damage in RAC have been developed by researchers, including models based on the Weibull distribution [51], the GM method [20,21], models developed from the Aas-Jakobsen fatigue theory [52], and classical damage evolution models such as the Chaboche model [53]. Among these, the Weibull distribution model effectively captures performance variability caused by the uneven distribution of internal defects in concrete; however, its prediction accuracy is highly sensitive to the number of test samples [54]. Freeze–thaw damage is inherently a complex process involving coupled physical and chemical interactions, which differ significantly from the mechanical fatigue damage mechanisms observed in metallic materials. Consequently, directly applying the Aas-Jakobsen fatigue theory struggles to accurately capture specific damage mechanisms prevalent in freeze–thaw processes, such as salt crystallization and moisture migration [51,55]. Although the Chaboche damage evolution model can meticulously describe the nonlinear accumulation of damage, it involves numerous material parameters,

making practical calibration challenging [51,55]. In contrast, the GM offers distinct advantages in handling data characterized by "small sample sizes and limited information." It enables effective prediction of long-term material durability based on limited initial experimental data, providing an efficient and economical approach for rapidly assessing the frost resistance of RAC. Therefore, the GM was selected in this study to establish the freeze–thaw damage prediction model for RAC.

The first-order, one-variable grey model, GM(1, 1), is effective for modeling systems with limited data [56]. It processes original, non-negative, discrete data sequences through accumulation to reveal underlying patterns [57]. GM(1, 1) is more accurate at modeling monotonic data, can retain the characteristics of the original system, and better reflects the real situation of the system [58]. Therefore, in this experiment, GM(1, 1) is used to establish a prediction model for the degree of damage D_N. For the detailed modeling steps, see the literature [33,59].

The freeze–thaw damage data of the RAC are shown in Table 6. The freeze–thaw damage data of the RAC were brought into the GM (1, 1), where n (n = 10 k) represents the number of FTCs and $X^{(0)}$ represents the freeze–thaw damage value of the RAC.

Table 6. Raw data of D_N after FTCs (%).

FTC (Times)	$X^{(0)} \times 100$				
	NC	R30	R50	R70	R100
10	2.76	4.76	6.88	9.23	11.02
20	5.34	9.89	10.57	12.91	16.09
30	10.67	11.66	14.67	16.82	19.9
40	14.88	15.29	17.03	19.61	22.89
50	19.22	21.51	24.4	26.08	28.01

3.2.2. Validation and Analysis of GM(1, 1) Model

The accuracy of the GM(1, 1) model was further tested on the calculation results via the posterior difference test method [18]. The specific formula is as follows:

$$\bar{\varepsilon} = \frac{1}{m}\sum_{k=1}^{m} \varepsilon_k \tag{6}$$

where $\bar{\varepsilon}$ represents the mean of the residuals, ε_k denotes the residual of the k-th sample, and m indicates the total number of samples.

$$S_1{}^2 = \frac{1}{m}\sum_{k=1}^{m} (\varepsilon_k - \bar{\varepsilon})^2 \tag{7}$$

where $S_1{}^2$ represents the variance of the residuals, $\bar{\varepsilon}$ represents the mean of the residuals, ε_k denotes the residual of the k-th sample, and m indicates the total number of samples.

$$\overline{X} = \frac{1}{m}\sum_{k=1}^{m} X^{(0)}{}_k \tag{8}$$

where $\overline{X}$ represents the mean of the original sequence, $X^{(0)}{}_k$ denotes the k-th sample in the original sequence, and m indicates the total number of samples.

$$S_2{}^2 = \frac{1}{m}\sum_{k=1}^{m} (X_k{}^{(0)} - \overline{X})^2 \tag{9}$$

where $S_2{}^2$ represents the variance of the original sequence, $\overline{X}$ represents the mean of the original sequence, $X_k{}^{(0)}$ denotes the k-th sample in the original sequence, and m indicates the total number of samples.

$$c = \frac{S_1}{S_2} \tag{10}$$

where c denotes the posteriori error ratio, S_1 represents the standard deviation of the residuals, and S_2 signifies the standard deviation of the original sequence.

$$\begin{aligned} p &= P((\varepsilon_k - \overline{\varepsilon}) < 0.6745 S_2) \\ u &= (\varepsilon_k - \overline{\varepsilon}) < 0.6745 S_2 \\ P &= \tfrac{u}{m} \end{aligned} \tag{11}$$

In the equation, both u and P denote probability values, where p signifies the small error probability, $\overline{\varepsilon}$ represents the mean of the residuals, ε_k denotes the residual of the k-th sample, m indicates the total number of samples, and S_2 signifies the standard deviation of the original sequence.

The accuracy test results and accuracy level comparison tables for the G(1, 1) model are shown in Tables 7 and 8, respectively. Both the posteriori error ratio (c) and the small error probability (p) attained Grade I, indicating that the GM(1, 1) model exhibits high accuracy and provides reliable predictions for the freeze–thaw damage of RAC.

Table 7. Accuracy test results of the GM(1, 1) model.

Type	*c*	*p*	Accuracy Class
NC	0.16263	1	Grade I
R30	0.12308		
R50	0.09466		
R70	0.06736		
R100	0.09152		

Table 8. Comparison of accuracy grades.

Accuracy Class	*c*	*p*
Grade I (Good)	0–0.35	0.95–1
Grade II (eligible)	0.35–0.5	0.8–0.95
Grade III (badly qualified)	0.5–0.65	0.7–0.8
Grade IV (Failed)	0.65–1	0–0.7

The damage data of the RAC before 50 FTCs were brought into the GM(1, 1) model for fitting, and the fitting results are shown in Table 9. When $R^2 > 0.92$, the fitting accuracy of the GM(1, 1) model is high.

Table 9. Results of the fitting and prediction of freeze–thaw damage.

n	$X^{(0)} \times 100$				
	NC	R30	R50	R70	R100
0	0	0	0	0	0
10	0.0503	6.172	7.6034	9.826	12.4634
20	6.5301	8.4099	10.1202	12.4985	15.2942
30	9.6147	11.4592	13.4699	15.898	18.7679
40	14.1564	15.6141	17.9285	20.2219	23.0307
50	20.8433	21.2756	23.8628	25.722	28.2616
R^2	0.96797	0.98506	0.99125	0.99556	0.99168

The freeze–thaw damage value D_N of the RAC is shown in Figure 10. According to GB/T 50082-2009 [37], D_N = 40% is the critical value for the freeze–thaw damage of a test sample. After 50 RAC FTCs, the D_N ranged from 20.84% to 28.26%. Through the R^2 and posterior difference tests, the G(1, 1) prediction model had higher accuracy and could better predict the RAC frost resistance.

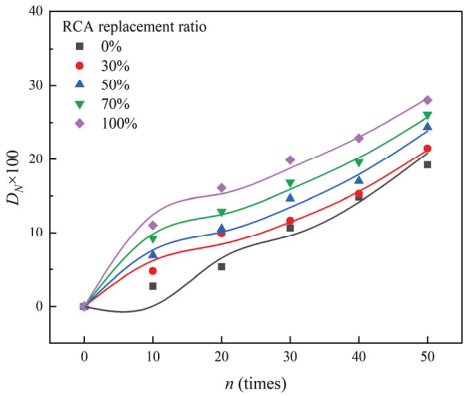

Figure 10. Predicted freeze–thaw damage value D_N.

3.3. Freeze–Thaw Damage Mechanism

To thoroughly elucidate the freeze–thaw damage mechanism of RAC in depth, a systematic analysis of the ITZ structures of NCA and RCA is necessary. A schematic diagram comparing the ITZ structures of NCA and RCA is presented in Figure 11. It can be observed that the ITZ structure of RCA is relatively simple, consisting only of the transition zone formed between the NCA and the new mortar (ITZ1). In contrast, the ITZ structure of RAC is more complex. In addition to ITZ1, it includes the transition zone between the new mortar and the old adhered mortar (ITZ2), as well as the transition zone between the original aggregate (within the RCA) and the old adhered mortar (ITZ3). This multi-layered ITZ system in RAC contributes to its higher susceptibility to freeze–thaw damage.

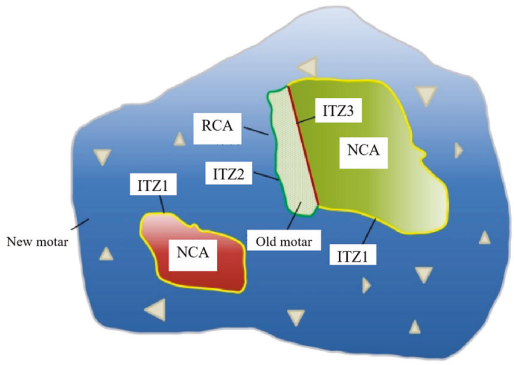

Figure 11. Schematic diagram comparing the ITZ structures of NCA and RCA.

The DMD and SEM images of the NCA before and after freeze–thaw cycling are shown in Figure 12. As shown in Figure 12a, in the early stage of FTCs (after 10 FTCs), the NCA cement stone had no cracks, and the main cracks appeared in the mortar and ITZ [60]. The interior of the NCA is very dense with almost no cracks; therefore, its deformation (contraction and expansion) during the freeze–thaw process is relatively small. When the NCA cement mortar region freezes, the aqueous solution in the gel pores is absorbed by the capillary pores and air bubbles, and the volume decreases; the gel pores absorb the aqueous solution from the outside when melting, and the volume expands. During the freeze–thaw process, the mortar region experienced large deformation, which caused the cracks in the

ITZ region to propagate continuously. In addition, owing to the high water–cement ratio in the ITZ region during the condensation and hardening process, the NCA concrete has more pores in the ITZ region, and its strength is lower; thus, the ITZ region of the test piece is the most prone to stress concentration.

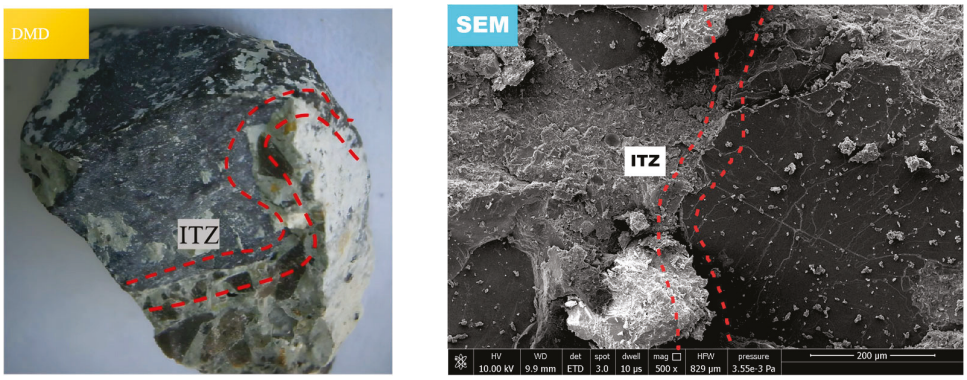

(**a**) Early freeze–thaw period

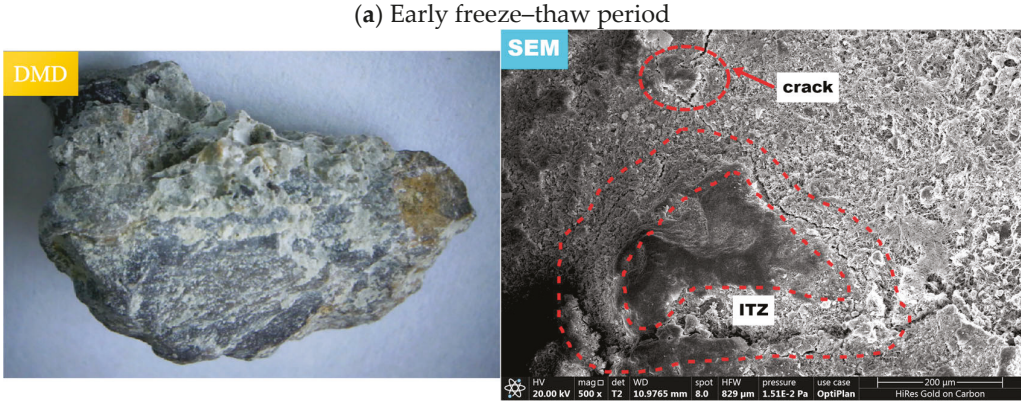

(**b**) Later stage of freeze–thawing

Figure 12. DMD and SEM images of NCA cement stones. (Note: 3.55E-3 represents 3.55×10^{-3}, 1.51E-2 represents 1.51×10^{-2}).

As shown in Figure 12b, at the later stage of the FTC (after 50 FTCs), the ITZ of the NCA cement was severely damaged. As the number of FTCs increases, the cracks in the ITZ continue to develop, the diameter of the bubbles increases, the number of fractures in the ITZ increases, and the pore spacing decreases, as shown in Figure 13. Scherer et al. [61] and Powers et al. [62] reported that the diameter r_2 of the bubbles in the ITZ at the later stage of freeze–thawing is greater than the diameter r_1 of the early stage of freeze–thawing, and the spacing L_2 of the air bubbles in the ITZ is smaller than the number of bubbles L_1 at the early stage of freeze–thawing; therefore, in the NCA, the hydrostatic pressure and crystallization pressure in the cement ITZ decrease as the cracks on the pore wall propagate. On the other hand, in the early stage of freeze–thawing, c_1 (the concentration of the aqueous solution in the air bubbles in the early stage of freeze–thawing) > c_2 (the concentration of the aqueous solution in the capillary pores in the early stage of freeze–thawing) > c_3 (the concentration of the aqueous solution in the gel pores in the early stage of freeze–thawing); therefore, in terms of the difference in concentration, the aqueous solution in the gel pores continuously flows to the capillary pores and air bubbles, and during this process, osmotic pressure is generated on the pore walls. During the later stage of freeze–thawing, the diameters of the air bubbles and capillary pores in the ITZ expand, and the volume of the ice crystals increases; as a result, the concentrations of c_4 (the concentration of the aqueous solution in the bubbles during the later stage of freeze–thawing) and c_5 (the concentration of the aqueous solution in the capillary pores during the later stage of freeze–thawing) increase,

c_5, c_4 and c_6 (the concentration of the aqueous solution in the gel pores during the later stage of freeze–thawing) further increase, resulting in an increase in the osmotic pressure in the ITZ region.

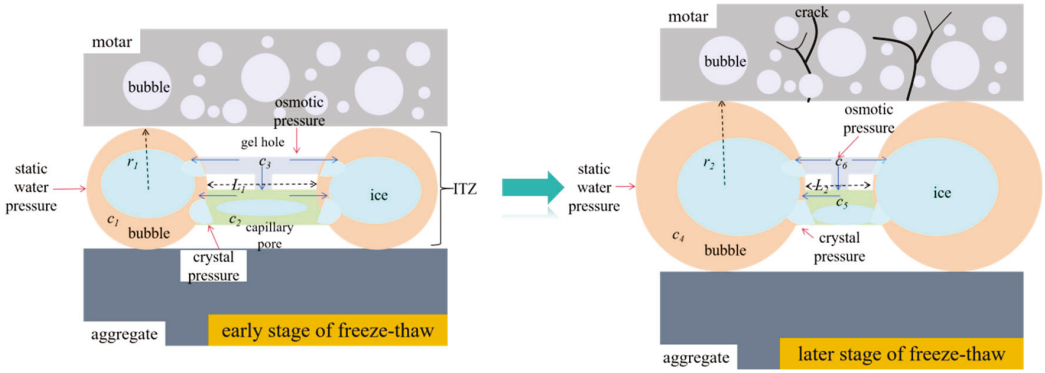

Figure 13. Diagram of the freeze–thaw mechanism of NCA cement.

During the initial stage of freeze–thawing, the crystallization pressure and hydrostatic pressure inside the bubbles increased. As the number of FTCs increases, the bubbles experience fatigue failure, the pore wall is damaged, the size expands, and the internal pressure (hydrostatic pressure and crystallization pressure) of the bubbles decreases, whereas the pressure (osmotic pressure) on the capillary pores and gel pores increases, which is referred to as the "pressure shift down" phenomenon. As the number of FTCs increases, the pressure of the larger air bubbles shifts to smaller capillary pores and gel pores. Therefore, as the number of FTCs increased, the internal stress of the test sample tended to increase overall. In addition, when the test piece melts, the air bubbles and ice in the capillary pores melt, the aqueous solution flows back into the gel pores, and the tensile stress in the test piece decreases. As the number of FTCs increases, the pores will suffer fatigue breakage. When the pore size reaches a certain stage, the test piece will suffer from global failure.

The DMD and SEM images of RCA before and after freeze–thaw cycles are shown in Figure 14. Figure 14a reveals that during the initial freeze–thaw stages, the aggregate particles within the RCA cement paste remain relatively dense and suffer minor damage, whereas the old mortar, along with the old and new ITZs, exhibits a porous and microcracked structure, becoming the primary zones of damage concentration [63,64]. The propagation and interconnection of these microcracks manifest macroscopically as initial surface roughening and localized minor spalling, leading to the observed mass loss in the concrete specimens. Furthermore, the differential thermal expansion coefficients between the aggregate and the mortar result in more initial microcracks within the old ITZ, exacerbating its freeze–thaw damage [65]. Consequently, damage in RAC typically initiates at the internal old mortar interfaces and is more severe than in conventional concrete, macroscopically evidenced by greater mass loss and a more significant reduction in the RDEM for RAC. Figure 14b demonstrates that in the later freeze–thaw stages, the old ITZ experiences the most severe damage, culminating in paste-aggregate separation and ultimately leading to specimen failure. This key microstructural failure directly corresponds to the macroscopic phenomena of extensive mortar and aggregate spalling and a sharp decline in mass.

As freeze–thaw cycling progresses, a "stress shift" phenomenon also occurs within the RCA cement paste. However, due to the pre-existing abundance of microcracks and larger defect zones in RCA, cracks within the ITZ propagate rapidly, as illustrated in Figure 15. This allows water and ice crystallization pressures to penetrate deeper into the material. Macroscopically, this is reflected by damage progression not being limited to the surface but extending inwards, leading to a continuous decline in the RDEM with increasing FTCs. Moreover, under the same number of cycles, RCA cement paste suffers greater damage

than NCA cement paste [66], specifically manifested as a much larger reduction in the relative dynamic modulus for RAC. This is attributed to the higher number of microcracks in RCA, which severely impair the material's ability to transmit elastic waves, indicating a rapid loss of load-bearing stiffness. Additionally, the significant difference in the thermal expansion coefficients between the aggregate and the mortar causes the old and new ITZs to endure the most severe damage, leading to paste-aggregate separation [67]. In summary, the macroscopic spalling, mass loss, and deterioration of the dynamic modulus of elasticity in RAC are the direct external manifestations of the initiation, propagation, and ultimate failure of its internal weak interfaces under freeze–thaw action.

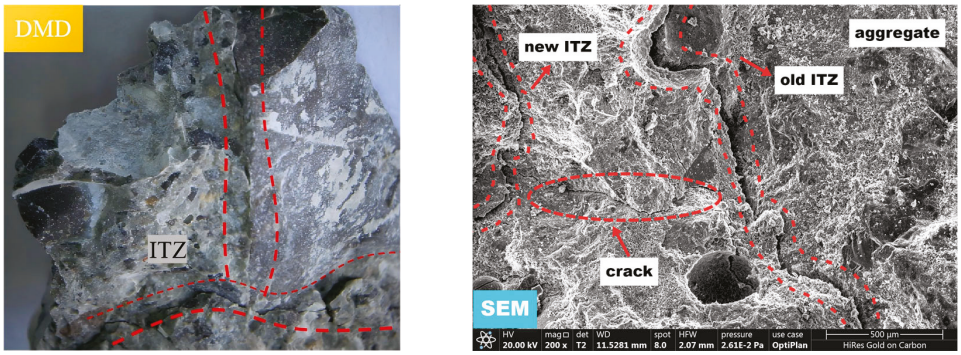

(**a**) Early freeze–thaw period.

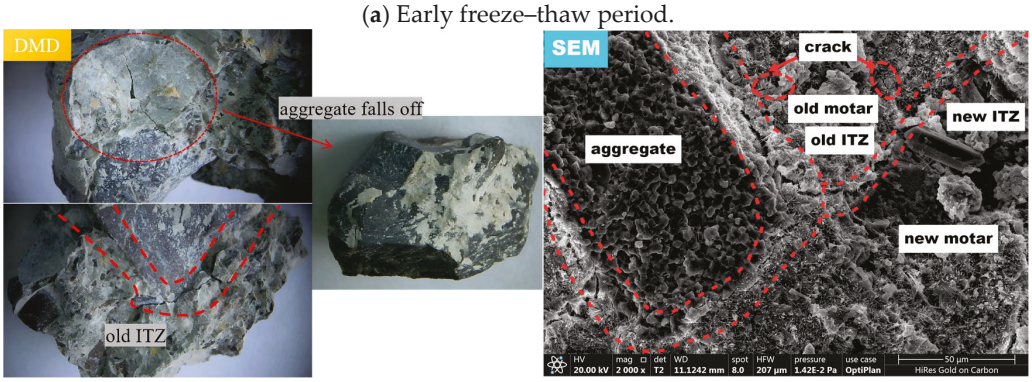

(**b**) Late stage of freeze–thaw period.

Figure 14. DMD and SEM images of RCA cement stones. (Note: 2.61E-2 represents 2.61×10^{-2}, 1.42E-2 represents 1.42×10^{-2}).

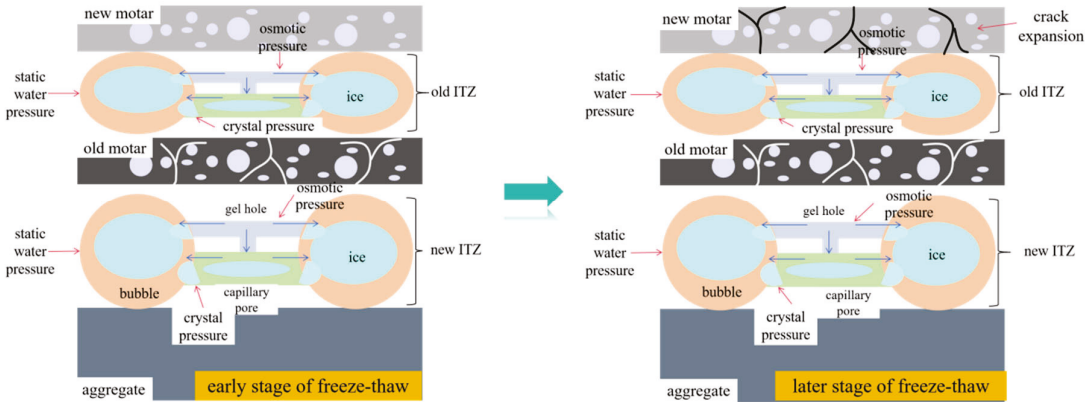

Figure 15. Diagram of the freeze–thaw mechanism of the RCA cement stone.

4. Conclusions

1. The degree of freeze–thaw damage in concrete intensifies with increasing RCA replacement ratios and number of FTCs. When the RCA replacement ratio exceeds 50%, specimens exhibit extensive mortar spalling and aggregate exposure after only

50 cycles, indicating a significant acceleration of apparent damage. It is therefore recommended to strictly limit the RCA replacement ratio to below 50% in critical structures located in severe cold regions to ensure adequate frost durability.

2. The minimum mass loss rate of RAC (averaging −0.92%) is considerably lower than that of conventional concrete (−0.08%), attributable to a more pronounced initial "weight gain" effect due to the continued hydration of the adhered old mortar. The mass loss rate of RAC demonstrates an initial decrease followed by an increase with progressing FTCs, with this transition typically occurring around 20 cycles. This threshold can serve as a criterion for assessing the stage of freeze–thaw damage development in RAC.
3. A GM(1, 1) prediction model for freeze–thaw damage was established based on the RDEM of RAC. Evaluation via the R^2 value and the posteriori error test method confirmed that the GM(1, 1) model achieves a high precision level (Grade I), providing a highly reliable theoretical basis for predicting the freeze–thaw service life of RAC.
4. This study elucidates the origin and evolution of freeze–thaw damage in RAC from a microstructural perspective, offering a mechanistic explanation for its performance degradation. Microstructural testing unequivocally confirmed that the old ITZ between the adhered old mortar and the original aggregate within the RCA is the primary site and the weakest link for damage initiation. The propagation of microcracks from this zone is identified as the fundamental cause of the observed macroscopic performance deterioration.

Author Contributions: M.L.: Writing—original draft, data curation, and investigation. H.L. and S.G.: Methodology and writing—review and editing. C.X.: Data curation, writing—review and editing. B.L.: Data curation and funding acquisition. X.M.: Writing—review and editing. S.X.: Writing—review and editing, and funding acquisition. T.S.: Writing—review and editing, Writing—original draft, supervision, investigation, and funding acquisition. All authors have read and agreed to the published version of the manuscript.

Funding: This work was supported by the National Natural Science Foundation of China (52309137 (Bangxiang Li)), the Natural Science Foundation of Shandong Province (ZR2025MS802 (Tian Su); ZR2024QE218 (Bangxiang Li)), and the Natural Science Foundation of Inner Mongolia Autonomous Region (2025MS05007 (Xuefeng Mei); 2025FX037 (Sheng Xu)).

Institutional Review Board Statement: Not applicable.

Informed Consent Statement: Not applicable.

Data Availability Statement: The data presented in this study are available on request from the corresponding author.

Conflicts of Interest: The authors declare that they have no known competing financial interests or personal relationships that could have appeared to influence the work reported in this paper.

References

1. Bai, G.; Zhu, C.; Liu, C.; Liu, B. An evaluation of the recycled aggregate characteristics and the recycled aggregate concrete mechanical properties. *Constr. Build. Mater.* **2020**, *240*, 117978. [CrossRef]
2. Wang, B.; Yan, L.; Fu, Q.; Kasal, B. A comprehensive review on recycled aggregate and recycled aggregate concrete. *Resour. Conserv. Recycl.* **2021**, *171*, 105565. [CrossRef]
3. Zhang, L.; Ding, D.; Zhao, J.; Zhou, G.; Wang, Z. Mixture Design and Mechanical Properties of Recycled Mortar and Fully Recycled Aggregate Concrete Incorporated with Fly Ash. *Materials* **2022**, *15*, 8143. [CrossRef] [PubMed]
4. Yuan, H.; Zhu, L.; Wang, X.; Yang, H. Effect of microstructure on the mechanical properties of steel fiber-reinforced recycled concretes. *Materials* **2022**, *15*, 4018. [CrossRef]
5. Yan, H.; Liu, Q.; Han, F.; Liu, S.; Han, T.; He, B. Frost Durability of Self-Compacting Concrete Prepared with Aeolian Sand and Recycled Coarse Aggregate. *Materials* **2023**, *16*, 6393. [CrossRef]

6. Zhu, P.; Chen, X.; Liu, H.; Wang, Z.; Chen, C.; Li, H. Recycling of waste recycled aggregate concrete in freeze-thaw environment and emergy analysis of concrete recycling system. *J. Build. Eng.* **2024**, *96*, 110377. [CrossRef]
7. Zhang, M. *Research on Mechanics and Durability Performance of Recycled Concrete*; Hefei University: Hefei, China, 2024. (In Chinese)
8. Song, Y.; Zhou, W.; Zhang, C.; Yang, C. Frost Resistance and Microscopic Properties of Recycled Coarse Aggregate Concrete Containing Chemical Admixtures. *Materials* **2024**, *17*, 4687. [CrossRef]
9. Omidinasab, F.; Moazami Goodarzi, S.; Sahraei Moghadam, A. Characterization and optimization of mechanical and impact properties of steel fiber reinforced recycled concrete. *Int. J. Civ. Eng.* **2022**, *20*, 41–55. [CrossRef]
10. Ahmed, T.W.; Ali, A.A.M.; Zidan, R.S. Properties of high strength polypropylene fiber concrete containing recycled aggregate. *Constr. Build. Mater.* **2020**, *241*, 118010. [CrossRef]
11. Xue, G. *Investigation on Influence of Strengthening of Coarse Aggregate on Performance of Recycled Concrete*; Xi'an University of Science and Technology: Xian, China, 2022. (In Chinese)
12. Su, T.; Wang, T.; Zhang, Z.; Sun, X.; Gong, S.; Mei, X.; Tan, Z.; Cui, S. Mechanical properties and frost resistance of recycled brick aggregate concrete modified by nano-SiO_2. *Nanotechnol. Rev.* **2023**, *12*, 20230576. [CrossRef]
13. Ji, Y.; Zhang, H. Frost resistance investigation of fiber reinforced recycled brick aggregate cementitious materials. *Sci. Rep.* **2022**, *12*, 15311. [CrossRef]
14. Fu, K.; Sang, Y.; Chen, C.; Liu, K. Frost resistance of recycled aggregate concrete subjected to coupling sustained compressive load and freeze–thaw cycles. *Constr. Build. Mater.* **2024**, *448*, 138219. [CrossRef]
15. Yu, Z.; Zhang, H.; Bao, J.; Zhang, P.; Ding, Y.; Chen, X.; Qin, L.; Sun, J.; Song, Q. Coupled effects of the freeze–thaw cycles and salt erosion on the performance of recycled aggregate concrete. *J. Build. Eng.* **2024**, *95*, 110212. [CrossRef]
16. Xiao, Q.; Wu, Z.; Qiu, J.; Dong, Z.; Shi, S. Capillary water absorption performance and damage constitutive model of recycled concrete under freeze–thaw action. *Constr. Build. Mater.* **2022**, *353*, 129120. [CrossRef]
17. Niu, H.; Fan, Y.; Zhang, X.; Ying, X. Experimental study on frost resistance of recycled concrete with different replacement ratios. *J. Mater. Sci. Eng.* **2018**, *36*, 615–620. (In Chinese)
18. Deng, J. *Grey System Theory Tutorial*; Huazhong University of Science and Technology Press: Wuhan, China, 1990. (In Chinese)
19. Liu, S. *Grey System Theory and Its Applications*; Science Press: Beijing, China, 2017. (In Chinese)
20. Liu, Q.; Shen, X.; Wei, L.; Dong, R.; Xue, H. Gray model research based on the pore structure fractal and strength of NMR Aeolian sand lightweight aggregate concrete. *JOM* **2019**, *72*, 536–543. [CrossRef]
21. Feng, Z.; Chen, S.; Xu, H.; Yao, X. Durability evaluation of concrete in alpine salt marsh area based on gray system theory. *J. Traffic Transp. Eng.* **2018**, *18*, 18–26.
22. Gao, C.; Kong, Z.; Shen, X. Freeze-thaw Resistance Evaluation of Lightweight Aggregate Concrete with Stress Damage Based on GM(1,1). *Adv. Eng. Sci.* **2021**, *53*, 184–190. (In Chinese)
23. Powers, T.C. A working hypothesis for further studies of frost resistance of concrete. *J. Proc.* **1945**, *41*, 245–272.
24. Powers, T.C.; Helmuth, R.A. Theory of volume changes in hardened portland-cement paste during freezing. *Highw. Res. Board Proc.* **1953**, *32*, 285–297.
25. Zhang, S.; Tian, B.; Chen, B.; Lu, X.; Xiong, B.; Shuang, N. The influence of freeze–thaw cycles and corrosion on reinforced concrete and the relationship between the evolutions of the microstructure and mechanical properties. *Materials* **2022**, *15*, 6215. [CrossRef] [PubMed]
26. Zhou, J.; Wang, G.; Xu, J. Experimental evaluation of the concrete damage and pore characteristics under salt-freezing cycles. *Materials* **2022**, *15*, 4454. [CrossRef] [PubMed]
27. Kong, L.; Meng, Y.; Gu, Y.; Wang, W. Study on freeze-thaw resistance of granite waste recycled concrete pavement bricks. Bull. *Chin. Ceram. Soc.* **2021**, *40*, 1545–1553+1563. (In Chinese)
28. Qiu, J.; Li, L.; Li, L.; Luan, X.; Guan, X.; Niu, G. Study on the deterioration characteristics and mechanisms of recycled brick-concrete aggregate concrete under load-freeze–thaw coupling. *Constr. Build. Mater.* **2024**, *413*, 134817. [CrossRef]
29. Bai, W.; Wang, X.; Yuan, C.; Guan, J.; Cao, K.; Xie, C. Study on dynamic mechanical properties and meso-damage mechanism of carbon fibers recycled aggregate concrete under freeze–thaw environment. *J. Build. Eng.* **2023**, *79*, 107768. [CrossRef]
30. *GB/T 39698-2020*; Confirmation Methods for Delivering Common Portland Cement. State Market Regulatory Administration: Beijing, China, 2020. (In Chinese)
31. *JGJ 52-2006*; Standard for Technical Requirements and Test Method of Sand and Crushed Stone for Ordinary Concrete. China Academy of Building Research: Beijing, China, 2006. (In Chinese)
32. Gong, S.; Wang, T.; Hasan, M.M.; Mei, X.; Tan, Z.; Su, T.; Cao, F. Effect of polypropylene fiber and nano-silica on the compressive strength and frost resistance of recycled brick aggregate concrete. *Nanotechnol. Rev.* **2023**, *12*, 20230174. [CrossRef]
33. Tan, G.; Gong, S.; Wang, T.; Li, M.; Li, J.; Ren, X.; Zhang, W.; Wang, C.; Cao, F.; Su, T. Mechanical Damage and Freeze–Thaw Damage of Concrete with Recycled Brick Coarse Aggregate. *Sustainability* **2024**, *16*, 5643. [CrossRef]
34. *JGJ 55-2019*; Specification for Mix Proportion Design of Ordinary Concrete. Ministry of Housing and Urban-Rural Development of the People's Republic of China: Beijing, China, 2019. (In Chinese)

35. Yu, Z.; Hou, Y.; Zhu, J.; Tian, Y. Frost resistance and service life prediction of recycled aggregate concrete (RAC) under flexural fatigue damage. *Constr. Build. Mater.* **2025**, *458*, 139787. [CrossRef]
36. Wang, C.; Zhang, M.; Pei, W.; Lai, Y.; Zhang, R.; Sun, J.; Zhao, T. Deterioration process and damage constitutive model of concrete under freeze-thaw circumstance of severely cold regions. *Cold Reg. Sci. Technol.* **2024**, *226*, 104290. [CrossRef]
37. *GB/T 50082-2009*; Standard for Test Methods of Long-Term Performance and Durability of Ordinary Concrete. China Architecture & Building Press: Beijing, China, 2009. (In Chinese)
38. Hu, A.; Chen, X.; Du, X.; Wang, F. Dynamic Compressive Damage Constitutive Correction of Concrete Under Freeze-Thaw Cycle. *Materials* **2025**, *18*, 1238. [CrossRef]
39. Chen, M.; Yang, S.; Wang, S.; Zhou, Y. Experimental study on pore structure and dynamic mechanical properties of modified rubber concrete after freeze-thaw cycle. *Sci. Rep.* **2025**, *15*, 5384. [CrossRef] [PubMed]
40. Qian, J.; Zhou, L.; Wang, X.; Yang, J. Degradation of Mechanical Properties of Graphene Oxide Concrete under Sulfate Attack and Freeze–Thaw Cycle Environment. *Materials* **2023**, *16*, 6949. [CrossRef] [PubMed]
41. Guo, L. *Application of Nano-Silica in Polypropylene Fiber Reinforced Concrete*; Heilongjiang University: Haerbin, China, 2021. (In Chinese)
42. Wei, P. *Experimental Study on Properties of Basalt Fiber and Nano-SiO_2 Mixed Concrete*; Xi'an University of Technology: Xian, China, 2022. (In Chinese)
43. Wei, S. *Research on Influence of Mineral Admixture on Chloride Corrosion Resistance and Frost Resistance of Recycled Concrete*; China University of Mining and Technology: Xuzhou, China, 2020. (In Chinese)
44. Luan, H.; Wu, J.; Pan, J. Freeze-thaw durability of recycled aggregate concrete: An overview. *J. Wuhan Univ. Technol. (Mater. Sci. Ed.)* **2021**, *36*, 58–69. [CrossRef]
45. Gong, J.; Zhang, W. The effects of pozzolanic powder on foam concrete pore structure and frost resistance. *Constr. Build. Mater.* **2019**, *208*, 135–143. [CrossRef]
46. Lin, H.; Takasu, K.; Suyama, H.; Koyamada, H.; Liu, S. A study on properties, static and dynamic elastic modulus of recycled concrete under the influence of modified fly ash. *Constr. Build. Mater.* **2022**, *347*, 128585. [CrossRef]
47. Fu, H.; Tian, J.; Chin, C.L.; Liu, H.; Yuan, J.; Tang, S.; Mai, R.; Wu, X. Axial compression behavior of GFRP-steel composite tube confinedseawater sea-sand concrete intermediate long columns. *Eng. Struct.* **2025**, *333*, 120157. [CrossRef]
48. He, Z.; Shen, A.; Wu, H.; Wang, W.; Wang, L.; Guo, Y. Properties and mechanisms of brick-concrete recycled aggregate strengthened by compound modification treatment. *Constr. Build. Mater.* **2022**, *315*, 125678. [CrossRef]
49. Zhu, C.; Zhao, W.; Yu, W. Basic Mechanical Properties and Constitutive Model of Recycled Brick-Concrete Aggregate Concrete. *Acta Mater. Compos. Sin.* **2024**, *41*, 898–910. (In Chinese)
50. Tam, V.W.Y.; Le, K.N.; Evangelista, A.C.J.; Butera, A.; Tran, C.N.; Teara, A. Effect of fly ash and slag on concrete: Properties and emission analyses. *J. Hazard. Mater.* **2019**, *6*, 395–405. [CrossRef]
51. Cheng, Y.; Sun, L.; Li, Y.; Liu, M.; He, R.; Jin, X.; Jin, H. Damage model of steel fiber-reinforced coal gangue concrete under freeze–thaw cycles based on Weibull distribution. *Materials* **2023**, *16*, 6775. [CrossRef]
52. Zhao, N.; Meng, J.; Jia, J.; Bai, Y.; Du, X. Freeze-thaw damage and life prediction model of seawater and sea sand concrete (SWSSC). *Constr. Build. Mater.* **2025**, *475*, 141157. [CrossRef]
53. Zhang, F.; Li, X.; Wang, L.; Xue, Z.; Guo, Z. Effects of freeze-thaw cycles on fatigue performance of asphalt mixture and a fatigue-freeze-thaw damage evolution model. *Constr. Build. Mater.* **2024**, *449*, 138427. [CrossRef]
54. Zhou, D.; Chen, D.; Yang, F.; Mei, J.; Yao, Y.; Deng, Y. Freeze–thaw damage analysis and life prediction of modified pervious concrete based on Weibull distribution. *Case Stud. Constr. Mater.* **2024**, *20*, e03305. [CrossRef]
55. Fu, H.; Tian, J.; Chen, S.; Chin, C.L.; Ma, C.K. Axial compressive performance of CFRP-steel composite tubeconfined seawater sea-sand concrete intermediate slender columns. *Constr. Build. Mater.* **2024**, *441*, 137399. [CrossRef]
56. Tien, T.L. A research on the gray prediction model GM (1, n). *Appl. Math. Comput.* **2012**, *218*, 4903–4916.
57. Yu, J.; Qiao, H.; Zhu, F.; Wang, X.K. Research on damage and deterioration of fiber concrete under acid rain environment based on GM (1, 1)-Markov. *Materials* **2021**, *14*, 6326. [CrossRef]
58. Qin, Y.; Guan, K.; Kou, J.; Ma, Y.; Zhou, H.; Zhang, X. Durability evaluation and life prediction of fiber concrete with fly ash based on entropy weight method and gray theory. *Constr. Build. Mater.* **2022**, *327*, 126918. [CrossRef]
59. Fu, H.; Zhao, H.; Pan, Z.; Wu, Z.; Chin, C.L.; Ma, C.K. Behaviour of corroded circular steel tube strengthened with externalFRP tube grouting under eccentric loading: Numerical study. *Structures* **2023**, *56*, 104810. [CrossRef]
60. Lu, B.; Shi, C.; Cao, Z.; Guo, M.; Zheng, J. Effect of carbonated coarse recycled concrete aggregate on the properties and microstructure of recycled concrete. *J. Clean. Prod.* **2019**, *233*, 421–428. [CrossRef]
61. Scherer, G.W. Crystallization in pores. *Cem. Concr. Res.* **1999**, *29*, 1347–1358. [CrossRef]
62. Powers, T.C.; Willis, T.F. The air requirement of frost-resistant concrete. *Proc. Highway Res. Board.* **1949**, *6*, 184–211.
63. Yang, W.; Huang, Y.; Li, C.; Tang, Z.; Quan, W.; Xiong, X.; Jia, H.; Wu, W. Damage prediction and long-term cost performance analysis of glass fiber recycled concrete under freeze-thaw cycles. *Case Stud. Constr. Mater.* **2024**, *21*, e03795. [CrossRef]

64. Guan, T.; Zhang, L.; Zheng, Y.; Guan, J.; Zhang, Y.; Zhang, Y. Frost resistance and damage evolution model of basalt fiber-reinforced recycled concrete based on recycled coarse aggregate strengthening and vibration mixing processes. *J. Build. Eng.* **2024**, *91*, 109627. [CrossRef]
65. Li, H.; Liang, K.; Chen, H.; Su, R. The effect of carbonated recycled coarse aggregate on the fracture properties of concrete. *Constr. Build. Mater.* **2024**, *442*, 137562. [CrossRef]
66. Abuowda, E.; El-Hassan, H.; El-Maaddawy, T. Synergistic impact of geopolymer binder and recycled coarse aggregates on the performance of concrete masonry units. *Cleaner Mater.* **2024**, *14*, 100272. [CrossRef]
67. Zhang, W.; Duan, Z.; Liu, H.; Yao, Y.; Zhang, Z.; Liu, C. Salt freezing-thawing damage evolution model based on the time-dependent hydration reaction incorporating rice husk ash and recycled coarse aggregate. *Constr. Build. Mater.* **2024**, *440*, 137179. [CrossRef]

Disclaimer/Publisher's Note: The statements, opinions and data contained in all publications are solely those of the individual author(s) and contributor(s) and not of MDPI and/or the editor(s). MDPI and/or the editor(s) disclaim responsibility for any injury to people or property resulting from any ideas, methods, instructions or products referred to in the content.

coatings

MDPI

Article

Simulation of Macroscopic Chloride Ion Diffusion in Concrete Members

Zhaorui Ji, Bin Peng *, Wendong Guo and Mingyang Sun

School of Environment and Architecture, University of Shanghai for Science and Technology, Shanghai 200093, China; 242291859@st.usst.edu.cn (Z.J.); 243441950@st.usst.edu.cn (W.G.); 2335053021@st.usst.edu.cn (M.S.)
* Correspondence: binpeng@usst.edu.cn

Abstract

To quantitatively analyze the macroscopic diffusion process of chloride ions in existing concrete members, the Peridynamic Differential Operator (PDDO) was introduced to formulate a discrete format for Fick's second law, and a simulation model was established and validated. Subsequently, the influence of specific or randomly distributed defects in the concrete is reflected by adjusting the coefficients in the model's global matrix. Moreover, the complex geometry of concrete members is captured by employing a point set-based spatial discretization approach. The model also accommodates for the complex corrosion conditions encountered in practice by imposing different boundary conditions. These features allowed for the simulation and validation of chloride ion diffusion experiments on concrete under natural environmental conditions. The study further analyzed how factors such as defects, diffusion coefficients, boundary conditions, and the geometric shape of members influence the macroscopic diffusion process. The findings indicate that the numerical model based on the PDDO can effectively quantify the macroscopic diffusion of chloride ions in existing concrete members. It provides fundamental data for the durability maintenance of concrete infrastructures and potentially reduces their carbon footprint by preventing unnecessary rehabilitation or reconstruction.

Keywords: chloride ion; macroscopic diffusion; concrete member; peridynamic differential operator; simulation

1. Introduction

Chloride ion ingress to the steel reinforcement surface of existing concrete members, initiating corrosion, is a significant factor in the degradation of their structural durability [1–4]. In China, conditions such as the coastal salt spray environment, the extensive saline soil conditions in the western regions, and the widespread use of deicing salts in practical engineering scenarios present considerable opportunities for chloride ingress. This issue poses a risk to the durability of numerous significant infrastructures, including coastal and high-altitude buildings, high-speed rail lines, docks, sea-crossing bridges, breakwaters, and undersea tunnels [5,6]. Maintaining the durability of these infrastructures can postpone the rehabilitation or reconstruction of them, which will result in huge greenhouse gas emissions. Therefore, to support the durability maintenance of infrastructures and then to significantly reduce their carbon footprint, it is essential to quantitatively analyze the chloride ion transport process in existing concrete members.

Apparent diffusion is the macroscopic mechanism governing the transport of chloride ions within concrete, which can be described using Fick's second law and its modified

models [7–11]. This framework is characterized by its simplicity and clear meaning, allowing for the coupling effects of other transport mechanisms to be reflected through the model parameters, thereby effectively addressing engineering problems [12–14]. However, during quantitative analysis, the inherent pores and microcracks in concrete materials (collectively referred to as defects) lead to discontinuities in the solution domain. The varying geometries of different concrete members result in irregular solution domains, while differing environmental influences contribute to complex boundary conditions. These macro features render the analytical solutions of Fick's second law inapplicable and necessitate the use of numerical methods for resolution. The finite volume method (FVM) can effectively simulate chloride diffusion under complex boundary conditions, enabling accurate predictions of the chloride distribution and service life of concrete structures exposed to chloride environments [12]. The finite element model (FEM) can effectively be used to solve for multiphase chloride diffusion in concrete, incorporating the influence of the interfacial transition zone (ITZ) [15]. The FEM can be further used to solve three-phase and multi-component ionic transport models [16].

Although the aforementioned methods are applicable and can give meaningful results, they assume the solution domain is a continuous medium or a medium with minimal defects at specified locations. Such an assumption diverges significantly from the characteristics of existing concrete materials and members. Furthermore, these methods discretize the solution domain into a grid, making them less adaptable to complex geometries and resulting in pronounced grid dependency in the solution outcomes. Additionally, difference methods often struggle to satisfy the conservation principles expressed in integral form [17].

Under conditions of discontinuity in the medium (solution domain), employing nonlocal numerical methods to solve differential equations offers distinct advantages [18,19]. In scenarios in which the geometries of the solution domain and the boundary conditions are complex, nonlocal numerical methods based on point cloud discretization provide better adaptability compared to local methods that rely on grid discretization [20]. Researchers have utilized the nonlocal bond-based peridynamics (BBPD) method to conduct in-depth analyses of the diffusion process of chloride ions in saturated concrete at the mesoscale [21–23]. The approach based on the Peridynamic Differential Operator (PDDO) [24] retains the characteristics and advantages of the aforementioned peridynamic methods: it does not require the assumption of medium continuity; it introduces nonlocal (non-contact) interactions between material points, using the weighted averages of differences within neighborhoods to represent differentiation, thereby transforming differential equations into integral equations; and it effectively computes derivative values within the domain, whether at smooth, continuous, or discontinuous points. Furthermore, this method is more flexible than other implementations of peridynamics, allowing for irregular family shapes, or influence domains, of points and not requiring specialized modifications for boundaries. The computational process preserves the original macroscopic parameters and their physical significance, avoiding the introduction of difficult-to-calibrate mesoscopic parameters [25,26].

This study attempts to apply the PDDO to quantify the macroscopic diffusion process of chloride ions based on a modified form of Fick's second law. Initially, we provide a brief introduction to the theory of the PDDO. Subsequently, we simulate the three-dimensional diffusion process in concrete under ideal conditions and validate the reliability of the PDDO-based method by comparing it with analytical solutions. Building on this foundation, we consider engineering factors such as the discontinuity of concrete materials, the complex geometries of diffusion regions, and the diversity of diffusion boundary conditions to quantify the macroscopic diffusion phenomena of chloride ions in concrete

members under practical engineering scenarios. Finally, based on the simulation results from the PDDO-based method, we analyze the characteristics of chloride ion diffusion within concrete members. The results indicate that the proposed PDDO-based method can quantify macroscopic chloride ion diffusion in concrete. It can aid in the durability maintenance of infrastructures and potentially help to reduce their carbon footprint. To the best of the authors' knowledge, this is the first attempt to apply the PDDO to a simulation of macroscale chloride diffusion under engineering scenarios.

2. Discrete Solution Format of Fick's Second Law Using PDDO

2.1. Peridynamic Differential Operator

As illustrated in Figure 1, the solution domain can be discretized into a set of PD points. Each PD point $\boldsymbol{x}\ (\mathrm{x}_1,\ \mathrm{x}_2,\ \mathrm{x}_3)$ has multiple member points within its influence domain $H_{\mathbf{x}}$ (shaded gray area). Interactions occur through bonds between the PD point $\boldsymbol{x}$ and any member point $\boldsymbol{x}'\left(\mathrm{x}_1',\ \mathrm{x}_2',\ \mathrm{x}_3'\right)$, regardless of whether they are in contact. The initial length of the bond is defined as the magnitude of the initial relative position vector between the two points. The characteristic length (radius) of the influence domain is referred to as the horizon.

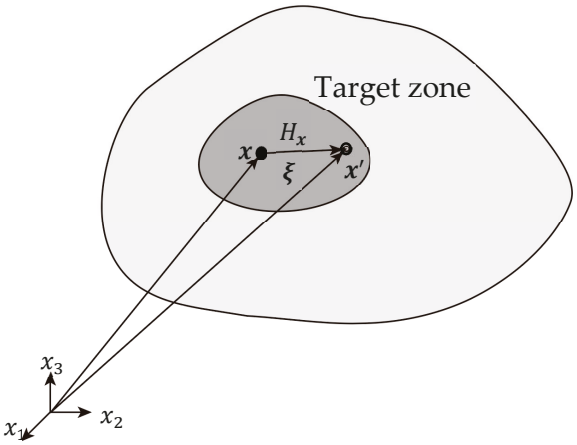

Figure 1. PD discretization of the target zone.

The Peridynamic Differential Operator (PDDO) for the field function $f(\mathrm{x})$ at point $\boldsymbol{x}$ is defined as follows [25]:

$$\frac{\partial^{p_1+p_2+p_3} f(x)}{\partial x_1^{p_1} \partial x_2^{p_2} \partial x_3^{p_3}} = \int_{H_x} f\left(x_1',\ x_2',\ x_3'\right) g_n^{p_1 p_2 p_3}(\xi) dV \tag{1}$$

where n is the sum of the highest order of the differential in the $x_1,\ x_2,\ x_3$ dimension; $p_1,\ p_2,\ p_3$ are the order of the differential in the $x_1,\ x_2,\ x_3$ dimension, respectively; $0 \le p_1 + p_2 + p_3 \le n$; $dV = d\xi_1 d\xi_2 d\xi_3$ denotes the micro-volume, represented by the member point $\left(x_1',\ x_2',\ x_3'\right)$; and $g_n^{p_1 p_2 p_3}(\boldsymbol{\xi})$ is the peridynamic (PD) function as follows:

$$g_n^{p_1 p_2 p_3}(\xi) = \sum_{q_1=0}^{n} \sum_{q_2=0}^{n-q_1} \sum_{q_3=0}^{n-q_1-q_2} a_{q_1 q_2 q_3}^{p_1 p_2 p_3} \omega_{q_1 q_2 q_3}(|\xi|) \xi_1^{q_1} \xi_2^{q_2} \xi_3^{q_3} \tag{2}$$

where $a_{q_1 q_2 q_3}^{p_1 p_2 p_3}$ are the undetermined coefficients, $|\boldsymbol{\xi}|$ is the magnitude of the relative position vector, and $\omega_{q_1 q_2 q_3}(|\boldsymbol{\xi}|)$ is the weight function. The weight function represents the physical characteristic parameters of the material and reflects the intensity of interactions between material points, providing a theoretical foundation for handling discontinuities in the

solution domain. Based on its statistical mechanical meaning and the required conditions of non-negativity and normalization, the form selected in this study is as follows [24]:

$$\omega(|\boldsymbol{\xi}|) \;=\; \pi^{-\frac{l}{2}}\left(\frac{s}{\delta}\right)^{l}\exp\left(-\frac{s^2}{\delta^2}|\xi|^2\right) \tag{3}$$

where l denotes the number of dimensions of the problem, with l = 1, 2, or 3, and $s > 0$ is the shape parameter, which is set to 4 in this study.

To determine the undetermined coefficients $a_{q_1q_2q_3}^{p_1p_2p_3}$, Equation (2) can be substituted into the orthogonality condition as follows:

$$\frac{1}{n_1!n_2!n_3!}\int_{H_x}\xi_1^{n_1}\xi_2^{n_2}\xi_3^{n_3}g_n^{p_1p_2p_3}(\boldsymbol{\xi})d\xi_1d\xi_2d\xi_3 \;=\; \delta_{n_1p_1}\delta_{n_2p_2}\delta_{n_3p_3} \tag{4}$$

where $n_1,\ n_2,\ n_3$, respectively, represent the highest order of expansion in the $x_1,\ x_2,\ x_3$ dimension after neglecting the remainder, and δnp is the Kronecker delta.

Then, by rearranging this, a system of linear equations is obtained as follows:

$$\sum_{q_1=0}^{n}\sum_{q_2=0}^{n-q_1}\sum_{q_3=0}^{n-q_1-q_2}A_{(n_1,n_2,n_3)(q_1,q_2,q_3)}a_{q_1q_2q_3}^{p_1p_2p_3} \;=\; b_{n_1n_2n_3}^{p_1p_2p_3} \tag{5}$$

where the shape coefficients $A_{(n_1,n_2,n_3)(q_1,q_2,q_3)} = \int_{H_x}\omega_{q_1q_2q_3}(|\boldsymbol{\xi}|)\xi_1^{n_1+q_1}\xi_2^{n_2+q_2}\xi_3^{n_3+q_3}d\xi_1d\xi_2d\xi_3$, and on the right-hand side, $b_{n_1n_2n_3}^{p_1p_2p_3} \;=\; n_1!n_2!n_3!\delta_{n_1p_1}\delta_{n_2p_2}\delta_{n_3p_3}$.

After solving Equation (5) to obtain all the coefficients $A_{(n_1,n_2,n_3)(q_1,q_2,q_3)}$, we can substitute them into Equation (2) to determine the PD function $g_n^{p_1p_2p_3}(\boldsymbol{\xi})$. Consequently, the PDDO form of the differential operator can be established from Equation (1).

It is important to note that as the order of differentiation n increases, the shape coefficient matrix defined by Equation (5) may become ill-conditioned, leading to significant rounding errors. To achieve convergence and sufficient accuracy within a reasonable computation time, it is essential to ensure that the size of the horizon is appropriately chosen.

2.2. Spatial Discretization of Fick's Law Using PDDO

Fick's second law, which describes the transient diffusion process of chloride ions in saturated concrete, is given as follows:

$$\frac{\partial c(x_1,\ x_2,\ x_3,\ t)}{\partial t} \;=\; D\left[\frac{\partial^2 c(x_1,\ x_2,\ x_3,\ t)}{\partial x_1^2}+\frac{\partial^2 c(x_1,\ x_2,\ x_3,\ t)}{\partial x_2^2}+\frac{\partial^2 c(x_1,\ x_2,\ x_3,\ t)}{\partial x_3^2}\right] \tag{6}$$

where c is the time-dependent distribution function of the chloride ion concentration, D is the apparent diffusion coefficient of chloride ions in concrete, and t denotes time.

The conditions for determining solutions include the initial and boundary conditions. The initial condition is as follows:

$$c(x_1,\ x_2,\ x_3,\ 0) \;=\; c_0 \tag{7}$$

where c_0 is the initial concentration.

The boundary conditions are specified as follows:

$$c(\overline{x}_1,\overline{x}_2,\overline{x}_3,\ t) \;=\; \overline{c}(t) \tag{8}$$

where $\overline{x}_i(i \;=\; 1 \sim 3)$ represents the spatial coordinates of the boundaries of the solution domain, and $\overline{c}(t)$ is the chloride ion concentration measured at the boundaries.

By applying the third-order PDDO as given in Equation (1), the spatial differential Equation (6) can be expressed in the following differential/integral equation:

$$\frac{\partial c(x_1,\ x_2,\ x_3,\ t)}{\partial t} \ = \ D\int_{H_x} c(x_1',\ x_2',\ x_3',\ t)[g_3^{200}(\xi_1,\ \xi_2,\ \xi_3) + g_3^{020}(\xi_1,\ \xi_2,\ \xi_3) + g_3^{002}(\xi_1,\ \xi_2,\ \xi_3)]dV \tag{9}$$

Discretizing the spatial domain into a set of PD points results in the discrete form of Equation (9), given as follows:

$$\frac{\partial c(x_1,\ x_2,\ x_3,\ t)}{\partial t} \ = \ D\sum_{i=1}^{N} c(x_{i1},\ x_{i2},\ x_{i3},\ t)[g_3^{200}(\xi_{i1},\ \xi_{i2},\ \xi_{i3}) + g_3^{020}(\xi_{i1},\ \xi_{i2},\ \xi_{i3}) + g_3^{002}(\xi_{i1},\ \xi_{i2},\ \xi_{i3})]V_i \tag{10}$$

where N is the total number of member points within the near field of PD point $\boldsymbol{x}$, $x_{i1},\ x_{i2},\ x_{i3}$ represent the coordinates of the i-th member point, $\xi_{i1},\ \xi_{i2},\ \xi_{i3}$ denote the components of the initial relative position vector between the PD point and the i-th member point, and V_i is the representative volume of the i-th member point.

For each spatially discretized PD point, Equation (10) can be established. By assembling the equations corresponding to all discretized points, we obtain the following:

$$\frac{\partial}{\partial t}\boldsymbol{c} \ = \ \boldsymbol{T}\boldsymbol{c} \tag{11}$$

where $\boldsymbol{c}$ is the vector composed of chloride ion concentration values at all discretized points, and $\boldsymbol{T}$ is the coefficient matrix formed by the results of the right-hand side of Equation (10).

2.3. Time Domain Difference

Equation (11) shows the trend of the diffusion: it increases if the production of the apparent diffusion coefficients, which form the matrix $\boldsymbol{T}$, and the current concentration is high. To quantify the trend, the time domain is discretized as follows.

By applying finite differences to Equation (11) in the time domain, we obtain the following:

$$\frac{\boldsymbol{c}^{t+\Delta t} - \ \boldsymbol{c}^t}{\Delta t} \ = \ \boldsymbol{T}\boldsymbol{c}^{t+\Delta t}$$

or

$$(\boldsymbol{I} - \Delta t\boldsymbol{T})\boldsymbol{c}^{t+\Delta t} = \ \boldsymbol{c}^t \tag{12}$$

where $\boldsymbol{c}^{t+\Delta t}$ and $\boldsymbol{c}^t$ are the column vectors of chloride ion concentration values at times $t+\Delta t$ and t, respectively, Δt is the time step, and $\boldsymbol{I}$ is the identity.

The Lagrange multiplier is employed to incorporate the boundary conditions (8) [27]:

$$\begin{bmatrix} \boldsymbol{I} - \boldsymbol{\Delta t T} & \boldsymbol{I}^T \\ \boldsymbol{I} & \boldsymbol{0} \end{bmatrix} \begin{Bmatrix} \boldsymbol{c}^{t+\Delta t} \\ \boldsymbol{\lambda} \end{Bmatrix} = \begin{Bmatrix} \boldsymbol{c}^t \\ \bar{\boldsymbol{c}}^t \end{Bmatrix} \tag{13}$$

where $\boldsymbol{\lambda}$ is the Lagrange multiplier.

Then, based on the initial condition (7), we can solve Equation (13) step by step. In the calculations at each time step, this study utilizes the Intel Math Kernel Library (MKL) to implement heterogeneous parallel computing on shared or distributed memory systems, effectively enhancing the efficiency of solving Equations (5) and (12). Figure 2 illustrates the workflow for solving the macroscopic diffusion problem of chloride ions.

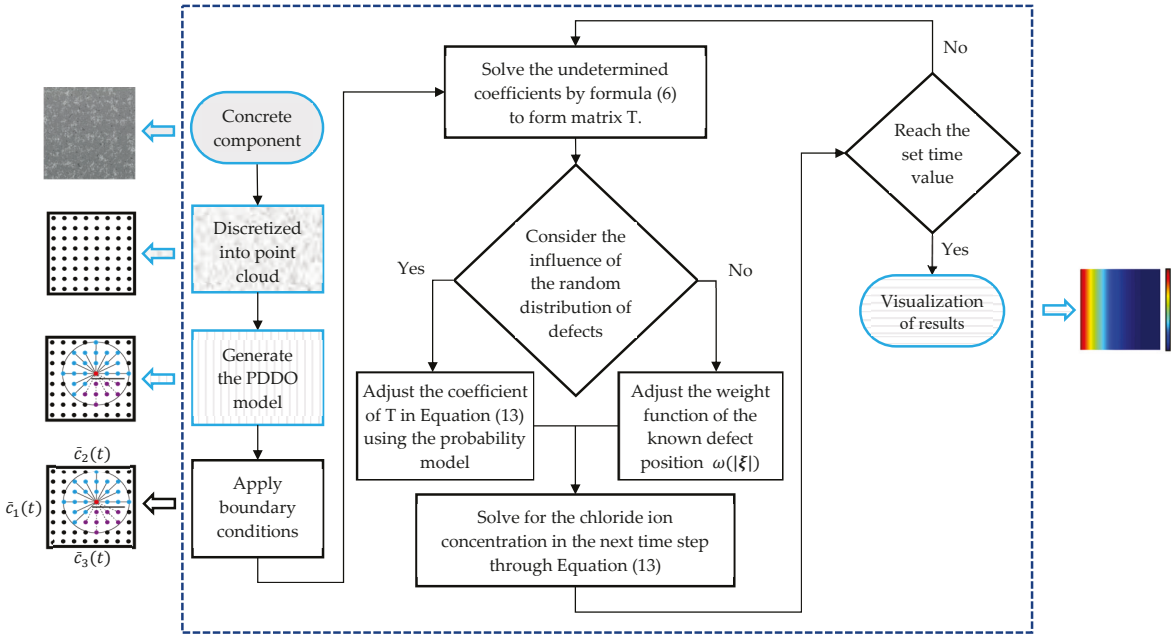

Figure 2. Simulation of macroscopic diffusion of chloride ions based on PDDO.

3. Validation of the PDDO Discrete Solution Format

3.1. Determination of the Horizon

The horizon comprehensively reflects the microscopic characteristics of the material and the specific features of the problem being solved. It determines the integration range that represents the cross-scale influence of microscopic features on macroscopic performance [28,29].

When spatially discretizing the solution, a horizon that is too small will lead to too few member points within the neighborhood, resulting in an ill-conditioned shape coefficient matrix in Equation (5), and may also produce unrealistic zero-energy deformation modes. Conversely, a horizon that is too large will significantly increase the computational workload without necessarily improving the accuracy. A horizon value equal to 3.015 times the distance between discretized points has been proposed [30]. For diffusion differential equations, after preliminary calculations and corrections, a value of four times the distance between discretized points is adopted for the horizon.

3.2. Diffusion Analysis Under Ideal Conditions

Figure 3a shows a cubic concrete specimen (150 mm × 150 mm × 150 mm) with three surfaces (the left side, bottom, and back) exposed to a chloride salt environment, where the chloride ion concentration at the exposed surfaces is 5% and the diffusion coefficient $D = 3 \times 10^{-6}$ mm^2/s. The specimen is discretized into PD points with a spacing of 6 mm, and the representative volume for each point is 216 mm^3, as illustrated in Figure 3b.

This example features a regular shape and simple boundary conditions. Assuming that the solution domain is continuous, the analytical solution for the diffusion Equation (6) can be readily obtained as follows [12]:

$$c(x_1,\ x_2,\ x_3,\ t)\ =\ c_0(1-erf(\frac{x_1}{2\sqrt{Dt}})erf(\frac{x_2}{2\sqrt{Dt}})erf(\frac{x_3}{2\sqrt{Dt}})) \tag{14}$$

where $erf(.)\ =\ \frac{2}{\sqrt{\pi}}\int_0 e^{-t^2}dt$ is the error function.

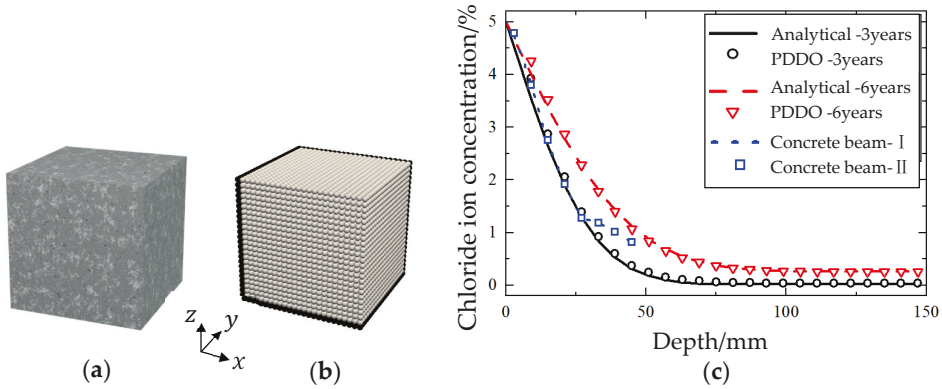

Figure 3. 3-Dimensional model for chloride ion diffusion and the calculation results. (**a**) Test cube; (**b**) PDDO model; (**c**) Chloride ion concentration distribution.

The spatial diffusion process of chloride ions is calculated using Equation (12). By placing the coordinate origin at the lower-left corner of the model, the computed results along the z-axis at x = 75 mm and y = 75 mm are shown in Figure 3c. It demonstrates an ideal accuracy when comparing the analytical results and the test results from the literature [31], in which the test was conducted according to the standard for test methods of long-term performance durability of concrete [32].

It can be proven that as the horizon decreases (while keeping the number of member points constant or increasing), the peridynamic solution converges to the analytical solution of the general local theory [24,33]. Therefore, simulating the diffusion process of chloride ions in concrete using the PDDO-based method has a reliable theoretical foundation.

4. Simulation of Macroscopic Chloride Ion Diffusion in Concrete

In practical engineering scenarios, the apparent diffusion coefficient of chloride ions in concrete varies over time, the shapes of members are diverse, and the erosion conditions are complex, with defects such as pores and microcracks present. This results in a significant deviation from the boundary conditions and analytical solutions discussed in the previous section, making it impossible to obtain analytical solutions. In such cases, the PDDO model can still effectively simulate practical engineering situations.

Taking a concrete slab exposed to a chloride salt environment as an example, Figure 4 illustrates the slab's side edges being exposed to the chloride salt environment in different configurations, neglecting the effects in the thickness direction. The initial apparent diffusion coefficient of chloride ions is 3×10^{-6} mm^2/s. The slab is discretized into PD points with a spacing of 2 mm, and the representative area for each point is 4 mm^2.

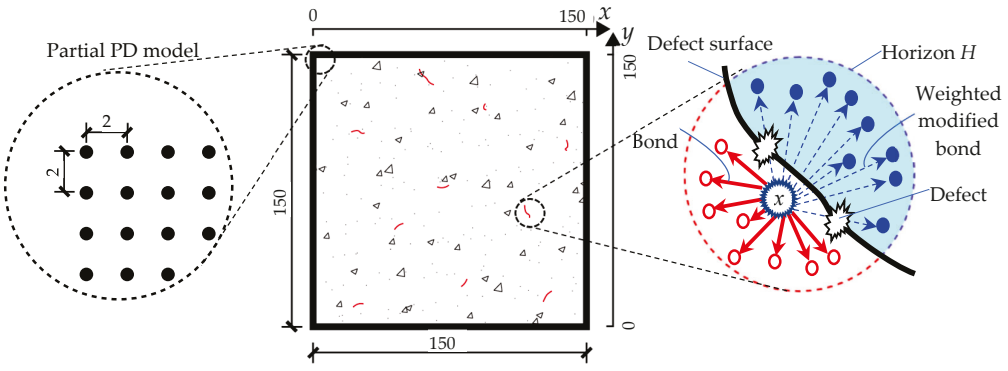

Figure 4. PD model of a concrete slab (unit: mm).

4.1. Influence of Time-Dependent Diffusion Coefficient

The apparent diffusion coefficient is a macroscopic expression of various transport mechanisms and exhibits significant time-dependent characteristics, which can be represented by Equation (15) [34]:

$$D = D_R(\frac{t_R}{t})^m \tag{15}$$

where D_R is the initial (reference) apparent diffusion coefficient, t_R and t represent the reference age and the age at which the solution is sought, respectively, with t_R set to 1 year, and m is the deterioration coefficient, taken as 0.19. Figure 5 presents the computational results considering the time-dependent behavior of the apparent diffusion coefficient as per the above equation. It is clear that the diffusion slightly relives considering its time-dependent nature. Therefore, improving the apparent diffusion coefficient of concrete should be considered in maintenance strategies.

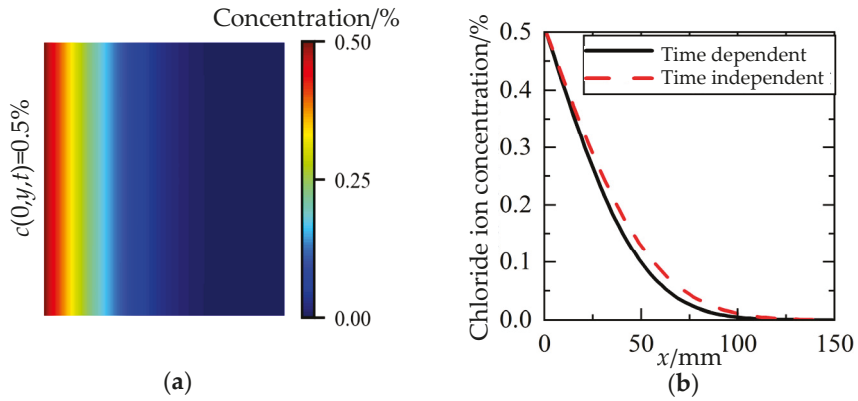

Figure 5. Influence of diffusion coefficient (t = 10 years). (**a**) Results of chloride ion diffusion; (**b**) Chloride ion concentration distribution at y = 75 mm.

4.2. Influence of Complex Boundary Conditions

Due to varying environmental conditions, the different ways in which members are exposed to corrosive environments, and the differing corrosion protection measures, there exist various erosion surfaces in practical engineering scenarios. For cases in which the surface chloride ion concentration varies according to a known pattern, this can be abstracted as Dirichlet boundary conditions for Fick's second law. For cases in which the flux of chloride ions across the surface changes according to a known pattern, this can be abstracted as Neumann boundary conditions for Fick's second law. In the PDDO-based computational model represented by Equation (12), these two types of boundary conditions can be uniformly introduced using the Lagrange multiplier [24].

Figure 6 presents the computational results considering multiple boundary conditions. It shows that it is unfavorable if the chloride exposure surfaces are near or adjacent to each other. An appropriate coating strategy that separates the chloride exposure surfaces should be considered.

4.3. Influence of Shape of Members

The PDDO discretizes the solution domain into a point cloud rather than a grid, providing excellent adaptability to the solution domain and being largely unaffected by the complexity of its geometric shape. This allows for effective simulations of concave and convex polyhedral as well as simply and multiply connected domains. Additionally, the PDDO relaxes the requirement in conventional PD models that the influence domains of PD points must be symmetric around themselves, and it does not necessitate the special treat-

ment of boundary points as some meshless methods do, further enhancing the flexibility of modeling.

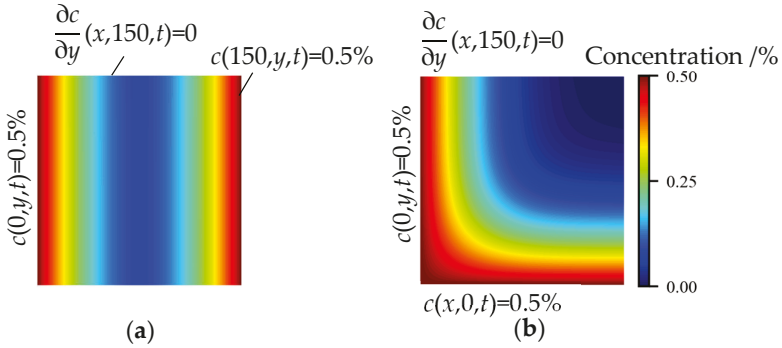

Figure 6. Influence of complex boundary conditions (t = 10 years). (**a**) Boundary condition 1; (**b**) Boundary condition 2.

Figure 7 presents the computational results for irregular regions. It indicates that the corner of members results in the superimposition of diffusion zones and the accumulation of chloride ion concentration. Therefore, the corners should be carefully protected in maintenance strategies.

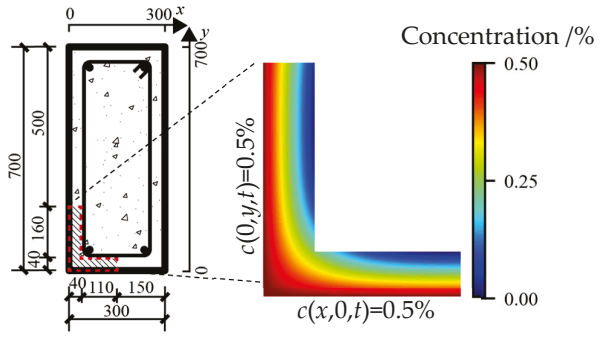

Figure 7. Influence of geometry (t = 10 years, unit: mm).

4.4. Influence of Defects

Defects such as pores and cracks are randomly distributed in concrete. A porous hardened paste with large and less tortuous capillary pores presents an easier path for chloride ion diffusion. Meanwhile, the cracks act as preferential, high-speed pathways for the ingress of chlorides, water, and oxygen, allowing these aggressive agents to bypass the protective concrete cover. When simulating the diffusion of chloride ions, the defects can be abstracted as discontinuities within the solution domain. Discontinuities are present at multiple locations throughout the solution domain, and this characteristic can be reflected by adjusting the weight function in the PDDO or the coefficients of the matrix $\boldsymbol{T}$ in Equation (12).

When discussing the influence of a small number of defects with known locations, defect planes can be set at the corresponding positions in the model, as illustrated in Figure 8. When the bond between a PD point and its member point traverses a defect, the weight function value corresponding to that bond is modified based on the blocking, delaying, or accelerating effects of the solution or air within the defect on the diffusion process.

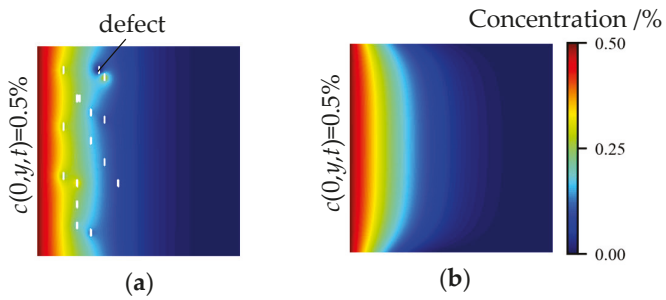

Figure 8. Influence of defects (t = 10 years). (**a**) The impact of known defects; (**b**) The impact of random defects.

When discussing the impact of the random distribution of defects on the macroscopic diffusion process, the matrix $\boldsymbol{T}$ in Equation (12) can be directly utilized. According to the physical meaning of the macroscopic diffusion equation, each coefficient t_{ij} in $\boldsymbol{T}$ represents the intensity of the diffusion influence between material point i and its j-th member point [12]. Therefore, a probabilistic model can be specified based on the random distribution pattern of the defects, allowing for the sampling of coefficients to adjust t_{ij}. For concrete with normal quality, the volume of defects is relatively small compared to the member, so the adjustment will not lead to an ill-conditioned matrix $\boldsymbol{T}$.

Neither of these methods increase the complexity of the model, require re-discretization during the calculation process, or increase the number of computations; therefore, they do not add to the overall accumulated error.

Figures 8a and 8b present the computational results for defects with specified locations and randomly distributed defects, respectively. A normal distribution with a mean of 1 and a standard deviation of 5×10^{-5} is used to sample coefficients for adjusting t_{ij}. It indicates that random distributed defects will push the peak of the chloride ion concentration forward into the concrete. That means the chloride ions will penetrate the concrete cover and reach the rebars faster. This quantitively demonstrates the importance of using good-quality concrete with fewer defects.

5. Simulation and Prediction of Macroscopic Chloride Ion Diffusion in Concrete Members Under Natural Environments

5.1. Simulation of Experiments

Using the method outlined in Section 3, the experiments from reference [30] that were conducted under natural environments were simulated. Considering both computational accuracy and scale, the spacing between discretized points was set to 10 mm. The intrusion surfaces were subjected to Dirichlet boundary conditions based on on-site measurements. The apparent diffusion coefficient was determined according to reference [30], as shown by Equation (15) with $D_R = 2.96 \times 10^{-6}$ mm^2/s, t_R = 1.3 years, and m = 0.19. The value is calibrated by field measurements and includes the influence of defects. Therefore, the distribution of defects is not explicitly considered again in this validation case. The time-dependent boundary chloride ion concentration was also calculated using the experimental results in reference [30], as shown by Equation (16):

$$c(\overline{x}_1,\ \overline{x}_2,\ \overline{x}_3,\ t)\ =\ c_0 t^n \tag{16}$$

where c_0 and n were determined through a regression after excluding outliers: c_0 = 3.72% and n = 0.31, yielding a coefficient of determination of R^2 = 0.88 with the experimental results.

Figure 9a illustrates the computational model, while Figure 9b presents a comparison of the simulation results with the experimental results.

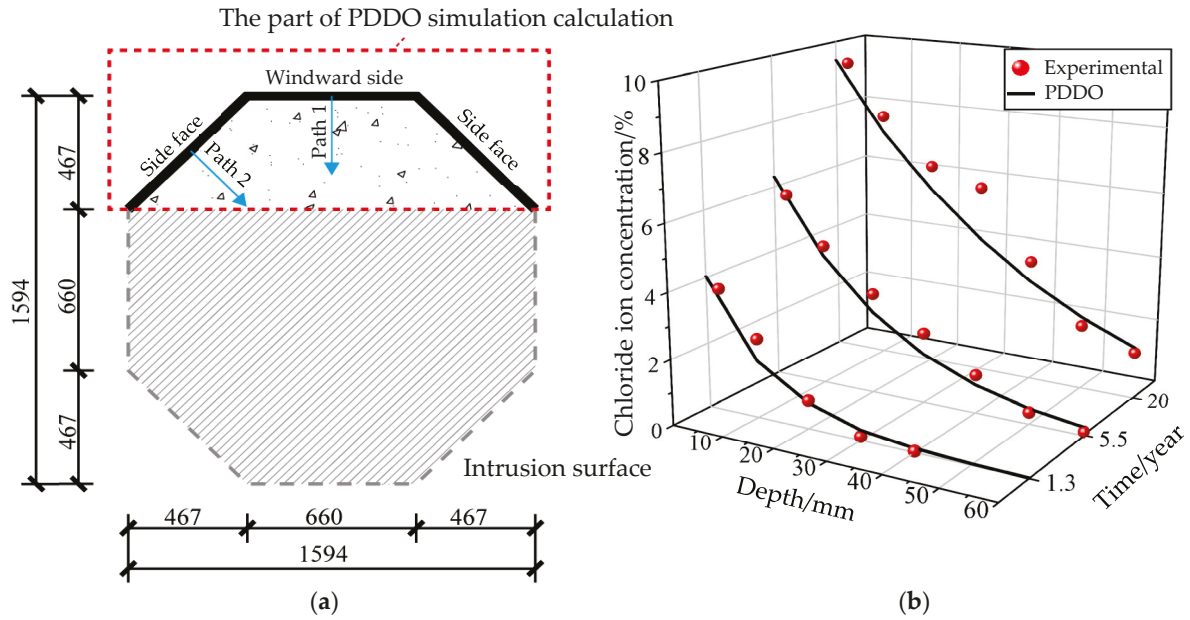

Figure 9. Comparison of PDDO results with experimental results. (**a**) Concrete specimen section model (unit: mm); (**b**) Chloride ion concentration distribution along the direction perpendicular to the intrusion surface (Path 1).

The results from Figures 5–9 validate the flexibility and fidelity of simulating the macroscopic diffusion of chloride ions in concrete using the PDDO, demonstrating that this method can offer quantitative data to aid in explaining the mechanisms of the diffusion process and can also reliably predict the diffusion process.

5.2. The Impact of Boundary Conditions

Building upon Section 5.1, we consider the differences in chloride ion concentration between the windward surface and the side surfaces. We reduce the chloride ion concentration on the side surfaces, denoting it as $c = 0.0372t^{0.31} \mid cos\ \theta \mid$, where θ is the angle between the windward surface and the side surface, which is 120° in this case.

The calculation results are shown in Figure 10: after reduction, the rate of change of the chloride ion concentration in the direction of the vertical intrusion surface is significantly slowed down. It shows that the windward surfaces that are exposed to the chloride ion attack directly are more vulnerable than other surfaces. They determine the locations of the peak chloride ion concentration in existing concrete members and they are the key factor in service life predictions for existing concrete members. Appropriate coating or other measures should be applied in the case of these windward surfaces. Such maintenance measures can significantly reduce the chloride ion attack, delay the diffusion, and extend the members' service life.

5.3. The Impact of Concrete Quality

It has been proposed that the diffusion of chloride ions will influence the structural or deformation parameters of concrete [35–37]. Building upon Section 4.1, we consider the random distribution of defects in concrete. We generate coefficients by sampling from a normal distribution with a mean of 1 and a standard deviation of 0.004 to adjust the coefficients t_{ij} in Equation (12).

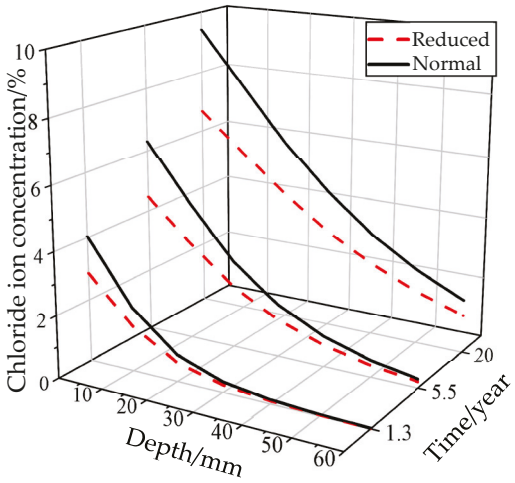

Figure 10. Influence of boundary conditions (Path 2).

The calculation results are illustrated in Figure 11: the influence of random defects causes significant fluctuations in the chloride ion concentration values at the same depth. The peaks of the chloride ion concentration shift forward in the depth direction, and this trend becomes more pronounced with higher concentration levels. The situation is in agreement with that revealed in Section 4.4: it potentially hastens the erosion of rebars in existing concrete members and shortens their service life. Therefore, maintenance would only be effective if based on good commerce, i.e., the members to be maintained use good-quality concrete with fewer defects.

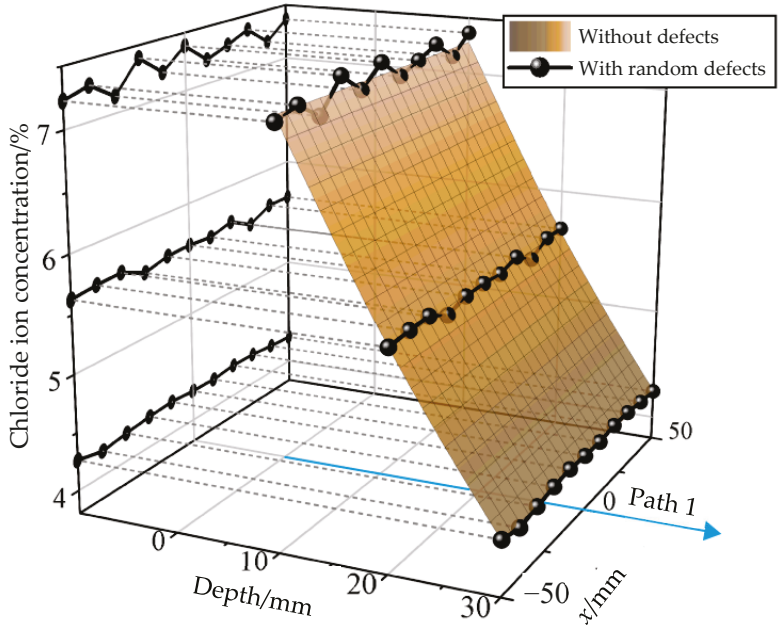

Figure 11. Influence of the quality of concrete (t = 20 years).

6. Conclusions

This paper introduces the PDDO to establish a peridynamic model, taking into account the complex geometry of concrete members, different corrosion conditions, and the effects of random defects in concrete to quantitatively simulate the diffusion process of chloride ions. The research findings are as follows:

1. Comparisons with analytical or experimental results show the peridynamic model based on the PDDO can effectively simulate the macroscopic diffusion process of

chloride ions in concrete. Moreover, the model can be conveniently applied to concrete members with complex geometries and diverse corrosion conditions, while these conditions would result in challenges for other grid-dependent methods;

2. The peridynamic model based on the PDDO can effectively quantify the impacts of known and random defects in concrete without the need to re-discretize the solution domain, and it does not increase computational iterations or cumulative errors. This could be difficult for other methods based on the assumption of continuous fields;
3. The simulation based on the PDDO suggests specific measures in maintenance strategy for concrete members, including an improvement of the apparent diffusion coefficient of concrete, an appropriate coating that separates adjacent chloride exposure surfaces, and the careful protection of corners in concrete members;
4. It is quantitively demonstrated that the defects in concrete result in the peaks of chloride ion concentration shifting forward in the depth direction, and this trend becomes more pronounced with higher concentrations. Under such circumstances, the chloride ions will penetrate the concrete cover and reach the rebars faster. Therefore, to slow the erosion of rebars in existing concrete members and extend their service life, it is important to use good-quality concrete with fewer defects.

The peridynamic model based on the PDDO provides an effective tool for simulating the macroscopic diffusion process of chloride ions in concrete members, thereby offering foundational data for the durability maintenance of a wide range of existing concrete structures. Proper maintenance will significantly reduce their carbon footprint by preventing unnecessary rehabilitation or reconstruction.

Author Contributions: Conceptualization, B.P.; data curation, Z.J., W.G. and M.S.; funding acquisition, B.P.; methodology, B.P.; supervision, B.P.; validation, Z.J.; visualization, W.G.; writing—original draft, Z.J.; writing—review and editing, B.P. All authors have read and agreed to the published version of the manuscript.

Funding: This research was funded by the National Natural Science Foundation of China (No. 51978401), the Key Laboratory of Performance Evolution and Control for Engineering Structures (Tongji University) (No. 2019KF5), and the Open Fund of Shanghai Key Laboratory of Engineering Structure Safety (No. 2019-KF07).

Institutional Review Board Statement: Not applicable.

Informed Consent Statement: Not applicable.

Data Availability Statement: Data are contained within the article.

Conflicts of Interest: The authors declare no conflicts of interest.

References

1. Miao, C.W.; Gu, X.L.; Zhang, W.P.; Guo, H.Y. State-of-the-art on performance evolution and control of concrete structures subjected to environmental actions. *J. Build. Struct.* **2019**, *40*, 1–10.
2. Gu, X.L.; Zhang, W.P.; Jiang, C.; Huang, Q.H.; Xu, N. *Environmental Actions of Concrete Structures*; Science Press: Beijing, China, 2021.
3. Fu, C.Q.; Tu, Y.J.; Jin, X.Y.; Fang, D.M.; Zhou, J.B. Experimental study on chloride ion transport in concrete under the combined action of load and environment. *J. Hydraul. Eng.* **2016**, *47*, 674–684.
4. Sun, J.; Jin, Z.Q.; Chang, H.L.; Zhang, W. A review of chloride transport in concrete exposed to the marine atmosphere zone environment: Experiments and numerical models. *J. Build. Eng.* **2024**, *84*, 108591. [CrossRef]
5. Zhao, Y.X.; Wang, C.K.; Jin, W.L.; Chen, X. Experimental analysis on time-dependent law of surface chloride ion concentration of concrete. *J. Civ. Environ. Eng.* **2010**, *32*, 8–13.
6. Li, P.; Li, C.F.; Jia, C.H.; Li, D.W. A comparative study on chloride diffusion in concrete exposed to different marine environment conditions. *J. Build. Eng.* **2024**, *94*, 109845. [CrossRef]

7. Yan, S.J.; Liu, Y.; Liang, Y.J. A space fractal derivative crack model for characterizing chloride ions superdiffusion in concrete in the marine tidal zone. *Constr. Build. Mater.* **2024**, *450*, 138585. [CrossRef]
8. Xi, Y.; Bažant, Z.P. Modeling chloride penetration in saturated concrete. *J. Mater. Civ. Eng.* **1999**, *11*, 58–65. [CrossRef]
9. Du, T.; Xiao, J.; Li, C.Y.; Gan, Y.D.; Jiang, X.L. Experimental and numerical study on the chloride ions penetration in recycled aggregate concrete. *Constr. Build. Mater.* **2024**, *451*, 138702. [CrossRef]
10. Tang, L.; Utgenannt, P. *Validation of Models and Test Methods for Assessment of Durability of Concrete Structures in the Road Environment*; Betonginstitutet: Lund, Sweden, 2012.
11. Zhang, W.P.; Zhang, Q.Z.; Gu, X.L.; Zhong, L.J.; Huang, Q.H. Effects of environmental conditions and stress level on chloride ion transport in concrete. *J. Jiangsu Univ. Nat. Sci. Ed.* **2013**, *34*, 101–106.
12. Zhou, X.G.; Li, K.F.; Chen, Z.Y. Simulation analysis of chloride penetration in concrete with finite volume method. *Eng. Mech.* **2013**, *30*, 34–39.
13. Engelund, S.; Mohr, L.; Edvardsen, C. *General Guidelines for Durability Design and Redesign*; CUR: Gouda, The Netherlands, 2000.
14. Samson, E.; Marchand, J. Modeling the transport of ions in unsaturated cement-based materials. *Comput. Struct.* **2007**, *85*, 1740–1756. [CrossRef]
15. Tian, Y.; Tian, Z.; Jin, N.; Jin, X.; Yu, W. A multiphase numerical simulation of chloride ions diffusion in concrete using electron microprobe analysis for characterizing properties of ITZ. *Constr. Build. Mater.* **2018**, *178*, 432–444. [CrossRef]
16. Liu, Q.; Easterbrook, D.; Yang, J.; Li, L.-Y. A three-phase, multi-component ionic transport model for simulation of chloride penetration in concrete. *Eng. Struct.* **2015**, *86*, 122–133.
17. Hu, H.Y.; Chen, J.S.; Hu, W. Error analysis of collocation method based on reproducing kernel approximation. *Numer. Methods Partial Differ. Equ.* **2011**, *27*, 554–580. [CrossRef]
18. Du, Q.; Gunzburger, M.; Lehoucq, R.B.; Zhou, K. Analysis and approximation of nonlocal diffusion problems with volume constraints. *SIAM Rev.* **2012**, *54*, 667–696. [CrossRef]
19. Du, Q.; Gunzburger, M.; Lehoucq, R.B.; Zhou, K. A nonlocal vector calculus, nonlocal volume-constrained problems, and nonlocal balance laws. *Math. Models Methods Appl. Sci.* **2013**, *23*, 493–540. [CrossRef]
20. Yu, H.; Sun, Y. Bridging the gap between local and nonlocal numerical methods—A unified variational framework for non-ordinary state-based peridynamics. *Comput. Methods Appl. Mech. Eng.* **2021**, *384*, 113962.
21. Silling, S.A.; Lehoucq, R.B. Peridynamic theory of solid mechanics. *Adv. Appl. Mech.* **2010**, *44*, 73–168.
22. Li, W.J.; Guo, L.; Zhou, X.; Hong, J. Peridynamic simulation of chloride penetration into concrete and the influences of mesoscopic parameters. *J. Southeast Univ. Nat. Sci. Ed.* **2021**, *51*, 30–37.
23. Chen, X.; Gu, X.; Liu, P.; Zhang, J.; Xia, X.; Zhang, Q. Peridynamic model for chloride diffusion–reaction in concrete reflecting mesostructure characteristic. *Int. J. Fract.* **2024**, *245*, 121–135.
24. Madenci, E.; Barut, A.; Futch, M. Peridynamic differential operator and its applications. *Comput. Methods Appl. Mech. Eng.* **2016**, *304*, 408–451. [CrossRef]
25. Madenci, E.; Barut, A.; Dorduncu, M. *Peridynamic Differential Operator for Numerical Analysis*; Springer International Publishing: Berlin, Germany, 2019.
26. Gu, X.; Madenci, E.; Zhang, Q. Revisit of non-ordinary state-based peridynamics. *Eng. Fract. Mech.* **2018**, *190*, 31–52.
27. Burman, E. Projection stabilisation of Lagrange multipliers for the imposition of constraints on interfaces and boundaries. *Numer. Methods Partial Differ. Equ.* **2014**, *30*, 567–592.
28. Bažant, Z.P.; Luo, W.; Chau, V.T.; Bessa, M.A. Wave dispersion and basic concepts of peridynamics compared to classical nonlocal damage models. *J. Appl. Mech.* **2016**, *83*, 111004. [CrossRef]
29. Bessa, M.A.; Foster, J.T.; Belytschko, T.; Liu, W.K. A meshfree unification: Reproducing kernel peridynamics. *Comput. Mech.* **2014**, *53*, 1251–1264. [CrossRef]
30. Madenci, E.; Oterkus, E. *Peridynamic Theory and Its Applications*; Springer: New York, NY, USA, 2014.
31. Li, D.; Wang, X.; Li, L.-Y. An analytical solution for chloride diffusion in concrete with considering binding effect. *Ocean Eng.* **2019**, *191*, 106549. [CrossRef]
32. *GB/T 50082-2024*; Standard for Test Methods of Long-Term Performance and Durability of Concrete. Standards Press of China: Beijing, China, 2024.
33. Silling, S.A.; Lehoucq, R.B. Convergence of peridynamics to classical elasticity theory. *J. Elast.* **2008**, *93*, 13–37. [CrossRef]
34. Kim, J.; McCarter, W.J.; Suryanto, B.; Nanukuttan, S.; Basheer, P.A.M.; Chrisp, T.M. Chloride ingress into marine exposed concrete: A comparison of empirical- and physically-based models. *Cem. Concr. Compos.* **2016**, *72*, 133–145.
35. Cheng, X.; Peng, J.; Cai, C.S.; Zhang, J. Experimental Study on Chloride Ion Diffusion in Concrete under Uniaxial and Biaxial Sustained Stress. *Materials* **2020**, *13*, 5717. [CrossRef]

36. Zhang, Q.; Zhao, M.; Song, L.; Yang, Y.; He, J. The Evolution of Concrete Microstructure and Chloride-Ion Diffusion Coefficient Under Cyclic Axial Compression. *Int. J. Concr. Struct. Mater.* **2025**, *19*, 56. [CrossRef]
37. Wang, J.; Ng, P.-L.; Wang, W.; Du, J.; Song, J. Modelling chloride diffusion in concrete with influence of concrete stress state. *J. Civ. Eng. Manag.* **2017**, *23*, 955–965. [CrossRef]

Disclaimer/Publisher's Note: The statements, opinions and data contained in all publications are solely those of the individual author(s) and contributor(s) and not of MDPI and/or the editor(s). MDPI and/or the editor(s) disclaim responsibility for any injury to people or property resulting from any ideas, methods, instructions or products referred to in the content.

coatings

MDPI

Article

Influence of Wood Fiber on Mechanical and Thermal Insulation Properties of Lightweight Mortar

Mo Zhou [1], Guimeng Ban [2,3], Yuanming Luo [2,3], Qin Hu [2,*], Jintuan Zhang [2], Ke Yu [4], Xue Hong [4] and Huixin Zhong [2]

[1] College of Architectural Engineering, Tianjin University, Tianjin 300072, China
[2] College of Architecture and Electrical Engineering, Hezhou University, Hezhou 542899, China; 15907886612@163.com (G.B.)
[3] College of Civil Engineering, Guilin University of Technology, Guilin 541004, China
[4] College of Economics and Management, Jingdezhen Ceramic University, Jingdezhen 333403, China
* Correspondence: huqin051@hzxy.edu.cn

Abstract

To advance the development of green building materials and achieve high-value utilization of waste resources, this study investigates the mechanistic influence of incorporating waste wood fibers on the mechanical and thermal insulation properties of lightweight mortar. Five fiber contents were designed—0%, 0.4%, 0.8%, 1.2%, and 1.6%—to systematically evaluate their effects on compressive strength, flexural strength, and tensile bond strength, as well as thermal conductivity, pore structure, and microstructural interfaces. The results demonstrate that at low fiber dosages (particularly 0.4% and 0.8%), wood fibers can significantly enhance both the mechanical strength and thermal insulation performance of mortar. Specifically, at a fiber content of 0.8%, the 28-day compressive strength increased by 10.62%, and the flexural strength by 23.8%; the tensile bond strength reached its peak at 0.4%, with a 14.8% improvement. The lowest thermal conductivity recorded was 0.16 W/(m· K), accompanied by a remarkable 61.9% reduction in porosity compared to the control group. Low-field nuclear magnetic resonance (LF-NMR) analysis revealed that wood fiber incorporation markedly increased the proportion of capillary pores, reduced total porosity, and enhanced mortar compactness; scanning electron microscopy (SEM) observations further indicated that the honeycomb-like morphology and surface roughness of wood fibers substantially improved interfacial bonding performance and microcrack-bridging capacity. The findings suggest that an optimal fiber content—recommended to not exceed 0.8%—can synergistically improve the mechanical and thermal insulation properties of lightweight mortar, providing both theoretical support and practical guidance for its application in green building wall materials.

Keywords: wood fiber; lightweight mortar; mechanical properties; thermal insulation performance; pore structure

1. Introduction

In recent years, under the strategic guidance of the "dual-carbon" objectives, China's construction industry has been accelerating its transition toward energy efficiency and environmental sustainability [1]. Among the key energy-saving materials, lightweight mortar—enhanced by the incorporation of lightweight aggregates such as expanded glass beads and expanded perlite—has been extensively employed in wall insulation systems due to its ability to markedly reduce matrix density and improve thermal performance [2–4]. However, lightweight aggregate

mortars are often plagued by insufficient compressive strength and weak interfacial bonding [5,6]. More critically, issues such as stratification and segregation caused by the flotation of lightweight aggregates during construction, as well as plastic shrinkage cracking induced by their high water absorption, further constrain their practical engineering applications [7,8].

In recent years, natural plant fibers—sourced primarily from agricultural and forestry residues or other renewable resources such as hemp, coconut shells, palm fibers, and wood-processing by-products—have become increasingly accessible and cost-effective. With simple and environmentally friendly processing requirements, their overall cost is significantly lower than that of synthetic fibers, making them widely adopted as reinforcement materials in lightweight mortars [9–11]. Sari et al. [12] treated corn husk fibers (CHFs) with a 5% NaOH solution, effectively removing non-cellulosic components and exposing a greater proportion of cellulose structures. This modification enhanced fiber crystallinity, resulting in a substantial increase in tensile strength. Merta et al. [13] conducted wedge-splitting tests using three types of natural fibers—hemp, elephant grass, and wheat straw—and found that the extent of fracture toughness enhancement varied among fiber types, with hemp fibers exhibiting the most pronounced effect. Teixeira et al. [14] investigated the mechanical performance and fracture mechanisms of cementitious composites reinforced with palm and jute fibers, reporting that palm fibers displayed superior bonding when favorably oriented, whereas jute fibers, due to partial surface coverage, induced matrix porosity and compromised interfacial efficiency. Hwang et al. [15] examined the influence of varying contents of short coconut shell fibers on the mechanical performance of cement-based composites, revealing that increased fiber dosage markedly improved toughness and crack resistance. Similarly, Soltan et al. [16] demonstrated that incorporating 2 vol% short Curauá fibers enhanced the tensile strain-softening behavior of cementitious composites. Collectively, these studies indicate that different fiber types exert significant reinforcing effects on mechanical properties, with fiber dosage variation and targeted fiber application further optimizing toughness and interfacial performance.

In addition, the industrial utilization rate of wood residues in China is estimated to be only about 17.4%, indicating that the vast majority of these residues are currently not employed for industrial purposes [17]. Unrecycled waste wood is typically either left in open-air stockpiles for natural degradation or incinerated as waste [18]. Such open-air storage not only consumes valuable land resources but also leads to the loss of organic constituents such as lignocellulose. Notably, natural plant fibers such as jute, palm, hemp, and coconut have been used to enhance the performance of cement mortars; however, systematic comparative studies among different fiber types remain limited. Wood fibers, by contrast, are more widely available and cost-effective, and their lightweight nature, porous structure, and low thermal conductivity make them well suited for improving both the thermal insulation and mechanical properties of lightweight mortars [19]. Nevertheless, publications directly comparing the performance of wood fibers with other long fibers in cement mortars are scarce. Therefore, this study focuses on elucidating the mechanisms of wood fiber reinforcement and determining its optimal dosage to address this research gap.

Therefore, this study employs waste wood fibers as reinforcing agents and systematically investigates, through dosage regulation, their effects on the mechanical properties, thermal conductivity, pore structure, and interfacial microcharacteristics of lightweight mortar. By integrating multi-scale testing techniques, including low-field nuclear magnetic resonance (LF-NMR) and scanning electron microscopy (SEM), the interaction mechanisms between wood fibers and the mortar matrix are elucidated. The findings are intended to provide both theoretical foundations and practical guidance for the engineering application of waste wood fibers in high-performance building mortars.

2. Experiment Overview

2.1. Experimental Materials

The water, P●O 42.5 ordinary Portland cement, manufactured sand, and expanded glass beads used in this study were all supplied by Hezhou Guangsha Environmental Protection Co., Ltd. (Hezhou, China). The physical properties of the water, P●O 42.5 ordinary Portland cement, manufactured sand, and expanded glass beads are presented in Tables 1–4, respectively. Representative appearances of the manufactured sand and expanded glass beads are shown in Figure 1a,b.

Table 1. Physical properties of tap water.

Property	PH Value	Chemical Content (mg/L)	Carbonate Content (mg/L)	Bicarbonate Content (mg/L)
Value	7.3	51	65	60

Table 2. Physical properties of cement.

Specific Surface Area (m^2/kg)	Setting Time (min)		Flexural Strength (MPa)		Compressive Strength (MPa)		Loss on Ignition (%)
	Initial setting	Final setting	3 d	28 d	3 d	28 d	
364	158	256	5.7	8.5	27.5	53.6	3.16

Table 3. Physical properties of manufactured sand.

Apparent Density (kg/m^3)	Loose Bulk Density (kg/m^3)	Voids Ratio (%)	Content of Fine Particles (%)	Content of Mud Lumps (%)	Water Content (%)	Crushing Value (%)
2520	1510	40	10.9	1.2	20	2.3

Table 4. Physical properties of vitrified microspheres.

Property	Density (Kg/m^3)	Compressive Strength (KPa)	Thermal Conductivity (W/(m·K))	Water Absorption Rate (%)	Surface Porosity (%)	Water Retention Rate (%)
Performance	102	196	0.042	16	95	93



(**a**) Mechanized sand (**b**) Vitrified microspheres

Figure 1. Mechanical sand and vitrified microspheres used in the experiment.

The wood fibers used in this study were supplied by Guangxi Huaqiang Building Materials Co., Ltd. (Beihai, China), which had pretreated them using a sodium hydroxide wet-immersion modification process (as shown in Figure 2). Under ambient temperature and pressure, the fibers were immersed in a 0.5% NaOH solution for 6 h, thoroughly rinsed with tap water, and then dried for subsequent use. The physical properties of the fibers are summarized in Table 5. The cellulose ether employed was BNE-119C (100,000 viscosity

grade) produced by Benor(Beijing, China), while the redispersible latex powder was BNE-7030, also manufactured by Benor.



Figure 2. Wood fiber samples.

Table 5. Physical properties of wood fiber.

Fiber Type	Water Absorption Rate (%)	Water Content (%)	Bulk Density (kg/m^3)	Length to Diameter Ratio (%)
Wood Fiber	310.5	12	170	1.14–3.28

Figure 3 presents the SEM micrograph of the wood fibers at 5000× magnification. It can be clearly observed that the fiber surface exhibits pronounced roughness and irregularity, with widespread presence of lamellar or granular attachments and debris. Such surface characteristics are expected to exert a substantial influence on the interfacial interactions and bonding performance between the fibers and the cementitious matrix.

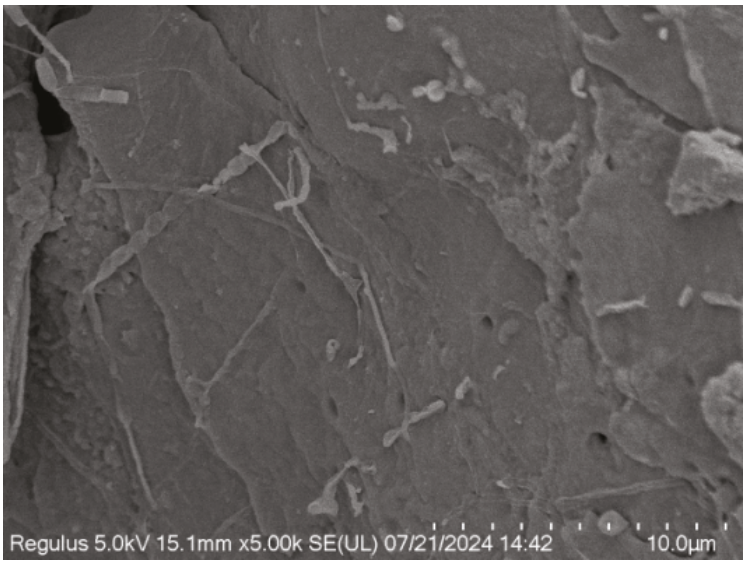

Figure 3. 5000× SEM image of wood fiber.

2.2. Sample Design

In this study, a systematic experimental investigation was conducted on the influence of wood fibers on the properties of lightweight mortar. Based on practical engineering requirements, the volume fraction of wood fibers relative to the total mortar volume was used as the variable, with five dosage levels set at 0%, 0.4%, 0.8%, 1.2%, and 1.6%. Preliminary tests indicated that at a dosage of 2%, the mortar exhibited performance trends similar to those observed at 1.2%–1.6%, while workability and fiber dispersion deteriorated noticeably. Therefore, the maximum dosage was limited to 1.6% to ensure both practicality and engineering feasibility. For ease of identification, the specimens were designated as JC (control group), WF4, WF8, WF12, and WF16, where "WF" denotes the wood fiber series, and the accompanying numeral represents the corresponding fiber content (%). The detailed mix proportions of each mortar group are provided in Table 6.

Table 6. Experimental design of wood fiber vitrified microsphere lightweight mortar.

Sample	Cement (g)	Mechanical Sand (g)	Glass Microspheres (g)	Water (g)	Cellulose (g)	Expansive Agent Powder (g)	Fiber (%)
JC	350	500	150	400	2.5	4	0
WF4	350	500	150	400	2.5	4	4
WF8	350	500	150	400	2.5	4	8
WF12	350	500	150	400	2.5	4	12
WF16	350	500	150	400	2.5	4	16

2.3. Test Method

2.3.1. Mechanical Property Test

In this study, the mechanical properties of the lightweight mortar specimens were tested at curing ages of 7 and 28 days under standard curing conditions to evaluate their performance over time. Considering that the incorporation of wood fibers makes the early-age strength highly sensitive to humidity and prone to significant fluctuations, the analysis focused primarily on the long-term (28-day) strength to more accurately reflect the material's actual performance. The compressive and flexural strengths of the cement mortar were evaluated in accordance with the Methods of Testing Cements—Determination of Strength (ISO Method) (GB/T 17671-2021) [20]. The preparation procedure was as follows: the admixture was first dissolved in the mixing water and then poured into the mixing bowl, followed by the addition of cement. The mixer was run at low speed for 30 s while the wood fibers were gradually introduced. To ensure proper dispersion of the fibers within the cement paste, the fibers were added manually in small increments to prevent clumping and excessive water absorption. Subsequently, the mixture of manufactured sand and expanded glass beads was added, and mixing continued according to the standard cement mortar mixing protocol. For fiber-reinforced specimens, an additional 30 s of high-speed mixing was applied to further improve homogeneity. Finally, the mixture was cast into prismatic molds measuring 40 mm × 40 mm × 160 mm, with three specimens prepared for each group. Testing was conducted using a WANCE computer-controlled universal testing machine in accordance with the three-point bending method specified in GB/T 17671-2021, with a span of 100 mm and a loading rate of 50 N/s. Compressive strength tests were carried out on the same equipment under static loading at a rate of 2.4 kN/s. For each data point, the average value of three specimens was calculated, and the standard deviation was determined to assess repeatability.

2.3.2. Tensile Bond Strength

The tensile bond strength of cement mortar represents a critical performance indicator, as it reflects the mortar's ability to maintain adhesion under tensile stresses. This property

directly governs the structural integrity and service life of buildings. The evaluation of bond strength was conducted in accordance with the Standard for Test Methods of Basic Properties of Building Mortar (JGJ/T 70-2009) [21].

2.3.3. Thermal Conductivity Testing Method

The thermal conductivity of cement mortar reflects its ability to conduct heat during the process of heat transfer, thereby directly influencing the thermal insulation performance and energy efficiency of buildings. The testing procedure was carried out in strict accordance with the Measurement of Steady-State Thermal Resistance and Related Properties of Thermal Insulation Materials—Heat Flow Meter Apparatus (GB/T 10295-2008) [22], which specifies the standardized methodology for determining material thermal conductivity.

2.3.4. LF-NMR Measurements

In this study, a low-field nuclear magnetic resonance (LF-NMR) analyzer was employed to systematically investigate the pore distribution within mortar after the incorporation of plant fibers.

2.3.5. Scanning Electron Microscopy (SEM)

According to the procedures described in Sections 2.3.1 and 2.3.2, hydration product samples of neat cement paste at the specified ages were prepared and then examined using a scanning electron microscope (SEM, Sigma 300 model, manufactured by Carl Zeiss AG, Germany, Oberkochen) to observe and analyze their microstructure.

3. Results and Discussion

3.1. Compressive Strength Test

Figure 4 illustrates the effects of varying wood fiber dosages on the compressive and flexural strengths of lightweight mortar specimens at 7 and 28 days. The results indicate that at 7 days, the compressive strengths of mortars with 0.4%, 0.8%, 1.2%, and 1.6% fiber contents decreased by 37.4%, 40.8%, 46.7%, and 72.3%, respectively, compared with the control group. This decline is primarily attributed to the high water absorption capacity of wood fibers, which sequesters a considerable amount of free water during the early mixing stage, thereby delaying cement hydration and hindering early strength development [23].

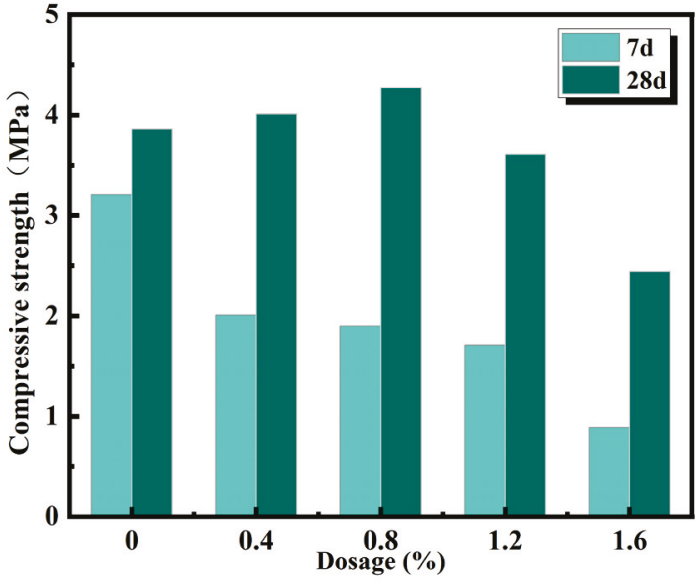

Figure 4. Compressive strength of wood fiber lightweight mortar.

With prolonged curing, the water absorbed within the wood fibers may gradually be released, potentially providing an "internal curing" effect that promotes further cement hydration and helps compensate for the early strength loss. This hypothesis is consistent with the conclusions of Chakraborty et al. [24] on polymer-modified jute fiber mortars, although differences in the absorption–release capacity and interfacial behavior of wood fibers may lead to variations in the extent of strength recovery. At 28 days, the compressive strength increased by 3.9% and 10.6% for fiber contents of 0.4% and 0.8%, respectively, relative to the control, whereas the strengths decreased by 6.5% and 36.8% at dosages of 1.2% and 1.6%. The maximum strength enhancement was observed at 0.8% fiber content. This improvement can be ascribed to the formation of a fiber-reinforced skeleton structure within the mortar, which enhances the compressive stability of the matrix. At dosages of 0.8% and below, fibers are uniformly dispersed, effectively filling voids, improving compactness, and providing structural reinforcement under compressive loading [25].

Conversely, when the fiber content exceeds 1.2%, agglomeration readily occurs, leading to non-uniform fiber distribution, the introduction of additional pores, and the disruption of matrix continuity and homogeneity. These defects result in stress concentration and a subsequent reduction in strength [26]. Therefore, the optimal fiber dosage should be controlled within 0.8% to achieve a balanced enhancement of mechanical performance and structural stability.

3.2. Flexural Strength Test

Figure 5 illustrates the influence of wood fibers on the flexural strength of mortar. Unlike compressive performance, the improvement in flexural strength was more pronounced at early ages, particularly at 7 days and under low fiber dosages ($\leq$0.8%). At fiber contents of 0.4% and 0.8%, the flexural strength increased by 25.4% and 29.2%, respectively, compared with the control group. In contrast, when the dosage reached 1.2% and 1.6%, the flexural strength decreased by 34.6% and 38.5%, respectively. At low dosages, the tensile properties and good dispersion of wood fibers help form a uniform reinforcing network within the mortar, effectively sharing tensile stresses and suppressing microcrack propagation under flexural loading. This is consistent with the findings of Zhao et al. [27], although the improvement observed in this study was more pronounced, likely due to differences in fiber surface roughness, interfacial bonding, and length distribution.

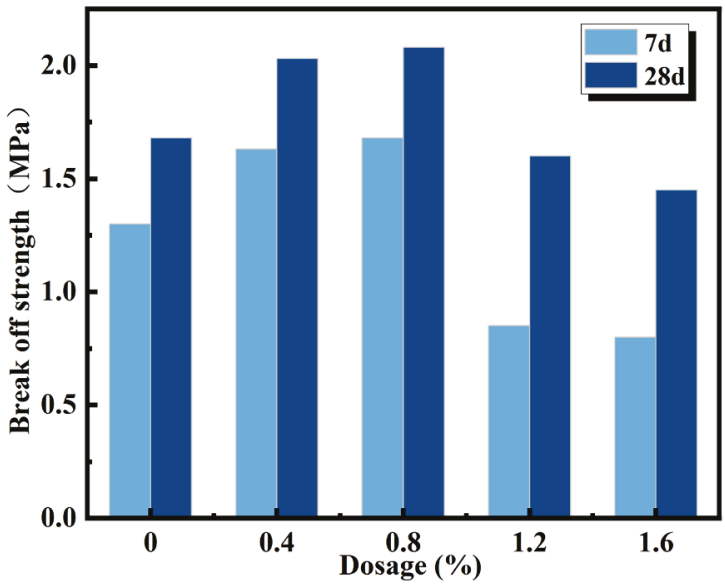

Figure 5. Flexural strength of wood fiber lightweight mortar.

As the curing age extended to 28 days, further cement hydration enhanced the interfacial bonding between fibers and the matrix, leading to additional improvements in flexural strength. The 0.8% group exhibited the greatest enhancement, with a 23.8% increase over the control, indicating that the reinforcing effect remained stable and reliable [28]. However, at dosages exceeding 1.2%, pronounced fiber agglomeration occurred, resulting in localized "bridging" structures and excess porosity, which compromised the microstructural integrity and led to a decline in flexural performance [29].

Therefore, to achieve desirable crack resistance and toughness in lightweight mortar, the fiber content should be controlled at no more than 0.8%.

3.3. Tensile Bond Testing of Mortars

Figure 6 presents the influence of wood fibers on the tensile bond strength of lightweight mortar. At 14 days, specimens containing 0.4% and 0.8% fiber exhibited increases of 34.7% and 43.1%, respectively, compared with the control group, indicating that low fiber dosages can markedly enhance interfacial bonding performance. This study shows that at low dosages, wood fibers significantly enhance interfacial bonding performance. This trend aligns with the findings of Awwad et al. [30] on industrial hemp fibers, but here the wood fibers exhibited superior interfacial bonding performance, likely due to their smaller aspect ratio and better dispersion, which promote a more uniform three-dimensional reinforcing network within the matrix.

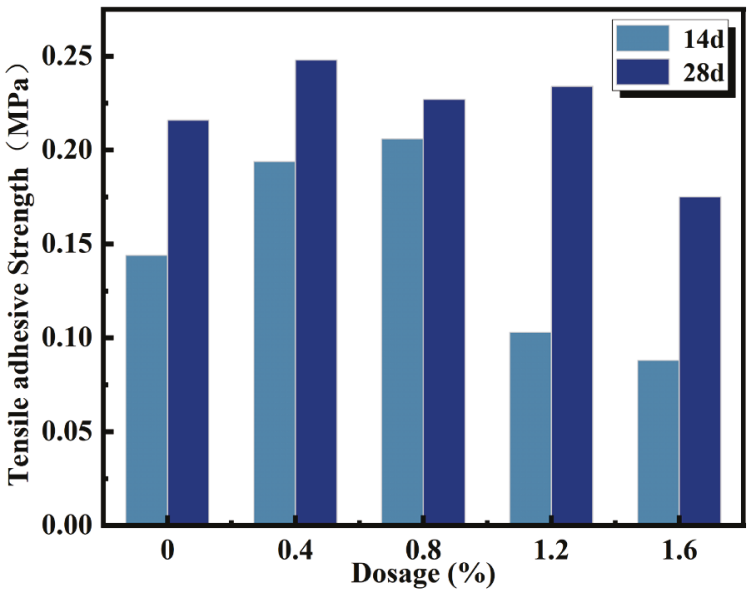

Figure 6. Tensile bond strength of wood fiber lightweight mortar.

With continued curing to 28 days, the overall bond strength further increased; however, the differences between dosages diminished. Relative to the control, the 0.4%, 0.8%, and 1.2% groups showed enhancements of 14.8%, 5.1%, and 8.3%, respectively. Among these, the 0.4% dosage maintained the most pronounced reinforcing effect, while the improvement at 0.8% stabilized. In contrast, the 1.6% group exhibited a 19.0% reduction in bond strength compared with the control at 28 days, highlighting that excessive fiber content can cause agglomeration and introduce additional porosity, thereby disrupting interfacial continuity and weakening adhesion.

Accordingly, the optimal fiber dosage is recommended to be maintained around 0.8%, ensuring a balance between significant early-age enhancement and long-term structural stability.

3.4. Thermal Conductivity Test

As shown in Figure 7, the regulation of thermal conductivity in lightweight mortar by wood fibers exhibited a nonlinear trend. At a dosage of 0.4%, the thermal conductivity reached its minimum value of 0.16 W/(m·K), representing a 23.8% reduction compared with the control group, thereby demonstrating a remarkable improvement in thermal insulation. This enhancement can be attributed to the hydrophilic nature of wood fibers, which promotes moisture evaporation and the formation of micropores, while their hollow structure and random distribution disrupt heat transfer pathways, effectively lowering thermal conduction efficiency [31].

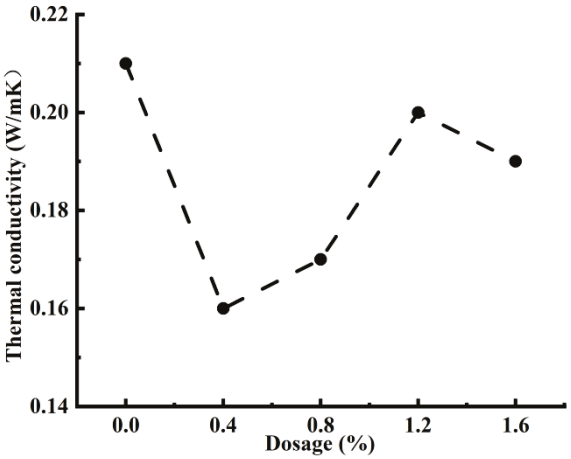

Figure 7. Thermal conductivity of wood fiber mortar.

For the 0.8% dosage group, the thermal conductivity was measured at 0.17 W/(m·K), a 19.0% reduction relative to the control, indicating that good insulation performance was still maintained. When the dosage increased further to 1.2%, the thermal conductivity rose to 0.20 W/(m·K), approaching the baseline value. This suggests that fiber agglomeration and heterogeneity in the pore structure compromised the original thermal resistance system, thereby weakening the insulating effect. At 1.6% dosage, the thermal conductivity slightly decreased to 0.19 W/(m·K), but the improvement was limited, with only a 9.5% reduction compared to the control.

These findings reveal that low fiber dosages ($\leq$0.8%) effectively enhance the thermal insulation performance of lightweight mortar, whereas excessive incorporation can disrupt the microstructural stability and diminish thermal efficiency. Therefore, it is recommended that the wood fiber content be maintained within the range of 0.4%–0.8% to achieve an optimal balance between thermal resistance and structural stability.

3.5. T_2 Spectrum of Mortar

To quantitatively elucidate the regulatory mechanism of plant fibers on the pore structure of lightweight mortar, low-field nuclear magnetic resonance (LF-NMR) technology was employed to characterize the pore features of the specimens. This technique, based on the principle of proton nuclear magnetic resonance, analyzes the spin behavior of hydrogen nuclei in saturated water to obtain information such as porosity, pore size distribution, and fluid states within the material. It offers the advantages of strong non-destructiveness, operational simplicity, and suitability for in situ measurements.

In the NMR signal, the transverse relaxation time (T_2) serves as a key parameter for evaluating pore characteristics. Its relaxation process is jointly influenced by bulk

fluid relaxation (T_{2B}), surface relaxation (T_{2S}), and diffusion relaxation (T_{2D}), as expressed in Equation (1):

$$\frac{1}{T_2} = \frac{1}{T_{2B}} + \frac{1}{T_{2S}} + \frac{1}{T_{2D}} \quad (1)$$

Under the experimental conditions of this study, the diffusion effect can be considered negligible, and the relaxation of bulk free water is comparatively weak; therefore, the transverse relaxation time (T_2) is predominantly governed by surface relaxation. Typically, shorter T_2 times correspond to smaller pore sizes, whereas longer T_2 times indicate larger pores. Consequently, the T_2 distribution curve can be effectively employed to capture the specific influence of fiber incorporation on the pore size distribution and overall pore structure of mortar. The relaxation time can be approximately expressed as

$$T_2 \approx \rho_2 \frac{V}{S} \quad (2)$$

In Equation (2): T_2 denotes the transverse relaxation time, ρ_2 is the transverse surface relaxivity, V represents the pore volume, and S is the pore surface area.

Accordingly, the pore radius r can be expressed as

$$r \approx \rho_2 F_s T_2 \quad (3)$$

In Equation (3), F_s is a dimensionless geometric shape factor of the pore structure. In this study, the internal pores were assumed to be cylindrical, for which $F_s = 2$. When the surface relaxivity ρ_2 is taken as 5 nm/ms, the relaxation times obtained for mortar specimens align well with the pore radius at all scales [32].

Furthermore, following the pore-scale classification method commonly adopted in cementitious materials, the pore structure can be divided into four categories according to pore radius: macropores ($r > 1$ μm), capillary pores (0.1 μm $< r \leq 1$ μm), transitional pores (0.01 μm $< r \leq 0.1$ μm), and gel pores ($r \leq 0.01$ μm) [33]. This classification system was also employed in the present study.

As illustrated in Figure 8, after the incorporation of wood fibers into lightweight mortar, the T_2 relaxation spectra consistently exhibited a characteristic three-peak distribution, corresponding to gel pores, capillary pores, and macropores, respectively. Compared with the control group (0%), all fiber-reinforced mortars showed a leftward shift in the signals, indicating a reduction in pore size and an overall densification of the pore structure. At a dosage of 0.4% (WF4), the main peak (gel pores) was significantly intensified, while the secondary peaks of capillary and macropores were notably diminished. This suggests that, at this dosage, the fibers were uniformly dispersed within the matrix, effectively filling larger voids and forming a dense multiscale structure, representing the most pronounced pore refinement effect. When the dosage increased to 0.8% (WF8), the main peak continued to intensify and the proportion of gel pores further increased; however, a slight resurgence of the capillary pore peak was observed, indicating the onset of fiber agglomeration, which began to impair pore continuity, although the overall pore-regulating capacity remained satisfactory. At 1.6% dosage (WF16), the macropore peak reappeared prominently, suggesting severe fiber agglomeration that resulted in the re-emergence of large pore structures, thereby compromising matrix compactness and diminishing the pore-regulating effect.

In summary, wood fibers effectively refine the pore structure of lightweight mortar, particularly at a dosage of 0.4%, where the proportion of gel pores is maximized and the formation of capillary and macropores is suppressed. Beyond 0.8% dosage, however, the benefits are progressively offset by agglomeration effects. Therefore, maintaining the fiber content within the range of 0.4%–0.8% is recommended to achieve comprehensive optimization of pore structure alongside mechanical and thermal performance.

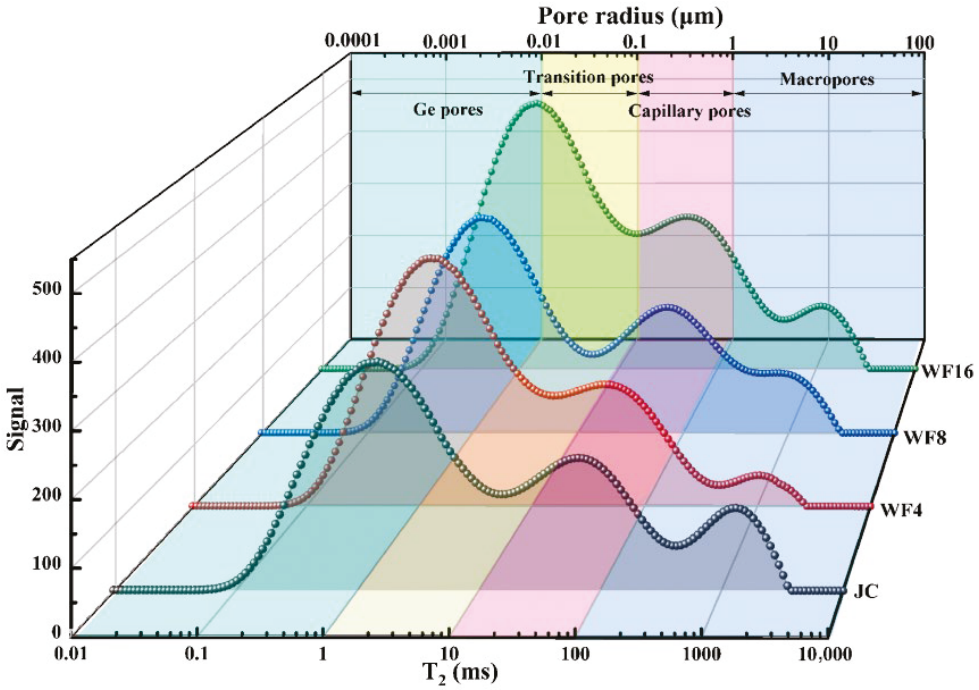

Figure 8. Changes of T_2 relaxation time spectrum in wood fiber reinforced lightweight mortar.

Variations in relaxation time can effectively reflect the trends of porosity within mortar [34]. Figure 9 presents the relaxation characteristics of lightweight mortar modified with different wood fiber dosages. After the incorporation of fibers, the porosity of all mortar groups exhibited a "decrease–increase" trend with increasing fiber content. Specifically, the porosity decreased in the order SJ (0%) > WF16 (1.6%) > WF8 (0.8%) > WF4 (0.4%). In particular, the 0.4% fiber-content group showed a markedly lower porosity than the control group (approximately 61.9%, estimated based on model assumptions), indicating that an appropriate amount of wood fiber can effectively fill the voids between aggregates, form a denser fiber skeleton, reduce heat-conduction pathways, and thereby enhance both the thermal insulation and mechanical strength of the mortar. However, as the fiber content increased further, agglomeration effects became more pronounced, leading to the formation of localized voids. Consequently, porosity increased again, compactness declined, and both thermal insulation and mechanical performance were adversely affected.

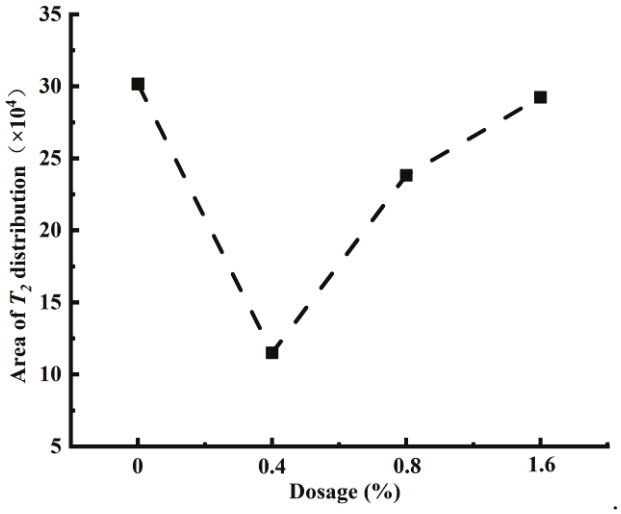

Figure 9. Relaxation time signal area.

Therefore, the wood fiber dosage should be carefully controlled to maintain optimal porosity regulation, ensuring simultaneous enhancement of both insulation efficiency and mechanical strength.

Previous studies have demonstrated that capillary pores and macropores together constitute the dominant portion of the mortar pore system, and their volumetric proportion largely determines the overall porosity distribution. More importantly, they are the primary factors influencing the thermal insulation performance of mortar [35]. Figure 10 presents the effects of varying wood fiber dosages on the relative contents of capillary pores and macropores in lightweight mortar. At low fiber dosages (0.4% and 0.8%), the relative content of capillary pores increased markedly by 14.89% and 7.52%, respectively, while the proportion of macropores decreased correspondingly. This indicates that wood fibers preferentially fill the mesopores formed by the packing of expanded glass beads, leading to the formation of a new capillary pore network. Such structural optimization not only enhances the mechanical properties of mortar but also improves its thermal insulation performance.

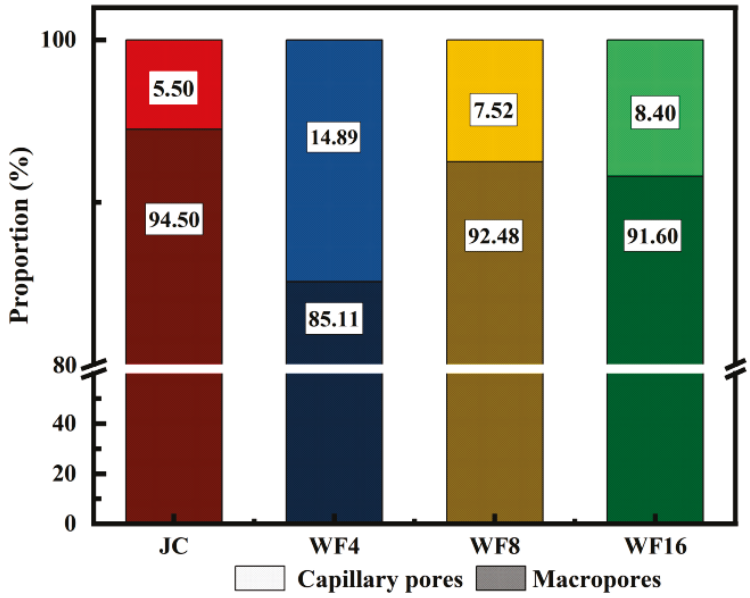

Figure 10. Evolution of the relative content of capillary and macropores.

However, when the fiber dosage increased to 1.6%, the relative content of capillary pores continued to rise, yet macropores still remained predominant. Although this configuration may be beneficial for thermal insulation, it adversely affects mechanical performance. In particular, an excessive proportion of macropores can induce air convection, thereby increasing heat loss and diminishing insulation efficiency.

In summary, the appropriate incorporation of wood fibers can optimize the pore structure of lightweight mortar, achieving a balance between mechanical performance and thermal insulation, while also mitigating issues associated with the particle size distribution of expanded glass beads and their weak interfacial bonding.

3.6. SEM Analysis of the Interface Between Plant Fiber and Lightweight Mortar

To investigate the influence of different plant fibers on the microstructure of the interfacial transition zone (ITZ) in lightweight mortar, scanning electron microscopy (SEM) was employed. The microstructural observations are presented in Figure 11A,B. As shown in Figure 11A, the surface of the control mortar (JC) exhibited a relatively fine, irregular granular morphology. The interior of the mortar matrix was primarily composed of lamellar and irregular cement hydration products. The ITZ displayed relatively uniform bonding, without any evident reinforcing structures or complexity at the interface.

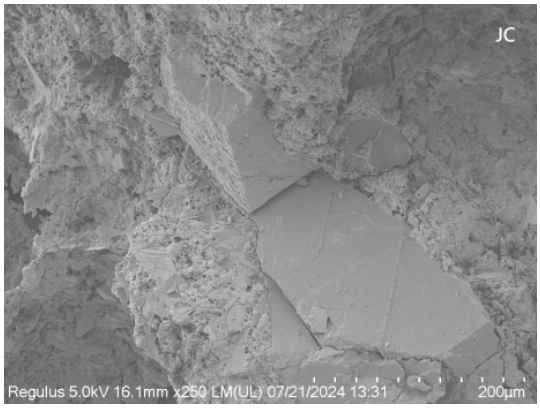

(**A**) JC control group.

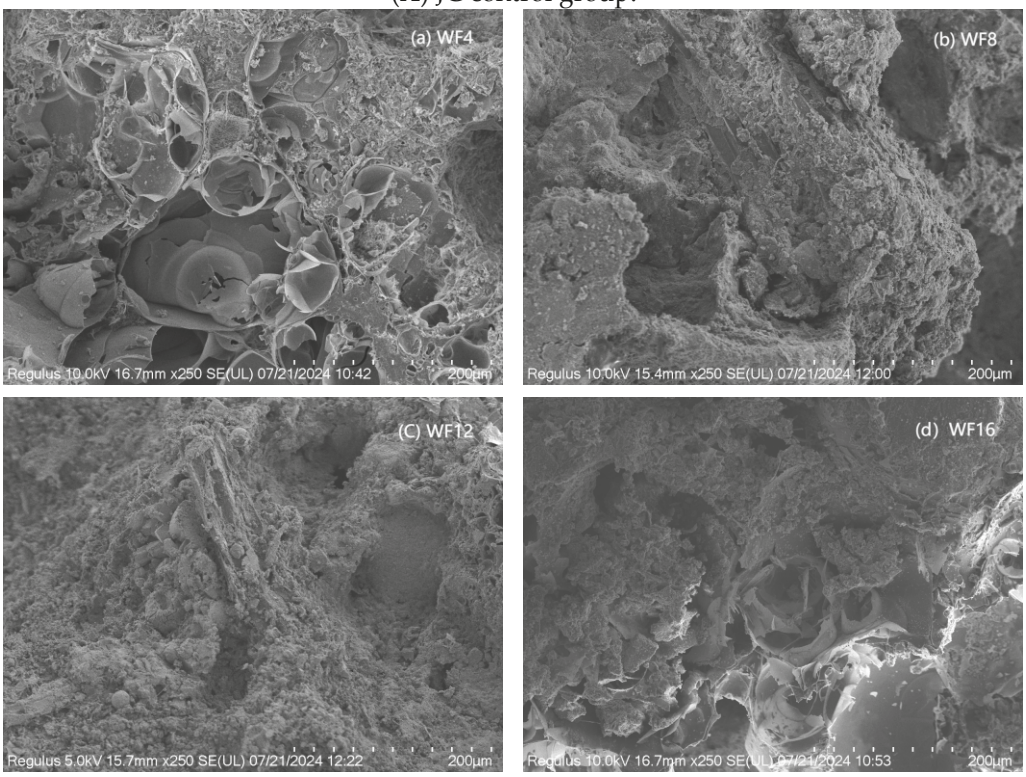

(**B**) Wood fiber modification group.

Figure 11. Effect of wood fiber on the microstructure of lightweight mortar.

As shown in Figure 11B, the incorporation of wood fibers induced pronounced changes in the microstructure of lightweight mortar. The SEM images reveal that the fibers formed a highly porous, honeycomb-like network within the matrix, with considerable internal porosity. These honeycomb structures markedly enhanced the thermal insulation performance of the mortar. During the hydration curing process, the inherent porosity and strong hydrophilicity of the fibers allowed them to absorb large amounts of mixing water at early stages, leading to swelling. Subsequently, as the fibers gradually released water, shrinkage occurred. This "swelling–desorption" cycle generated numerous irregular voids and macropores around the fibers. Moreover, the rough surface and irregular cross-sections of the fibers further promoted the formation of pores. Collectively, these structural features optimized the internal pore distribution, effectively suppressing heat conduction and thereby improving thermal insulation performance.

It is noteworthy, however, that if the absorption–desorption cycle of the fibers is not properly controlled, early-age cracking may occur, adversely affecting the mechanical

properties of the mortar. Hence, in practical applications, the dosage of wood fibers should be carefully regulated to preserve the thermal insulation benefits without compromising the structural integrity and long-term stability of the mortar.

4. Conclusions

This study investigated the effects of wood fiber incorporation on the mechanical and thermal insulation properties of lightweight mortar, with particular attention to compressive strength, flexural strength, tensile bond strength, and thermal conductivity. In addition, low-field nuclear magnetic resonance (LF-NMR) and scanning electron microscopy (SEM) were employed to analyze the pore structure and interfacial transition zone microstructure. The key conclusions are as follows:

1. Appropriate wood fiber dosages (0.4%–0.8%) significantly improved the mechanical properties of lightweight mortar. At 28 days, compressive strength increased by up to 10.6%, while flexural strength and tensile bond strength were enhanced by approximately 23.8% and 14.8%, respectively. These improvements can be attributed to the fibers' ability to fill voids, form reinforcing skeleton structures, and bridge microcracks.
2. Wood fibers exhibited a positive effect on the thermal performance of mortar. At a dosage of 0.4%, the thermal conductivity decreased to a minimum of 0.16 W/(m·K), owing to the fibers' hollow and porous structures combined with their uniform dispersion, which optimized pore morphology, reduced heat conduction pathways, and suppressed convective heat transfer.
3. Pore structure analysis revealed that low fiber dosages markedly reduced total porosity (by as much as 61.9%) while simultaneously increasing the proportion of capillary pores. This dual effect contributed to both improved thermal insulation and enhanced mechanical strength. However, when the fiber dosage reached or exceeded 1.2%, agglomeration effects introduced structural heterogeneity and stress concentrations, leading to performance deterioration.
4. The optimal wood fiber content in lightweight mortar should be kept below 0.8%, within which it can significantly improve mechanical and thermal insulation properties while promoting the reuse of forestry residues and supporting green building. Future work will verify these findings on larger elements and under on-site conditions to assess feasibility and long-term performance.

Author Contributions: Methodology, J.Z.; Investigation, Q.H.; Resources, Y.L.; Data curation, Y.L., Q.H., K.Y. and H.Z.; Writing—original draft, M.Z.; Writing—review & editing, G.B. and X.H.; Project administration, Q.H.; Funding acquisition, J.Z. All authors have read and agreed to the published version of the manuscript.

Funding: The authors gratefully acknowledge the financial support from the Doctoral Scientific Research Start-up Fund of Hezhou University (HZUBS202207), the Science and Technology Program of the Guangxi Department of Housing and Urban-Rural Development (R&D, 2024), the Special Project in Key Fields of the Guangdong Provincial Department of Education (No. 2023ZDX3106), and the Guangxi Program for Fostering Research Capacity of Young University Faculty (No. 2025KY0792).

Data Availability Statement: The original contributions presented in this study are included in the article. Further inquiries can be directed to the corresponding author.

Acknowledgments: Sincere appreciation is extended to all supporting institutions and funding agencies.

Conflicts of Interest: The authors declare that they have no known competing financial interests or personal relationships that could have appeared to influence the work reported in this paper.

References

1. Wan, Y.; Zhang, W.; Chen, R.; Zhang, L.; Zhang, Y. A novel cellulose ether cross-linking modification and its effect mechanism on the properties of cementitious materials. *Constr. Build. Mater.* **2024**, *447*, 138150. [CrossRef]
2. Liu, S.; Li, Q.; Zhang, J.; Zhao, K.; Wang, L.; Zhang, Z. Research on mechanical properties of high-strength thermal insulation mortar. *Constr. Build. Mater.* **2024**, *420*, 135260. [CrossRef]
3. Zelder, S.; Rosin, A.; Helling, D.; Gerdes, T.; Scharfe, F.; Schafföner, S. Mineral composite plaster containing hollow glass microspheres and CSA cement for building insulation. *Appl. Sci.* **2022**, *12*, 1152. [CrossRef]
4. Romero, M.; Padilla, I.; García Calvo, J.L.; Carballosa, P.; Pedrosa, F.; López-Delgado, A. Development of lightweight mortars using sustainable low-density glass aggregates from secondary raw materials. *Materials* **2023**, *16*, 6281. [CrossRef]
5. Ma, Y.; Zhang, C.; Lin, X.; Ye, Y.; Ye, X.; Ji, T. Bond between alkali-activated steel slag/fly ash lightweight mortar and concrete substrates: Strength and microscopic interactions. *Constr. Build. Mater.* **2024**, *449*, 138401. [CrossRef]
6. Zhang, X.; Liu, W.; Zhang, S.; Hou, J. Performance study of lightweight insulating mortar reinforced with straw fiber. *Materials* **2023**, *16*, 2266. [CrossRef] [PubMed]
7. Wyrzykowski, M.; Trtik, P.; Münch, B.; Weiss, J.; Vontobel, P.; Lura, P. Plastic shrinkage of mortars with shrinkage reducing admixture and lightweight aggregates studied by neutron tomography. *Cem. Concr. Res.* **2015**, *73*, 238–245. [CrossRef]
8. Solak, A.M.; Tenza-Abril, A.J.; Baeza-Brotons, F.; Benavente, D. Proposing a new method based on image analysis to estimate the segregation index of lightweight aggregate concretes. *Materials* **2019**, *12*, 3642. [CrossRef] [PubMed]
9. Guo, W.; Wang, Z.; Bao, F.; Chang, L. The status and trend of natural fiber/biodegradable plastic bio-composites. *Sci. Silvae Sin.* **2008**, *44*, 157–162.
10. Adamu, M.; Alanazi, F.; Ibrahim, Y.E.; Alanazi, H.; Khed, V.C. A comprehensive review on sustainable natural fiber in cementitious composites: The date palm fiber case. *Sustainability* **2022**, *14*, 6691. [CrossRef]
11. Jaffur, N.; Jeetah, P. Production of low cost paper from Pandanus utilis fibres as a substitution to wood. *Sustain. Environ. Res.* **2019**, *29*, 20. [CrossRef]
12. Sari, N.H.; Wardana, I.N.G.; Irawan, Y.S.; Siswanto, E. The effect of sodium hydroxide on chemical and mechanical properties of corn husk fiber. *Orient. J. Chem.* **2017**, *33*, 3037–3042. [CrossRef]
13. Merta, I.; Tschegg, E.K. Fracture energy of natural fibre reinforced concrete. *Constr. Build. Mater.* **2013**, *40*, 991–997. [CrossRef]
14. Teixeira, F.P.; Lima, V.N.; Moutinho, D.J.C.; Fujiyama, R.T. Mechanical properties and fractography of cement-based composites reinforced by natural piassava and jute fibers. *Cerâmica* **2022**, *68*, 60–66. [CrossRef]
15. Alvarez, V.A.; Ruscekaite, R.A.; Vazquez, A. Mechanical properties and water absorption behavior of composites made from a biodegradable matrix and alkaline-treated sisal fibers. *J. Compos. Mater.* **2003**, *37*, 1575–1588. [CrossRef]
16. Soltan, D.G.; das Neves, P.; Olvera, A.; Junior, H.S.; Li, V.C. Introducing a curauá fiber reinforced cement-based composite with strain-hardening behavior. *Ind. Crops Prod.* **2017**, *103*, 1–12. [CrossRef]
17. Chen, X. Appendix 1 Assessment of wood residues in China. In *ASIA-PACIFIC FORESTRY COMMISSION, Trash or Treasure? Logging and Mill Residues in Asia and the Pacific*; FAO: Rome, Italy, 2001.
18. Fang, W.; Evangeliou, N.; Eckhardt, S.; Xing, J.; Zhang, H.; Xiao, H.; Zhao, M.; Kim, S.-W. Increased contribution of biomass burning to haze events in Shanghai since China's clean air actions. *Commun. Earth Environ.* **2023**, *4*, 310. [CrossRef]
19. Qiu, Y.; Pang, Q.; He, Y.; Cui, X. Extraction of xylan from sugarcane bagasse through mild hydrothermal treatment with phosphoric acid-based porous geopolymers. *J. Clean. Prod.* **2024**, *448*, 141640. [CrossRef]
20. *GB/T 17671-2021*; Test Method for Strength of Cementitious Sand (ISO Method). Chinese Standard Press: Beijing, China, 2021. (In Chinese)
21. *JGJ/T70-2009*; Standard Test Methods for Basic Performance of Building Mortar. Chinese Standard Press: Beijing, China, 2009. (In Chinese)
22. *GB/T 10295-2008*; Determination of Steady-State Thermal Resistance and Related Properties of Thermal Insulation Materials—Heat Flow Meter Method. Chinese Standard Press: Beijing, China, 2008. (In Chinese)
23. Li, G.; Yu, Y.; Li, J.; Wang, Y. Research on adaptability between crop-stalk fibers and cement. *Cem. Concr. Res.* **2004**, *34*, 1081–1085. [CrossRef]
24. Chakraborty, S.; Kundu, S.P.; Roy, A.; Adhikari, B.; Majumder, S. Polymer modified jute fibre as reinforcing agent controlling the physical and mechanical characteristics of cement mortar. *Constr. Build. Mater.* **2013**, *49*, 214–222. [CrossRef]
25. Santos, R.F.; Ribeiro, J.C.L.; De Carvalho, J.M.F.; Magalhães, W.L.E.; Pedroti, L.G.; Nalon, G.H.; De Lima, G.E.S. Nanofibrillated cellulose and its applications in cement-based composites: A review. *Constr. Build. Mater.* **2021**, *288*, 123122. [CrossRef]
26. Gbekou, F.K.; Boudenne, A.; Eddhahak, A.; Benzarti, K. Mechanical and thermal properties of cement mortar composites incorporating micronized miscanthus fibers. *J. Mater. Res. Technol.* **2023**, *26*, 7649–7664. [CrossRef]
27. Zhao, K.; Xue, S.; Zhang, P.; Tian, Y.; Li, P. Application of natural plant fibers in cement-based composites and the influence on mechanical properties and mass transport. *Materials* **2019**, *12*, 3498. [CrossRef]

28. Jiang, D.; Lv, S.; Cui, S.; Sun, S.; Song, X.; He, S.; Zhang, J.; An, P. Effect of thermal insulation components on physical and mechanical properties of plant fibre composite thermal insulation mortar. *J. Mater. Res. Technol.* **2020**, *9*, 12996–13013. [CrossRef]
29. Ajabshir, S.; Gupta, R. Effects of Pretreatment Methods and Physical Properties of Cellulose Fibers on Compatibility of Fiber-Cement Composites: A Review. In *Interdisciplinary Symposium on Smart & Sustainable Infrastructures*; Springer Nature: Cham, Switzerland, 2023; pp. 253–264.
30. Awwad, E.; Mabsout, M.; Hamad, B.; Farran, M.T.; Khatib, H. Studies on fiber-reinforced concrete using industrial hemp fibers. *Constr. Build. Mater.* **2012**, *35*, 710–717. [CrossRef]
31. Mydin, M.A.O.; Abdullah, M.M.A.B.; Sor, N.H.; Omar, R.; Dulaimi, A.; Awoyera, P.O.; Althoey, F.; Deifalla, A.F. Thermal conductivity, microstructure and hardened characteristics of foamed concrete composite reinforced with raffia fiber. *J. Mater. Res. Technol.* **2023**, *26*, 850–864. [CrossRef]
32. Yu, B.; Li, S.; Zhu, H.; Jiang, Q.; Wang, D.; Chen, Y. A composite phase change material for improving the freeze–thaw resistance performance of cement mortars. *Constr. Build. Mater.* **2023**, *387*, 131657. [CrossRef]
33. Yu, L.; Zhang, J.; Zhang, J.; Ma, B. Quantitative relationship model between macroscopic properties and pore structure of cement concrete. *J. Harbin Eng. Univ.* **2015**, *36*, 1459–1464. (In Chinese)
34. Dong, M.; Li, S.; Yu, B.; Jiang, Q.; Zhu, H.; Zhao, J.; Huang, J.; Tao, S. Experimental investigation on the freeze-thaw durability of a phase change concrete in cold regions. *Cold Reg. Sci. Technol.* **2024**, *218*, 104102. [CrossRef]
35. Xiong, H.; Yuan, K.; Xu, J.; Wen, M. Pore structure, adsorption, and water absorption of expanded perlite mortar in external thermal insulation composite system during aging. *Cem. Concr. Compos.* **2021**, *116*, 103900. [CrossRef]

Disclaimer/Publisher's Note: The statements, opinions and data contained in all publications are solely those of the individual author(s) and contributor(s) and not of MDPI and/or the editor(s). MDPI and/or the editor(s) disclaim responsibility for any injury to people or property resulting from any ideas, methods, instructions or products referred to in the content.

coatings

MDPI

Article

Dynamic Response and Energy Dissipation Mechanisms of Soil–Lightweight Foam Composite Protective Layers Under Impact Loading

Jianping Gao [1], Le Liu [1,2,*], Xuefeng Mei [3], Dengfeng Li [4], Jianli Wu [4,5,6] and Peng Cui [7]

[1] School of Civil Engineering, Chongqing Jiaotong University, Chongqing 400074, China
[2] Chongqing Jiangjin District Highway Affairs Center, Chongqing 400074, China
[3] College of Civil Engineering, Inner Mongolia University of Science and Technology, Baotou 014010, China
[4] China 19th Metallurgical Group Co., Ltd., Chengdu 610036, China
[5] College of Civil Engineering and Architecture, Zhejiang University of Water Resources and Hydropower, Hangzhou 310018, China
[6] State Key Laboratory of Geohazard Prevention and Geoenvironment Protection, Chengdu University of Technology, Chengdu 610059, China
[7] Shandong Energy Group Luxi Mining Co., Ltd., Heze 274900, China
* Correspondence: 611200111010@mails.cqjtu.edu.cn

Abstract

Engineering structures often face safety risks under impact or explosion loading, making the design of lightweight and efficient cushioning systems crucial. This study investigates the dynamic response and energy-dissipation characteristics of Expanded Polystyrene (EPS), Expanded Polyethylene (EPE), and soil–foam composite cushion layers under impact loading, using a Split Hopkinson Pressure Bar (SHPB) testing apparatus. The tests include pure foam layers (lengths ranging from 40 to 300 mm) and a soil–foam composite layer with a total length of 60 mm (soil/foam ratio 1:1 to 1:3), subjected to impact velocities of 9.9–15.4 m/s. The results show that the stress wave propagation velocity of EPE is 149.6 m/s, lower than that of EPS at 249.3 m/s. At higher velocities, the attenuation coefficient for the 40 mm EPE sample reaches as low as 0.22, while EPS is 0.31. Furthermore, the maximum energy absorption coefficient of EPE exceeds 98%, with better stability at high impact velocities. In composite cushion layers, both soil and foam collaborate in energy absorption, but an increased proportion of soil leads to a decrease in energy absorption efficiency and attenuation capacity. Under equivalent ratios, the soil–EPE combination performs better than the soil–EPS combination. By constructing a comprehensive evaluation system based on three indices: stress wave attenuation coefficient, energy absorption coefficient, and energy absorption density, this study quantifies the impact resistance performance of different cushioning layers, providing theoretical and parametric support for material selection in engineering design.

Keywords: soil–foam composite; dynamic response; stress wave attenuation; energy dissipation; Split Hopkinson pressure Bar (SHPB)

1. Introduction

In modern engineering practice, the loading conditions faced by structures are becoming increasingly complex, particularly with extreme loads such as explosions [1] and impacts [2], which are characterized by nonlinearity, high-velocity propagation, and localized damage [3]. These loads pose a growing threat to engineering structures, making the

enhancement of impact resistance a core issue in fields such as civil and protective engineering. Research has demonstrated that adding cushion layers can absorb the significant energy generated by dynamic loads, ensuring that the primary structure of the engineering system is not damaged under high-pressure peak loads. For instance, in traditional rockfall protection structures, such as protective rock-shed and pile-slab barriers (Figure 1), materials like sand and soil are often added to the impact side to absorb the massive impact forces from falling rocks. However, these materials are heavy, have low energy absorption efficiency, and require large foundations for support [4–6]. With the rapid development of new materials and technologies, the use of multi-layered, multi-material-composite "layered cushioning" structures has proven to be an effective approach for improving impact resistance and energy dissipation efficiency. Expanded Polystyrene (EPS) and Expanded Polyethylene (EPE), due to their lightweight, porous, and high energy absorbing properties, are widely used in impact protection, vibration damping, and other engineering applications [7–9]. Therefore, utilizing the advantages of different energy absorbing materials and constructing well-designed composite-layered wave-damping structures is crucial. These structures dissipate high-peak transient shock waves into lower peak, longer rise-time weak shock waves, thereby reducing the intensity of shock waves transmitted to the protected structural surface. This approach is key to enhancing structural safety and significantly improves the impact and blast resistance of layered protective structures.

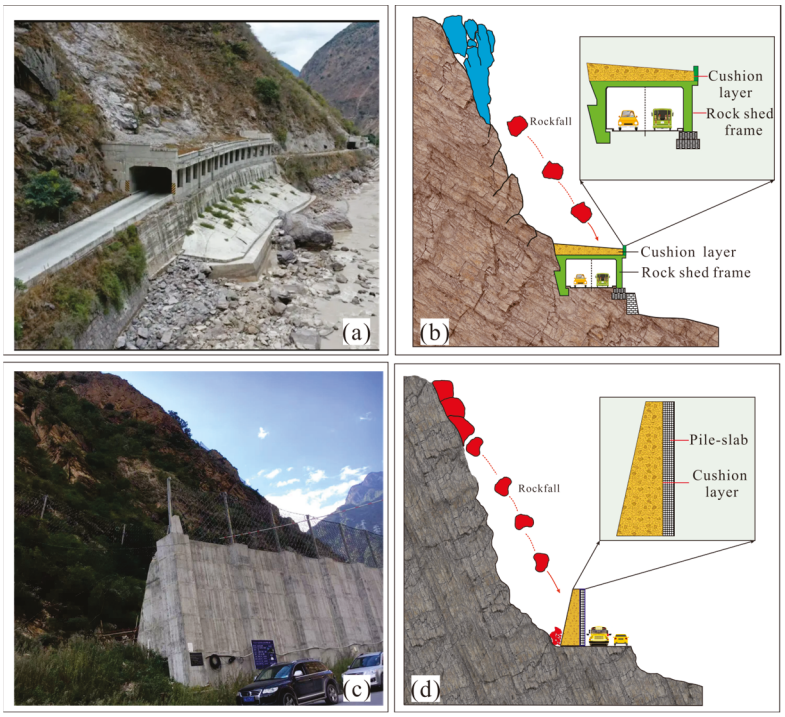

Figure 1. Engineering application background: (**a**,**b**) rock-shed; (**c**,**d**) pile-slab and cushion layer rockfall barrier.

Similar granular materials exhibit porous and loose characteristics, making them complex, non-equilibrium energy dissipation systems [10]. These materials have been widely applied in the design of protective engineering structures, particularly in impact- and blast-resistant structural design. Through the disruption of the inherent structure between particles, such materials cause particle sliding, displacement, and even fragmentation, which weakens the peak stress of the applied shock waves [11]. Moreover, the irreversible plastic deformation of sand and soil under loading leads to additional energy loss, further increasing the attenuation of the stress wave. To investigate the propagation characteristics

of stress waves in particles, shock tubes [12,13], drop-weight devices [14,15], and physical model experiments [16,17] are commonly used. However, shock tubes and drop-weight devices face challenges in obtaining the mechanical response of materials under medium-to-high strain rate conditions [18], while model experiments typically rely on embedded pressure gauges to capture stress data. Due to the significant difference in wave impedance between the pressure gauges and the materials, as well as the interference caused by the gauges on the stress waves, this can result in the transmitted stress being greater than the incident stress, leading to calibration difficulties [19]. For instance, Hampton et al. [20] found that the transmitted stress measured by pressure gauges was higher than the actual incident pressure due to interactions between the gauges and the soil, with the maximum deviation reaching 50%. Schindler [21] pointed out that the placement of the pressure gauges could cause significant sample disturbance, making calibration within the sample difficult. The Split Hopkinson Pressure Bar (SHPB) resolves the issue of simultaneously measuring stress and strain at the same position in the sample over time by measuring the elastic deformation at the ends of the incident and transmission bars. This approach provides more accurate results than embedded pressure gauges and allows high strain-rate loading by varying the bars' diameters and increasing projectile velocity. Yu et al. [22] noted that using SHPB to analyze stress wave propagation in "long specimens" does not require the assumption of stress uniformity. Based on one-dimensional stress wave theory, they discussed the propagation characteristics of stress waves in coral sand samples of varying lengths. Lyu et al. [23] and Yu et al. [24] studied the attenuation effects of stress waves in silica sand and calcareous sand using SHPB. Cui [25] investigated the attenuation of stress waves in sand samples and provided a quantification model. Additionally, to explain the propagation characteristics of stress waves in granular media, numerical analysis methods such as the Finite Element Method (FEM), Discrete Element Method (DEM), and Smoothed Particle Hydrodynamics (SPH) have been extensively used by researchers [26–28], yielding promising results.

Traditional sand and soil cushion layers require significant thickness to resist high-impact energy. According to the "Highway Tunnel Design Code" in China [29], the thickness of the soil cushion layer should exceed 1.5 m to resist rockfalls, and in areas with frequent rockfalls, even thicker sand and soil layers are required. However, excessively thick cushions result in greater self-weight, which reduces the design efficiency of protective structures such as shelters [30]. To enhance both energy absorption efficiency and structural stability under extreme dynamic loads, researchers have increasingly introduced lightweight foam materials into wave-damping energy dissipation systems [31]. Typical lightweight damping and cushioning materials can absorb substantial dynamic energy through deformation, the rupturing of cell walls, and the collapse of porous structures [32–35]. Studies have shown that combining sand and foam materials to form composite cushion layers can fully leverage the advantages of both materials, improving the overall impact and blast resistance of the structure. According to experimental results from Zhao et al. [36], EPS foam tends to undergo permanent deformation after multiple impacts, leading to a decrease in energy absorption capacity. However, Expandable Polyethylene (EPE) exhibits excellent elasticity and cushioning properties, with nearly no residual deformation after compression. Meree et al. [37] proposed a new EPS particle–sand composite cushion layer based on drop-weight impact tests, achieving a 90% reduction in weight while improving energy dissipation efficiency by 84.3%. Wu et al. [38] found in their experimental study that embedding EPS foam boards in sand layers can effectively delay the propagation velocity of stress wave fronts, reduce stress peaks, and enhance the cushioning effect of the structure. Additionally, some studies have employed an alternating foam–sand layering design. By optimizing the foam thickness and interlayer

contact interfaces, energy dissipation can be achieved in a gradient manner across the layers, effectively reducing the intensity of stress waves on the protected side of the structure and improving protective performance [39,40]. With the advancement of numerical simulation techniques, three-dimensional models including foam materials, sand, and structural components have been developed to precisely simulate the propagation of shock waves in composite structures. These models can analyze the impact resistance performance of different material parameters and structural configurations [41–44]. This approach not only reduces experimental costs but also allows for the optimization of the structure during the design phase, thereby improving its impact resistance performance. Overall, significant progress has been made in understanding the energy absorption characteristics of lightweight cushion layers under dynamic loading. However, most studies compare the energy absorption performance of different materials based on experimental observations, lacking a unified mathematical model to describe the quantitative relationship between the material's energy absorption properties, sample length, and loading conditions. This limitation hinders a deeper understanding and the efficient design of lightweight cushion materials.

This study is based on the SHPB testing system and investigates two typical lightweight foams, EPS and EPE. Pure foam and soil–foam composite specimens were constructed by varying sample lengths (40–300 mm), the foam-to-soil ratio (1:1 to 1:3), and impact velocities (9.9–15.4 m/s). The propagation characteristics of stress waves and the energy dissipation mechanisms in different layered structures under impact loading conditions were systematically studied. The effects of sample length and material composition ratio on the propagation characteristics and energy dissipation behavior of stress waves were analyzed. Innovative mathematical models for the stress attenuation coefficient, energy absorption coefficient, and energy absorption density have been proposed, enabling multidimensional quantification and comprehensive evaluation of the cushioning and energy absorption performance of different materials. These models provide experimental evidence and a theoretical foundation for the design and protective applications of composite structures under dynamic loading.

2. Experimental Design

2.1. Test Material

The sand used in the tests was sourced from Zibo City, Shandong Province (Figure 2a,b). According to the results of the geotechnical tests, the natural water content of the soil sample was 32.3%. As this study does not consider the impact of water content on stress wave propagation, the soil was dried at 105 °C for 48 h during preparation. Subsequently, sieve analysis was conducted using sieves with apertures of 5 mm, 2.5 mm, 1.25 mm, 0.6 mm, 0.3 mm, and 0.08 mm. Based on the particle size distribution curve (Figure 3), particles larger than 2 mm accounted for 5.0% of the total mass, while particles larger than 0.075 mm constituted 67.0% of the total mass. According to national standards [45], the soil sample was classified as sandy soil. Additionally, the median particle size (d_{50}) of the soil was 0.58 mm, with a uniformity coefficient (C_u) of 5.00 and a curvature coefficient (C_c) of 0.91. Scanning Electron Microscopy (SEM) images of the soil sample show that the soil particles consist of irregularly shaped particles with sharp edges and high surface roughness. Numerous micro-cracks and pores are visible on the particle surfaces, with particles primarily in point or mixed point-face contact. XRD (X-ray diffraction) analysis results (Figure 4) indicate that quartz and albite are the main mineral components in the soil samples, with a relatively high intensity of quartz diffraction peaks, accompanied by multiple sets of feldspar diffraction peaks.

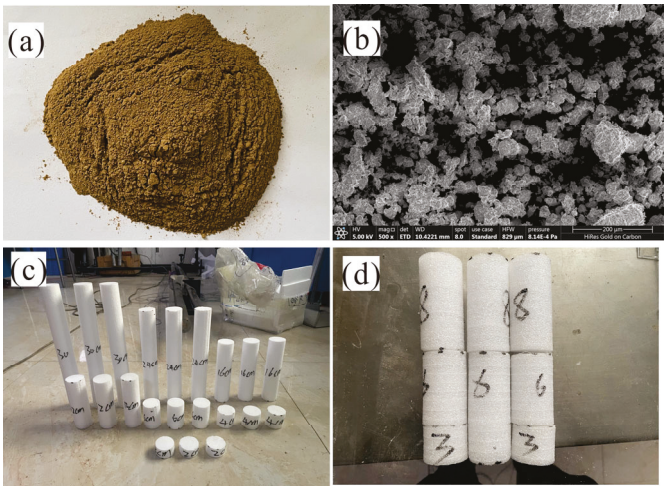

Figure 2. Specimen electron microscope scanning morphology: (**a**,**b**) soil; (**c**) EPS cushion layer; (**d**) EPE cushion layer.

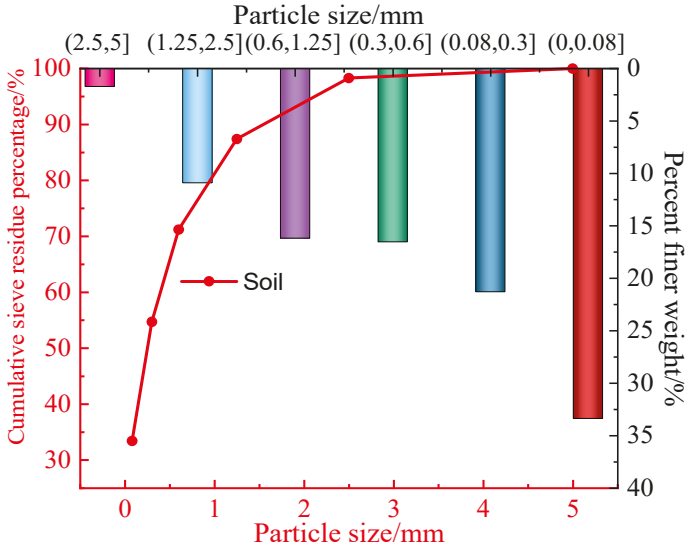

Figure 3. Particle size distribution.

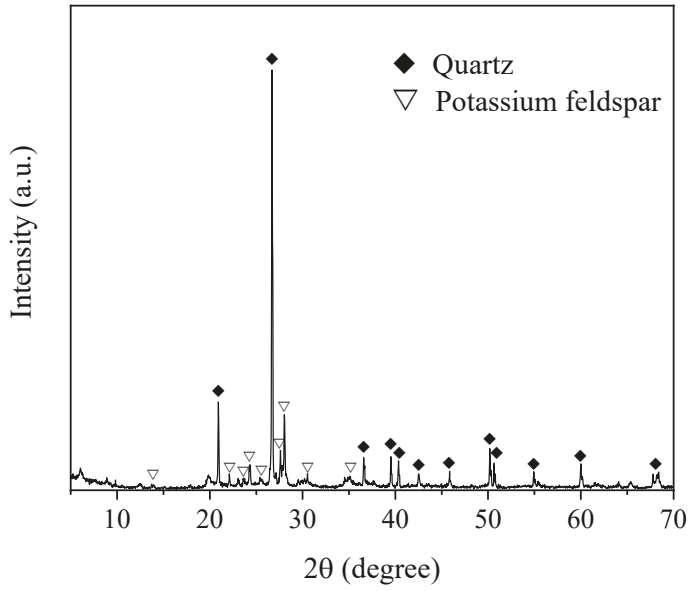

Figure 4. XRD Spectrum of the soil sample.

EPS and EPE materials used in this study were both commercially available lightweight foams (Chengdu Xuchuan Building Materials Co., Ltd., Chengdu, China). EPS has a density of 15 kg/m^3 (Figure 2c). According to the study by Sarmiento et al. [46] on the microscopic characteristics of EPS, foam cell morphology is regular, with distinct boundaries, representing a typical closed-cell structure. Thin walls separate the cells, forming the unique 'foam skeleton' of EPS material, which deforms, collapses, and ruptures during compression, playing a key role in its energy absorption performance. Based on the experimental design, 18 groups of EPS samples with different lengths were tested in this study.

EPE foam used in the experiment has a density of 20 kg/m^3 (Figure 2d). According to Tan's study [47], EPE material exhibits a typical foam cell structure, with polyhedral closed cells and a relatively uniform pore size distribution. Additionally, the cells are large, and the cell walls are thick, providing good deformation stability. The cells are interconnected through the cell walls, forming a complex spatial network skeleton. To compare the energy absorption performance with that of EPS, 18 groups of EPE samples with different lengths were also tested in this study.

2.2. SHPB Testing Apparatus and Improved Sleeve

Experiments were conducted using the Split Hopkinson Pressure Bar (SHPB) system provided by the Archimedes Dynamic Testing Laboratory (Tianjin, China) with modifications made to the setup to accommodate testing of particulate materials (Figure 5). The system consists of three main modules: the power module, the pressure bar system, and the data acquisition module. The power module compresses nitrogen gas, stores it, and drives a metal projectile to impact the incident bar, generating a compressive stress wave. The projectile velocity is controlled by adjusting the nitrogen pressure, allowing for loading at different strain rates. The bar system comprises a 2.4 m long incident bar and a 2.0 m long transmission bar, both made from 7075 aluminum alloy, with an elastic modulus of 71 GPa and a stress wave propagation velocity of approximately 5000 m/s. Due to the significant wave impedance mismatch between the specimen and the bars, semiconductor strain gauges were selected for signal acquisition. The strain gauges have a nominal resistance of 120 Ω and are amplified by a factor of 1000. The strain gauges are positioned 850 mm from each end of the specimen. Data acquisition is performed at a frequency of 10 MHz, ensuring accurate capture of the entire stress wave propagation process under impact loading, thus guaranteeing data timeliness and integrity.

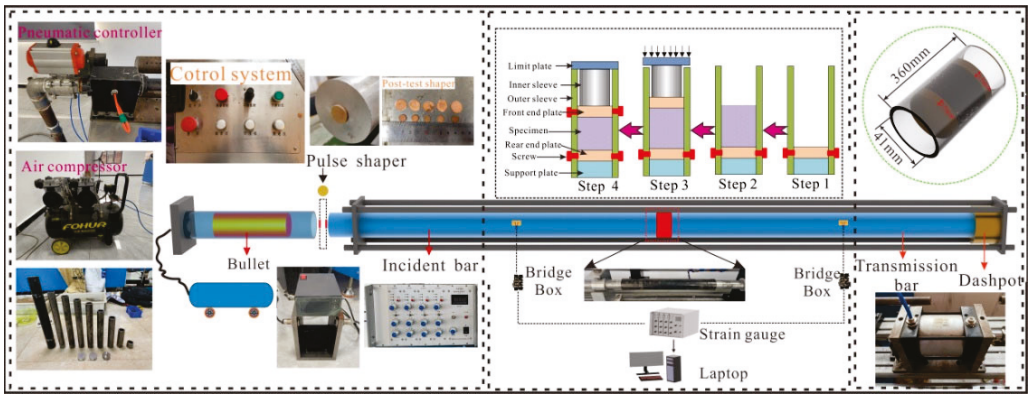

Figure 5. Modified SHPB apparatus.

The specimen housing sleeve consists of an outer sleeve, an inner sleeve, and front, rear, and support plates. The outer sleeve is made from high-strength steel, with a total length of 360 mm, an inner diameter of 40.1 mm, and a wall thickness of 2.0 mm, providing

ideal lateral confinement. The sleeve is pre-equipped with a series of threaded holes for installing and adjusting the plate positions, allowing for precise control of the specimen's initial length and density before loading. All bolts must be removed during loading to prevent interference with the propagation of the stress wave. The inner sleeve is made of the same material as the outer sleeve, with a diameter of 25 mm, and its primary function is to further restrict the specimen's length and packing density, enhancing the repeatability and consistency of the test. The front and rear plates are made from the same material as the SHPB bars, with a diameter of 40.0 mm and a thickness of 15 mm. These plates help reduce wave impedance mismatch caused by interface discontinuities and prevent specimen particle leakage. The support plate is 10 mm thick and made from high-strength steel, positioned below the rear plate to ensure the plates do not tilt when bolted.

In this study, EPS and EPE were solid materials that could theoretically have been directly loaded. However, to maintain consistent testing conditions for different sample types under the same constraints and improve the comparability and data consistency, all samples were loaded using the same sleeve device. The test conditions are summarized in Table 1.

Table 1. Test conditions.

Material	Length of Cushion Layer (mm)	Impact Velocity (m/s)
EPS	40	10.7; 12.6; 15.3
	60	10.5; 12.4; 15.2
	120	10.6; 12.9; 15.3
	160	10.4; 12.5; 15.4
	240	10.0; 11.7; 14.3
	300	10.0; 11.7; 14.4
EPE	40	10.1; 12.1; 15.1
	80	10.1; 12.0; 15.3
	120	10.0; 12.5; 15.3
	160	10.1; 12.4; 15.1
	240	10.6; 12.1; 15.1
	300	10.5; 12.1; 15.1
Soil + EPS	30 + 30	10.2; 11.9; 14.8
	40 + 20	9.9; 12.2; 14.8
	45 + 15	10.2; 12.3; 15.2
Soil + EPE	30 + 30	10.6; 12.7; 15.4
	40 + 20	10.6; 12.5; 15.3
	45 + 15	10.6; 12.5; 15.3

2.3. Sample Preparation and Testing Procedure

This study primarily tests different lengths of EPS and EPE, as well as soil–EPS and soil–EPE composite specimens with varying proportions under a fixed length. The experimental procedure is as follows: (1) Positioning the Plates: Place the support plate on a level working surface and stack the rear plate. Secure the outer sleeve and the rear plate with bolts to ensure the bottom structure is stable and reliable. (2) Filling the Test Material: For pure EPS and EPE materials, place them directly inside the sleeve according to the designed length, and position a plate on top of the test material before applying the impact load. For composite material layers, first place the designed length of EPS or EPE foam material on the rear plate, then fill the calculated amount of soil on top of the foam material to form a layered structure with a total length of 60 mm. The foam-to-soil layer length ratios are 1:1, 1:2, and 1:3. (3) Density Control for Composite Layers: To ensure uniform density of the soil across different impact conditions, a constant-mass filling method is used. The soil density is maintained at 1.6 g/cm^3 through multiple pre-compression and

leveling adjustments. It is important to note that the applied pre-compression is minimal and does not alter the initial density of the foam. When the top of the inner sleeve is aligned with the end of the outer sleeve, the limiting plate should be in contact with the outer sleeve, ensuring that the specimen length is precisely set. (4) Assembly and Impact Loading: The assembled specimen is placed between the SHPB incident and transmission bars. The sleeve's orientation is adjusted to maintain a horizontal position, ensuring full contact between the plate ends and the bar ends. The fixing bolts are then removed, and impact loading is applied. To reduce interface friction and improve experimental accuracy, graphite powder is evenly applied on the contact surfaces between the incident bar and the front plate, and between the transmission bar and the rear plate.

3. Results and Analysis

3.1. Test Validity Verification

Figure 6 displays the typical incident, reflected, and transmitted wave signals, all of which are smooth and continuous without noticeable jumps or oscillations. Figure 7 compares stress wave propagation before and after introducing the pulse shaper. Without it, the incident waveform is sharp and exhibits high-frequency oscillations, while the transmitted wave shows pronounced distortion—indicating a steep shock front prone to reflection and interface interference. With the pulse shaper, the incident waveform is smoother, its rising edge broader, and oscillations greatly reduced; the transmitted signal becomes more stable, and its main peak is delayed. These improvements signify that the pulse shaper prolongs the loading duration and optimizes the stress wave delivery process. Overall, compared to tests without a pulse shaper, the application of the pulse shaper increased the pulse duration by 60%, greatly enhancing the reliability of the experiment. Figure 8 compares no-load conditions before and after adding the sleeve and plates. Before this modification (Figure 8a), the incident and transmitted signals overlap significantly. Afterward (Figure 8b), using matching materials for plates and bars eliminates waveform changes, confirming that the sleeve and plates have negligible impact on the signals and satisfy experimental requirements.

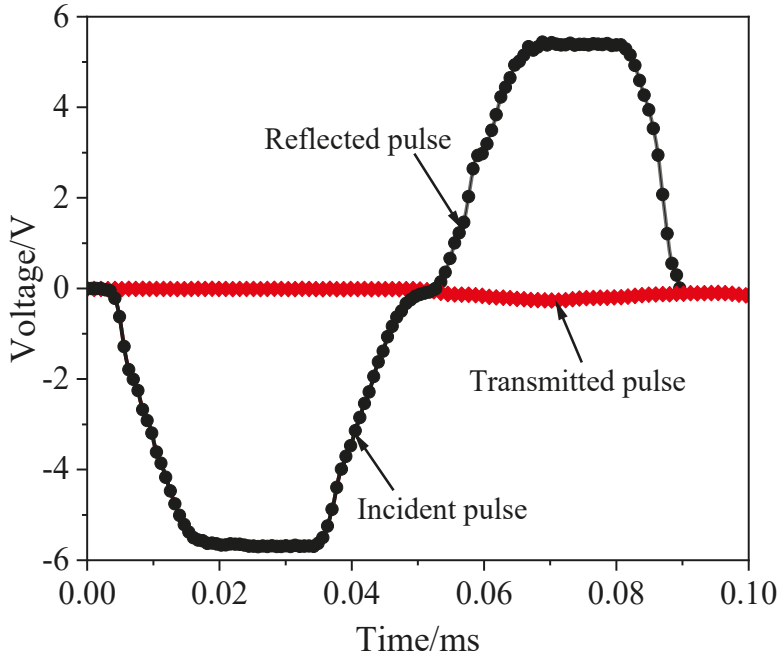

Figure 6. Test validity verification.

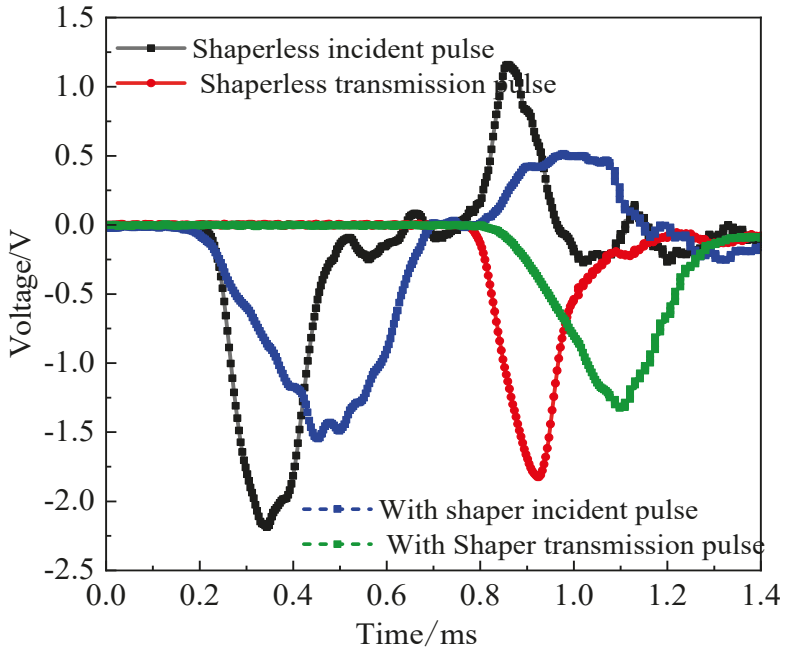

Figure 7. Effect of shapers on waveform.

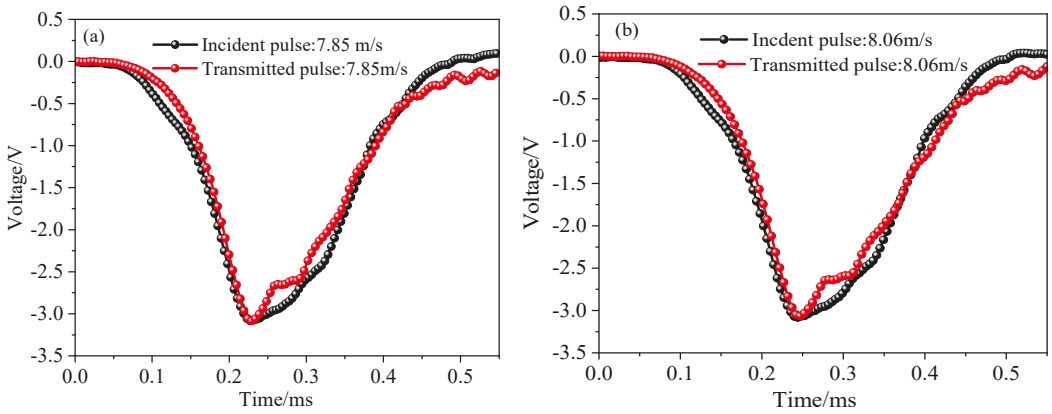

Figure 8. Sleeve and plate calibration: (**a**) pre-improvement waveform; and (**b**) improved waveform.

3.2. Compressive Stress Wave Propagation and Attenuation Characteristics

Figure 9 illustrates the propagation process of the stress wave in the specimen. At the start of the experiment, the impact bar, driven by the actuator, strikes the free end of the incident bar at a certain velocity, generating a compressive stress wave that propagates axially along the incident bar, referred to as the incident wave. This wave propagates through the incident bar at the material's elastic wave velocity until it reaches the interface between the incident bar and the specimen. Upon reaching the interface, due to the difference in wave impedance between the two materials, a portion of the wave is reflected back into the incident bar, forming the reflected wave. The reflected wave propagates in the opposite direction along the incident bar and is recorded by the strain gauges. At the same time, another portion of the energy from the incident wave passes through the interface into the specimen and continues to propagate. When the wave passes through the specimen and reaches the interface between the specimen and the transmission bar, part of the wave is transmitted into the transmission bar, forming the transmitted wave, which is recorded by the strain gauges installed on the transmission bar.

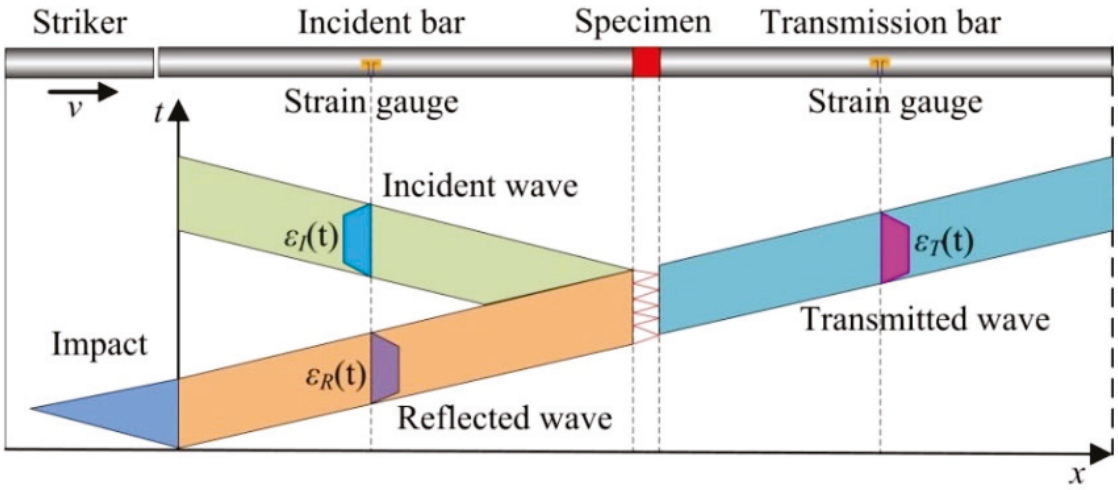

Figure 9. Schematic diagram of stress wave generation and propagation process.

The propagation velocity of stress waves in a medium is crucial for studying wave propagation characteristics and the constitutive model of materials. Based on the SHPB stress wave time history curve, the velocity of the compressive stress wave and the peak stress velocity in soil can be calculated as Equations (1) and (2):

$$C = L_S/(t_c - t_I - t_T) \tag{1}$$

$$C_{max} = L_S/(t_m - t_I - t_T) \tag{2}$$

where C is the stress wave velocity, C_{max} is the peak stress velocity, L_S is the specimen length, t_c is the time difference between the initial starting points of the incident and transmitted waves, t_m is the time difference between the peak points of the incident and transmitted waves, t_I is the time for the incident bar strain gauge to reach the specimen's front end, and t_T is the time for the specimen's rear end to reach the transmission bar strain gauge.

Figure 10 illustrates the effect of specimen length on stress wave propagation velocity. For EPS foam (Figure 10a), the stress wave velocity ranges from 162.8 to 354.1 m/s, with an average velocity of approximately 249.3 m/s. Additionally, the peak stress velocity decreases significantly with increasing specimen length and shows a strong negative linear relationship. For EPE foam (Figure 10c), the velocity ranges from 81.2 to 199.6 m/s, with an average velocity of 149.6 m/s, which is notably lower than the average velocity of stress waves in EPS foam. Aside from the stress wave propagation characteristics, the specimen length of foam materials also has a significant impact on the propagation characteristics of shock waves. The average velocity in EPS foam is consistently higher than in EPE foam, indicating that EPS material has a weaker damping effect on shock wave propagation and transmits waves more quickly. In addition, the difference in peak stress velocity between EPS and EPE is primarily attributed to the attenuation of stress waves during propagation through the materials (Figure 10b,d). As the sample length increases, the propagation path of the stress wave becomes longer, leading to greater energy dissipation. Moreover, EPE foam, compared to the more rigid and brittle EPS foam, exhibits greater flexibility, resilience, and a closed-cell structure, providing higher damping and cushioning capabilities. Consequently, at the same thickness, EPE foam is more effective in absorbing and attenuating shock waves, resulting in a lower peak stress velocity. Furthermore, in EPE foam, the peak stress velocity decreases more significantly with increasing length, with the slope of the fitted curve being steeper. This suggests that EPE foam has a stronger

shock wave cushioning capability and can more effectively reduce the intensity of the shock waves.

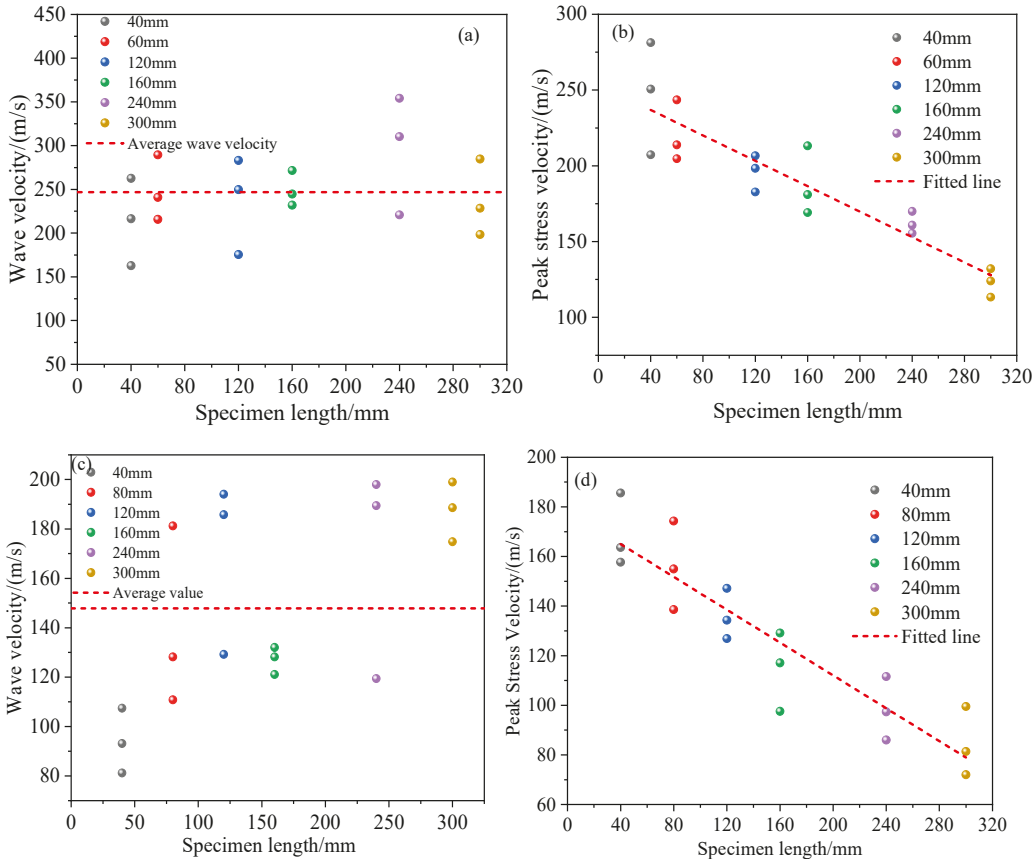

Figure 10. Effect of EPS layer specimen length on stress wave propagation characteristics: (**a**) wave velocity in EPS cushion layer; (**b**) peak stress velocity in EPS cushion layer; (**c**) wave velocity in EPE cushion layer; and (**d**) peak stress velocity in EPE cushion layer.

Figure 11a,b show the propagation characteristics of the average wave velocity and peak stress velocity in the soil–EPS composite layer. The results indicate that as the soil length increases, the propagation velocity of the stress wave significantly decreases. For a 1:1 ratio, the average wave velocity is 246.7 m/s, while for the 2:1 and 3:1 ratios, the average velocities are 272.4 m/s and 283.6 m/s, respectively. Furthermore, the peak stress velocity increases linearly with the increase in the soil-to-EPS ratio. In the soil–EPE composite layer (Figure 11c,d), both the average wave velocity and peak stress velocity exhibit the same trend as in the soil–EPE composite layer. However, for the same ratios, both the average wave velocity and peak stress velocity are significantly lower. Compared to EPS, EPE foam has a softer structure and undergoes more complete compressive deformation, which allows it to dissipate shock energy more effectively, resulting in a more significant reduction in wave velocity. Fang and Liu [48] suggested that the peak stress velocity is typically treated as a constant without considering the effects of particle size. However, based on the results of the present analysis, peak stress velocity is shown to be dependent on specimen length and layer material properties. Thus, simplifying the peak stress velocity as a constant may underestimate the actual impact of the cushion layer on the shock response, which would be unsafe for engineering design.

In SHPB experiments, as the stress wave propagates through the specimen, the amplitude of the stress wave experiences attenuation. Traditional wave theory primarily focuses on wave propagation velocity, waveform, and other characteristics, but lacks a quantitative description of wave amplitude attenuation. To address this, the attenuation coefficient

is introduced to quantify the wave-shaping characteristics of the specimen. It is defined as follows:

$$\eta = \frac{T_{max}}{I_{max}} \tag{3}$$

where T_{max} is the maximum stress at the transmission bar end and I_{max} is the maximum stress at the incident bar end. η reflects the specimen's ability to attenuate the energy of the incident stress wave. A smaller η value indicates stronger attenuation of the stress wave by the specimen, leading to a smaller amplitude of the transmitted wave.

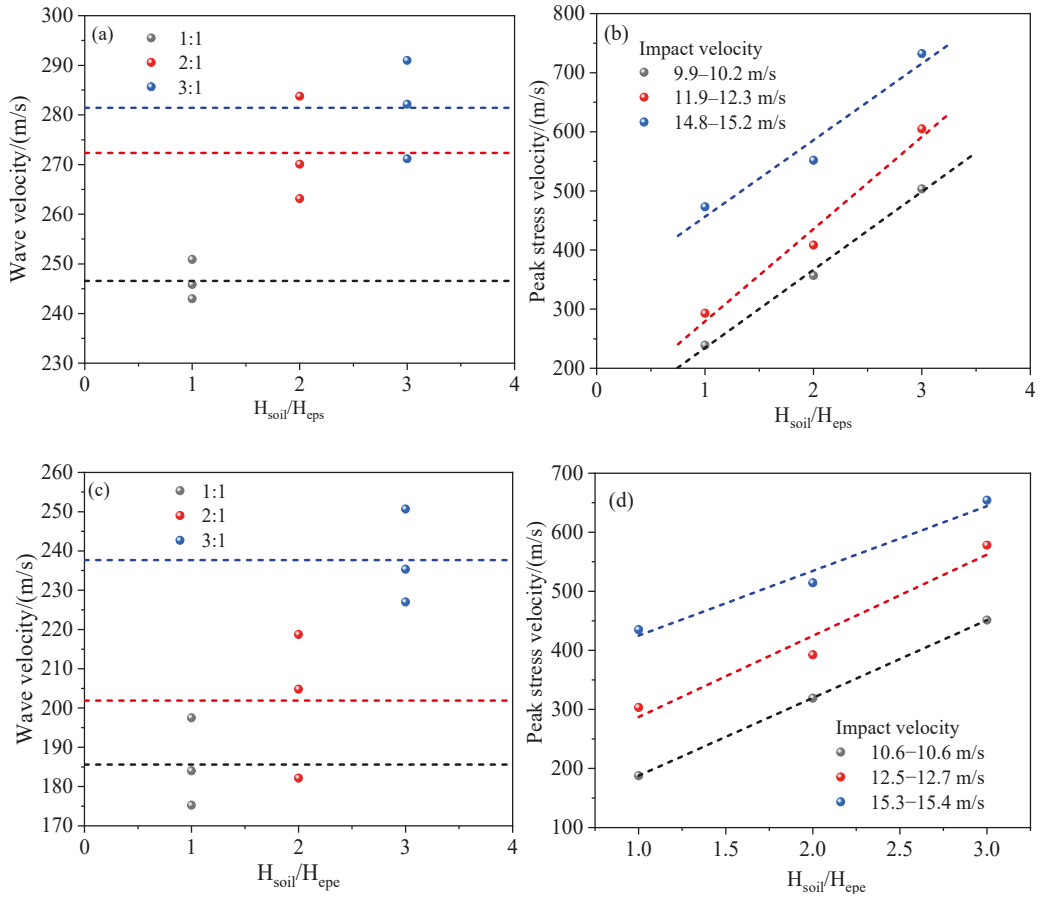

Figure 11. Effect of composite cushion layer on stress wave propagation characteristics: (**a**) wave velocity in soil–EPS cushion layer; (**b**) peak stress velocity in soil–EPS cushion layer; (**c**) wave velocity in soil–EPE cushion layer; (**d**) peak stress velocity in soil–EPE cushion layer.

For both EPS and EPE, the stress wave attenuation coefficient decreases exponentially with increasing specimen length (Figure 12a,b). In the case of EPS, when the specimen length is less than 50 mm, the attenuation coefficient decreases rapidly, indicating that most of the stress waves are either reflected or absorbed in EPS. As the specimen length increases beyond 100 mm, the transmission coefficient stabilizes, suggesting that the dissipation of stress waves by the cushion layer gradually saturates. For the same specimen length, a higher impact velocity results in a larger proportion of transmitted stress, showing that the attenuation effect in the medium is strain rate-sensitive. Figure 12b shows the relationship between the stress wave attenuation coefficient and specimen length for EPE material. Compared to the EPS medium, the relationship between the attenuation coefficient and specimen length is approximately the same. However, for specimens shorter than 50 mm, the attenuation coefficient of EPS is significantly higher than that of EPE. Moreover, in EPS, a larger thickness is required to reduce the attenuation coefficient to a level similar to that of EPE. Overall, under the same conditions, EPE foam exhibits a generally superior attenuation

capacity compared to EPS foam, particularly under short-range and high-intensity impacts, demonstrating better cushioning performance for stress wave attenuation.

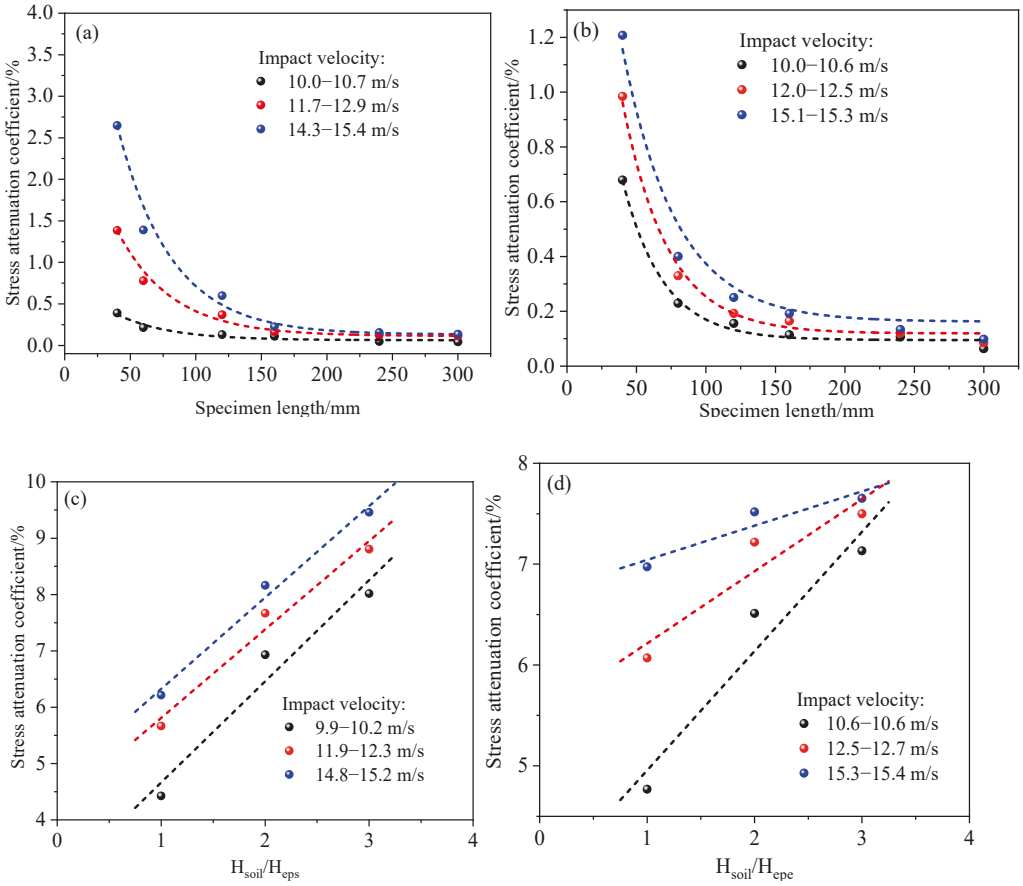

Figure 12. Stress wave attenuation characteristics in different cushion layers: (**a**) EPS cushion layer; (**b**) EPE cushion layer; (**c**) soil–EPS cushion layer; and (**d**) soil–EPE cushion layer.

Figure 12c,d show the attenuation characteristics of stress waves in composite specimens. The results indicate that the attenuation coefficient increases with the soil-to-foam ratio, suggesting that as the proportion of soil increases, the specimen's ability to attenuate stress waves decreases. Additionally, the impact velocity negatively correlates with the attenuation coefficient. Under the same soil-to-foam ratio, higher velocity results in a more compact specimen, leading to a larger attenuation coefficient. Comparing different composite specimens, the attenuation coefficient of the EPE composite layer is lower than that of the EPS composite layer, indicating that the former exhibits more significant attenuation of stress waves.

3.3. Laws of Energy Evolution and Dissipation

3.3.1. Characterization of Energy Evolution

In energy absorbing materials in protective structures, compression deformation and friction under impact loading are accompanied by energy transfer and conversion. The peak stress attenuation index can be used to quantify the changed characteristics of the compressive wave in granular materials. Additionally, the energy variation during the impact process can also describe the energy absorption characteristics of granular media. In the SHPB test, the incident energy W_I, reflected energy W_R, transmitted energy W_T, and absorbed energy W_S can be calculated using Equations (4)–(7) [49]:

$$W_I = A_C E_C C_C \int_0^t \varepsilon_I^2(t) d_t \tag{4}$$

$$W_R = A_C E_C C_C \int_0^t \varepsilon_R^2(t) d_t \tag{5}$$

$$W_T = A_C E_C C_C \int_0^t \varepsilon_T^2(t) d_t \tag{6}$$

$$W_S = W_I - W_R - W_T \tag{7}$$

where W_I, W_R, W_T, and W_S represent the incident energy, reflected energy, transmitted energy, and absorbed energy, respectively. A_C and E_C are the cross-sectional area and the elastic modulus of the bar, respectively. C_C is the propagation velocity of the compressive stress wave in the bar. ε_I and ε_R are the incident and reflected strains, respectively, and ε_T is the transmitted strain. t represents time.

Figure 13 illustrates the variation in energy with time for a typical specimen during the SHPB test, reflecting the material's energy absorption characteristics. During the test, incident energy rapidly increases with loading time and stabilizes after 0.032 ms. Both reflected and transmitted energies rise synchronously, but their amplitudes are much lower than that of the incident energy. Absorbed energy shows a continuous increase with time, indicating the specimen's dissipation effect on incident energy. Furthermore, soil particles are a low wave impedance material, resulting in most of the incident energy being converted into reflected energy, with relatively small proportions of transmitted and absorbed energies.

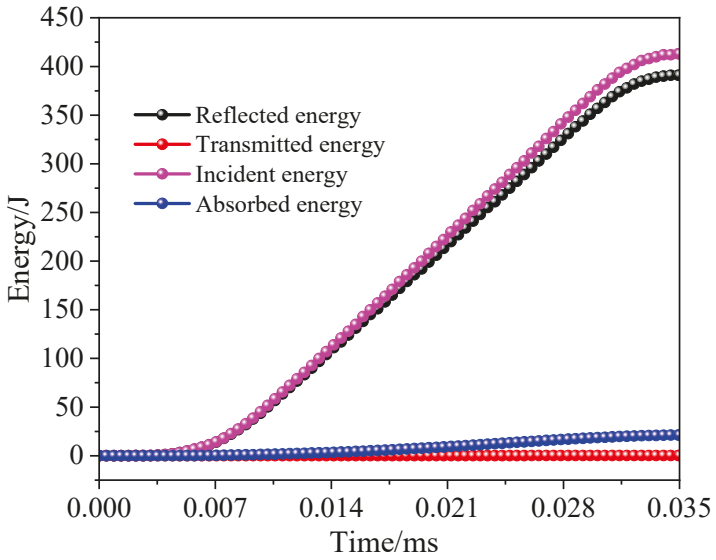

Figure 13. Typical energy change time course curve.

3.3.2. Energy Dissipation Characteristics

Although the incident energy, reflected energy, and transmitted energy all increase with the impact velocity, the ratio of absorbed energy to the total energy entering the specimen can describe the material's energy dissipation characteristics. According to the law of energy conservation, the energy absorption coefficient α is defined as:

$$\alpha = \frac{W_s}{W_I - W_R} \tag{8}$$

where α is the energy absorption coefficient, W_s is the absorbed energy, and W_I and W_R are the incident energy and reflected energy, respectively.

Figure 14a,b show the variation in the energy absorption coefficient with specimen length for EPS and EPE foam materials under different impact velocities. As the specimen length increases, the energy absorption coefficient increases and stabilizes once the specimen length exceeds 100 mm. This indicates that the material's energy absorption effect rapidly diminishes within a certain propagation distance. Comparing the two materials, EPE exhibits a higher energy absorption coefficient than EPS under the same conditions, with a steeper increase in the curve, demonstrating superior energy dissipation properties.

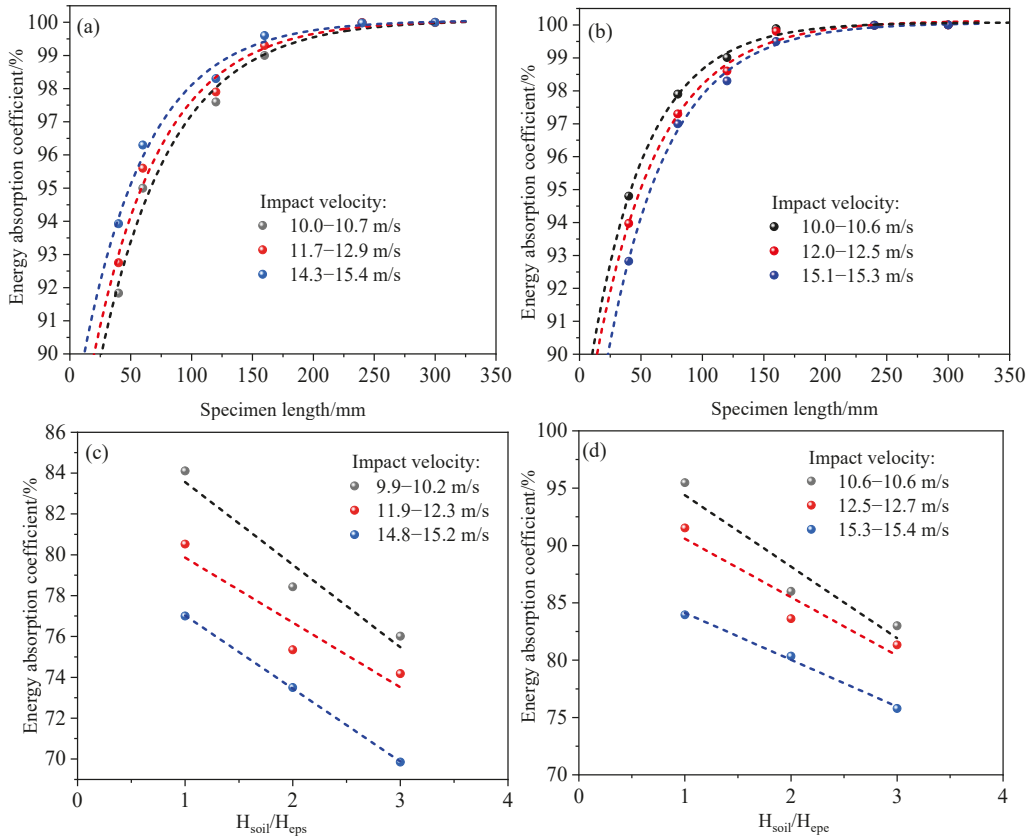

Figure 14. Energy absorption coefficients in different cushion layers: (**a**) EPS cushion layer; (**b**) EPE cushion layer; (**c**) soil–EPS cushion layer; (**d**) soil–EPE cushion layer.

Figure 14c,d show the trend of the energy absorption coefficient with the soil-to-foam material ratio in composite specimens under different impact velocities. Overall, both composite specimens exhibit similar patterns. The energy absorption coefficient of the soil–EPE composite cushion layer is significantly higher than that of the soil–EPS composite cushion layer, especially when the soil-to-foam ratio is low, with the energy absorption coefficient of soil–EPE reaching nearly 95%, compared to around 84% for the soil–EPS layer. Additionally, the energy absorption coefficient decreases significantly as the soil proportion increases, indicating that the foam material plays the primary energy-dissipating role in the composite layer, with EPE performing better in energy absorption. In contrast, the energy absorption performance of the EPS layer decreases more significantly under higher soil proportions and increased impact velocities, with slightly lower stability.

The energy absorption density index is further used to reflect the energy dissipation characteristics of the specimens [50]:

$$W_\rho = W_S / V \tag{9}$$

where W_ρ represents the energy absorption density, W_S denotes the absorbed energy, and V is the sample volume. The energy absorption density is a measure of the material's efficiency in absorbing impact energy. The higher its value, the greater the proportion of incident energy effectively absorbed by the material, indicating better energy absorption performance.

Figure 15a,b show that the energy absorption density significantly decreases with increasing foam specimen length and eventually stabilizes at a lower value. This indicates that shorter specimen segments can absorb more energy per unit volume, while as the length increases, the volume expands, but the energy absorption contribution from the added volume diminishes. Therefore, in practical engineering, infinitely increasing the cushion layer thickness has certain limitations in improving its energy dissipation capacity.

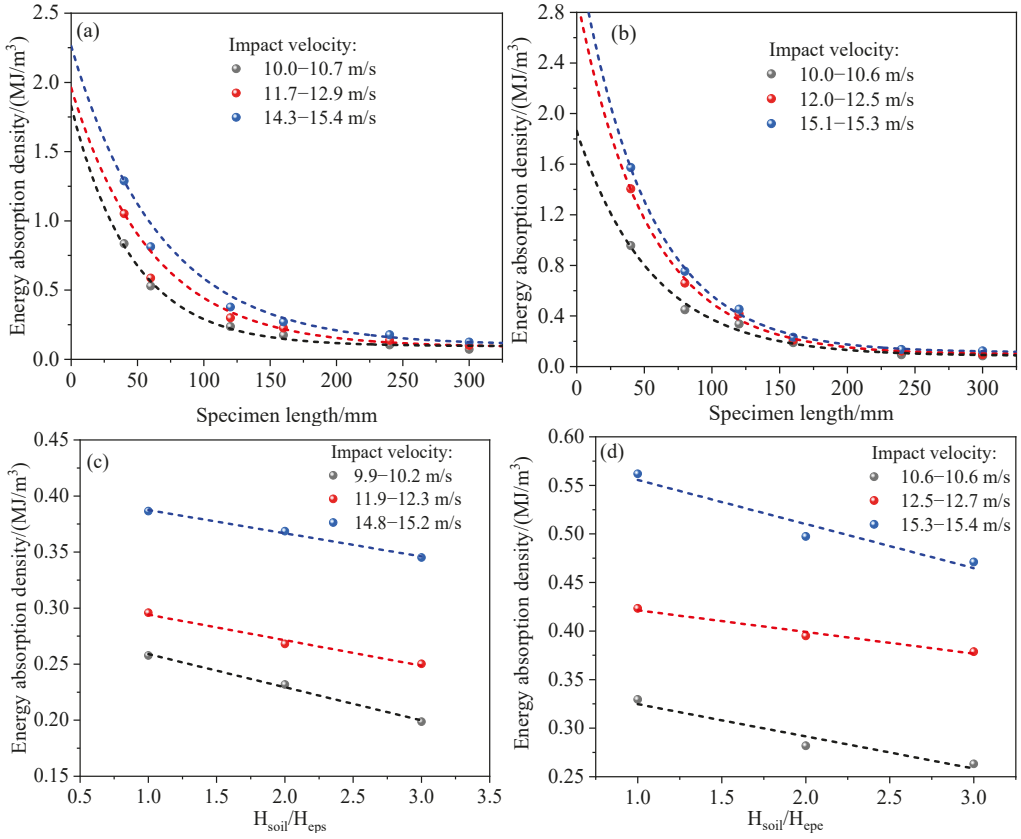

Figure 15. Energy absorption density in different cushion layers: (**a**) EPS cushion layer; (**b**) EPE cushion layer; (**c**) soil–EPS cushion layer; and (**d**) soil–EPE cushion layer.

Figure 15c,d show the variation trends of energy absorption density for composite specimens under different impact velocities. The results indicate that for both soil–EPS and soil–EPE composite layers, the energy absorption density significantly decreases as the soil specimen length ratio increases. This suggests that as the soil content increases, the overall energy absorption capability of the material deteriorates. Therefore, although soil may provide some structural support, its inherently weak energy absorption capacity actually dilutes the energy absorption contribution of the foam.

3.3.3. Compression Properties of Foam

In the SHPB foam impact test, the degree of pore collapse can be quantified by comparing the initial density ρ_0 and the final density ρ_f, revealing the dynamic energy dissipation characteristics and stress wave attenuation behaviors of different density foams. This

provides a basis for evaluating their cushioning performance under high-velocity impact environments. The density variation ratio is defined as:

$$\Delta\rho = \frac{\rho_f - \rho_0}{\rho_0} \times 100\% \tag{10}$$

where ρ_0 is the initial density of the specimen, ρ_f is the final density after impact, and $\Delta\rho$ represents the density variation ratio.

The results shown in Figure 16 indicate that the density variation ratio of EPS material significantly increases with the impact velocity. At impact velocities between 14.3 and 15.4 m/s, the density variation ratio of a 40 mm short specimen exceeds 100%, suggesting substantial compression. As the specimen length increases, the density variation ratio gradually decreases, especially at 300 mm, where it drops below 30%. This reflects a decline in the impact energy absorption and transmission capabilities of longer specimens, as well as a weakening of the compaction effect. In contrast, EPE material exhibits a similar trend, but the overall density variation ratio is lower than that of EPS. For example, under impact velocities of 15.1–15.3 m/s, the density variation ratio of a 40 mm EPE specimen is about 85%, lower than the over 100% observed for EPS, thus maintaining better structural integrity. Therefore, EPE can absorb some of the impact energy and achieve partial stress release through elastic deformation, making it suitable for engineering scenarios that require high cushioning repeatability and structural integrity.

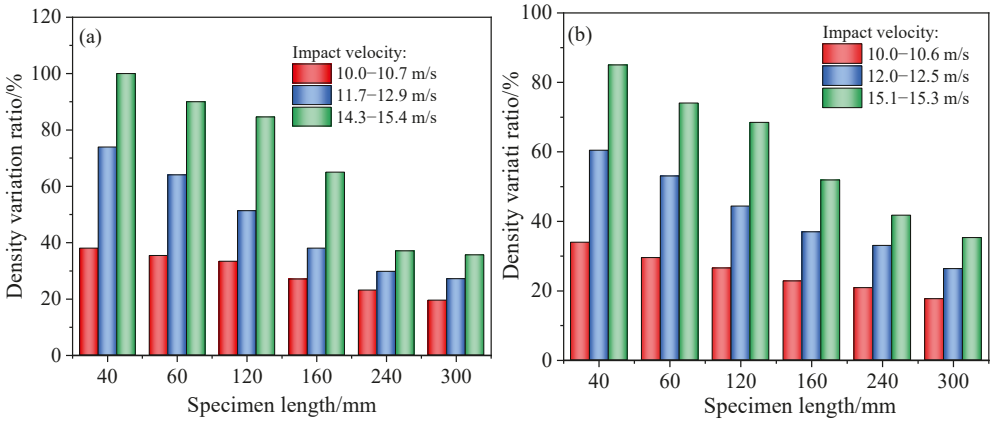

Figure 16. Density variation ratio of specimens: (**a**) EPS cushion layer; and (**b**) EPE cushion layer.

Figure 17 compares the variations in the stress attenuation coefficient of EPS and EPE foams under different impact velocities and density variation ratio conditions. The results show that EPE foam consistently exhibits lower stress attenuation coefficients and superior energy absorption capabilities compared to EPS foam. The stress wave dissipation effect of EPE foam is more effective than that of EPS foam, with EPE displaying lower sensitivity to changes in impact velocity. Moreover, under the same impact velocity, the density variation ratio decreases as the specimen length increases. This is because longer specimens extend the stress wave propagation path, leading to a more uniform distribution of strain energy within the unit volume, which mitigates local compaction damage and reduces the density variation ratio. In EPE foam, longer specimens not only have smaller density variation ratios but also exhibit lower attenuation coefficients. In contrast, EPS foam is more prone to early collapse under shorter specimen lengths or higher impact velocities, leading to significantly higher transmitted stress, increased attenuation coefficients, and reducing energy absorption performance. In summary, EPE foam demonstrates superior energy dissipation and structural adaptability under various impact conditions, indicating its higher potential for engineering applications.

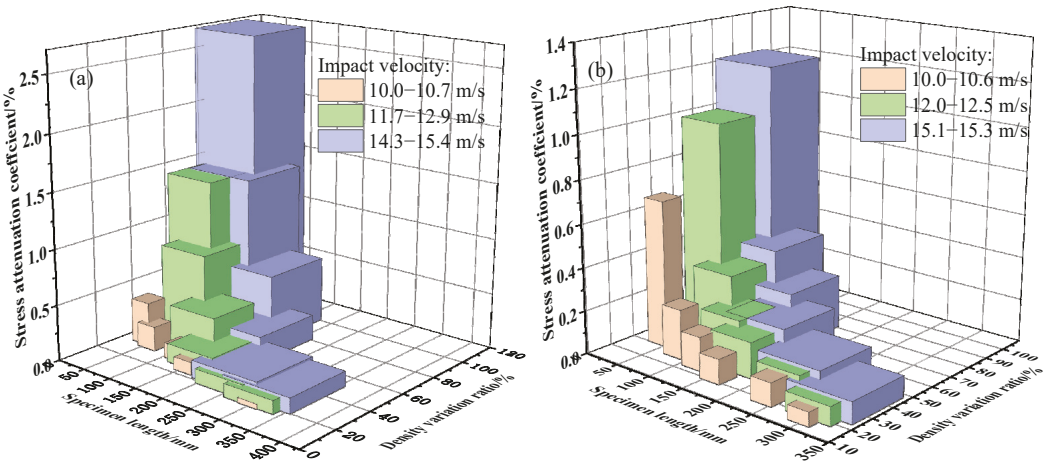

Figure 17. Stress attenuation coefficient in foam: (**a**) EPS cushion layer; and (**b**) EPE cushion layer.

Figure 18 analyzes the variation trends of the energy absorption coefficient for EPS and EPE foams under different impact velocities and density variation ratio conditions. The energy absorption coefficient of EPE foam fluctuates very little with compression, while that of EPS foam decreases significantly as the density variation ratio increases. Under different impact velocities, EPE foam not only exhibits a higher overall energy absorption coefficient but also remains almost stable, with minimal influence from the density variation ratio. In contrast, EPS foam shows a noticeable decrease in the energy absorption coefficient at higher density variation ratios, particularly at higher impact velocities, indicating that the material is more prone to localized failure or stress concentration under large deformations. Furthermore, EPE foam maintains nearly 100% energy absorption at higher velocity ranges, while EPS foam experiences significant degradation under the same conditions. A similar trend is observed in the effect of density variation ratio on energy absorption density (Figure 19). Overall, EPE foam demonstrates better extensibility and structural recovery throughout the compression process, providing sustained energy absorption capacity and good deformation coordination, which makes it more suitable for applications under high-energy impact loads.

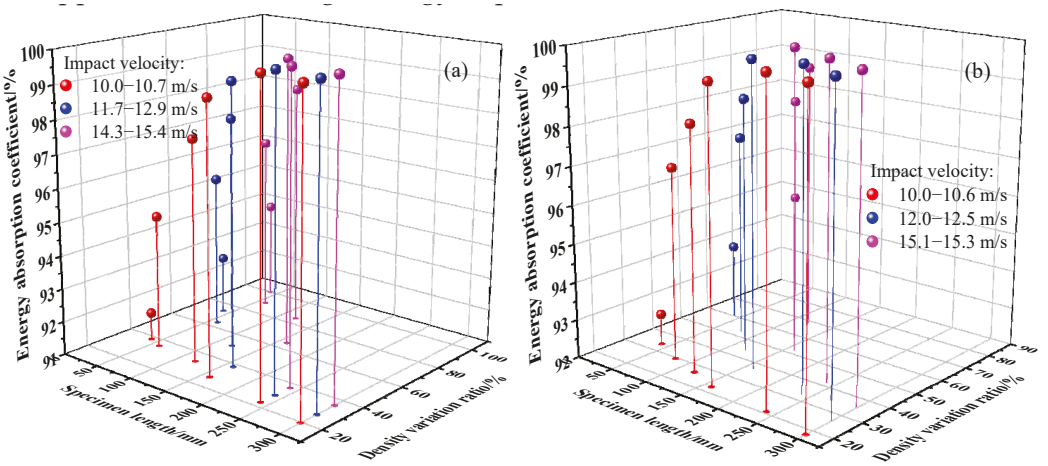

Figure 18. Effect of density variation ratio on energy absorption coefficient: (**a**) EPS cushion layer; and (**b**) EPE cushion layer.

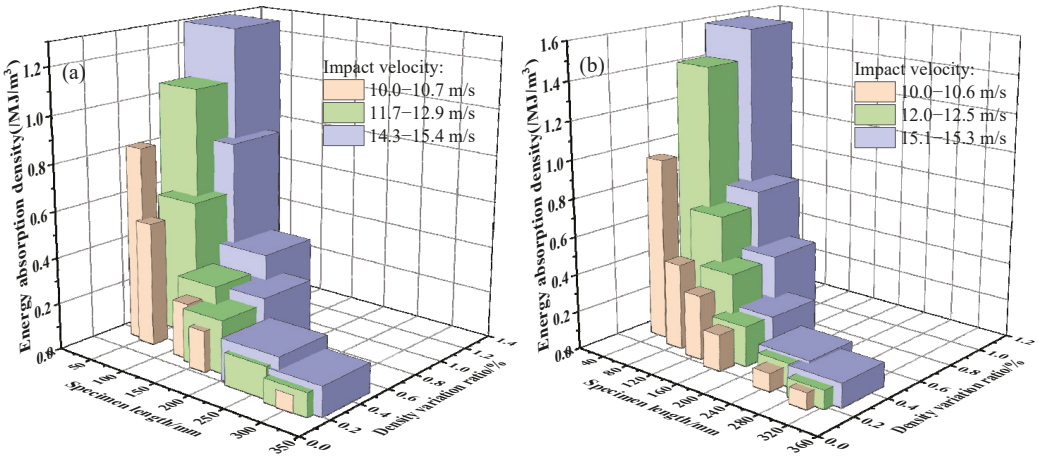

Figure 19. Effect of density variation ratio on energy absorbing density: (**a**) EPS cushion layer; and (**b**) EPE cushion layer.

4. Conclusions

This study systematically investigates the dynamic response characteristics of EPS and EPE foams and their composite cushion layers with soil under impact loading, through SHPB experimental testing and energy evolution analysis. The main conclusions are as follows:

(1) In a single foam material structure, the average stress wave propagation velocity in EPE foam is 149.6 m/s, significantly lower than the 249.3 m/s in EPS foam, indicating stronger wave resistance in EPE. For the 40 mm specimen, the stress attenuation coefficient in EPE is as low as 0.22, compared to 0.31 in EPS at the same velocity. Additionally, in the 14.3–15.4 m/s velocity range, the density variation ratio for EPS can reach up to 100%, whereas EPE only reaches 87% under similar impact conditions. Therefore, EPE exhibits stronger plastic cushioning and structural stability, making it more suitable for energy dissipation under repeated impacts. It is recommended to use EPE instead of traditional EPS for structural design in engineering.

(2) The energy absorption effect of the soil–foam composite layer decreases as the proportion of soil increases. A higher foam proportion leads to more significant energy dissipation. When the foam-to-soil ratio is 1:1, the energy absorption coefficient of the soil–EPE composite structure reaches 94.7%, significantly higher than the 84% for the soil–EPS composite cushion layer. As the soil proportion increases to 1:2 and 1:3, the energy absorption coefficient decreases significantly, indicating that soil, while providing support, has limited energy dissipation capacity. A higher soil proportion weakens the overall energy absorption effect of the structure. Therefore, in practical engineering design, the foam layer should occupy at least 50% of the total volume to maximize energy absorption.

(3) As the foam specimen length increases from 40 mm to 300 mm, the stress wave propagation velocity continuously decreases, the peak stress response significantly weakens, and the energy absorption coefficient gradually increases. This indicates that increasing the thickness helps enhance wave attenuation and energy dissipation. However, the energy absorption density per unit volume decreases as the length increases, indicating that the additional volume contributes less to energy absorption. Longer foam layers extend the stress wave path and reduce local compaction. Thus, cushion layer thickness should not be arbitrarily increased. The relationship between foam thickness and energy absorption density should be optimized, considering impact energy, available space, and structural load capacity, to balance energy dissipation with structural dimensions and weight.

(4) The SHPB testing method employed in this study is suitable for investigating the dynamic behavior of different cushioning materials at high strain rates. However, the small

size of the specimens does not fully account for the effects of specimen size and the influence of macroscopic structures on the overall response. Future research should integrate SHPB testing with large-scale model experiments to more comprehensively evaluate the dynamic protective performance of material systems under real engineering conditions.

Author Contributions: Conceptualization, J.G. and L.L.; methodology, X.M.; validation, D.L., J.W., and P.C.; formal analysis, J.W. and P.C.; investigation, D.L.; resources, D.L. and P.C.; data curation, D.L. and J.W.; writing—original draft preparation, D.L. and J.W.; writing—review and editing, P.C.; visualization, D.L. and J.W.; supervision, P.C. All authors have read and agreed to the published version of the manuscript.

Funding: This work was supported by the Natural Science Foundation of Inner Mongolia, China (Grant No. 2025MS05007), the Projects of the Guizhou Provincial Department of Transportation (Grant No. 2024-122-022), and the Projects of the Sichuan Provincial Department of Transportation (Grant No. 2022-A-1).

Institutional Review Board Statement: Not applicable.

Informed Consent Statement: Not applicable.

Data Availability Statement: Data are contained within the article.

Conflicts of Interest: Authors Dengfeng Li and Jianli Wu were employed by the China 19th Metallurgical Group Co., Ltd. Author Peng Cui was employed by the Shandong Energy Group Luxi Mining Co., Ltd. The remaining authors declare that the research was conducted in the absence of any commercial or financial relationships that could be construed as a potential conflict of interest.

References

1. Li, X.M.; Wang, M.; GUO, X.; Yan, J.L.; Ying, C.P. Measurement of stress attenuation effect in the sand under explosion wave. *Appl. Mech. Mater.* **2014**, *556–562*, 3187–3190. [CrossRef]
2. Yu, X.; Wang, J.R.; Zhou, B.K.; Chen, L.; Fang, Q. Experimental study on the mechanical behavior and energy absorption capacity of coral sand at high strain rates. *Ocean Eng.* **2024**, *291*, 116343. [CrossRef]
3. Song, B.; Chen, W.W.; Luk, V. Impact compressive response of Dry sand. *Mech. Mater.* **2009**, *41*, 777–785. [CrossRef]
4. US Department of the Army. *Structures to Resist the Effects of Accidental Explosions: TM5-1300*; US Department of the Army: Washington, DC, USA, 1990.
5. Jia, J.X.; Tang, H.P.; Chen, H.J. Dynamic mechanical properties and energy dissipation characteristics of frozen soil under passive confined pressure. *Acta Mech. Solida Sin.* **2021**, *34*, 184–203. [CrossRef]
6. Ma, Q.; Cao, Z. Experimental study on fractal characteristics and energy dissipation of stabilized soil based on SHPB test. *J. Mater. Civ. Eng.* **2019**, *31*, 04019264. [CrossRef]
7. Yan, S.; Wang, Y.; Wang, D.P.; He, S.M. Application of EPS geofoam in rockfall galleries: Insights from large-scale experiments and FDEM simulations. *Geotext. Geomembr.* **2022**, *50*, 677–693. [CrossRef]
8. Zhao, P.; Yuan, S.; Li, L.; Ge, Q.; Liu, J.; Du, L. Experimental study on the multi-impact resistance of a composite cushion composed of sand and geofoam. *Geotext. Geomembr.* **2021**, *49*, 45–56. [CrossRef]
9. Ouyang, C.J.; Liu, Y.; Wang, D.; He, S.M. Dynamic Analysis of Rockfall Impacts on Geogrid Reinforced Soil and EPS Absorption Cushions. *KSCE J. Civ. Eng.* **2019**, *23*, 37–45. [CrossRef]
10. Cui, P.; Luo, G.; Liu, L.; Cao Xi Li, B.; Mei, X. Experimental study on crushing characteristics and energy absorption effect of silica sand under dynamic loading. *Explos. Shock. Waves* **2025**, *45*, 093101. [CrossRef]
11. Lv, Y.R.; Li, X.; Wang, Y. Particle breakage of calcareous sand at high strain rates. *Powder Technol.* **2020**, *366*, 776–787. [CrossRef]
12. Bakken, J.; Slungaard, T.; Engebretsen, T.; Christensen, S.O. Attenuation of shock waves by granular filters. *Shock Waves* **2003**, *13*, 33–40. [CrossRef]
13. Balan, S.G.; Raj, A.S. Impact load bearing and energy absorption in sandwich polymer composites: Projectile versus shock loadings. *Results Eng.* **2025**, *25*, 103815. [CrossRef]
14. Wu, J.L.; Hu, X.W.; Mei, X.F. Dynamic response of a combined structure of falling stone impacted concrete slab and buffer layer. *Hydrogeol. Eng. Geol.* **2021**, *48*, 78–87.
15. Guo, Q.; Gou, Y.; Chen, J. Dynamic response of foam concrete under low-velocity impact: Experiments and numerical simulation. *Int. J. Impact Eng.* **2020**, *146*, 103693. [CrossRef]

16. Pan, Y.H.; Zong, Z.H.; QIAN H., M.; Huang, J.; Shan, Y.L. Experiment study on blast wave propagation in calcareous sand. *Explos. Shock Waves* **2023**, *43*, 1–15.
17. Peila, D.; Oggeri, C.; Castiglia, C. Ground reinforced embankments for rockfall protection: Design and evaluation of full scale tests. *Landslides* **2007**, *4*, 255–265. [CrossRef]
18. Wu, L.; Lyu, Y.R.; Zhang, S.; Din, S.C. Research progress and discussion on problems of sandy soil SHPB impact tests and numerical simulations. *Rock Soil Mech.* **2024**, *45*, 3461–3480. [CrossRef]
19. Yu, X.; Chen, L.; Fang, Q. Experimental study on the attenuation of stress wave in coral sand. *Chin. J. Rock Mech. Eng.* **2018**, *37*, 1520–1529.
20. Hampton, D.; Wetzel, R.A. Stress Wave Propagation in Confined Soils. *IIT Res. Inst Chic. IL* **1966**, AFWL-TR-66-56. Available online: https://www.semanticscholar.org/paper/STRESS-WAVE-PROPAGATION-IN-CONFINED-SOILS-Hampton-Wetzel/8898a6a555062f1682757ae19d62278ccd6573dd (accessed on 6 September 2025).
21. Schindler, L. *Design and Evaluation of a Device for Determining the One-Dimensional Compression Characteristics of Soils Subjected to Impulse-Type Loads*; Army Engineer Waterways Experiment Station: Vicksburg, MS, USA, 1968.
22. Yu, X.; Chen, L.; Fang, Q. A testing method on the attenuation of stress waves in loose porous media and its application to coral sand. *Eng. Mech.* **2019**, *36*, 44–52.
23. Lv, Y.; Ng, C.W.; Wang, Y. Evaluation of wave dissipation in sand under impact loading. *J. Geotech. Geoenvironmental Eng.* **2019**, *145*, 06019007. [CrossRef]
24. Yu, X.; Chen, L.; Zhou, B. Discussion of "Evaluation of Wave Dissipation in Sand under Impact Loading" by Yaru Lv, Charles, W.W. Ng, and Yuan Wang. *J. Geotech. Geoenviron. Eng.* **2019**, *145*, 06019007.
25. Cui, P.; Su, T.; Liu, L.; Wang, T.; Li, B.X.; Guan, X.T.; Mei, X.F. Characteristics of compression wave propagation and energy absorption effects in dry sandy soil. *Sci. Rep.* **2024**, *14*, 31625. [CrossRef]
26. Prabhu, S.; Qiu, T. Simulation of split Hopkinson pressure bar tests on sands with low water content. *J. Eng. Mech.* **2020**, *146*, 04020082. [CrossRef]
27. Prabhu, S.; Qiu, T. Modeling of sand particle crushing in split Hopkinson pressure bar tests using the discrete element method. *Int. J. Impact Eng.* **2021**, *156*, 103974. [CrossRef]
28. Lv, Y.R.; Wu, L.; Zhang, S.; Ding, S.C. Macro and micro quantitative study on impact behavior of glass beads by SHPB tests and FEM-DEM coupling analysis. *Eng. Mech.* **2023**, *40*, 245–256.
29. *JTGT D70-2010*; Guidelines for Design of Highway, Tunnel. Ministry of Transport of the People's Republic of China: Beijing, China, 2010. Available online: https://www.doc88.com/p-7327311462091.html (accessed on 6 September 2025).
30. Zhao, P.; Xie, L.Z.; He, B.; Zhang, Y. Experimental study of rock-sheds constructed with PE fibres and composite cushion against rockfall impacts. *Eng. Struct.* **2018**, *177*, 175–189. [CrossRef]
31. Huang, B.K.; Kin, S.K.; Kim, J.H.; Kim, J.D.; Lee, J.M. Dynamic compressive behavior of rigid polyurethane foam with various densities under different temperatures. *Int. J. Mech. Sci.* **2020**, *180*, 105657. [CrossRef]
32. Mazek, S.A.; Mostafa, A.A. Impact of a shock wave on a structure strengthened by rigid polyurethane foam. *Struct. Eng. Mech.* **2013**, *48*, 569–585. [CrossRef]
33. De, A.; Morgante, A.N.; Zimmie, T.F. Numerical and physical modeling of geofoam barriers as protection against effects of surface blast on underground tunnels. *Geotext. Geomembr.* **2016**, *44*, 1–12.
34. Gupta, N. A functionally graded syntactic foam material for high energy absorption under co repression. *Mater. Lett.* **2007**, *61*, 979–982. [CrossRef]
35. Hu, J.; Sun, Q.; Wu, X.T. Numerical analysis of the anti-explosion properties of tunnel constructions with EPS geofoam inclusions of different density. *Proective Eng.* **2012**, *34*, 38–43. Available online: https://kns.cnki.net/kcms2/article/abstract?v=Y2E-z2Sa5CMREp4uuR0fBdO2V7BoDY0AFcWlTikysKIj33sTDlGWbxXroreKhz4RE7-xx1VoqprnGF0Ngt-zYleLm1Uv_t8gHfOhKP8hzY3AjXO0Lr5OlV1_B20T9ZGkqvPwLAYgTjbk3CNL2FmsFHV3EoxHs6j6ECQx4oRiSKwoo0xMkUJJXg==&uniplatform=NZKPT&language=CHS (accessed on 6 September 2025).
36. Zhao, P.; Xie, L.; Li, L.; Liu, Q.; Yuan, S.X. Large-scale rockfall impact experiments on a RC rock-shed with a newly proposed cushion layer composed of sand and epe. *Eng. Struct.* **2018**, *175*, 386–398.
37. Hani, M.; Wang, D.P.; Yan, S.X.; Stéphane, L.; Chen, Y.H.; Qi, D. Optimization and performance analysis of novel waste EPS bead-sand composite cushions for rockfall mitigation: An integrated experimental and numerical study. *Geotext. Geomembr.* **2025**, *53*, 1314–1331.
38. Wu, J.; Ma, G.; Zhou, Z.; Mei, X.F.; Hu, X.W. Experimental Investigation of Impact Response of RC Slabs with a Sandy Soil Cushion Layer. *Adv. Civ. Eng.* **2021**, *2021*, 1562158. [CrossRef]
39. Ren, F.; Liu, J.; Huang, Q.; Ding, H.; Hu, Z.; Wang, G. Experimental study on the buffering mechanism of EPS bead-sand cushions under single and multiple impacts. *Geoenviron. Disasters* **2024**, *11*, 31. [CrossRef]
40. Alaie, R.; Chenari, R.J. Dynamic Properties of EPS-Sand Mixtures Using Cyclic Triaxial and Bender Element Tests. *Geosynth. Int.* **2019**, *26*, 563–579. [CrossRef]

41. Bhatti; Qadir, A. Computational Modeling of Energy Dissipation Characteristics of Expanded Polystyrene (EPS) Cushion of Reinforce Concrete (RC) Bridge Girder Under Rockfall Impact. *Int. J. Civ. Eng.* **2018**, *16*, 1635–1642. [CrossRef]
42. Özgür, A.; Erdem, R.T.; Kantar, E. Improving the impact behavior of pipes using geofoam layer for protection. *Int. J. Press. Vessel. Pip.* **2015**, *132–133*, 52–64. [CrossRef]
43. Wang, D.P.; Zhou, L.K.; Pei, X.J.; Huang, R.Q.; Liu, X.R. Experimental and numerical study on rockfall impacts on sand-soil cushions. *J. Vib. Shock* **2020**, *39*, 195–202.
44. Pham, T.T.; Kurihashi, Y.; Masuya, H. Impact response of reinforced concrete beam with cushion using finite-element analysis. *Case Stud. Constr. Mater.* **2022**, *17*, e1147. [CrossRef]
45. *GB/T 50123–2019*; Standard for Geotechnical Testing Method. Ministry of Housing and Urban-Rural Development of the People's Republic of China : Beijing, China; Planning Press: Beijing, China, 2019.
46. Sarmientom, A.M.; Guzman, H.L.; Morales, G. Expanded Polystyrene (EPS) and Waste Cooking Oil (WCO): From Urban Wastes to Potential Material of Construction. *Waste Biomass Valorization* **2016**, *7*, 1245–1254. [CrossRef]
47. Tan, Y. Preparation and Properties of Room Temperature Vulcanized Silicone Foam Packaging Material. Ph.D. Thesis, Hunan University of Technology, Zhuzhou, China, 2020. Available online: https://kns.cnki.net/kcms2/article/abstract?v=Y2E-z2Sa5COK4_fBFkgt42UT6jokDbeDkS48CZDWwAegs3Qx2gjGY94YMgVSCASdpeoPIoDuQEAHokQByNg-23pWZwohr17z1zaCFJqX0KYtRQboinonr1aFGqOOVnC23eGjjWq1tHi3UfWBnFK3C9IkKBKal2EQGFjnwRC0scm2aW7jsLBBQ6n1WDTDg7SN&uniplatform=NZKPT&language=CHS (accessed on 6 September 2025).
48. Fang, Q.; Liu, J.C. *Underground Protective Structure*; China Water and Power Press: Beijing, China, 2010.
49. Fu, T.; Zhu, Z.; Cao, C. Simulating the dynamic behavior and energy consumption characteristics of frozen sandy soil under impact loading. *Cold Reg. Sci. Technol.* **2019**, *166*, 102821. [CrossRef]
50. Yu, T.X.; Lu, G.X. *Energy Absorption of Structures and Materials*; Chemical Industry Press: Beijing, China, 2006.

Disclaimer/Publisher's Note: The statements, opinions and data contained in all publications are solely those of the individual author(s) and contributor(s) and not of MDPI and/or the editor(s). MDPI and/or the editor(s) disclaim responsibility for any injury to people or property resulting from any ideas, methods, instructions or products referred to in the content.

coatings

MDPI

Article

Frost Resistance and Life Prediction of Waste Polypropylene Fibre-Reinforced Recycled Aggregate Concrete

Xuechao Yang [1], Zehui Zhang [2], Hsing-Wei Tai [3,4], Bangxiang Li [1], Jiahui Li [1], Weishen Zhang [1], Tian Su [1,4,*] and Jianping Liu [1,*]

[1] Department of Civil Engineering, School of Civil Engineering and Geomatics, Shandong University of Technology, Zibo 255000, China; yxc1790772857@163.com (X.Y.); libangxiang@mail.sdu.edu.cn (B.L.); 13331271436@163.com (J.L.); zws22188@163.com (W.Z.)
[2] China Design Testing Technology Co., Ltd., Nanjing 210000, China; m18252582690@163.com
[3] Department of Civil Engineering, School of Higher-Educational Engineering Research Centre for Intelligence and Automation in Construction, Huaqiao University, Xiamen 361021, China; rt007204@gmail.com
[4] Department of Engineering and Management, International College, Krirk University, No. 3 Soi Ramintra 1, Ramintra Road, Anusaowaree, Bangkhen, Bangkok 10220, Thailand
* Correspondence: sutiancivil@foxmail.com (T.S.); liujp@sdut.edu.cn (J.L.)

Abstract

The inherent defects of recycled coarse aggregate (RCA) lead to poor frost resistance in recycled aggregate concrete (RAC), limiting its application in cold coastal regions. Waste polypropylene fibre (WPF), utilized as a reinforcement material, can improve the frost resistance of RAC. This study systematically analyzes the influence of WPF on the frost resistance of RAC and establishes a life prediction model. The results indicate that the damage to concrete in a saline freeze–thaw environment is significantly greater than that in a freshwater environment. WPF mitigates the development of freeze–thaw damage in RAC effectively by bridging microcracks and segmenting interconnected pores, thereby optimizing the pore structure and enhancing the matrix compactness. After 125 freeze–thaw cycles, the attenuation amplitude of the relative dynamic elastic modulus (RDEM) for RAC incorporated with WPF decreased by 9.69% and 5.77% in freshwater and saline environments, respectively, while the compressive strength increased by 20.65% and 18.57%. Concurrently, the negative mass growth rate of RAC in freshwater decreased by 20.62%, and the mass loss in the salt solution decreased by 5.84%. Furthermore, life predictions based on both RDEM and the compressive strength loss rate demonstrate that WPF extends the service life of RAC. Notably, the RDEM-based prediction yields a longer life but corresponds to a larger strength loss, whereas the prediction based on the compressive strength loss rate, although slightly shorter, corresponds to a more stable residual strength.

Keywords: waste polypropylene fibre; recycled aggregate concrete; frost resistance; life prediction

1. Introduction

With the continuous advancement of global urbanization, the demand for natural aggregates in the construction industry has increased significantly, triggering a series of serious problems such as over-exploitation of natural sand and gravel resources, deterioration of the ecological environment, and depletion of mineral resources [1,2]. Concurrently, the production of construction and demolition waste (CDW) generated from building demolition and construction activities has increased dramatically. It is projected that annual

CDW production in the United States will reach 330 million tons from 2022 to 2026 [3]. Meanwhile, China's annual CDW production has already reached a staggering 2.4 billion tons [4]. Faced with such massive quantities of CDW, traditional landfill disposal methods not only encroach upon valuable land resources but also pose potential risks of soil and groundwater contamination. This makes the resource utilization of CDW a critical challenge that must be addressed to achieve sustainable development [5]. Against this backdrop, recycled aggregate concrete (RAC) technology has emerged. This technology processes CDW into recycled coarse aggregate (RCA) to replace natural coarse aggregate (NCA), demonstrating significant environmental benefits in reducing natural resource consumption, lowering carbon emissions, and alleviating landfill pressure [6,7].

Concrete structures located in mid-to-high latitude cold regions are universally subjected to freeze–thaw damage [8]. This issue is particularly prominent in offshore and coastal engineering, where freeze–thaw damage in saline environments is characterized by more severe, deeper, and faster deterioration [9]. Consequently, frost resistance and its performance in saline environments are key indicators for evaluating the durability and service life of concrete. However, compared to natural aggregate concrete (NAC), RAC exhibits significantly degraded mechanical properties and frost resistance due to the high porosity, high water absorption, and complex multi-interface transition zone (ITZ) structure resulting from the residual old mortar adhered to the RCA surface. This degradation constrains the wider application of RAC [2]. Research has indicated that incorporating RCA reduces the frost resistance of concrete, and the degree of performance deterioration has intensified with increasing RCA replacement ratios and the accumulation of freshwater freeze–thaw cycles [10,11]. Notably, studies by Bogas et al. have presented a contrasting view, suggesting that the higher permeability of RCA could potentially improve the frost resistance of RAC [12].

In a saline freeze–thaw environment, the trends of decreasing compressive strength and relative dynamic elastic modulus (RDEM) of RAC with increasing freeze–thaw cycles are consistent with those observed in a freshwater environment, but the damage caused by freeze–thaw in salt solution is more severe [13]. After 125 freeze–thaw cycles, the compressive strength loss rates of RAC in saline and freshwater environments were 36.70% and 22.89%, respectively, significantly higher than those of NAC at 9.78% and 9.13% [14]. This difference is primarily attributed to the greater initial defects in RAC. Cl^- penetration not only lowers the freezing point of pore water and increases the degree of saturation but also generates osmotic pressure. The combined action of osmotic pressure, salt crystallization pressure, and ice crystal expansion pressure creates a multi-directional destructive stress field, accelerating the material deterioration process [15,16]. The freeze–thaw cycles themselves also significantly accelerate the transport of salt solution within the concrete, further exacerbating the increase in internal Cl^- concentration and the deterioration of the pore structure [17]. As the number of freeze–thaw cycles gradually increases, porosity increases, small pores degenerate into larger ones, and the number of connected pores rises [18]. This continuously deteriorating pore structure directly leads to a decline in the macro-mechanical properties of concrete and a significant increase in permeability. When the number of freeze–thaw cycles in salt solution reached 300, the concrete exhibited severe external damage: new cracks were initiated, propagated, and connected along pores and interface zones in the outer section, leading to aggregate spalling from the surface inward [19].

To improve the frost resistance of RAC, researchers have conducted extensive studies and achieved certain results. For instance, methods such as reducing the water–cement ratio, optimizing the screening and processing techniques for recycled aggregates, and rationally using air-entraining agents have all been demonstrated to enhance the frost resistance

of RAC to some extent [20–23]. In recent years, fibre-reinforced concrete technology has attracted widespread attention due to its potential in inhibiting crack initiation and propagation and improving material toughness. Researchers have attempted to enhance the frost resistance and other comprehensive properties of concrete by incorporating fibres. Studies show that fibre incorporation can effectively improve the performance of concrete under freeze–thaw conditions. Various fibres, such as steel, basalt, and glass fibres, primarily function through mechanisms like crack bridging, pore refinement, and matrix densification [24–28]. Among these, polypropylene fibre (PPF) has become a research hotspot due to its characteristics of being lightweight, having strong chemical inertness, having good flexibility, and easily mixing with concrete. PPF can effectively inhibit the development of microcracks and surface scaling in concrete, thereby enhancing frost resistance, reducing strength loss, improving impermeability and resistance to freeze–thaw damage in salt solution, while simultaneously enhancing flexural and splitting tensile strength [29–31].

Specifically, recent research has focused on utilizing waste textiles (such as carpets) to prepare waste polypropylene fibre (WPF) for engineering applications, aligning with reverse management in the textile industry and the principles of a circular economy [32–34]. Compared to virgin PPF, WPF not only alleviates resource shortages and environmental pressure but also demonstrates significant potential in enhancing concrete durability. Studies indicate that WPF can reduce freeze–thaw damage, drying shrinkage, and the Cl^- penetration coefficient by 47%, 79%, and 50%, respectively, effectively extending the service life of concrete [32,33]. However, existing research has predominantly focused on the frost resistance improvement of NAC or within a single freeze–thaw environment. Investigations into the frost resistance of waste polypropylene fibre-reinforced recycled aggregate concrete (FRAC) under freeze–thaw conditions in salt solution remain relatively scarce, particularly regarding the mechanism of fibre action on the multiple ITZs within RAC. Furthermore, while Cui et al. [33] studied frost resistance and life prediction of recycled brick aggregate concrete with WPF, their work primarily utilized brick-based recycled aggregates and focused on a single freeze–thaw medium. In contrast, the present study employs conventional concrete-sourced RCA, systematically compares performance in both saline and freshwater environments, and specifically investigates the role of WPF in mitigating damage within the complex multi-ITZ structure of RAC. Moreover, most existing life prediction models use a 60% reduction in RDEM as the failure criterion [33]. However, the synergistic damage from freeze–thaw in salt solution and the heterogeneity of recycled materials may alter this critical value, leading to prediction deviations. Therefore, a dual-parameter approach considering both RDEM and compressive strength loss rate is necessary for more accurate and conservative life assessment.

To address these research gaps, the present study systematically evaluates the improvement effect of WPF on the frost resistance of RAC in both saline and freshwater environments, reveals its enhancement mechanism particularly at the multi-ITZs, and proposes novel life prediction models based on both RDEM and compressive strength loss rate. This work aims to provide a theoretical basis for the durability design and life assessment of RAC structures in cold coastal regions, promoting the resource utilization of CDW and the development of high-performance, low-carbon building materials.

2. Experimental Materials and Methods

2.1. Raw Materials

The coarse aggregates used in this study were recycled coarse aggregate (RCA) and natural coarse aggregate (NCA) with a continuous gradation of 5–26.5 mm. The RCA was sourced from construction and demolition waste (CDW) of a demolition project in Zibo City and prepared through mechanical crushing, sieving, and grading processes. The NCA was

conventional crushed stone. The performance indices of the coarse aggregates complied with the technical requirements of JGJ 52-2006 [35]. It is worth noting that the continuous gradation of 5–26.5 mm for coarse aggregates was chosen to achieve a dense particle packing structure, minimizing the void content and improving the overall compactness of the concrete, which is especially critical for frost resistance.

Manufactured sand produced by a dry grinding process was selected as the fine aggregate, with a particle size distribution of 0–5 mm and a fineness modulus of 2.8, classifying it as medium sand. The appearance and morphology of the aggregates and their gradation curves are shown in Figures 1 and 2, respectively. The main physical properties of the coarse aggregates are shown in Table 1.



(**a**) Recycled coarse aggregate (**b**) Natural coarse aggregate (**c**) Fine aggregate

Figure 1. Surface morphology of aggregates.

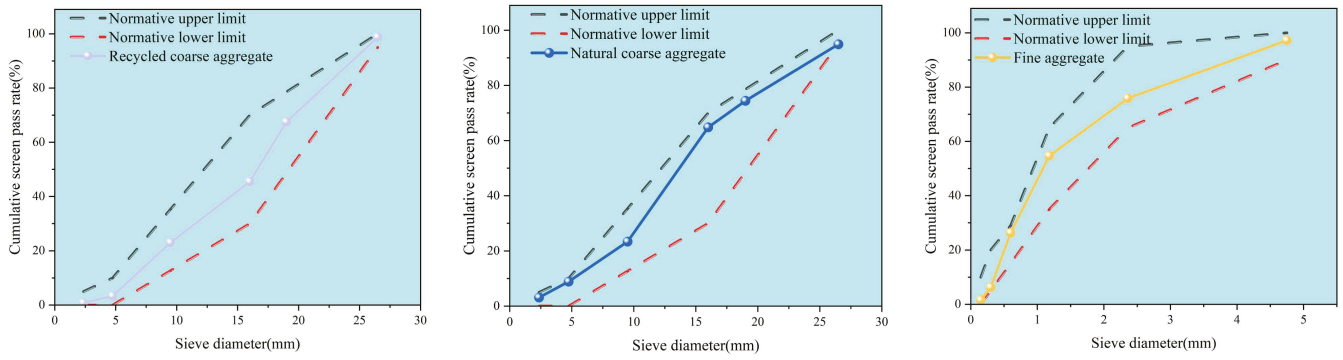

(**a**) Recycled coarse aggregate (**b**) Natural coarse aggregate (**c**) Fine aggregate

Figure 2. Aggregate grading curve.

Table 1. Coarse aggregate physical properties.

Type of Coarse Aggregates	Apparent Density (kg/m^3)	Crushing Index (%)	Water Absorption (%)	Mud Content (%)
RCA	2541	16	3.5	1.5
NCA	2635	7.5	1.3	0.5

The cementitious material was Shanlv brand P·O 42.5 ordinary Portland cement produced by Shandong Zibo Shanlv Cement Co., Ltd. in China. Its physical property indices are listed in Table 2. Tap water from the municipal supply network was used as the concrete mixing water. The water quality met the requirements for mixing water specified in JGJ 63-2006 [36] and was left standing for 24 h before use to eliminate the effect of residual chlorine. The admixtures employed were a composite polycarboxylic acid high-efficiency water-reducing agent and a concrete air-entraining agent.

Table 2. Test results of physical performance indicators of cement [37].

Cement Grade	Density (g/cm^3)	Specific Surface Area (m^2/kg)	Initial/Final Condensation Time (min)	3d/28d Compressive Strength (MPa)
P O 42.5	3.21	312	195/259	24.6/45.2

Discarded polypropylene fibre (PPF) carpets were selected as the source material for the test fibres. The fibre material for testing was prepared through manual processing. After the raw fibre material underwent disassembly and sorting, it was successively subjected to pre-treatment processes of cleaning, disinfecting, and natural air-drying. Subsequently, manual sorting and precise cutting processes were employed to control the fibre bundle length parameter (19 mm), ultimately yielding fibre material that met the test requirements. The relevant performance parameters of the waste polypropylene fibre (WPF) are listed in Table 3. The specific processing flow chart for the WPF is shown in Figure 3.

Table 3. Fibre performance parameters [37].

Monofilament Diameter (mm)	Elastic Modulus (MPa)	Tensile Strength (MPa)	Water Absorption (%)	Ultimate Elongation (%)	Density (g/cm^3)
0.043	3.67×10^3	380	<0.10	1.81	0.91



Figure 3. Disposal process of WPF.

The release agent for freeze–thaw testing was selected in compliance with the relevant provisions of GB/T 50082-2024 [38]. This standard explicitly prohibits the use of hydrophobic release agents. Therefore, the F-198 hydrophilic release agent was selected for the tests. Its active ingredients are polymeric organic compounds with a pH value of 6–8 (in a 1% aqueous solution). Before use, it was prepared as an aqueous solution at a 1:1 volume ratio and brushed onto the mold surfaces.

2.2. Mix Proportion Design

The concrete mix proportions were designed according to the technical specifications of JGJ55-2011 [39]. Due to the high water absorption of RCA, which can lead to mixing water loss and reduced slump during pouring while also exacerbating shrinkage crack formation during the curing period, additional water was incorporated to compensate for water loss to maintain concrete workability and test reliability. Specifically, additional water equivalent to 85% of the 24 h water absorption of the pre-dried RCA (3.5%, see Table 1) was added in the RAC and FRAC mixes [40].

Previous studies have shown that excessive fibre content or excessive fibre length readily leads to fibre agglomeration, forming fibre bundles. Therefore, based on multiple preliminary experiments and existing research, this study determined fibre parameters that are relatively easy to disperse (length 19 mm, volume fraction 0.12%) [41,42]. The final concrete mix proportions obtained through trial mixing are shown in Table 4. Herein, NAC denotes natural aggregate concrete, while RAC and FRAC represent recycled aggregate concrete and waste polypropylene fibre-reinforced recycled aggregate concrete, respectively.

Table 4. Mix proportions of the concrete.

Specimens	NAC	RAC	FRAC
Cement (kg/m^3)	485	485	485
Sand (kg/m^3)	540	540	540
Water (kg/m^3)	184	184	184
RCA (kg/m^3)	-	1150	1150
NCA (kg/m^3)	1150	-	-
Additional water (%)	-	34	34
WPF volume fraction (%)	-	-	0.12
Water-reducing agent (%)	0.11	0.11	0.11
Air-entraining agent (%)	0.11	0.11	0.11
Air content (%)	4.3	4.5	4.6

2.3. Specimen Preparation

To ensure uniform distribution of fibres during mixing with concrete, the dry mixing method was adopted in this test. The specific procedure is shown in Figure 4.

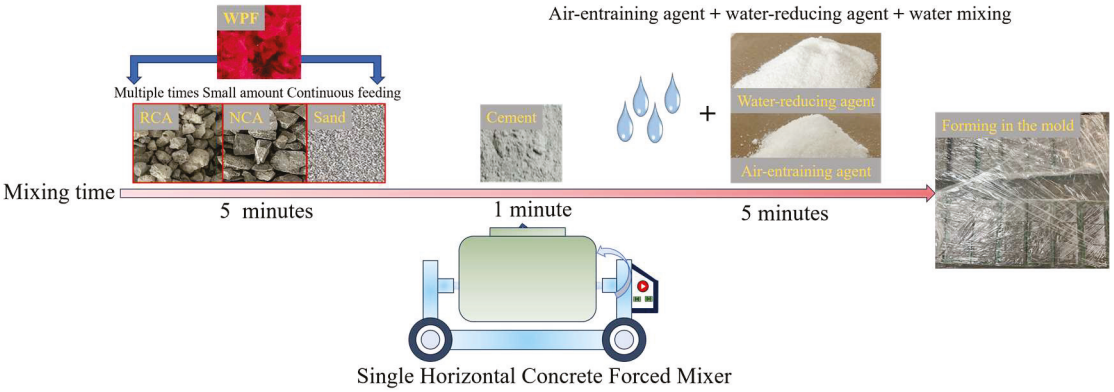

Figure 4. Mixing process.

According to the provisions of GB/T 50476-2019 [43], two standard specimen sizes were used: cube specimens measuring 100 mm × 100 mm × 100 mm for testing compressive strength changes before and after freeze–thaw cycles, and prism specimens measuring 100 mm × 100 mm × 400 mm for determining mass loss rate and relative dynamic elastic

modulus (RDEM). Three parallel specimens were prepared for each group. The specimen grouping design scheme is shown in Table 5. After casting, the specimens were covered with curing membranes. They were demolded after 24 h of curing and subsequently placed in a standard concrete curing room with a relative humidity of 95% and a temperature of 20 ± 2 °C for 28 days of curing before testing.

Table 5. Specimen design group.

Specimen Grouping	Medium	Specimen Size (mm^3)	Number of Freeze–Thaw Cycles
NAC-F	freshwater	100 × 100 × 100 100 × 100 × 400	0, 25, 50, 60, 75, 100, 110, 125
NAC-S	salt solution	100 × 100 × 100 100 × 100 × 400	0, 25, 50, 60, 75, 100, 110, 125
RAC-F	freshwater	100 × 100 × 100 100 × 100 × 400	0, 25, 50, 60, 75, 100, 110, 125
RAC-S	salt solution	100 × 100 × 100 100 × 100 × 400	0, 25, 50, 60, 75, 100, 110, 125
FRAC-F	freshwater	100 × 100 × 100 100 × 100 × 400	0, 25, 50, 60, 75, 100, 110, 125
FRAC-S	salt solution	100 × 100 × 100 100 × 100 × 400	0, 25, 50, 60, 75, 100, 110, 125

Note: F denotes the freeze–thaw medium as freshwater; S denotes the freeze–thaw medium as a 3.5% mass fraction NaCl solution (salt solution).

2.4. Testing Methods

The test procedure for this study is shown in Figure 5 and mainly comprises the following three parts: specimen preparation, macroscopic testing, and microscopic testing. The specific testing methods are described below.

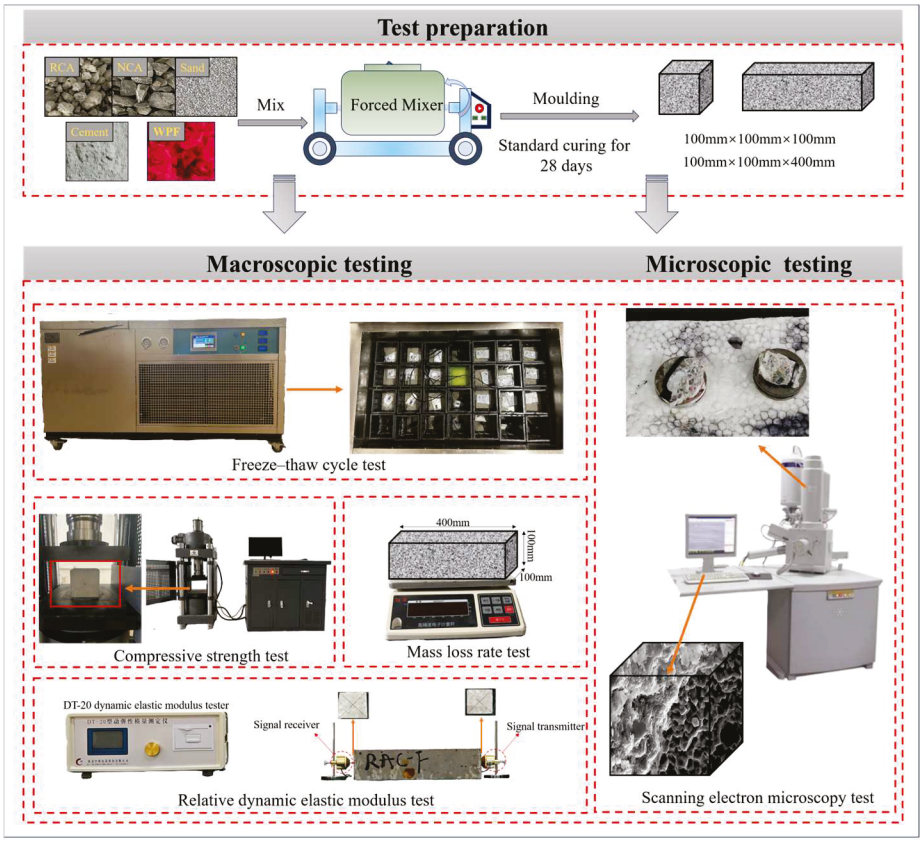

Figure 5. Test procedure.

2.4.1. Freeze–Thaw Cycle Test

The freeze–thaw cycle test employed the "rapid freezing method". The freeze–thaw equipment was a KDR-V9 concrete rapid freeze–thaw cycling testing machine, produced by Beijing Road Construction Science Instrument Co., Ltd. in China. Following the specifications of GB/T 50082-2024 and relevant research [13,15,38], concrete specimens cured for 28 days underwent rapid freeze–thaw testing. The specific procedure was as follows: Specimens were removed from the curing room 4 days before the test. After screening for qualified specimens, they were immersed in freshwater or salt solution maintained at 20 ± 2 °C, with the liquid level 20–30 mm above the top surface of the specimen. After 4 days, the specimen surfaces were dried, and the initial mass and RDEM were measured. During the test, the same type of solution was injected into the specimen container, maintaining a liquid level 5 mm above the top surface of the specimen. The temperature-controlled specimens were placed in the core area of the freeze–thaw chamber. After sensor calibration, the testing instrument was activated. The freeze–thaw cycle parameters were controlled to meet the following requirements: a single cycle duration of 2–4 h (with the thawing duration accounting for ≥25% of the total), the specimen center temperature strictly limited to the range of −18 ± 2 °C (minimum low temperature) to 5 ± 2 °C (maximum high temperature), the time taken for the temperature to decrease from 3 °C to −16 °C and the time for the reverse heating both exceeding 50% of the duration of the corresponding phase, and the phase transition time ≤10 min.

2.4.2. Mass Loss Rate Test

The mass loss rate can be used for quantitative analysis of the degree of surface scaling in concrete [44]. The masses of specimens in each group were measured using an electronic platform balance with an accuracy of 0.1 g. The mass loss rates were calculated according to Equation (1). The average value of the calculation results from three specimens was taken as the test result:

$$\triangle W_n = \frac{W_0 - W_n}{W_0} \times 100\% \quad (1)$$

where w_0 is the initial mass of the specimen before freeze–thaw cycles (g); w_n is the mass of the specimen after n freeze–thaw cycles (g).

2.4.3. RDEM Test

The RDEM of specimens reaching the target number of freeze–thaw cycles were tested using a DT-20 dynamic elastic modulus tester produced by Beijing Zhongke Dongchen Technology Co., Ltd., China. The RDEM of concrete was calculated according to Equation (2). The average value of the calculation results from three specimens was taken as the test result:

$$P_n = \frac{f_n^2}{f_0^2} \times 100\% \quad (2)$$

where f_0 is the transverse fundamental frequency of the specimen before freeze–thaw cycles; f_n is the transverse fundamental frequency after n freeze–thaw cycles.

2.4.4. Compressive Strength Test

The compressive strength test was conducted using an HYE-2000 microcomputer-controlled electro-hydraulic servo pressure testing machine produced by Hebei Sanyu Testing Machine Co., Ltd. in China. Testing was performed according to GB/T 50081-2019 [45]. Continuous and uniform vertical loading was maintained during the test at a loading rate of 0.5 MPa/s to determine the compressive strength of concrete cubes after different numbers of freeze–thaw cycles. The compressive strength of concrete was

calculated according to Equation (3). It is important to note that due to size limitations of the freeze–thaw specimen containers, this study used 100 mm × 100 mm × 100 mm cube specimens for testing. In accordance with the provisions of GB/T 50081-2019 [45], the calculation results were multiplied by a size conversion factor of 0.95, and the average value of the strengths from three specimens was taken as the final test result.

$$f_{cu} = 0.95 \times \frac{F}{A} \tag{3}$$

where f_{cu} is the cube compressive strength (MPa); F is the failure load of the specimen (N); A is the bearing area of the specimen (mm^2).

Based on Equation (3), the compressive strength loss rate for each specimen group was further calculated according to Equation (4):

$$\triangle fcu(n) = \frac{f_{cu,0} - f_{cu,n}}{f_{cu,0}} \times 100\% \tag{4}$$

where $\triangle f_{cu(n)}$ is the compressive strength loss rate after n freeze–thaw cycles (%); $f_{cu,0}$ is the initial compressive strength before any freeze–thaw cycles (MPa); $f_{cu,n}$ is the compressive strength after n freeze–thaw cycles (MPa).

2.4.5. Scanning Electron Microscopy (SEM) Test

This study used a Sirion 200 SEM produced by FEI Company in Oregon, USA, to scan RAC and FRAC specimens after the freeze–thaw cycles. Sample blocks were cut from the core of the tested specimens to avoid edge effects, with a specific focus on areas containing the interface transition zone (ITZ) between aggregate and mortar. These samples were then dried, and sputter-coated with a thin layer of gold to ensure electrical conductivity. The scanning acceleration voltage ranged from 0.2 to 30 kV, and the image resolution was 1.5 nm.

3. Results and Analysis

3.1. Evolution of Apparent Damage

The apparent morphological characteristics of concrete specimens from each group after freeze–thaw cycles are shown in Figure 6. Before testing, all specimen surfaces were dense and smooth, showing no significant differences. With increasing freeze–thaw cycles, surface damage to the concrete continuously intensified, and its deterioration process can be divided into three stages: (1) Initial deterioration stage (0 < freeze–thaw cycles $\leq$ 25)—pits appeared on the concrete surface accompanied by surface mortar spalling, making the entire specimen very rough. (2) Damage propagation stage (25 < freeze–thaw cycles $\leq$ 75)—as the number of freeze–thaw cycles increased, the size of surface pits enlarged and connected, leading to large-area mortar spalling; the specimen surface became distinctly pitted and uneven; some aggregates were exposed and exhibited edge/corner defects. (3) Severe damage stage (freeze–thaw cycles > 75)—the degree of aggregate exposure and edge/corner defects increased dramatically. Because the corners of the concrete have the largest contact area with the freeze–thaw environment, their damage was the most severe. After 125 freeze–thaw cycles, more severe aggregate spalling occurred at the corners, exposing internal mortar and aggregates, severely compromising the integrity of the specimens. It is noteworthy that concrete subjected to freeze–thaw cycles in freshwater exhibited overall lighter damage without severe apparent deterioration. In contrast, damage was significantly exacerbated in the saline environment. This is attributed to the combined effect of non-uniform phase transition of ice crystals and salt crystallization precipitation, triggered by the elevated degree of saturation from the salt solution, which produced superimposed expansion stresses [9,14]. Furthermore, NAC demonstrated the best apparent integrity

in both environments. This is because its raw materials possess higher compactness and superior frost resistance, enabling effective resistance to freeze–thaw damage.

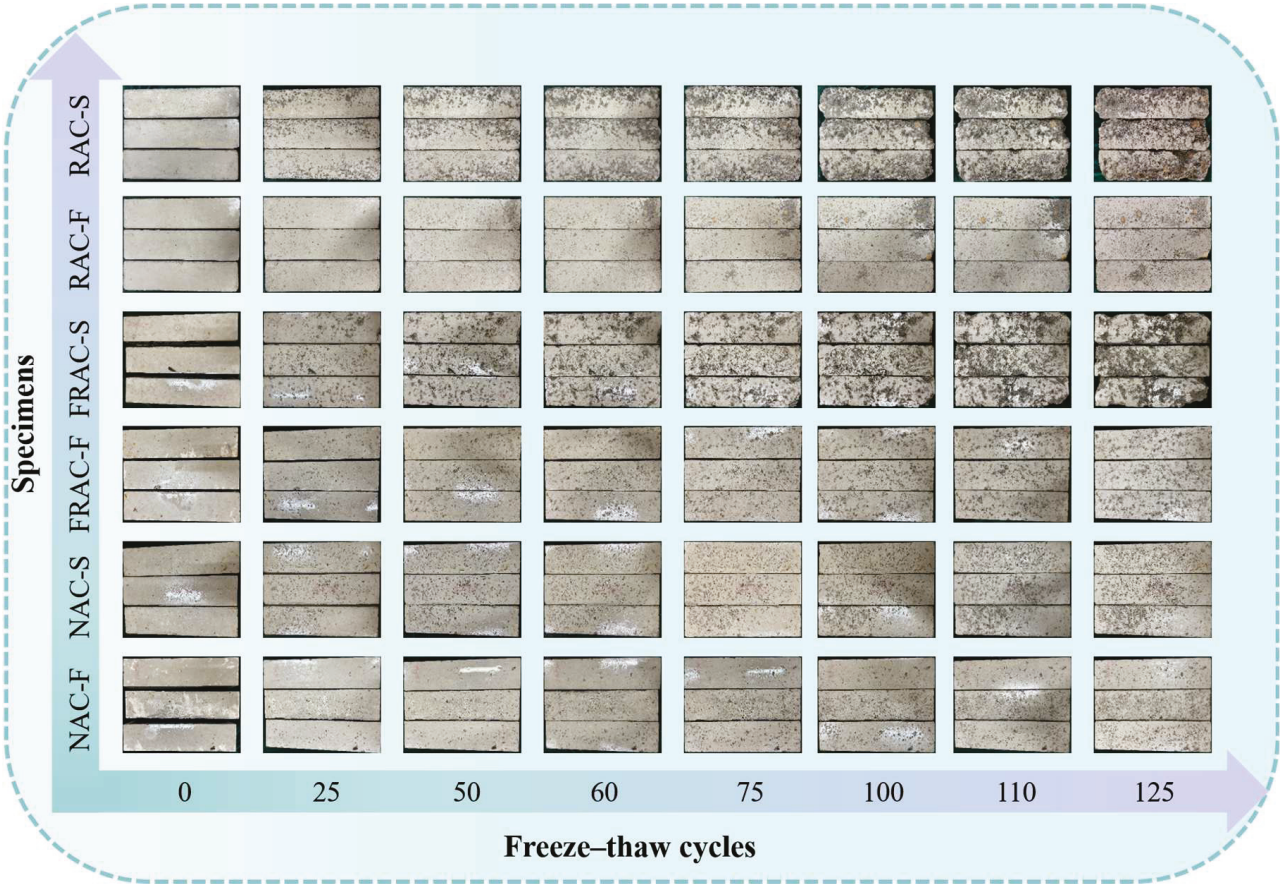

Figure 6. Surface morphology of each group of specimens under different freeze–thaw cycles.

The comparison in Figure 6 reveals that the incorporation of WPF effectively reduced the apparent damage in RAC. After experiencing the same number of freeze–thaw cycles, the amount of surface mortar and aggregate spalling in FRAC was significantly lower. WPF formed a three-dimensional network within RAC. When freeze–thaw cycles induced microcrack initiation, the fibres bridging the crack sides exerted a bridging effect. This bridging action effectively inhibited the occurrence and propagation of cracks, dispersing the concentrated stress at the crack tip and transferring it to the surrounding concrete matrix [46]. WPF segmented large pores, refined the pore structure of the matrix, and blocked potentially interconnected microcracks. This restricted the migration of water between pores and the continuous growth of ice crystals, thereby significantly weakening the frost heave pressure and inhibiting the development of macro-damage and the spalling of surface mortar [47,48]. Furthermore, the improvement effect of WPF on apparent damage was more pronounced in the saline environment. In the early stage of freeze–thaw in salt solution, the surface of RAC without WPF exhibited densely pitted surfaces with concentrated spalling. In contrast, after incorporating WPF, the damage manifested as discrete pits with dispersed spalling. In the later stage of freeze–thaw in salt solution, RAC without WPF showed large areas of exposed aggregates and severe edge/corner damage. Comparatively, RAC incorporating WPF exhibited significantly reduced overall damage severity. However, in the freshwater freeze–thaw environment, where the damage level itself was lighter, RAC did not exhibit severe apparent damage, regardless of whether WPF was incorporated.

3.2. Mass Loss Rate

The relationship between the mass loss rate and the number of freeze–thaw cycles for each group of specimens is shown in Figure 7. As the number of freeze–thaw cycles increased, all specimen groups exhibited a trend of initial decrease (including negative values, indicating mass gain) followed by an increase in mass loss rate, which is consistent with literature reports [49,50]. The negative mass loss rate, i.e., mass gain, occurred despite pre-soaking because the specimens were not fully saturated at the start of the test. Early freeze–thaw cycles promoted the development and interconnection of microcracks, facilitating the infiltration of external solution into these newly formed micropores. This ingress of water contributed temporarily to mass gain, outweighing the limited mortar spalling at this stage. The subsequent increase in loss rate was due to the increasing number of freeze–thaw cycles exacerbating surface mortar spalling of the specimens, where the resulting mass loss surpassed the compensatory effect of solution infiltration [13]. It is worth noting that including mass gain in the analysis is relevant for frost damage assessment, as it provides insight into early micro-damage development prior to macroscopic material loss. The presence of this phase underscores the importance of considering both mass gain and loss to fully understand the deterioration mechanism of concrete under freeze–thaw conditions.

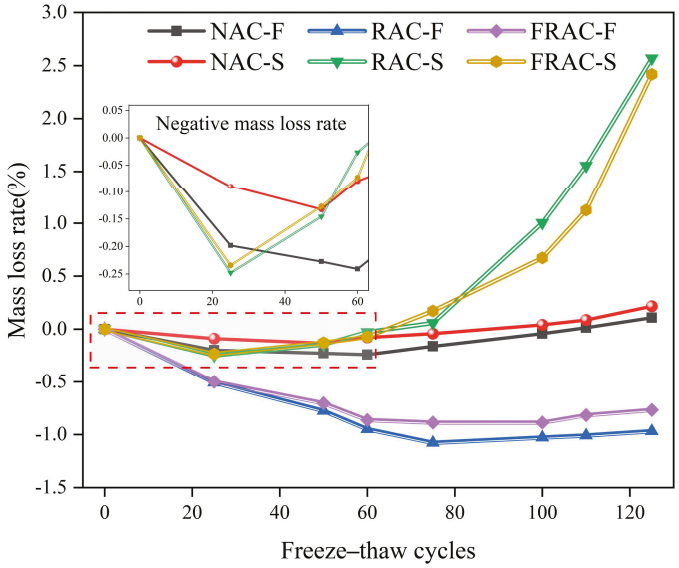

Figure 7. Mass loss rate of concrete specimens in each group under freeze–thaw cycles.

Comparative analysis showed that NAC exhibited minimal change in mass loss rate during freeze–thaw cycling (maximum only 0.22%), significantly lower than RAC (maximum reaching 2.57%). This is attributed to the low porosity and dense ITZ of NAC, which effectively restricted the development of microcracks and the compensatory effect of solution infiltration. In contrast, the inherent high porosity and weak ITZ of RCA within RAC significantly reduced its resistance to freeze–thaw damage. Furthermore, freeze–thaw in salt solution significantly exacerbated the mass loss of concrete. After 125 freeze–thaw cycles in salt solution, the mass loss rate of RAC dramatically increased by 365% compared to the freshwater environment. This is because the high permeability of the salt solution elevated the degree of saturation of the concrete. The combined action of its non-uniform phase transition and salt crystallization precipitation produced superimposed expansion stresses, accelerating microcrack propagation and resulting in a substantial increase in mortar spalling [9].

The incorporation of WPF effectively mitigated the mass loss in RAC. During freshwater freeze–thaw cycling, the mass loss rates of both RAC and FRAC remained negative

(i.e., indicating mass increase). After 125 freshwater freeze–thaw cycles, the mass loss rate of RAC without WPF was −0.97%, while that of RAC with WPF increased to −0.77%. The incorporation of WPF reduced the negative mass loss rate of RAC by 20.62%. After 125 freeze–thaw cycles in salt solution, the mass loss rate of RAC without WPF reached 2.57%, while that with WPF decreased to 2.42%, representing a reduction of 5.84%. The reasons for the improved mass damage resistance in RAC after WPF incorporation are as follows: (1) WPF formed a three-dimensional randomly distributed network within the RAC matrix, bridging microcracks and effectively restricting their chained propagation, thereby reducing aggregate and mortar spalling caused by continuous crack development [46]. (2) The presence of WPF obstructed the migration paths of water and salt within the pore solution in RAC, reducing the freezable water content inside pores. This effectively alleviated the frost heave pressure generated by ice crystal expansion and inhibited the increase in mass loss rate [48]. (3) WPF optimized the microstructure of RAC and enhanced matrix compactness. On one hand, this suppressed the initiation and development of microcracks; on the other hand, it reduced the number of newly formed water-bleeding channels generated by freeze–thaw cycles, thereby decreasing the secondary absorption of water in subsequent cycles and consequently reducing secondary mass gain [50].

3.3. RDEM Attenuation

As a key indicator for evaluating the elastic properties of materials, the continuous attenuation of the RDEM directly reflects the irreversible accumulation process of freeze–thaw damage. The RDEM of specimens in all groups exhibited a continuous decreasing trend with increasing freeze–thaw cycles, as shown in Figure 8. This is primarily because freeze–thaw cycles caused coarsening of the concrete pore structure and aggravated interconnection of microcrack networks, compromising the continuity of the matrix and hindering ultrasonic wave propagation [49]. Furthermore, the attenuation amplitude of RDEM in RAC was significantly higher than that in NAC. The reason is that the inherent microcracks and weak interfaces within RCA provided preferential paths for freeze–thaw damage development, thereby accelerating performance deterioration [51]. The damaging effect of the saline freeze–thaw environment on RDEM was more severe compared to the freshwater environment. This stemmed from the high crystallization expansion pressure generated by salt solution, which far exceeded that of freshwater freeze–thaw, intensifying microcrack development and further compromising the continuity of the matrix [15].

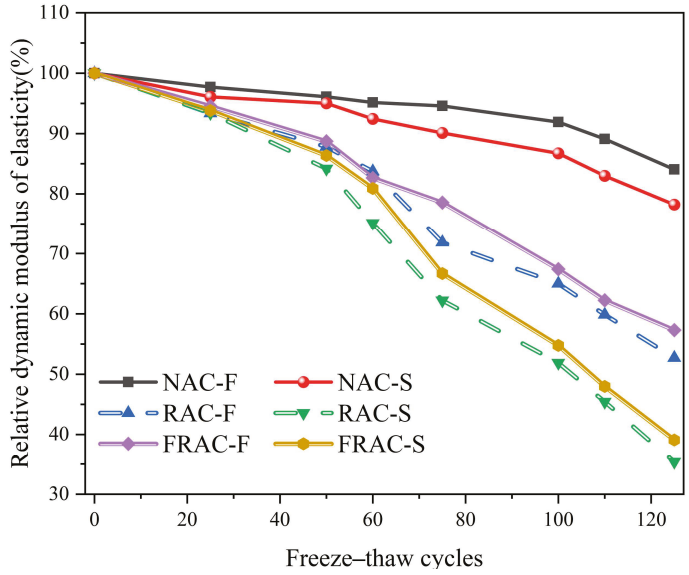

Figure 8. Influence of freeze–thaw cycles on the RDEM of specimens.

WPF effectively inhibited the attenuation of the RDEM in RAC. After 125 freshwater freeze–thaw cycles, the RDEM attenuation of RAC without WPF reached 47.29%, while that incorporating WPF decreased to 42.71%, representing a reduction in attenuation amplitude of 9.69%. After 125 freeze–thaw cycles in salt solution, the RDEM attenuation of RAC without WPF reached 64.64%, while that with WPF decreased to 60.91%, representing a reduction in attenuation amplitude of 5.77%. WPF formed a three-dimensional randomly distributed network within the matrix. Through its bridging effect, it effectively inhibited the initiation and propagation of initial microcracks and reduced the connectivity of the crack network, thereby maintaining the structural continuity of the matrix and the integrity of the ultrasonic wave propagation path [52]. Furthermore, WPF obstructed the migration of water and salt, reducing the amount of freezable water within pores and dispersing the expansion stresses generated by ice crystals and salt crystallization. This significantly alleviated the destructive pressure exerted on the matrix by freeze–thaw phase transitions [30]. It is noteworthy that although the incorporation of WPF effectively improved the RDEM attenuation of RAC, the degree of improvement differed significantly between environments. In the freshwater environment, incorporating WPF reduced the RDEM attenuation of RAC by 9.69%, whereas in the saline environment, the reduction was only 5.77%. The reason is that salt solution erosion damaged the bonding interface between WPF and the matrix, weakening the fibre's bridging effect, particularly its crack-restraining capacity, which resulted in diminished improvement effectiveness [53].

3.4. Compressive Strength

3.4.1. Compressive Strength Loss Rate

The variations in compressive strength and compressive strength loss rate with the number of freeze–thaw cycles for each specimen group are shown in Figure 9a,b. The compressive strength of all specimen groups continuously decreased with increasing freeze–thaw cycles, while the compressive strength loss rate correspondingly increased. This strength deterioration pattern is consistent with reports in existing studies [54]. The primary reason is that the repeated cyclic stress induced by frost heave pressure caused progressive propagation of microcracks and weakening of interfacial bonding between the aggregate and the mortar. This reduced the effective load-bearing area and induced stress concentration, leading to a macroscopic decline in compressive strength.

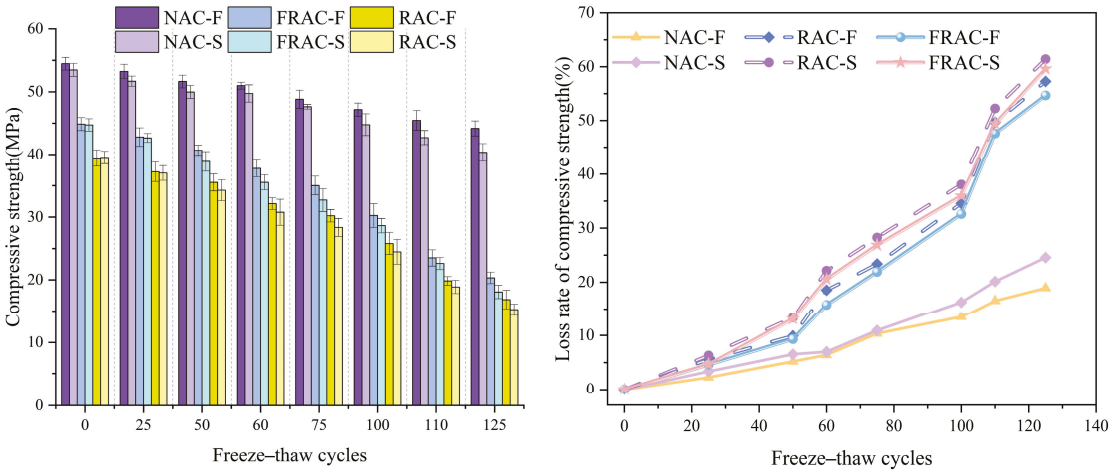

(**a**) Compressive strength (**b**) Compressive strength loss rate

Figure 9. Influence of freeze–thaw cycles on the compressive strength of concrete.

Comparative analysis revealed that the strength loss rate of RAC was consistently significantly higher than that of NAC (Figure 9b). The reason is that the microcracks intro-

duced by RCA and the multiple weak ITZs (aggregate-old mortar-new mortar) possessed high porosity and water absorption, accelerating the accumulation and propagation of freeze–thaw damage within the interfacial zones [41]. Furthermore, the damaging effect of the saline freeze–thaw environment on strength far exceeded that of the freshwater environment. After 125 cycles, the strength loss rate of RAC in salt solution increased by 7.28% compared to the freshwater environment. The reason is that the salt solution elevated the degree of saturation of RAC. The combined action of non-uniform ice formation and salt crystallization precipitation generated a superimposed expansion pressure differential, creating multi-directional destructive stresses [9,55].

WPF effectively inhibited the strength damage in RAC. After 125 freshwater freeze–thaw cycles, the compressive strength loss rate of RAC without WPF reached 57.27%; after incorporating WPF, it decreased to 54.68%, representing a reduction of 4.52%. After 125 freeze–thaw cycles in salt solution, the compressive strength loss rate of RAC without WPF was 61.44%; after incorporating WPF, it decreased to 59.60%, representing a reduction of 3.00%. The improvement mechanism of WPF on RAC strength damage can be attributed to the following two aspects: (1) Enhanced crack resistance—when microcracks occurred, WPF bridged the cracks and transferred stress, effectively restricting further crack propagation and reducing the connectivity between cracks. This enhanced the crack resistance of concrete, thereby delaying the specimen failure process [56,57]. (2) Improved matrix structure—the three-dimensional network formed by WPF within the matrix effectively connected its various components, enhancing overall compactness. This network reduced the connectivity of capillary pores, decreased the number of large pores, increased the proportion of small pores, and made the pore distribution more uniform. Consequently, it mitigated the destructive pressure exerted on RAC by ice crystal and salt crystallization expansion [50]. Furthermore, although the strength damage of RAC was effectively improved after incorporating WPF, the degree of improvement differed between saline and freshwater environments. In the freshwater environment, incorporating WPF reduced the strength loss rate of RAC by 4.52%, whereas in the saline environment, the reduction was only 3.00%. The improvement effect in saline was reduced by 33.63% compared to freshwater. This is because salt solution erosion weakened the interfacial bonding between WPF and the matrix, reducing the fibre's stress transfer efficiency and crack-restraining capacity, resulting in limited enhancement effectiveness.

To further investigate the improvement effect of WPF on the compressive strength of RAC under different numbers of freeze–thaw cycles and in different environments, this study calculated the enhancement rate of WPF on RAC compressive strength according to Equation (5):

$$\triangle U(n) = (\frac{f_{F,cu,n}}{f_{R,cu,n}} - 1) \times 100\% \quad (5)$$

where $\triangle U(n)$ is the enhancement rate of WPF on RAC compressive strength after n freeze–thaw cycles (%); $f_{F,cu,n}$ and $f_{R,cu,n}$ are the compressive strength of FRAC and RAC after n freeze–thaw cycles (MPa), respectively.

The improvement effect of WPF on the compressive strength of RAC after freeze–thaw cycles is shown in Figure 10. The enhancement rate of WPF on RAC compressive strength generally exhibited an increasing trend with the number of freeze–thaw cycles, with a peak increase reaching 20.65%. This is consistent with the pattern reported in the existing literature [33]. In the early stages of freeze–thaw cycles, matrix damage was minor, and the fibre reinforcement effect had not been fully exerted. As the number of freeze–thaw cycles increased, the internal microcrack network in concrete continuously developed. The crack-bridging and three-dimensional restraining effects of the fibres became significantly enhanced, effectively inhibiting the loss of load-bearing cross-section caused by crack inter-

connection. Consequently, the fibre improvement effect increased with the intensification of freeze–thaw damage. It was noteworthy that the enhancement effect of WPF on RAC compressive strength in the freshwater environment was generally slightly higher than that in the saline environment. This may be related to the chemical erosion effect of salt solution. Salt solution damaged the compactness of the fibre-matrix interface, reducing the friction coefficient and stress transfer efficiency, thereby weakening the bridging effect and consequently diminishing the fibre's enhancement effect on compressive strength.

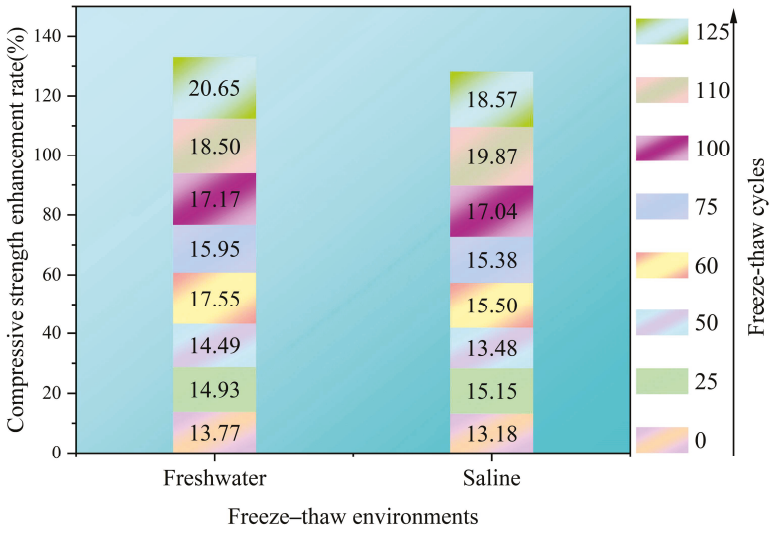

Figure 10. Enhancement of RAC compressive strength by WPF for different freeze–thaw environments and freeze–thaw cycles.

3.4.2. Compressive Strength Prediction Model

Based on the test results, a predictive model for the compressive strength of RAC in a freshwater freeze–thaw environment was developed through polynomial regression analysis. The model was fitted using experimental data obtained from eight different freeze–thaw cycles (n = 0, 25, 50, 60, 75, 100, 110, and 125), with three parallel specimens for each data point, thus constituting a robust dataset for the analysis. The specific expression is shown in Equation (6):

$$f_{R,n} = f_{R,0} - 0.06n - 6.39 \times 10^{-4}n^2 - 3.03 \times 10^{-6}n^3 \qquad R^2 = 0.98 \tag{6}$$

where $f_{R,0}$ is the compressive strength of the RAC specimen before freeze–thaw cycles (MPa); n is the number of freeze–thaw cycles.

Considering the influence of WPF and salt solution on compressive strength, a fibre enhancement coefficient (β_ε) and a salt solution attenuation coefficient (α_ω) were defined to characterize the effect degree of WPF and salt solution on compressive strength. The specific expressions are shown in Equations (7) and (8):

$$\alpha_\omega = 1 - \frac{\omega_{s,n}}{\omega_{f,n}} \tag{7}$$

$$\beta_\varepsilon = \frac{\varepsilon_{FRAC,n}}{\varepsilon_{RAC,n}} - 1 \tag{8}$$

where $\omega_{s,n}$ and $\omega_{f,n}$ represent the compressive strengths of the specimen after n freeze–thaw cycles in salt solution and freshwater (MPa), respectively; $\varepsilon_{FRAC,n}$ and $\varepsilon_{RAC,n}$ represent the compressive strengths of FRAC and RAC after n freshwater freeze–thaw cycles (MPa), respectively.

After substituting the test data into Equations (7) and (8), the relationships between the fibre enhancement coefficient (β_ε), the salt solution attenuation coefficients for RAC ($\alpha_{\omega,1}$) and FRAC ($\alpha_{\omega,2}$), and the number of freeze–thaw cycles were determined through regression analysis ($R^2 \geq 0.88$). The specific expressions are shown in Equations (9) to (11):

$$\beta_\varepsilon = 0.14 + 8.3 \times 10^{-4} n - 1.29 \times 10^{-5} n^2 + 8.53 \times 10^{-8} n^3 \quad (9)$$

$$\alpha_{\omega,1} = -0.00147 - 0.00192n + 1.17466 \times 10^{-4} n^2 - 1.59 \times 10^{-6} n^3 + 6.5539 \times 10^{-9} n^4 \quad (10)$$

$$\alpha_{\omega,2} = 0.00383 - 0.00356n + 1.94258 \times 10^{-4} n^2 - 2.64246 \times 10^{-6} n^3 + 1.09538 \times 10^{-8} n^4 \quad (11)$$

Substituting Equations (9)–(11) into Equation (6) yielded the compressive strength prediction model that comprehensively considered the number of freeze–thaw cycles, the enhancement effect of WPF, and the deterioration effect of salt solution, as shown in Equation (12):

$$f_{cu,n} = (1 - \alpha_\omega)(1 + \beta_\varepsilon) f_{R,n} \quad (12)$$

where for RAC specimens, α_ω takes the value $\alpha_{\omega,1}$; for FRAC specimens, α_ω takes the value $\alpha_{\omega,2}$.

The predicted compressive strength results calculated using Equation (12) are shown in Figure 11. The results indicate that the model predictions were highly consistent with the test results. This prediction model can accurately predict the effects of freeze–thaw cycles, WPF, and salt solution on compressive strength.

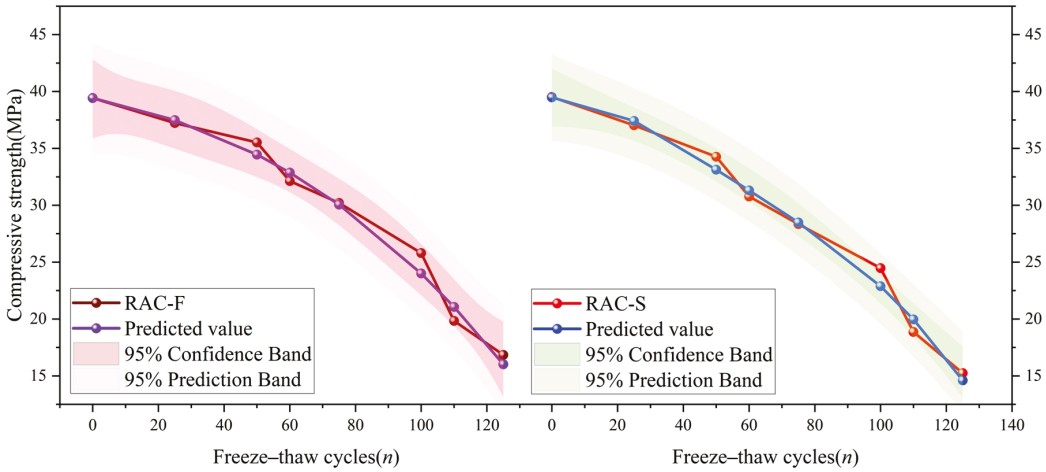

(**a**) RAC compressive strength prediction results

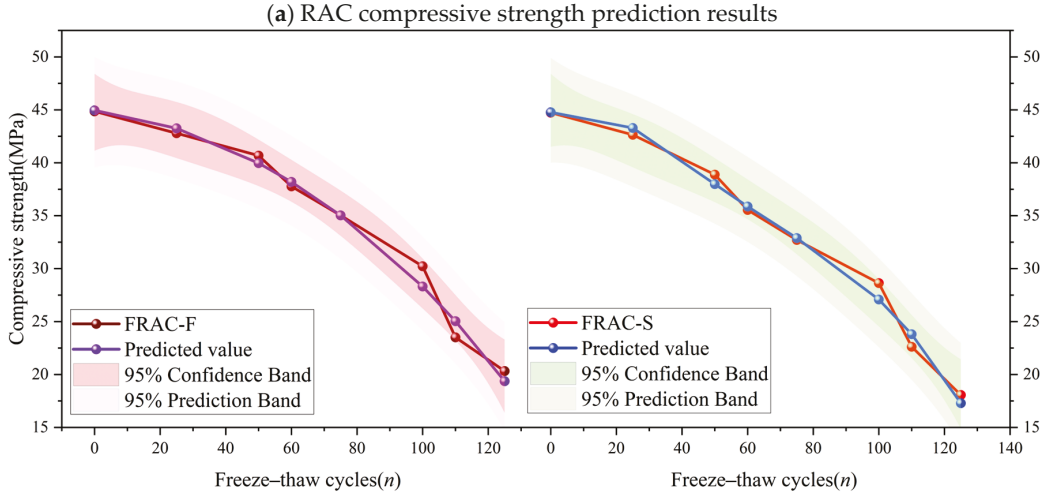

(**b**) FRAC compressive strength prediction results

Figure 11. Compressive strength prediction results.

3.5. Systematic Quantitative Comparison of Frost Resistance

To provide a clear and systematic overview of the deterioration degree of different specimens, the key indicators (mass loss rate, RDEM attenuation, and compressive strength loss rate) at critical freeze–thaw cycles (0, 75, 125) are summarized in Table 6.

Table 6. Key frost resistance indicators for test specimens at different critical freeze–thaw cycles.

	Freeze–Thaw Cycles	NAC-F	NAC-S	RAC-F	RAC-S	FRAC-F	FRAC-S
Mass loss rate (%)	0	0	0	0	0	0	0
	75	−0.16	−0.04	−1.08	0.06	−0.89	0.17
	125	0.11	0.22	−0.97	2.57	−0.77	2.42
RDEM attenuation (%)	0	100	100	100	100	100	100
	75	94.58	90.11	71.85	62.21	78.55	66.67
	125	84.05	78.21	52.71	35.36	57.29	39.09
Compressive strength loss rate (%)	0	0	0	0	0	0	0
	75	10.34	10.91	23.38	28.26	21.91	26.87
	125	18.91	24.56	57.27	61.44	54.68	59.6

As presented in Table 6, the degradation of all specimens exhibited a consistent pattern where NAC demonstrated the best performance, followed by FRAC, with plain RAC showing the most severe deterioration. This pattern was particularly evident when examining the compressive strength loss after 125 freeze–thaw cycles in salt solution, where RAC-S experienced 61.44% strength loss compared to 24.56% for NAC-S while FRAC-S showed a noticeable improvement of 59.6% strength loss. These results clearly demonstrated that RAC was more susceptible to freeze–thaw damage than NAC, and that the incorporation of WPF effectively mitigated this damage in RAC.

The damaging effect of the saline environment was clearly observable in the experimental data. For all recycled aggregate specimens, the damage was significantly more severe in salt solution than in freshwater across all evaluation metrics. This was well illustrated by the RDEM values after 125 cycles, where RAC-S dropped to 35.36% compared to 52.71% for RAC-F, confirming the synergistic damaging effect of salt solution in combination with freeze–thaw cycles.

The effectiveness of WPF in enhancing frost resistance was quantitatively demonstrated in the results. In the freshwater environment, the addition of fibre reduced the compressive strength loss from 57.27% to 54.68% after 125 cycles, representing a 4.52% reduction in strength loss. Although the improvement was less pronounced in the more challenging saline environment, with the strength loss decreasing from 61.44% to 59.60%, the fibre reinforcement still consistently enhanced the durability performance under these severe conditions.

Additionally, the table clearly shows the initial mass gain phase, represented by negative values, for samples tested in freshwater at 75 cycles, which subsequently transitioned to mass loss at later stages. This quantitative information effectively supports and complements the qualitative description of this phenomenon presented earlier in Section 3.2.

3.6. Dual-Damage Parameter Life Prediction

3.6.1. Life Prediction Based on RDEM Threshold

Based on damage mechanics principles, internal damage in concrete gradually accumulates under freeze–thaw cycles. Using dynamic elastic modulus as the damage characterization index, its damage degree D_n was defined as follows:

$$D_n = 1 - \frac{E_n}{E_0} \tag{13}$$

where D_n is the damage degree after n freeze–thaw cycles; E_n is the dynamic elastic modulus after n freeze–thaw cycles; E_0 is the initial dynamic elastic modulus of the concrete. A two-parameter Weibull model with high conformity to concrete behavior was adopted to predict the service life of concrete structures. Assuming the service life was T, its probability density function and cumulative distribution function are shown in Equations (14) and (15), respectively:

$$f(T) = \frac{\beta}{\alpha}\left(\frac{T}{\alpha}\right)^{(\beta-1)} exp[-\left(\frac{T}{\alpha}\right)^{\beta}] \tag{14}$$

$$F(T) = 1 - exp[-\left(\frac{T}{\alpha}\right)^{\beta}] \tag{15}$$

where α is the scale parameter and β is the shape parameter. The failure probability $P_f(n_1)$ after n_1 freeze–thaw cycles is shown in Equation (16):

$$P_f(n_1) = 1 - exp[-\left(\frac{n_1}{\alpha}\right)^{\beta}] \tag{16}$$

When the structure reaches its service life (i.e., failure), $P_f(n_1) \to 1$. At this point, the damage degree $D(n_n) \to 1$, meaning $(n_n/\alpha)^{\beta} \to \infty$. The reliability function $R(n)$ derived from the Weibull distribution function is as follows:

$$R(n) = 1 - F(n) = exp[-\left(\frac{n}{\alpha}\right)^{\beta}] \tag{17}$$

Performing a Weibull transformation on Equation (17) and taking the logarithm twice yielded a linear relationship:

$$\ln[(\ln(\frac{1}{R(n)}))] = \beta(\ln(n) - \ln(\alpha)) \tag{18}$$

Let $Y = ln[ln(1/R(n))]$, $X = ln(n)$, $A = \beta$, $B = -\beta ln(\alpha)$. Then, Equation (18) simplifies to $Y = Ax + B$. If the life prediction data conforms to the Weibull distribution, Y and X should exhibit a strong linear relationship. The least squares method was used to fit parameters A, B, and the correlation coefficient R^2. If $R^2 > 0.90$, it indicates the life prediction data conforms to the Weibull distribution.

Based on the Weibull correlation test equation (Equation (18)), correlation analysis was performed on the RDEM of the concrete to obtain its Weibull distribution values for life prediction, shown in Table 7. The data in Table 7 was linearly fitted using OriginPro 2022 software; the fitting results are shown in Figure 12 and Table 8. The results show that the R^2 values for all specimens were very close to 1, confirming the data highly conforms to the Weibull distribution. The fitted life prediction models are as follows:

$$\text{RAC} - \text{F}: \ Y = ln[\ln(1/R(n))] = 1.43677ln(n) - 7.44156 \tag{19}$$

$$\text{RAC} - \text{S}: \ Y = ln[\ln(1/R(n))] = 1.71116ln(n) - 8.25331 \tag{20}$$

$$\text{FRAC} - \text{F}: \ Y = ln[\ln(1/R(n))] = 1.46745ln(n) - 7.69048 \tag{21}$$

$$\text{FRAC} - \text{S}: \ Y = ln[\ln(1/R(n))] = 1.72544ln(n) - 8.44831 \tag{22}$$

According to specifications and previous research [33], concrete components are considered to have failed when the RDEM drops to 60%, i.e., when the reliability $R(n) = 0.6$. Substituting this critical value into Equations (19)–(22) yielded predicted life for RAC-F, RAC-S, FRAC-F, and FRAC-S of 111, 83, 119, and 90 freeze–thaw cycles, respectively.

Table 7. Weibull distribution value.

Specimen Grouping	Freeze–Thaw Cycle	1/*R*(*n*)	*X* = *ln*(*n*)	*Y* = *ln*[*ln*(1/*R*(*n*))]	Specimen Grouping	Freeze–Thaw Cycle	1/*R*(*n*)	*X* = *ln*(*n*)	*Y* = *ln*[*ln*(1/*R*(*n*))]
RAC-F	25	1.071	3.219	−2.678	RAC-S	25	1.071	3.219	−2.686
	50	1.139	3.912	−2.041		50	1.188	3.912	−1.759
	60	1.194	4.094	−1.730		60	1.331	4.094	−1.252
	75	1.392	4.277	−1.107		75	1.607	4.277	−0.745
	100	1.538	4.605	−0.842		100	1.927	4.605	−0.422
	110	1.670	4.700	−0.667		110	2.201	4.700	−0.237
	125	1.897	4.828	−0.446		125	2.828	4.828	0.039
FRAC-F	25	1.058	3.219	−2.882	FRAC-S	25	1.066	3.219	−2.750
	50	1.127	3.912	−2.123		50	1.158	3.912	−1.920
	60	1.210	4.094	−1.657		60	1.236	4.094	−1.551
	75	1.273	4.277	−1.421		75	1.500	4.277	−0.903
	100	1.484	4.605	−0.930		100	1.826	4.605	−0.507
	110	1.607	4.700	−0.746		110	2.084	4.700	−0.309
	125	1.746	4.828	−0.585		125	2.558	4.828	−0.063

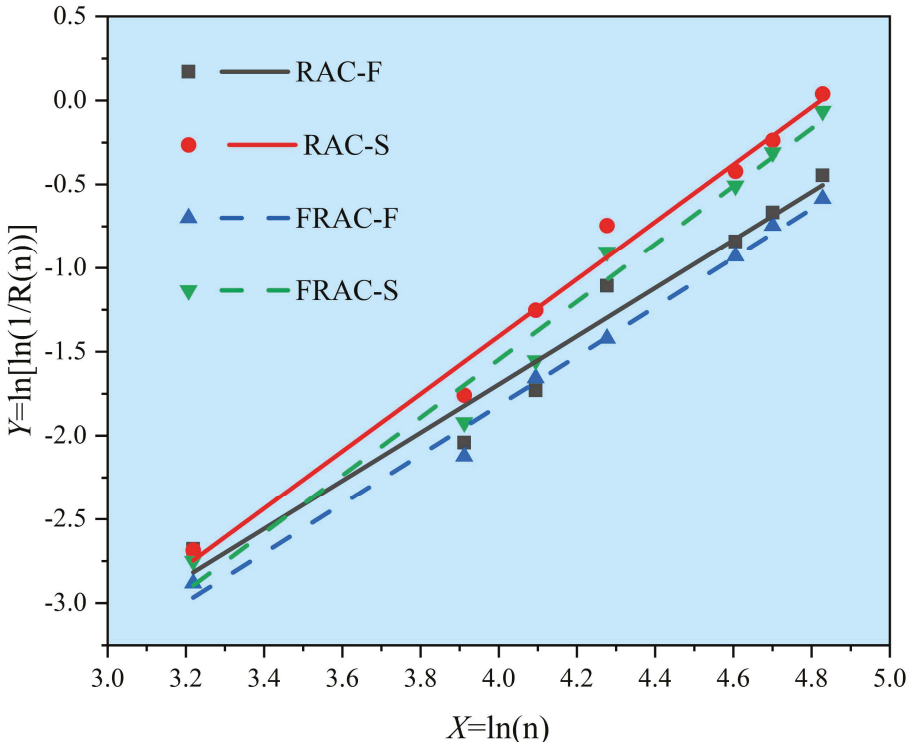

Figure 12. Fitting result.

Table 8. Weibull parameter values.

Specimen Grouping	*A*	*B*	R^2	Specimen Grouping	*A*	*B*	R^2
RAC-F	1.43677	−7.44156	0.96556	RAC-S	1.71116	−8.25331	0.98491
FRAC-F	1.46745	−7.69048	0.99001	FRAC-S	1.72544	−8.44831	0.97722

To verify the reliability of this model's predictions, the compressive strength and loss rate of each specimen group at the predicted life cycle number were calculated using Equation (12). The calculation results are shown in Table 9. The results indicate that there were significant differences in the service life and strength loss rate among the four specimen groups under freeze–thaw conditions. The service lives of RAC-F and RAC-S were 111 and 83 cycles, respectively, while those of the fibre-reinforced groups FRAC-F and FRAC-S increased to 119 and 90 cycles. This demonstrates that WPF effectively delayed the freeze–thaw damage process in RAC and significantly enhanced its service life. It is noteworthy that although the life of FRAC-F was longer than that of RAC-F, its compressive strength loss rate reached 51.59%, notably higher than the 47.37% for the RAC-F group.

Concurrently, the strength loss rate in the freshwater freeze–thaw environment was also significantly higher than that in the saline environment. This anomalous relationship between strength loss rate and life was also observed in the study by Cui et al. [33]. This suggests that relying solely on the RDEM threshold (e.g., 60%) to determine life may underestimate the risk associated with the concrete's residual load-bearing capacity.

Table 9. RDEM life prediction model validation.

Specimen Grouping	RAC-F	RAC-S	FRAC-F	FRAC-S
Service life	111	83	119	90
Predicted compressive strength (MPa)	20.75	26.89	21.76	29.70
Loss rate of maximum strength (%)	47.37	31.90	51.59	33.67

3.6.2. Life Prediction Based on Compressive Strength Loss Rate Threshold

Based on the compressive strength prediction formula (Equation (12)) from Section 3.4.2) the compressive strength damage degree G_n was defined as follows:

$$G_n = 1 - \frac{f_{cu,n}}{f_{cu,0}} \tag{23}$$

where G_n is the compressive strength damage degree after n freeze–thaw cycles; $f_{cu,n}$ is the compressive strength after n freeze–thaw cycles; $f_{cu,0}$ is the initial compressive strength of the concrete with the same mix proportion before any freeze–thaw cycles.

Similarly, using the Weibull correlation test equation (Equation (18)), correlation analysis was performed on the compressive strength loss rate of the concrete to obtain its Weibull distribution values for life prediction, shown in Table 10. Linear fitting was applied to the data in Table 10; the fitting results are shown in Figure 13 and Table 11. The results indicate that the correlation coefficient R^2 for all specimens was greater than 0.90, confirming that the strength prediction data also conforms to the Weibull distribution. The fitted life prediction models based on strength loss rate are as follows:

$$\mathrm{RAC-F}: \ Y = ln[\ln(1/R(n))] = 4.69317 - 1.04803ln(n) \tag{24}$$

$$\mathrm{RAC-S}: \ Y = ln[\ln(1/R(n))] = 4.74667 - 1.08344ln(n) \tag{25}$$

$$\mathrm{FRAC-F}: \ Y = ln[\ln(1/R(n))] = 4.79154 - 1.05605ln(n) \tag{26}$$

$$\mathrm{FRAC-S}: \ Y = ln[\ln(1/R(n))] = 4.95578 - 1.11818ln(n) \tag{27}$$

Table 10. Weibull distribution value.

Specimen Grouping	Freeze–Thaw Cycle	1/*R*(*n*)	*X* = *ln*(*n*)	*Y* = *ln*[*ln*(1/*R*(*n*))]	Specimen Grouping	Freeze–Thaw Cycle	1/*R*(*n*)	*X* = *ln*(*n*)	*Y* = *ln*[*ln*(1/*R*(*n*))]
RAC-F	25	20.255	3.219	1.101	RAC-S	25	19.086	3.219	1.081
	50	7.924	3.912	0.727		50	6.210	3.912	0.602
	60	6.015	4.094	0.585		60	4.826	4.094	0.454
	75	4.207	4.277	0.362		75	3.593	4.277	0.246
	100	2.557	4.605	−0.063		100	2.379	4.605	−0.143
	110	2.147	4.700	−0.269		110	2.023	4.700	−0.350
	125	1.685	4.828	−0.651		125	1.587	4.828	−0.772
FRAC-F	25	26.542	3.219	1.187	FRAC-S	25	30.048	3.219	1.225
	50	9.014	3.912	0.788		50	6.585	3.912	0.634
	60	6.653	4.094	0.639		60	5.028	4.094	0.479
	75	4.534	4.277	0.413		75	3.766	4.277	0.282
	100	2.702	4.605	−0.006		100	2.531	4.605	−0.074
	110	2.258	4.700	−0.205		110	2.135	4.700	−0.277
	125	1.758	4.828	−0.573		125	1.629	4.828	−0.717

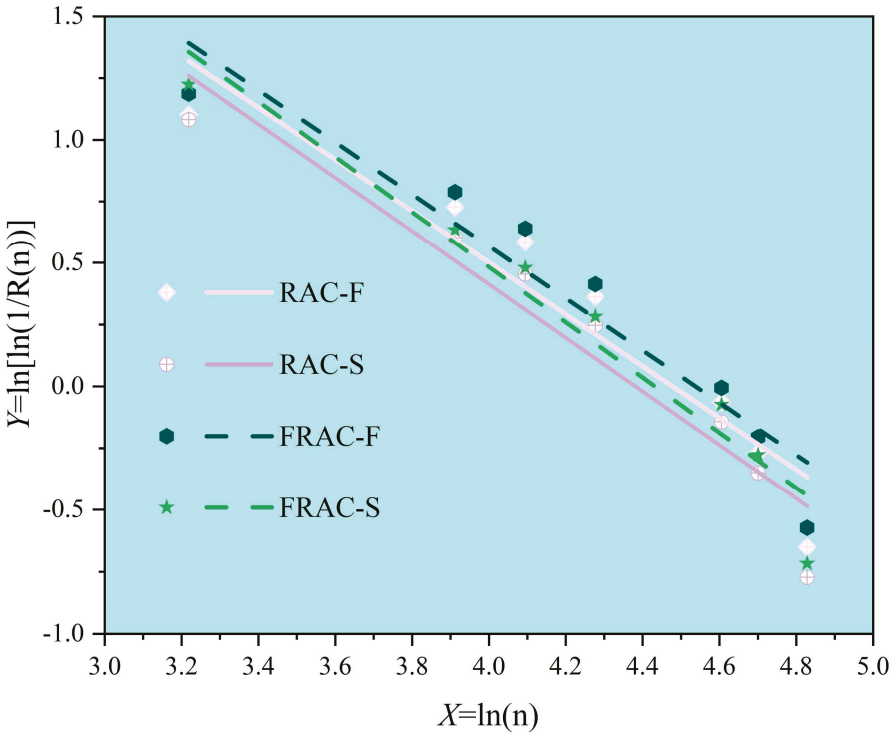

Figure 13. Fitting result.

Table 11. Weibull parameter values.

Specimen Grouping	*A*	*B*	R^2	Specimen Grouping	*A*	*B*	R^2
RAC-F	−1.04803	4.69317	0.90758	RAC-S	−1.08344	4.74667	0.92739
FRAC-F	−1.05605	4.79154	0.91925	FRAC-S	−1.11818	4.95578	0.94631

Currently, existing research has not established a unified standard for the strength attenuation threshold signifying failure of concrete structures. Dong et al. [58] proposed a compressive strength loss rate of 25% as the failure criterion whereas Wiyanto et al. [59] suggested that a strength loss rate of 50% should be required for failure determination. Furthermore, Ma et al. [60] advocated for an absolute value threshold method, i.e., failure is determined when the compressive strength drops to a specific critical value. Based on previous studies, a compressive strength loss rate of 35% (i.e., reliability R(n) = 0.35) was selected as the criterion for component failure. Substituting $R(n)$ = 0.35 into Equations (24)–(27) yielded a predicted life for RAC-F, RAC-S, FRAC-F, and FRAC-S of 84, 76, 89, and 84 freeze–thaw cycles, respectively. The model verification results are shown in Table 12. The residual strength of all specimen groups at their predicted life stabilized between 28 and 32 MPa, and the strength loss rate converged within 28%–31%. This indicates that specimens successively failed when the strength loss rate approached approximately 30%, and the attenuation of load-bearing capacity is the core mechanism determining ultimate failure.

Table 12. Validation of compressive strength life prediction model.

Specimen Grouping	RAC-F	RAC-S	FRAC-F	FRAC-S
Service life	84	76	89	84
Predicted compressive strength (MPa)	28.09	28.30	31.51	31.04
Loss rate of maximum strength (%)	28.77	28.32	29.89	30.67

Furthermore, comparing Tables 9 and 12 reveals that both prediction methods demonstrate that WPF incorporation significantly enhanced the service life of RAC. However, the life predicted based on RDEM was generally greater than that predicted based on strength loss rate. Critically, the former exhibited a strength loss rate as high as 47%–52% at the end of its predicted life, far exceeding established engineering safety thresholds. In contrast, the latter method constrained the loss rate to around 30%. Although its predicted life was shortened by approximately 16% on average, it effectively avoided the structural risk associated with low residual strength accompanying long life. Therefore, when assessing the service life of concrete structures in freeze–thaw environments, the evolution patterns of both RDEM and compressive strength should be comprehensively considered to more accurately evaluate their safe service period.

3.6.3. Sensitivity Analysis and Engineering Failure Thresholds

The selection of failure thresholds (60% for RDEM and 35% for compressive strength loss) significantly influences the predicted service life and residual strength of concrete. To evaluate the sensitivity of these thresholds, this study conducted a supplementary analysis by varying the failure criteria and observing the corresponding changes in predicted life and strength loss. When the RDEM threshold was tightened to 70%, the predicted service life of FRAC-S decreased from 90 to 74 cycles, while the compressive strength loss rate at failure decreased to 26.11%. Conversely, relaxing the RDEM threshold to 50% extended the predicted life to 108 cycles, with a strength loss rate of 45.23%. Similarly, if the compressive strength loss threshold was adjusted to 25%, the predicted life of FRAC-S decreased to 65 cycles; if the compressive strength loss threshold raised to 40%, the predicted life of FRAC-S increased to 96 cycles.

These variations highlight a trade-off between service life and structural safety. The 60% RDEM threshold, while widely adopted in standards and previous studies [33], may lead to an overestimation of usable life under high residual strength requirements. In contrast, the 35% strength loss threshold provides a more conservative estimate, ensuring that the residual strength remains above 28 MPa, which is critical for load-bearing structures in harsh environments. The 35% strength loss criterion is further justified by its alignment with practical engineering safety margins. For instance, many existing studies stipulate that when predicting the service life of concrete structures, the maximum allowable strength of concrete should be reduced by 25%–50% [58,59]. Moreover, the 60% RDEM threshold is primarily based on acoustic and elastic properties, which may not fully capture the mechanical degradation under combined freeze–thaw. Therefore, for applications where residual strength is a primary concern (e.g., structures in coastal regions), the strength-based model is recommended. For non-structural or lightly loaded structures, the RDEM-based model may suffice.

In summary, the dual-parameter approach allows engineers to select the appropriate failure criterion based on specific performance requirements, thereby enhancing the flexibility and reliability of life prediction for RAC structures in freeze–thaw environments.

3.7. Microstructure Analysis

The micro-morphological characteristics of RAC and FRAC after freeze–thaw cycles are shown in Figures 14 and 15, respectively. SEM images of RAC reveal that, compared to NAC which exhibits only a single NCA-new mortar ITZ, the inherent characteristics of RCA lead to the formation of three distinct types of ITZ structures with different morphological features within RAC. These are the new mortar–old mortar ITZ, the RCA–old mortar ITZ, and the RCA–new mortar ITZ [42]. Among these, the bonding state between the new mortar and the RCA surface, as well as the interfacial bonding between the old

and new mortars, is relatively dense. Hydration products at these interfaces are densely interwoven with low porosity, indicating good mechanical continuity. However, during the secondary crushing process of RCA, the old mortar adhering to its surface inevitably suffers mechanical damage. This results in the generation of microcracks within the old mortar layer and localized debonding from the aggregate substrate. This process-induced damage is visually manifested in SEM images as significantly widened crack structures within the ITZ between the RCA and the old mortar layer. The interface connection is loose and exhibits discontinuous defects. The microcracks in this region not only weaken the integrity between the aggregate and mortar but, more critically, due to their significant geometric discontinuity and mechanical weakness, become preferential paths for stress concentration and crack propagation. Ultimately, this region evolves into a key damage evolution zone, influencing the macroscopic performance degradation of RAC.

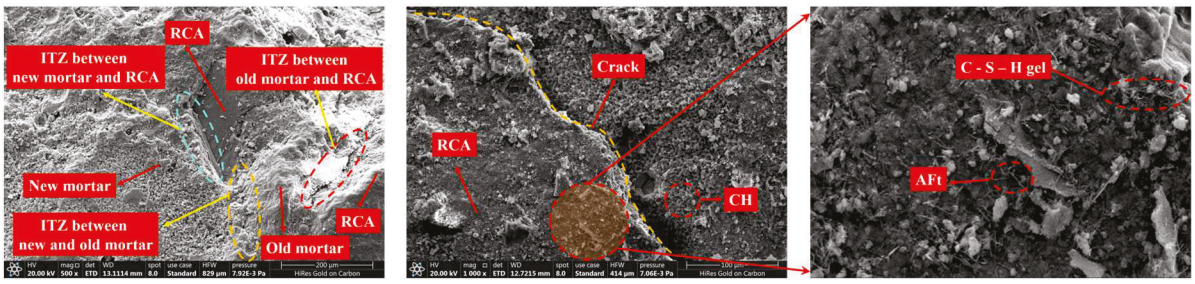

(**a**) Three categories of ITZ (**b**) Crack (**c**) Hydration products

Figure 14. SEM images of RAC.

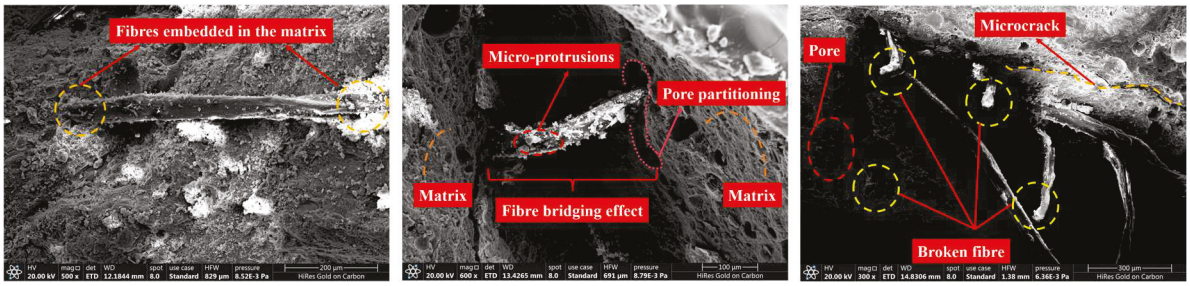

(**a**) Fibre embedding (**b**) Fibre bridging (**c**) Broken fibre

Figure 15. SEM images of FRAC.

Furthermore, three typical micro-morphological features of cement hydration products can be clearly identified from Figure 14b,c. For instance, layered crystalline calcium hydroxide (CH) densely fills capillary pores in the form of hexagonal plate-like crystals. Its flaky structure forms physical barriers within the mortar matrix, effectively reducing the connectivity of pores. Needle-columnar ettringite (AFt) exhibits a distribution of slender radiating clusters, penetrating pores and interfacial regions. Its rigid skeleton structure provides microscale support to the matrix. Amorphous calcium silicate hydrate gel (C-S-H gel), as the primary cementing phase, envelops aggregates with a dense reticular network. Its high specific surface area and cohesive properties constitute the core source of matrix strength [61,62]. It is noteworthy that these products can provide a certain degree of protection to the matrix during the initial stages of freeze–thaw by reducing water infiltration channels, restricting pore deformation, and enhancing matrix cohesion. However, if the equilibrium between hydration products is disrupted, such as excessive consumption of CH or over-expansion of Aft, it can compromise the frost resistance of concrete [50].

Typical micro-SEM images of FRAC are shown in Figure 15. WPF is distributed within the concrete matrix in a tightly embedded state. Its surface is encased by hydration products and exhibits micro-protrusions, forming a significant mechanical anchorage enhancement effect [63]. This bonding in the fibre-matrix interfacial zone effectively fills local pores and enhances the overall compactness of the matrix. Figure 15b shows that when crack propagation reaches a fibre location, the fibre bridges both sides of the crack, effectively restraining the separated matrix fragments. This bridging force retards the speed of crack interconnection and imparts higher fracture toughness to the material [64]. It is noteworthy that in this image, a fibre traverses a large pore, dividing it into two isolated smaller pores. This phenomenon visually demonstrates the pore structure refinement capability of fibres. By transforming interconnected large pores into dispersed micropores, the stress concentration effect of the pores is weakened. Furthermore, Figure 15c reveals that numerous fibres exhibit random, non-directional distribution within the matrix, interwoven into a continuous three-dimensional network skeleton. This multi-directional confinement system can effectively transfer loads and inhibit crack initiation. Meanwhile, dense micropores are observable surrounding the fibres. Significantly, the exposed fibre fracture surfaces after matrix failure all present smooth single fracture planes. This fracture morphology indicates that the fibres provided effective stress transfer and fully exerted their crack-blocking function.

A comparative analysis of SEM images revealed that the incorporation of WPF significantly refined the pore structure. Compared to plain RAC, the addition of fibres reduced the number of large, interconnected pores and promoted the formation of a more dispersed and finer pore structure in FRAC. This microstructural improvement is consistent with the enhancement in its macro-scale durability performance. Furthermore, research by Ren et al. indicated that incorporating PPFs could reduce concrete porosity by 17.4% and significantly decrease the proportion of large pores greater than 5000 nm [48]. Studies by Wu et al. also pointed out that after adding fibres and undergoing 200 freeze–thaw cycles, the proportion of large pores greater than 1000 nm decreased by 50.22%, the total porosity was reduced by 50.39%, and the fibre–matrix interfacial bonding performance was noticeably enhanced [65]. Research by Huang further demonstrated that the introduction of an appropriate amount of fibre could reduce concrete porosity by 30.65%, decrease the peak signal of large pores by 68.84%, and increase the proportion of small pores, thereby optimizing the pore size distribution, enhancing the fibre-matrix interfacial density, and effectively inhibiting crack propagation [66]. These studies consistently indicate that the incorporation of fibres, by optimizing the pore structure and enhancing interfacial properties, is a key mechanism for improving the durability of concrete.

3.8. Mechanism Analysis

Schematic diagrams illustrating the damage mechanisms of RAC under different freeze–thaw environments and the improvement mechanism of WPF on RAC are shown in Figure 16. The failure of RAC under freeze–thaw cycles is a progressive deterioration process originating from its unique microstructure. Its core weak link lies in the multiple ITZs formed by RCA, old mortar, and new mortar [67,68], as shown in Figure 16a. This region's inherent characteristics of high tortuous porosity, propensity for Cl^- enrichment, and relatively weak bond strength make it the origin for the initiation and development of freeze–thaw damage. In the freshwater freeze–thaw environment, water penetrating the matrix preferentially fills and is retained in the high-porosity areas of the ITZ. Upon freezing, this water forms ice crystals and generates expansion pressure. Due to the higher degree of saturation and tortuous pores in the ITZ, the degree of ice formation far exceeds that in other parts of the matrix. The ice crystal expansion pressure amplifies sharply with increasing saturation, directly causing debonding in the ITZ region and damage to the

interfacial bonding. After multiple freeze–thaw cycles, the pore area in RAC increases, and freeze–thaw cracks propagate from the outer surface towards the interior.

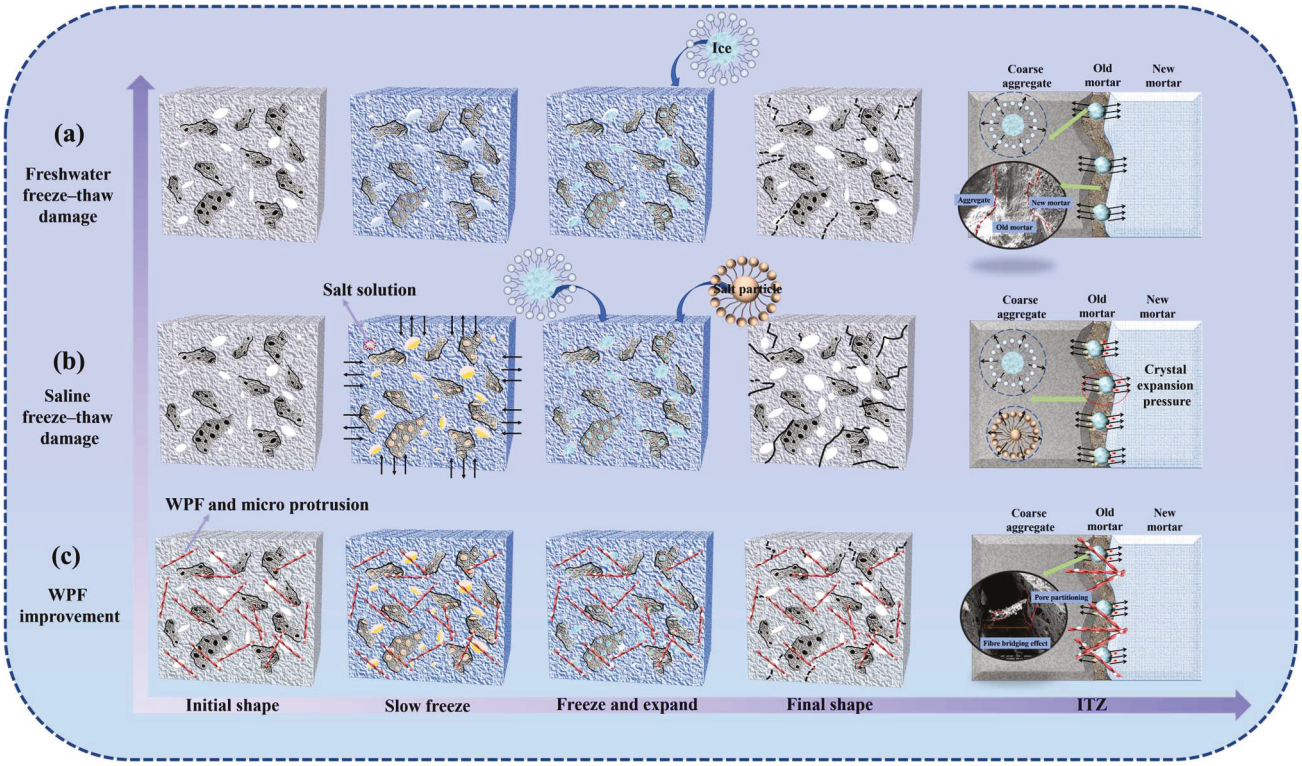

Figure 16. Mechanism diagram of freeze–thaw.

Figure 16b shows that the saline freeze–thaw environment induces a more complex multi-stress damage mechanism. The intrusion of salt solution brings not only water but also Cl^-. During freezing, the Cl^- enriched in the ITZ forms a high-concentration salt solution, creating a significant concentration gradient with the external solution, which induces osmotic pressure. This osmotic pressure continuously attracts external water to infiltrate, further substantially increasing the degree of saturation and freezable water content within the ITZ. Consequently, a larger ice crystal expansion pressure is generated compared to the freshwater environment [9]. Furthermore, as water freezes and ice crystals precipitate, the salt concentration in the remaining solution sharply increases, forming a supersaturated solution. With the gradual increase in salt solution concentration, crystallization eventually occurs, precipitating salt particles. These precipitated salt particles are squeezed and wedged into the matrix during ice crystal expansion, exerting a physical wedging action that further weakens the interfacial bonding [9,55]. The synergistic effect of osmotic pressure, ice crystal expansion pressure, and salt crystallization pressure at the vulnerable ITZ promotes the initiation of microcracks and accelerates their propagation and interconnection. Therefore, the damage to RAC under freeze–thaw in salt solution is more severe, manifested by a further increase in internal pore area, an increase in the number, width, and penetration depth of freeze–thaw damage cracks developing from the outside inward, leading to rapid loss of structural integrity.

The improvement mechanism of WPF on the frost resistance of RAC is shown in Figure 16c. The beneficial effect of WPF originates from its three-dimensional randomly distributed structure within the RAC matrix and the synergistic effects it triggers. Firstly, WPF effectively optimizes the pore structure: its incorporation blocks capillary water infiltration channels, reducing the penetration of water and Cl^-; simultaneously, it segments and refines large, interconnected pores within the matrix into isolated micropores, increasing

the proportion of small pores and decreasing the number of large pores, resulting in a more uniform pore distribution [69]. This optimized structure not only provides buffer space for crystal volume expansion, significantly alleviating the direct destructive pressure exerted on pore walls by ice crystal frost heave and salt crystallization pressure [30], but also reduces the amount of freezable water and inhibits the migration and local accumulation of Cl^- within the pore network, thereby mitigating the risk of freeze–thaw damage [50]. Secondly, WPF significantly enhances the crack resistance and toughness of the material: During freeze–thaw cycles, when microcracks form in the matrix (particularly in vulnerable ITZ regions) due to ice crystal expansion and salt crystallization, fibres bridging the cracks, leveraging their high elastic modulus and tensile strength, effectively transfer and disperse stress. This avoids stress concentration at the crack tip and absorbs energy through their own deformation, thereby retarding crack propagation [63,70]. This bridge-like effect is particularly prominent at the ITZ. Fibres traversing the ITZ effectively inhibit interfacial debonding failure in RAC under freeze–thaw conditions and enhance the overall toughness of the concrete.

In summary, RAC undergoes an irreversible process in freeze–thaw (especially saline freeze–thaw) environments, driven by ITZ deterioration, involving microcrack initiation and propagation that ultimately lead to structural disintegration. However, with the improvement provided by WPF, RAC not only exhibits a significantly reduced rate of freeze–thaw deterioration but also effectively limits the depth and extent of internal damage (particularly ITZ degradation). It suppresses the propagation and interconnection of cracks, thereby significantly enhancing the structural stability and frost resistance of RAC.

4. Conclusions

This study systematically analyzed the influence of WPF on the frost resistance of RAC under freshwater and saline freeze–thaw environments, revealed the improvement mechanism of WPF on the frost resistance of RAC, and established life prediction models. The main conclusions are as follows:

(1) With increasing freeze–thaw cycles, the mass loss rate of concrete first decreased and then increased, while the compressive strength and RDEM continuously decreased. Freeze–thaw in salt solution exacerbated the structural damage of RAC, and the frost resistance of RAC was significantly lower than that of NAC.

(2) WPF effectively enhanced the frost resistance of RAC. The improvement was more pronounced in freshwater. After 125 freeze–thaw cycles, the RDEM attenuation amplitude of FRAC decreased by 9.69% (freshwater) and 5.77% (salt solution) compared to RAC. The compressive strength increased by 20.65% and 18.57%, respectively. The negative mass growth rate in freshwater decreased by 20.62%, and the mass loss rate in salt solution decreased by 5.84%.

(3) WPF optimized the pore structure of RAC and enhanced the density of the matrix by bridging microcracks and dividing connected pores, effectively inhibiting the penetration of water and salt, delaying the debonding failure and crack propagation of the ITZ, and thereby improving the frost resistance of RAC.

(4) Life prediction demonstrated that WPF increased the service life of RAC. The RDEM-based model predicted longer lives (119/90 cycles for FRAC-F/FRAC-S) but corresponded to higher strength loss rates (34%–52%). Conversely, the strength-based model predicted shorter lives (89/84 cycles) but more stable residual strength (30%–31% loss rate). A comprehensive analysis using both models is recommended for accurate life assessment.

5. Limitations and Future Research

This study provides insights into FRAC's frost resistance under laboratory conditions but has certain limitations. For example, the 125 freeze–thaw cycles, while sufficient to reveal trends, limit the understanding of long-term durability. Additionally, this study only conducted qualitative pore structure observations via SEM; the lack of quantitative analysis (e.g., pore size distribution, fibre-matrix bonding) limits in-depth understanding of WPF's reinforcement mechanism. Future research should consider increasing the number of freeze–thaw cycles to investigate FRAC's long-term durability performance. It is also recommended to use advanced techniques like X-ray CT for quantitative microstructural analysis, such as measuring pore size distribution and quantifying fibre–matrix bonding, to better clarify WPF's reinforcement mechanism.

Author Contributions: X.Y.: Writing—original draft, investigation. Z.Z.: Writing–review and editing. H.-W.T.: Writing—review and editing. B.L.: Investigation, data curation, funding acquisition. J.L. (Jiahui Li): Writing—original draft, methodology, investigation. W.Z.: Writing—review and editing. T.S.: Writing–review and editing, writing—original draft, supervision, investigation, funding acquisition. J.L. (Jianping Liu): Writing—review and editing, investigation. All authors have read and agreed to the published version of the manuscript.

Funding: This research was supported by the National Natural Science Foundation of China (52309137), the China Postdoctoral Science Foundation (2022M723687; 2024M751866), the Natural Science Foundation of Shandong Province, China (ZR2024QE218; ZR2025MS802).

Data Availability Statement: Data will be made available upon request.

Conflicts of Interest: Author Zehui Zhang was employed by the company China Design Testing Technology Co., Ltd. The remaining authors declare that the research was conducted in the absence of any commercial or financial relationships that could be construed as a potential conflict of interest.

Abbreviations

The following abbreviations are used in this manuscript:

RCA	Recycled coarse aggregate
RAC	Recycled aggregate concrete
NCA	Natural coarse aggregate
NAC	Natural aggregate concrete
SEM	Scanning electron microscopy
WPF	Waste polypropylene fibre
FRAC	Waste polypropylene fibre-reinforced recycled aggregate concrete
RDEM	Relative dynamic elastic modulus
ITZ	Interface transition zone
CDW	Construction and demolition waste

References

1. Pandey, B.; Brelsford, C.; Seto, K.C. Rising infrastructure inequalities accompany urbanization and economic development. *Nat. Commun.* **2025**, *16*, 1193. [CrossRef]
2. Bai, G.; Zhu, C.; Liu, C.; Liu, B. An evaluation of the recycled aggregate characteristics and the recycled aggregate concrete mechanical properties. *Constr. Build. Mater.* **2020**, *240*, 117978. [CrossRef]
3. Wu, L.; Sun, Z.; Cao, Y. Modification of recycled aggregate and conservation and application of recycled aggregate concrete: A review. *Constr. Build. Mater.* **2024**, *431*, 136567. [CrossRef]
4. Cho, N.; El Asmar, M.; Aldaaja, M. An analysis of the impact of the circular economy application on construction and demolition waste in the United States of America. *Sustainability* **2022**, *14*, 10034. [CrossRef]
5. Liu, H.; Guo, D.; Xu, H. Pathway selection to achieving synergistic benefits of pollution and carbon reduction through solid waste resource utilization based on system dynamics. *Environ. Impact Assess. Rev.* **2025**, *115*, 108053. [CrossRef]

6. Salgado, F.D.A.; Silva, F.D.A. Recycled aggregates from construction and demolition waste towards an application on structural concrete: A review. *J. Build. Eng.* **2022**, *52*, 104452. [CrossRef]
7. Xiao, J.; Zhang, K.; Ding, T.; Zhang, Q.; Xiao, X. Fundamental issues towards unified design theory of recycled and natural aggregate concrete components. *Engineering* **2023**, *29*, 188–197. [CrossRef]
8. Hao, L.; Liu, Y.; Wang, W.; Zhang, J.; Zhang, Y. Effect of salty freeze-thaw cycles on durability of thermal insulation concrete with recycled aggregates. *Constr. Build. Mater.* **2018**, *189*, 478–486. [CrossRef]
9. Luan, H.; Wu, J.; Xu, C.; Hu, J.; Guo, S.; Wang, Y.; Geng, F.; Li, Z. Freeze-thaw deterioration development characterization and mechanism investigation of recycled coarse aggregate concrete under deicing salt exposure. *Constr. Build. Mater.* **2025**, *489*, 142232. [CrossRef]
10. Huda, S.B.; Alam, M.S. Mechanical and freeze-thaw durability properties of recycled aggregate concrete made with recycled coarse aggregate. *J. Mater. Civ. Eng.* **2015**, *27*, 04015003. [CrossRef]
11. Yuan, C.; Qu, S.; Bai, W.; Guan, J.; Xie, Y. Study on the mechanical properties and mesoscopic damage mechanism of recycled aggregate concrete under different dynamic strain rates after freeze-thaw cycles. *Case Stud. Constr. Mater.* **2025**, *22*, e04182. [CrossRef]
12. Bogas, J.A.; Gomes, A. Non-steady-state accelerated chloride penetration resistance of structural lightweight aggregate concrete. *Cem. Concr. Compos.* **2015**, *60*, 111–122. [CrossRef]
13. Hu, J.; Wu, J. Mechanical properties and uni-axial compression stress-strain relation of recycled coarse aggregate concrete subjected to salt-frost cycles. *Constr. Build. Mater.* **2019**, *197*, 652–666. [CrossRef]
14. Su, T.; Wu, J.; Yang, G.; Zou, Z. Bond behavior between recycled coarse aggregate concrete and steel bar after salt-frost cycles. *Constr. Build. Mater.* **2019**, *226*, 673–685. [CrossRef]
15. Su, T.; Wang, T.; Wang, C.; Yi, H. The influence of salt-frost cycles on the bond behavior distribution between rebar and recycled coarse aggregate concrete. *J. Build. Eng.* **2022**, *45*, 103568. [CrossRef]
16. Thaulow, N.; Sahu, S. Mechanism of concrete deterioration due to salt crystallization. *Mater. Charact.* **2004**, *53*, 123–127. [CrossRef]
17. Du, X.; Li, G.; Cao, A.; Wang, A.; Zhou, Y. Study of transport and binding behavior of chloride ions in concrete under single-sided salt-freezing cycle. *Constr. Build. Mater.* **2025**, *471*, 140749. [CrossRef]
18. Chen, C.; Zhang, K.; Yin, Z.; Zhou, J. Deterioration performance of recycled aggregate Pervious concrete under freezing-thawing cycle and chloride environment. *Buildings* **2023**, *13*, 645. [CrossRef]
19. Chen, S.; Ren, J.; Li, Y.; Ren, X.; Song, Y.; Sun, J. Macroscopic and mesoscopic deterioration behaviors of concrete under the coupling effect of chlorine salt erosion and freezing-thawing cycle. *Materials* **2021**, *14*, 6471. [CrossRef]
20. Zhu, H.; Li, X. Experiment on freezing and thawing durability characteristics of recycled aggregate concrete. *Key Eng. Mater.* **2009**, *400–402*, 447–452. [CrossRef]
21. Richardson, A.; Coventry, K.; Bacon, J. Freeze/thaw durability of concrete with recycled demolition aggregate compared to virgin aggregate concrete. *J. Clean. Prod.* **2011**, *19*, 272–277. [CrossRef]
22. Atasham ul haq, M.; Wang, P.; Wang, Y.; Cui, H.; Tahir, M.; Gong, F.; Li, W. Optimization and utilization of air-entrained recycled brick aggregate concrete under freeze-thaw environment. *Case Stud. Constr. Mater.* **2025**, *23*, e04941. [CrossRef]
23. GivKashi, M.R.; Tohidloo, M. The effect of freeze-thaw cycles and sulfuric acid attack separately on the compressive strength and microstructure of 3D-printed air-entrained concrete. *Constr. Build. Mater.* **2024**, *440*, 137411. [CrossRef]
24. Gao, D.; Zhang, L.; Zhao, J.; You, P. Durability of steel fibre-reinforced recycled coarse aggregate concrete. *Constr. Build. Mater.* **2020**, *232*, 117119. [CrossRef]
25. Zhang, P.; Yang, Y.; Wang, J.; Hu, S.; Jiao, M.; Ling, Y. Mechanical properties and durability of polypropylene and steel fiber-reinforced recycled aggregates concrete (FRRAC): A review. *Sustainability* **2020**, *12*, 9509. [CrossRef]
26. Fan, X.; Wu, D.; Chen, H. Experimental research on the freeze-thaw resistance of basalt fiber reinforced concrete. *Adv. Mater. Res.* **2014**, *919–921*, 1912–1915. [CrossRef]
27. Liu, J.; Zhao, S.; Liu, R. Study on antifreeze properties and pore structure of basalt fiber reinforced concrete. *J. Phys. Conf. Ser.* **2020**, *1605*, 012151. [CrossRef]
28. Moceikis, R.; Kičaitė, A.; Sahmenko, G.; Selsekienė, A. Durability characterisation of glass fibre reinforced concrete by resistance to freezing and thawing. *J. Sustain. Archit. Civ. Eng.* **2020**, *26*, 98–109. [CrossRef]
29. Al-Lebban, M.F.; Khazaly, A.I.; Shabbar, R.; Jabal, Q.A.; Asadi, L.A.R.A.I. Effect of polypropylene fibers on some mechanical properties of concrete and durability against freezing and thawing cycles. *Key Eng. Mater.* **2021**, *895*, 130–138. [CrossRef]
30. Wang, C.; Chen, F. Durability of polypropylene fiber concrete exposed to freeze-thaw cycles with deicing salts. In Proceedings of the 2019 International Conference on Electronical, Mechanical and Materials Engineering, Wuhan, China, 20–21 January 2019; pp. 203–206. [CrossRef]
31. Richardson, A. Polypropylene fibres in concrete with regard to durability. *Struct. Surv.* **2003**, *21*, 87–94. [CrossRef]
32. Idrees, M.; Saeed, F.; Farooq, Z.; Köksal, F.; Shi, J. Production of waste carpet fiber-reinforced concrete as sustainable material. *J. Build. Eng.* **2023**, *77*, 107499. [CrossRef]

33. Cui, S.; Wang, T.; Zhang, Z.; Sun, X.; Li, J.; Li, B.; Zhang, W.; Su, T.; Cao, F. Frost resistance and life prediction of recycled brick aggregate concrete with waste polypropylene fiber. *Rev. Adv. Mater. Sci.* **2023**, *62*, 20230154. [CrossRef]
34. Han, F.; Lang, C.; Qiu, Y. Cleaning behavior based on waste textile before resource conversion and its challenges in China–A comprehensive review. *J. Clean. Prod.* **2022**, *370*, 133509. [CrossRef]
35. *JGJ 522006*; Standard for Quality and Test Methods of Ordinary Concrete Sand and Stone. China Architecture & Building Press: Beijing, China, 2006. (In Chinese)
36. *JGJ 632006*; Standard for Water of Concrete. China Architecture & Building Press: Beijing, China, 2006. (In Chinese)
37. Zhang, W.; Wang, T.; Cao, F.; Wang, C.; Mei, X.; Shao, J.; Su, T. Improvement effect assessment of waste fibre on the comprehensive performance of mixed recycled aggregate concrete. *Constr. Build. Mater.* **2025**, *491*, 142633. [CrossRef]
38. *GB/T 50082-2024*; Standard for Test Methods of Long-Term Performance and Durability of Ordinary Concrete. China Architecture & Building Press: Beijing, China, 2024. (In Chinese)
39. *JGJ 552011*; Specification for Mix Proportion Design of Ordinary Concrete. China Architecture & Building Press: Beijing, China, 2011. (In Chinese)
40. Ferreira, L.; Brito, J.D.; Barra, M. Influence of the pre-saturation of recycled coarse concrete aggregates on concrete properties. *Mag. Concr. Res.* **2011**, *63*, 617–627. [CrossRef]
41. Liu, Y.; Zhou, J.; Wu, D.; Kang, T.; Liu, A. Bond behavior of recycled fiber recycled concrete with reinforcement after freeze-thaw cycles. *Crystals* **2021**, *11*, 1506. [CrossRef]
42. Zhou, J.; Kang, T.; Wang, F. Study on mesostructure of recycled concrete with waste fiber. *Concrete* **2019**, *11*, 78–82. [CrossRef]
43. *GB/T 50476-2019*; Code for Durability Design of Concrete Structures. China Architecture & Building Press: Beijing, China, 2019. (In Chinese)
44. Duan, M.; Qin, Y.; Li, Y.; Zhou, H. Durability and damage model of polyacrylonitrile fiber reinforced concrete under freeze-thaw and erosion. *Constr. Build. Mater.* **2023**, *29*, 132238. [CrossRef]
45. *GB/T 50081-2019*; Standard for Test Methods of Physical and Mechanical Properties of Concrete. China Architecture & Building Press: Beijing, China, 2019. (In Chinese)
46. Wang, J.; Dai, Q.; Si, R.; Guo, S. Mechanical; durability, and microstructural properties of macro synthetic polypropylene (PP) fiber-reinforced rubber concrete. *J. Clean. Prod.* **2019**, *234*, 1351–1364. [CrossRef]
47. Lu, J.; Liu, J.; Yang, H.; Wan, X.; Gao, J.; Zhang, J.; Li, P. Experimental investigation on the mechanical properties and pore structure deterioration of fiber-reinforced concrete in different freeze-thaw media. *Constr. Build. Mater.* **2022**, *350*, 128887. [CrossRef]
48. Ren, J.; Lai, Y. Study on the durability and failure mechanism of concrete modified with nanoparticles and polypropylene fiber under freeze-thaw cycles and sulfate attack. *Cold Reg. Sci. Technol.* **2021**, *188*, 103301. [CrossRef]
49. Zhang, W.; Pi, Y.; Kong, W.; Zhang, Y.; Wu, P.; Zeng, W.; Yang, F. Influence of damage degree on the degradation of concrete under freezing-thawing cycles. *Constr. Build. Mater.* **2020**, *260*, 119903. [CrossRef]
50. Wu, C.; Jierula, A.; Fu, Z.; Chen, Y.; Kuang, Y.; Xia, J. Study on the mechanism of anti sulfate freeze-thaw, dry wet cycle of polypropylene fiber foam concrete. *Constr. Build. Mater.* **2025**, *463*, 140144. [CrossRef]
51. Feng, Z.; Wu, J.; Hu, D.; Zhao, L. Uniaxial compressive behavior and unified damage constitutive model of various types of recycled coarse aggregate concrete under freeze-thaw action. *Mater. Today Commun.* **2024**, *41*, 110976. [CrossRef]
52. Yang, W.; Tang, Z.; Wu, W.; Zhang, K.; Yuan, J.; Li, H.; Feng, Z. Effect of different fibers on impermeability of steam cured recycled concrete. *Constr. Build. Mater.* **2022**, *328*, 127063. [CrossRef]
53. Li, S.; Yin, S.; Gao, Y. Analysis of interface properties between TRC and concrete under chloride attack based on fracture energy. *Int. J. Concr. Struct. Mater.* **2020**, *14*, 28. [CrossRef]
54. Xiao, Q.; Wu, Z.; Qiu, J.; Dong, Z.; Shi, S. Capillary water absorption performance and damage constitutive model of recycled concrete under freeze-thaw action. *Constr. Build. Mater.* **2022**, *353*, 129120. [CrossRef]
55. Valenza, J.J.; Scherer, G.W. A review of salt scaling: II. Mechanisms. *Cem. Concr. Res.* **2007**, *37*, 1022–1034. [CrossRef]
56. Gong, S.; Bai, L.; Tan, Z.; Xu, L.; Bai, X.; Huang, Z. Mechanical properties of polypropylene fiber recycled brick aggregate concrete and its influencing factors by gray correlation analysis. *Sustainability* **2023**, *15*, 11135. [CrossRef]
57. Xu, F.; Li, T.; Li, C.; Li, Z.; Wang, S.; Zhao, N. Compressive behavior, microstructural properties, and freeze-thaw behavior of tailing recycled aggregate concrete with waste polypropylene fiber addition. *Materials* **2021**, *14*, 6712. [CrossRef]
58. Dong, W.; Ji, Y.; Zhou, M. Microstructure and service-life prediction models of aeolian sand concrete under freeze-thaw damage. *Int. J. Pavement Res. Technol.* **2024**, *17*, 908–917. [CrossRef]
59. Wiyanto, H.; Makarim, C.A.; Gondokusumo, O.; Siregar, J.P.; Irawan, A.P.; Cionita, T.; Najid, N. Determining concrete structure condition rating based on concrete compressive strength. *Buildings* **2022**, *12*, 776. [CrossRef]
60. Ma, S.; Wu, Y.; Bao, P. Study on damage mechanism and residual life of clay brick in central plains of China under freeze-thaw environment. *Arab. J. Sci. Eng.* **2022**, *47*, 13317–13331. [CrossRef]

61. Liu, Y.; Yuan, N.; Xu, H.; Yang, Q. Evaluation of ZIF-67 particle size and dosage on cement paste strength, microstructural development and calcium hydroxide morphology. *Powder Technol.* **2025**, *464*, 121271. [CrossRef]
62. Liu, H.; Liu, C.; Wu, J.; Gao, Y.; Shao, J.; Wang, C.; Su, T.; Cao, F.; Zhang, W.; Yang, Q.; et al. Preparation of high-belite calcium sulfoaluminate cement and calcium sulfoaluminate cement from industrial solid waste: A Review. *Sustainability* **2025**, *17*, 4269. [CrossRef]
63. Yuan, Z.; Jia, Y. Mechanical properties and microstructure of glass fiber and polypropylene fiber reinforced concrete: An experimental study. *Constr. Build. Mater.* **2021**, *266*, 121048. [CrossRef]
64. Tang, Z.; He, X.; Wei, B.; Wang, H.; Zhou, M.; Wu, C. Flexural capacity of concrete beams reinforced by different types of polypropylene fibers and FRP bars. *J. Build. Eng.* **2025**, *106*, 112650. [CrossRef]
65. Wu, J.; Liu, K.; Wang, S.; Quan, X.; Tian, P.; Tian, Z.; Ying, H. Evaluation of hybrid steel-polyethylene fiber-reinforced aggregated solid waste cementitious composites subjected to seawater freeze-thaw cycles attack: Durability, 3D pore structure, and microstructure. *Constr. Build. Mater.* **2025**, *493*, 143069. [CrossRef]
66. Huang, D.; Wang, X.; Li, X.; Su, L.; Tian, J. Advanced nuclear magnetic resonance technology analysis of hybrid fiber reinforced concrete for optimized pore structure and strength. *Constr. Build. Mater.* **2025**, *467*, 140383. [CrossRef]
67. Gokce, A.; Nagataki, S.; Saeki, T.; Hisada, M. Freezing and thawing resistance of air-entrained concrete incorporating recycled coarse aggregate: The role of air content in demolished concrete. *Cem. Concr. Res.* **2004**, *34*, 799–806. [CrossRef]
68. Fu, K.; Sang, Y.; Chen, C.; Liu, K. Frost resistance of recycled aggregate concrete subjected to coupling sustained compressive load and freeze-thaw cycles. *Constr. Build. Mater.* **2024**, *448*, 138219. [CrossRef]
69. Liang, N.; Geng, S.; Mao, J.; Liu, X.; Zhou, X. Investigation on cracking resistance mechanism of basalt-polypropylene fiber reinforced concrete based on SEM test. *Constr. Build. Mater.* **2024**, *411*, 134102. [CrossRef]
70. Liang, N.; You, X.; Yan, R.; Miao, Q.; Liu, X. Experimental investigation on the mechanical properties of polypropylene hybrid fiber-reinforced roller-compacted concrete pavements. *Int. J. Concr. Struct. Mater.* **2022**, *16*, 3. [CrossRef]

Disclaimer/Publisher's Note: The statements, opinions and data contained in all publications are solely those of the individual author(s) and contributor(s) and not of MDPI and/or the editor(s). MDPI and/or the editor(s) disclaim responsibility for any injury to people or property resulting from any ideas, methods, instructions or products referred to in the content.

coatings

MDPI

Article

Effect of Y_2O_3 Particle Size on the Microstructure and Properties of Ni-Co-Y_2O_3 Composite Coatings

Linxin Qi [1], Hongmin Kan [1,2,*], Tingting Yue [1] and Jiang Wu [1]

[1] School of Mechanical Engineering, Shenyang University, Shenyang 110044, China; qilinxin1005@163.com (L.Q.); 13399506895@163.com (T.Y.); 15242606273@163.com (J.W.)
[2] Key Laboratory of Research and Application of Multiple Hard Films of Liaoning Province, Shenyang University, Shenyang 110044, China
* Correspondence: kanhongmin2002@163.com

Abstract

In this study, Ni-Co-Y_2O_3 composite coating was prepared by electrodeposition, and the effect of Y_2O_3 particle size on the microstructure and properties of the coating was investigated. The samples were analyzed by XRD, SEM, AFM, EDS, cyclic voltammetry, XPS, hardness, and corrosion resistance test. The results indicate that the diffraction peak of the coating prepared with 50 nm particles exhibits reduced intensity and broadening, whereas the coating prepared with 100 nm particles displays a sharper and more pronounced peak. The onset reduction potential and the performance of the reduction reaction are influenced by particle size. When the particle size is 50 nm, the reduction process is less favorable, with an onset reduction potential of −0.9 V; in contrast, when the particle size is 100 nm, the reduction occurs more readily, with an onset reduction potential of −0.8 V. XPS analysis reveals that the chemical environment of elements varies with particle size. Regarding hardness, the coating prepared by combining different Y_2O_3 particle sizes exhibits higher hardness compared to that prepared using a single particle size, which can be attributed to the synergistic effect. In terms of corrosion resistance, the coating prepared with 100 nm Y_2O_3 particles demonstrates superior corrosion resistance, whereas the coating prepared with mixed particle sizes shows reduced stability and is more susceptible to corrosion. The coating prepared by mixing Y_2O_3 with particle size of 50 nm and 100 nm has a small friction coefficient. In summary, the particle size of Y_2O_3 has a significant influence on the microstructure, hardness, and corrosion resistance of Ni-Co-Y_2O_3 composite coatings.

Keywords: electrodeposition; Ni-Co-Y_2O_3 composite coating; Y_2O_3 particle size; hardness; corrosion resistance

1. Introduction

In the field of modern materials science, surface engineering technologies are rapidly advancing. As a key approach to surface modification, composite coatings have attracted extensive attention and have been the subject of in-depth research. Composite coatings prepared by electrodeposition exhibit smooth surface morphology, strong adhesion to various substrates, high hardness, excellent oxidation resistance, and superior corrosion resistance. These properties enable them to demonstrate broad application potential across multiple industrial sectors, including aerospace, automotive manufacturing, and electronic equipment [1–7].

Among them, Ni-Co coatings offer advantages such as high hardness, excellent wear resistance, and superior corrosion resistance, and have been widely applied across various

industries. Cobalt atoms in the Ni-Co alloy coating substitute for nickel atoms in the lattice, causing lattice distortion and increasing the number of grain boundaries. Co addition refines the grain size and enhances the compactness of the composite coating. Consequently, the corrosion resistance and high-temperature stability of the composite coating are significantly improved compared to pure Ni coatings. Moreover, the Ni-Co structure exhibits hydrogen evolution catalytic activity [8–11]. However, the demand for enhanced performance to meet increasingly challenging applications has driven researchers to explore novel strategies for improving its properties. To enhance the performance of nickel-based coatings under harsh conditions, various types of ceramic reinforcement particles have been incorporated, including SiC [12], Y_2O_3 [13], SiO_2 [14], ZrO_2 [15], Al_2O_3 [16], WC [17], CNTs [18], CeO_2 [19], and MoS_2 [20].

Among these nanoparticles, Y_2O_3 serves as an additive in ceramic materials and can improve the grain boundary structure of ceramics, promoting uniform grain growth and thereby enhancing mechanical properties such as hardness, toughness, and wear resistance. Y_2O_3 offers multiple advantages in composite coatings. As a rare earth element compound, Y_2O_3 enhances the adhesion of oxide films and inhibits elemental interdiffusion through grain boundary segregation. Y_2O_3 promotes the formation of a protective oxide film, improves compactness, and exhibits excellent hot corrosion resistance, particularly in environments containing sulfur or salt fog [10]. Additionally, Y_2O_3 can act as a heterogeneous nucleation site during electrodeposition, refining grains and reducing electrochemical resistance more effectively than Al_2O_3 [16]. By refining the microstructure and reducing the number of active sites for corrosion microcells, Y_2O_3 significantly enhances corrosion resistance across various environments. In contrast, Al_2O_3 can lead to localized porosity, while SiO_2 may dissolve in acidic conditions [14]. Moreover, Y_2O_3 possesses a high melting point, excellent high-temperature phase stability, and strong chemical inertness. In comparison, Al_2O_3 nanoparticles tend to agglomerate, and SiO_2 may undergo phase transformations or form volatile oxides at elevated temperatures. As hard particles, Y_2O_3 has advantages over MoS_2 in enhancing hardness [20].

In addition, Y_2O_3 is also widely used in the fabrication of high-temperature transparent ceramics, electronic ceramics, and structural ceramics. When incorporated into Ni-Co alloy coatings, Y_2O_3 can inhibit grain growth during the deposition process, promoting grain refinement and an increase in grain boundary area. This facilitates the formation of a new phase structure in the Ni-Co alloy, which hinders dislocation movement, thereby improving coating hardness and enhancing resistance to deformation [21–24].

Y. J. Xue et al. [25] electrodeposited a Ni-Y_2O_3 nanocomposite coating from a nickel sulfamate solution containing Y_2O_3 particles. The results showed that, compared with the pure Ni coating, the Ni-Y_2O_3 nanocomposite coating exhibited finer grains and enhanced corrosion resistance. Furthermore, the Ni-Y_2O_3 nanocomposite coating prepared under ultrasonic conditions displayed a denser microstructure, finer grains, and superior corrosion resistance. Xiaofang Yi et al. [26] prepared both Ni-Co composite coatings and Ni-Co-Y_2O_3 composite coatings via electrodeposition. The results indicate that the Ni-Co-Y_2O_3 composite coating exhibits higher electrocatalytic activity for the hydrogen evolution reaction compared to the Ni-Co composite coating. Y. B. Zhou [27] prepared a Ni-Y_2O_3 composite coating through the co-deposition of Ni and Y_2O_3 particles. Compared with the electrodeposited pure Ni coating, the Ni-Y_2O_3 composite coating exhibits superior corrosion resistance and alters the oxidation growth mechanism of nickel. Tian et al. [28] co-deposited nano-Y_2O_3 particles and Ni from a plating solution via electroplating to fabricate a Ni-Y_2O_3 composite coating. As the Y_2O_3 concentration increased from 20 g/L to 80 g/L, the Y_2O_3 content in the coating rose from 1.56% to 4.4%. The co-deposition of Y_2O_3 reduced the friction coefficient and wear weight loss. Under the experimental conditions,

the coating exhibited optimal microhardness and tribological properties when the Y_2O_3 content reached 4.4%.

The performance of the coating is largely determined by its microstructure, and the particle size of the reinforcing phase is also a key influencing factor. So far, numerous studies have been conducted on Ni-Co coatings and Ni-Y_2O_3 composite coatings. However, limited research has focused on the influence of Y_2O_3 particle size on the microstructure and properties of the coating. Y_2O_3 particles of different sizes exhibit variations in specific surface area, surface energy, and reactivity, which directly affect their dispersion behavior in the plating solution. Meanwhile, the incorporation of particles with different sizes can alter the internal stress distribution and surface roughness of the coating, thereby influencing its overall performance. Smaller particles are more readily dispersed in the electrolyte through mechanical stirring or ultrasonic treatment, which helps reduce coating defects. However, if the particle size is excessively small, surface energy increases significantly, leading to particle agglomeration and the formation of micron-sized aggregates, which compromises coating uniformity. Conversely, excessively large particles may cause stress concentration at the coating–substrate interface, potentially resulting in delamination or spalling. Therefore, in this paper, Ni-Co-Y_2O_3 composite coatings were prepared by incorporating Y_2O_3 particles with individual particle sizes of 50 nm and 100 nm, as well as a 1:1 mixture of both sizes. The microstructure, surface properties, and electrochemical properties of the three types of Ni-Co-Y_2O_3 composite coatings were systematically analyzed using XPS, AFM, and electrochemical techniques. The influence of Y_2O_3 particle size on the microstructure and performance of the Ni-Co-Y_2O_3 composite coatings was investigated.

2. Preparation and Characterization

Ni-Co-Y_2O_3 composite coatings were prepared using an electrodeposition technique, with a copper sheet serving as the cathode substrate. The preparation steps and deposition process are illustrated in Figure 1. A 99% pure nickel sheet was utilized as the anode, maintaining a distance of 2 cm between the cathode and anode. The electrolyte composition and operating conditions for the preparation of Ni-Co-Y_2O_3 coatings are detailed in Table 1. Y_2O_3 nanoparticles were homogeneously dispersed in the solution through rotor agitation using a magnetic stirrer (DF-101S Suzhou Weier Laboratory Supplies Co., Ltd., Suzhou, China). The copper substrate was polished sequentially with 600#, 1200#, and 1500# sandpaper, followed by cleaning with deionized water after alkaline and acid washing treatments. Subsequently, the substrate was dried and set aside. This pretreatment process effectively enhances the adhesion strength between the coating and the substrate. After pretreatment, the samples were immersed in the solution for electrodeposition to prepare the Ni-Co-Y_2O_3 coating. The manufacturer of Y_2O_3 is Epure, with a purity of $\geq$ 99.9%. Mixed particle size group: 50 nm and 100 nm Y_2O_3 particles were pre-mixed in a 1:1 mass ratio, then ultrasonically dispersed to form a uniform mixed suspension. The suspension was added to the electrolyte at the same total concentration as the single particle size group, and the particles were kept in suspension in the electrolyte by magnetic stirring. The electrodeposition duration was 75 min, after which the prepared samples were rinsed with distilled water and dried using an air blower.



Figure 1. Electrodeposition coating process diagram.

Table 1. Process conditions of electrodeposition coating preparation.

Electrolyte Components	Concentration (g/L)
$NiSO_4 \cdot 7H_2O$	300
$NiCl_2 \cdot 6H_2O$	80
$CoSO_4 \cdot 7H_2O$	15
H_3BO_3	40
SDS	4
Y_2O_3 (50 nm)	6
Y_2O_3 (100 nm)	6
Y_2O_3 (50 nm and 100 nm mixed)	6
Deposition parameters	Amount
Solution pH	4.3
Temperature (°C)	55
Current density (A/dm^2)	4
Magnetic agitation rate (rpm)	350
Electrodeposition cell voltage (V)	1.1
Deposition time (minute)	75
Bath volume (mL)	100
Y_2O_3 particle size	50 nm; 100 nm

The surface morphology of the Ni-Co-Y_2O_3 composite coatings was investigated using a Hitachi S4800 scanning electron microscope (SEM; Hitachi, Tokyo, Japan). An energy dispersive X-ray detector (EDS; Oxford, UK) coupled with the SEM was employed to determine the chemical composition and Y_2O_3 content of the coating. The impact of varying particle sizes on the surface roughness of the deposited nanocoatings was assessed using atomic force microscopy (AFM; Dimension Icon). Additionally, the influence of different particle sizes on the phase structure of the deposited nanocoatings was analyzed using X-ray diffraction (XRD; D8 Advance; the ceramic closed tube is the core, and the Cu target is standard. Japanese scientific instrument manufacturers, Japan). The effect of particle size on the chemical composition of the deposited nanocoatings was further evaluated using X-ray photoelectron spectroscopy (XPS; Thermo Escalab 250 Xi). Vickers microhardness measurements were conducted using a 402 MVD hardometer (Shanghai Takezu Analytical Instruments Co., Ltd., Shanghai, China). The hardness test conditions included an objective lens magnification of 40×, a brightness value of 100, a loading pressure of 100 g held for 15 s, and the final hardness value of the composite coating was calculated as the average of five measurements. Electrochemical experiments were conducted using a three-electrode cell at the IVIUM electrochemical workstation (Ivium Technologies, Eindhoven, The Netherlands). The platinum wire (1 mm in diameter) was connected as the working electrode (WE), with 1 cm × 1 cm platinum plate as the counter electrode (CE) and saturated calomel electrode as the reference electrode (RE). Cyclic voltammograms were recorded at a potential scanning rate of 5 mV/s, with test voltages ranging from −2.5 V to 1.5 V and a step size of 10 mV. The corrosion resistance of the composite coatings was evaluated using both the polarization curve method and the AC impedance method. The AC impedance tests were performed in a 3.5% NaCl corrosive medium over a frequency range of 0.01 Hz to 100,000 Hz, maintaining a scanning rate of 5 mV/s. The polarization curves were scanned from potentials of −0.8 V to 0.2 V, while the remaining parameters were consistent with those described above.

3. Results and Discussion

3.1. Cyclic Voltammetry Tests

Figure 2 shows the cyclic voltammetry curves of three Ni-Co-Y_2O_3 composite coatings. The reduction potential of Ni-Co-Y_2O_3 (50 nm) coating is −0.9 V. The Y_2O_3 particles with a

50 nm particle size are smaller, reducing the effective reaction area, thereby increasing the resistance of electron transfer, resulting in the reduction reaction requiring a more negative potential to drive. In addition, particle agglomeration restricts the diffusion of reactant ions (Ni^{2+}, Co^{2+}), further increasing reaction resistance. The negative reduction potential (−0.9 V) indicates that the reduction reaction is more difficult and that the deposition process demands higher energy input. In contrast, the reduction potential of the Ni-Co-Y_2O_3 (100 nm) coating is −0.8 V. The larger Y_2O_3 particles at this size enhance the effective reaction area and facilitate electron conduction, thereby reducing electron transfer resistance. The increased particle spacing also improves the diffusion of reactants and mitigates diffusion limitations [29].

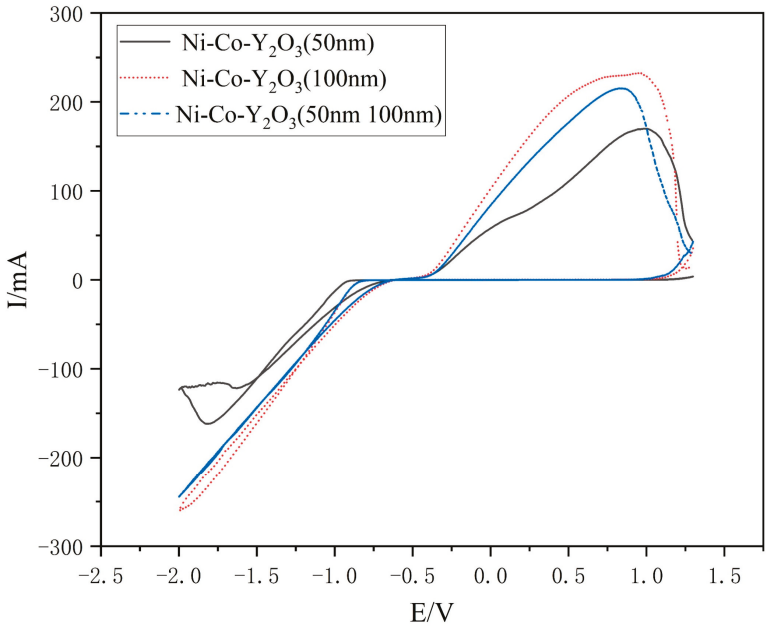

Figure 2. Cyclic voltammograms of electrolytes with different particle sizes.

3.2. Phase Analysis

Figure 3 shows the XRD patterns of Ni-Co-Y_2O_3 composite coatings (50 nm, 100 nm, and 50 nm and 100 nm mixed) prepared by different particle sizes of Y_2O_3, and analyzes the crystal structure characteristics of the coating. The XRD pattern of the Ni-Co-Y_2O_3 composite coating was presented by comparing the diffraction peaks of the coating with the standard diffraction peaks compiled by the Joint Committee on Powder Diffraction Standards (JCPDS). The diffraction peaks corresponding to Ni, Co, and Y_2O_3 could be identified in the composite coating. The XRD pattern reflects the phase composition and crystal structure of the material by measuring the X-ray diffraction intensity at different 2θ angles. There is a weak peak between 40° and 45°, which corresponds to the diffraction peak of Y_2O_3. Moreover, there are phases formed by Ni and Co in the coating, and Y_2O_3 particles are successfully compounded. Compared with Ni-Co-Y_2O_3 (50 nm) coating, the change of Co/Ni peak position and strength may be caused by the change of stress state and crystal growth direction caused by the increase in coating thickness, which also indicates that Y_2O_3 is successfully compounded.

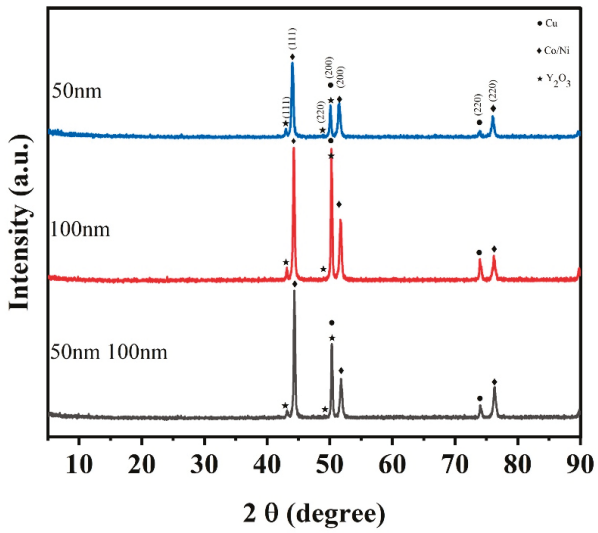

Figure 3. XRD patterns of coatings prepared by Y_2O_3 with different particle sizes.

3.3. XPS Analysis

The spectral peak characteristics of Ni, Co, and Y elements in the coatings were systematically investigated and compared. Figure 4 presents the XPS survey spectrum of the composite coating. Figure 5 shows the XPS detection diagrams of the coatings prepared with 50 nm and 100 nm. Table 2 presents the content of each element. In the Ni 2p spectrum, the Ni $2p_{3/2}$ peaks for the Ni-Co-Y_2O_3 (50 nm) coating were observed at 852.83 eV and 873.35 eV, whereas those for the Ni-Co-Y_2O_3 (100 nm) coating were located at 851.93 eV and 873.06 eV, indicating a shift towards lower binding energy by approximately 0.9 eV. The peak intensity of the Ni-Co-Y_2O_3 (100 nm) coating is significantly higher, suggesting modifications in the chemical environment of Ni, variations in its relative content, or alterations in surface enrichment. The Co $2p_{3/2}$ peaks are observed at 779.94 eV and 795.68 eV in (a), and at 780.57 eV and 796.09 eV in (b). These peaks exhibit a shift towards lower binding energy, accompanied by an increase in peak intensity, which indicates changes in the valence state, content, or surface distribution of Co. The Y $3d_{5/2}$ peak is located at 158.03 eV in (a) and shifts to 158.21 eV in (b), corresponding to a shift towards higher binding energy by approximately 0.18 eV. Additionally, the peak intensity is enhanced, implying modifications in the chemical environment of Y, variations in its relative content, or an increase in surface distribution density [30,31].

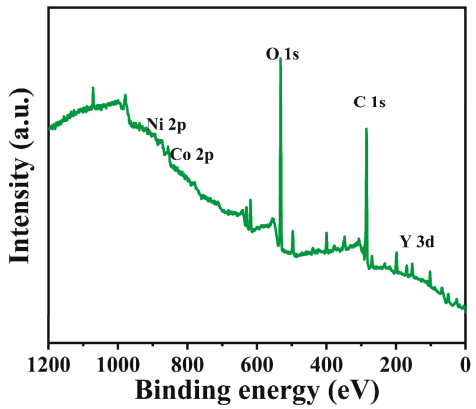

Figure 4. XPS survey spectrum of the composite coating.

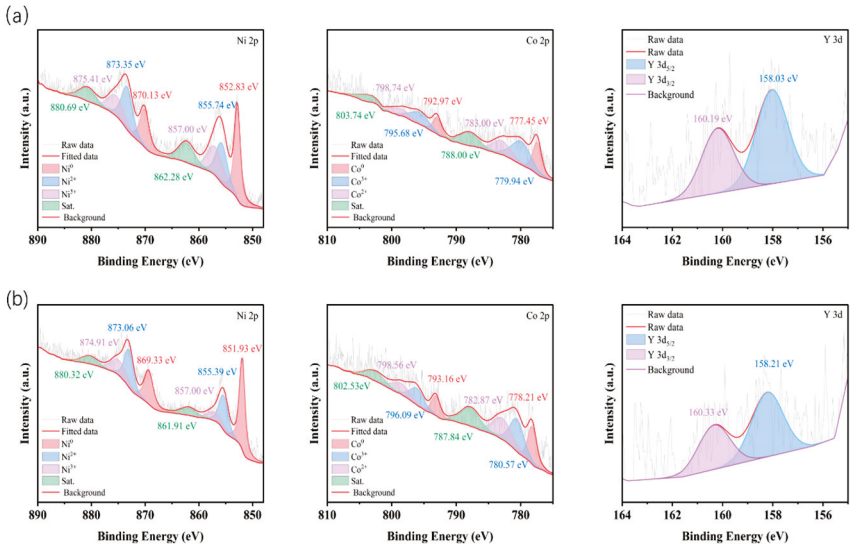

Figure 5. XPS test of composite coatings: (**a**) 50 nm Y_2O_3, (**b**) 100 nm Y_2O_3.

Table 2. The content of each element.

Sample	Y 3d	C 1s	O 1s	Co 2p	Ni 2p
50 nm	0.75	69.9	27	0.73	1.63
100 nm	0.98	64.42	31.07	1.07	2.47
mixed	1.81	56.14	34.25	1.87	5.92

As illustrated in Figure 6, in the Ni 2p spectrum, the Ni $2p_{3/2}$ peak is observed at approximately 852.32 eV and 872.44 eV, exhibiting a relatively weak intensity. A peak potentially associated with metallic nickel (Ni^0) may be present at lower binding energies, indicating a low content of metallic Ni in the coating. The peak at 869.50 eV is potentially associated with Ni^+, indicating that nickel in the coating exhibits multiple oxidation states. In the Co 2p spectrum, the Co $2p_{3/2}$ peak is observed at approximately 779 eV and 795 eV, with the peak at 778–780 eV being correlated with Co^{2+}. The broadened peak suggests that cobalt exists in multiple chemical states or distinct crystal structures. During the growth of the coating, Co forms alloys or compounds with Ni and Y, leading to changes in the electronic structure, which are manifested as broad peaks in the XPS spectrum. In the Y 3d spectrum, the Y $3d_{5/2}$ peak is located near 158.40 eV and 160.48 eV, corresponding to Y^{3+} in Y_2O_3. The mixture of Y_2O_3 particles with sizes of 50 nm and 100 nm results in the broadening or shifting of the Y binding energy, and the variations in the local chemical environment of Y influence its distribution and chemical state.

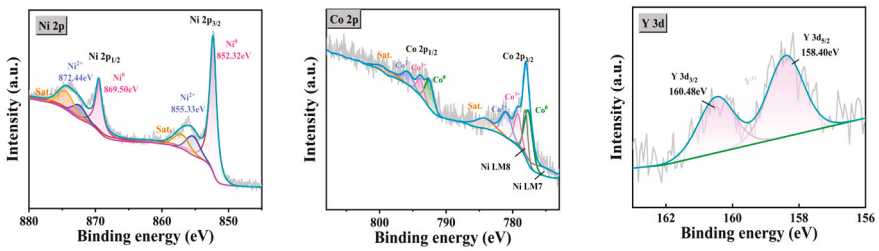

Figure 6. XPS test of Ni-Co-Y_2O_3 (50 nm and 100 nm mixed) coatings.

3.4. Microstructure of the Plated Layer

Figure 7 shows the cross-sectional morphology of the coatings prepared with different particle sizes and mixed particle sizes. The thickness of the coating was 38 μm, 32 μm, and 33 μm, respectively. Figure 8 shows the surface morphology of the coatings prepared

with different particle sizes and mixed particle sizes. At a magnification of 2000× and 5000×, the Ni-Co-Y_2O_3 (100 nm) coating exhibits uniformly distributed surface particles with consistent spacing, indicating that the nanoparticles were well dispersed during the deposition process. The EDS spectrum reveals that the coating primarily consists of Ni, Co, and Y elements, with Ni and Co present in higher concentrations and Y in a relatively lower amount. Since EDS cannot distinguish between nanoparticles of different sizes, only the total Y content can be determined. The Y content in the three composite coatings is 1.3 wt%, 1.4 wt%, and 1.7 wt%, respectively. These results demonstrate that during the electroplating process, metal ions and nanoparticles were uniformly deposited onto the substrate surface, and Y_2O_3 nanoparticles participated stably in the deposition reaction without significant agglomeration or loss.

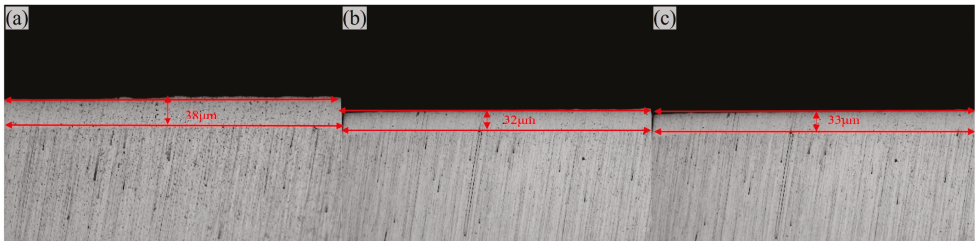

Figure 7. Sections of the three coatings: (**a**) 50 nm Y_2O_3, (**b**) 100 nm Y_2O_3, (**c**) 50 nm and 100 nm Y_2O_3 mixture.

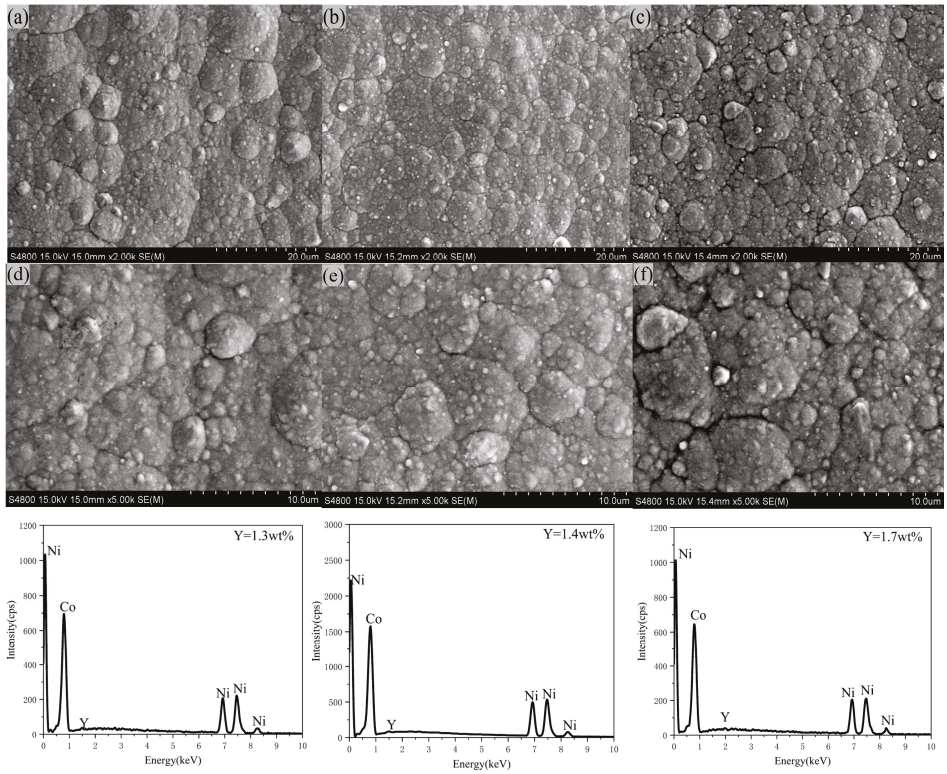

Figure 8. SEM and EDS analysis of the three coatings: (**a**,**d**) 50 nm Y_2O_3, (**b**,**e**) 100 nm Y_2O_3, (**c**,**f**) 50 nm and 100 nm Y_2O_3 mixture.

Figure 9 is the AFM image of the composite coating. From the 3D image, the surface of Ni-Co-Y_2O_3 (50 nm) coating shows more peak–valley structures, and the height difference is relatively large. This may be due to the formation of relatively dense and irregular accumulation of 50 nm particles during the coating process. The surface of Ni-Co-Y_2O_3 (100 nm) coating is relatively flat, the peak–valley structure is relatively small and the

height difference is small. The peak–valley structure on the surface of Ni-Co-Y_2O_3 (50 nm and 100 nm mixed) coating is very significant, and the height difference is also very large. This may be due to the complex microstructure formed by the mixing of 50 nm and 100 nm particles, and the interaction of particles with different sizes.

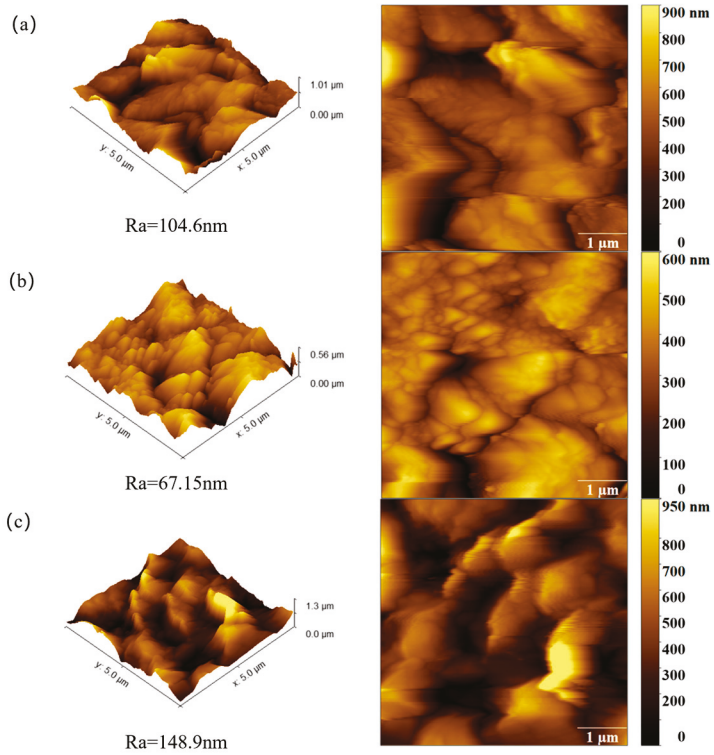

Figure 9. AFM images of composite coatings: (**a**) 50 nm Y_2O_3, (**b**) 100 nm Y_2O_3, (**c**) 50 nm and 100 nm Y_2O_3 mixture.

3.5. Hardness Analysis

Figure 10 is the hardness analysis histogram. Table 3 presents the hardness measurement data of the composite coating. It can be observed from the chart that the hardness of the Ni-Co-Y_2O_3 (50 nm and 100 nm mixed) coating is significantly higher than that of the other two coatings. In the Ni-Co-Y_2O_3 (50 nm) composite coating, the relatively small nanoparticle size leads to a higher proportion of grain boundaries. An excessive number of grain boundaries can impede dislocation movement, thereby increasing the hardness to some extent. When the nanoparticle size increases to 100 nm, a more favorable microstructure may form. This results in reduced local stress concentration and improved overall load-bearing capacity and hardness. The coating prepared with a mixture of particle sizes contains a larger number of 50 nm particles per unit volume, which can more effectively pin dislocation movement, hinder lattice slip, and provide high-frequency short-range obstacles [32]. During the electrodeposition process, 50 nm particles inhibit the local migration of grain boundaries, while 100 nm particles hinder the movement of large-scale grain boundaries. Under this synergistic effect, the grain structure is significantly refined [33]. From the perspective of nanoparticle synergy, the 50 nm particles effectively impede dislocation movement due to their small size, thereby enhancing grain boundary strengthening. Meanwhile, the 100 nm particles may improve stress distribution over a larger scale, enhance load transfer capability, and thus synergistically improve the overall hardness of the coating [34–36]. Tables 4 and 5 present comparative data graphs for hardness. The hardness of Ni-Co-Y_2O_3 (50 nm and 100 nm mixed) coating is significantly higher than that of the coating prepared by Lin Shengnan [36].

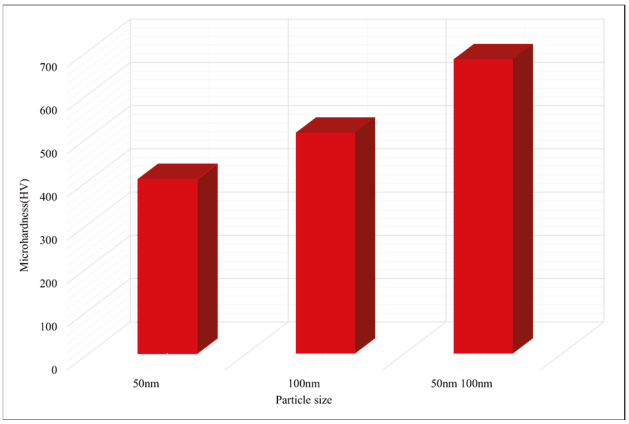

Figure 10. Histogram of hardness analysis of three composite coatings.

Table 3. Hardness measurement results data of composite coatings.

Sample	1 Hardness (HV)	2 Hardness (HV)	3 Hardness (HV)	4 Hardness (HV)	5 Hardness (HV)
50 nm	400.7	402.5	404.1	406.3	400.4
100 nm	509.2	510.4	511.3	511.3	510.0
mixed	675.8	679.2	683.5	687.1	675.9

Table 4. Comparison table of hardness data.

Y_2O_3 (size)	50 nm	50 nm	100 nm	mixed
Hardness (HV)	538.85 [36]	402.8	510.6	680.3

Table 5. Hardness data statistics chart.

Statistics	Error Bars	Standard Deviation	Statistical Significance
50 nm	1.10	2.46	$p < 0.0001$
100 nm	0.505	1.13	$p < 0.001$
mixed	2.21	4.93	$p < 0.0001$

3.6. Corrosion Resistance Analysis

Figure 11 shows the polarization curves of the three coatings. Table 6 presents the parameters of the polarization curve. Table 7 is the statistical table of corrosion results. Among them, the corrosion current density of Ni-Co-Y_2O_3 (100 nm) coating is relatively low and lower than the other two, the corrosion rate is slow and the corrosion resistance is good. The corrosion potential of the coating is relatively positive, which means that the coating is less prone to oxidation reaction in the corrosion system. The corrosion current density of Ni-Co-Y_2O_3 (50 nm and100 nm mixed) coating is relatively high, and the corrosion potential is relatively negative, which means that the coating is more prone to oxidation in the corrosion system, in a more unstable state, and more susceptible to corrosion [37,38].

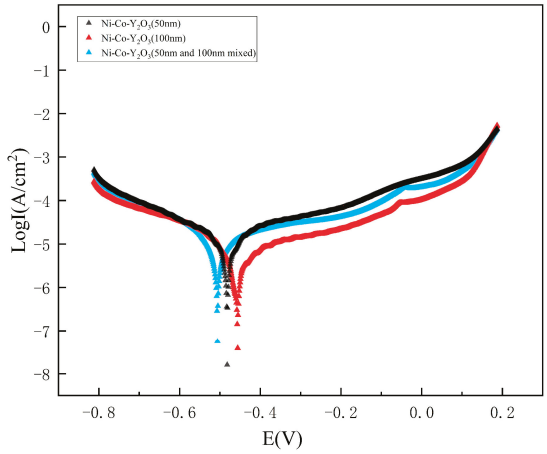

Figure 11. Polarization curves of three Ni-Co-Y_2O_3 coatings.

Table 6. Polarization curve parameter table.

Samples	Ecorr (V)	Icorr (A/cm^2)	β_a (V/dec)	$-\beta_c$ (V/dec)	Corrosion Rate (mm/y)
50 nm	−0.48	2.036×10^{-5}	82.4	96.4	0.0137
100 nm	−0.46	8.719×10^{-6}	63.5	82.6	0.0091
mixed	−0.51	2.381×10^{-5}	75.9	90.7	0.0106

Table 7. Statistical table of corrosion results.

Statistics	Error Bars	Standard Deviation
data	0.0146	0.0252

Figure 12 presents the Nyquist plots of the three coatings. As shown in the diagram, the Ni-Co-Y_2O_3 (100 nm) coating exhibits a high charge transfer resistance, indicating that the electron transfer between the coating and the corrosive medium is significantly hindered, thereby effectively suppressing the corrosion reaction. This suggests that the Ni-Co-Y_2O_3 (100 nm) coating can efficiently prevent the electrochemical interaction between ions in the corrosive medium and the metallic components of the coating, thus enhancing its corrosion resistance. In contrast, the Ni-Co-Y_2O_3 (50 nm and 100 nm mixed) coating shows a lower charge transfer resistance in the Nyquist plot. During the corrosion process, electrons are more readily transferred between the coating and the corrosive medium, facilitating the corrosion reaction and resulting in relatively weaker corrosion resistance. When 50 nm and 100 nm Y_2O_3 particles are combined to prepare the coating, the significant difference in particle size makes it difficult to form a uniform microstructure during deposition. In a corrosive environment, the aggressive medium is more likely to penetrate through these non-uniform interfaces and structural defects, reaching the substrate surface and initiating a corrosion reaction.

Figure 13 presents the Bode plots of the three coatings. The Ni-Co-Y_2O_3 (100 nm) coating exhibits a large phase angle in the low-frequency region. A larger phase angle indicates stronger capacitive behavior, suggesting that the coating possesses significant capacitance characteristics. During the corrosion process, these characteristics can function similarly to a capacitor by storing and releasing charges, thereby suppressing the initiation of corrosion reactions. According to Table 8, the charge transfer resistance (Rct) of the Ni-Co-Y_2O_3 (100 nm) coating is 16,050 Ω, which is considerably higher than that of the other two coatings. This further supports the conclusion drawn from the Nyquist diagram—that a higher charge transfer resistance effectively inhibits the corrosion reaction. In contrast,

the Ni-Co-Y_2O_3 (50 nm and 100 nm mixed) coating shows a relatively small phase angle in the low-frequency region, indicating weaker capacitance characteristics and a higher susceptibility to corrosion.

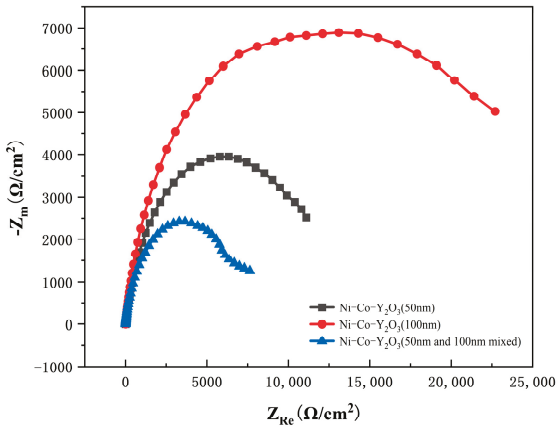

Figure 12. Impedance curves of three Ni-Co-Y_2O_3 coatings.

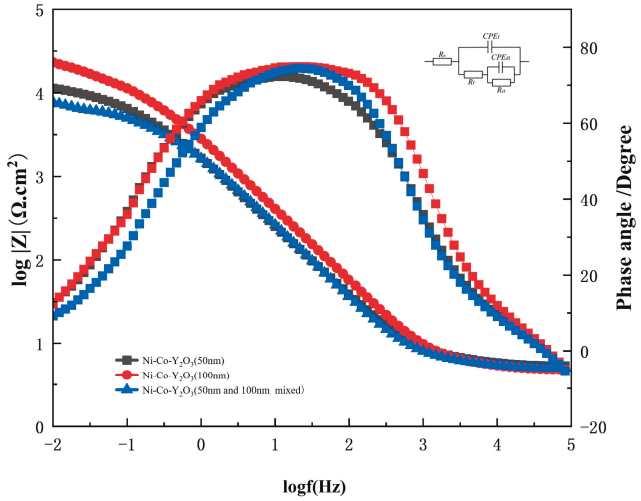

Figure 13. Bode plots of three Ni-Co-Y_2O_3 coatings.

Table 8. Electrochemical analysis data.

Samples	R_S (Ω)	CPE_f (μF.cm^{-2})	R_f (Ω)	CPE_{dl} (μF.cm^{-2})	Rct (Ω)	χ^2
50 nm	5.587	128.2	4163	292.3	4286	≈0.002
100 nm	5.061	67.47	8620	387	16050	≈0.004
mixed	5.297	106.2	3213	130.8	9458	≈0.005

3.7. Frictional Wear

Figure 14 shows the friction and wear diagram of the three composite coatings. As shown in Figure 14, when the 50 nm and 100 nm Y_2O_3 particles are mixed, the prepared coating has a smaller friction coefficient. On the one hand, the surface microstructure is optimized. Small particles fill the gap of large particles to make the surface smoother and reduce the occlusion of surface protrusions during friction. As the strengthening phase, Y_2O_3 particles with different particle sizes work together to form a more effective strengthening network inside the coating. The larger particles provide a larger support skeleton, while the smaller particles hinder the movement of dislocations, making it more difficult for the coating material to deform plastically. At the same time, the particles with

different particle sizes are evenly distributed in the Ni-Co matrix and support each other to form a denser structure. As a strengthening phase, the microstructure is refined and the dislocation movement is hindered by the synergistic effect, which makes the coating more difficult to deform and have higher hardness.

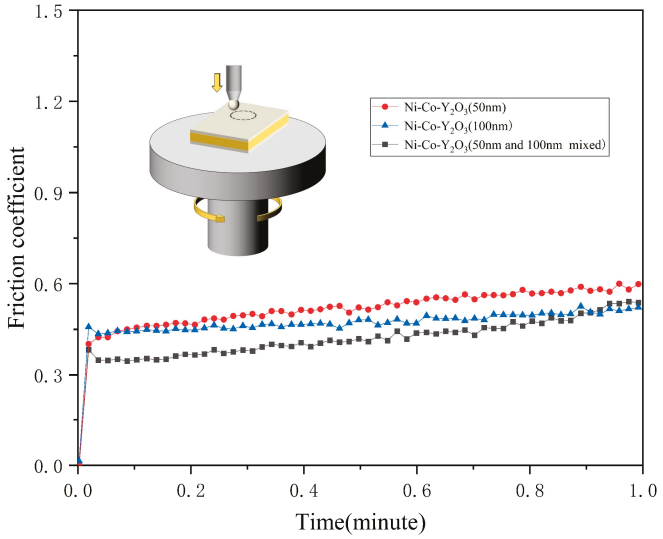

Figure 14. Friction and wear diagram of composite coating.

4. Conclusions

Ni-Co-Y_2O_3 composite coatings were successfully prepared by electrodeposition. The effects of Y_2O_3 particle size on the microstructure and properties of Ni-Co-Y_2O_3 coating were studied.

1. The particle size of Y_2O_3 has a significant influence on the reduction potential of the coating. XPS analysis reveals that the chemical environment of the elements changes with increasing particle size. Hardness testing indicates that the Ni-Co-Y_2O_3 (50 nm and 100 nm mixed) coating benefits from the synergistic effect between large and small particles, which effectively hinders dislocation movement and optimizes load transfer. As a result, its hardness is higher than that of coatings with a single particle size.
2. The Ni-Co-Y_2O_3 (50 nm and 100 nm mixed) coating showed poor stability and was prone to corrosion through the corrosion resistance test, and the particle adhesion was weak. The coating prepared by mixing Y_2O_3 with particles of 50 nm and 100 nm in size had a smaller friction coefficient.

Author Contributions: Data curation, investigation, writing—original draft, L.Q.; supervision, H.K.; investigation, T.Y.; writing—original draft preparation, J.W. All authors have read and agreed to the published version of the manuscript.

Funding: This research was funded by Applied Basic Research Program of Liaoning Provincial Department of Science and Technology of China, grant Number 2025JH2/101300035.

Institutional Review Board Statement: Not applicable.

Informed Consent Statement: Not applicable.

Data Availability Statement: All data that support the findings of this study are included within the article.

Conflicts of Interest: The authors declare no conflict of interest.

References

1. Bakonyi, I.; Hansal, W.E.G. Development of pulse-plating technology for the preparation of coatings with varying composition along their thickness: A historical overview. *Trans. IMF* **2018**, *96*, 237–243. [CrossRef]
2. Aliofkhazraei, M.; Walsh, F.C.; Zangari, G.; Köçkar, H.; Alper, M.; Rizal, C.; Magagnin, L.; Protsenko, V.; Arunachalam, R.; Rezvanian, A.; et al. Development of electrodeposited multilayer coatings: A review of fabrication, microstructure, properties and applications. *Appl. Surf. Sci. Adv.* **2021**, *6*, 100141. [CrossRef]
3. Li, B.; Li, D.; Chen, W.; Liu, Y.; Zhang, J.; Wei, Y.; Zhang, W.; Jia, W. Effect of current density and deposition time on microstructure and corrosion resistance of Ni-W/TiN nanocomposite coating. *Ceram. Int.* **2019**, *45*, 4870–4879. [CrossRef]
4. Xia, F.; Li, Q.; Ma, C.; Guo, X. Preparation and characterization of Ni–AlN nanocoatings deposited by magnetic field assisted electrodeposition technique. *Ceram. Int.* **2020**, *46*, 2500–2509. [CrossRef]
5. Xia, F.; Yan, P.; Ma, C.; Wang, B.; Liu, Y. Effect of different heat-treated temperatures upon structural and abrasive performance of Ni-TiN composite nanocoatings. *J. Mater. Res. Technol.* **2023**, *27*, 2874–2881. [CrossRef]
6. Ma, C.; He, H.; Xia, F.; Xiao, Z.; Liu, Y. Performance of Ni–SiC composites deposited using magnetic-field-assisted electrodeposition under different magnetic-field directions. *Ceram. Int.* **2023**, *49*, 35907–35916. [CrossRef]
7. Gao, M.; Liu, L.; Huang, Z.; Jiang, C.; Wang, X.; Huang, F.; Li, X.; Zhang, X. Electrodeposition and properties of Ni–W–Ti_2AlC composite coatings. *Ceram. Int.* **2024**, *50*, 18832–18842. [CrossRef]
8. Bakhit, B.; Akbari, A. Synthesis and characterization of Ni–Co/SiC nanocomposite coatings using sediment co-deposition technique. *J. Alloys Compd.* **2013**, *560*, 92–104. [CrossRef]
9. Karimzadeh, A.; Rouhaghdam, A.S.; Aliofkhazraei, M.; Miresmaeili, R. Sliding wear behavior of Ni–Co–P multilayer coatings electrodeposited by pulse reverse method. *Tribol. Int.* **2020**, *141*, 105914. [CrossRef]
10. Allahyarzadeh, M.H.; Aliofkhazraei, M.; Rouhaghdam, A.S.; Torabinejad, V. Electrochemical tailoring of ternary Ni-W-Co (Al_2O_3) nanocomposite using pulse reverse technique. *J. Alloys Compd.* **2017**, *705*, 788–800. [CrossRef]
11. Ranjith, B.; Kalaignan, G.P. Ni–Co–TiO_2 nanocomposite coating prepared by pulse and pulse reversal methods using acetate bath. *Appl. Surf. Sci.* **2010**, *257*, 42–47. [CrossRef]
12. Wasekar, N.P.; Latha, S.M.; Ramakrishna, M.; Rao, D.S.; Sundararajan, G. Pulsed electrodeposition and mechanical properties of Ni-W/SiC nano-composite coatings. *Mater. Des.* **2016**, *112*, 140–150. [CrossRef]
13. Zhang, R.; Li, Z.; Yu, X.; Cui, G. Characterisation and properties of Ni–W–Y_2O_3–ZrO_2 nanocomposite coating. *Surf. Eng.* **2019**, *35*, 578–587. [CrossRef]
14. Sadreddini, S.; Afshar, A. Corrosion resistance enhancement of Ni-P-nano SiO_2 composite coatings on aluminum. *Appl. Surf. Sci.* **2014**, *303*, 125–130. [CrossRef]
15. Beltowska-Lehman, E.; Bigos, A.; Indyka, P.; Chojnacka, A.; Drewienkiewicz, A.; Zimowski, S.; Kot, M.; Szczerba, M.J. Optimisation of the electrodeposition process of Ni-W/ZrO_2 nanocomposites. *J. Electroanal. Chem.* **2018**, *813*, 39–51. [CrossRef]
16. Li, B.; Zhang, W.; Huan, Y.; Dong, J. Synthesis and characterization of Ni-B/Al_2O_3 nanocomposite coating by electrodeposition using trimethylamine borane as boron precursor. *Surf. Coat. Technol.* **2018**, *337*, 186–197. [CrossRef]
17. Elkhoshkhany, N.; Hafnway, A.; Khaled, A. Electrodeposition and corrosion behavior of nano-structured Ni-WC and Ni-Co-WC composite coating. *J. Alloys Compd.* **2017**, *695*, 1505–1514. [CrossRef]
18. Firdouz, Z.; Tripathi, P.; Mondal, K.; Balani, K. Effect of carbonaceous reinforcements on anticorrosive and magnetic properties of Ni-Cu based composite coatings prepared by pulsed electrodeposition. *Surf. Coat. Technol.* **2022**, *441*, 128560. [CrossRef]
19. Wang, C.; Shen, L.; Qiu, M.; Tian, Z.; Jiang, W. Characterizations of Ni-CeO_2 nanocomposite coating by interlaced jet electrodeposition. *J. Alloys Compd.* **2017**, *727*, 269–277. [CrossRef]
20. He, Y.; Wang, S.C.; Walsh, F.C.; Chiu, Y.L.; Reed, P.A.S. Self-lubricating Ni-P-MoS_2 composite coatings. *Surf. Coat. Technol.* **2016**, *307*, 926–934. [CrossRef]
21. Li, B.; Zhang, W.; Mei, T.; Miao, Y. Fabrication of Ni–B/TiC–Y_2O_3 nanocomposites by one-step electrodeposition at different duty cycle and evaluation of structural, surface and performance as protective coating. *J. Alloys Compd.* **2020**, *823*, 153888. [CrossRef]
22. Yao, Q.L.; He, M.; Kong, Y.R.; Gui, T.; Lu, Z.H. Y_2O_3-functionalized graphene-immobilized Ni–Pt nanoparticles for enhanced hydrous hydrazine and hydrazine borane dehydrogenation. *Rare Met.* **2023**, *42*, 3410–3419. [CrossRef]
23. Zhou, X.; Wang, Y.; Liang, Z.; Jin, H. Electrochemical deposition and nucleation/growth mechanism of Ni–Co–Y_2O_3 multiple coatings. *Materials* **2018**, *11*, 1124. [CrossRef] [PubMed]
24. Zhang, Y.; Qian, S.Q.P.; Fu, X.F. Experimental study on friction-assisted electroforming of Ni-Co alloys. *Mater. Res. Express* **2023**, *10*, 026508. [CrossRef]
25. Xue, Y.J.; Shen, C.; Li, J.S.; Li, H.; Si, D.H. Corrosion resistance of Ni-Y_2O_3 composite coating prepared by electrodeposition under ultrasonic condition. *Adv. Mater. Res.* **2010**, *97*, 1235–1238. [CrossRef]
26. Yi, X.; He, P.; Chen, Y.; Wang, W.; Yang, D.; Dong, F. Y_2O_3-Modified Ni-Co Composite Coating as Cathode Materials for Hydrogen Evolution Reaction on Titanium Substrate. *ECS Trans.* **2010**, *28*, 13. [CrossRef]

27. Zhou, Y.B.; Sun, J.F.; Wang, S.C.; Zhang, H.J. Oxidation of an electrodeposited Ni–Y_2O_3 composite film. *Corros. Sci.* **2012**, *63*, 351–357. [CrossRef]
28. Tian, L.; Xu, J. Electrodeposition and characterization of Ni–Y_2O_3 composite. *Appl. Surf. Sci.* **2011**, *257*, 7615–7620. [CrossRef]
29. Kan, H.M.; Meng, Y.Y.; Reddy, R.G. Influence of particle size and surfactants on uniformity and quantity of silicon carbide particles in electrodeposited nickel-silicon carbide coatings. *J. Cent. South Univ.* **2021**, *28*, 1627–1636. [CrossRef]
30. Biesinger, M.C.; Lau, L.W.; Gerson, A.R.; Smart, R.S.C. Resolving surface chemical states in XPS analysis of first row transition metals, oxides and hydroxides: Sc, Ti, V, Cu and Zn. *Appl. Surf. Sci.* **2010**, *257*, 887–898. [CrossRef]
31. Grey, L.H.; Nie, H.Y.; Biesinger, M.C. Defining the nature of adventitious carbon and improving its merit as a charge correction reference for XPS. *Appl. Surf. Sci.* **2024**, *653*, 159319. [CrossRef]
32. Wu, G.; Li, N.; Zhou, D.; Cang, Z. The microstructure and high temperature properties of electrodeposited Co-Ni-Al_2O_3 composite coatings. *J. Compos. Mater.* **2004**, *02*, 8–13.
33. Zhao, M.; Wang, J.; Li, H.; Yang, H.; Zhou, Y.; Li, J. Grain size effects on mechanical behavior of $Al_{0.25}$CoCrFeNi high-entropy alloy at room and cryogenic temperatures. *Intermetallics* **2025**, *183*, 108792. [CrossRef]
34. Akbarpour, M.R.; Asl, F.G.; Rashedi, H. Pulse-reverse electrodeposition of Ni-Co/graphene composite films with high hardness and electrochemical behaviour. *Diam. Relat. Mater.* **2023**, *133*, 109720. [CrossRef]
35. Karmakar, R.; Maji, P.; Ghosh, S.K. A review on the nickel based metal matrix composite coating. *Met. Mater. Int.* **2021**, *27*, 2134–2145. [CrossRef]
36. Lin, S.N.; Niu, L.P.; Wang, Y.Y.; Zhou, X.Y.; Liang, Z.P.; Liu, X.; Zhang, T.A. Orthogonal optimization of composite electrodeposition nickel-cobalt-yttrium oxide process in sulfamate system. *Plat. Finish.* **2020**, *39*, 532–535.
37. Raghavendra, C.R.; Basavarajappa, S.; Sogalad, I.; Kumar, S. A review on Ni based nano composite coatings. *Mater. Today Proc.* **2021**, *39*, 6–16. [CrossRef]
38. Shozib, I.A.; Ahmad, A.; Abdul-Rani, A.M.; Beheshti, M.; Aliyu, A.A.A. A review on the corrosion resistance of electroless Ni-P based composite coatings and electrochemical corrosion testing methods. *Corros. Rev.* **2022**, *40*, 1–37. [CrossRef]

Disclaimer/Publisher's Note: The statements, opinions and data contained in all publications are solely those of the individual author(s) and contributor(s) and not of MDPI and/or the editor(s). MDPI and/or the editor(s) disclaim responsibility for any injury to people or property resulting from any ideas, methods, instructions or products referred to in the content.

MDPI AG
Grosspeteranlage 5
4052 Basel
Switzerland
Tel.: +41 61 683 77 34

Coatings Editorial Office
E-mail: coatings@mdpi.com
www.mdpi.com/journal/coatings



Disclaimer/Publisher's Note: The title and front matter of this reprint are at the discretion of the Guest Editors. The publisher is not responsible for their content or any associated concerns. The statements, opinions and data contained in all individual articles are solely those of the individual Editors and contributors and not of MDPI. MDPI disclaims responsibility for any injury to people or property resulting from any ideas, methods, instructions or products referred to in the content.





Academic Open
Access Publishing

mdpi.com

ISBN 978-3-7258-9264-8